DEPARTMENT OF THE AIR FORCE

AIR UNIVERSITY

AIR FORCE INSTITUTE OF TECHNOLOGY

Wright-Patterson Air Force Base, Ohio

1

AFIT/GAE/AA/88D-31

THE EFFECTS OF INCIDENCE ANGLE AND
FREE STREAM TURBULENCE ON THE
PERFORMANCE OF A VARIABLE GEOMETRY
TWO-DIMENSIONAL COMPRESSOR CASCADE
AT HIGH REYNOLDS NUMBERS

THESIS

EDWARD M. PONIATOWSKI
CAPTAIN, UNITED STATES ARMY

AFIT/GAE/AA/88D-31

AFIT/GAE/AA/88D-31

THE EFFECTS OF INCIDENCE ANGLE AND FREE STREAM TURBULENCE ON THE PERFORMANCE OF A VARIABLE GEOMETRY TWO-DIMENSIONAL COMPRESSOR CASCADE AT HIGH REYNOLDS NUMBERS

THESIS

Presented to the Faculty of the School of Engineering

of the Air Force Institute of Technology

Air University

In Partial Fulfillment of the

Requirements for the Degree of

Master of Science in Aeronautical Engineering

Edward M. Poniatowski, B.S.

Captain, United States Army

December 1988

Approved for public release; distribution unlimited

Preface

In the present study, the effects of incidence angle and free stream turbulence on the performance of a variable geometry, two-dimensional compressor cascade are investigated. The cascade design is such that angle of attack, angle of incidence, and stagger angle vary simultaneously. This is accomplished by rotating the five interior blades within the cascade in unison about similar fixed points. The design is similar in principle to the variable stator arrangements used on many current jet engines. This approach was taken not only to provide useful quantitative information on flow behavior through this type of cascade, but also to gain a qualitative appreciation for the factors involved in analyzing variable geometry designs. The limited scope of this investigation precludes a thorough design assessment of the particular blades used. It is hoped however, that this study will lay the groundwork for future efforts in this area. Having said all that, a few words of thanks are appropriate.

It is often said that we see as far as we do, because we stand on the shoulders of giants. To the "giants" who have supported me, I am grateful.

I thank the Lord Almighty for the continual challenges and good fortune He has brought me. I thank my parents for their love and support, and my colleagues for their wisdom and advice.

To my instructors I owe a special debt of gratitude. To my principal advisor Dr. William C. Elrod, I am especially grateful. His guidance and support were instrumental to my success. To my thesis committee; LTC King, Dr. Halim, and CPT. Fant, I am also grateful. Their keen interest and helpful suggestions served to sharpen my research abilities.

To the AFIT technicians, Mr. John Brohas, Mr. Jay Anderson, Mr. Leroy Cannon, Mr. Gerry Hild, and Mr. Nick Yardich, I owe a great deal. If not for their tireless efforts there would be no thesis to write.

Finally, to my family, my wife [redacted] and my children [redacted] I owe more than words can express. They have been my inspiration. Their love and support kept me going through many long hours. I am eternally grateful for their understanding all the times when daddy couldn't be there.

To these "giants" and all the rest: I salute you.

Edward M. Poniatowski

Table of Contents

List of Figures

Figure		Page

Figure		Page
36	Wake Velocity and Turbulence Intensity Profiles, X/C = 2.125, (i = -3, High Turb.) ..	101
37	Wake Velocity and Turbulence Intensity Profiles, X/C = 0.625, (i = 0, Low Turb.) ...	103
38	Wake Velocity and Turbulence Intensity Profiles, X/C = 1.125, (i = 0, Low Turb.) ...	104
39	Wake Velocity and Turbulence Intensity Profiles, X/C = 1.625, (i = 0, Low Turb.) ...	105
40	Wake Velocity and Turbulence Intensity Profiles, X/C = 2.125, (i = 0, Low Turb.) ...	106
41	Wake Velocity and Turbulence Intensity Profiles, X/C = 0.625, (i = 0, High Turb.) ...	108
42	Wake Velocity and Turbulence Intensity Profiles, X/C = 1.125, (i = 0, High Turb.) ...	109
43	Wake Velocity and Turbulence Intensity Profiles, X/C = 1.625, (i = 0, High Turb.) ...	110
44	Wake Velocity and Turbulence Intensity Profiles, X/C = 2.125, (i = 0, High Turb.) ...	111
45	Wake Velocity and Turbulence Intensity Profiles, X/C = 0.625, (i = +3, Low Turb.) ...	113
46	Wake Velocity and Turbulence Intensity Profiles, X/C = 1.125, (i = +3, Low Turb.) ...	114
47	Wake Velocity and Turbulence Intensity Profiles, X/C = 1.625, (i = +3, Low Turb.) ...	115
48	Wake Velocity and Turbulence Intensity Profiles, X/C = 2.125, (i = +3, Low Turb.) ...	116
49	Wake Velocity and Turbulence Intensity Profiles, X/C = 0.625, (i = +3, High Turb.) ..	118
50	Wake Velocity and Turbulence Intensity Profiles, X/C = 1.125, (i = +3, High Turb.) ..	119
51	Wake Velocity and Turbulence Intensity Profiles, X/C = 1.625, (i = +3, High Turb.) ..	120
52	Wake Velocity and Turbulence Intensity Profiles, X/C = 2.125, (i = +3, High Turb.) ..	121

Figure		Page

Figure		Page

Figure		Page

Figure		Page
206	Boundary Layer Turbulence Intensity Profile 65.62% Chord, (i = +3, High Turb.)	281
207	Boundary Layer Velocity Profiles 70.31% Chord, (i = +3, High Turb.)	282
208	Boundary Layer Turbulence Intensity Profile 70.31% Chord, (i = +3, High Turb.)	283
209	Boundary Layer Velocity Profiles 75% Chord, (i = +3, High Turb.)	284
210	Boundary Layer Turbulence Intensity Profile 75% Chord, (i = +3, High Turb.)	285
211	Boundary Layer Velocity Profiles 79.68% Chord, (i = +3, High Turb.)	286
212	Boundary Layer Turbulence Intensity Profile 79.68% Chord, (i = +3, High Turb.)	287
213	Boundary Layer Velocity Profiles 84.37% Chord, (i = +3, High Turb.)	288
214	Boundary Layer Turbulence Intensity Profile 84.37% Chord, (i = +3, High Turb.)	289

List of Tables

List of Symbols

Symbol	Name	Units
A	Area	in^2
A	Machine Axis of Rotation	
A	Constant in Calibration Equation	
a	Constant in Velocity Recovery Equation	
B	Constant in Calibration Equation	
b	Constant in Velocity Recovery Equation	
c	Chord Length	in
C_p	Pressure Coefficient	
C_p	Specific Heat at Constant Pressure	$\frac{BTU}{lbm\text{-}^{o}R}$
E_o	Anemometer Voltage	volts
k_t	*Coefficient of Thermal Conductivity*	$\frac{BTU}{s\text{-}ft\text{-}^{o}R}$
L	Length	feet
m	Variable in Carter's Rule	
N	Number of Data Points	
N_u	Nusselt Number	
P	Pressure	lbf/in^2
$\overline{P}$	Mass Averaged Pressure	lbf/in^2
R	Resistance	ohms
Re	Reynolds Number	
s	Cascade Blade Spacing	in
T	Temperature	^{o}R
TI	Turbulence Intensity	%
U	Anemometer Velocity Component	volts
V	Velocity	ft/sec

Symbol	Name	Units
X	Stream wise Direction	in
Y	Vertical Direction	in
Z	Lateral Direction	in
α	Air and Blade Cascade Angles	degrees
δ	Deviation Angle	degrees
δ	Boundary Layer Thickness	in
i	Incidence Angle	degrees
ε	Deflection Angle	degrees
γ	Ratio of Specific Heats	
ρ	Density	lbm/ft^3
μm	Micrometer	
θ	Blade Camber Angle	degrees
σ	Cascade Solidity	
ζ	Cascade Stagger Angle	degrees
$\bar{\omega}$	Total Pressure Loss Coefficient	

Sub-Superscripts	Name
BL	Boundary Layer
C	Calibrator
E	Edge
INV	Inviscid
L	Local
M	Mean
MEAS	Measured
MIN	Minimum

Sub-Superscripts	Name
RMS	Root Mean Square
TE	Trailing Edge
AW	Adiabatic Wall
T	Total
W	Wire
1	Upstream
2	Downstream
o	Reference Value
'	Designates Blade Angle

Acronyms	Name
AC	Alternating Current
AFIT	Air Force Institute of Technology
CTF	Cascade Test Facility
DC	Direct Current
HP	Hewlett Packard
NACA	National Advisory Committee on Aeronautics
TSI	Thermal Systems International

Abstract

The present study investigates the effects of incidence angle and free stream turbulence on the performance of a variable geometry, two-dimensional compressor cascade. A seven-blade cascade of NACA 65-A506 airfoils with two inch chord, aspect ratio of one, and solidity of 1.5 was used. This cascade used porous side wall suction to establish two-dimensional flow conditions. Flow Unit Reynolds numbers exceeding 2.5 million per foot, and average free stream turbulence levels of one and seven percent were used. Cascade geometry was varied in a manner similar to that used in current variable stator designs: maintaining axial direction and blade spacing constant, while varying incidence angle, stagger angle, and angle of attack. Incidence angles of -3, 0, and +3 degrees were investigated.

Total pressure loss coefficient decreases through the cascade and may increase in the wake as incidence angle or free stream turbulence increase. The change in loss coefficient with increasing incidence was determined to be insignificant when compared with the change as a result of increased free stream turbulence. Blade suction surface pressure coefficients decrease sharply along the first thirty percent chord as incidence increases. Additionally, the suction surface pressure coefficients show a uniform increase across the blade center span with additional free stream turbulence. Increases in incidence and free stream

turbulence result in thicker boundary layers and suggest both earlier transition and intermittent separation on the forward half of the blade. Evidence also suggests that the location of the minimum loss incidence angle may change with additional free stream turbulence.

THE EFFECTS OF INCIDENCE ANGLE AND FREE STREAM TURBULENCE ON THE PERFORMANCE OF A VARIABLE GEOMETRY TWO-DIMENSIONAL COMPRESSOR CASCADE AT HIGH REYNOLDS NUMBERS

I. Introduction

The historical development of the gas turbine engine has proven to be quite exciting and often dramatic.

> ...immediately, with a rising scream the engine began to accelerate out of control. I promptly shut the control valve, but the uncontrolled acceleration continued. Everyone around took to their heels except me...once again I found myself alone with the monster I had created. (36:8-9)

Indeed, this excerpt (told by Sir Frank Whittle) presents a seemingly discouraging picture of the future for the gas turbine engine. Yet this engine has, since that uncertain day in 1937, evolved into the most sophisticated and reliable power plant ever conceived. Men like Whittle foresaw this.

> I was well aware of the many prior failures in the gas turbine field early in the century, but was convinced that the causes of these--low compressor efficiency, low turbine efficiency, and lack of suitable materials--could be overcome.... (36:4)

The present effort is directed towards the quest for higher compressor efficiency and performance. Fundamental in this effort is understanding the nature of the airflow through the compressor. To this end, the most basic approach is the study of cascade flow.

In 1981, the Air Force Institute of Technology, in cooperation with the Air Force Wright Aeronautical Laboratories, built a facility to investigate two-dimensional cascade flow. Using this Cascade Test Facility (CTF), AFIT graduate students have conducted detailed investigations on the effects of both surface roughness and free stream turbulence on cascade performance. This series of studies forms the framework for the current investigation: the effects of cascade geometry on performance.

Objectives and Scope

The objectives of this investigation were to:

1. Modify the current cascade test section to permit varying geometry in a manner similar to current variable stator designs.

2. Determine the influence of incidence angle and free stream turbulence on the performance of a cascade of NACA 65-A506 compressor blades. Specifically; examine the influence on selected blade loss parameters, suction surface pressure profile behavior, and suction surface boundary layer behavior, at incidence angles of -3, 0, and +3 degrees, and average free stream turbulence levels of 1 and 7 percent.

3. Comment on any specific design considerations in variable geometry cascade performance analysis.

This investigation used one of the three compressor blade sets studied by Poulin (23) and Absar (1). As in their

studies, the flow across mid-span of the center blade in the cascade was considered to be most nearly two-dimensional, thus it was the source for all of the data collected. Several specific areas of interest were examined. The flow in the wake of the cascade center blade was studied using wake velocity and turbulence intensity profiles. Also, the center blade suction surface static pressure distribution was studied as was its boundary layer profile.

The cascade was modified to permit continuous variation of angle of attack, angle of incidence, and stagger angle, in a manner similar to many variable stator blade designs in current use. Additionally, an artificial free stream turbulence generator was used to provide the additional free stream turbulence (hereafter referred to as high turbulence) required in the investigation. The above modifications introduced effects on both the mass flow through and the total pressure upstream of the cascade. Specifically, the variable geometry design altered the cascade throughflow area, and the turbulence generator injected compressed air into the flow upstream from the cascade. These effects were assumed negligible in the current study.

The variable geometry method used was selected with the intent of both providing useful compressor design information, and developing a qualitative feel for the blade performance characteristics desired in a variable geometry design. To this end, a review of the theory is in order.

II. Theory

Cascade Geometry

"Careful design of compressor blading based on both aerodynamic theory and experiment is necessary..." (7:139). Cascade research provides much of the experimental data for engine designers, and understanding the basic geometry within the cascade is required. Figure 1 is adapted from Cohen and Rogers, and shows the relevant angles of interest within a two-dimensional cascade (7:188).

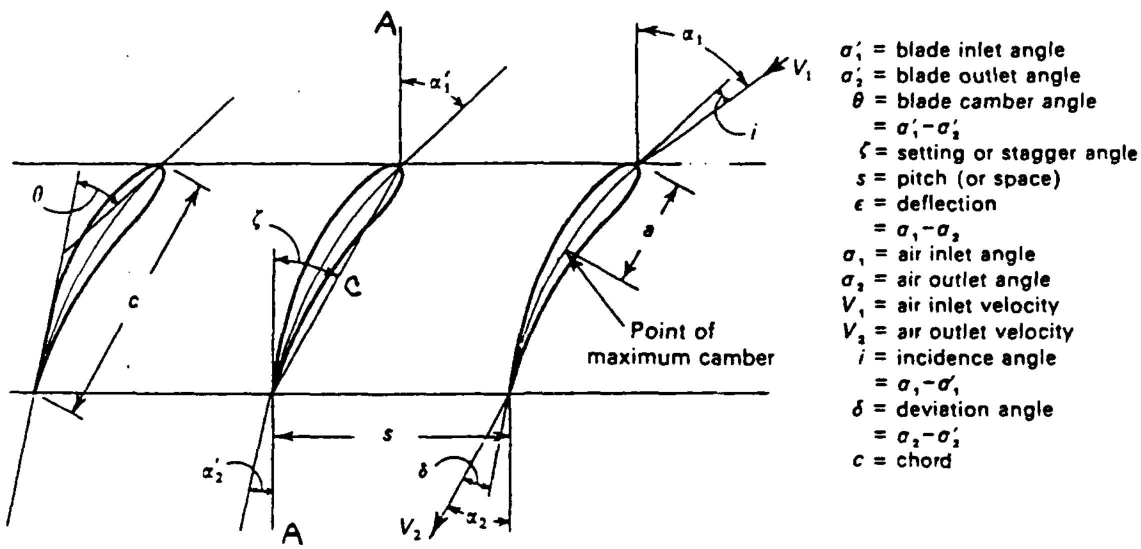

Fig. 1. Cascade Geometry
Cohen and Rogers (7:188)

Notation. All cascade angles with the exception of blade camber angle, are referenced to the turbomachine axis of rotation (A). In the current study, the NACA 65-A506

blades were of fixed geometry, with a blade camber angle (θ) of 19 degrees, chord (c) of 2 inches, span (b) of 2 inches, and planform area (s) of 4 square inches. The resulting aspect ratio (b^2/s) was 1. The air inlet angle (α_1) and exit angle (α_2) are measured from the machine axis of rotation (A) to the inlet velocity vector (V_1) and exit velocity vector (V_2) respectively. The blade inlet angle (α_1') and blade exit angle (α_2') are measured from the machine axis of rotation to a line tangent with the blade camber line at the leading and trailing edge respectively. The angle between the blade chord line (c) and the machine axis (A) is called the stagger angle (ζ), and the angle between the chord line and the inlet velocity vector is the blade angle of attack (α). The flow incidence angle (i) is given by:

$$i = \alpha_1 - \alpha_1' \tag{1}$$

and the air deflection angle by:

$$\varepsilon = \alpha_1 - \alpha_2 \tag{2}$$

The cascade solidity (σ) is defined to be the ratio of blade chord (c) to spacing (s).

$$\sigma = \frac{c}{s} \tag{3}$$

In all cascades, the airflow is not completely turned by the blade, and thus the air exit angle deviates somewhat from the blade exit angle. This flow deviation angle (δ) was correlated by Carter (7:192) and using the present notation is expressed as:

$$\delta = \frac{m\theta}{\sqrt{\sigma}} \tag{4}$$

where for this study:

$$m \approx 0.23 + 0.002(\alpha_2) \tag{5}$$

The five interior blades in the cascade were rotated about their rear attachment points (located at approximately 60 percent chord) so that the blade spacing, axial direction, and solidity remained constant. Three blade incidence angles were investigated. Idealizing each blade using the chord line, and assuming a constant inlet flow direction, the various physical angles are found based on the angle of attack. Table I shows the resulting angles for each setting studied.

Table I

Cascade Geometry Settings

α	ζ	α_1	α_1'	i	α_2 **	α_2'	δ
15*	16	31	31	0	13.5	12	1.50
18	13	31	28	+3	12.0	9	3.00
12	19	31	34	-3	16.0	15	1.00

*...Zero Incidence Setting
**...Based on Ave. Measured End Wall Angles
All Angles are in Degrees

Turbulence Intensity

Turbulence intensity may be expressed as the ratio of root mean square of velocity fluctuations to mean flow velocity.

$$TI = \frac{V'_{RMS}}{V_{MEAN}} \tag{6}$$

The AC (RMS) fluctuating voltage and the DC (MEAN) voltage outputs of the hot film anemometer represent the respective velocity components. Thus with the appropriate calibration information, Equation 6 may be used to calculate turbulence intensity from the measured anemometer voltage components. The result is TI as a percentage of the mean flow velocity. Absar investigated the effects of free stream turbulence on the performance of the same cascade (1). Some of his results are shown for comparison purposes in Chapter IV.

Blade Surface Roughness

The same blades were used in this investigation as were used by Poulin (23) and Absar (1). Specifically, their configuration number 2 was used. This configuration contained a strip of emery paper with an average roughness of 12.10 μm, bonded to the suction surface between 4 and 25 percent chord. This bonding was done during the blade casting process so as to retain the blade surface contour. The roughness definitions and measurement methods are described by Poulin (23:23), Williams (37:49), and Tanis (32:54).

Wake Flow Parameters

There are many approaches to analyzing the losses within the cascade. One method is to examine the blade wake. This wake is formed by the boundary layers of both the suction and pressure surfaces of the blade. As these boundary layers depart the trailing edge, they join together and thus create the wake. Assuming a uniform velocity profile at the inlet, the cascade loss presents itself as a deficit in velocity and thus total pressure. As the flow continues to mix down stream, the velocity deficit decreases. This down stream mixing further contributes to the total pressure loss. Thus, when the flow has travelled far enough down stream, the wake has completely mixed and a uniform flow at a lower total pressure exists (25:153, 20:4). Figure 2 shows the

development of the cascade wake.

Total Pressure Loss Coefficient. Examining the total pressure deficit described above is done using the total pressure loss coefficient $\bar{\omega}$ defined as:

$$\bar{\omega} = \frac{P_{T_1} - \overline{P_{T_2}}}{\left(\frac{1}{2}\right) \rho V_1^2} \tag{7}$$

where P_{T_1} is the total pressure upstream of the cascade, $\overline{P_{T_2}}$ is the mass averaged total pressure across the blade space downstream from the cascade and $(1/2)\rho V_1^2$ is the inlet dynamic pressure. In this study total pressures were calculated using the relation:

$$P_{T_i} = P_i \left[1 + \frac{V_i^2}{2\, C_p T_i} \right]^{\left(\frac{\gamma - 1}{\gamma}\right)} \tag{8}$$

where i = 1 upstream and i = 2 at the downstream measuring station. The mass averaged total pressure downstream is given as:

$$\overline{P_{T_2}} = \frac{\int P_{T_2} \rho V \, dA}{\int \rho V \, dA} \tag{9}$$

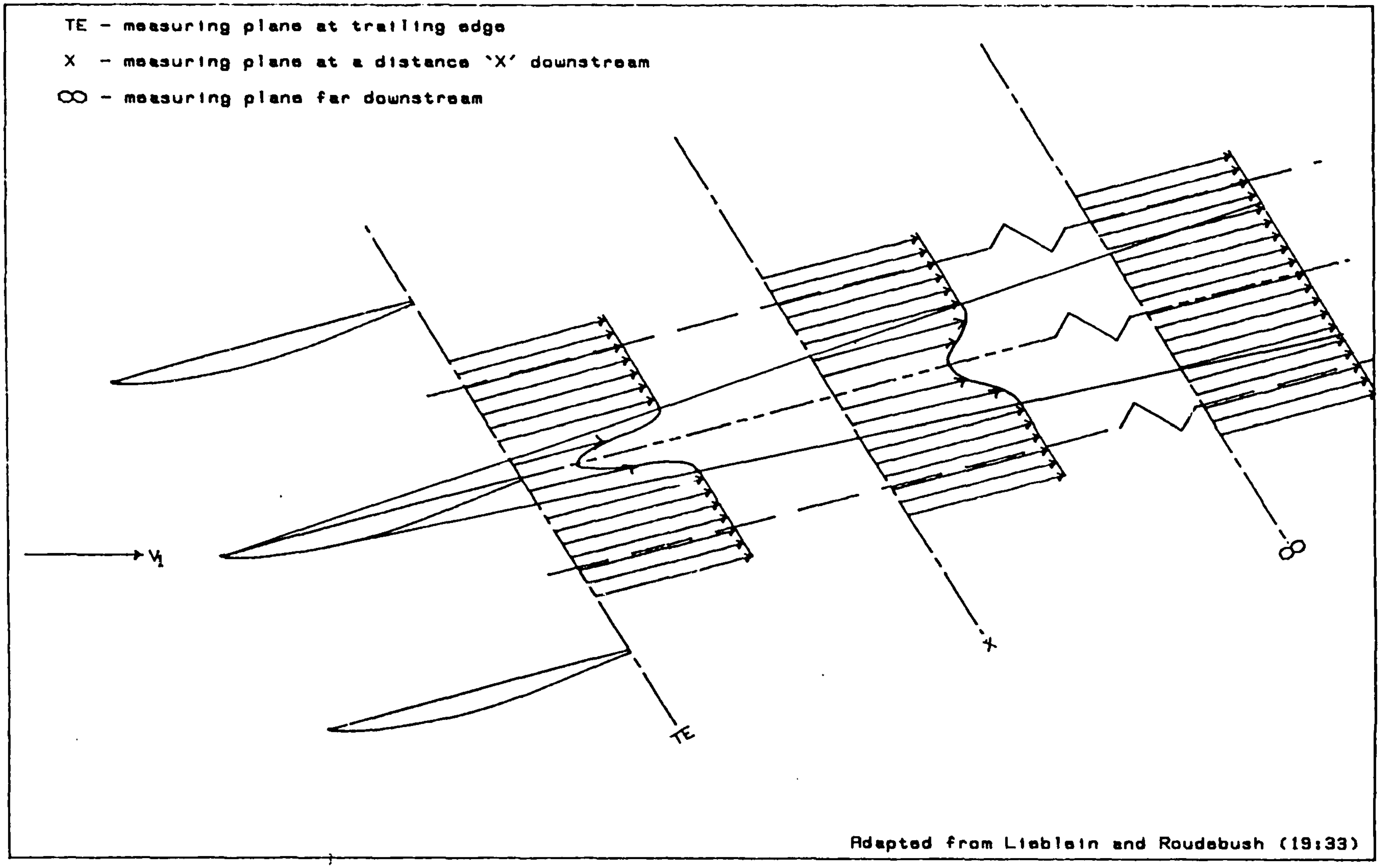

Fig. 2. Schematic Representation of Boundary Layer and Wake Development

Equation 9 is used by Lieblein and Roudebush (19:14). For the two-dimensional case, dA becomes dY, and the area integrals reduce to single integrals. The integrals were numerically evaluated using data points collected during the investigation.

Wake Minimum Velocity. Lieblein and Roudebush also discuss the concept of wake minimum velocity. From the previous discussion on what occurs within the wake, it is of interest to examine how the velocity deficit behaves with increasing downstream distance (19:6-7). Thus the wake minimum velocity ratio is defined as:

$$\frac{V_{MIN}}{V_o} = 1 - a \left[\frac{x}{c} + b \right]^{-\frac{1}{2}} \tag{10}$$

Where V_{MIN} is the minimum velocity within the wake and V_o is the free stream velocity at the same location x/c from the blade trailing edge. The constants a and b were determined experimentally by Lieblein and Roudebush to be (a = 0.13) and (b = 0.025). These values for a and b give a reasonable approximation for the velocity ratio in the cascade wake (19:7).

Using this correlation, one can track the intensity of the velocity deficit downstream. The wake thickness may also be determined by defining the wake boundary to be the point

where the local velocity (V_{LOCAL}) was 99.5 percent of the free stream velocity (V_o):

$$(V_{LOCAL} / V_O) = 0.995 \qquad (19:15)$$

Blade Pressure Profile

The blade pressure profile is also of great use when analyzing cascade losses. It provides a picture of the velocity distributicn on the surface of interest, as well as the blade loading. The shape of the pressure curve can be used to estimate optimum blade loading as well as boundary layer behavior (29:283). This study examines only the suction surface pressure distribution in terms of the non-dimensional pressure coefficient given by:

$$C_P = \frac{\left[P - P_1 \right]}{(1/2)\rho V_1^2} \qquad (11)$$

where:

P = Static Pressure at the Point on the Blade

P_1 = Measured Inlet Static Pressure

$(1/2)\rho V_1^2$ = Inlet Dynamic Pressure

Boundary Layer Flow

Studying the boundary layer flow in the cascade is important for several reasons. First, the information

gathered is helpful in finding solutions for the boundary layer equations. Second, this information helps to form a qualitative picture of boundary layer behavior (25:151).

In the present effort, only the suction surface boundary layer is examined in detail. In the compressor cascade, the flow along the suction surface encounters an adverse pressure gradient, and is thus very sensitive to both flow disturbances and surface condition. In addition, unlike an isolated airfoil, the flow past the suction surface is influenced by the flow past the pressure surface of the adjacent blade. Specifically, the static pressure at a specified point on the suction surface will be lower than the static pressure at the corresponding point on the pressure surface of the adjacent blade. Lieblein and Roudebush point out that the static pressure through the boundary layer is nearly constant (25:152). As a result, a normal pressure gradient between the two surfaces exists. The lower static pressure at the edge of the suction surface boundary layer yields a higher velocity than that for the corresponding point at the edge of the adjacent pressure surface boundary layer. The result is a sloped velocity profile between blades similar to that shown in Figure 3a. This sloped velocity profile makes both the boundary layer edge velocity and thickness difficult to determine (25:152, 23:4).

Deutsch and Zierke use an approximation scheme to circumvent this problem (8:8). The measured velocity profile

is assumed to be a composite of two distinct profiles, shown in Figure 3b. The first profile is essentially that of the boundary layer, where the effects of viscous forces dominate. The second profile is that of the "inviscid" region between the blades where the effects of the normal pressure gradient dominate. These profiles are matched at the point common to both. This common point is taken to be the edge of the boundary layer where the velocity is given as V_E. Mathematically, Deutsch and Zierke represent this composite profile using the following equation.

$$V_M = V_{BL} + V_{INV} - V_E \tag{12}$$

where:

V_M = Actual Measured Velocity

V_{BL} = Calculated Boundary Layer Velocity

V_{INV} = Actual Measured Inviscid Velocity

V_E = Calculated Boundary Layer Edge Velocity

Assuming a no-slip condition at the surface of the blade, both V_M and V_{BL} go to zero. Then by Equation 12, at the blade surface $V_{INV} = V_E$. Thus, if the measured inviscid velocity plot were extrapolated to the blade surface, the edge velocity (V_E) would be determined (23:38). This value for edge velocity can then be used in Equation 12 to determine V_{BL}.

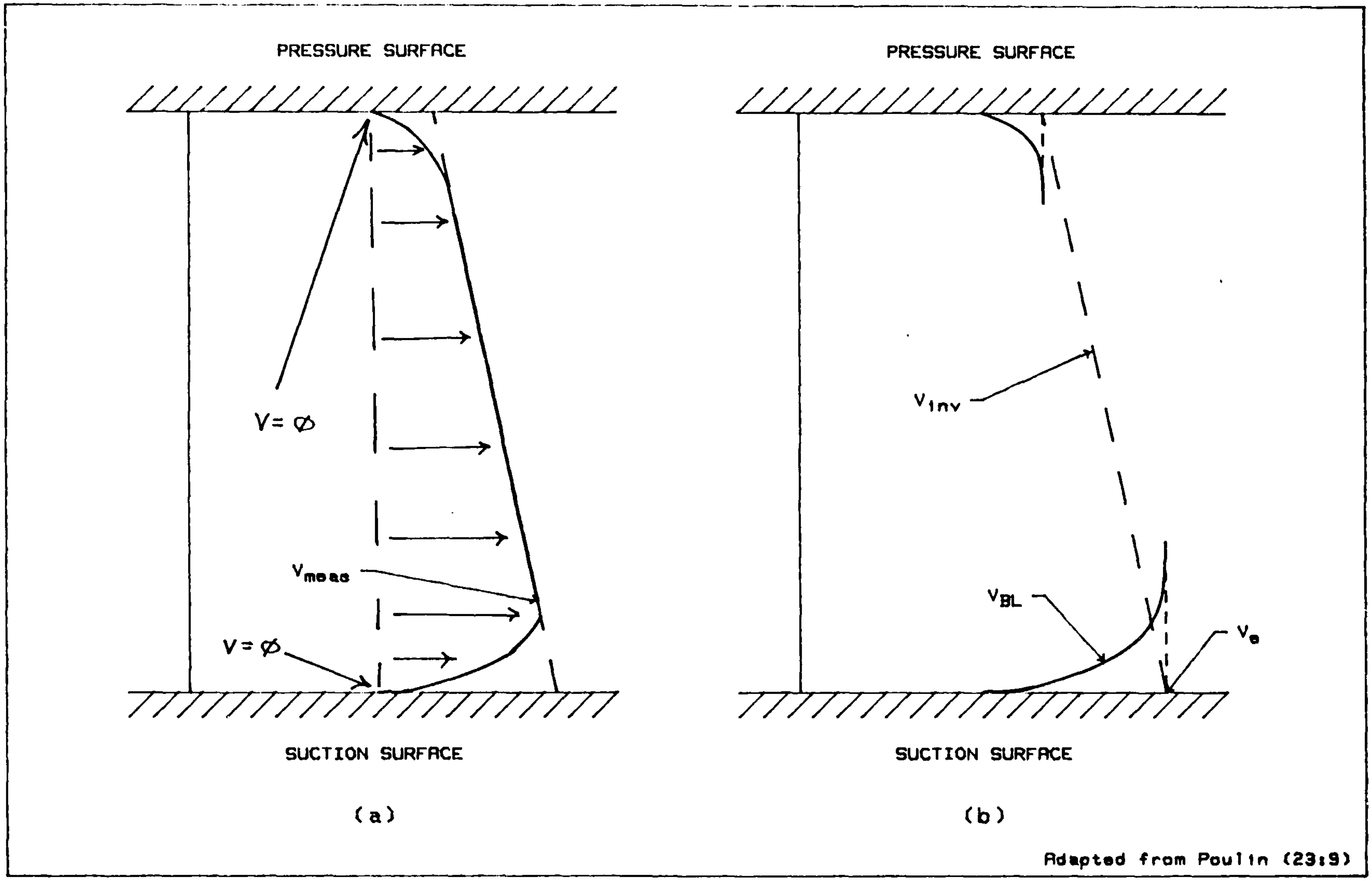

Fig. 3. Matching Channel and Boundary Layer Profiles

Deutsch and Zierke's method involved calculating a quadratic curve fit of a range of points in the inviscid region, and then extrapolating this curve to the blade surface. "This range was represented by ($N_{INV}/2$) ± ($N_{INV}/4$) where N_{INV} is the number of data points from the maximum velocity position to the measured point furthest from the blade" (23:39). This method produced edge velocities that were essentially constant.

The method used by Deutsch and Zierke to determine the inviscid velocity at the blade surface was adopted by Williams (37), and later modified by Poulin to account for velocity profile curvature towards the leading edge (23:40). Figures 105 and 159 show the curvature of the velocity profile near the leading edge for which Poulin's correction was effective.

III. Experimental Apparatus

Cascade Test Facility

This study was done using the Cascade Test Facility (CTF) at the Air Force Institute of Technology School of Engineering. The facility was designed and built in 1981, and has undergone several design modifications since its construction. Detailed design information is given by Allison (2). Figure 4 shows the CTF general schematic diagram.

The CTF is composed of several major sub-systems. Supply air is provided by a 40 horsepower centrifugal blower housed in a small containment room. The blower is rated to deliver 3000 cubic feet of air per minute at a discharge pressure of 1.66 psig. In this arrangement, supply air is drawn from outside through a 12 inch circular duct and passed through an electrostatic air cleaner prior to entering the blower. By opening doors in the containment room, laboratory air may be mixed with the outside air. This is useful for regulating the discharge air temperature, which varies from 30 to 40 degrees above outside ambient temperature.

From the blower, air passes through a converging nozzle/ejector assembly (not used in this study), a 9 foot diffuser assembly, and into a stilling tank. In the tank, air is radially diffused by a center-body plug that also serves to block acoustic signals from the blower. It is then

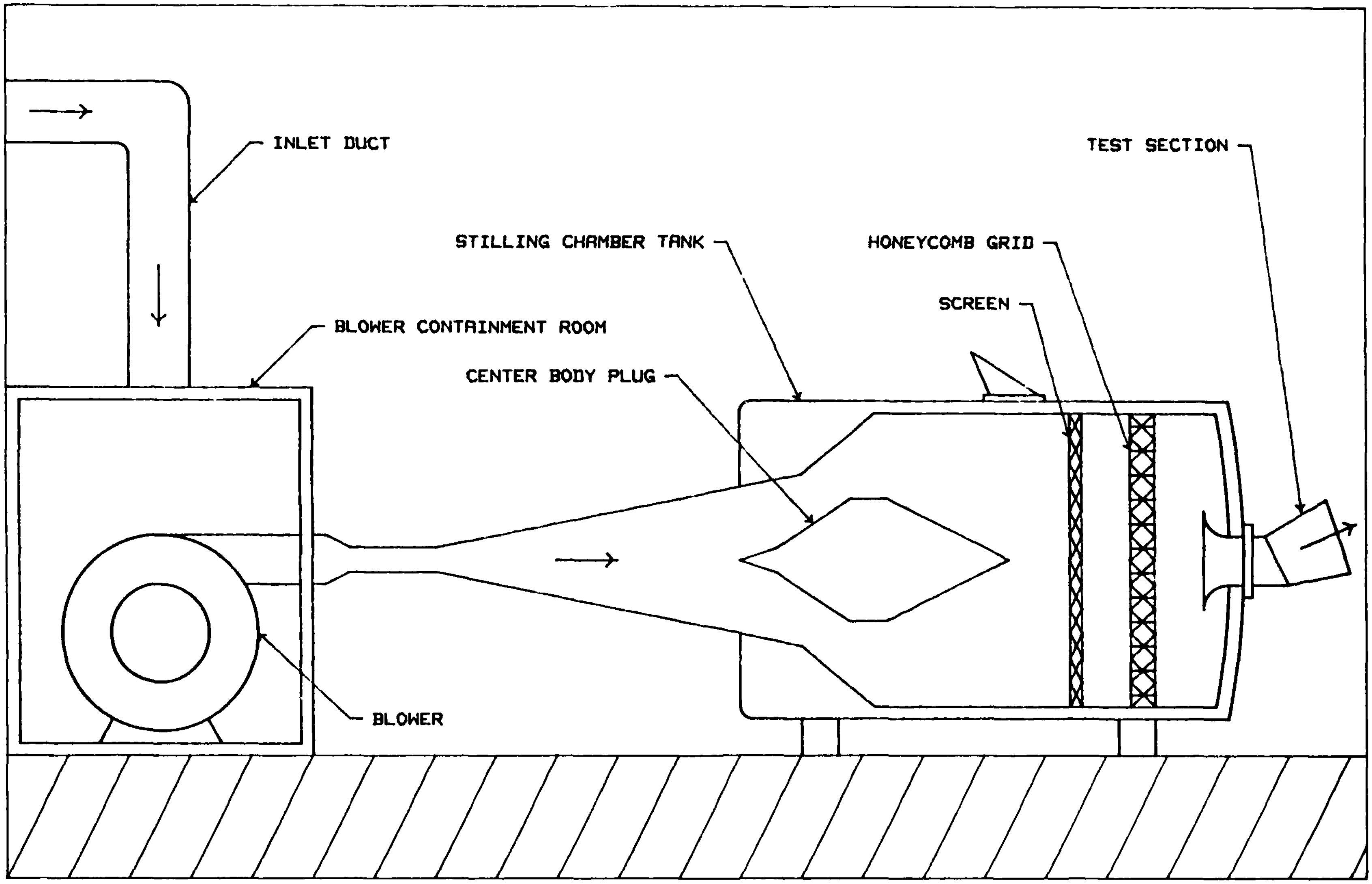

Fig. 4. General Schematic of the AFIT Cascade Test Facility

passed through a 40 mesh wire screen and a felt-type filter disk to screen out fine particulate matter. Finally, it passes through a 4 inch thick honeycomb flow straightener and exits the tank through a variable area two by eight inch rectangular nozzle. Measured Reynolds numbers per foot exceed 2.5 million, and measured free stream turbulence intensities average less than two percent as determined by hot film anemometer tests.

Turbulence Generation

Upon exiting the nozzle and prior to entering the test section, the flow passes through a free stream turbulence generator. This device was added by Absar (1), and is constructed to fit flush with the nozzle exit. The device injects 100 psig compressed air into the flow stream through a series of 1/16 inch holes. The air is injected perpendicular to the flow direction at the nozzle exit. As measured by Absar, this process generated free stream turbulence levels up to 7 percent, while changing the air flow total pressure less than 2 percent (1:14).

Test Section

The test section contains seven NACA 65-A506 blades. The NACA 65-A506 airfoil profile was generated as a test airfoil for compressor cascade research. In the central or neutral setting, the cascade has a measured stagger angle of

16 degrees, an angle of attack of 15 degrees, and a flow incidence angle of 0 degrees. Each blade has a chord length and span of 2 inches, resulting in an aspect ratio of 1. The blade spacing is 1.33 inches and the corresponding cascade solidity is 1.5. Additionally, the outer blade on each end of the row is imbedded into the end wall in order to better approximate an infinite cascade.

Downstream from the blade row, the flow passes into a variable area exit duct. This duct contains two plexiglas side walls and two 13 inch adjustable end walls. The end walls alter the duct shape, allowing it to function as a diffuser or nozzle as required. The duct exits directly into the laboratory.

The test section is fitted with 7 sets of static pressure taps. The first set is installed in the test section inlet and provides an inlet pressure profile. The second and third sets are installed in each end wall, and the remaining four sets are installed in one plexiglas side wall, perpendicular to the axial direction as defined in Chapter II. The four sets in the side wall are behind the center cascade blade at 1.25, 2.25, 3.25, and 4.25 inches from the trailing edge. These 7 sets of taps are used to balance the test section and calculate ideal velocities. Figure 5a shows the test section diagram.

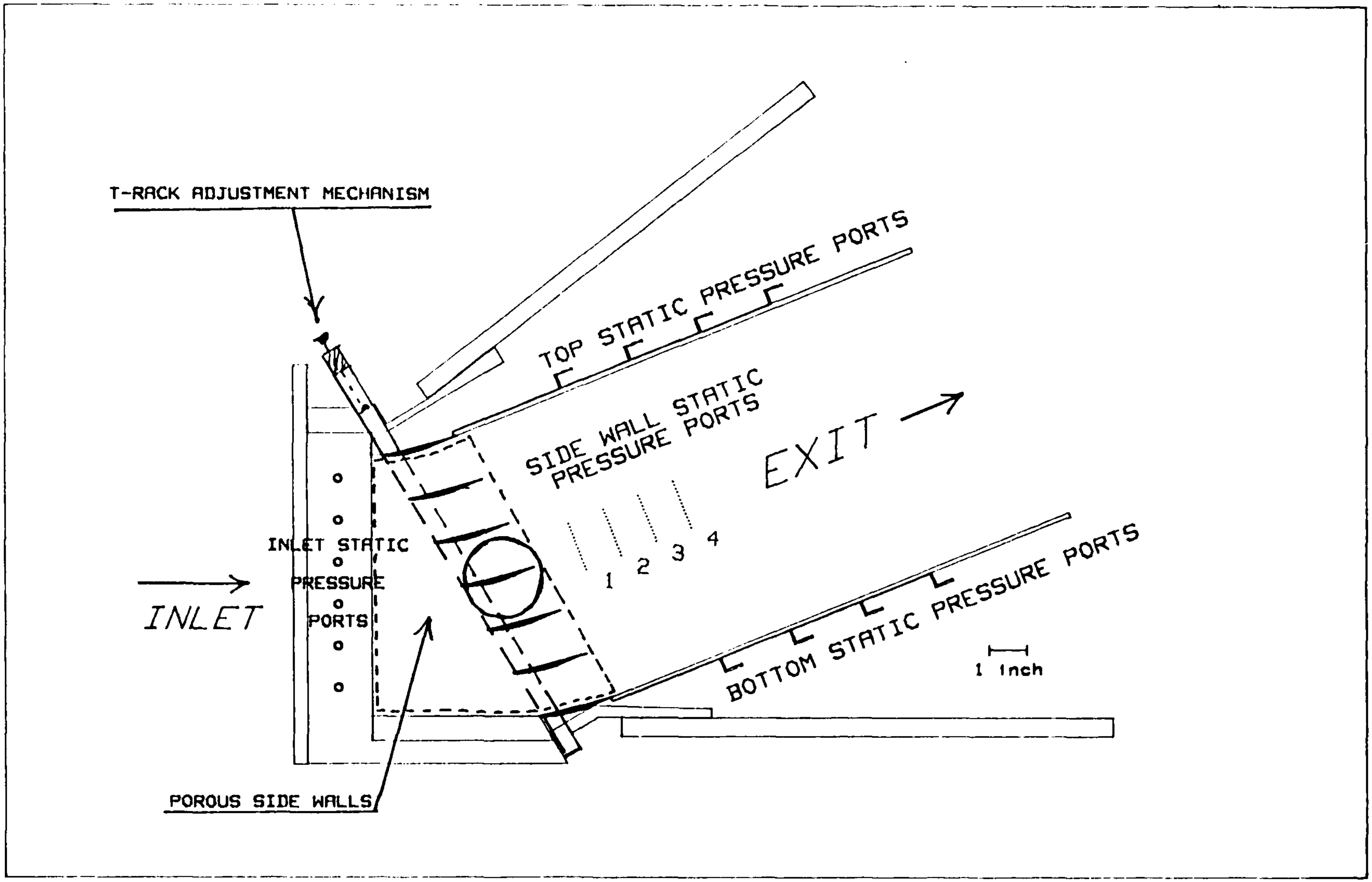

Fig. 5a. Test Section Schematic Diagram

Side Wall Suction System

A side wall suction system was added by Moe in order to draw off the test section boundary layer (21). This reduced the side wall boundary layer's influence on the flow through the cascade. As Moe reported, this boundary layer did not allow for the two-dimensional flow required for accurate experiments. By continually drawing off the boundary layer through porous side walls, the flow through the cascade can be made virtually two-dimensional over the middle two thirds of the center blade span (21:47). With side wall suction applied, the adjustable end walls are positioned so that the static pressure across the cascade inlet is uniform while the pressure measured at each end wall and from the side wall pressure taps is as near to ambient as possible. This "balancing" procedure produces the two-dimensional flow described above.

Cascade Geometry Control

As previously stated, an objective of this investigation was to modify the test section to allow for varying the cascade geometry. Initially, the effort centered on a method to vary the cascade incidence angle while holding the cascade geometry fixed. The goal being to study incidence angle effects alone. As shown in Cohen and Rogers (7:187), the most practical method of accomplishing this is to mount the entire blade row on a turntable, and rotate it about the

center blade while holding the flow inlet direction constant. This approach required that the test section be re-designed from scratch. Time and material constraints eliminated this option, so an alternate approach was devised by the author.

In this approach, the blade shape, spacing, and axial direction were fixed. The blade angle of attack was chosen as the parameter to vary. Specifically, the blades imbedded in each end wall remained fixed, and the five blades in the flow were rotated in unison about their rear attachment pins as shown in Figure 5b. This choice made the physical modifications easy, but also unalterably changed the test conditions as will be shown later.

Before modification, each blade was mounted in the section using four threaded pins. These mounting pins entered from the outside through threaded holes in the plexiglas. The pins then passed through holes in the porous metal to engage the blade. The end of each pin fit in a corresponding hole drilled into the end of each blade at approximately 30 and 60 percent chord. Figure 6 shows an exploded view of the blade mounting prior to modification. Since the rear attachment point for each blade was selected as the pivot point, it required no modification.

Next, using the rear attachment point as the center of a circle, an 18 degree arc was cut out of each porous metal side wall at the forward pin mounting hole of each blade except the center one. This arc was centered on the original

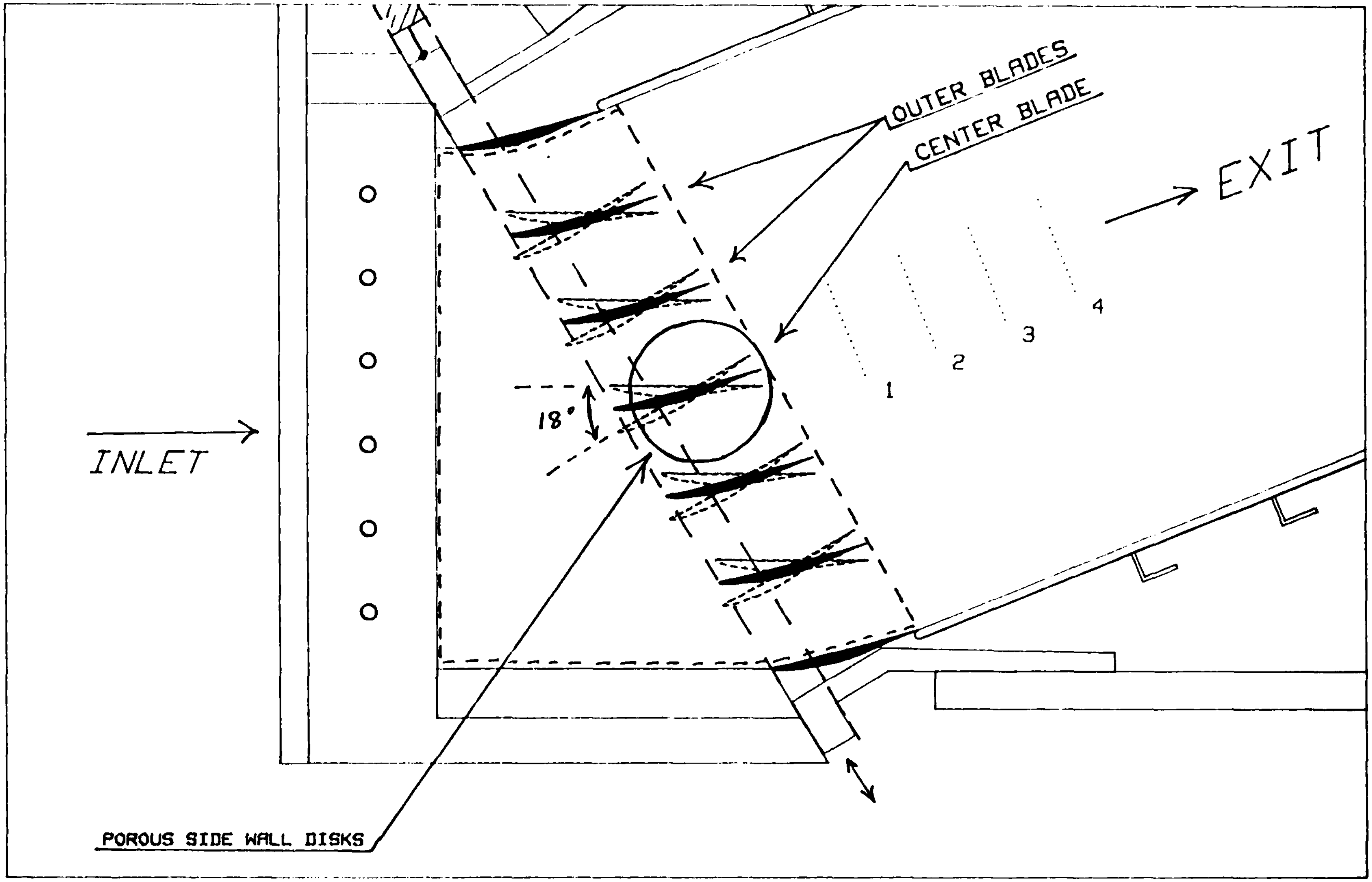

Fig. 5b. Test Section Closeup Schematic Diagram

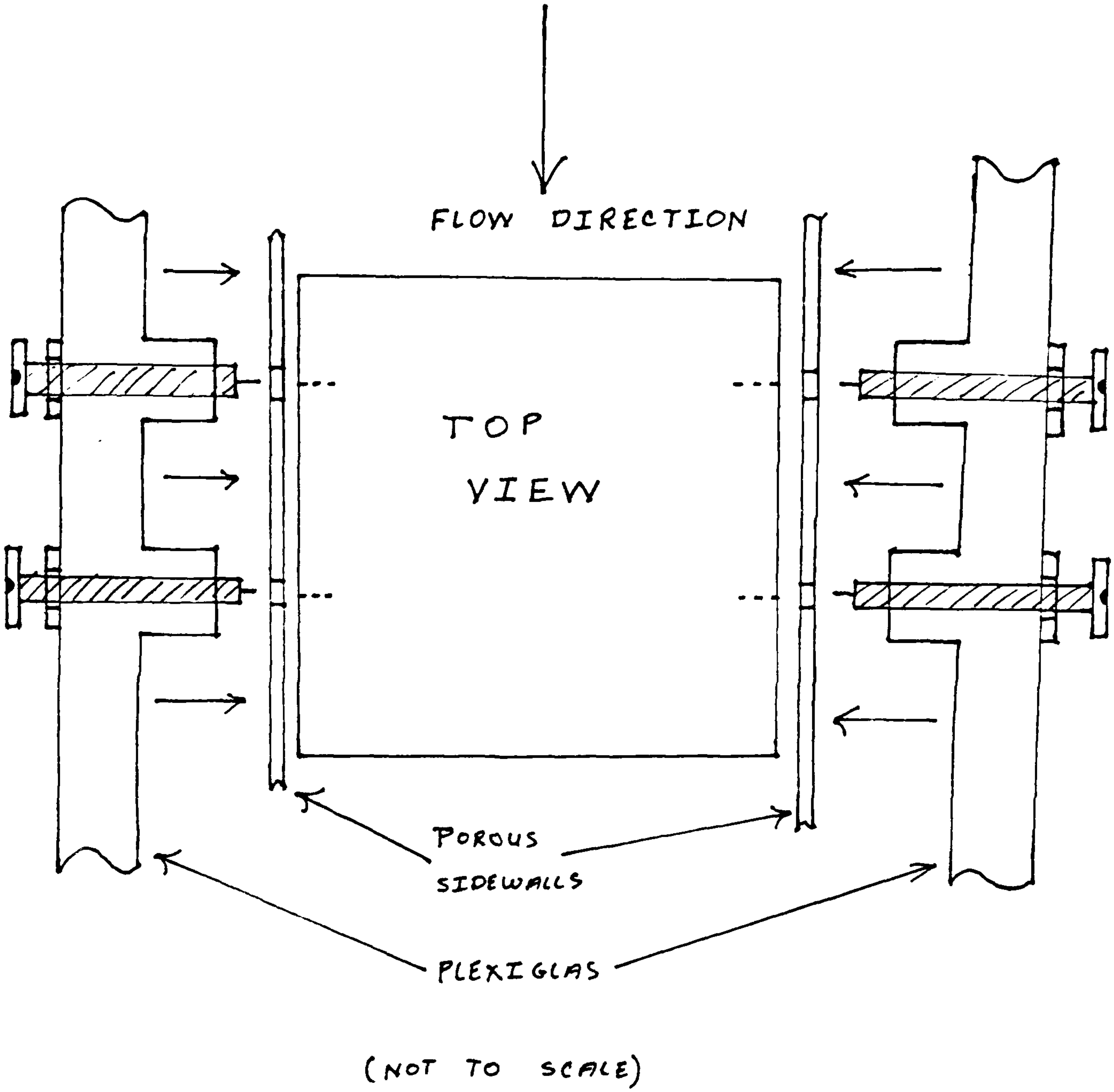

Fig. 6 Blade Mounting Prior To Modification

hole location, thus allowing a maximum of nine degrees rotation in both directions from the center position. An adapter/shim was then fabricated to fit snugly into both the forward mounting hole of the blade, and the arc cutout in the side wall. A thirty-thousandths inch deep by one half inch wide channel was then milled on the back side of each porous metal side wall along a line connecting each forward mounting hole. A T-shaped rack made of the same porous metal was then made to connect all the forward adapter/shims while smoothly sliding in the milled channel as shown in Figure 7. The racks on each side extend out the top of the test section where they are joined and fastened to a jack screw adjustment mechanism. A scale on each rack indicates the current angle of attack setting in three degree increments. Turning the adjustment screw moves each rack along an axis perpendicular to the cascade axial direction, and pivots all five interior blades in unison.

The center blade posed a unique problem. It is equipped with numerous pressure taps (discussed in the next section). Thus, it could not be rotated in the same way as the other blades. The center blade is mounted on each side to a disk of porous metal that is machined to fit flush to a corresponding hole in the side wall. In this way, the blade and disks rotate as a single unit (see Fig 8). The original forward mounting pins are retained and used to hold the rack assembly firmly in the milled channel.

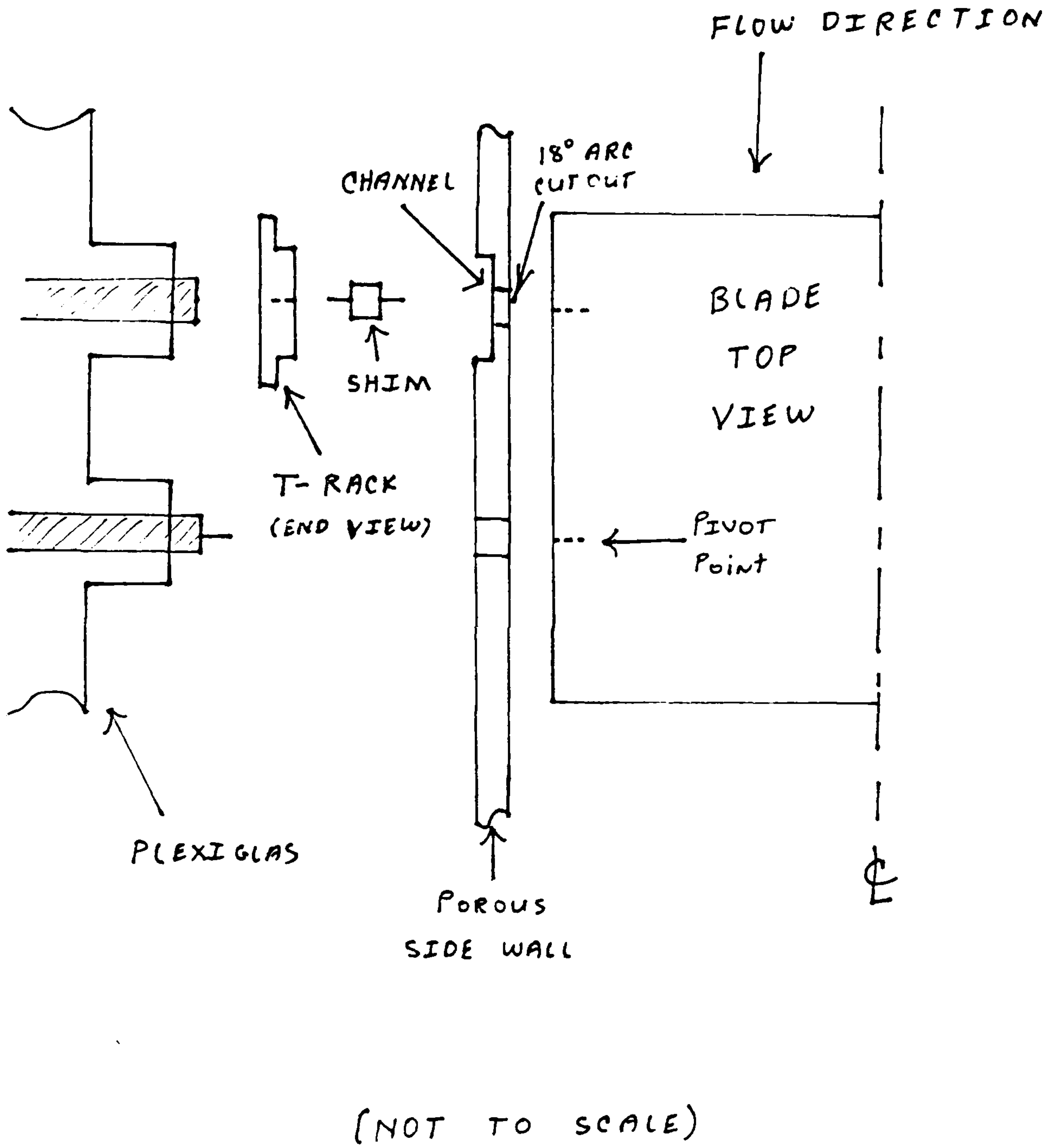

Fig. 7 Placement Of T-Rack

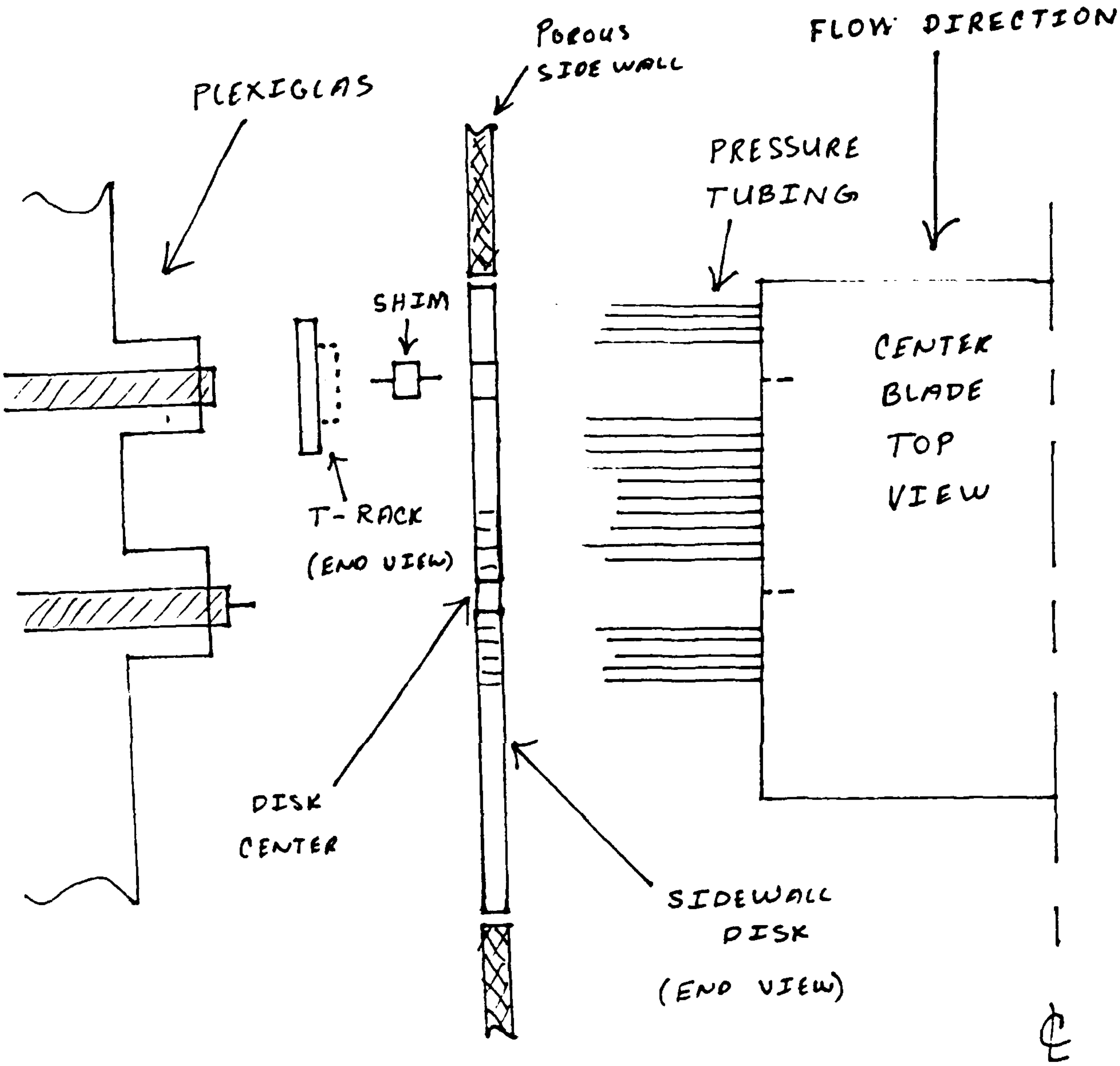

(NOT TO SCALE)

Fig. 8. Center Blade Mounting Arrangement

This arrangement admittedly sounds very complicated. The ultimate requirement was to develop a method to adjust all the blades together while not disturbing either the air flow or the side wall suction, and still provide secure mounting at all angles. Indeed, the original goal was to vary only the flow incidence angle. Now, incidence angle, stagger angle, and angle of attack vary together. Additionally, the flow area through the blade passage will also vary, and this must be considered in the data analysis.

Blade Roughness Configuration. The NACA 65-A506 blades used in this investigation are one set of three that were used by Poulin (23) and Absar (1). The specific set used is their configuration number 2. The blades are cast fiber resin material that has been cured at high temperature to improve performance in the cascade. The configuration number signifies the degree of roughness incorporated into the blade. This roughness was added by bonding a selected emery paper to the suction surface between the 4 and 25 percent chord point. The application was made in a way that minimizes surface distortion. Detailed roughness information is given by Poulin (23:90-92). The average roughness for the current configuration is 12.10 μm.

Suction Surface Pressure Measurement. The center blade is equipped with 38 static pressure taps drilled into the suction surface as shown in Figure 9. These taps are offset one sixteenth of an inch from the center line and alternate

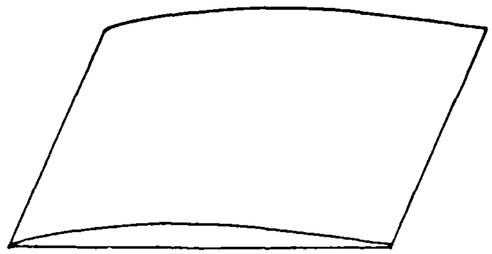

NACA 65-A506 Profile

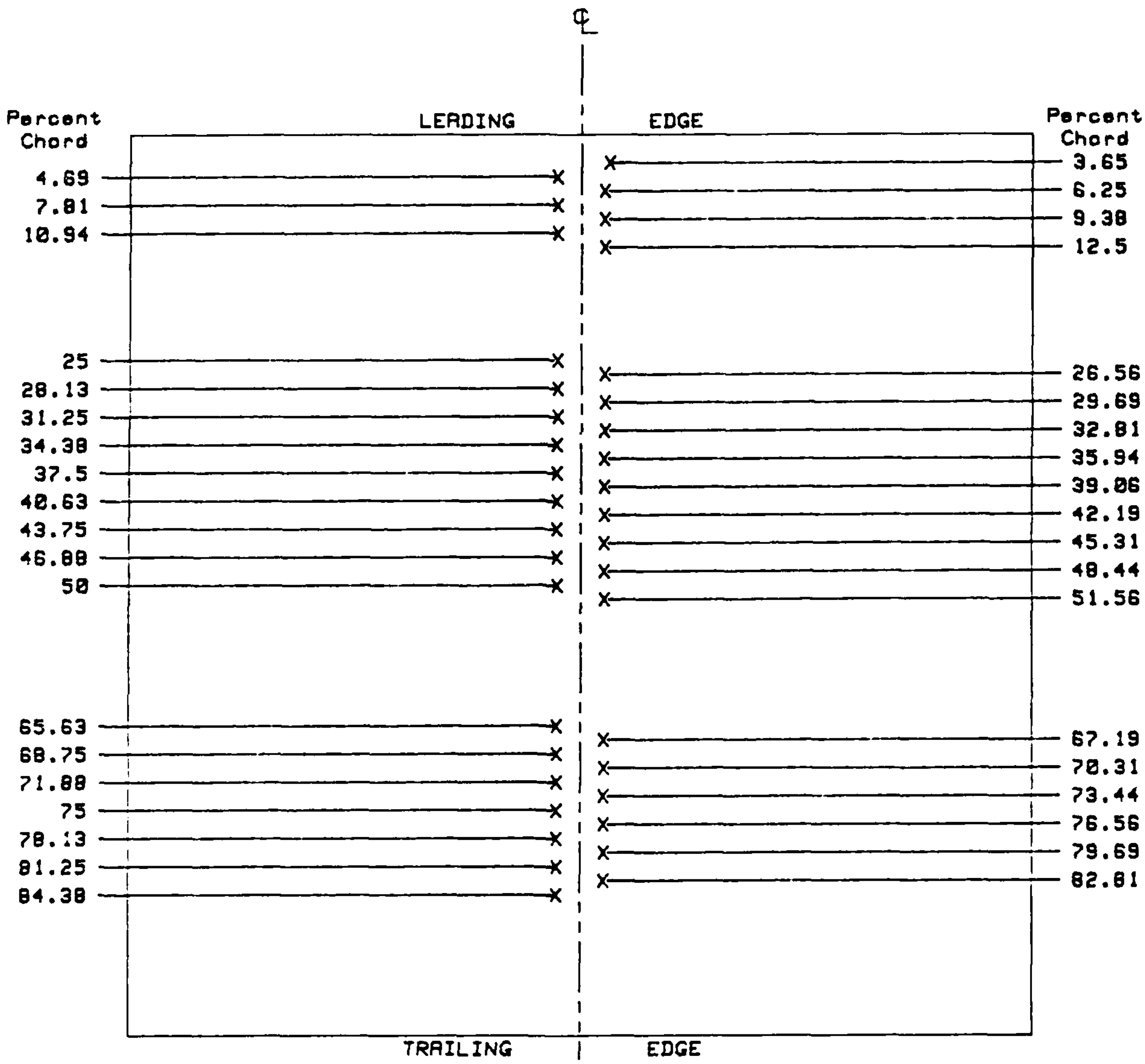

Top view of center blade, looking down at the suction surface, showing pressure tap locations (X) and tube arrangement.

Fig. 9. Blade Profile and Pressure Tap Arrangement

to either side. The taps are individually connected to a scanivalve measuring system. The computer controlled scanivalve samples each tap and can take one complete blade pressure measurement in ten seconds. Individual measurements can also be made by manually cycling the scanivalve controller.

Instrumentation

During this investigation, numerous pressure, temperature, and velocity measurements were taken. A complete instrument listing is given in Appendix A, and the general types of instruments used are reviewed here.

Pressure Measurements. Five different pressure measurements were taken during each test. The stilling chamber total pressure was measured in the chamber between the flow straightener and the nozzle. The cascade inlet and exit static pressures were measured upstream and downstream of the center blade. Also, ambient pressure, and the center blade suction surface static pressure were measured. All measurements were made with diaphragm type transducers. These transducers converted pressures to voltages, and were calibrated prior to each run as detailed in Appendix B. Additionally, eighteen 30 inch U-tube water manometers were connected to provide visual indications of the transducer-measured pressures as well as the additional inlet and exit duct static pressures, and side wall suction vacuum.

Temperature Measurements. Two temperatures were measured during the tests. Stilling chamber total temperature, and ambient temperature were measured using T-type copper constantan thermocouples. The voltages from these devices were converted to temperatures as described in Appendix B.

Velocity and Turbulence Intensity Measurements. The velocity and turbulence intensity both in the center blade wake and along its suction surface were measured using three TSI model 1050 anemometers. Measurements in the wake were made with a TSI model 1241-10 X-configuration hot film probe, while measurements along the suction surface boundary layer were made with a TSI model 1218-20 boundary layer probe. These probes were calibrated using a modified TSI model 1125 calibrator and the method detailed in Appendix B. The probes were calibrated over a range of temperatures and velocities. The detailed calibration procedure is that used by Poulin (23) and Absar (1). In an effort to increase accuracy, the calibration and data reduction software was modified to account for wire and probe angle errors as well as probe support and probe internal resistance at the elevated test temperatures. The calibrations produced curves as shown in Appendix B that were later used to obtain velocities and turbulence intensities. Additionally, the X-configuration probe measures two-dimensional velocity and turbulence intensity.

Traversing Mechanism. This unit positioned the hot film anemometer probes at the desired locations within the test section. Its range extends from the leading edge of the airfoils to the end of the 13 inch exit duct. The device contains an 18 inch probe support holder mounted in a modified NACA 66-007 airfoil faring (2:12). The faring provides a measure of stability for the support by reducing vibration. It also protects the probe, probe support and cables while in the flow. The traverser moves parallel to the exit flow (X axis), perpendicular to the exit flow (Y axis), and laterally within the exit channel (Z axis). Both the X and Y axis movements are performed using stepping motors connected to the data acquisition system. The probe position is automatically displayed and reported to the computer via two digital encoders within the mechanism. X direction resolution is 0.002 inches and Y direction resolution is 0.001 inches. The observed positioning accuracy was +/- 0.002 inches in Y and +/- 0.005 inches in X. The Z axis is adjusted manually, and was set so that the probe was centered in the exit channel for all tests.

Automated Data Acquisition System. All instruments are controlled by a HP-3052A data acquisition system. Using specific software, this system performs all data collection, recording, and reduction functions. The system components are listed in Appendix A.

IV. Experimental Procedure and Data Reduction

Methodology

A complete test run was divided into three phases; calibration/warm up, data collection, and data reduction. Calibration involved both the hot film probes and the pressure transducers. Hot film calibration was conducted when the velocity correction factor (to be discussed) fell below Ø.92. The pressure transducers were calibrated prior to each data run and hot film calibration.

Before the actual data collection began, the CTF was turned on and allowed to warm up. This warm up usually required two hours. During this period, the traverser was positioned as required by the particular test being run, and its encoders adjusted to the appropriate reference values. Traverse locations with respect to the cascade are shown in Figure 1Ø. Also, if the turbulence generator was to be used, it was turned on to bleed any water from the compressed air lines. All tests were run both with and without artificially generated free stream turbulence. When the system was warmed up, the exit duct end walls were adjusted so that the cascade inlet manometers indicated a uniform pressure across the inlet. This usually resulted in the end wall and wake manometers showing approximately ambient pressure. Once this ballancing was done, the end wall angles, temperature, pressure, relative humidity, and manometer readings were

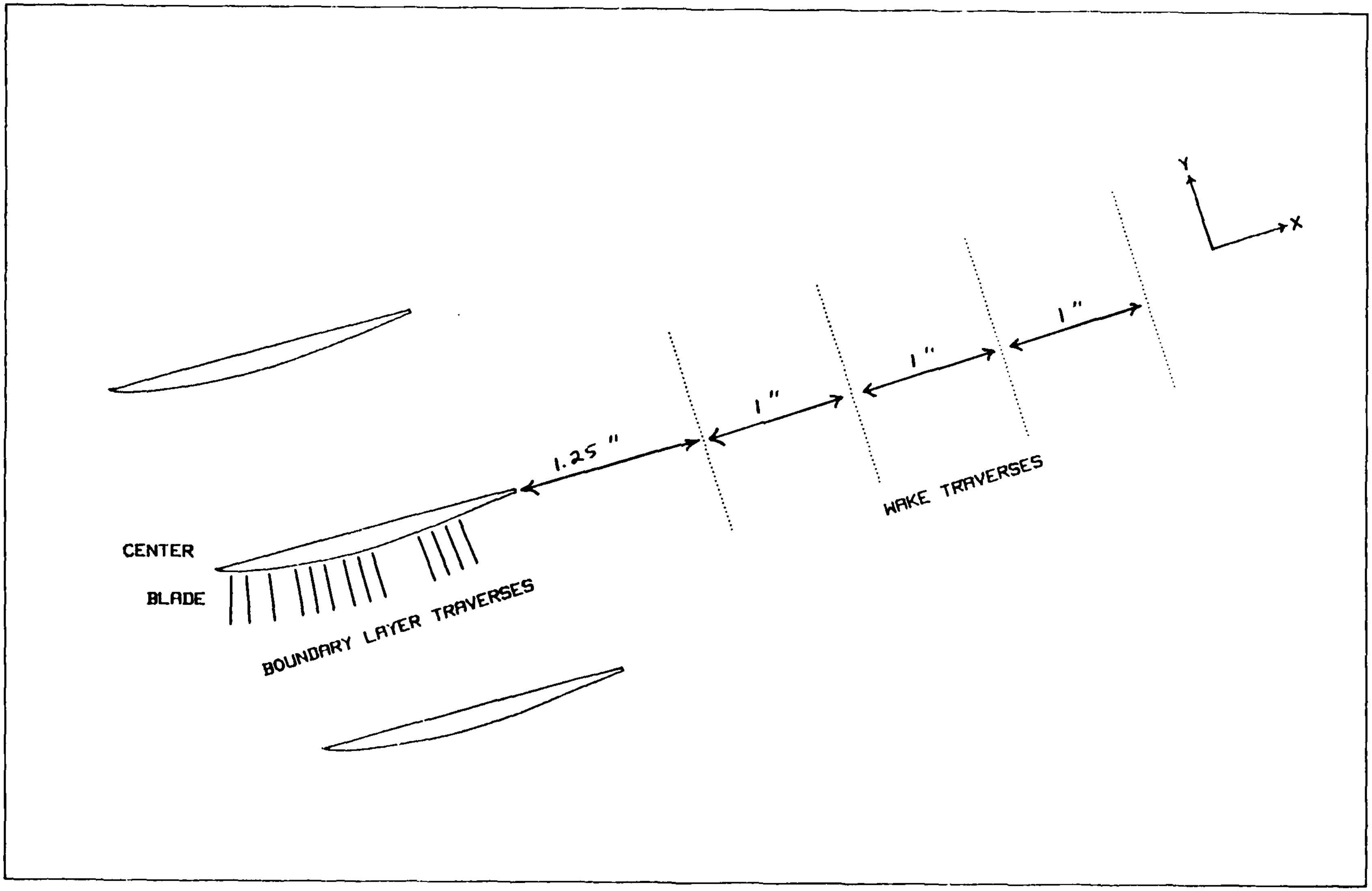

Fig.10. Representation of Wake and Boundary Layer Traverses

recorded. Then the data collection was started. Upon test completion, the raw data was recorded on magnetic disks. This data was later converted into engineering units and plotted as necessary. Repeat runs were made on different days for selected traverses to confirm data repeatability.

Automated Procedures

Virtually every part of the experimental process was automated. The existing software was quite sophisticated and certainly reduced the amount of work required in calibration, data collection, and data reduction. However, such software almost always has "bugs" of one form or another. Indeed, several such bugs were found and corrected. In addition, most of the programs were modified by the author to accommodate the specific requirements of the investigation. Overall, the software performed in accordance with the theory presented in Chapter II.

Error Predictions

Obviously, minimizing error in any scientific investigation is a basic objective. Thus, understanding error's effects is essential. Errors occur in numerous forms, and affect the two fundamental qualities in scientific measurement; precision and accuracy. Precision is the indicator of how exactly a given instrument measures a specified quantity such as voltage or resistance. Accuracy

is the indicator of how close the instrument's measured value is to the actual value.

Precision errors are usually a function of instrument design. As a result, there is little one can do other than to perform periodic servicing to minimize them. In the present case, instrument and computer values were assumed to be precise to three decimal places. On the other hand, accuracy errors are best controlled by rigorous and frequent instrument calibration, and understanding physical uncertainties such as instrument positioning.

In the current investigation, the most obvious error occurred in the measured anemometer velocities. As with all previous studies using this facility, the anemometer's measured velocities were usually between four and eight percent higher than those predicted using ideal compressible flow relations. Thus a correction or "scaling factor" as described by Tanis was used to correct the velocity in a way that satisfies continuity through the cascade (32:14-16). The equation is:

$$V' = sV \tag{13}$$

where:

s = scaling factor ($s \leq 1.00$)

V = the anemometer velocity

V' = the scaled velocity

The scaled velocity was then used to calculate the cascade performance parameters. Using this correction factor, accuracy errors were reduced to less than one percent.

Wake Survey

Wake traverses were conducted at 1.25, 2.25, 3.25, and 4.25 inches behind the center blade trailing edge. Each traverse contained 133 data points taken 0.01 inches apart for a total distance of 1.33 inches. The traverse direction was perpendicular to the mean flow direction, and the probe was positioned so that the center blade trailing edge bisected the traverse. The X-configuration hot film probe was used to measure X and Y velocity and turbulence intensity components as defined in Figure 10.

At the start of each data point, ten 1-second samples of the AC (true RMS) voltage component of sensor number one were taken. The arithmetic average of the ten samples was then computed and recorded as the U_{RMS} voltage for that sensor at that point. The process was then repeated for the second sensor. Following this, the DC voltage component of each sensor was sampled in an identical manner and recorded as U_{MEAN} for the appropriate sensor at that data point. After this was done, the remaining pressure and temperature transducer voltages were recorded and the probe was moved to the next data point. After moving the probe, a delay time of three seconds was observed before any data collection to

allow any movement vibrations to damp out.

As shown in Chapter II, the total pressure loss coefficient ($\bar{\omega}$) is used to measure the loss through the cascade. The measured stilling tank total pressure and inlet static pressure forward of the center blade were used to compute the inlet dynamic pressure. Finally the mass averaged total pressure given by Equation (9), was calculated. Since the flow was considered two-dimensional, the area integral reduces to single integrals as originally shown by Moe (21:16). These integrations were done on the HP 9845B computer. The results are discussed in the next chapter.

Suction Surface Pressure Survey

As previously stated, the center blade suction surface static pressure distribution was measured by a scanivalve system. Each pressure port was sampled for 0.5 seconds. These samples were then sorted in leading edge to trailing edge order. The resulting pressures were then converted to pressure coefficients using Equation (11). A minimum of three separate sampling runs were made during each test. The arithmetic average of the three pressure coefficients at each point were then plotted versus blade chord location. Since the results were used in reducing the boundary layer data, the pressure runs were made immediately prior to the boundary layer data collection run. At this point it is interesting

to note that the presence of the boundary layer probe within the cascade had a marked effect on the pressure distribution. This may be having a significant effect on data accuracy and will be discussed in the next chapter.

Suction Surface Boundary Layer Survey

The center blade suction surface was probed using a TSI Model 1218-20 hot film boundary layer probe as shown below.

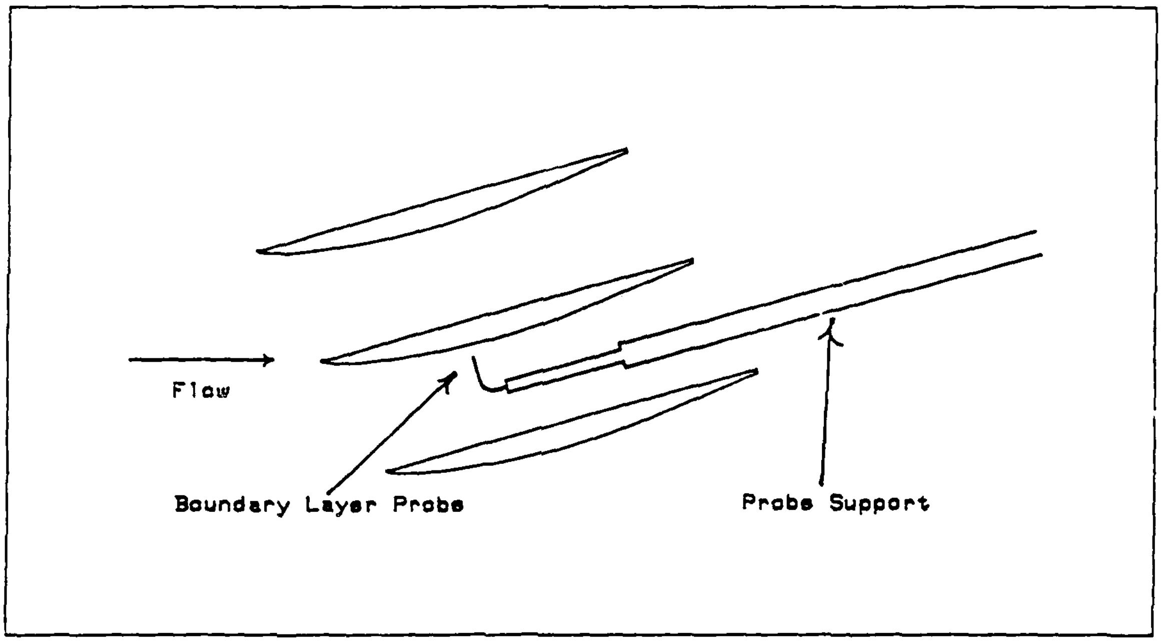

Fig. 11. Boundary Layer Probe Orientation

The film was first positioned at a preselected offset distance from the surface. It was then traversed away from the blade in a direction normal to the blade surface at the particular traverse point. The offset distance was usually

0.03 inches. For the test runs at $\alpha = 12$ degrees, the offset was reduced to 0.005 inches. However, at $\alpha = 18$ degrees, the offset had to be increased to 0.06 inches to avoid probe damage from vibration. Once the film was positioned, data was collected in the same way as for the wake traverses. Since the boundary layer probe had only one sensor, only one set of anemometer voltages was recorded as opposed to two sets for the X-configuration probe.

Normally, 13 traverses were made, one each at 4.6875, 9.375, 25, 29.6875, 34.375, 40.625, 45.3125, 50, 65.625, 70.3125, 75, 79.6875, and 84.375 percent chord. As testing continued, a 14th traverse was added at 16.5175 percent chord in an attempt to gain more boundary layer information there. Each traverse usually contained 60 data points spaced 0.005 inches apart. However, as with Absar's study, the last four chord locations required 90 data points when artificial free stream turbulence was used (1:32).

Using both the anemometer voltages recorded during the tests and the appropriate probe calibration data, the mean flow velocity (V_M) was calculated. The turbulence intensities were then calculated using Equation (6). As in previous studies using this facility, the boundary layer mean edge velocity (V_E) was computed using the scheme presented by Deutsch and Zierke and outlined in Chapter II (8:8-9). Using Equation (12), the composite boundary layer velocity profile was computed at each traverse location. Boundary layer

thickness (δ) was assumed to be the distance from the surface where:

$$U_{BL} = 0.99U_E \tag{13}$$

Finally, the distance from the surface where the turbulence intensity begins to increase (δ_{TI}) can be related to boundary layer thickness by:

$$\delta_{TI} = 1.25\delta_{BL} \tag{14}$$

This relation is gi e.. by Deutsch and Zierke and applies to an equilibrium boundary layer (8:9). It is used in this investigation for comparison purposes only. The distance from the surface where turbulence started to increase was used in Equation 14 to compute comparison boundary layer thicknesses.

The tabulated results and selected plots are discussed in the next chapter. As previously stated, selected traverses were repeated on different days to confirm data repeatability. The complete set of output plots for all tests are given in Appendices C through N.

V. Results and Discussion

Wake Surveys

As previously discussed, wake velocity and turbulence intensity were measured at 1.25, 2.25, 3.25, and 4.25 inches behind mid-span of the center blade trailing edge, using an X-configuration hot film probe. This allowed both velocity and turbulence intensity to be calculated two-dimensionally. A method to correct for errors in sensor angle and probe alignment was developed and integrated into the calibration and data reduction software. This was done as an additional effort to minimize accuracy errors.

There is much in the literature discussing the effects of incidence angle on the various cascade loss parameters. Therefore, the present results are presented as functions of incidence angle rather than angle of attack. On the surface, this may seem misleading. Indeed, angle of attack is actually changed. However, in light of the parameters being discussed, it is felt that presenting the results with respect to incidence angle will be more meaningful to the reader, and will make comparison with other investigations easier. One need only remember that in the current study, incidence, stagger, and angle of attack vary together.

Results. The wake traverse results are presented graphically in Appendices C through H. These appendices are arranged in order starting at -3 degrees incidence, and

proceeding next to 0 and +3 degrees respectively. For each incidence angle, the low free stream turbulence data are presented first, followed by the high free stream turbulence data.

Both velocity and turbulence intensity are shown as vectors. The coordinate axes are set with the X axis parallel to the mean exit flow direction, and the Y axis aligned perpendicular to the mean exit flow in the vertical plane of the exit duct. The light-black vectors show the velocity distribution behind the center blade at the given measuring station. Superimposed on these are a set of darker vectors indicating the local turbulence intensity across the blade. The center blade wake with its accompanying increase in turbulence is clearly visible in all cases. Using the scale factors listed on the plot of interest, one can measure a specific velocity or turbulence intensity vector and determine its magnitude.

<u>Minimum Velocity Ratio</u>. Figures 12 and 13 show the values of minimum velocity ratio for all three incidence angles at each downstream measuring station. The figures are for low and high free stream turbulence respectively. Equation 10 is also plotted for reference, using the values for the constants a and b recommended by Lieblein and Roudebush (19:7). Additionally, values are plotted from an investigation by Raj and Lakshminarayana for further comparison. Clearly, the velocity recovery is quite rapid

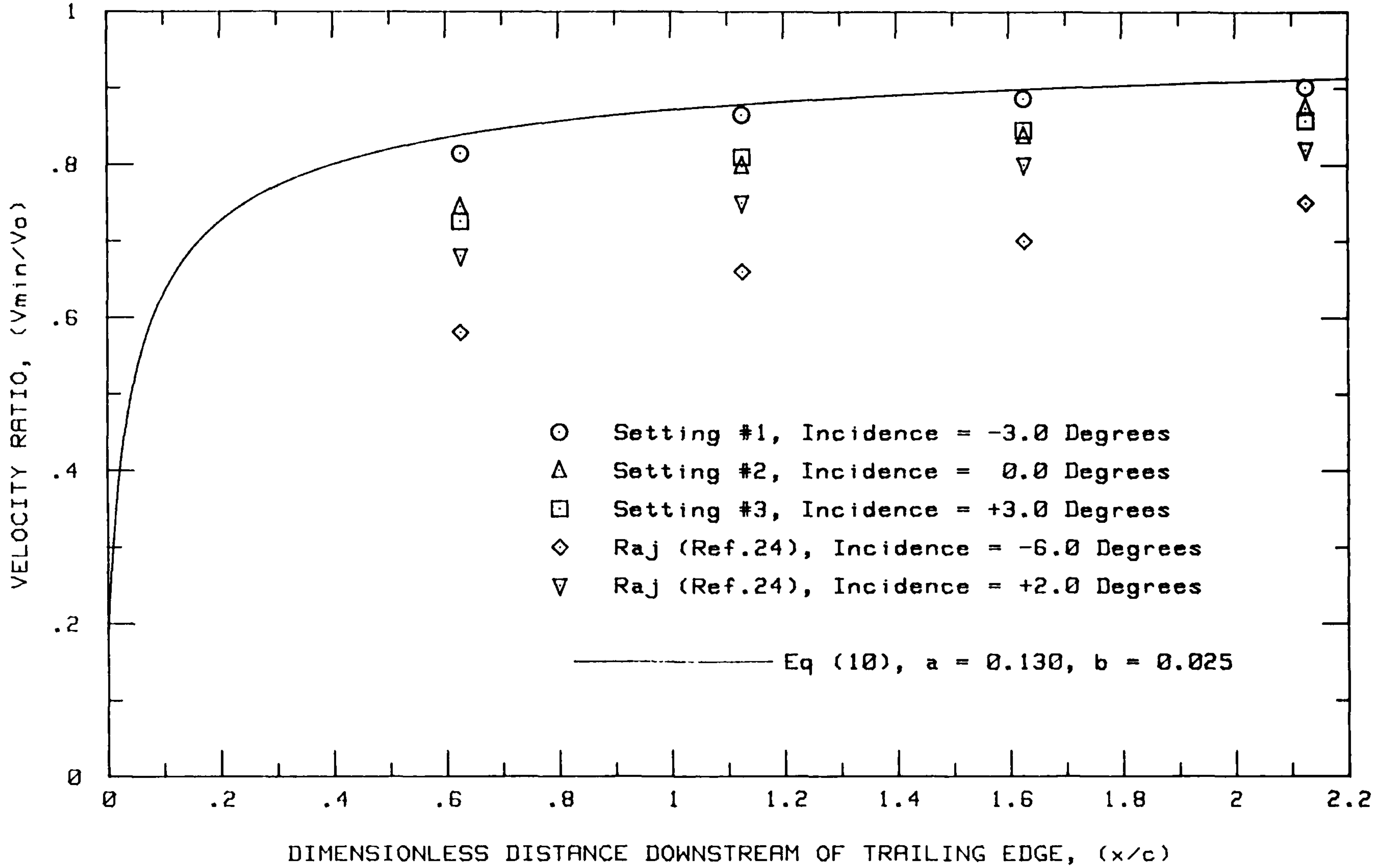

Fig. 12. Wake Velocity Recovery, Conf.#2, Low Turbulence

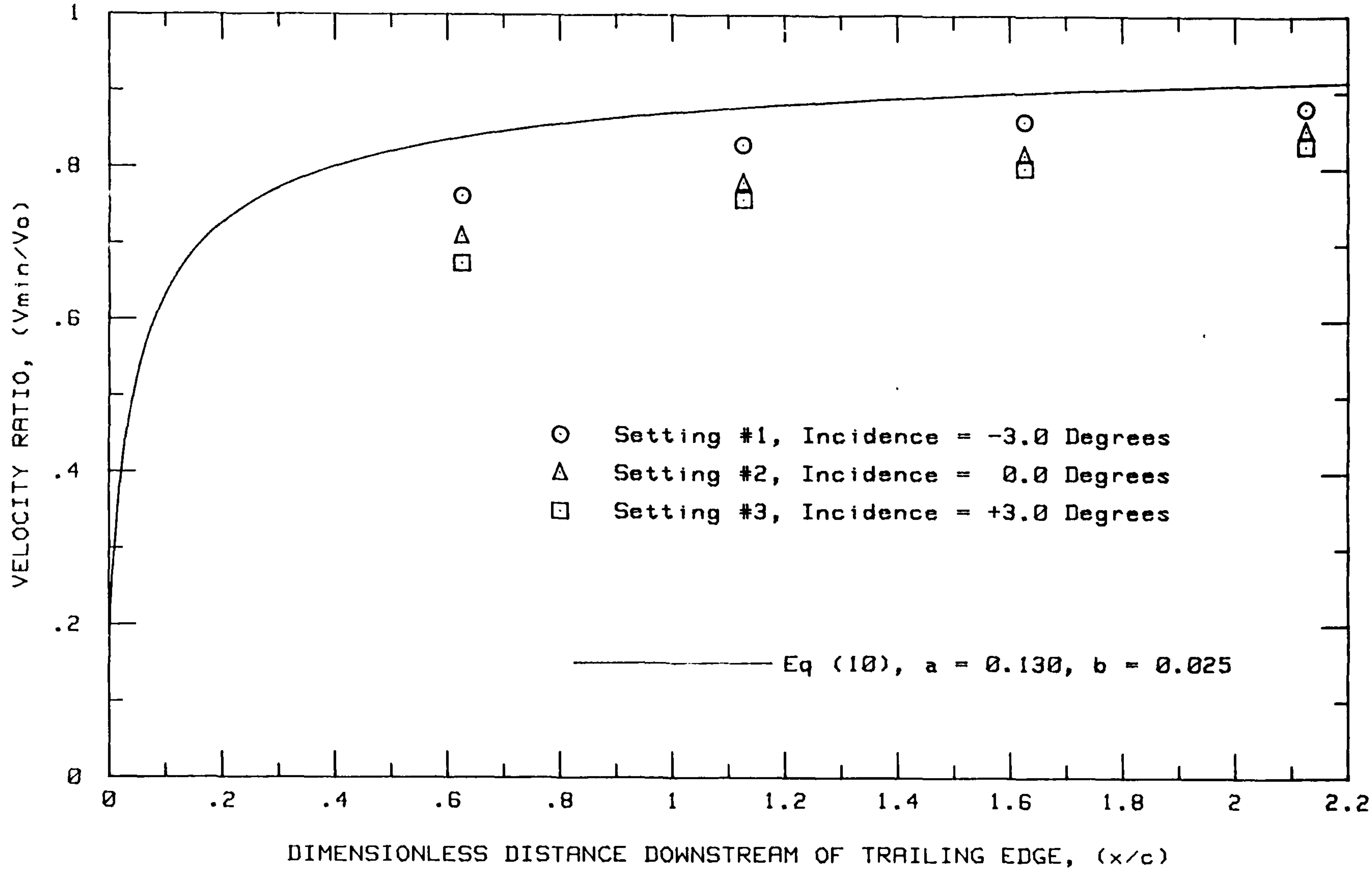

Fig. 13. Wake Velocity Recovery, Conf.#2, High Turbulence

for all configurations in both the low and high free stream turbulence tests, and reaches 70 to 80% within 1.5 chord lengths behind the cascade. This is consistent with the results obtained by Poulin (23:57-60), and Absar (1:38). The velocity recovery values are slightly lower for the high free stream turbulence runs.

In the current study, the wake velocity deficit was least at the negative incidence setting. As incidence increased, the velocity ratio decreased. This decrease is most pronounced from -3 degrees to 0 degrees. With the exception of the traverses at 2.25 and 3.25 inches in the low turbulence runs, this trend continued to +3 degrees. The cause can be traced to the boundary layer development on the blade. This development will be discussed in detail in an upcoming section. In brief, for both increased free stream turbulence and incidence angle, larger boundary layers develop on the blade. These larger boundary layers suggest that the streamwise adverse pressure gradient may be increasing. Also, the boundary layer may be undergoing transition from laminar to turbulent flow earlier along the blade. The thicker boundary layers result in correspondingly larger wakes with greater velocity deficits. Hence the lower velocity ratios. Interestingly enough, the gap between ratios (10% at X/C = 0.625) reduces to 5% at X/C = 2.125. This indicates a higher mixing rate with its associated losses as incidence angle and free stream turbulence are

increased. Overall, the effect of both increased incidence angle and increased free stream turbulence are most pronounced near the trailing edge and diminish with distance downstream.

Full Thickness Ratio. The wake thickness is an important parameter in analyzing cascade losses. The full thickness ratio is defined as

$$\frac{\delta}{c} = \frac{\text{Wake Thickness}}{\text{Chord}} \tag{14}$$

and is plotted in Figure 14 for low turbulence and Figure 15 for higher turbulence. For the low turbulence runs, the full thickness at a given measuring station nearly doubles over the range of incidence angles investigated. This trend is also present with high free stream turbulence. The high turbulence condition makes an additional contribution to the full thickness increase. This contribution is nearly equivalent in magnitude to that of incidence angle. It should be noted however, that with high free stream turbulence, an initial increase in incidence angle shows no appreciable increase in the full thickness ratio between -3 degrees and 0 degrees. The implication is that for incidence angles between -3 degrees and 0 degrees, the high turbulence may be somehow inhibiting the incidence effect on boundary layer growth. The author found no reference to this effect

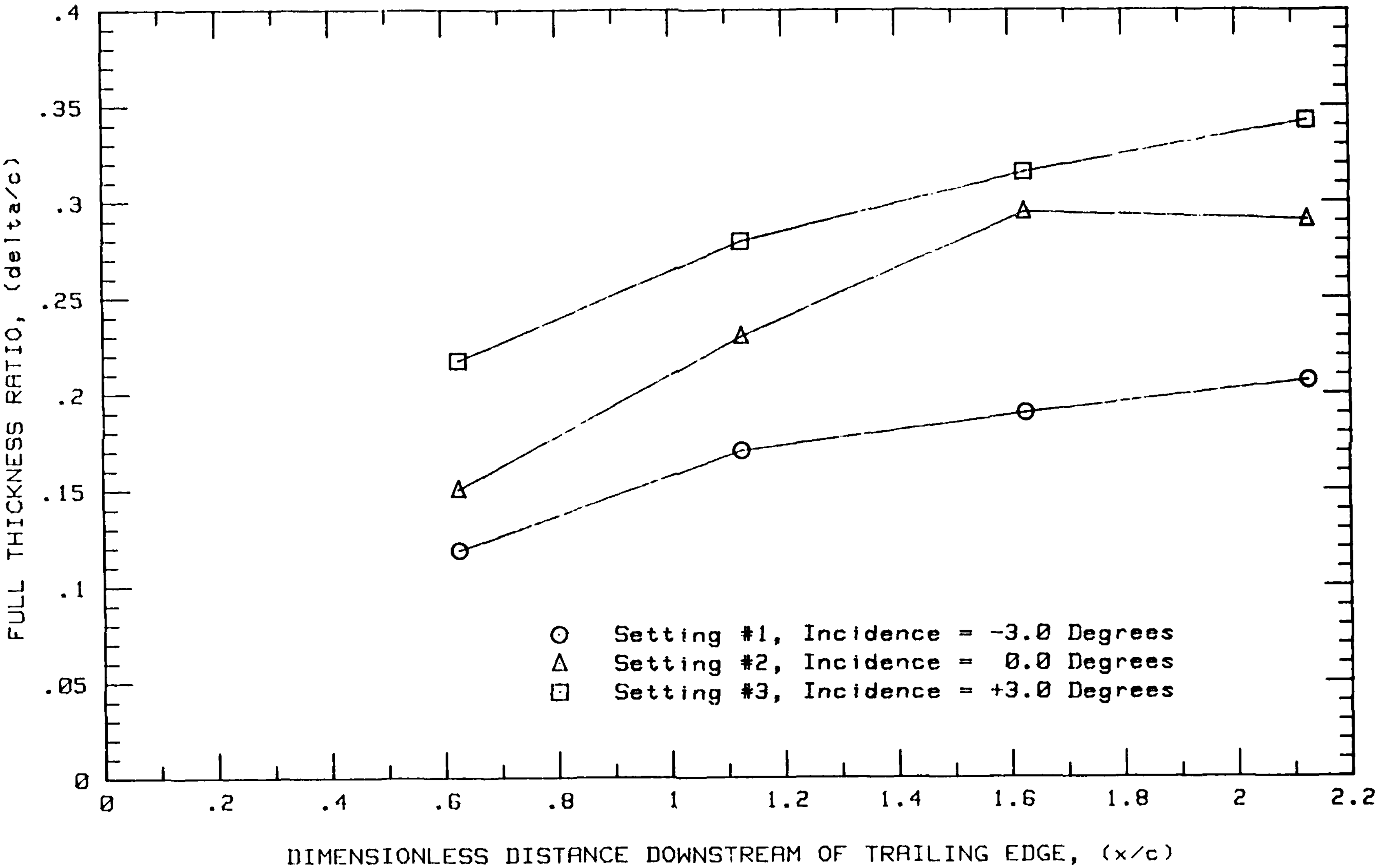

Fig. 14. Downstream Variation of Full Thickness Ratio, Low Turbulence

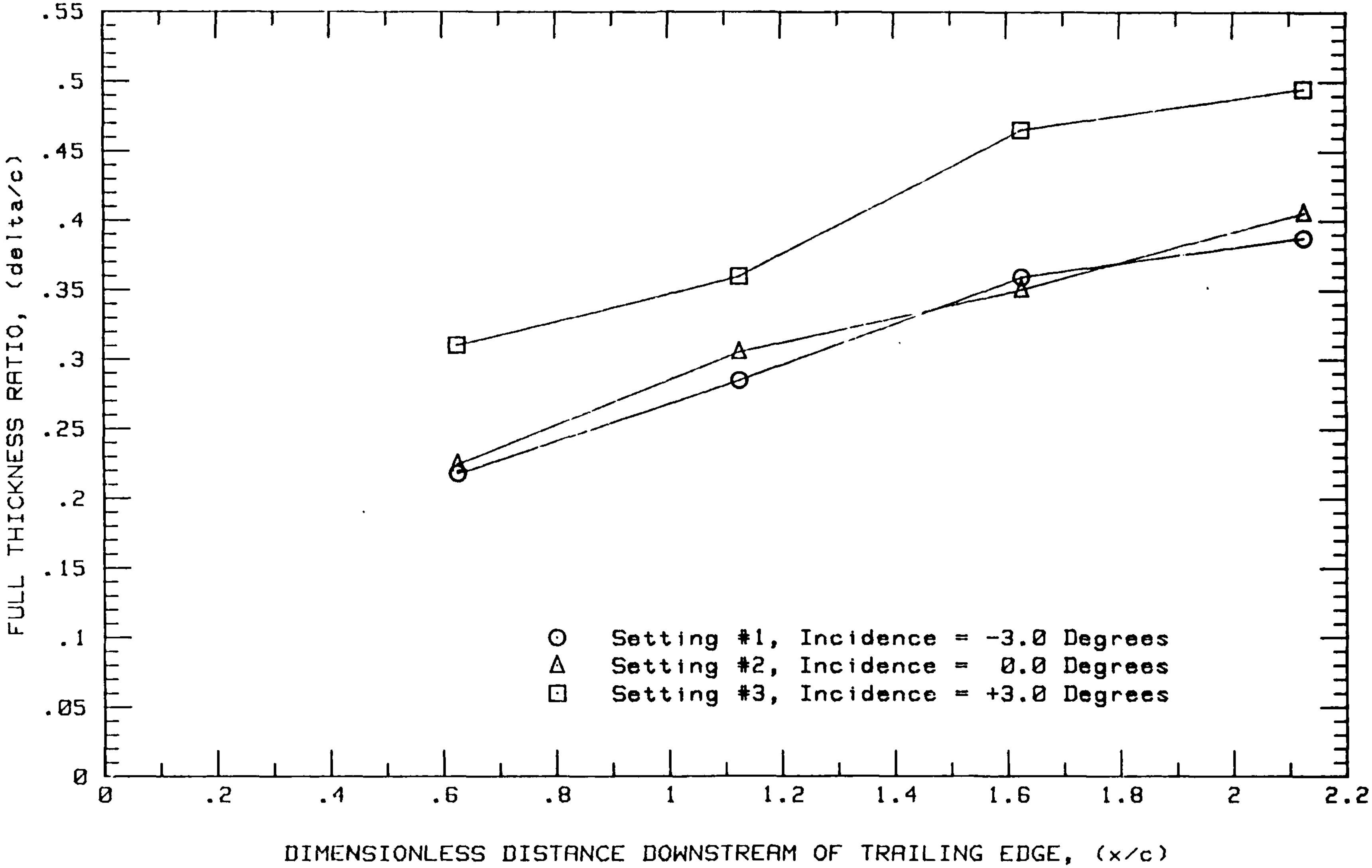

Fig. 15. Downstream Variation of Full Thickness Ratio, High Turbulence

in the literature, and is hesitant to comment on possible causes. However, the increased turbulence may be causing earlier transition at i = -3 degrees, perhaps as a result of the applied roughness on the suction surface. At i = 0 degrees, the flow stagnation point ideally is located at the leading edge of the blade, whereas at the negative incidence setting, the stagnation point would be slightly on the suction surface and closer to the beginning of the applied roughness. Although not specifically investigated in this study, roughness effects on cascade performance have been the primary interest of previous investigations using the present facility and test blades (1,11,21,23,32,35,37).

As with the velocity ratio, the full thickness increase can be traced to the overall thicker boundary layers that develop at the higher incidence angles and turbulence intensities. Since the wake defines the region of total pressure loss, one might expect that a larger wake implies a larger total pressure loss. As will be shown shortly, this is not always the case.

<u>Total Pressure Loss Coefficient</u>. Table II shows the values of the total pressure loss coefficient (as computed from Equation 7) for this investigation. The results from Poulin's and Absar's investigations are listed for comparison. Additionally, Figures 16 thru 19 show the trend of $\bar{\omega}$ with incidence angle at each measuring station, for both

low and high free stream turbulence.

Referring to Figures 16 through 19, the changes in $\bar{\omega}$ with incidence are not significant when compared with the changes resulting from additional free stream turbulence. The figures are presented in order beginning with the traverse closest to the blade trailing edge (X/C = 0.625) and ending with the farthest downstream traverse (X/C = 2.125). Note that for all traverses, the $\bar{\omega}$ values in the high turbulence runs are from 20 to 50 percent lower than those with low free stream turbulence; whereas, the differences in $\bar{\omega}$ with incidence angle average less than 5 percent. This significant reduction in $\bar{\omega}$ with increased turbulence is consistent with Absar's findings (1) and is a strong indicator that the loss through the cascade is reduced with increases in free stream turbulence. Note also how the difference between corresponding (same incidence angle) low and high turbulence loss coefficient values decreases with each successive downstream traverse. This decrease may be a result of the higher wake turbulence intensities present for the high free stream turbulence runs (reference Figures 29 through 52). The higher wake turbulence intensities may be intensifying the mixing process in the wake for the high free stream turbulence tests. If so, the ultimate losses far downstream may be higher with high free stream turbulence. An in-depth turbulence analysis is needed to show this. At a minimum, traverses farther downstream than those in the

Table II

Total Pressure Loss Coefficients

Low and High Free Stream Turbulence

		$\bar{\omega}$				
		Poulin	Absar		Poniatowski	
Incidence Angle	$\frac{x}{c}$	Low Turb	Low Turb	High Turb	Low Turb	High Turb
-3.0 °	0.625	—	—	—	.0459	.0260
	1.125	—	—	—	.0728	.0499
	1.625	—	—	—	.0763	.0584
	2.125	—	—	—	.0763	.0661
0.0 °	0.625	.0729	.0671	.0419	.0505	.0266
	1.125	.0770	.0755	.0635	.0737	.0567
	1.625	.0750	.0811	.0840	.0772	.0673
	2.125	.0770	.0844	.0940	.0724	.0669
+3.0 °	0.625	—	—	—	.0453	.0180
	1.125	—	—	—	.0679	.0465
	1.625	—	—	—	.0813	.0614
	2.125	—	—	—	.0833	.0727

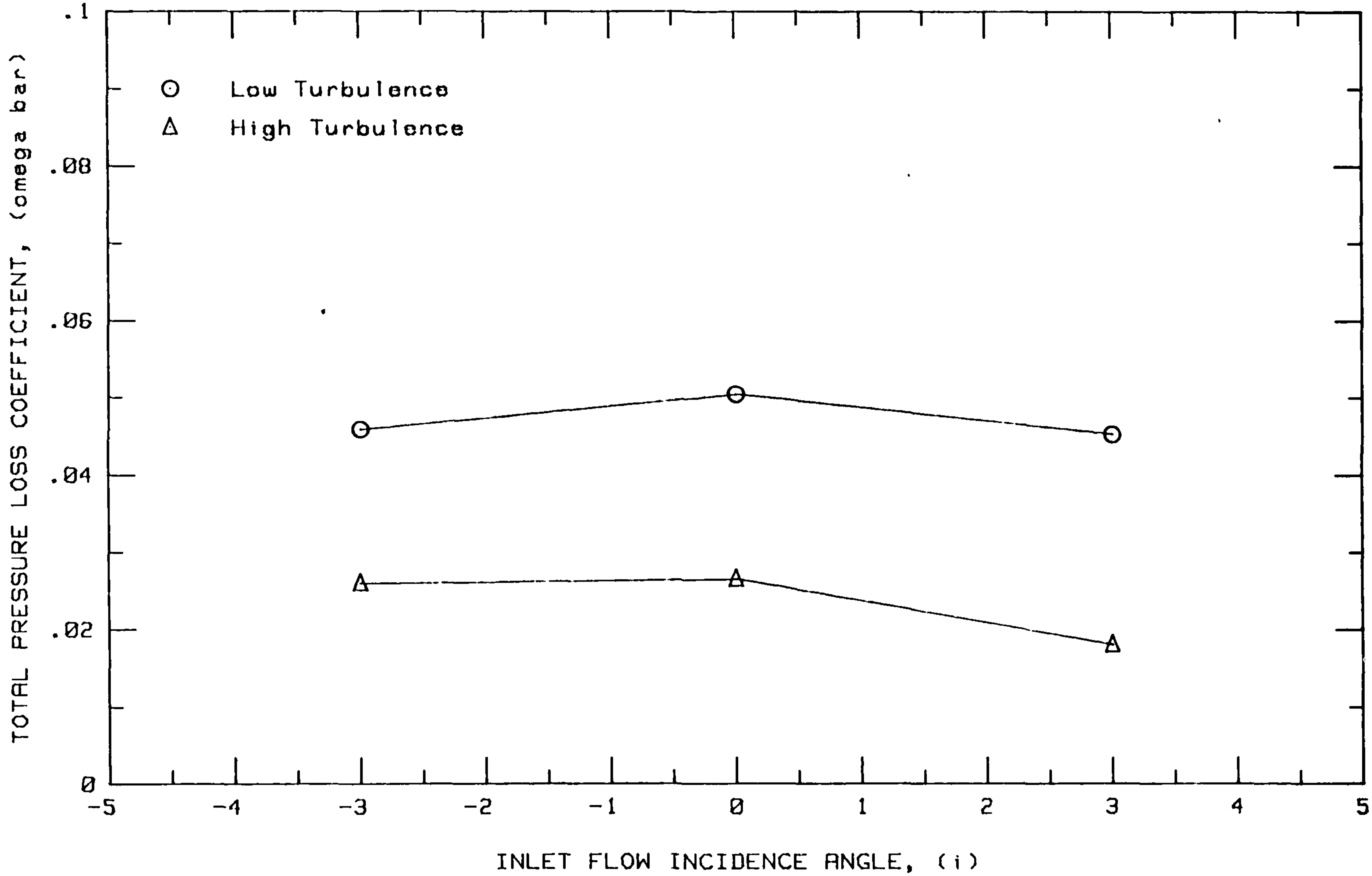

Fig. 16. Change in Total Pressure Loss Coefficient, X/C = 0.625

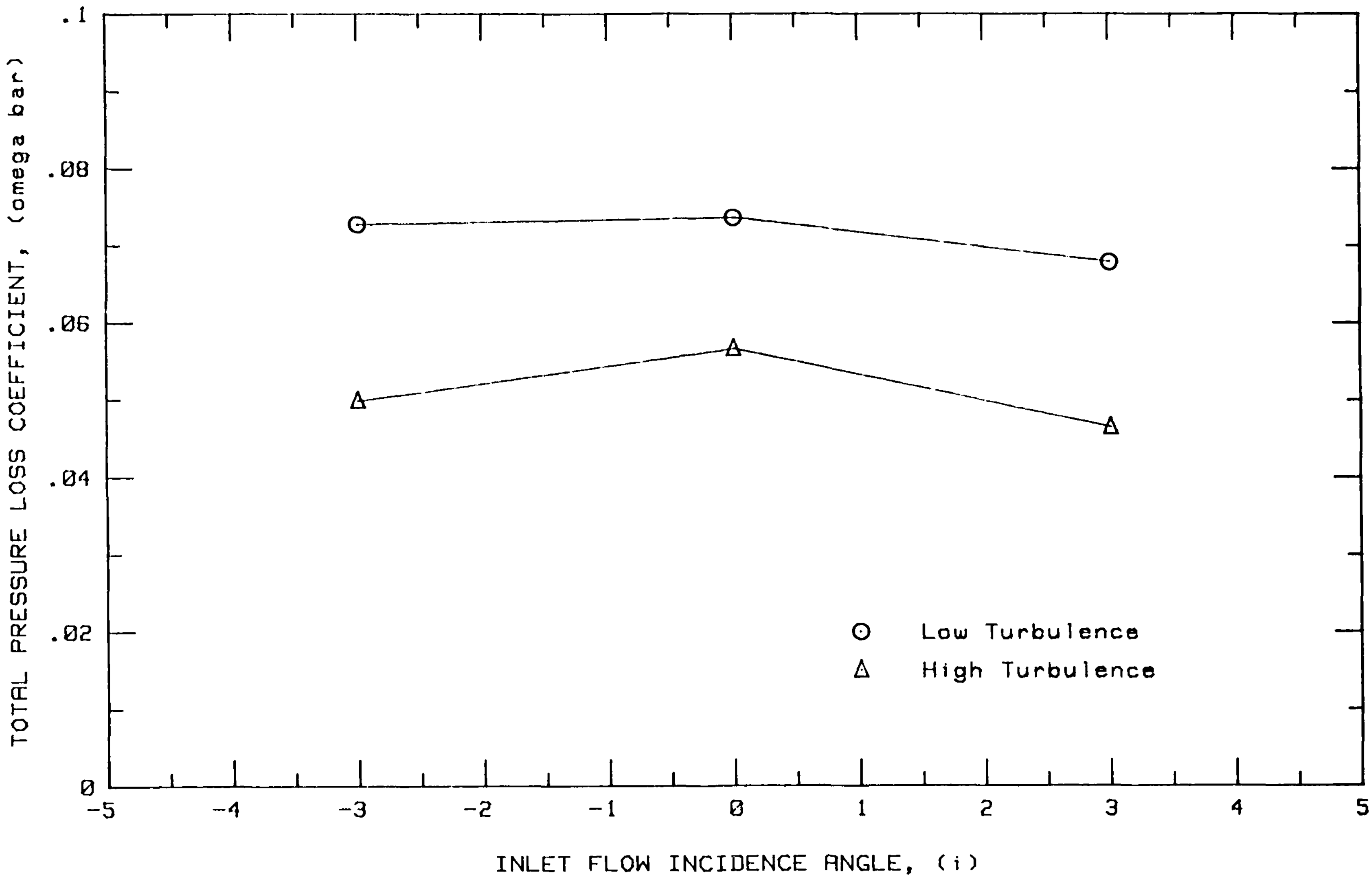

Fig. 17. Change in Total Pressure Loss Coefficient, X/C = 1.125

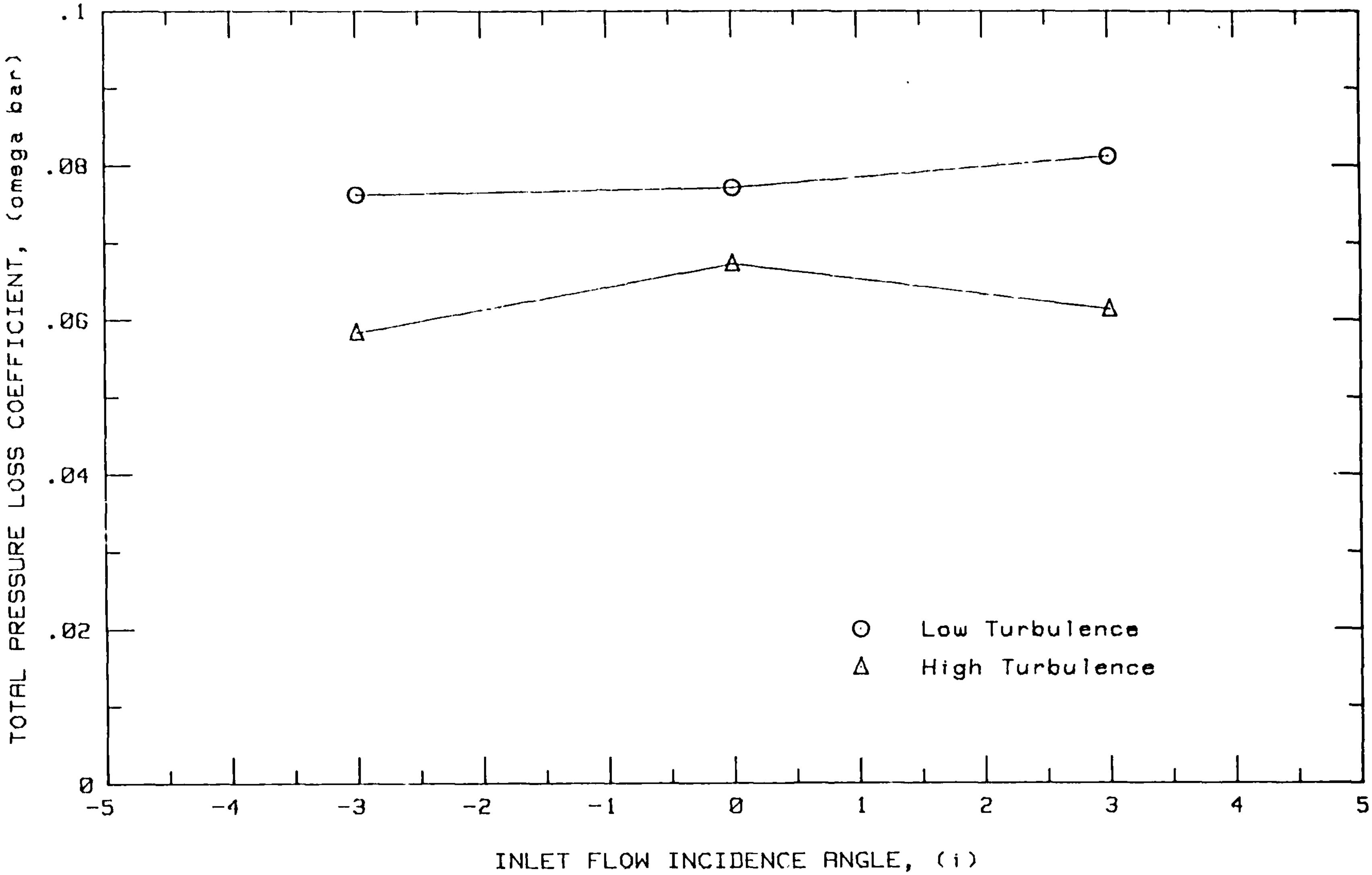

Fig. 18. Change in Total Pressure Loss Coefficient, X/C = 1.625

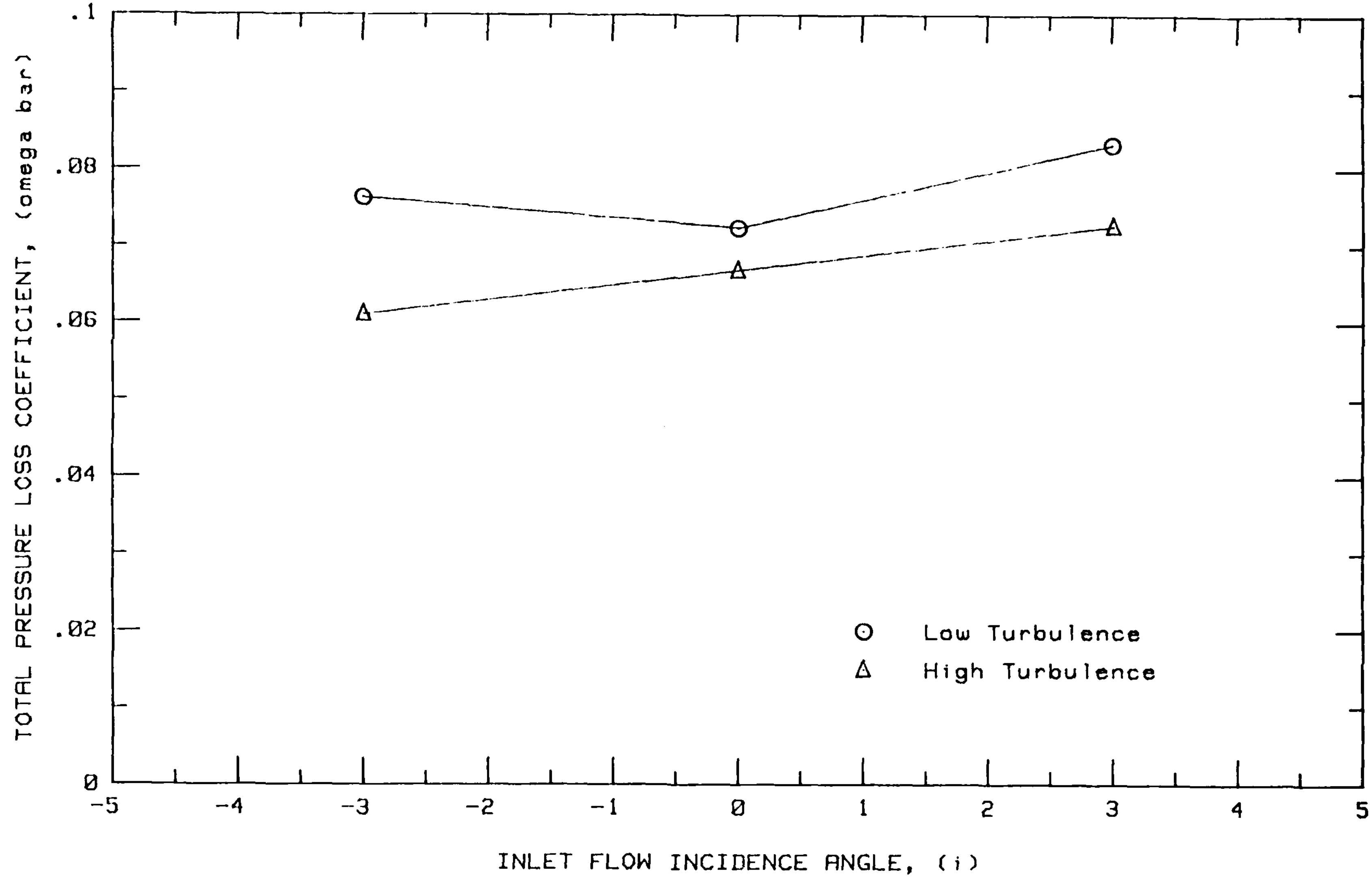

Fig. 19. Change in Total Pressure Loss Coefficient, X/C = 2.125

present investigation are needed to determine if higher ultimate losses actually occur with increased free stream turbulence.

Lieblein (17) and Cohen and Rogers (7) both show that the total pressure loss coefficient does indeed vary with incidence. The familiar "bucket plots" of $\bar{\omega}$ versus incidence angle are not shown in the present investigation. This is because of the relatively narrow range of incidence angles studied. An investigation of the current blades over a wider range of both positive and negative incidence angles is necessary to show where losses begin to increase with increase of positive and negative incidence.

The values of loss coefficient shown in Figure 19 and Table II, for the most downstream traverse, are most representative of the total pressure loss both through the cascade and by mixing in the wake. The variation of the low turbulence data with distance downstream suggests that the limiting values for total pressure loss have nearly been reached. This is not as evident for the high turbulence data. There is still a significant increase in $\bar{\omega}$ between traverse locations 1.625 and 2.125. This increase implies that for high free stream turbulence the wake takes longer to mix with the free stream. Longer mixing time consumes more energy, thus ultimately higher values for $\bar{\omega}$ may result with higher free stream turbulence. Again, an in-depth analysis of wake turbulence intensities is needed to confirm this.

Finally, studies of this nature have often determined a minimum-loss incidence angle for the cascade blades under investigation. Seymour Lieblein points out that this angle is positive for zero camber blades and decreases with increasing positive camber. He also states that this angle is characterized by the absence of large velocity peaks with their subsequent decelerations on either blade surface (18:577). In the current investigation, a conclusive minimum loss incidence angle was not established for the cascade. The pressure surface of the blade was not examined to determine a velocity profile; moreover, note the apparent trend shown by Figure 19. For low turbulence, the $\bar{\omega}$ plot indicates a minimum-loss incidence angle near 0 degrees. For high turbulence however, the plot shows a steady decrease in $\bar{\omega}$ with decreasing incidence. This trend suggests that the addition of high free stream turbulence may have an effect on the minimum loss incidence angle for the current blades. More testing over a wider range of incidence angles is necessary to establish this trend conclusively.

Turbulence Intensity. For the low free stream turbulence runs, the measured local turbulence intensity in the wake increased as incidence angle was increased. This increase varied from an average of 6% at $x/c = 0.625$ to 4% at $x/c = 2.125$. , the turbulence plots are shown with the velocity wake profiles in Appendices C through H. Free stream turbulence values for these runs averaged between 1

and 2 percent. The turbulence profiles remained symmetric for incidence angles of -3 and 0 degrees. However, at i = +3 degrees, the data shows an increase in turbulence intensity of about 1 percent on the pressure side of the blade. As a result, the plots show this change as a slight elongation. Additionally, the free stream turbulence vectors also seem to be influenced at the positive incidence setting. This influence seems to be in direction rather than magnitude.

At the +3 degree incidence setting, the flow "sees" the pressure surface slightly sooner than the suction surface. This may account for both the slight increase in turbulence intensity on the pressure side, and the change in the free stream turbulence direction. However, with the current cascade design, incidence angle, stagger angle, and angle of attack vary together. As the cascade geometry is changed, the flow area between blades is altered, and this may also be contributing to the effect. The same changes in turbulence intensity are observed at the high turbulence level runs. The increase in free stream turbulence between the low and high level tests averaged 5 percent. Corresponding increases in local turbulence intensities occurred at the 0.625 traverse point. The increases further downstream however, were progressively less then those associated with low free stream turbulence.

Suction Surface Pressure Distribution

Results. The pressures along the suction surface of the center blade were measured as discussed in Chapter IV. Figures 20 and 21 show the resulting pressure profile plots for low and high free stream turbulence respectively. Specifically, the pressure coefficient (C_p) was calculated using Equation 11, and plotted verses chord location. Each plot shows a representative profile from the -3, 0 and +3 degree incidence runs. As can be easily seen, the visible incidence angle effects were for the most part, limited to the first thirty percent chord of the blade. There appears to be a slightly larger effect beyond the 30 percent chord point at high free stream turbulence and a change of order of the curves.

Discussion. As incidence angle increases, the forward tap pressures drop substantially. This indicates a large increase in velocity at these points. Indeed, this is shown in the boundary layer velocity plots (to be discussed). Note the pressure curve at -3 degrees incidence. Although the pressures are slightly higher overall for the high turbulence run, (an effect also observed by Absar 1:51) the shape of the curves are virtually identical. The pressure rise and subsequent drop for the -3 degree incidence case at both turbulence levels, and the +3 degree incidence case at low turbulence suggests that some type of local separation and reattachment has occurred. Note also that for -3 degrees

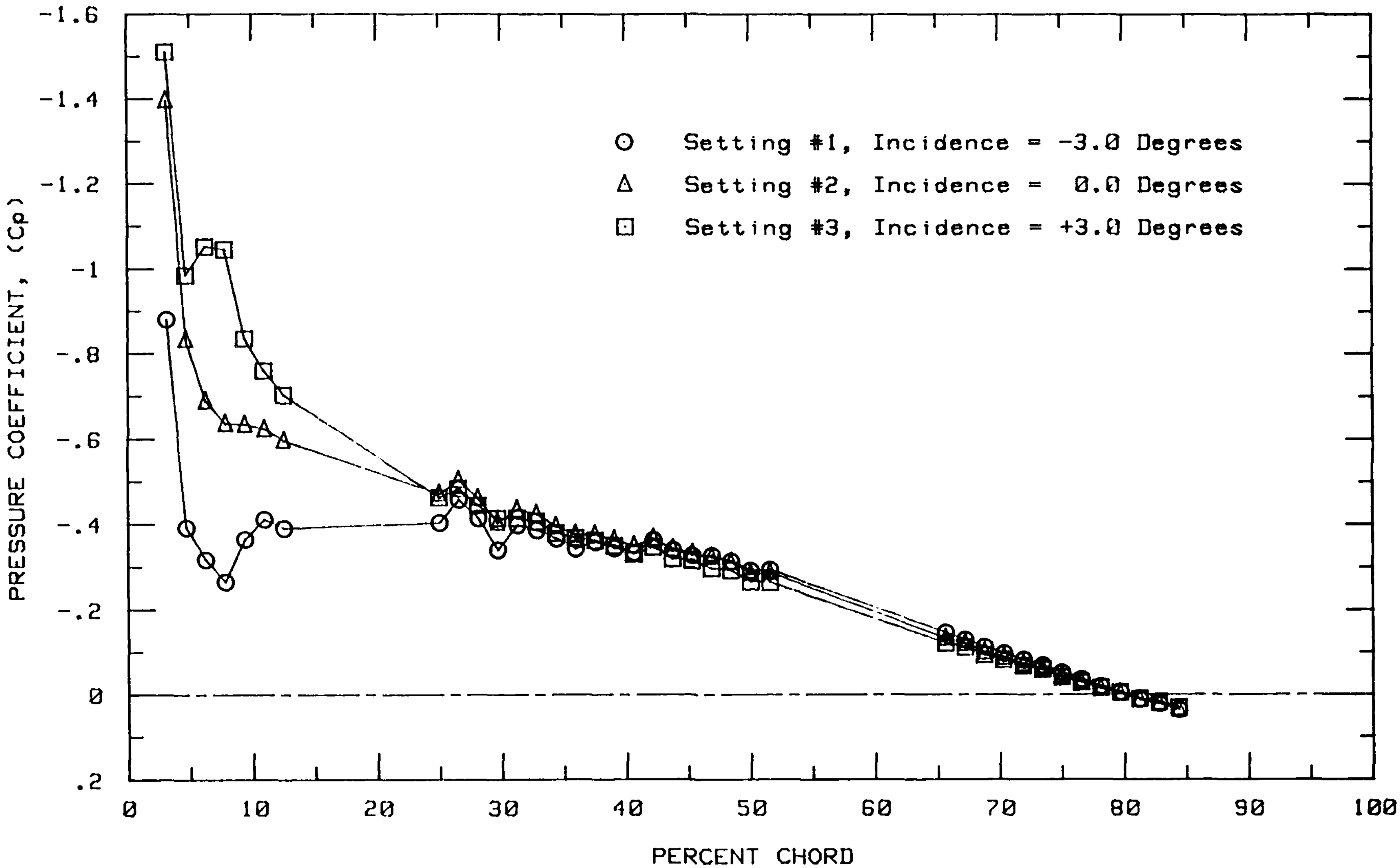

Fig. 20. Pressure Profile Comparison, Conf #2, Low Turbulence

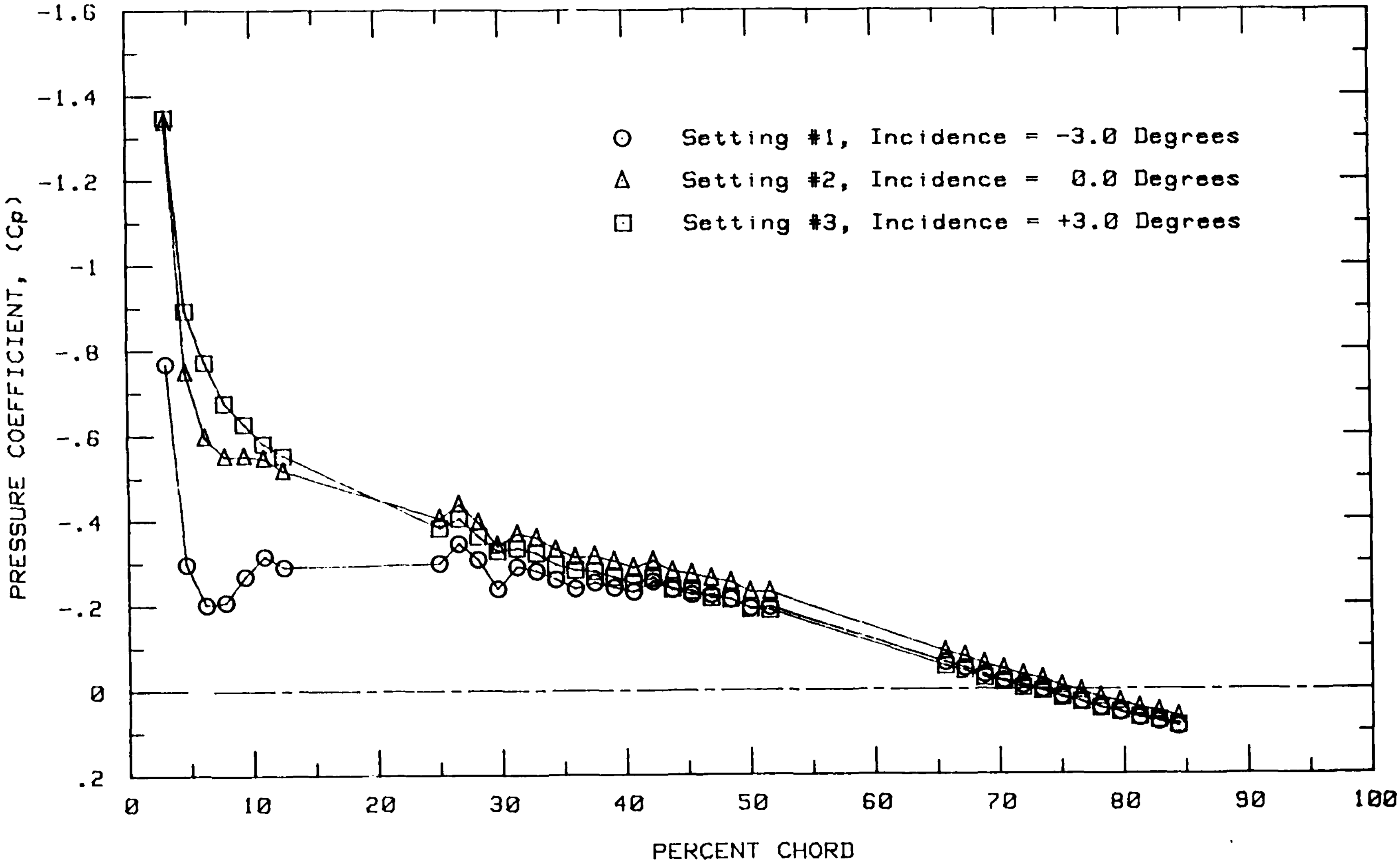

Fig. 21. Pressure Profile Comparison, Conf #2, High Turbulence

incidence between 10 and 30 percent chord, there is a region of essentially constant pressure (a relatively flat pressure profile). This suggests the presence of a separation bubble as described by Herrig, Emery, and Erwin (13:12). Unfortunately, attempts to probe this region with a hot film probe were inconclusive.

As incidence angle increases, the profile tends to smooth out. At +3 degrees incidence however, a pressure jump followed by a slight drop is again seen. This phenomenon was almost but not always repeatable. However, it appeared in most of the tests and again suggests that some type of flow separation is occurring near the leading edge of the blade. With high free stream turbulence, this pressure discontinuity was not observed at all.

As with the previous studies on these blades, a pressure fluctuation is observed between 25 and 30 percent chord. This fluctuation seems more pronounced at -3 degrees incidence but dampens out by the 50 percent chord point in all cases. Poulin suggests that this fluctuation may be caused by the method used to apply the surface roughness (23:46). Indeed this may be the case; however, the fluctuation previously discussed for the negative incidence curves is of similar appearance and directly over the roughened surface. The absence of pressure taps between the two points prevents one from determining if the two fluctuations are isolated, or part of the same effect.

Finally, the different pressure profiles provide information on the cascade optimum loading. It is generally felt that the suction surface pressure profile is triangular in shape under optimum loading (29:283). As incidence angle increases, the area under the pressure coefficient curve increases and the shape of the curve begins to form one leg of a triangle with the C_p axis and the percent chord axis serving as the other two legs. Thus the given profiles indicate that the blade loading is approaching optimum as incidence increases. A study over a wider incidence angle range would be necessary to determine a particular incidence angle that gives optimum blade loading. Such information is very useful in compressor design and particularly important when designing variable stator systems which must perform well over a wide incidence angle range.

Suction Surface Boundary Layer

Results. The center blade suction surface was investigated using a hot film boundary layer probe as discussed in Chapter IV. The resulting information is presented as a series of plots in Appendices I through N. The plots show the measured velocity profile (indicated by +), the results of the curve fit for the outer region points extrapolated to the wall (indicated by a dashed line), and the composite velocity profile calculated from Equation 12. Additionally, a comparison edge velocity computed from an

average of several curve fits for each traverse is shown as an E on the plot. Each velocity plot is accompanied by its respective turbulence intensity plot The plots are arranged in order similar to the wake traverse plots. The -3 degree incidence plots are presented first for both low and high free stream turbulence, followed by the Ø degree and + 3 degree plots. Also, selected boundary layer parameters are presented in Table III for low turbulence runs and Table IV for the high turbulence runs.

Discussion. Previous investigations using this facility have accrued much information on the boundary layer. However, these studies were limited in how close the boundary layer probe could be brought to the blade surface. In most cases, the boundary layer probe was maintained a minimum of .Ø3Ø inches from the surface. In the current study, traverses were also done using this same standoff distance. However, several repeat runs were conducted at standoff distances estimated to be as close as .ØØ5 inches to the blade surface. In contrast, traverses made at the +3 degree incidence setting could be done no closer than .Ø6Ø inches to the surface. This was due to increased probe vibration at this setting. An additional boundary layer traverse was added at 16.5 percent chord to selected runs. This was done in an attempt to detect any flow separation or other phenomenon over the area of the blade surface where the pressure fluctuations were observed.

Table III

Boundary Layer Parameters

Low Free Stream Turbulence

Incidence (DEGREES)	Chord (%)	U_E (FT/S)	$\frac{U_E}{U_1}$	δ_{BL} (IN)	δ_{TI} (IN)
-3	4.6875	592.86	1.264	---	---
	9.3750	601.44	1.282	---	---
	16.5175	----	----	---	---
	25.0000	614.26	1.310	---	---
	29.6875	612.60	1.306	---	---
	34.3750	611.44	1.304	---	---
	40.6250	606.92	1.294	---	---
	45.3125	603.61	1.287	---	---
	50.0000	599.56	1.278	.0038	.0045
	65.6250	570.21	1.216	.0158	.0131
	70.3125	559.96	1.194	.0198	.0174
	75.0000	550.02	1.173	.0292	.0269
	79.6875	541.84	1.155	.0364	.0309
	84.3750	533.44	1.137	.0602	.0397
Ø	4.6875	647.33	1.357	---	---
	9.3750	642.46	1.347	---	---
	16.5175	627.01	1.314	---	---
	25.0000	625.49	1.311	.0075	.0083
	29.6875	620.39	1.309	.0124	.0103
	34.3750	616.30	1.292	.0143	.0124
	40.6250	608.62	1.276	.0197	.0190
	45.3125	601.38	1.261	.0192	.0191
	50.0000	593.90	1.245	.0231	.0218
	65.6250	564.66	1.184	.0372	.0356
	70.3125	555.65	1.165	.0452	.0413
	75.0000	545.73	1.144	.0507	.0497
	79.6875	537.77	1.127	.0597	.0561
	84.3750	533.60	1.119	.1076	.0639
+3	4.6875	715.28	1.501	.0799	---
	9.3750	688.16	1.444	---	---
	16.5175	633.71	1.330	.0659	---
	25.0000	641.28	1.346	.0711	.0708
	29.6875	633.57	1.330	.0756	.0758
	34.3750	627.37	1.317	.0787	.0835
	40.6250	616.45	1.294	.0844	.0896
	45.3125	609.90	1.280	.0873	.0925
	50.0000	601.18	1.262	.0906	.0976
	65.6250	571.43	1.199	.1135	.1178
	70.3125	563.66	1.183	.1270	.1281
	75.0000	557.35	1.170	.1393	.1386
	79.6875	548.48	1.151	.1476	.1460
	84.3750	572.14	1.201	.2779	.1577

Table IV

Boundary Layer Parameters

High Free Stream Turbulence

Incidence (DEGREES)	Chord (%)	U_E (FT/S)	U_E / U_1	δ_{BL} (IN)	δ_{TI} (IN)
-3	4.6875	592.05	1.231	---	---
	9.3750	602.79	1.253	---	---
	16.5175	----	----	---	---
	25.0000	616.30	1.281	---	---
	29.6875	616.44	1.282	---	---
	34.3750	616.89	1.283	---	---
	40.6250	611.93	1.272	---	---
	45.3125	609.81	1.268	.0128	.0060
	50.0000	604.20	1.256	.0220	.0109
	65.6250	576.86	1.199	.0740	.0422
	70.3125	569.98	1.185	.1003	.0434
	75.0000	558.51	1.161	.1143	.0560
	79.6875	551.88	1.147	.1489	.0690
	84.3750	542.07	1.127	.1587	.0812
Ø	4.6875	652.23	1.342	---	---
	9.3750	642.51	1.322	---	---
	16.5175	----	----	---	---
	25.0000	621.77	1.279	.0329	---
	29.6875	615.81	1.267	.0371	---
	34.3750	611.81	1.259	.0395	---
	40.6250	604.84	1.245	.0412	.0302
	45.3125	597.72	1.230	.0425	.0359
	50.0000	591.83	1.218	.0515	.0408
	65.6250	562.52	1.157	.1027	.0642
	70.3125	576.96	1.187	.1973	.1133
	75.0000	562.95	1.158	.1991	.1185
	79.6875	563.50	1.159	.2677	.1265
	84.3750	553.88	1.140	.3128	.1387
+3	4.6875	724.50	1.483	.0723	---
	9.3750	691.45	1.415	.0732	---
	16.5175	645.21	1.321	.0742	---
	25.0000	651.31	1.333	.0917	.0727
	29.6875	643.17	1.317	.0952	.0770
	34.3750	636.23	1.302	.1043	.0805
	40.6250	623.53	1.276	.1052	.0873
	45.3125	616.33	1.262	.1045	.0889
	50.0000	608.93	1.247	.1161	.0923
	65.6250	581.43	1.190	.1722	.1185
	70.3125	572.58	1.172	.1944	.1292
	75.0000	563.63	1.154	.2123	.1410
	79.6875	560.72	1.148	.2527	.1508
	84.3750	550.39	1.127	.2633	.1665

For those traverses where a boundary layer is detected, the velocity plots show the sharp drop-off close to the surface that is characteristic of a turbulent boundary layer. One can also see the curvature in the inviscid velocity profiles near the leading edge, as shown in Figures 105, 133, and 159. As incidence or free stream turbulence increases, thicker boundary layer profiles are seen. The profiles also show the various offset distances used. Some plots seem to actually go below the blade surface. This was due to an intermittent plotter error. One very interesting event can be seen on the plots made at the 65 and 70 percent chord point with high free stream turbulence and -3 degrees incidence (Figures 95 and 97). A small but distinct bulge in the profile is indicated at approximately .020 inches from the surface. This bulge apparently disappears prior to the plot at 75 percent chord. The bulge appeared only on one particular test and was not repeatable.

Edge Velocities. The dimensionless edge velocities are listed in Tables III and IV for low and high free stream turbulence. Also, Figures 22 and 23 show these values plotted for each incidence angle verses percent chord.

The edge velocity is an important parameter. Under constant mass flow conditions, the edge velocity is a fair indicator of boundary layer thickness changes. The blade boundary layers actually restrict the flow through the cascade. The thicker the boundary layer, the greater the

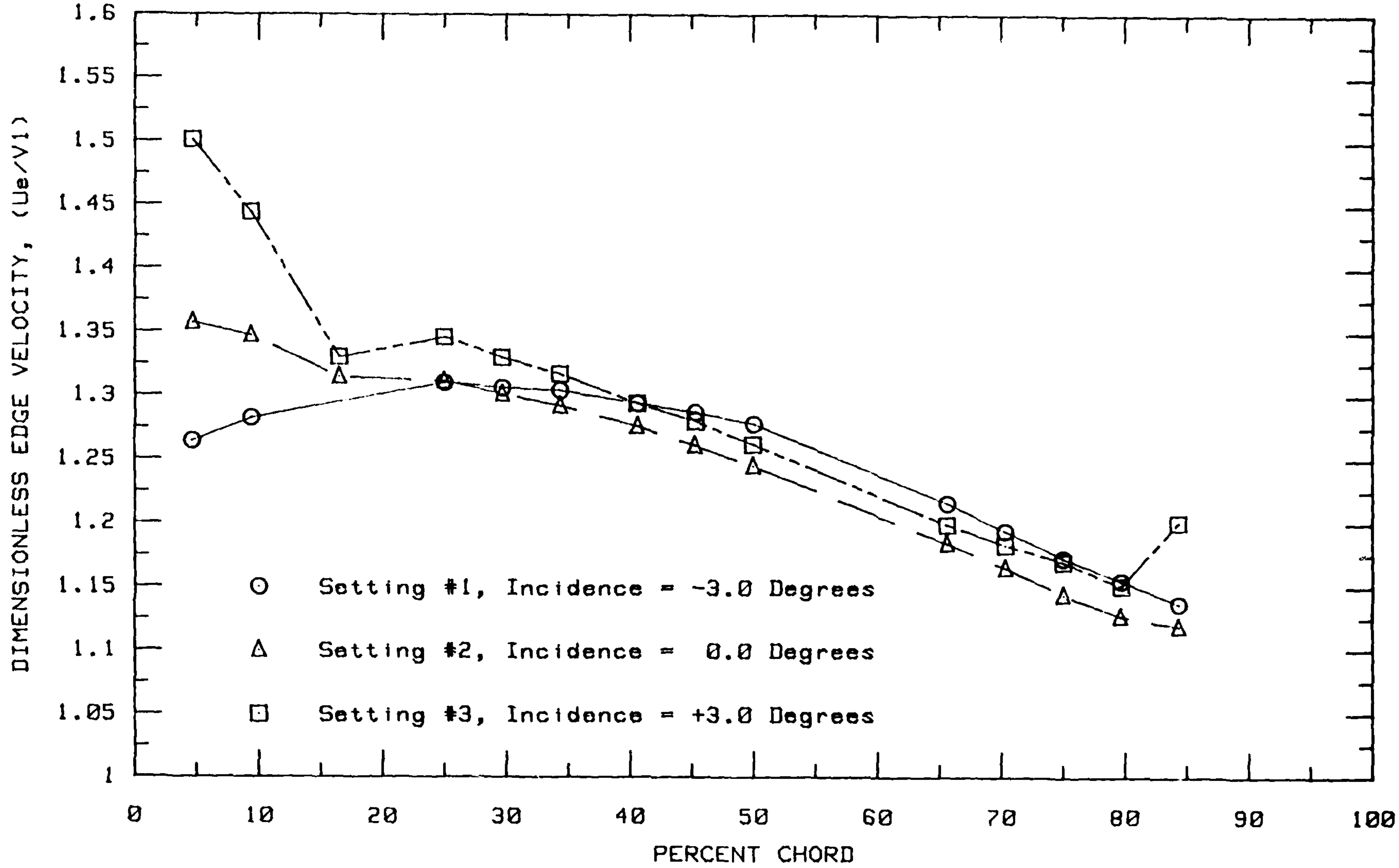

Fig. 22. Boundary Layer Edge Velocity Along the Suction Surface, Low Turbulence

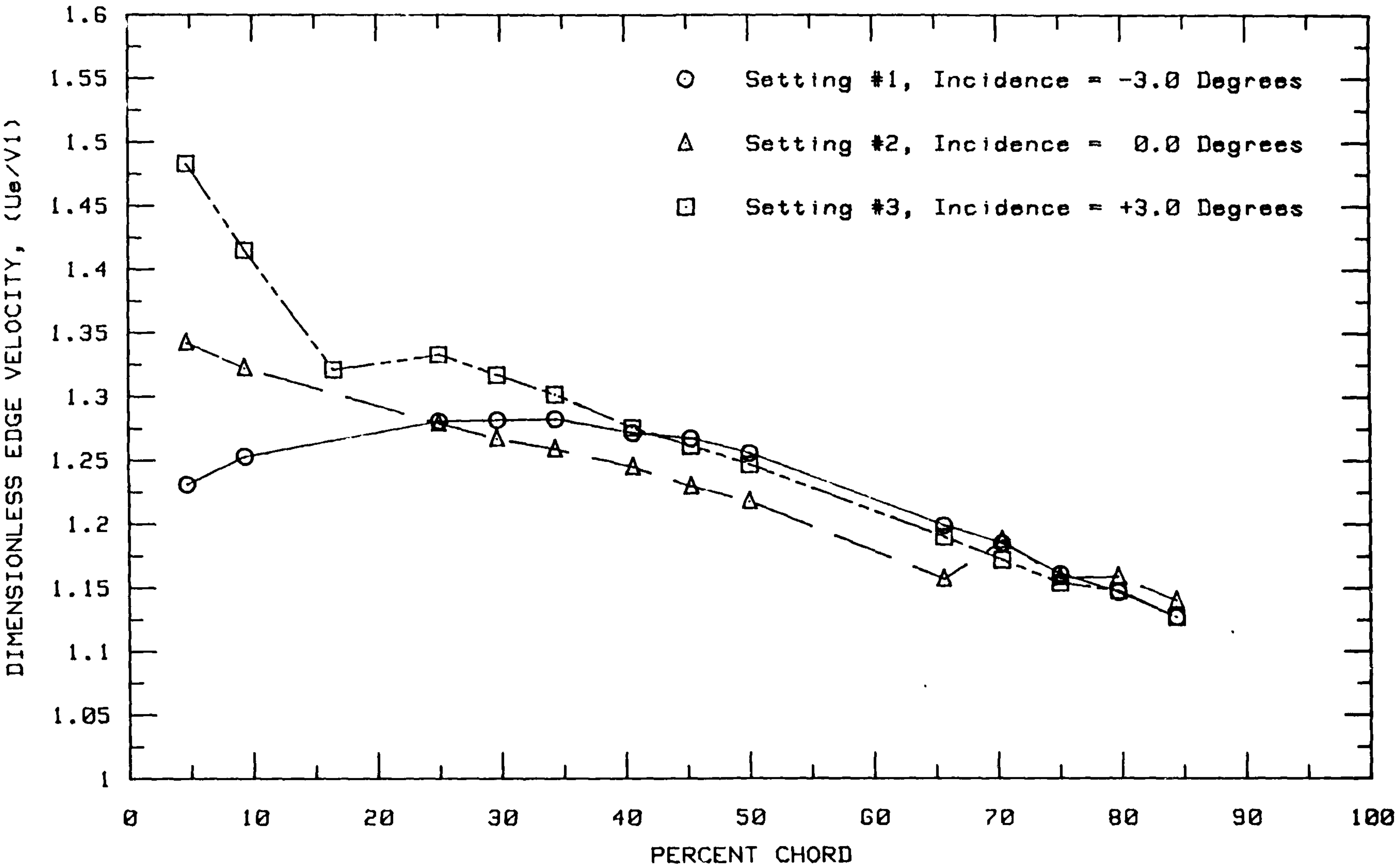

Fig. 23. Boundary Layer Edge Velocity Along the Suction Surface, High Turbulence

restriction. In order to maintain the same mass flow through the restricted channel, the flow velocity increases. Thus an increased edge velocity is an indicator that a thicker boundary layer is present. However, the current cascade design causes a change in flow area as the blades are moved. Specifically, as incidence angle increases, flow area increases. This undoubtedly influences the edge velocity and probably the boundary layer growth. The extent of this effect however, could not determined in the current investigation.

The plots show the same trends with increasing incidence for both low and high free stream turbulence, although the edge velocities overall are one to three percent lower with high free stream turbulence. This reduction in V_E with additional turbulence is in apparent contradiction to findings by Absar (1), using the same blades. An explanation may be a defect found within the modified test section during the course of the investigation. The initial data collected was at the zero incidence setting. After this data was collected, the test section was removed and inspected. Several gaps in both end walls upstream of the cascade were discovered. They were sealed by the author and repeat runs were conducted. The edge velocities of these runs were on the average 10 to 15 feet per second slower than the initial run values. This difference brings the edge velocities into closer agreement with prior studies.

Of noteworthy interest is the edge velocity profile at -3 degrees incidence. For both low and high free stream turbulence, it indicates that edge velocity increases along the blade surface from 4.68 to about 30 percent chord. This increase in V_E coupled with the flat pressure profile for that configuration, reinforces the idea that some type of boundary layer separation and reattachment may be occurring. However, along the forward portion of the blade no boundary layer was detected at that incidence angle. A small area of increasing edge velocity is also observed for the + 3 degree incidence configuration between 15 and 25 percent chord. Overall, the data indicates that edge velocities increase with incidence over the forward half of the blade and tend to decrease slightly with incidence over the rear half of the blade.

Boundary Layer Thickness. Boundary layer thickness was calculated using Equation 13. The values are listed in Tables III and IV, and are plotted in Figures 24 and 25 for low and high turbulence. The effects of both incidence angle and free stream turbulence are readily seen. As Absar reported (1), increased free stream turbulence primarily affects boundary layer growth on the rear portion of the blade. Incidence angle however has a pronounced effect over the entire blade surface. At -3 degrees incidence, the boundary layer was not detected at all forward of the 45 percent chord point. As incidence angle is increased, the

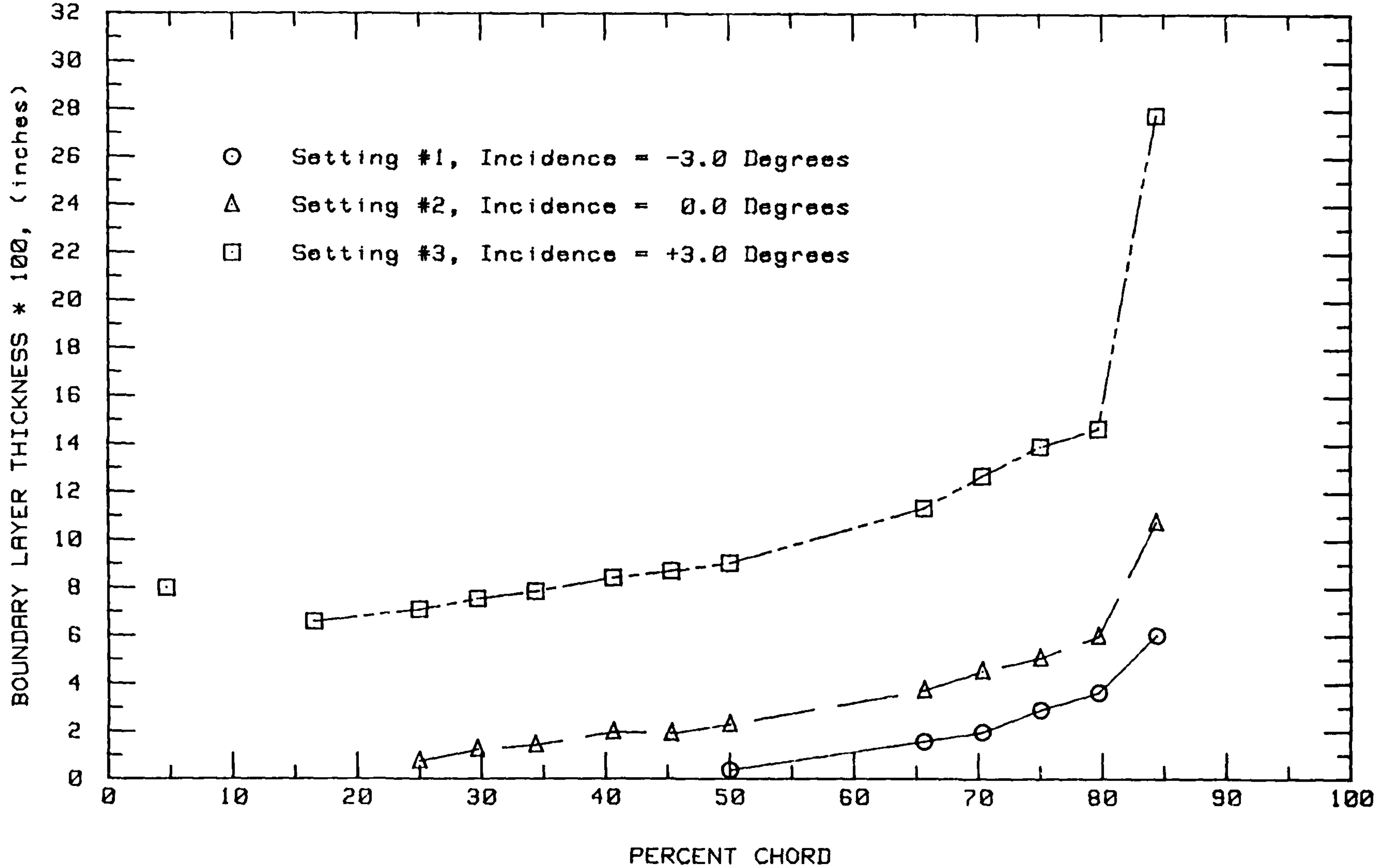

Fig. 24. Boundary Layer Growth Along the Suction Surface, Low Turbulence

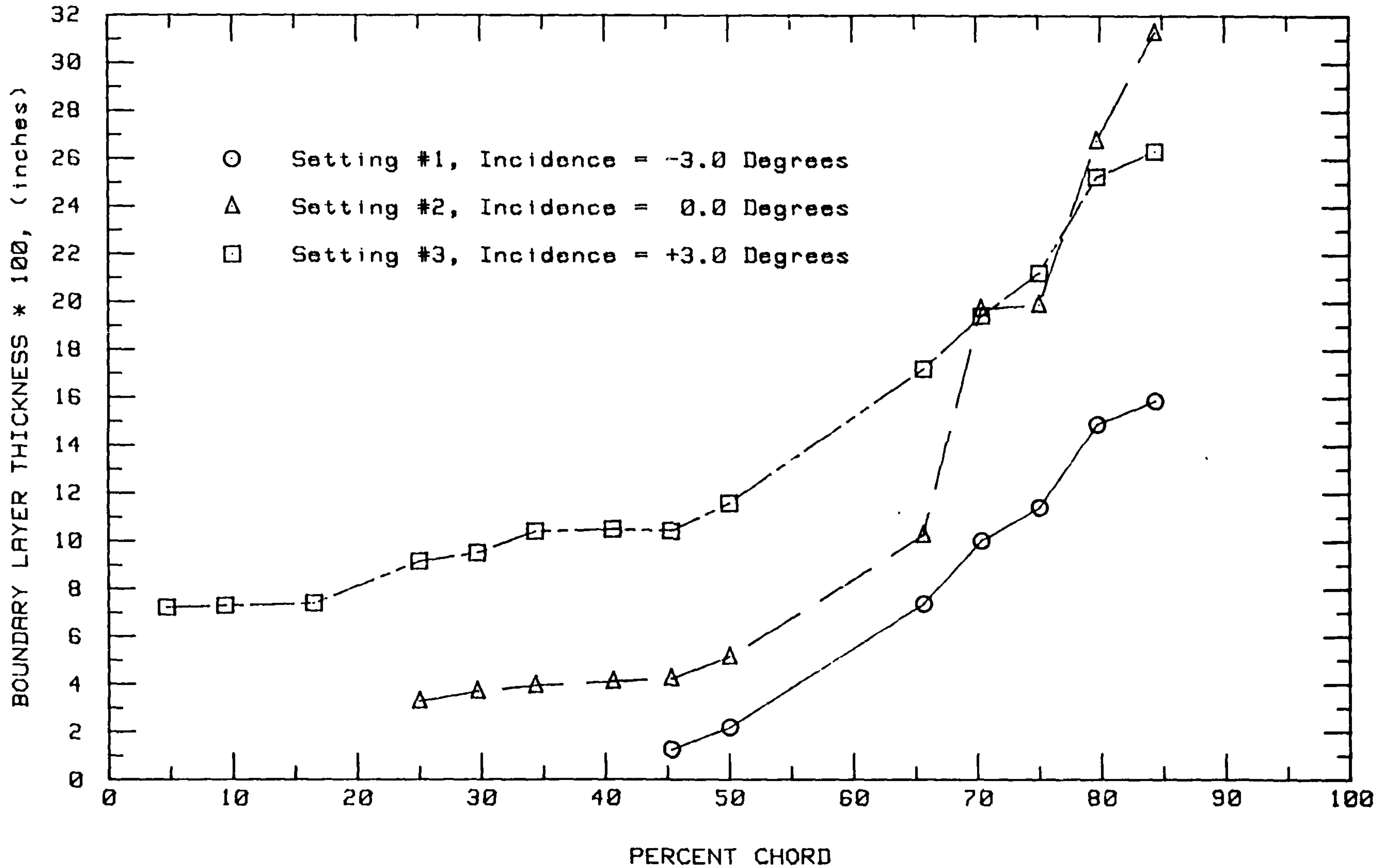

Fig. 25. Boundary Layer Growth Along the Suction Surface, High Turbulence

boundary layer thickens rapidly and becomes detectable farther forward on the blade. This information coupled with the increased edge velocities and steep pressure profile indicates that the boundary layer may be transitioning from laminar to turbulent farther forward on the blade. No conclusions can be drawn with respect to a possible transition point. However, at -3 degrees incidence with low turbulence, the presence of a boundary layer is detected at 4 percent chord (see Table III). This boundary layer is not detected again until 16 percent chord. Additionally, the suction surface pressure profile for this configuration (Figure 20) shows a pressure rise followed by a slight reduction between 5 and 10 percent chord. This information suggests possible separation and reattachment near the 4 percent chord point. More tests would be necessary to conclusively show this. One final comment on the thickness profiles. It seems that at +3 degrees incidence the boundary layer is on the verge of complete separation at the 84% chord in the low turbulence plot. This can be seen by the marked increase in thickness and steep curve slope. High free stream turbulence seems to delay this effect somewhat.

Local Turbulence Intensity. The local turbulence intensity for each boundary layer traverse was plotted verses distance above the blade surface. These plots are co-located with their respective velocity plots in Appendices I through N. As expected, turbulence intensities close to the surface

were high. As the probe moved away from the surface, they decreased to the levels associated with the free stream for the particular run being made. The distance from the surface where the turbulence intensity first increased was used in Equation 14 to calculate a comparison boundary layer thickness (δ_{TI}). These values are listed in Tables II and III. The values obtained using Equation 14 do not generally agree with those obtained from Equation 13. Equation 14 was formulated for use with an equilibrium boundary layer (23:56). Since the suction surface boundary layer is subject to an adverse pressure gradient, the general lack of good agreement between boundary layer thicknesses is not unexpected. However, in the high free stream turbulence tests, a rhythmic variation in intensity as a function of distance away from the blade is shown. The variance is as great as one percent and is most noticeable on the plots near the trailing edge of the blade at -3 degrees incidence. At first it was thought that this was caused by traverser error. However, the error is along the percent turbulence intensity axis and not along the distance axis. It is believed that this effect is present in the flow, and is a result of the method used to create the high free stream turbulence.

<u>Closure</u>.

The purpose of this study was to investigate the effects of incidence angle and free stream turbulence on the

performance of a two-dimensional cascade. The variable geometry approach was used with the additional objective of gaining some insight on the advantages of variable geometry compressor design. Indeed, both incidence angle and free stream turbulence influence cascade performance in the present effort. Equally important however is the fact that such influence, with intensive study, may be used to develop more efficient compressor designs. The variable stator systems already in use show the viability of variable geometry designs. The limited scope of this investigation does not allow for many concrete conclusions to be made, but as Cohen and Rogers point out, testing of variable geometry designs (stators in particular) must be done to optimize their performance (7:218). It is to this end that the current effort is dedicated.

VI. Conclusions and Recommendations

Conclusions

Based on the information obtained, within the scope of this investigation the following conclusions are made.

1. General. Free stream turbulence levels have significant effect on the performance of the two-dimensional, variable geometry cascade, while incidence angle does not.

2. Specific.

a. Cascade losses as measured by the total pressure loss coefficient do not significantly change with increases in incidence angle.

b. The addition of free stream turbulence reduces loss through the cascade, and may increase losses in the wake.

c. Velocity recovery downstream near the blade trailing edge is decreased by both the addition of free stream turbulence and an increase in incidence angle.

d. Wake thickness is increased with both higher free stream turbulence and increased incidence angle. This effect due to incidence angle is initially delayed with increased free stream turbulence.

e. Local turbulence intensity both near the blade surface and within the wake increases with incidence and additional free stream turbulence.

f. Incidence angle effects on the suction surface pressure distribution are generally limited to the first thirty percent chord, while increased free stream turbulence influences the pressure distribution along the entire blade.

g. Boundary layer thickness along the suction surface increases with both increased free stream turbulence and increased incidence angle. This effect due to free stream turbulence occurs primarily after fifty percent chord, while this effect due to incidence occurs over the majority of the blade surface.

In addition, the following general observations are made:

1. An increase in free stream turbulence may influence the location of the minimum loss incidence angle of the investigated airfoils.

2. Increasing free stream turbulence suggests that mixing within the wake may be affected to a degree that influences the ultimate total pressure loss downstream.

3. The current results suggest that the change in mass flow through the cascade caused by the variable geometry design may be a parameter of interest in future investigations of this type.

4. The intrusive data collection methods used may have a effect on the cascade flow particularly in the suction surface boundary layer.

Recommendations.

As with all research, finding the answer to one question usually results in two or more being asked. This being the case several recommendations are appropriate.

The cascade, by design, is very small. Tests conducted by the author show that the flow is very sensitive to intrusive measurement methods. Specifically, the presence of the boundary layer probe near the blade had a marked effect on the suction surface pressure distribution. Given the temperamental nature of boundary layers, it seems likely that the probe may be inducing a substantial effect on the boundary layer flow. Thus consideration should be given to investigating the extent of such effects to determine whether developing less intrusive means to probe the boundary layer flow are required.

The current methods used to calibrate both the hot wire probes and pressure transducers are both time consuming and complicated. These procedures should be examined and simplified if possible.

The current study did not determine a minimum loss incidence angle, but evidence suggests that it may vary with free stream turbulence level. It would be of significant interest to investigate both where the minimum loss incidence angle occurs and what effect surface roughness and free stream turbulence have on it.

Next, this is the eighth investigation conducted using this facility. These investigations have gathered much useful information on compressor cascade studies. However, the values of loss parameters such as $\bar{\omega}$ seem to vary significantly from one investigation to the next. Of course, experimental technique and a host of other variables will cause the data to vary somewhat. Yet, with the modifications made to the system in recent years, a re-evaluation of the CTF's capabilities and data processing/reduction procedures may be needed.

Finally, it follows that an analysis of the previous investigations conducted using the CTF may be in order. Such an analysis might provide data correlations useful in compressor design research. At a minimum it would consolidate the research to date, pinpoint any problem areas, and provide possible direction for future efforts.

APPENDIX A: Component Listing

Component	Type/Model #
Pressure Transducers	
Tank Total Pressure	Statham PM60TC
Test Section Inlet Static	Statham P6TC
Test Section Exit Static	Statham P6TC
Ambient Pressure	CEC 4-326
Bridge Balance	CEC type 8-108
DC Power Supply	HP 6205C
Scanivalve System	
Pressure Transducer	PDCR 23D
Scanivalve	48S9-3003
Controller	CTLR 2/S2-S6
Scanner Position Display	J102/J104
Thermocouples	
Copper-constantan (4)	Omega T-type
Ambient Temperature	
Tank Total Temperature	
Calibrator Top Total Temperature	
Calibrator Bottom Total Temperature	
Traversing Mechanism	
Motors (2)	North American Phillips Controls K82952-M
Encoder Transducers (2)	Astrosystems MT28-1/10
Hot Wire/Film Anemometer System	
Anemometers (3)	TSI Model 1050
Monitor and Power Supply	TSI Model 1051-6
Oscilloscope	B&K Model 1570A
Boundary Layer Hot Film	TSI Model 1218-20
X-configuration Hot Film	TSI Model 1241-10
Boundary Layer Probe Support	TSI Model 1150-18
X-configuration Probe Support	TSI Model 1155-18
Calibrator (modified)	TSI Model 1125
Transformer (to heat air for calibrator)	General Radio Co. Variac Type 50-B
Data Acquisition System	HP 3052A
Computer	HP 9845B
Disk Drives (2)	HP 9885M HP 9885S
Channel Scanner	HP 3495A
Digital Voltmeter	HP 3455A
System Voltmeter	HP
Printer	HP 2225A
Plotter	HP 9872S

APPENDIX B: Calibration

Pressure Transducers

The five pressure transducers used in this study were calibrated using a two-point linear method. Each transducer was first exercised over its rated pressure range. Next, a low end and high end reference pressure was applied to each transducer and its individual bridge output voltage recorded. These voltages and pressures were then used to calculate the slope and intercept of a linear curve of psi vs voltage for each transducer. The curves were used in the data reduction process to determine pressures based on output voltages. Although linearity was assumed in the calibration, the current calibration values were automatically compared with the previous values. A change in either slope or intercept of two percent or more generated an error/warning message.

The reference pressures were provided by regulated, 100 psig compressed air or a vacuum pump as required. Positive reference pressures were measured by a 100 inch water manometer, and were assumed accurate to 0.05 inches (1/2 of a scale graduation). The highest reference pressure used was 69.2 inches of water (2.5 psig). Vacuum was measured by a 100 inch mercury manometer and was also assumed accurate to 0.05 inches.

Temperature Transducers

The copper-constantan "T-Type" thermocouples used in this investigation were not "calibrated" by the author. Rather, each thermocouple voltage output was converted to temperature using a referencing program provided with the data acquisition system (14:8.78-8.85).

Hot Film Probes

The hot film probes used in this research were calibrated using an automated procedure developed by Rivir and Vonada (35). Because of the CTF design, and the length of each test, the air temperature within the test section varied considerably during a given run. Thus, an individual calibration curve for a specific temperature (typically 30 to 40 degrees above ambient) would not provide sufficient accuracy. Consequently, each hot film probe was calibrated over a range of temperatures and velocities.

The constant temperature anemometer was used in this investigation. The theory of operation of this device is presented in detail by Bradshaw (4:106-133), and will be briefly reviewed here.

Hot wire anemometry involves solving a heat transfer problem. The sensing element, usually a fine platinum or tungsten wire, or a tungsten coated quartz rod (called a film), is maintained at a constant temperature by an electrical potential (E_o). This is usually accomplished by

incorporating the sensor into one leg of a bridge circuit as shown in Figure 26.

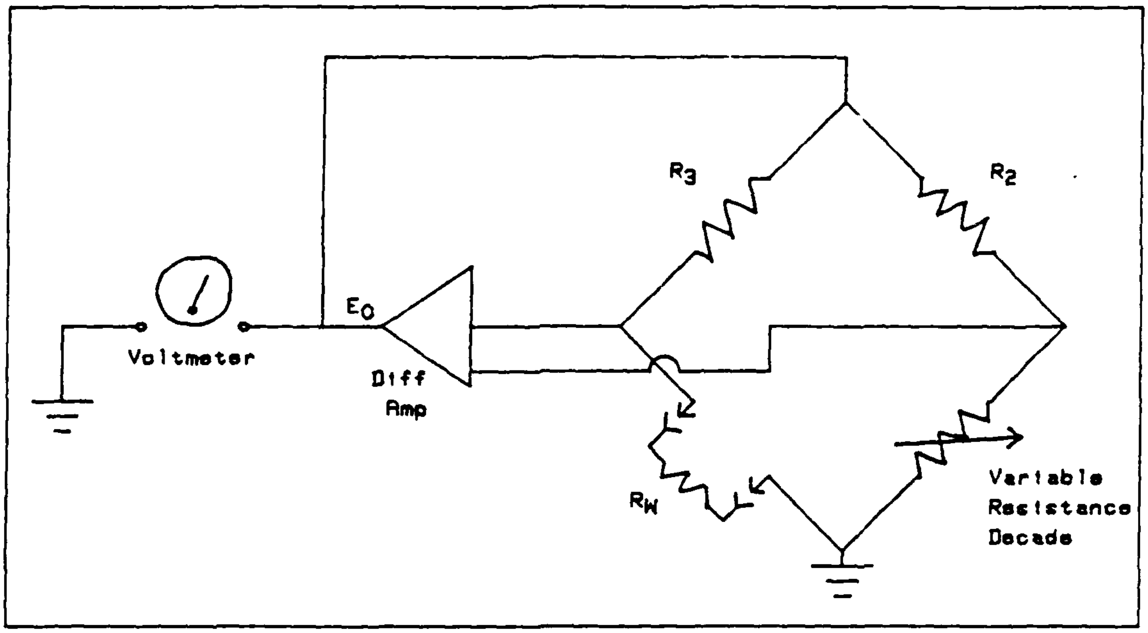

Fig. 26. Simplified Schematic of the Anemometer Bridge Circuit

When it is exposed to the flow of interest, heat is transferred between it and the flow. This transfer changes the sensor temperature and thus its resistance. Since the sensor is part of a bridge circuit, a voltage change occurs across the two legs of the bridge. A differential amplifier senses this voltage change and increases or decreases E_o as required to maintain the original bridge voltage. This has the effect of maintaining the sensor at its original temperature and resistance.

As the flow velocity changes, so does the heat transfer

rate of the sensor. Thus, a relationship exists between the anemometer voltage (E_o), the sensor resistance (R_w), and the sensor heat transfer characteristics. The Nusselt number (Nu) may be used to interpret the heat transfer relationship between the sensor and the flow (16:268). Thus, using the Nusselt number, one can develop a straightforward equation that models the sensor behavior in the flow. This relationship was worked out in detail by Poulin (23:86-87) and modified by Absar (1:70). It is an expression for the Nusselt number based on the sensor characteristics, flow characteristics, and anemometer voltage. This approach is advantageous, for once the Nusselt number is determined, one of several calibration schemes may be used to determine flow velocity at any point of interest within the test section. For the present case, this relationship is given as:

$$Nu = \frac{E_o^{2} R_w}{k_t \pi L (R_w + R_3 + R_c)^2 (T_w - T_o)} \tag{15}$$

where:

E_o = Anemometer Voltage

R_w = Film Resistance at operating temperature

k_t = Air Thermal Conductivity Coefficient

L = Film Length

R_3 = Bridge Resistance (upper leg)

R_c = Cable Resistance

T_w = Film (Sensor) Temperature

T_o = Flow Temperature

During the current investigation, this formula was modified slightly. The cable resistance (R_c) was modified to include the measured probe support and internal probe resistances.

With this formula in hand, one must now determine how the Nusselt number varies with flow velocity. This relationship has been the subject of extensive study and several empirical expressions have been developed (4:114). The form used for this study was first developed by King (4) and is given by:

$$Nu = A + B{*}Re^{N} \tag{16}$$

This formula, known as King's law, relates the Nusselt number of the sensor to the Reynolds number based on the sensor diameter using the constants A, B, and N. It defines a calibration curve with intercept A and slope B.

Bradshaw points out that there is usually a large difference between the sensor temperature and the fluid temperature. Thus a mean fluid temperature must be chosen (4:115). Based on the work of Collis and Williams, the final form of King's law becomes:

$$Nu\left(\frac{T_M}{T_o}\right)^{m} = A + BRe^{N} \tag{17}$$

where the term in parenthesis is a "temperature loading

factor". For the range of Reynolds numbers in this study, the exponent N was chosen to be 0.51, and the exponent m was chosen so that a linear regression analysis of the calibration data produced the smallest variance. The mean fluid temperature (T_M) is given by:

$$T_M = \frac{(T_W + T_O)}{2} + 0.22(T_{AW} - T_O) \qquad (18)$$

where T_{AW} is the equilibrium temperature of the sensor in the flow (also called Adiabatic Wall Temperature). The detailed calibration procedure is that used by Poulin (23:20-23,83-88). Sample calibration curves are shown in Figures 27 and 28.

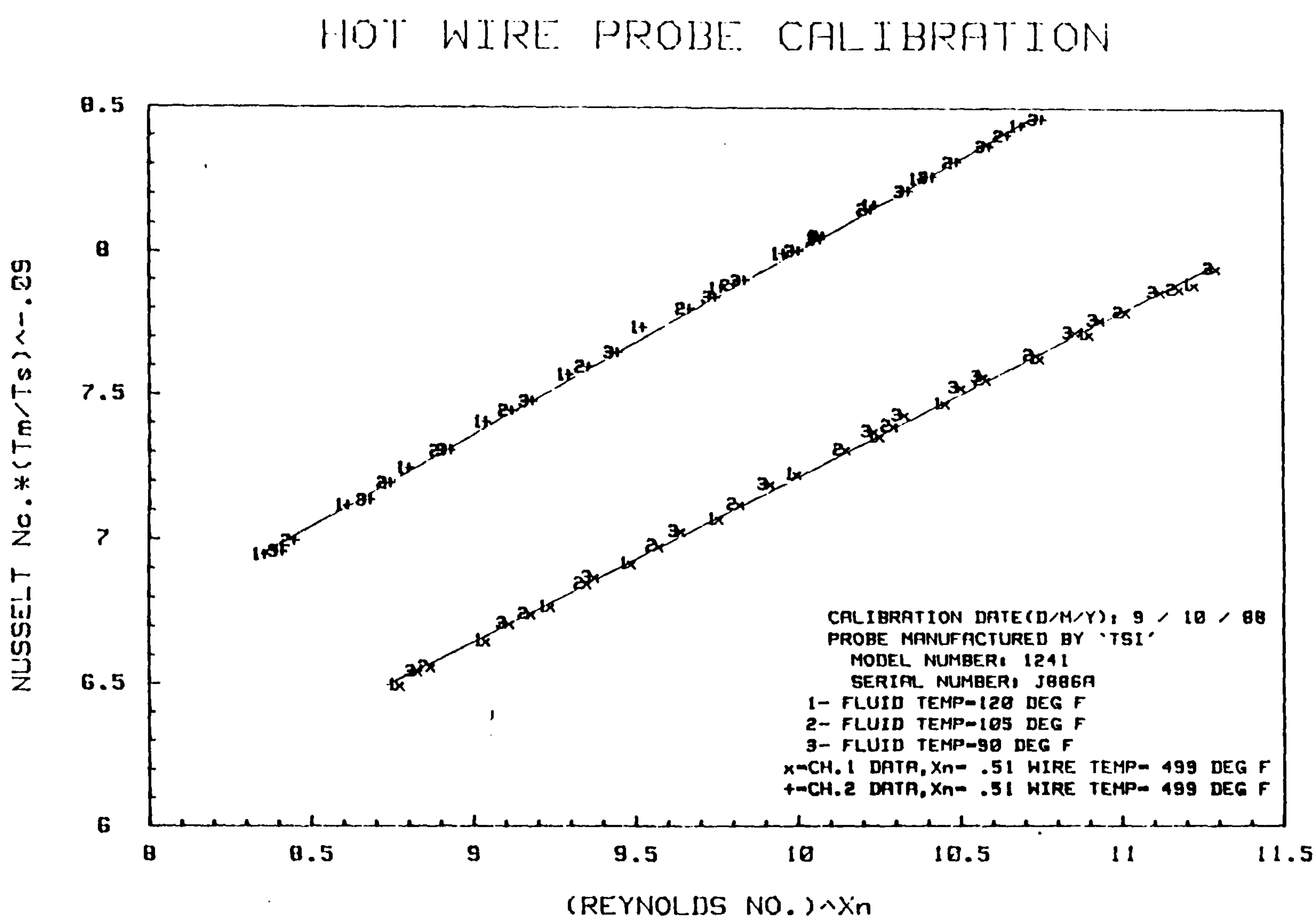

Fig. 27. Example X-Configuration Hot Film Calibration Curve

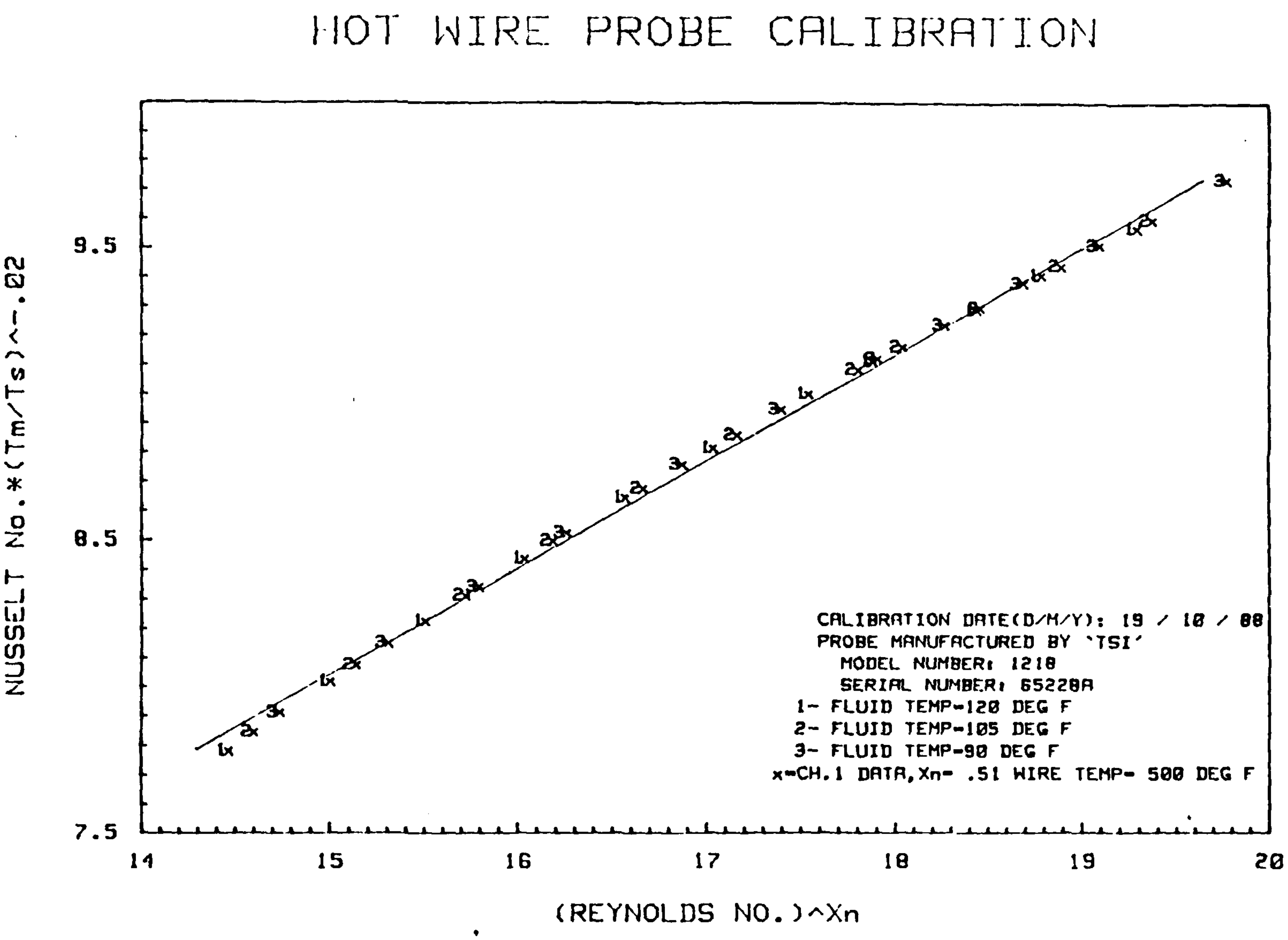

Fig. 28. Example Boundary Layer Hot Film Calibration Curve

Appendix C

Wake Velocity and Turbulence Intensity Profiles

Blade Configuration Number 2

Incidence Angle = -3.0 Degrees

Low Free Stream Turbulence

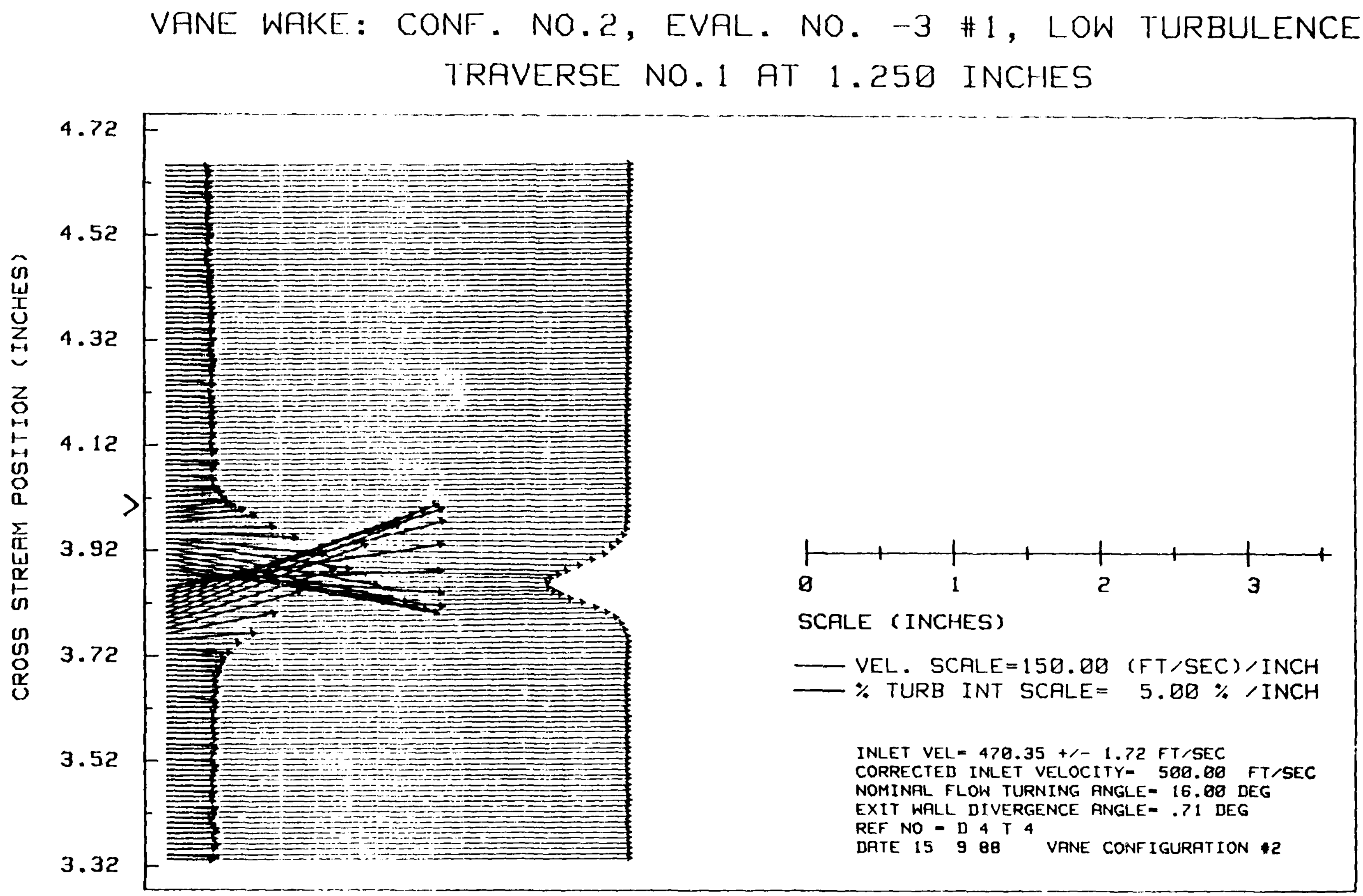

Fig. 29. Wake Velocity and Turbulence Intensity Profiles, Conf.#2, x/c = 0.625

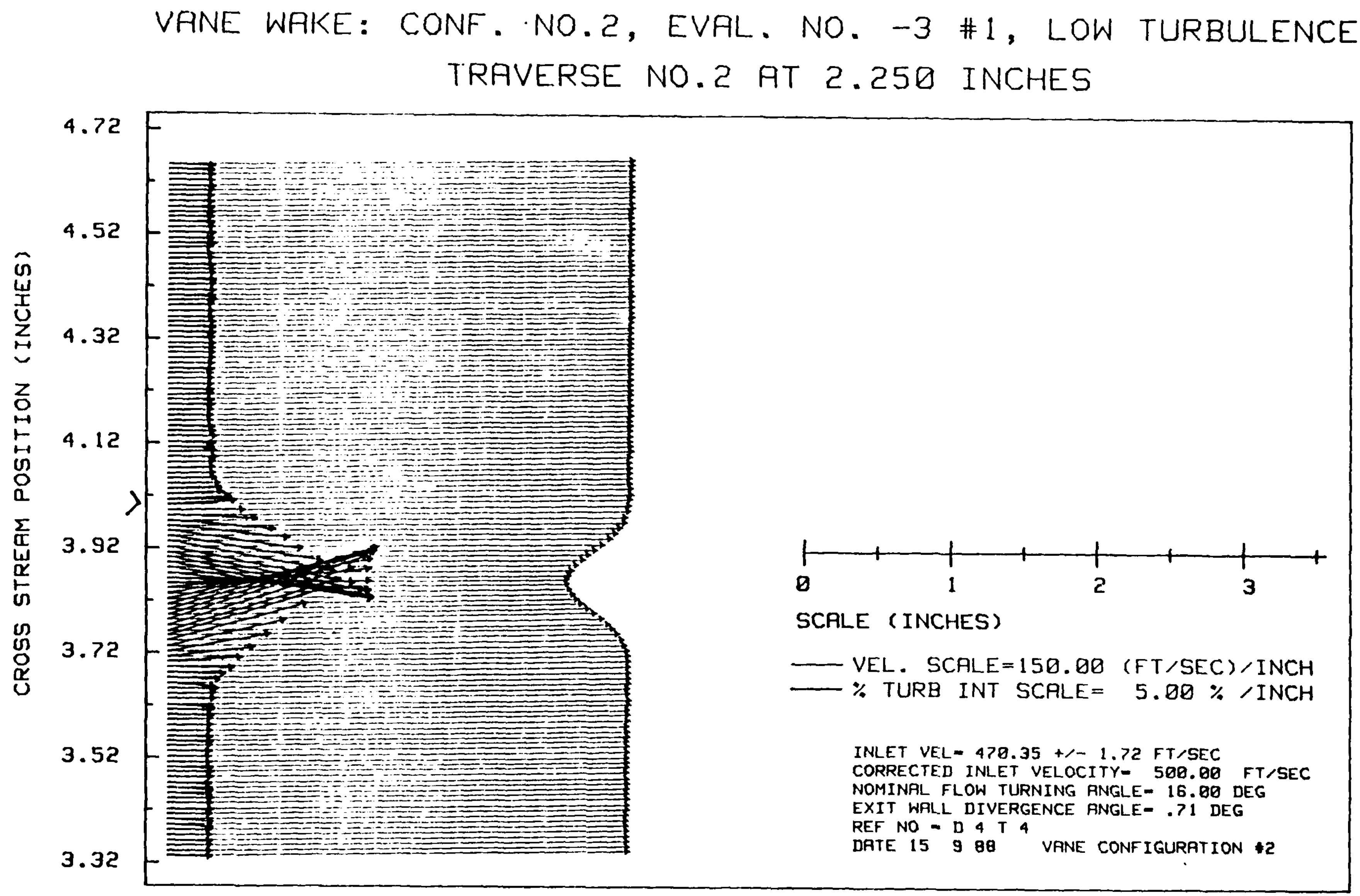

Fig. 30. Wake Velocity and Turbulence Intensity Profiles, Conf.#2, x/c = 1.125

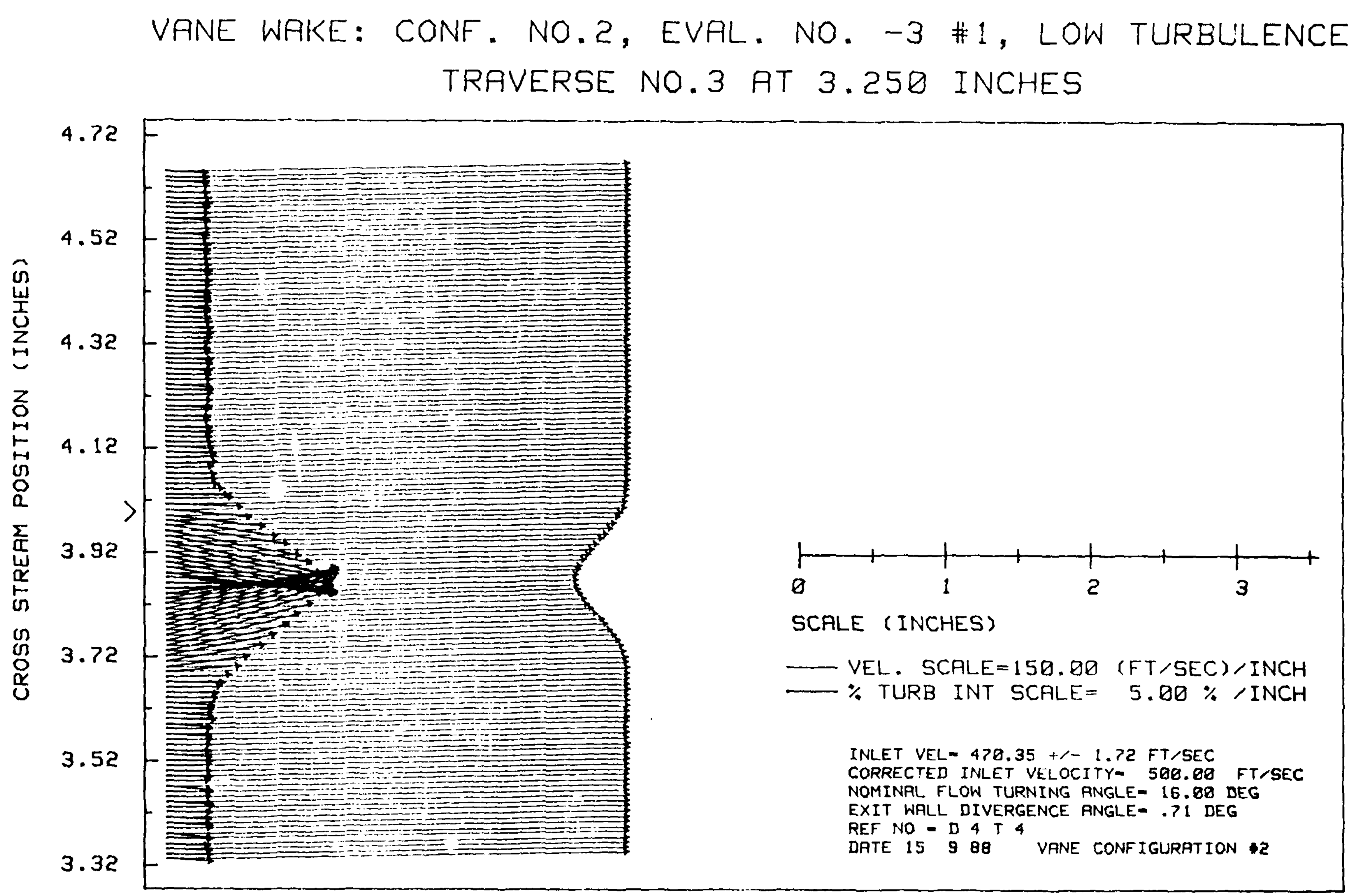

Fig. 31. Wake Velocity and Turbulence Intensity Profiles, Conf.#2, x/c = 1.625

VANE WAKE: CONF. NO.2, EVAL. NO. -3 #1, LOW TURBULENCE
TRAVERSE NO.4 AT 4.250 INCHES

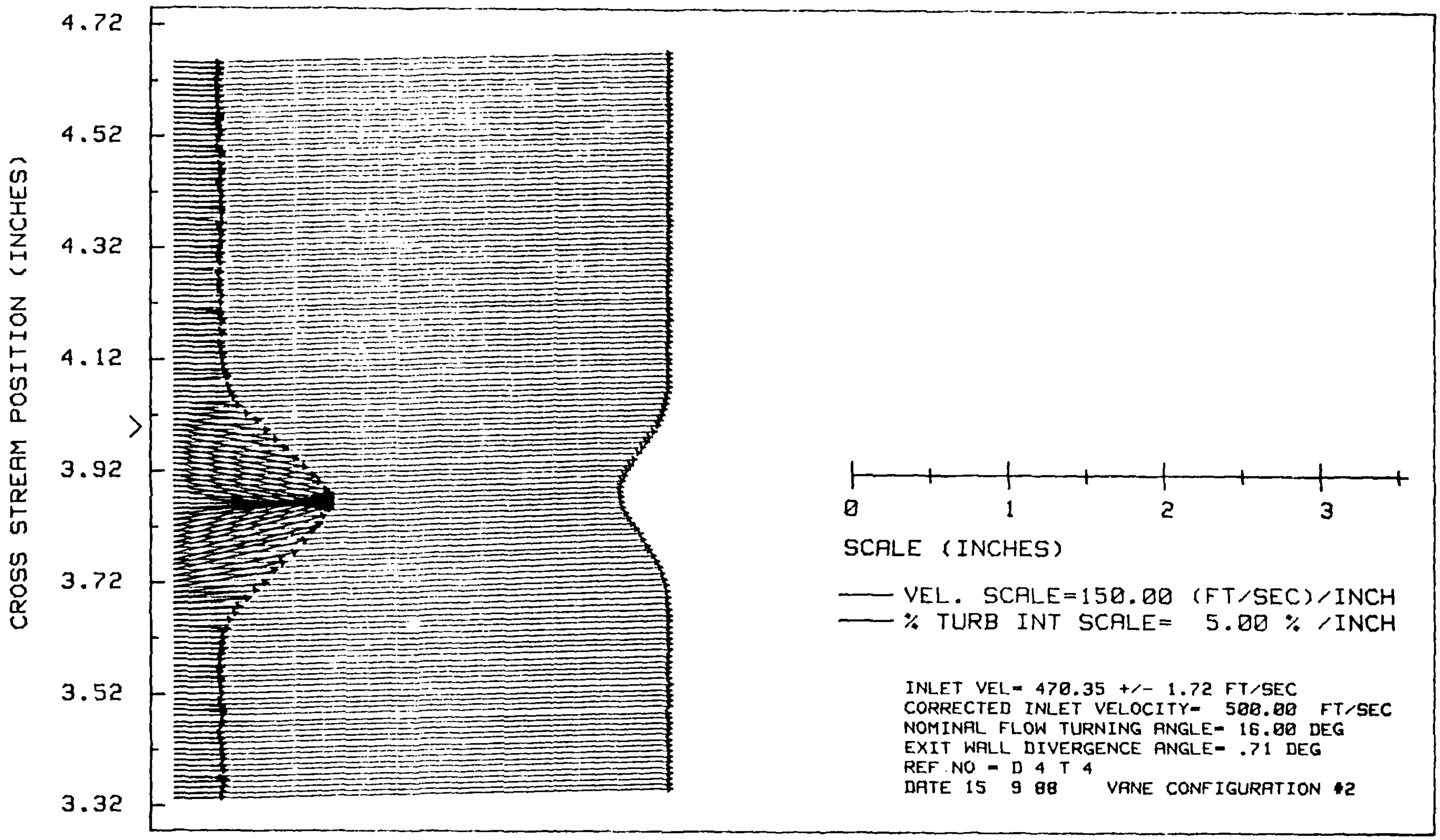

Fig. 32. Wake Velocity and Turbulence Intensity Profiles, Conf.#2, x/c = 2.125

Appendix D

Wake Velocity and Turbulence Intensity Profiles

Blade Configuration Number 2

Incidence Angle = -3.0 Degrees

High Free Stream Turbulence

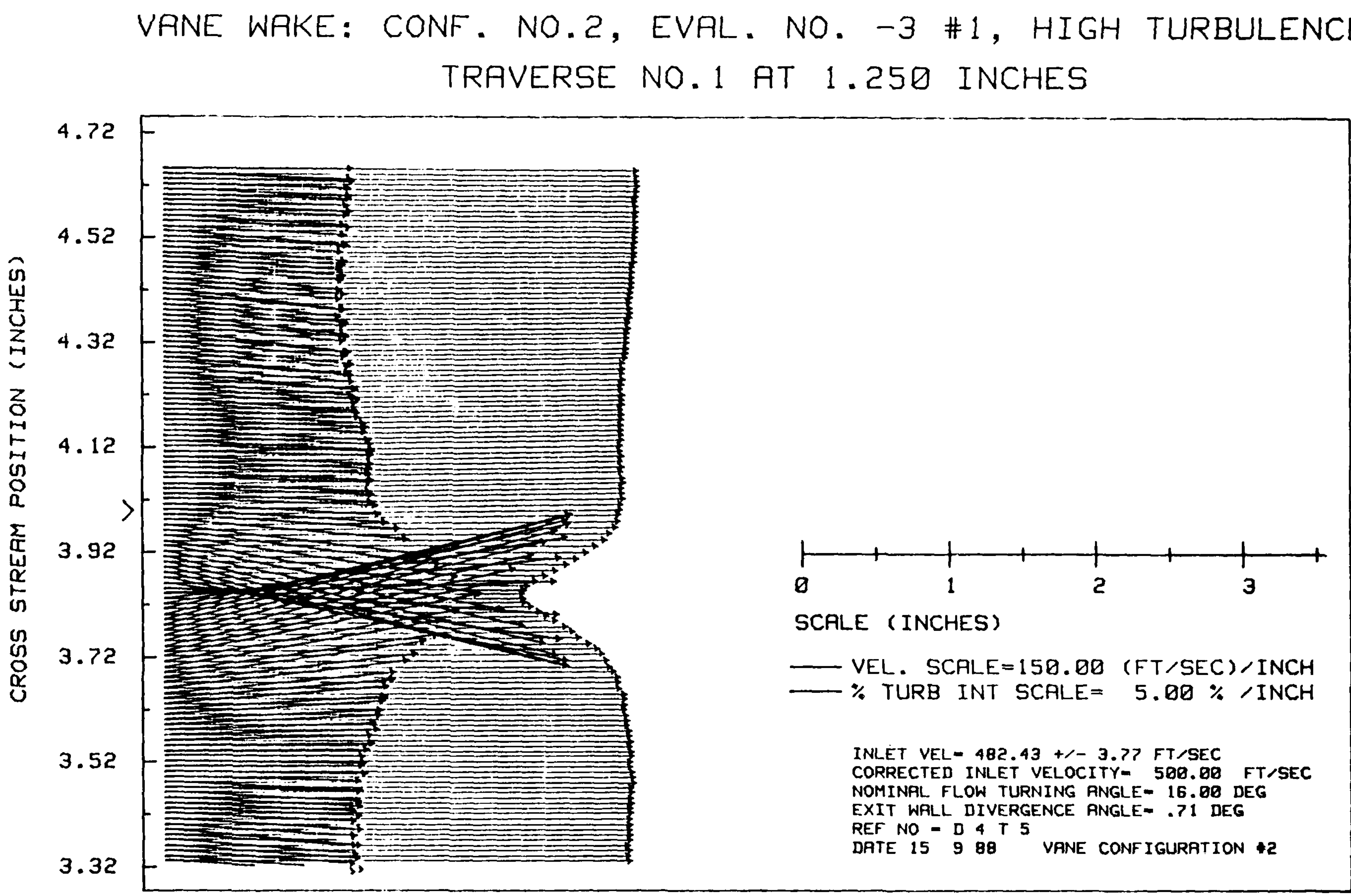

Fig. 33. Wake Velocity and Turbulence Intensity Profiles, Conf.#2, x/c = 0.625

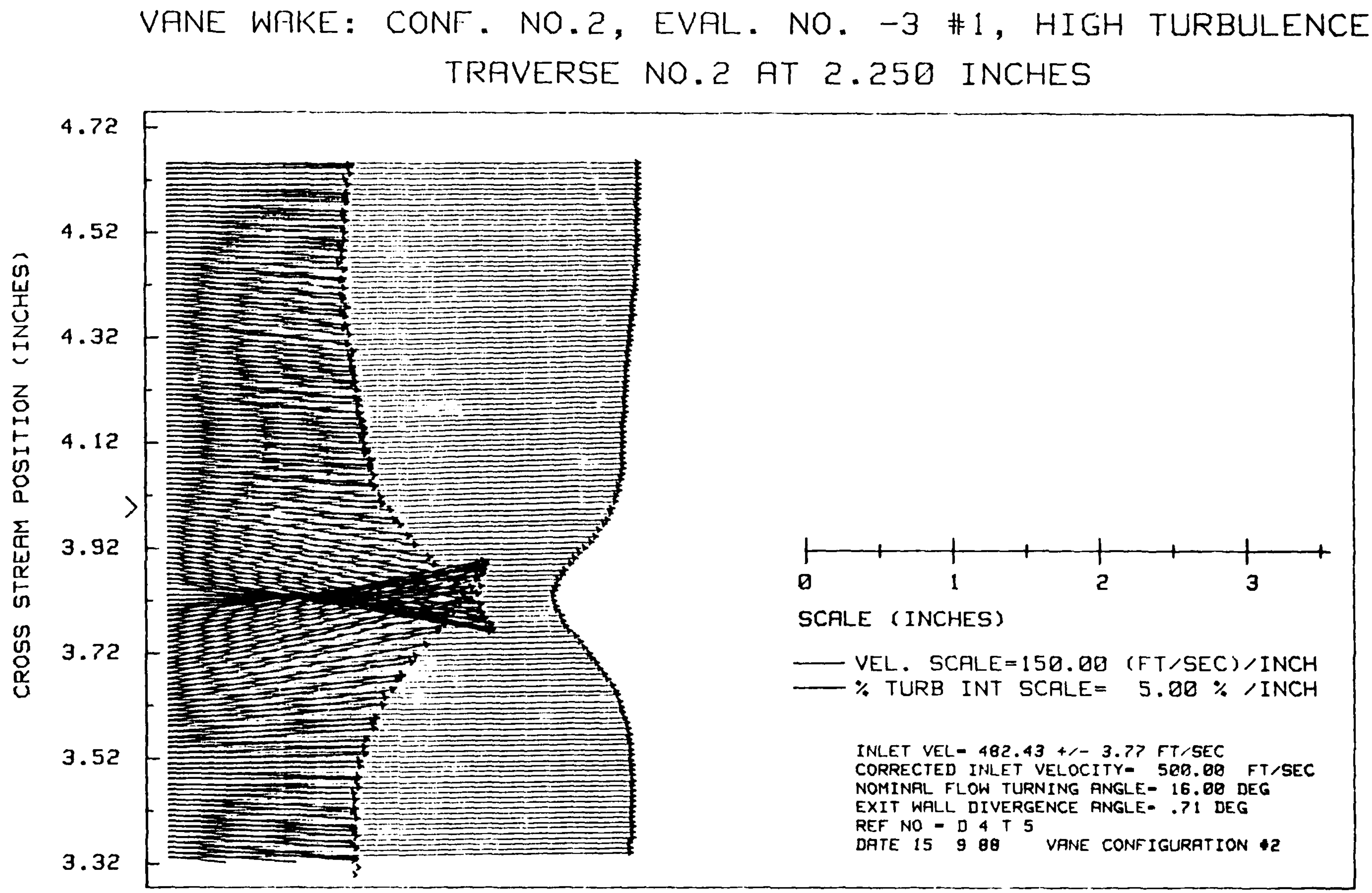

Fig. 34. Wake Velocity and Turbulence Intensity Profiles, Conf.#2, x/c = 1.125

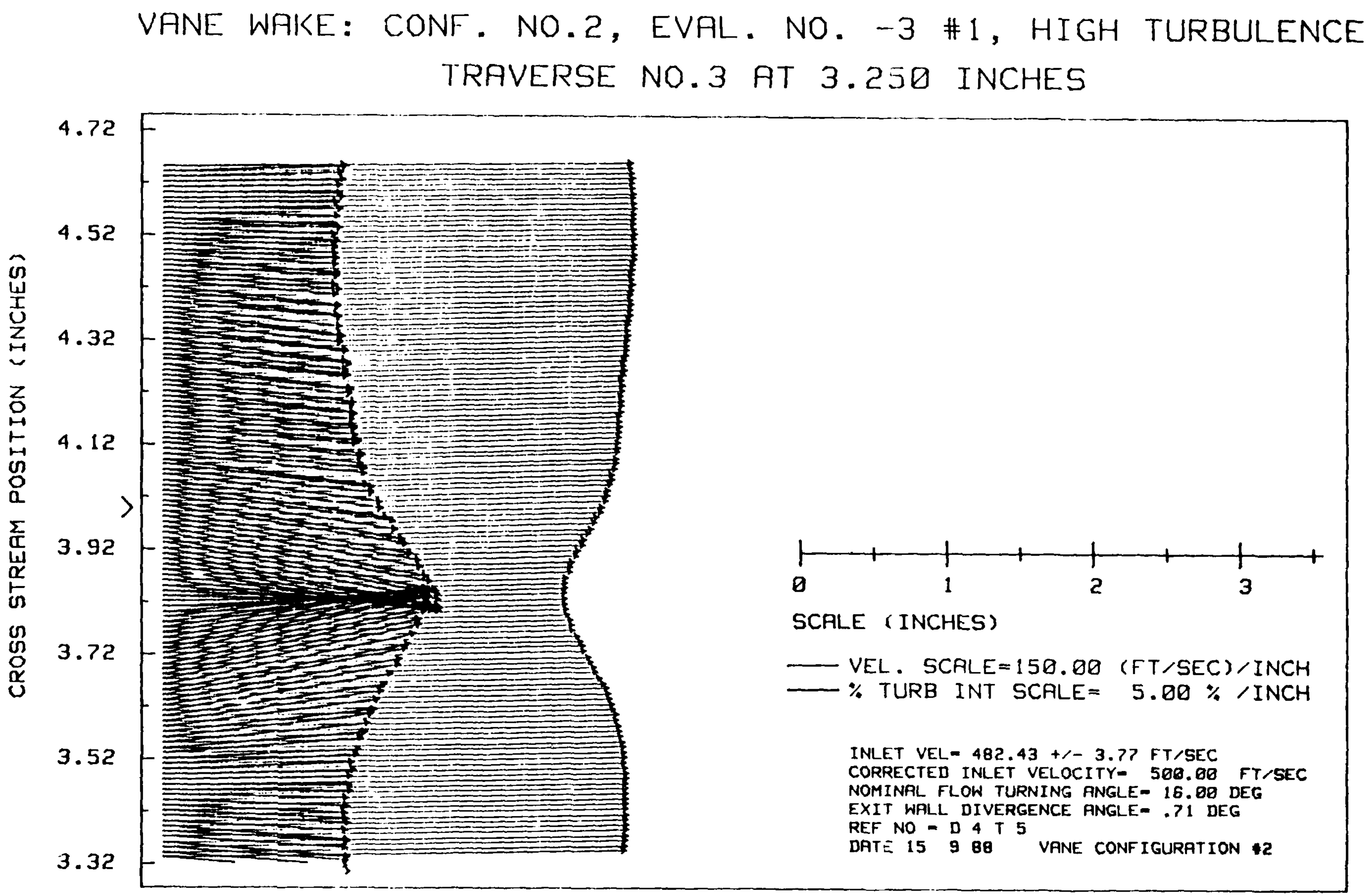

Fig. 35. Wake Velocity and Turbulence Intensity Profiles, Conf.#2, x/c = 1.625

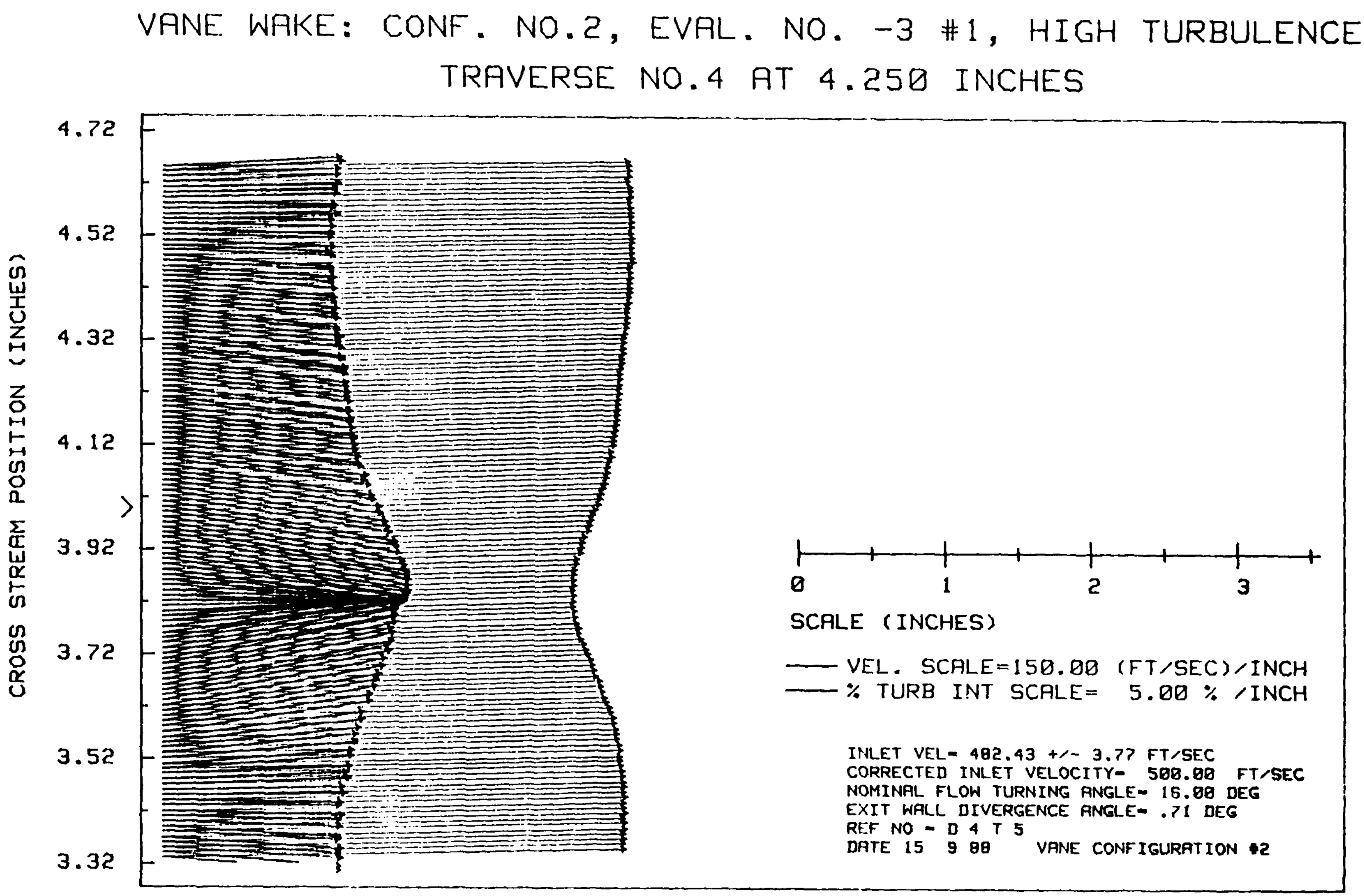

Fig. 36. Wake Velocity and Turbulence Intensity Profiles, Conf.#2, x/c = 2.125

Appendix E

Wake Velocity and Turbulence Intensity Profiles

Blade Configuration Number 2

Incidence Angle = 0.0 Degrees

Low Free Stream Turbulence

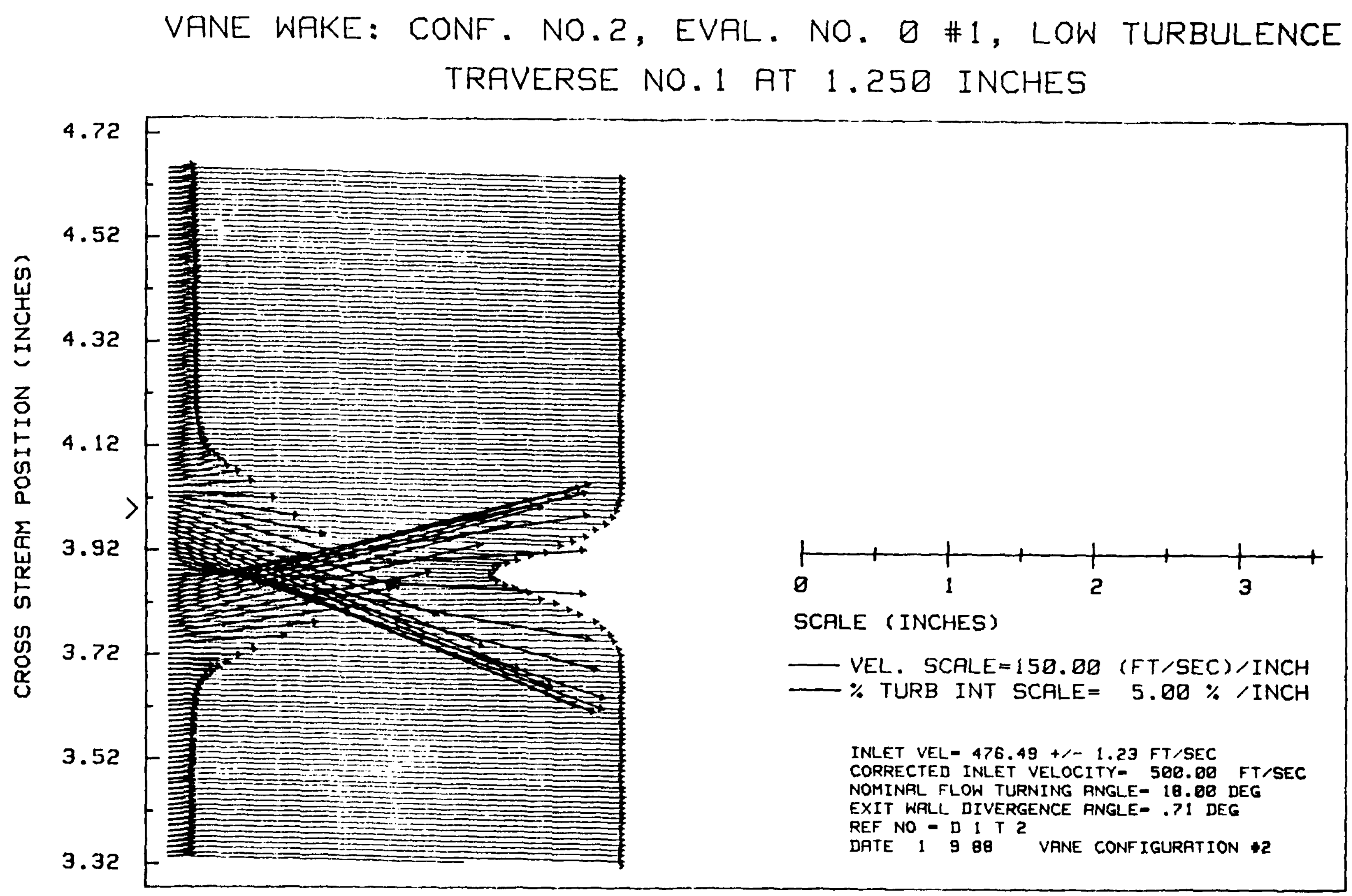

Fig. 37. Wake Velocity and Turbulence Intensity Profiles, Conf.#2, x/c = 0.625

VANE WAKE: CONF. NO.2, EVAL. NO. 0 #1, LOW TURBULENCE
TRAVERSE NO.2 AT 2.250 INCHES

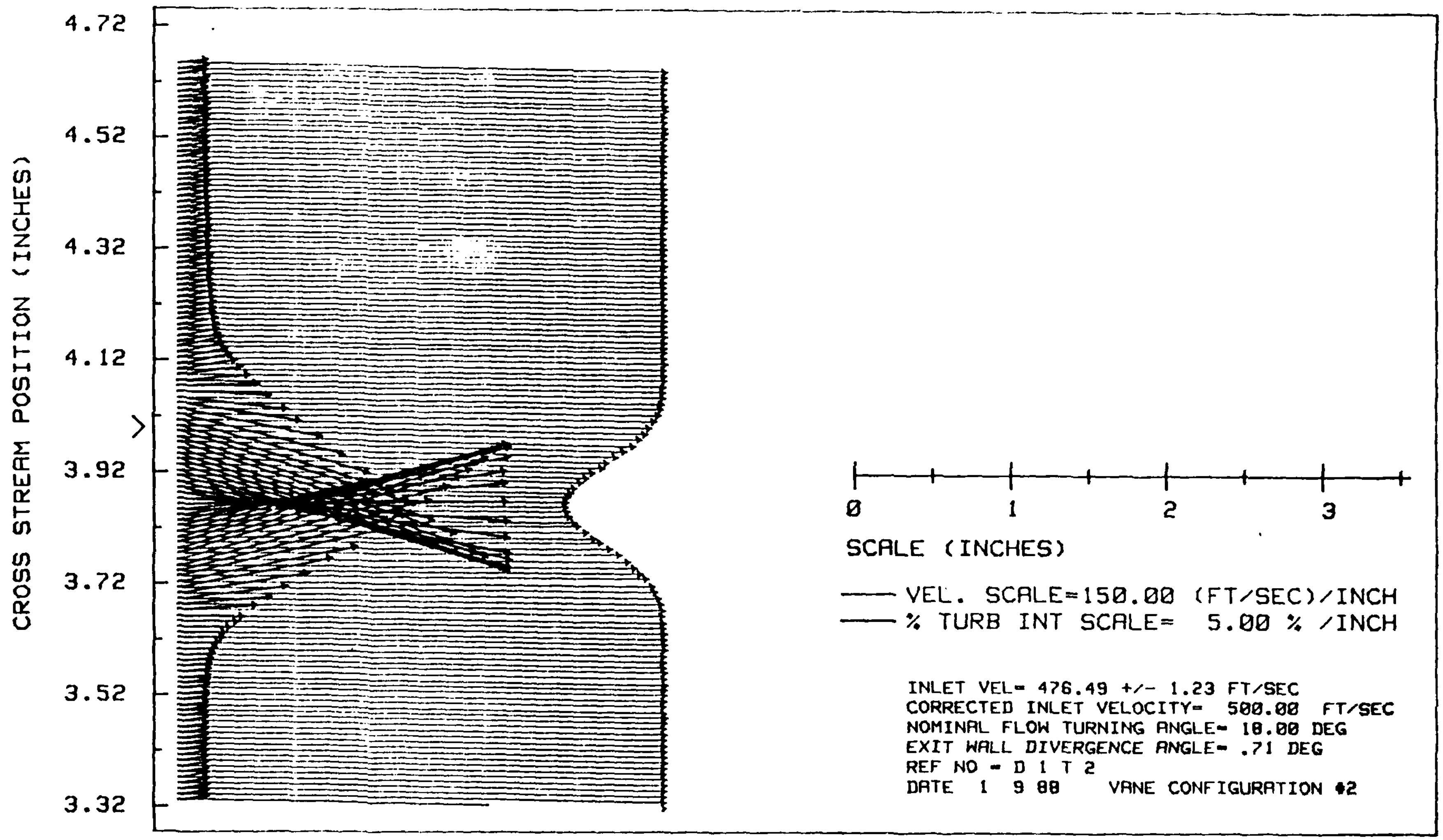

Fig. 38. Wake Velocity and Turbulence Intensity Profiles, Conf.#2, x/c = 1.125

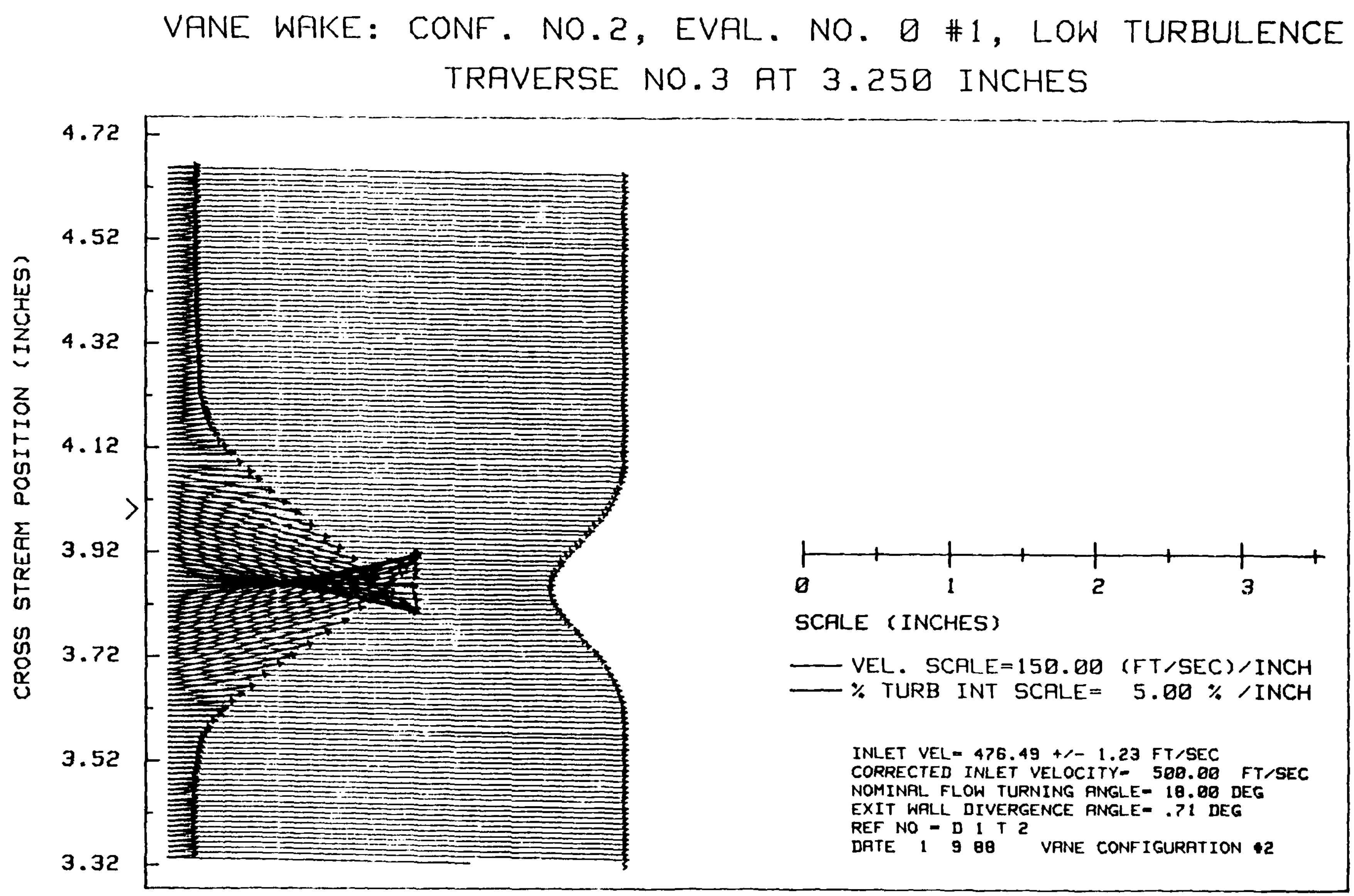

Fig. 39. Wake Velocity and Turbulence Intensity Profiles, Conf.#2, x/c = 1.625

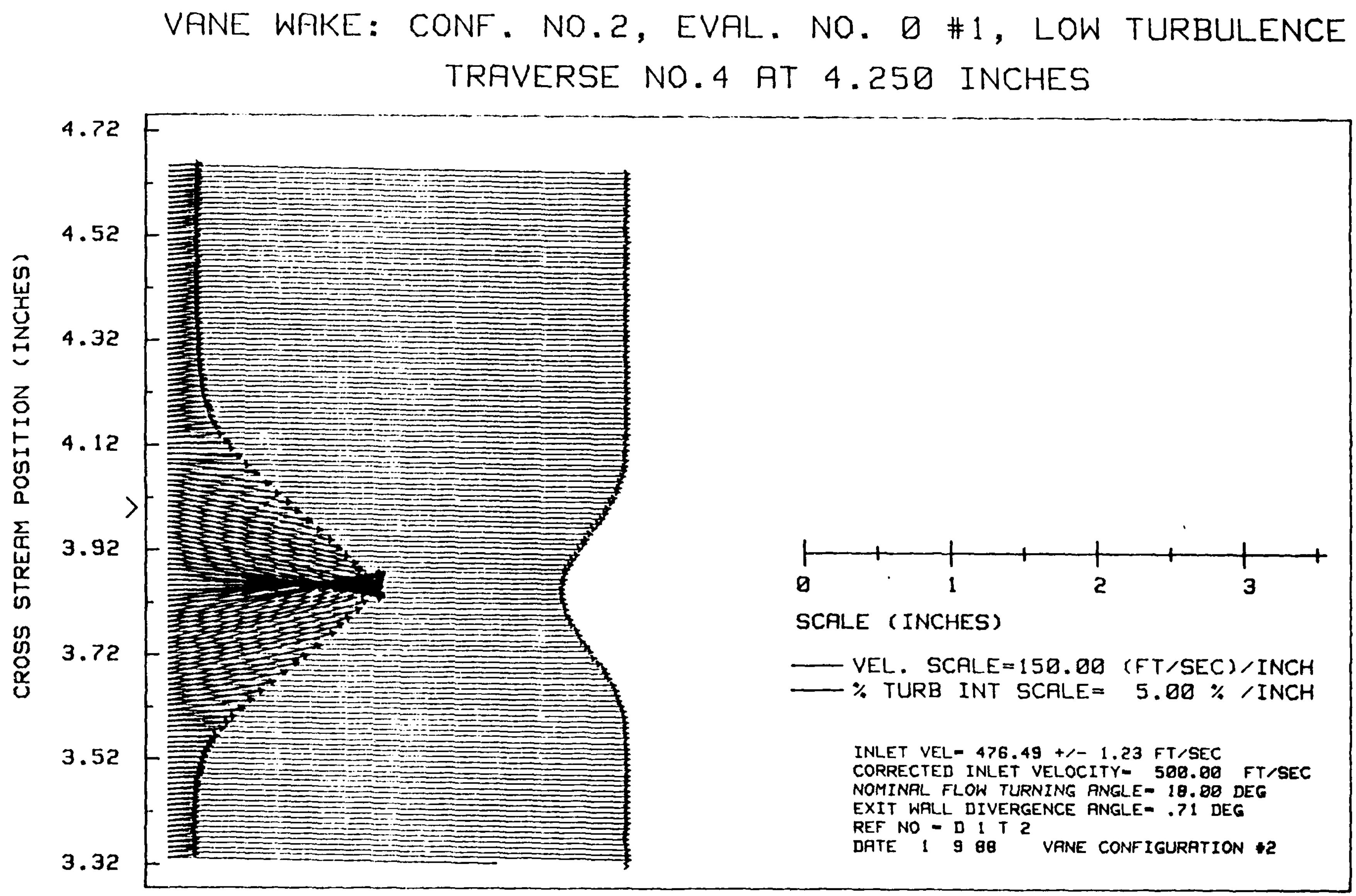

Fig. 40. Wake Velocity and Turbulence Intensity Profiles, Conf.#2, x/c = 2.125

Appendix F

Wake Velocity and Turbulence Intensity Profiles

Blade Configuration Number 2

Incidence Angle = 0.0 Degrees

High Free Stream Turbulence

VANE WAKE: CONF. NO.2, EVAL. NO. 0 #1, HIGH TURBULENCE
TRAVERSE NO.1 AT 1.250 INCHES

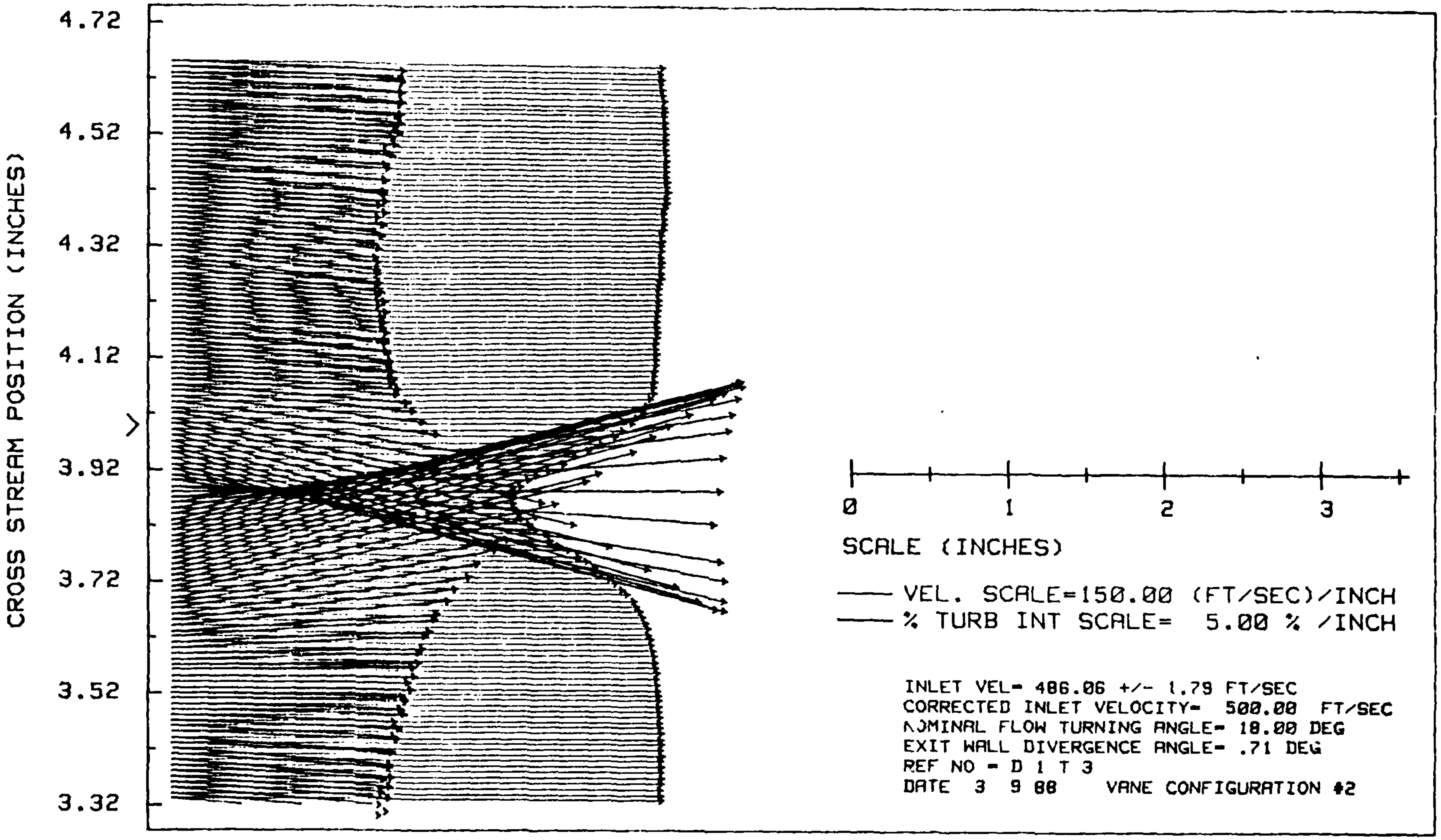

Fig. 41. Wake Velocity and Turbulence Intensity Profiles, Conf.#2, x/c = 0.625

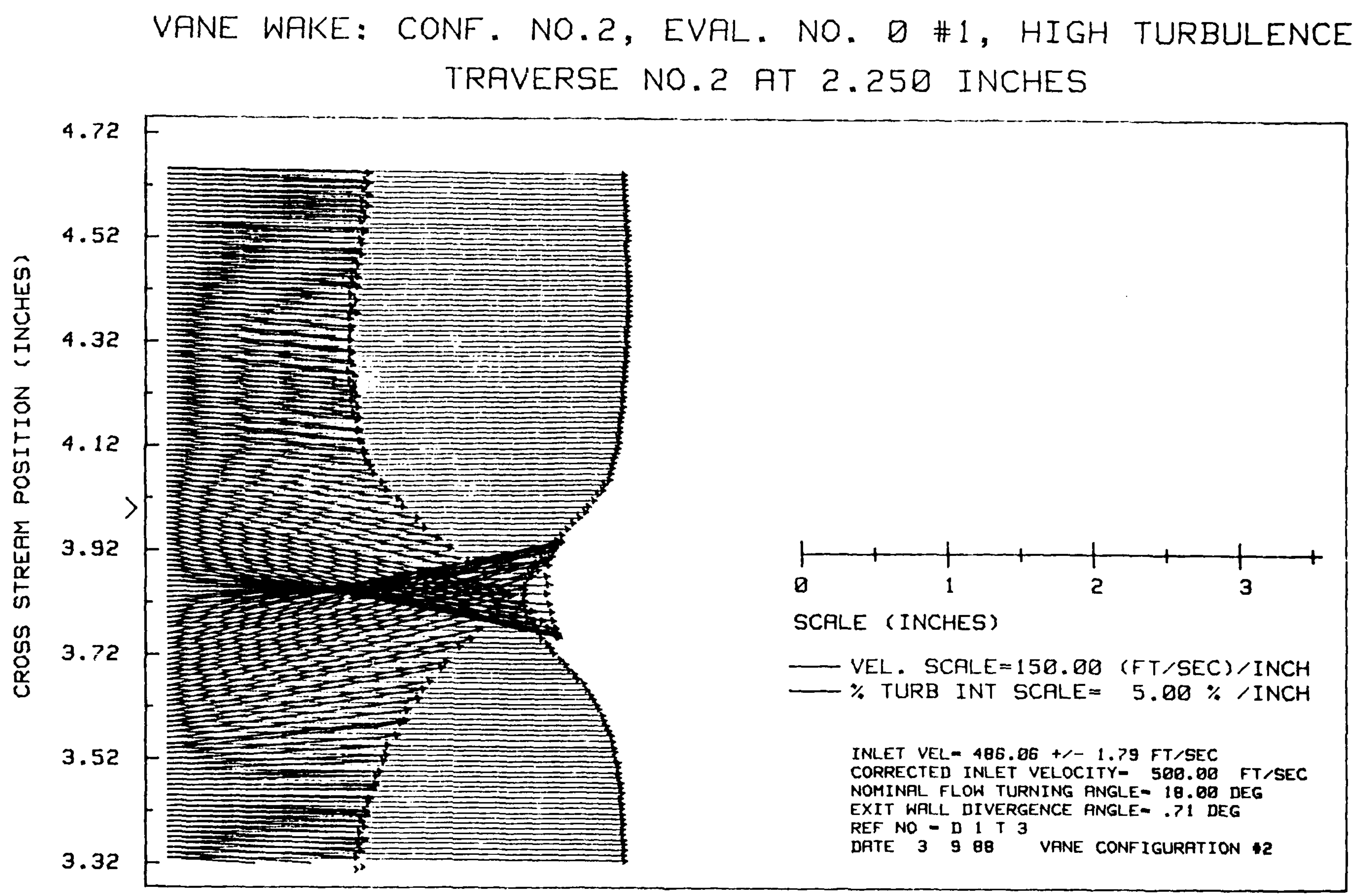

Fig. 42. Wake Velocity and Turbulence Intensity Profiles, Conf.#2, x/c = 1.125

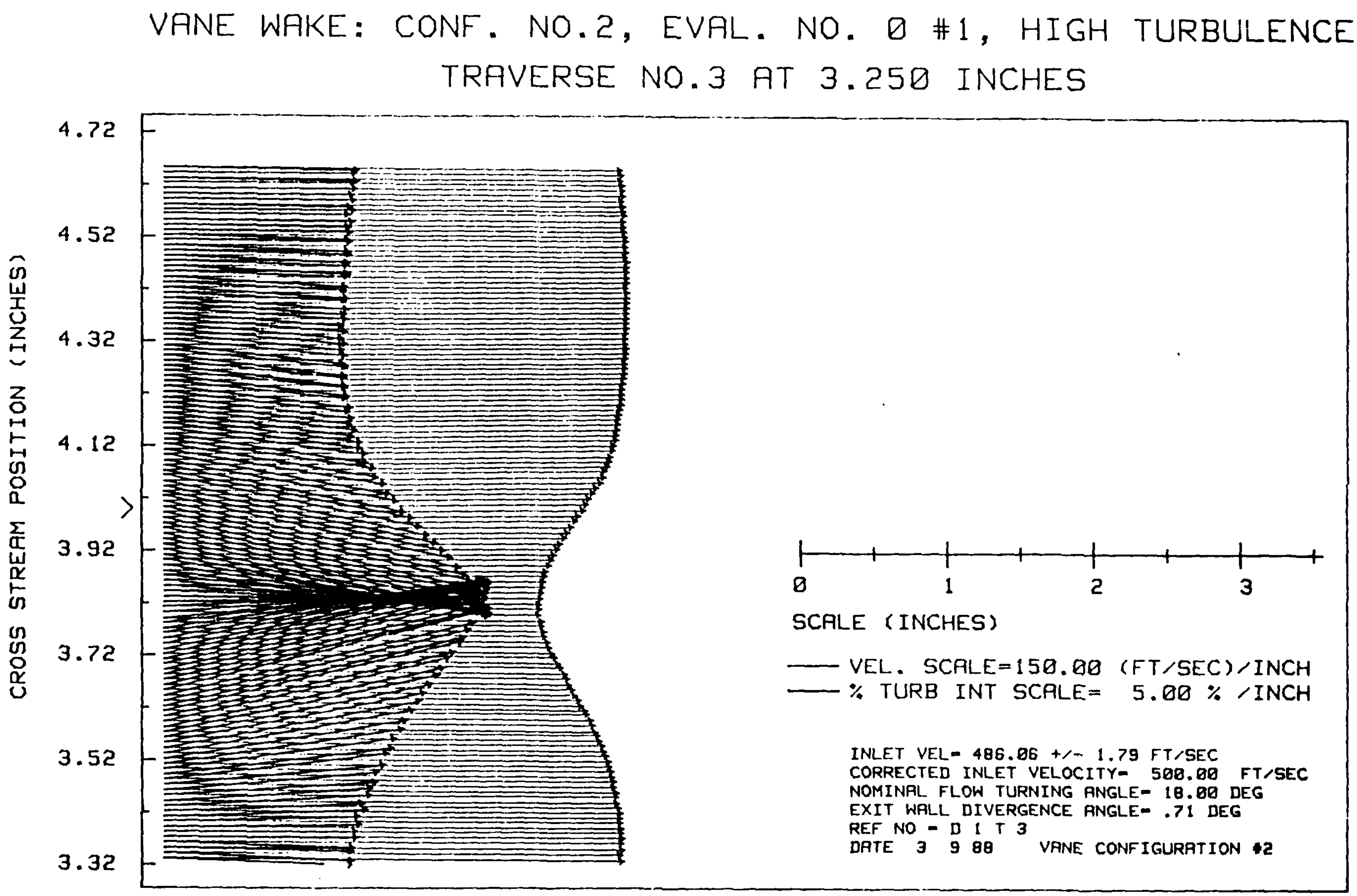

Fig. 43. Wake Velocity and Turbulence Intensity Profiles, Conf.#2, x/c = 1.625

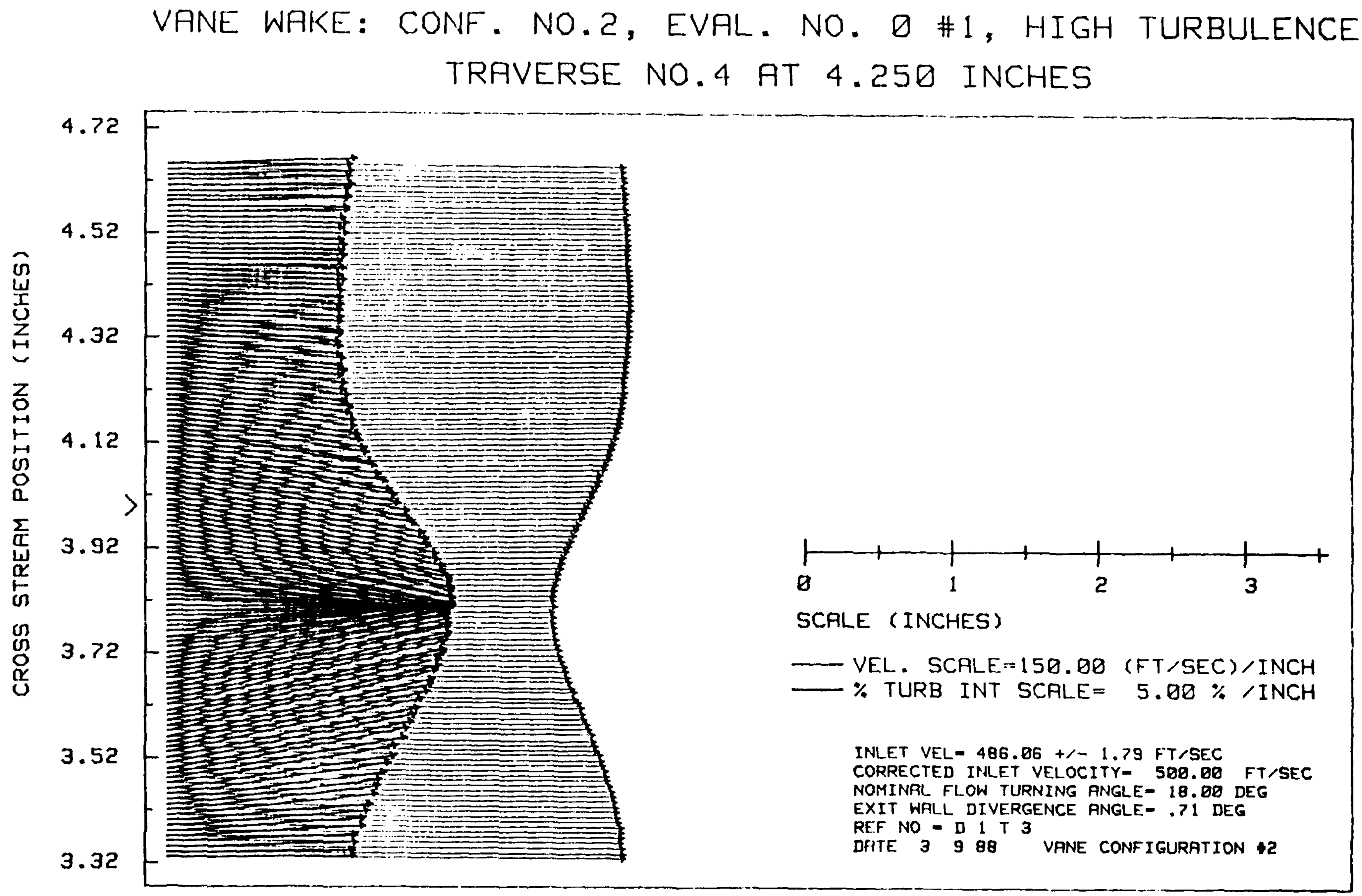

Fig. 44. Wake Velocity and Turbulence Intensity Profiles, Conf.#2, x/c = 2.125

Appendix G

<u>Wake Velocity and Turbulence Intensity Profiles</u>

<u>Blade Configuration Number 2</u>

<u>Incidence Angle = +3.0 Degrees</u>

<u>Low Free Stream Turbulence</u>

VANE WAKE: CONF. NO.2, EVAL. NO. +3 #1, LOW TURBULENCE
TRAVERSE NO.1 AT 1.250 INCHES

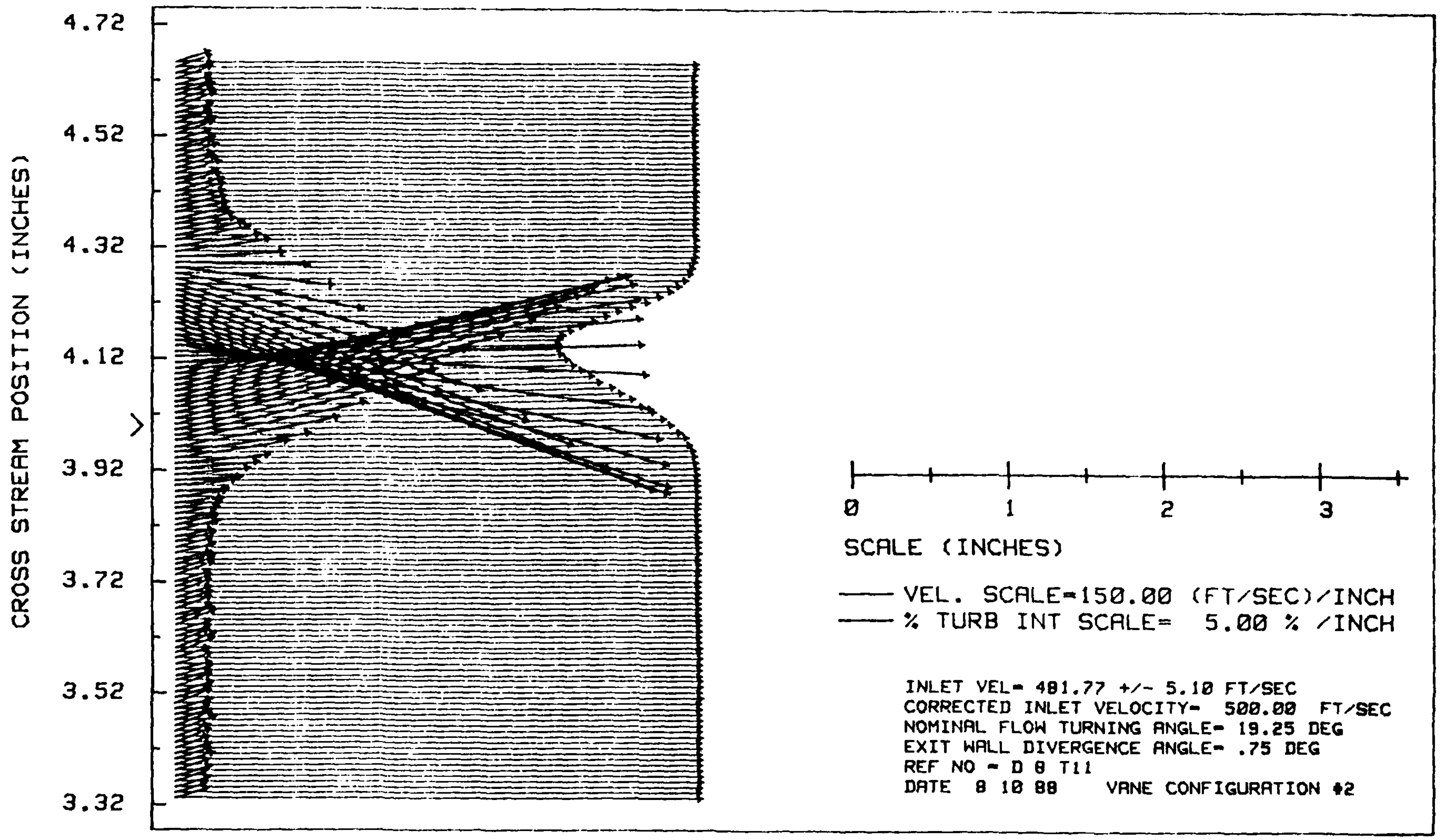

Fig. 45. Wake Velocity and Turbulence Intensity Profiles, Conf.#2, x/c = 0.625

VANE WAKE: CONF. NO.2, EVAL. NO. +3 #1, LOW TURBULENCE
TRAVERSE NO.2 AT 2.250 INCHES

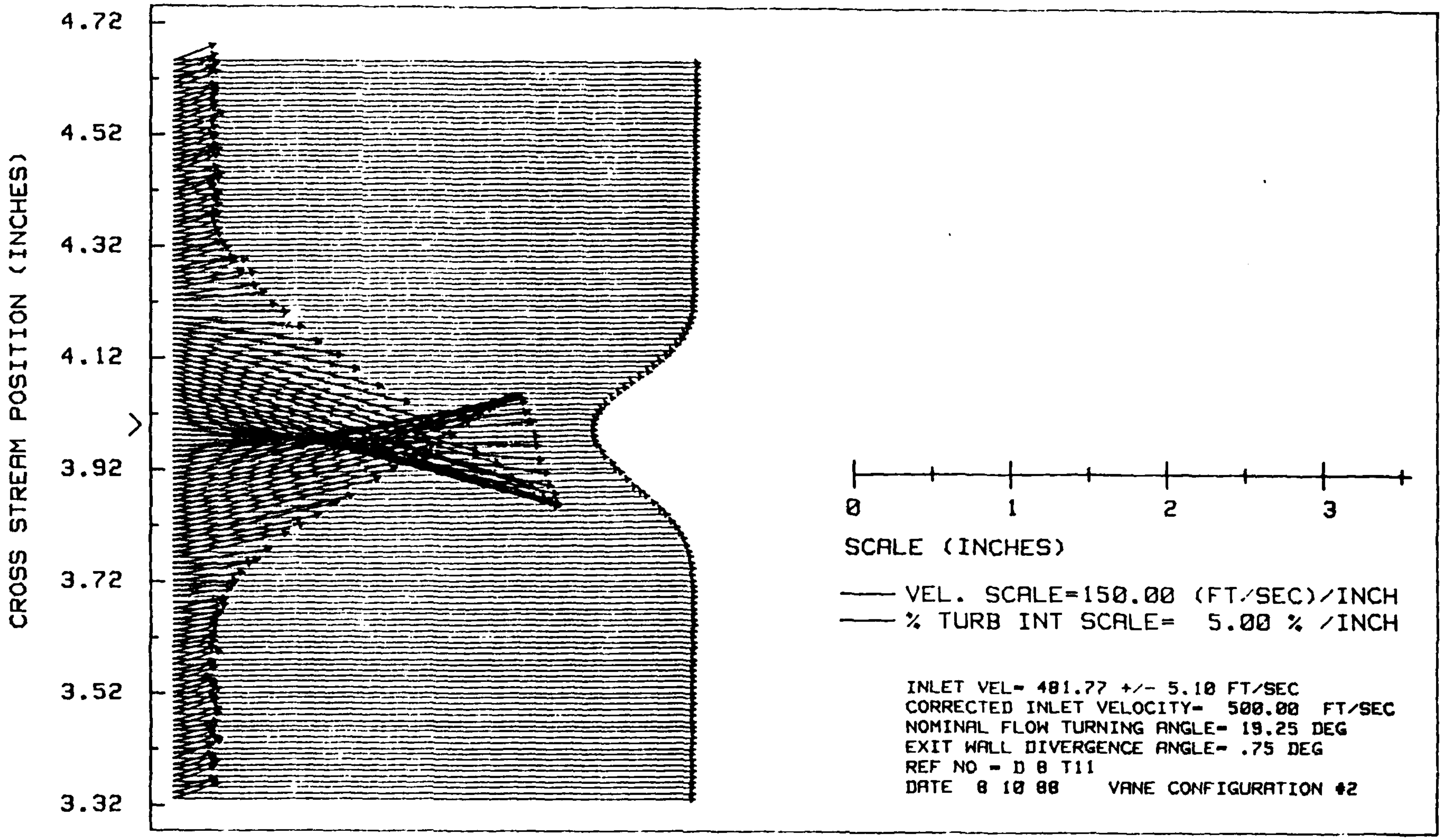

Fig. 46. Wake Velocity and Turbulence Intensity Profiles, Conf.#2, x/c = 1.125

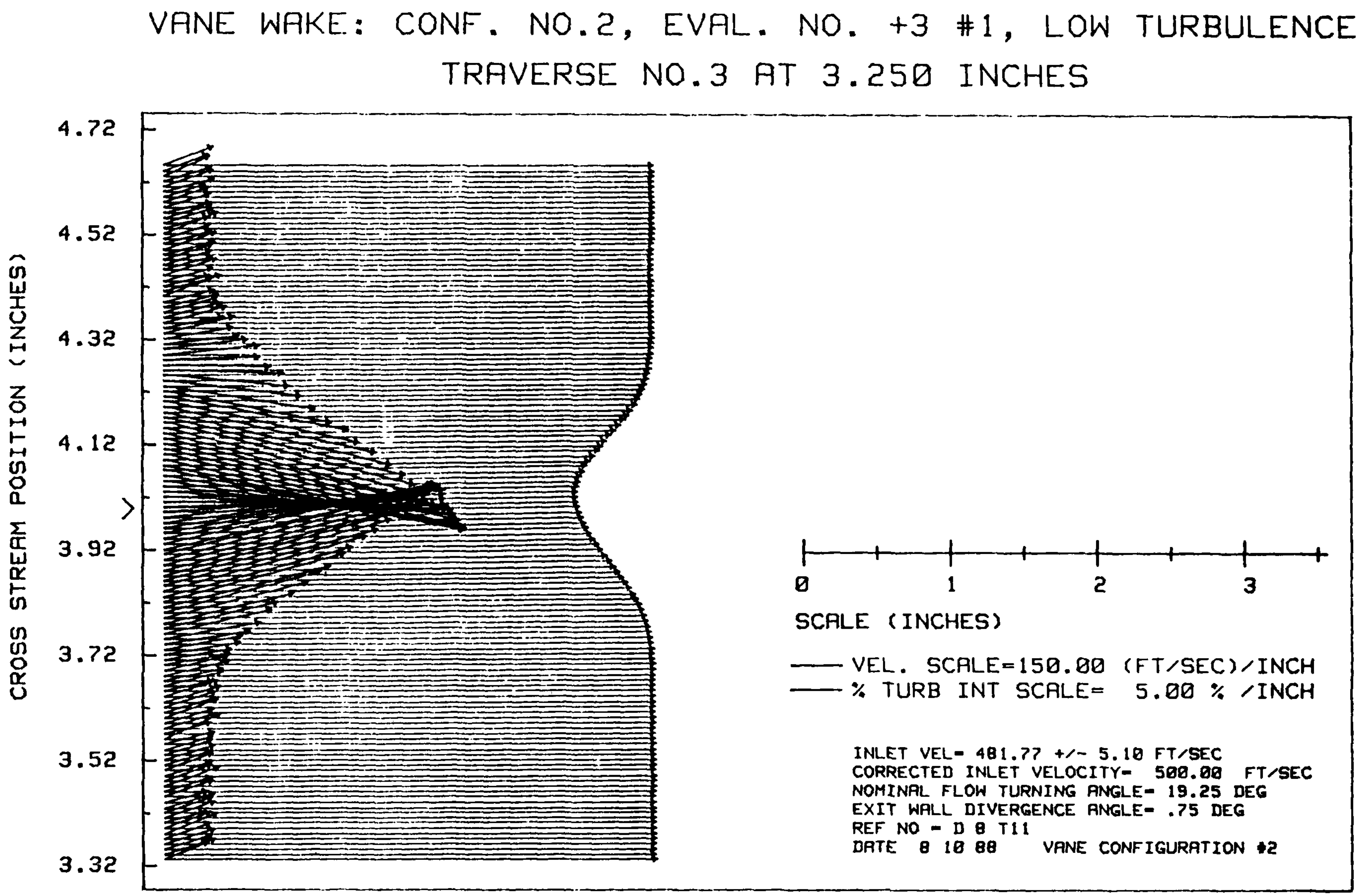

Fig. 47. Wake Velocity and Turbulence Intensity Profiles, Conf.#2, x/c = 1.625

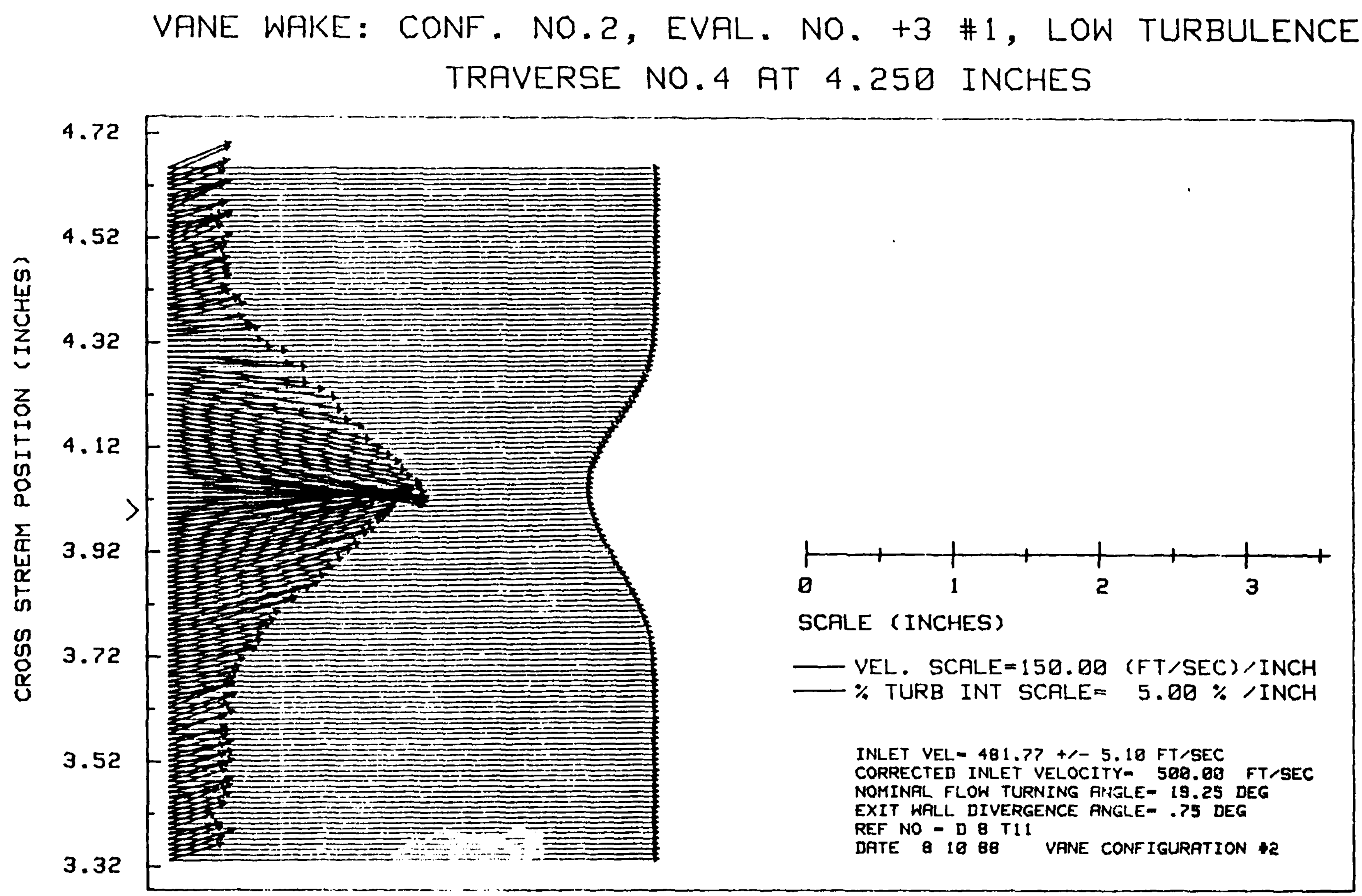

Fig. 48. Wake Velocity and Turbulence Intensity Profiles, Conf.#2, x/c = 2.125

Appendix H

Wake Velocity and Turbulence Intensity Profiles

Blade Configuration Number 2

Incidence Angle = +3.0 Degrees

High Free Stream Turbulence

VANE WAKE: CONF. NO.2, EVAL. NO. +3 #1, HIGH TURBULENCE
TRAVERSE NO.1 AT 1.250 INCHES

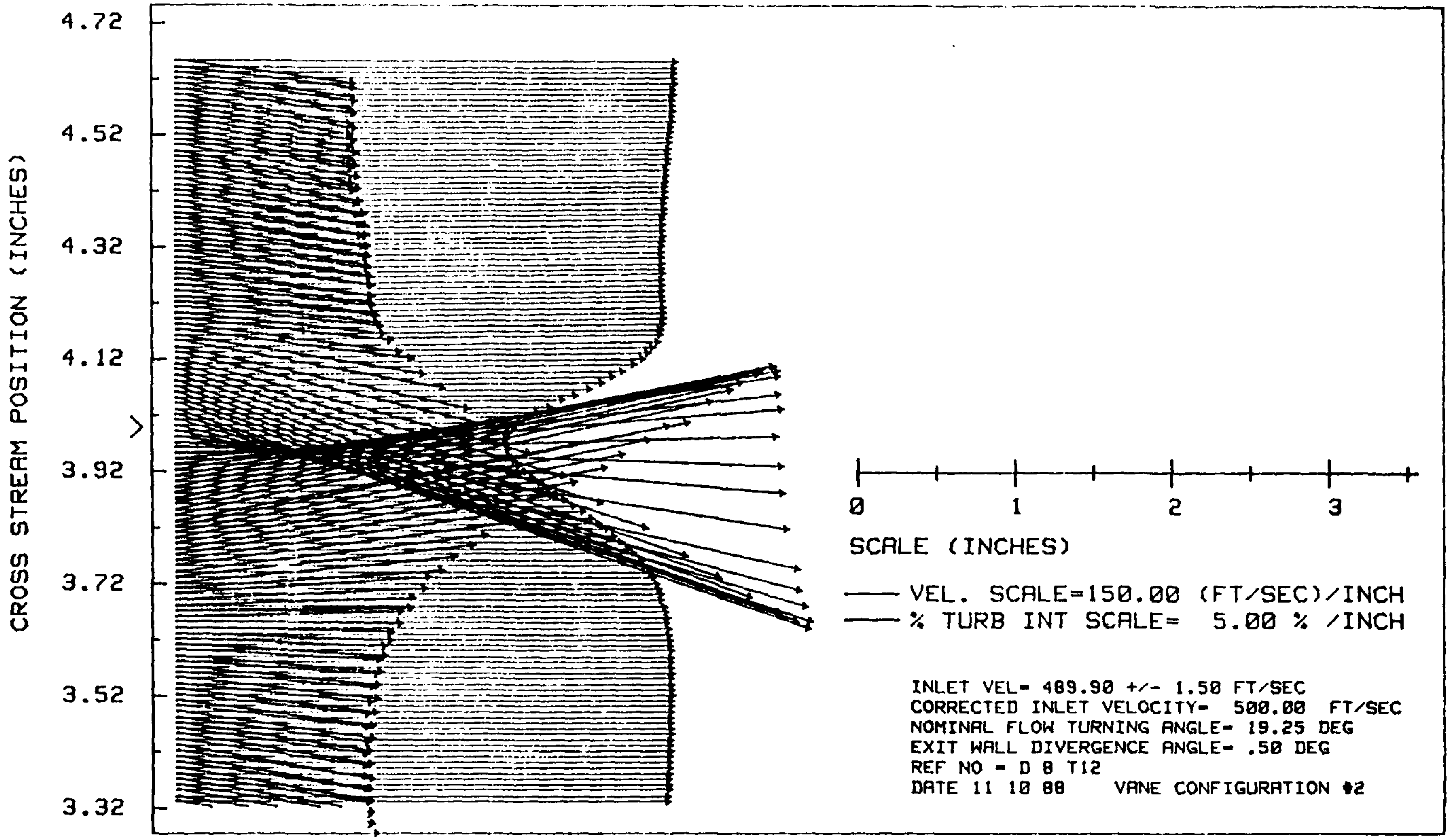

Fig. 49. Wake Velocity and Turbulence Intensity Profiles, Conf.#2, x/c = 0.625

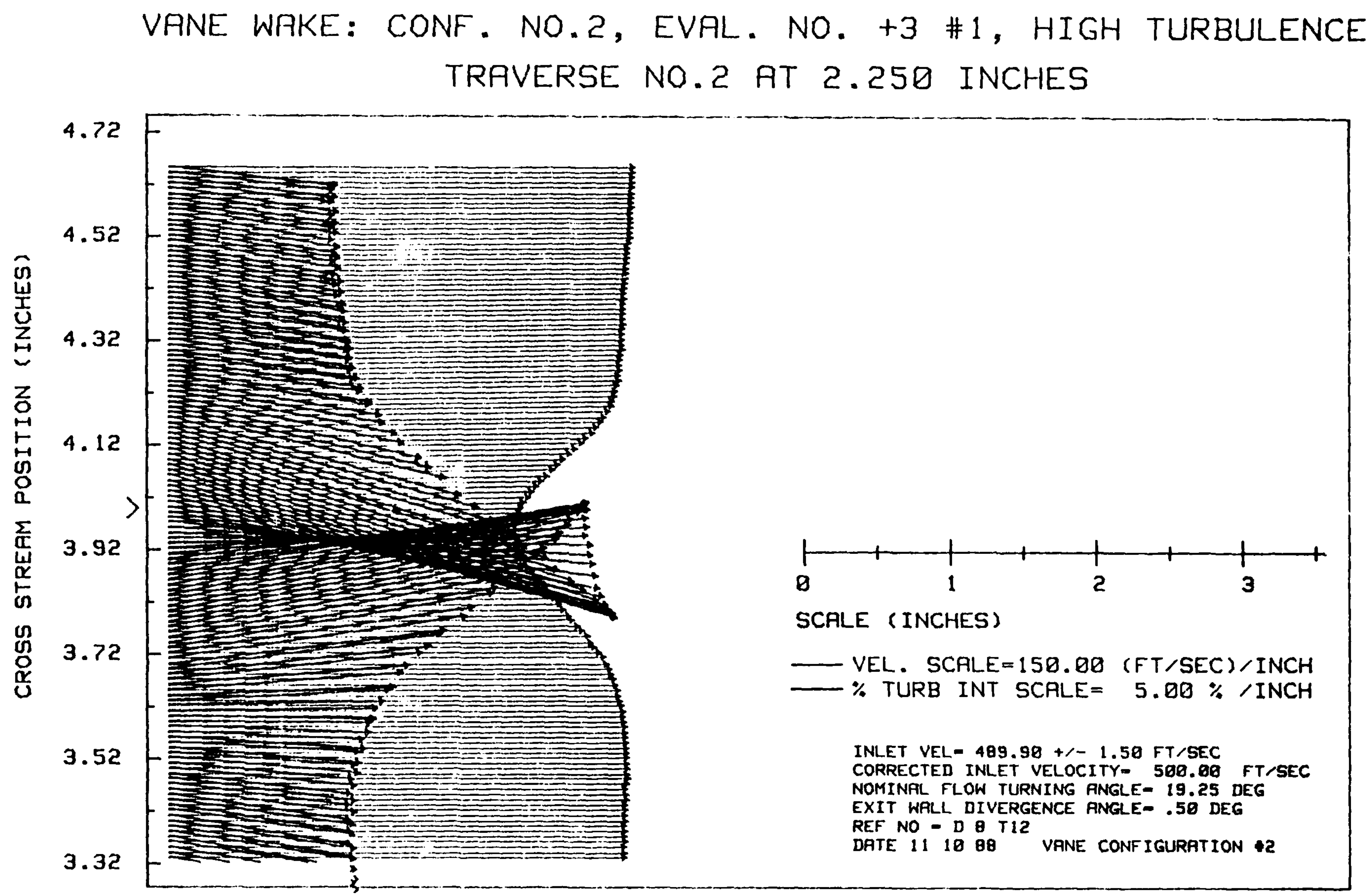

Fig. 50. Wake Velocity and Turbulence Intensity Profiles, Conf.#2, x/c = 1.125

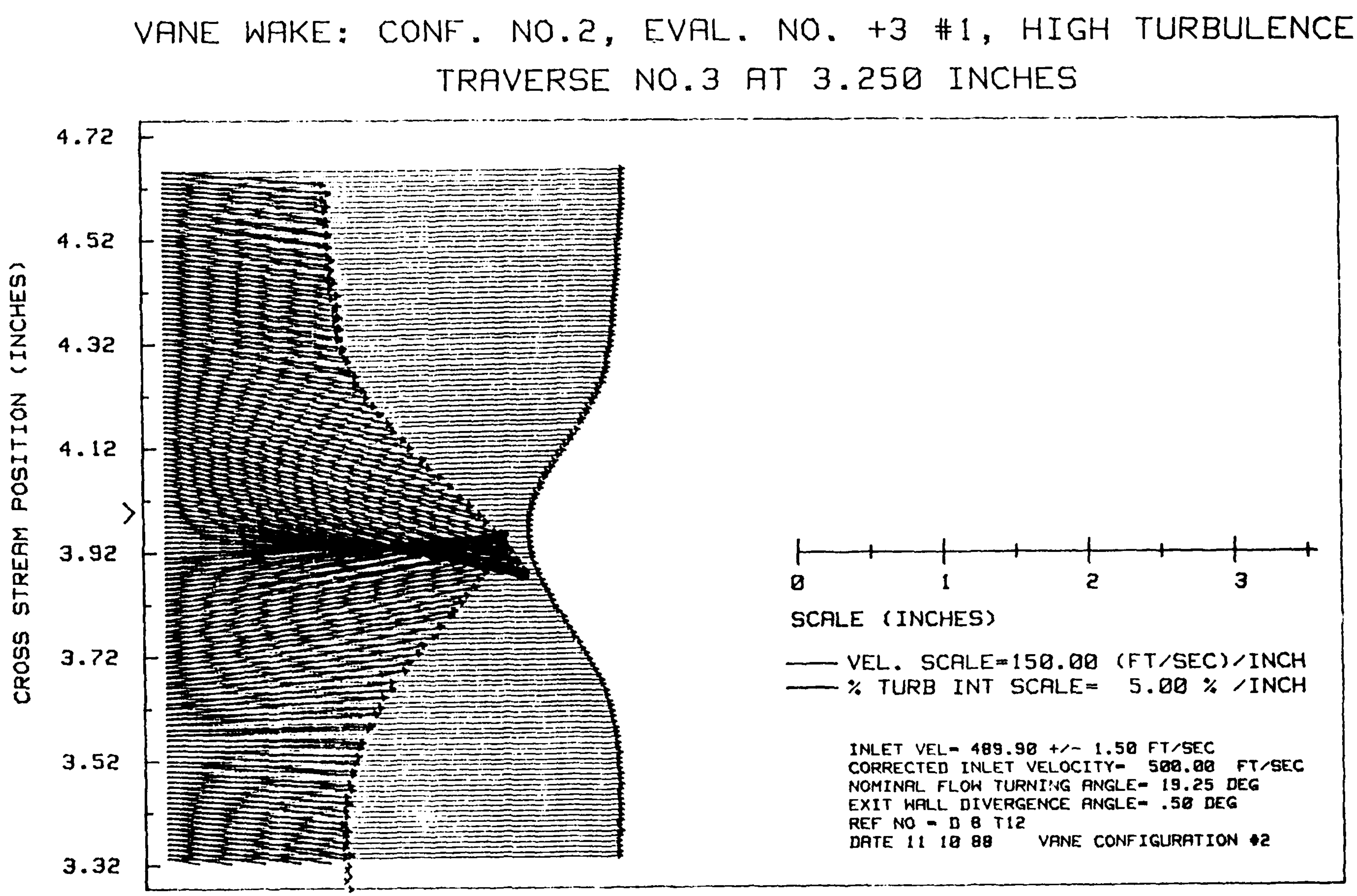

Fig. 51. Wake Velocity and Turbulence Intensity Profiles, Conf.#2, x/c = 1.625

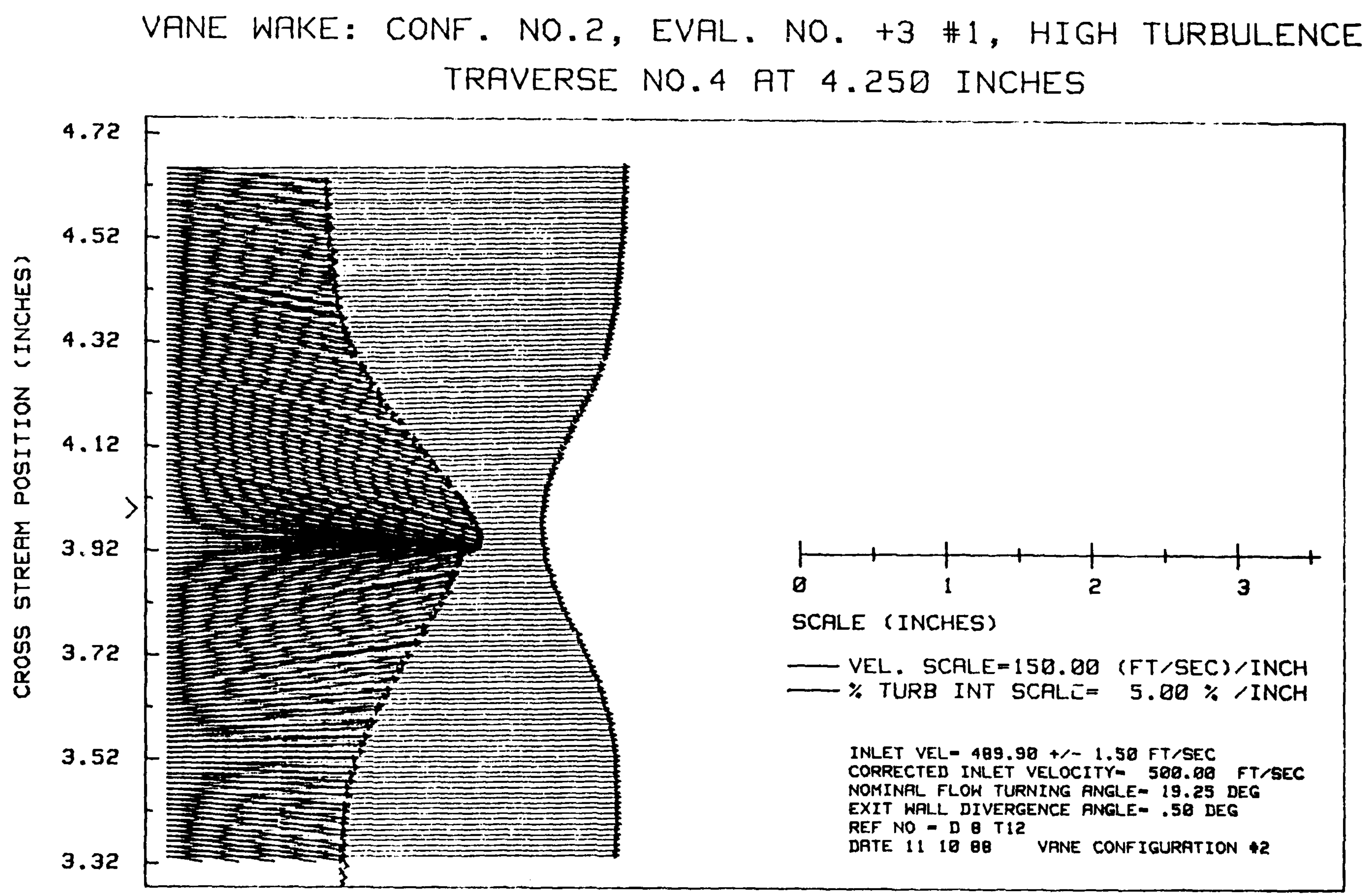

Fig. 52. Wake Velocity and Turbulence Intensity Profiles, Conf.#2, x/c = 2.125

Appendix I

Boundary Layer Velocity and Turbulence Intensity Profiles

Blade Configuration Number 2

Incidence Angle = -3.0 Degrees

Low Free Stream Turbulence

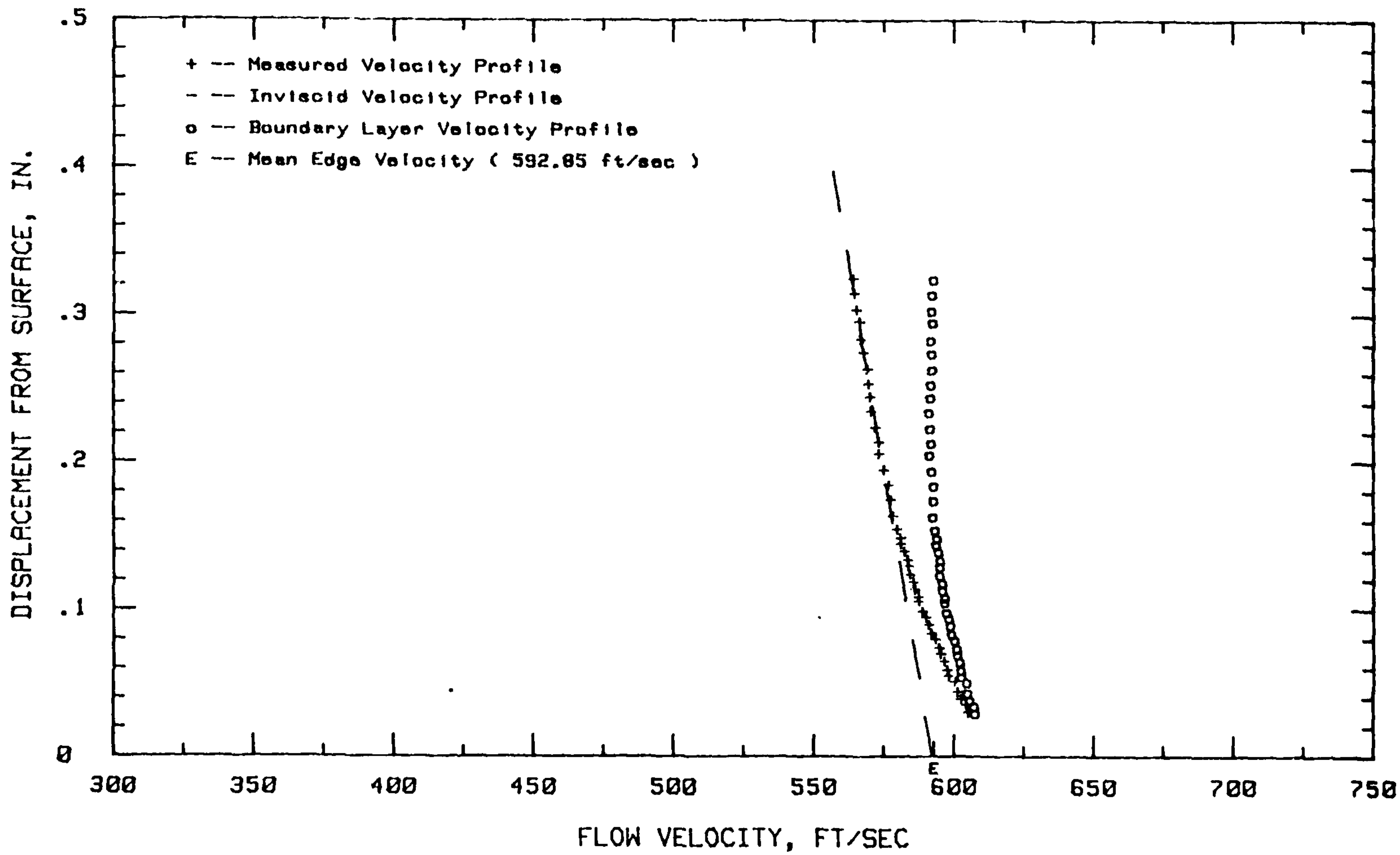

Fig. 53. Boundary Layer Velocity Profiles, i = -3 Deg, 4.68 % Chord

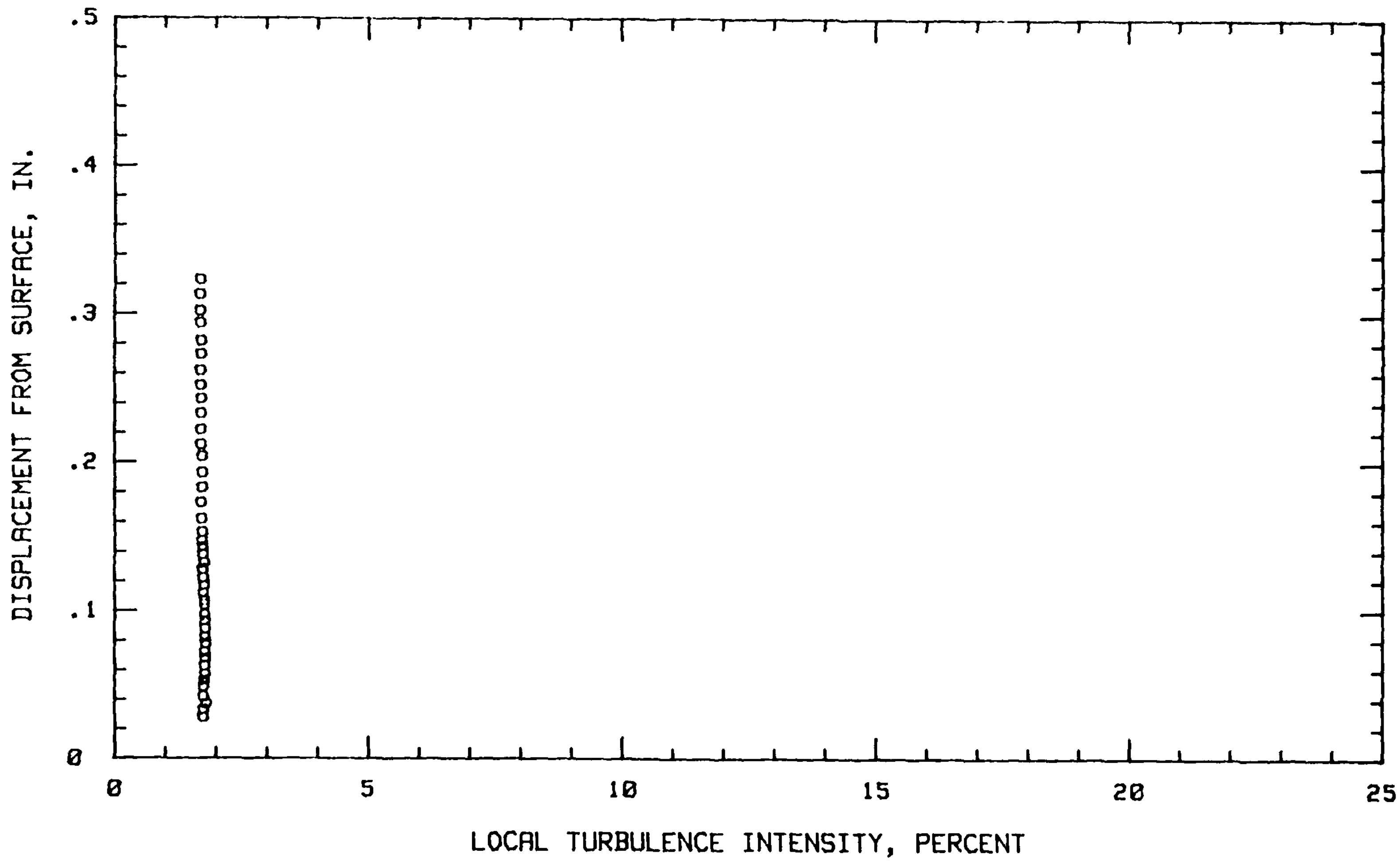

Fig. 54. Boundary Layer Turbulence Intensity Profile, i = -3 Deg, 4.68 % Chord

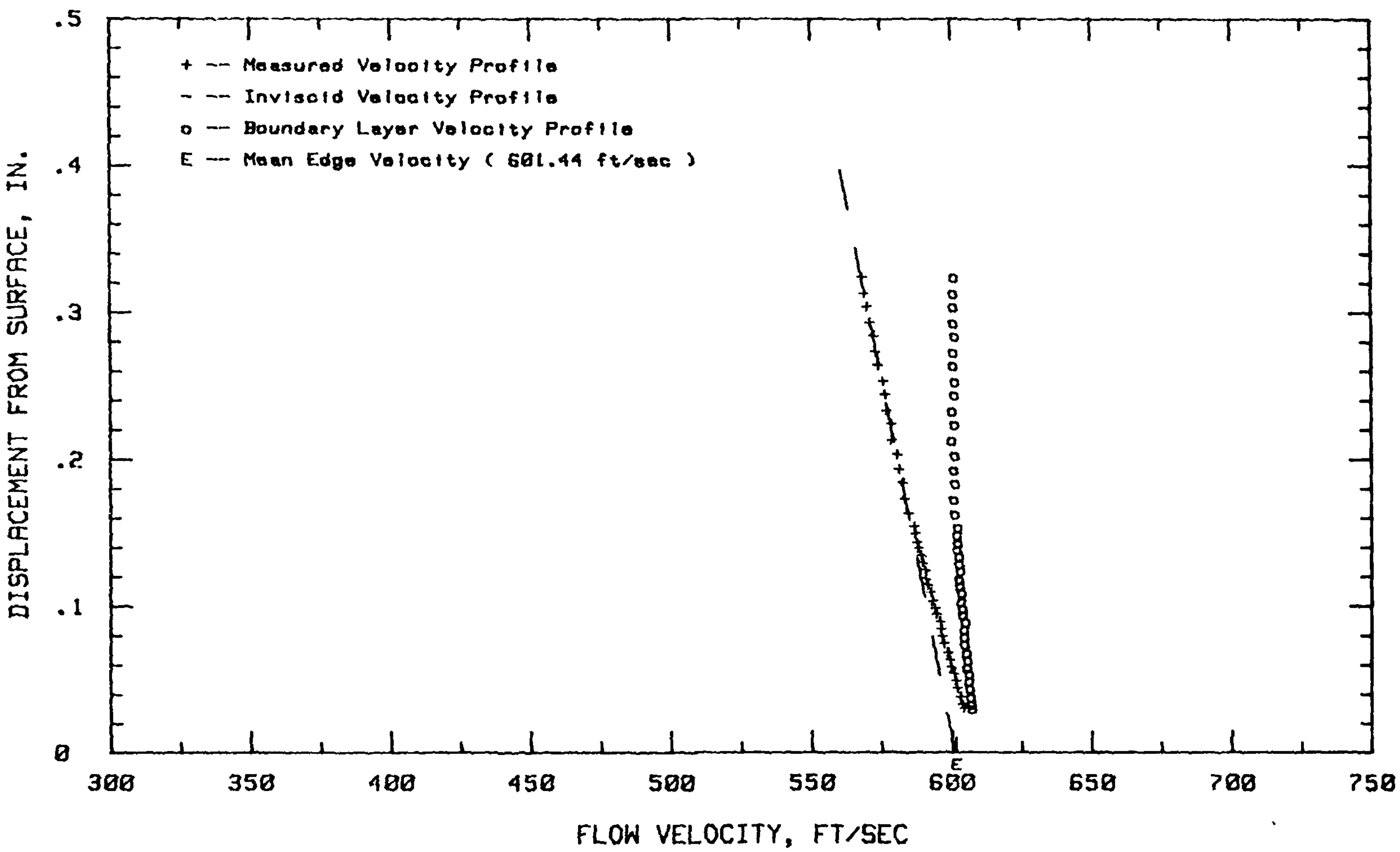

Fig. 55. Boundary Layer Velocity Profiles, i = -3 Deg, 9.37 % Chord

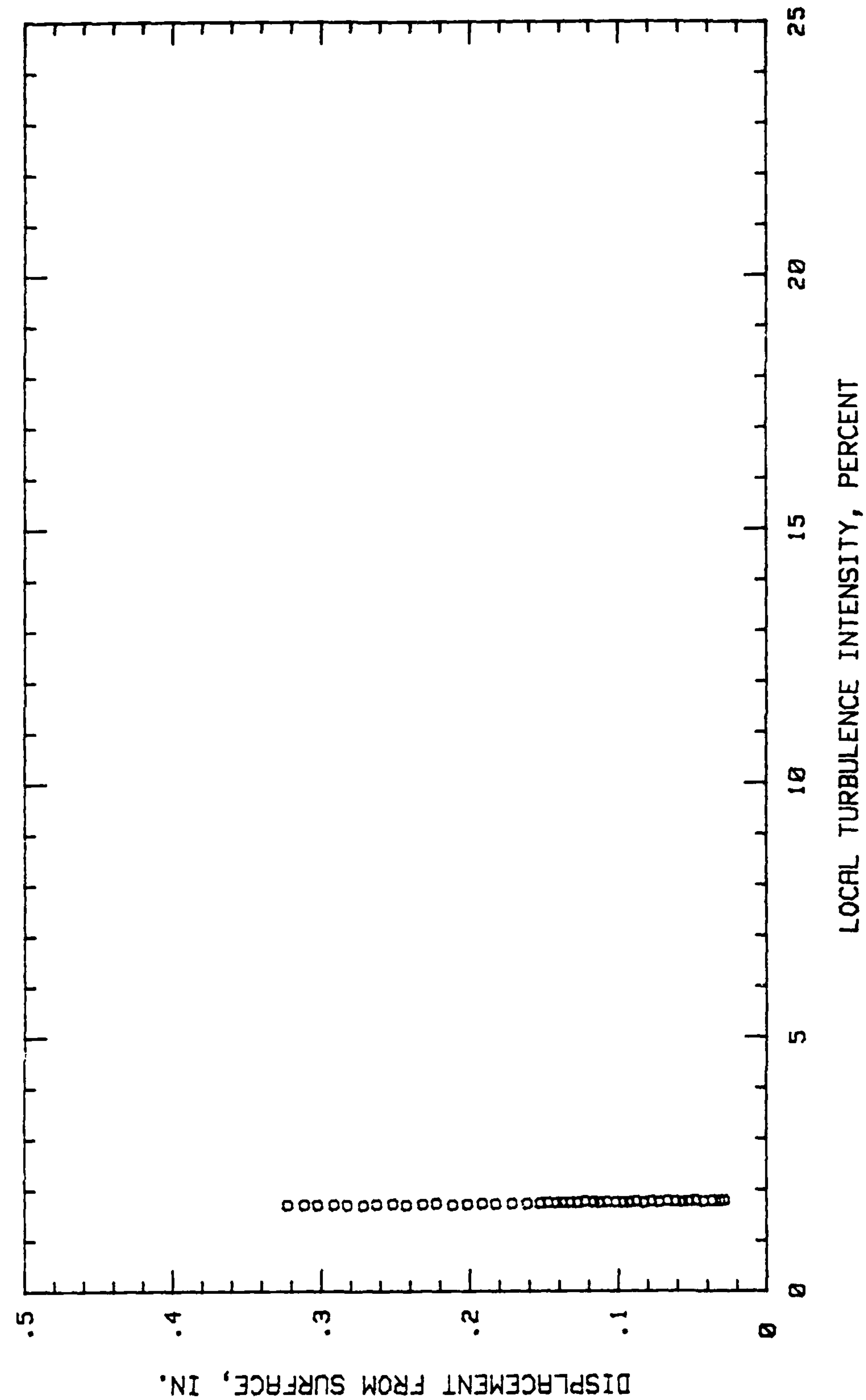

Fig. 56. Boundary Layer Turbulence Intensity Profile, i = -3 Deg, 9.37 % Chord

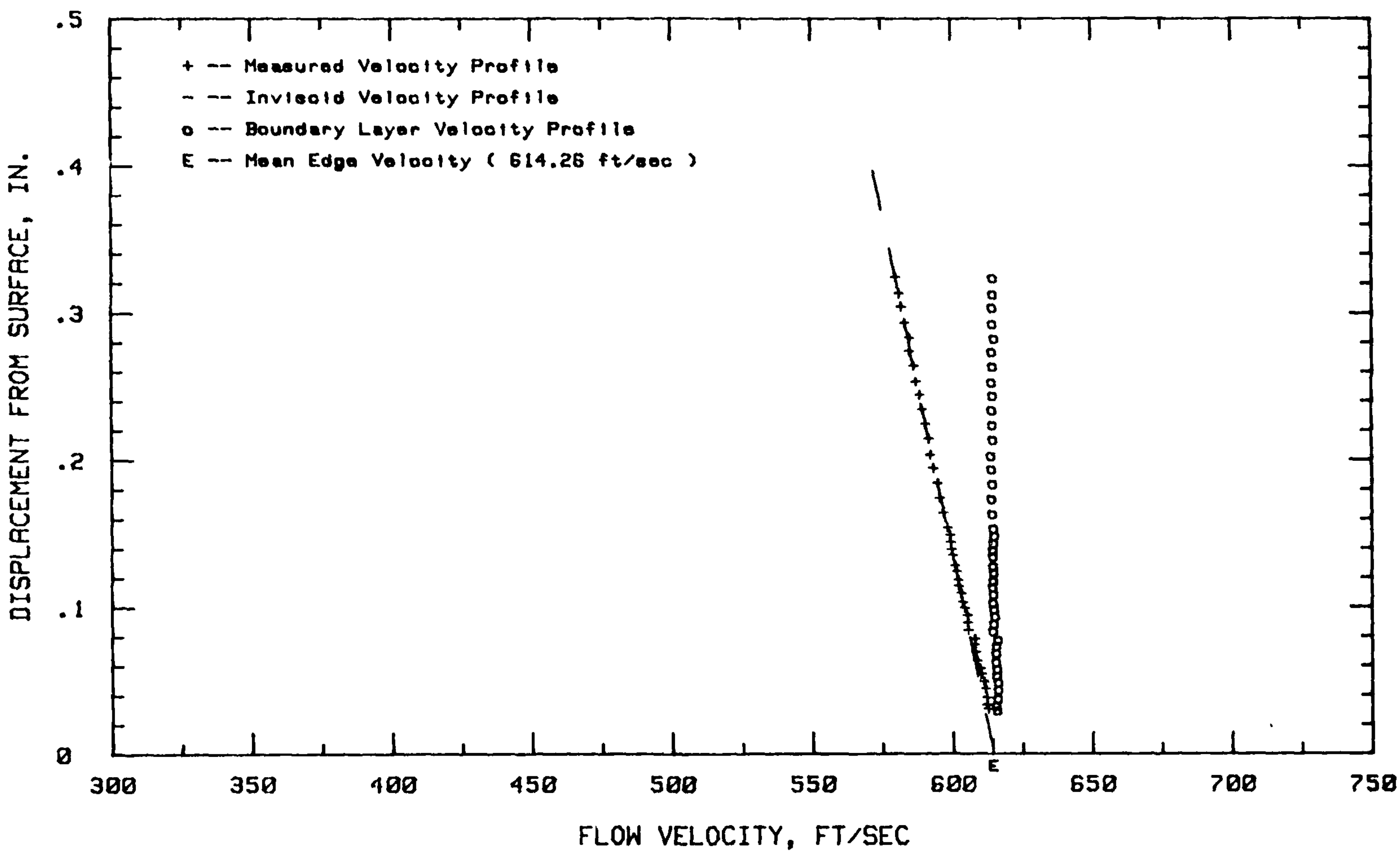

Fig. 57. Boundary Layer Velocity Profiles, i = -3 Deg, 25 % Chord

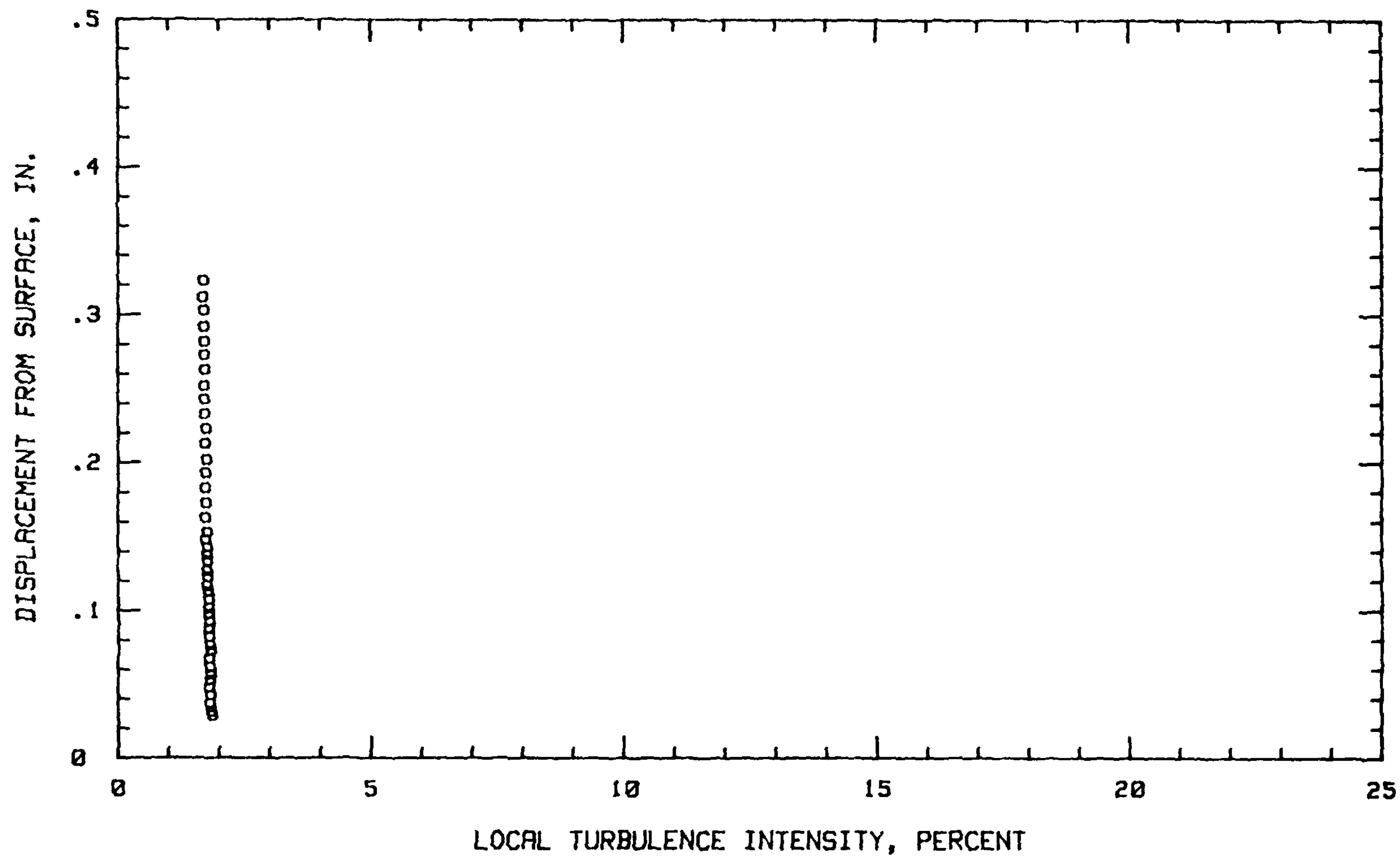

Fig. 58. Boundary Layer Turbulence Intensity Profile, i = -3 Deg, 25 % Chord

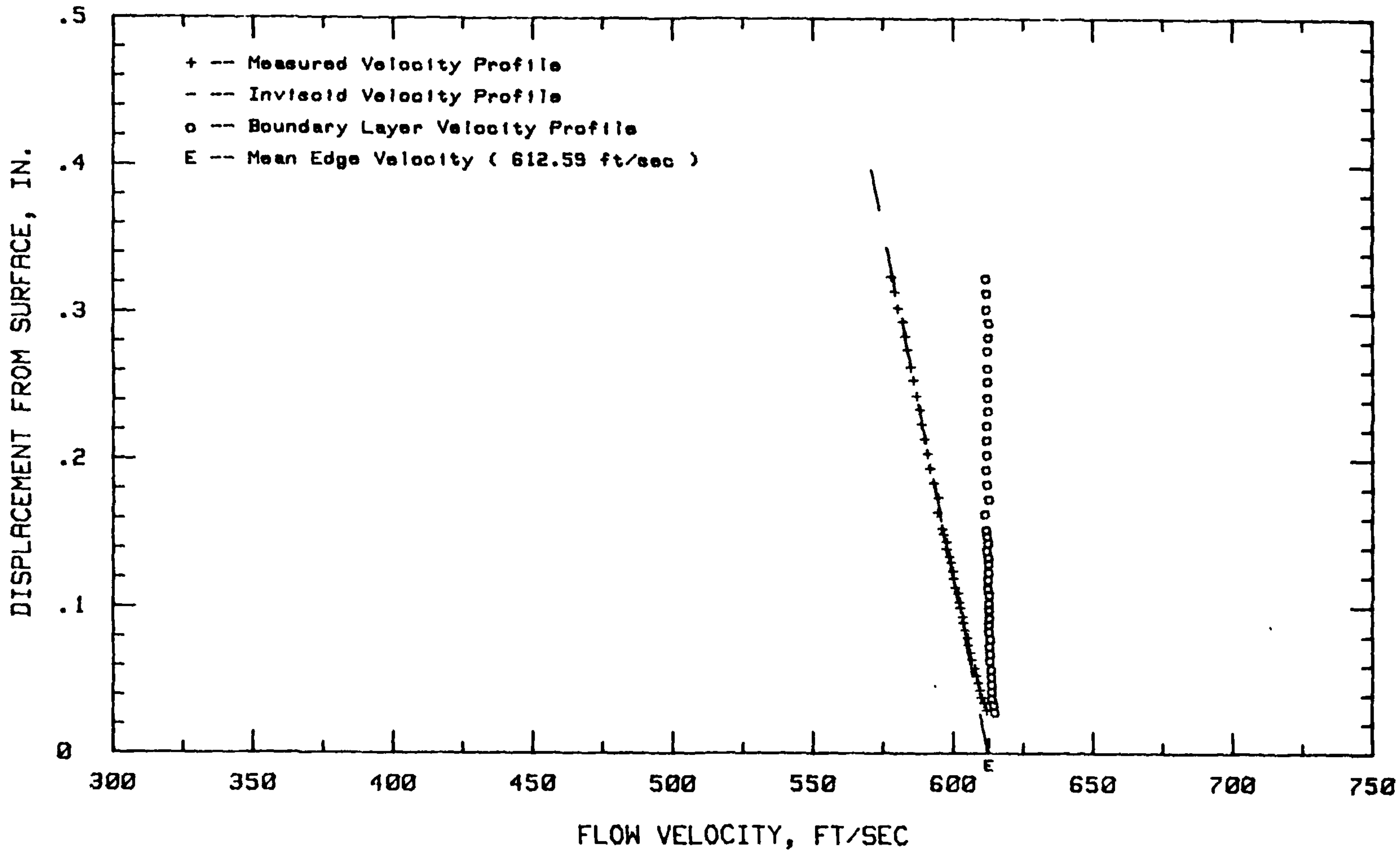

Fig. 59. Boundary Layer Velocity Profiles, i = -3 Deg, 29.68 % Chord

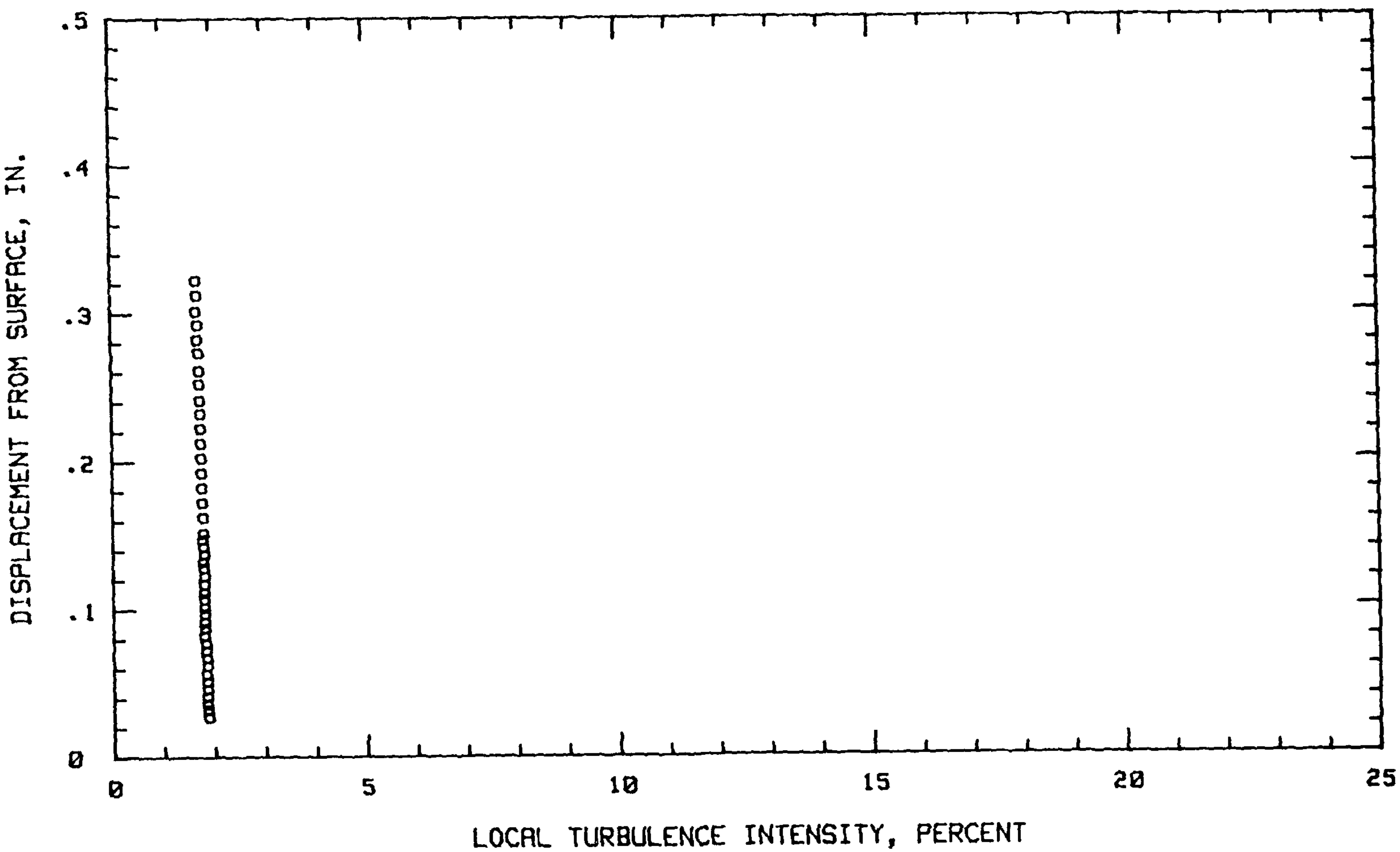

Fig. 60. Boundary Layer Turbulence Intensity Profile, i = -3 Deg, 29.68 % Chord

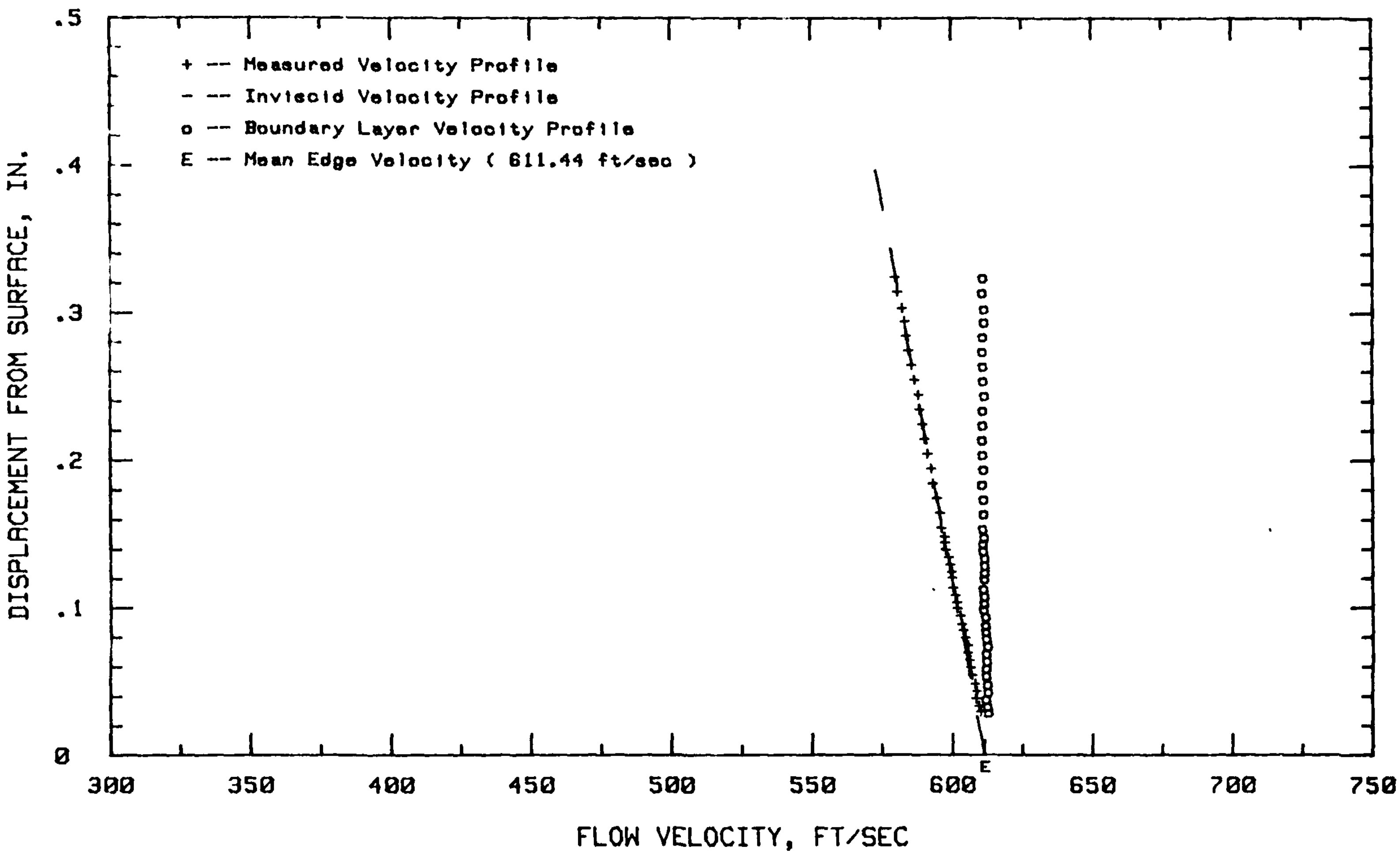

Fig. 61. Boundary Layer Velocity Profiles, i = -3 Deg, 34.37 % Chord

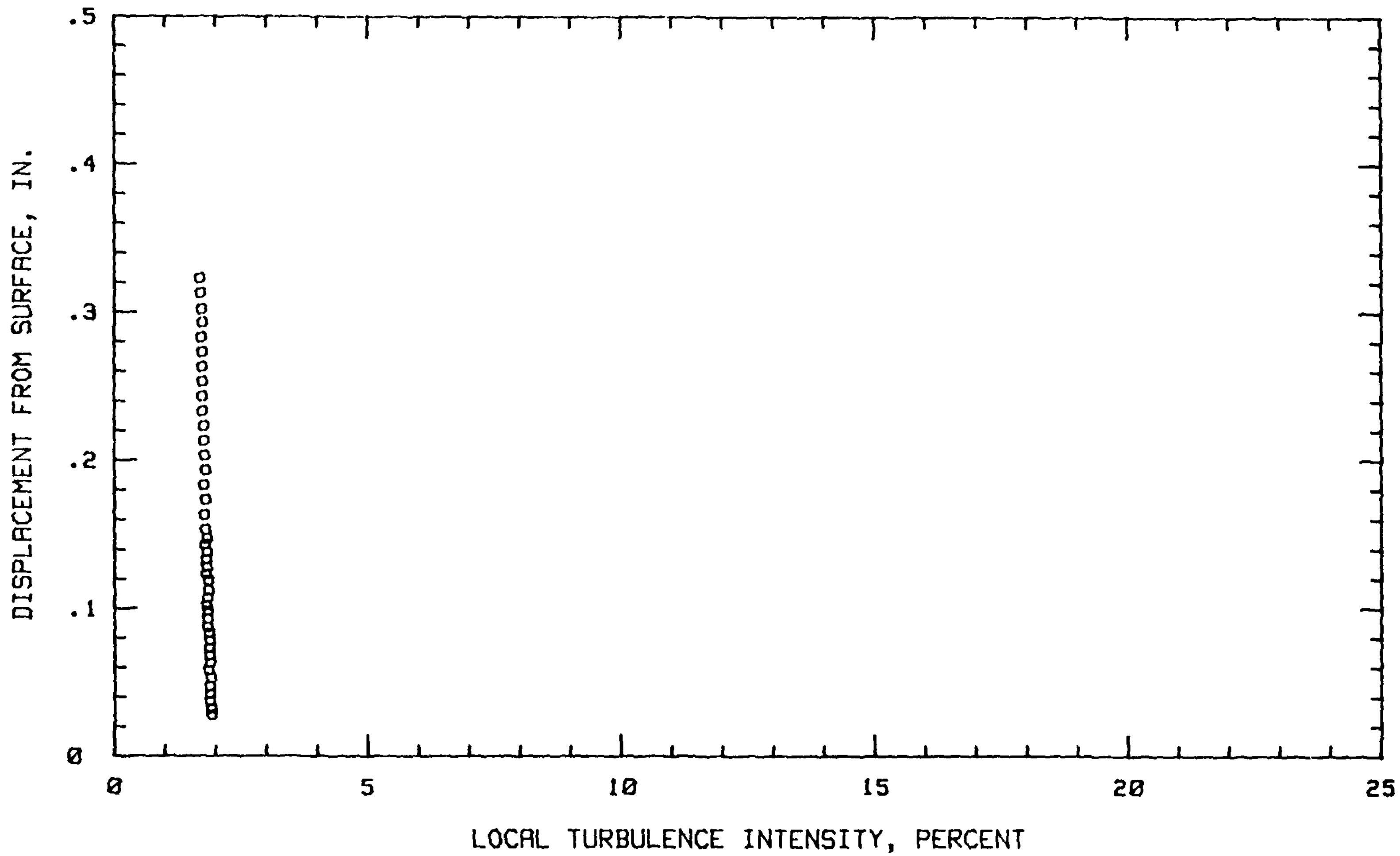

Fig. 62. Boundary Layer Turbulence Intensity Profile, i = -3 Deg, 34.37 % Chord

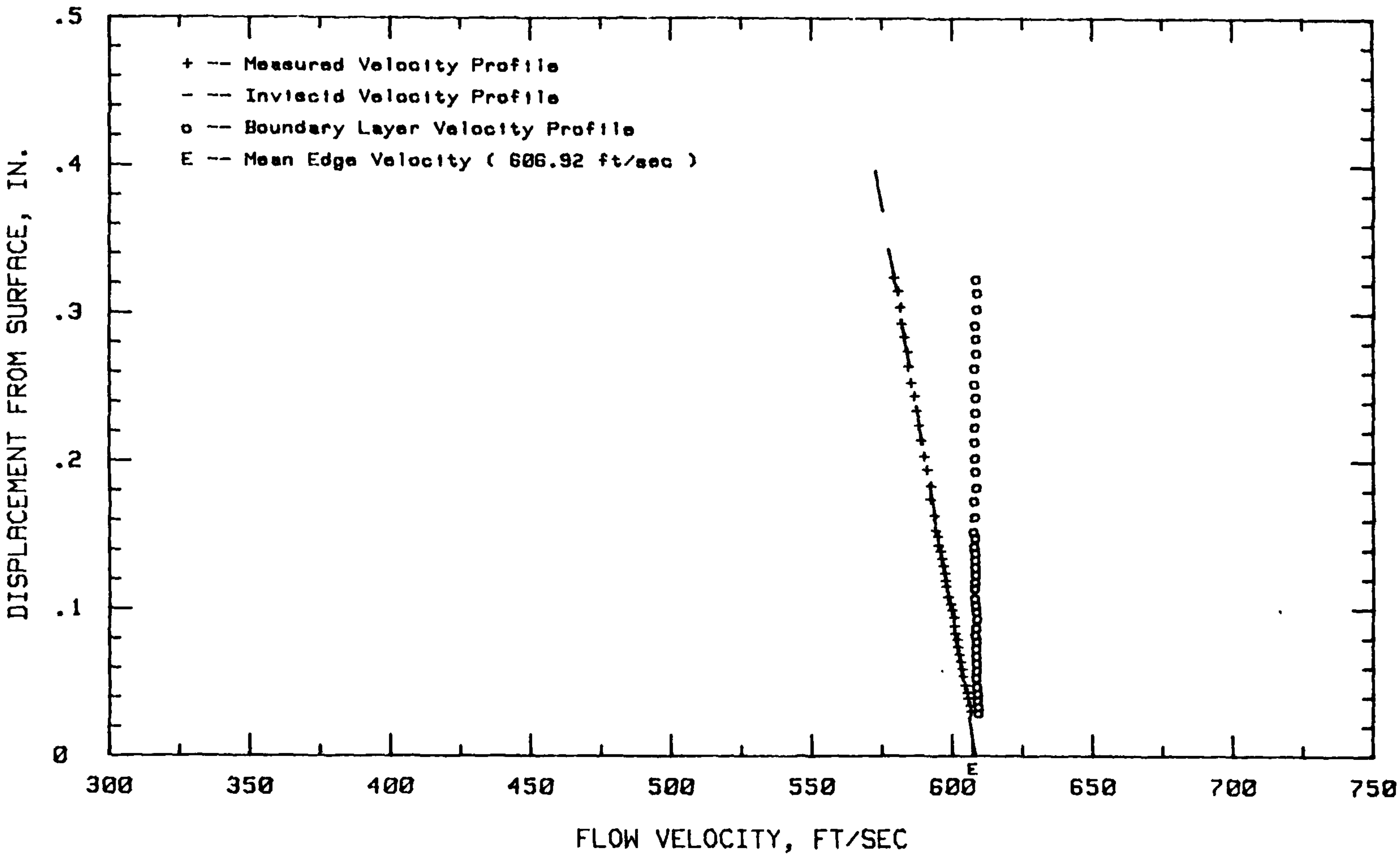

Fig. 63. Boundary Layer Velocity Profiles, i = -3 Deg, 40.62 % Chord

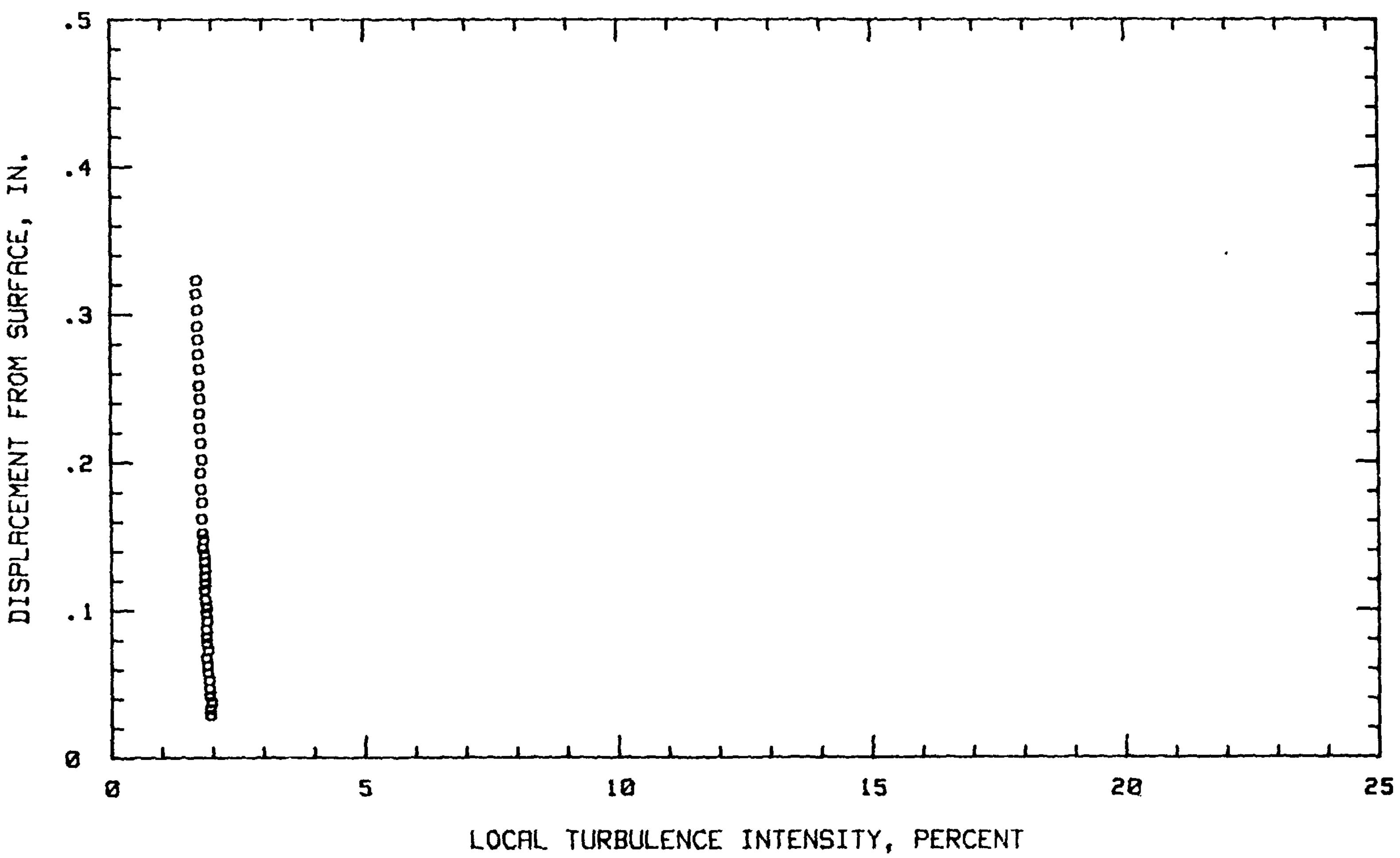

Fig. 64. Boundary Layer Turbulence Intensity Profile, i = -3 Deg, 40.62 % Chord

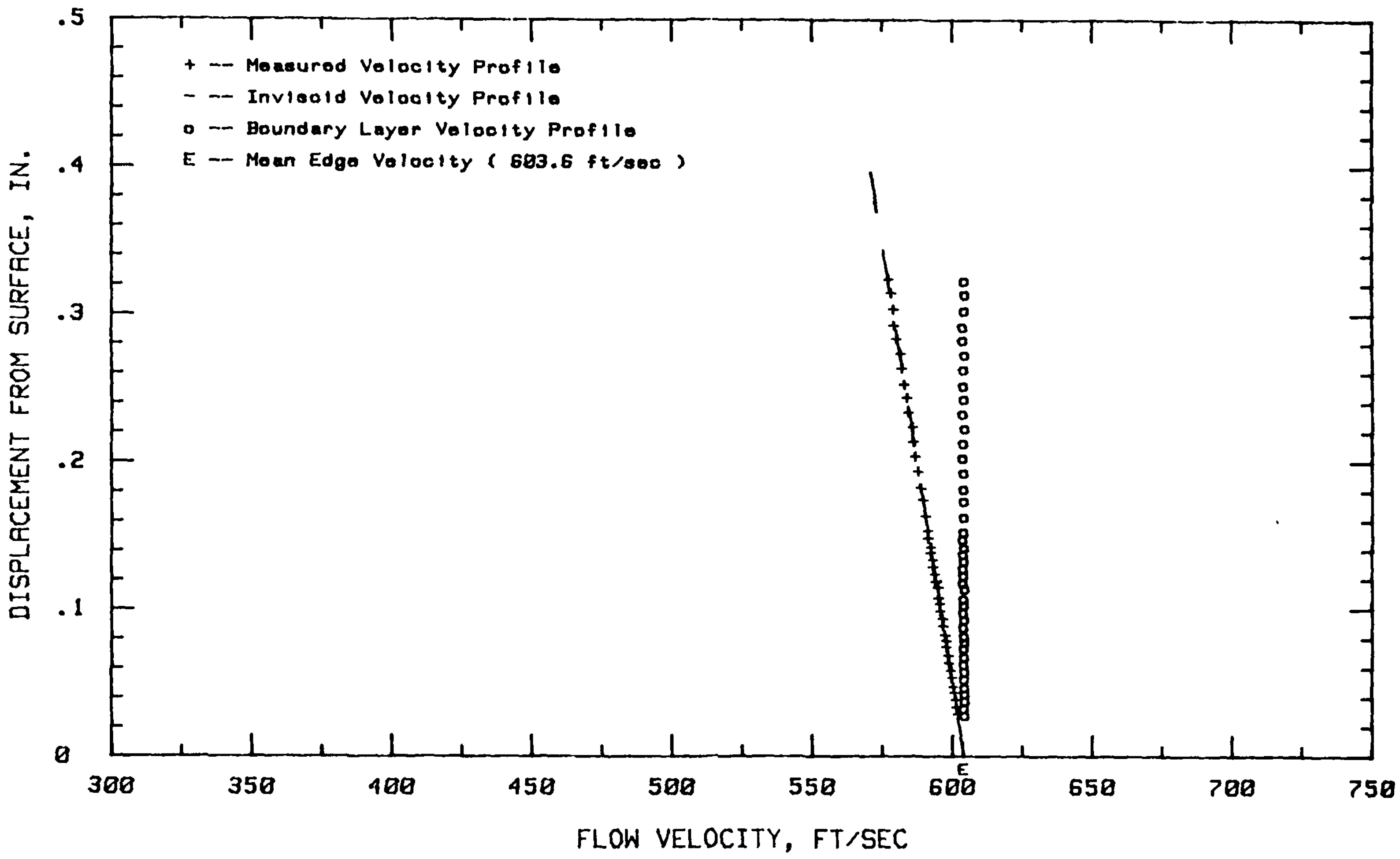

Fig. 65. Boundary Layer Velocity Profiles, i = -3 Deg, 45.31 % Chord

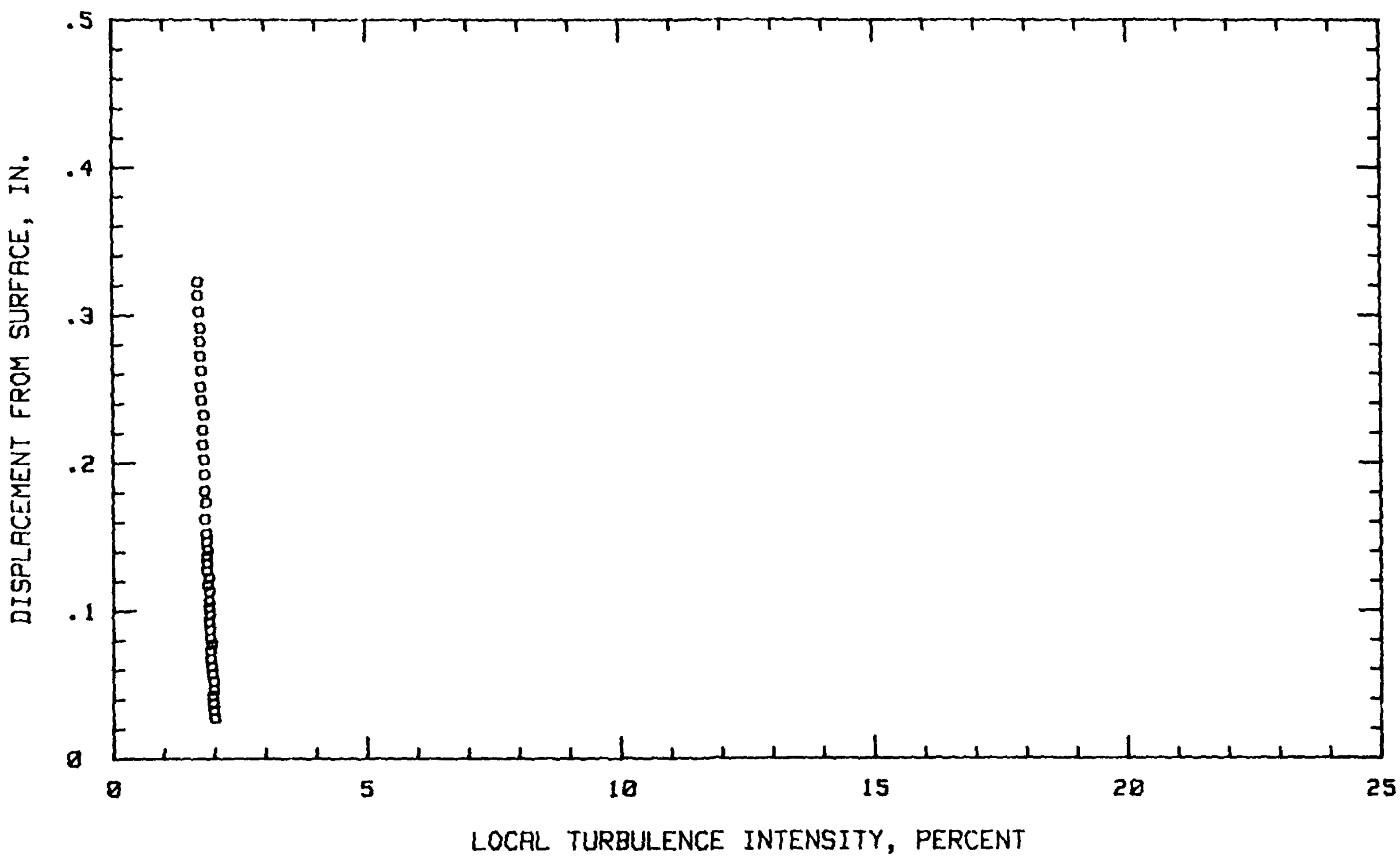

Fig. 66. Boundary Layer Turbulence Intensity Profile, i = -3 Deg, 45.31 % Chord

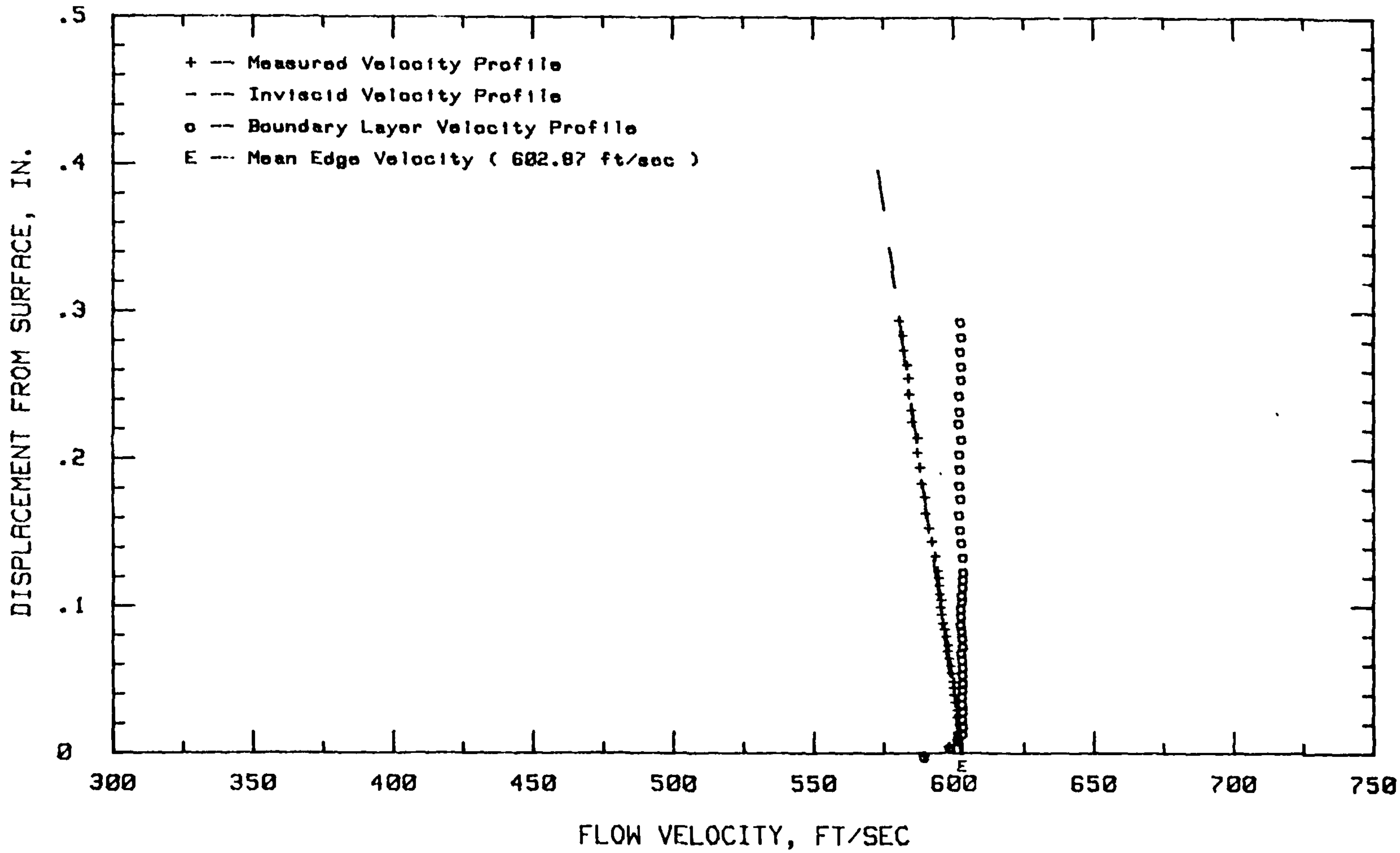

Fig. 67. Boundary Layer Velocity Profiles, i = -3 Deg, 50 % Chord

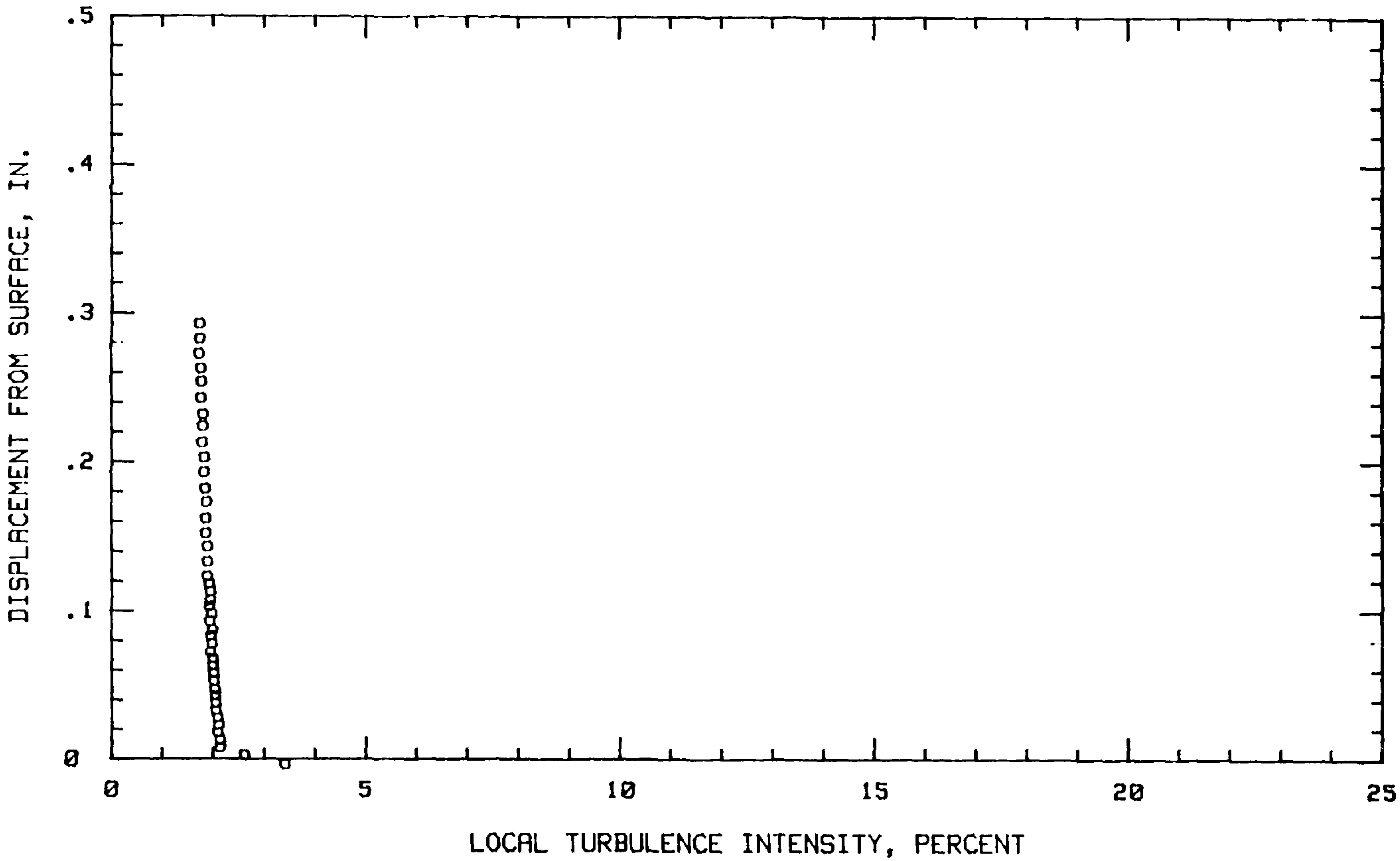

Fig. 68. Boundary Layer Turbulence Intensity Profile, i = -3 Deg, 50 % Chord

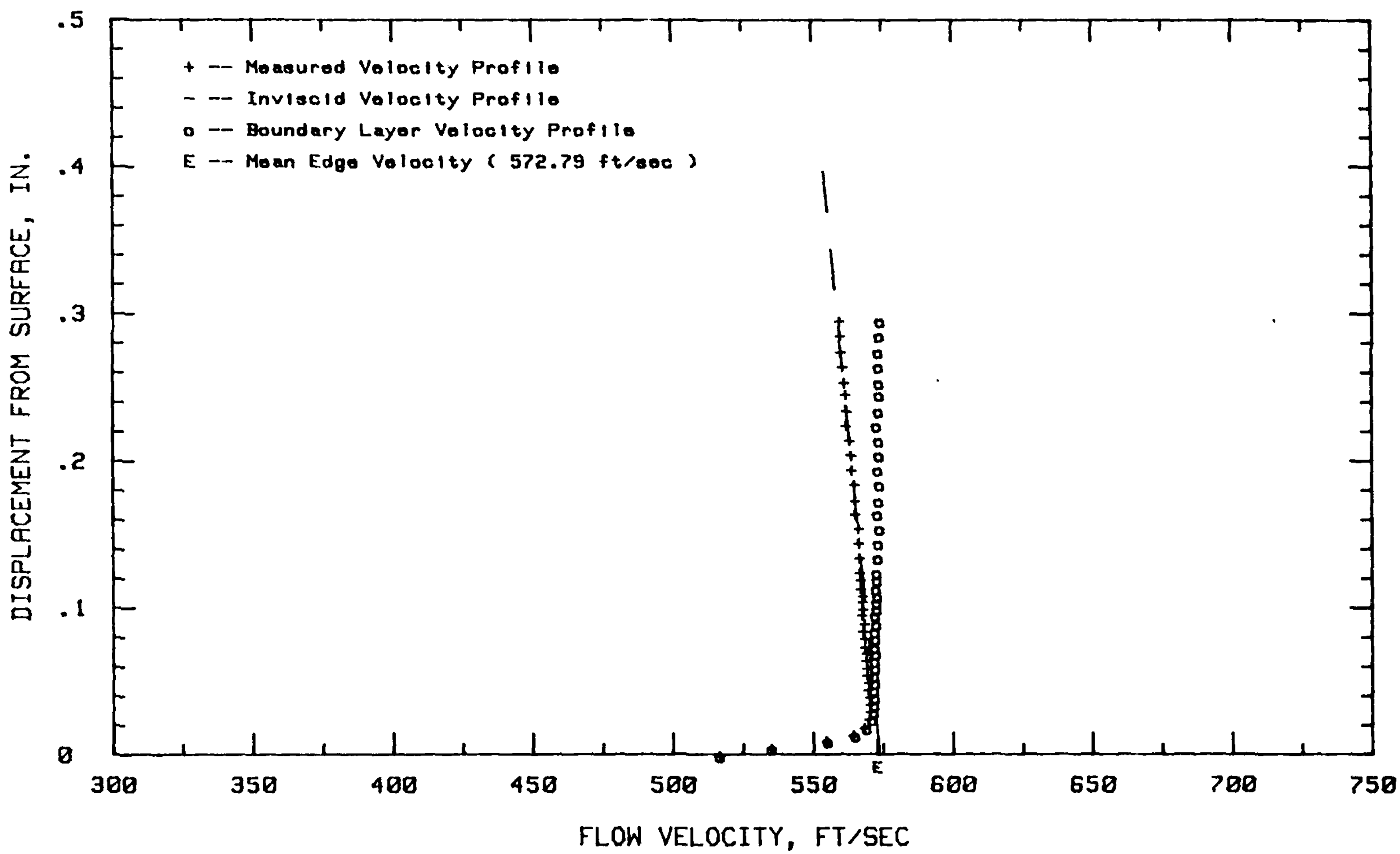

Fig. 69. Boundary Layer Velocity Profiles, i = -3 Deg, 65.62 % Chord

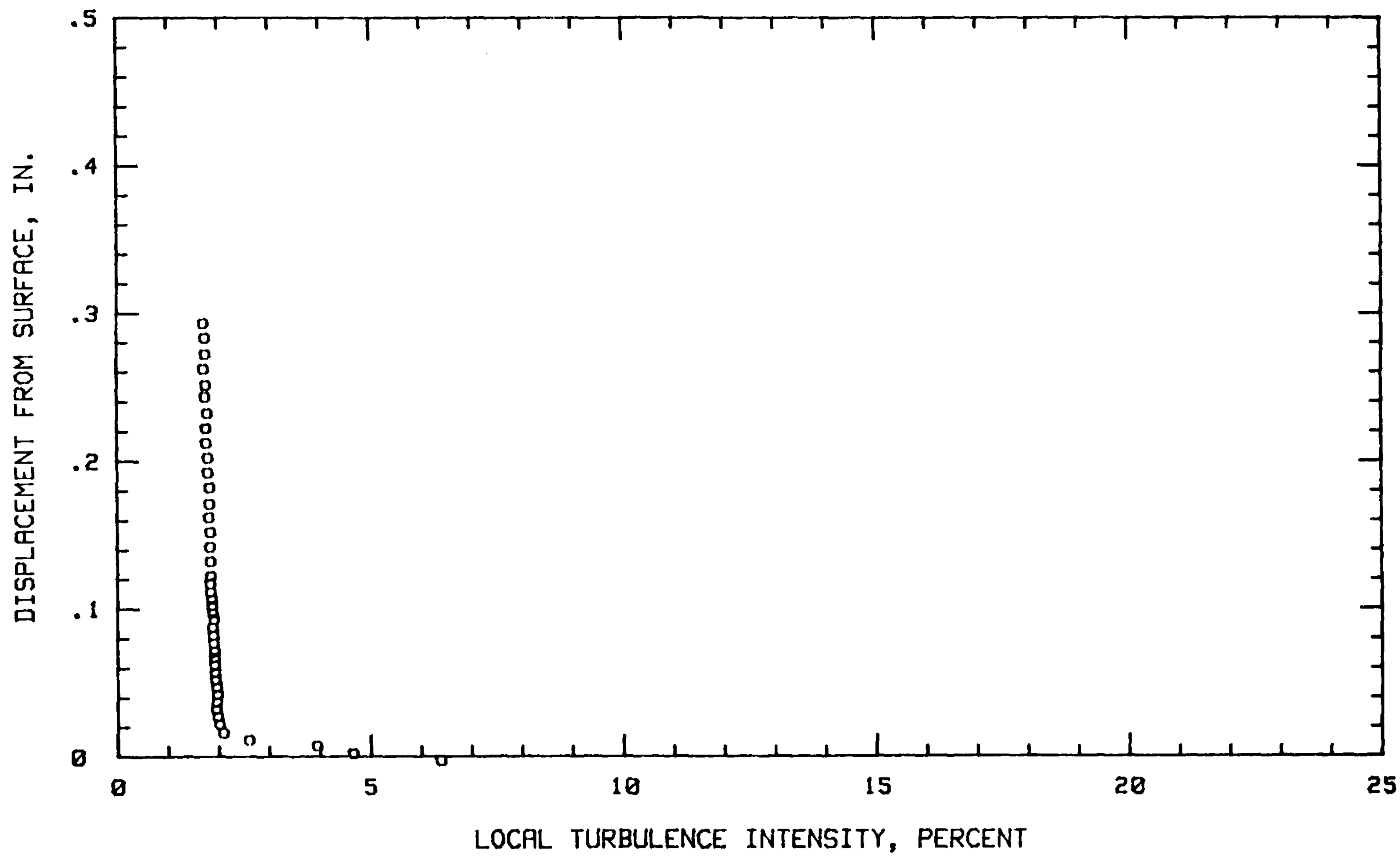

Fig. 70. Boundary Layer Turbulence Intensity Profile, i = -3 Deg, 65.62 % Chord

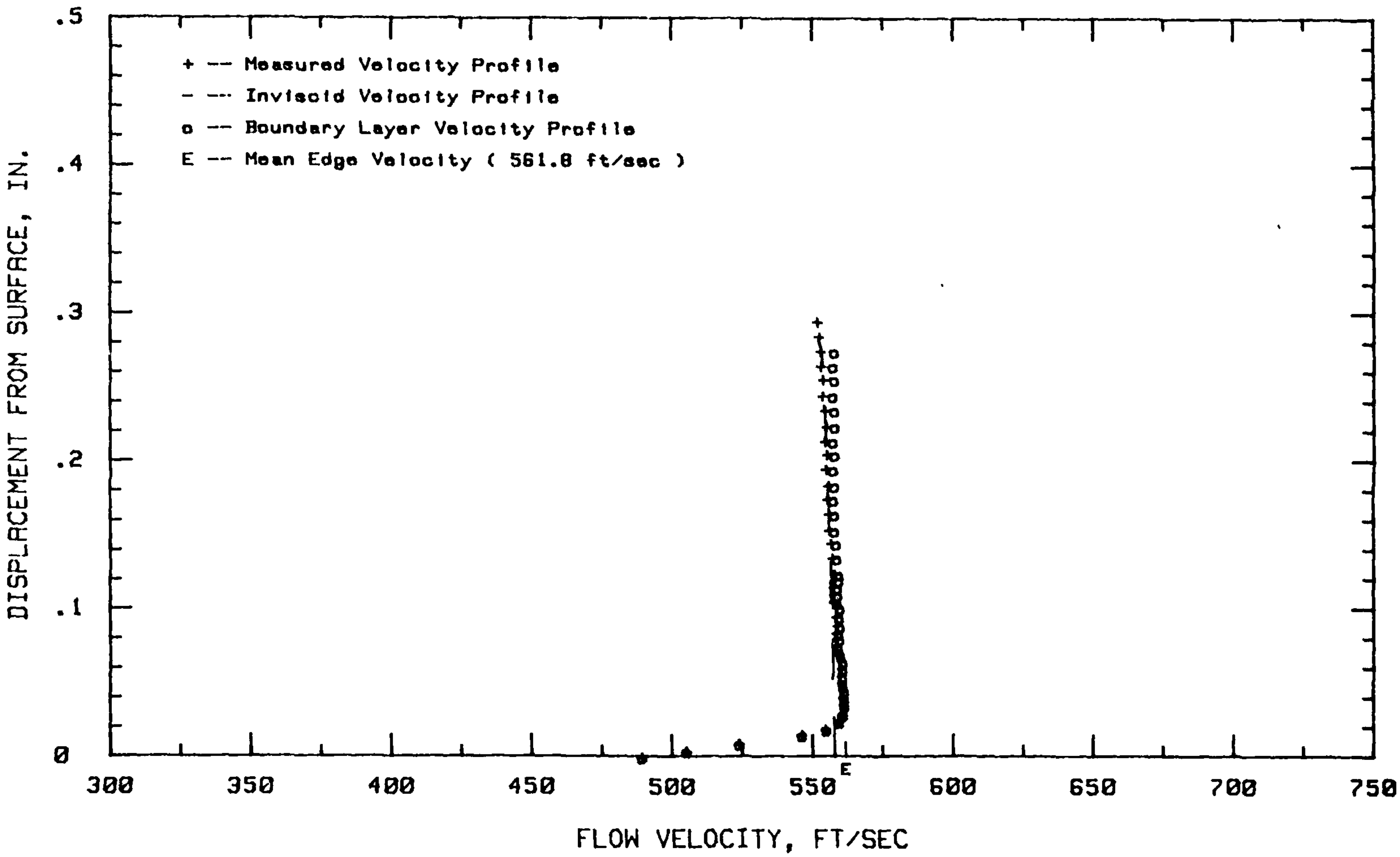

Fig. 71. Boundary Layer Velocity Profiles, i = -3 Deg, 70.31 % Chord

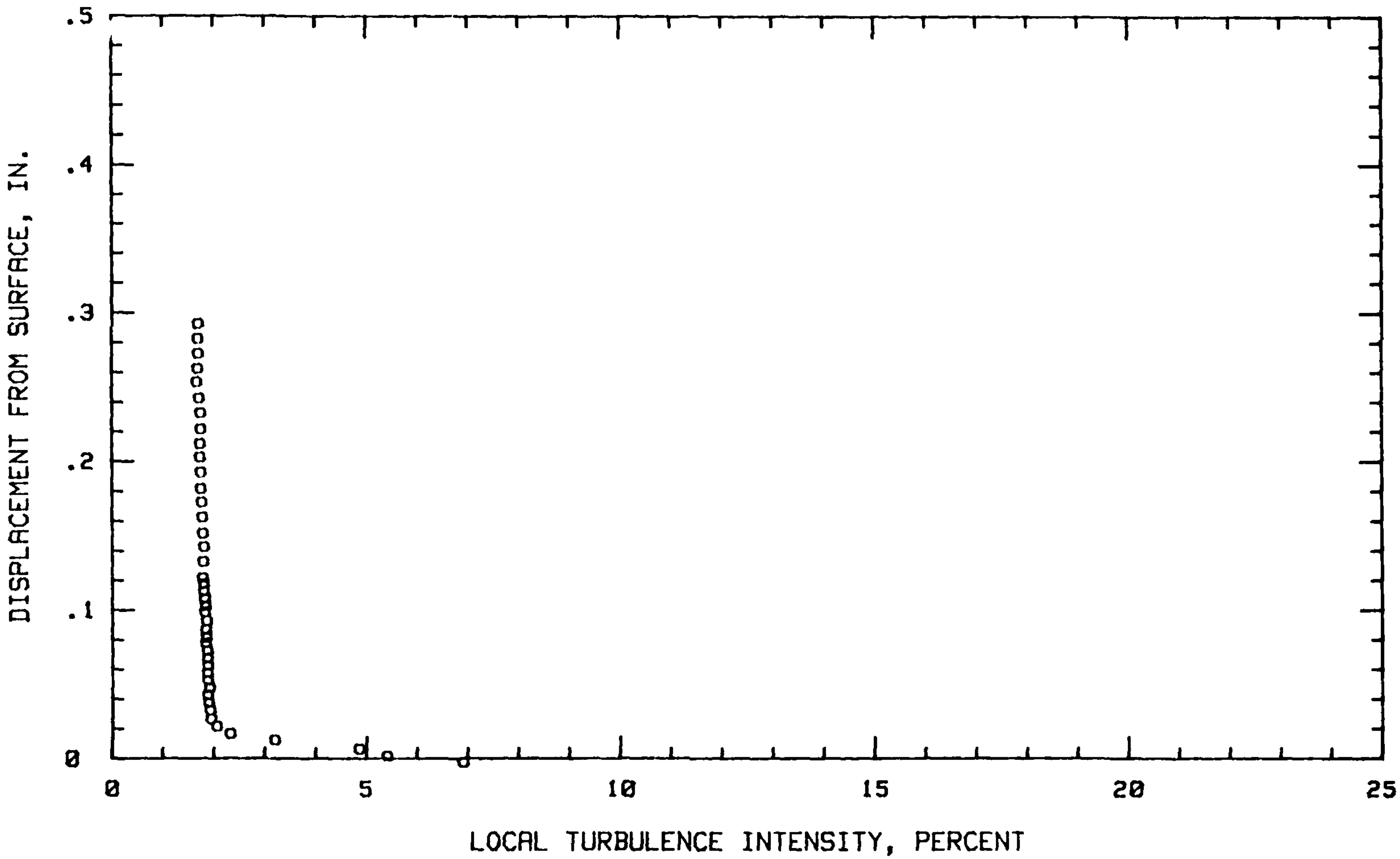

Fig. 72. Boundary Layer Turbulence Intensity Profile, i = -3 Deg, 70.31 % Chord

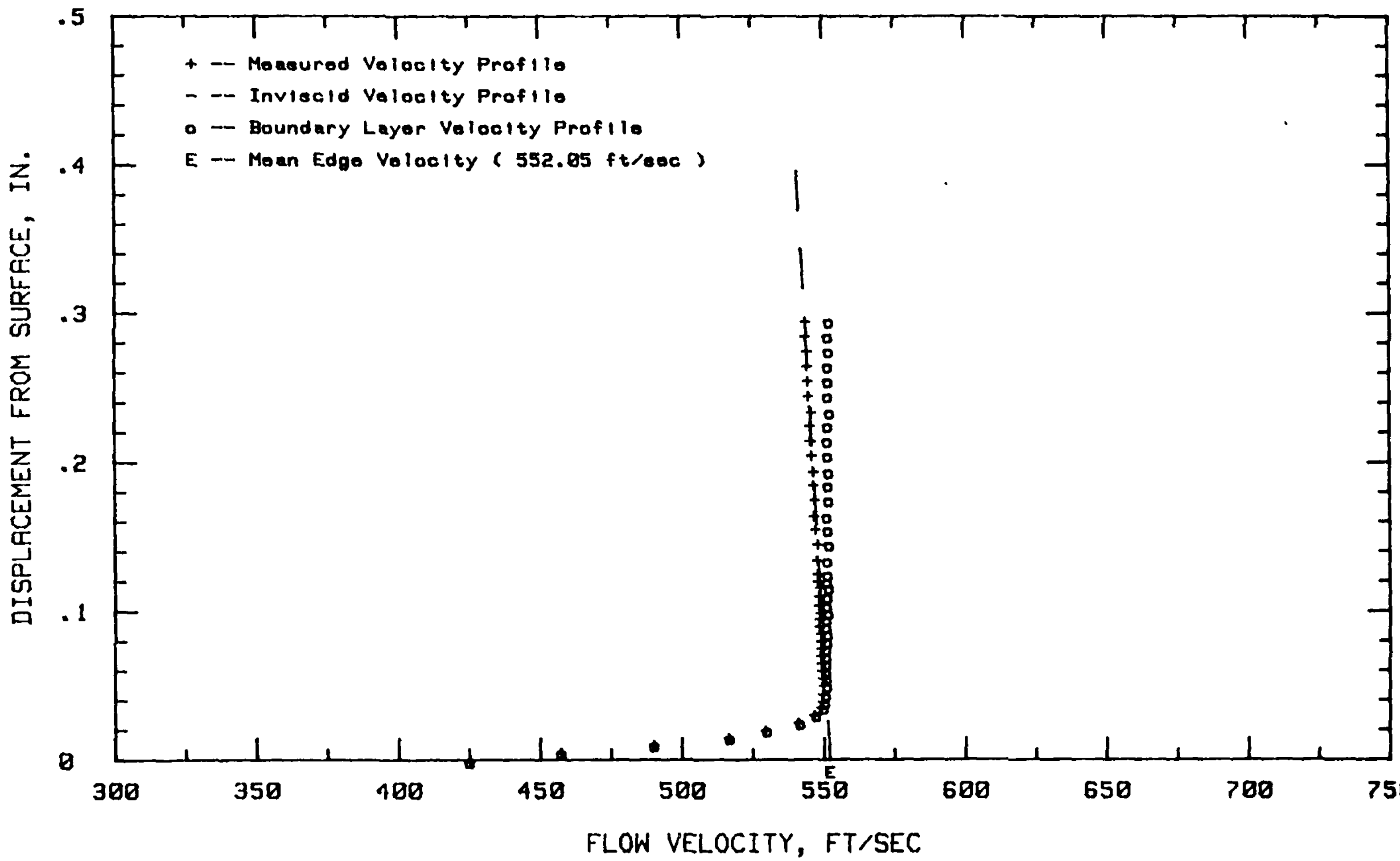

Fig. 73. Boundary Layer Velocity Profiles, i = -3 Deg, 75 % Chord

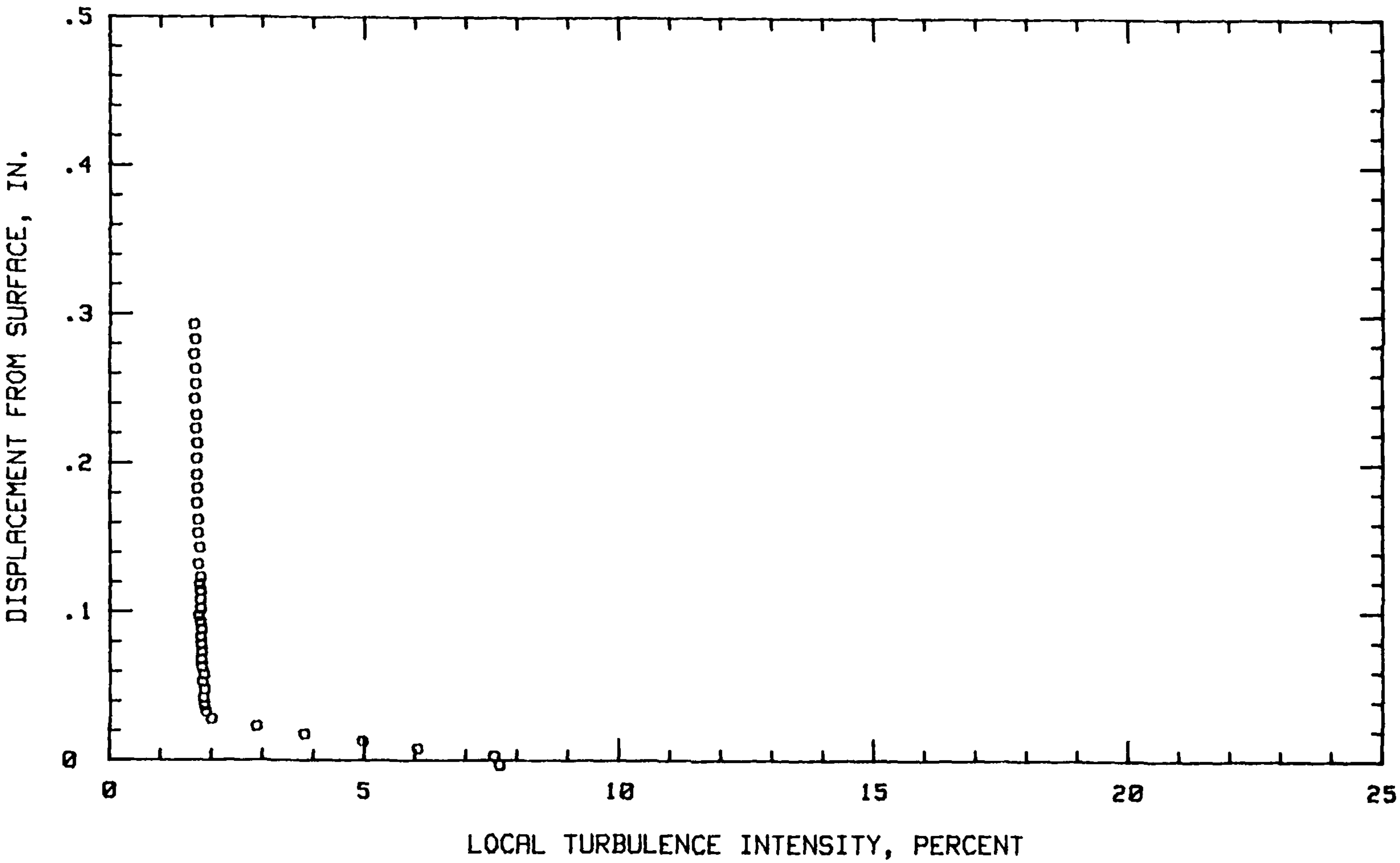

Fig. 74. Boundary Layer Turbulence Intensity Profile, i = -3 Deg, 75 % Chord

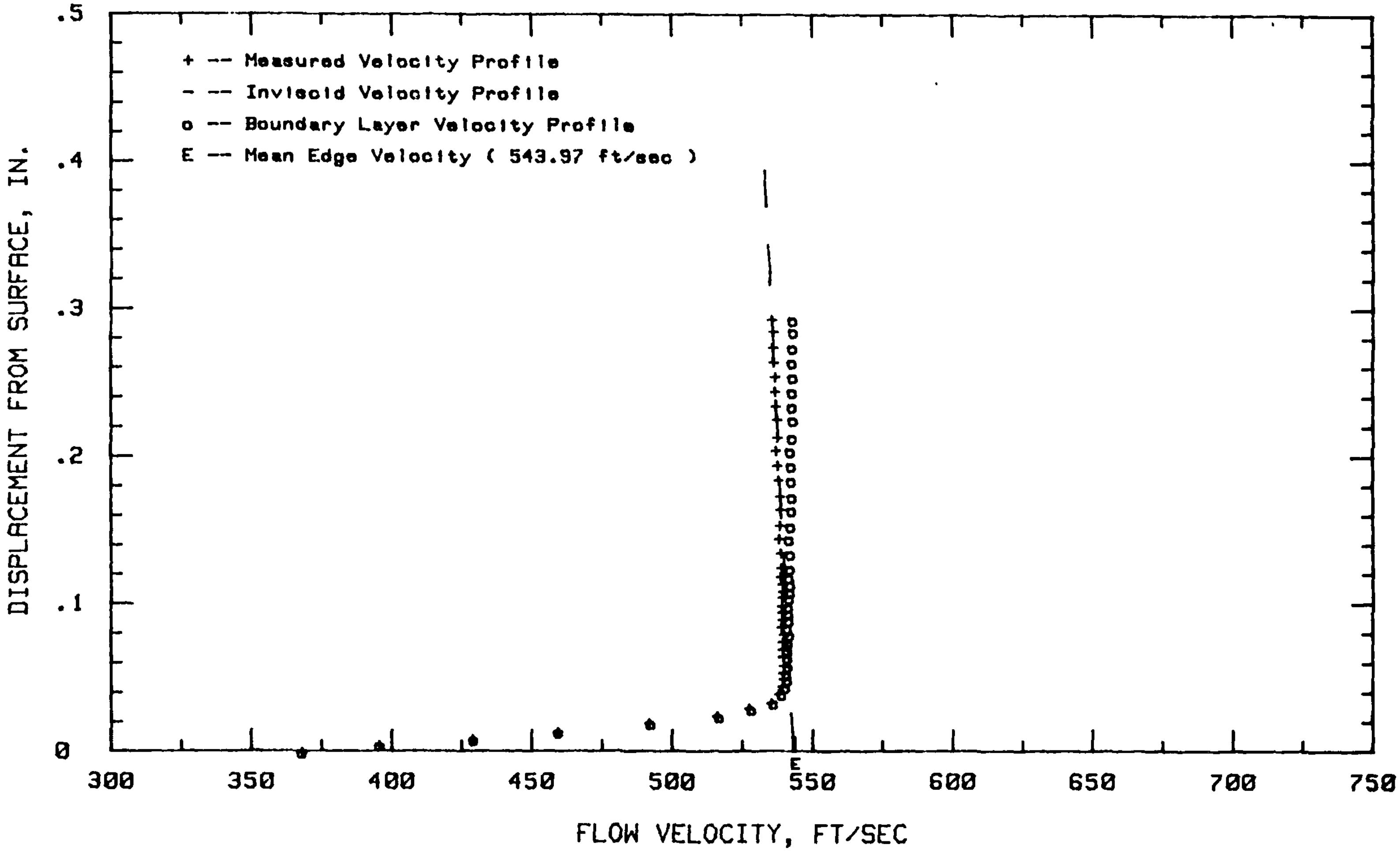

Fig. 75. Boundary Layer Velocity Profiles, i = -3 Deg, 79.68 % Chord

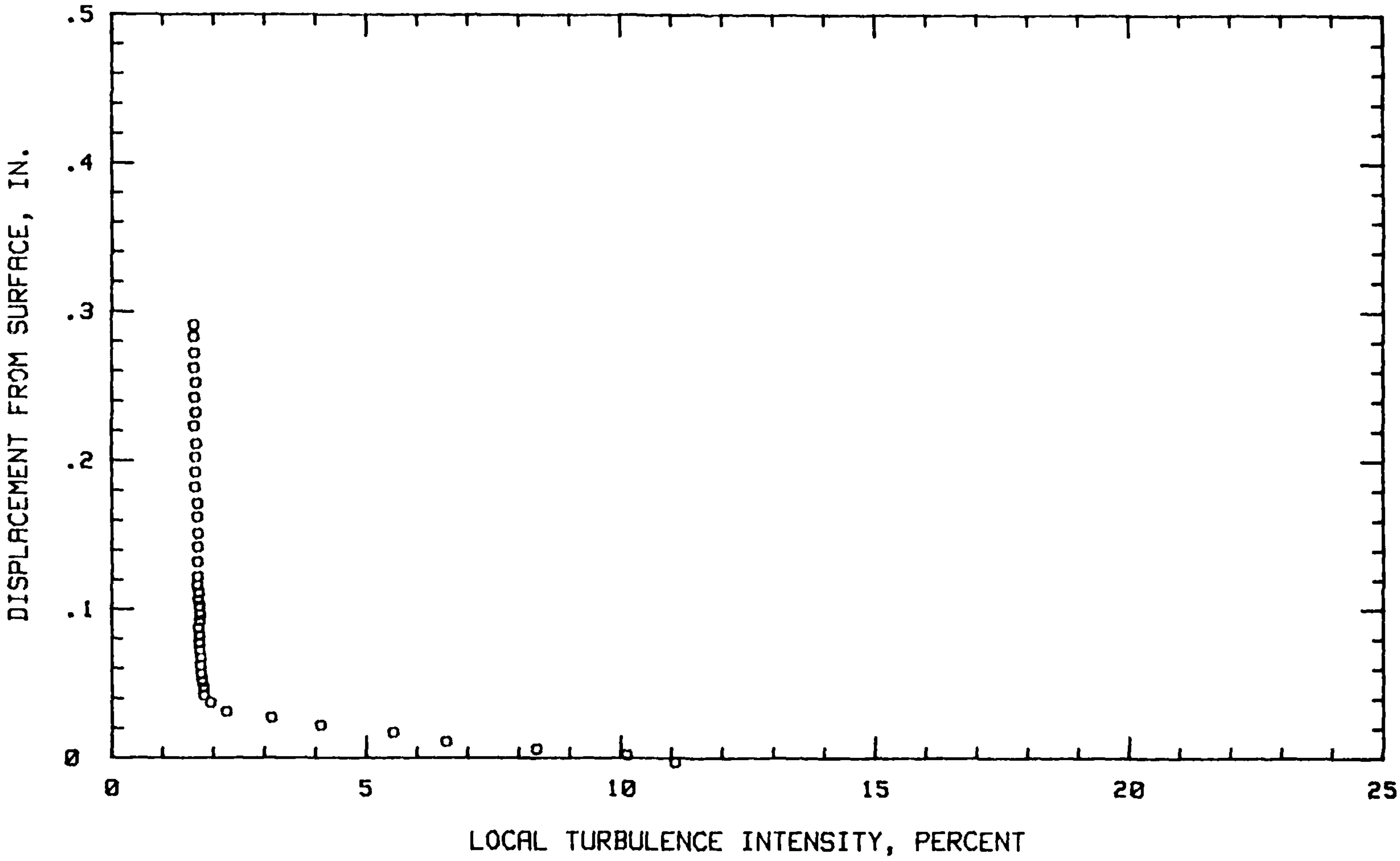

Fig. 76. Boundary Layer Turbulence Intensity Profile, i = -3 Deg, 79.68 % Chord

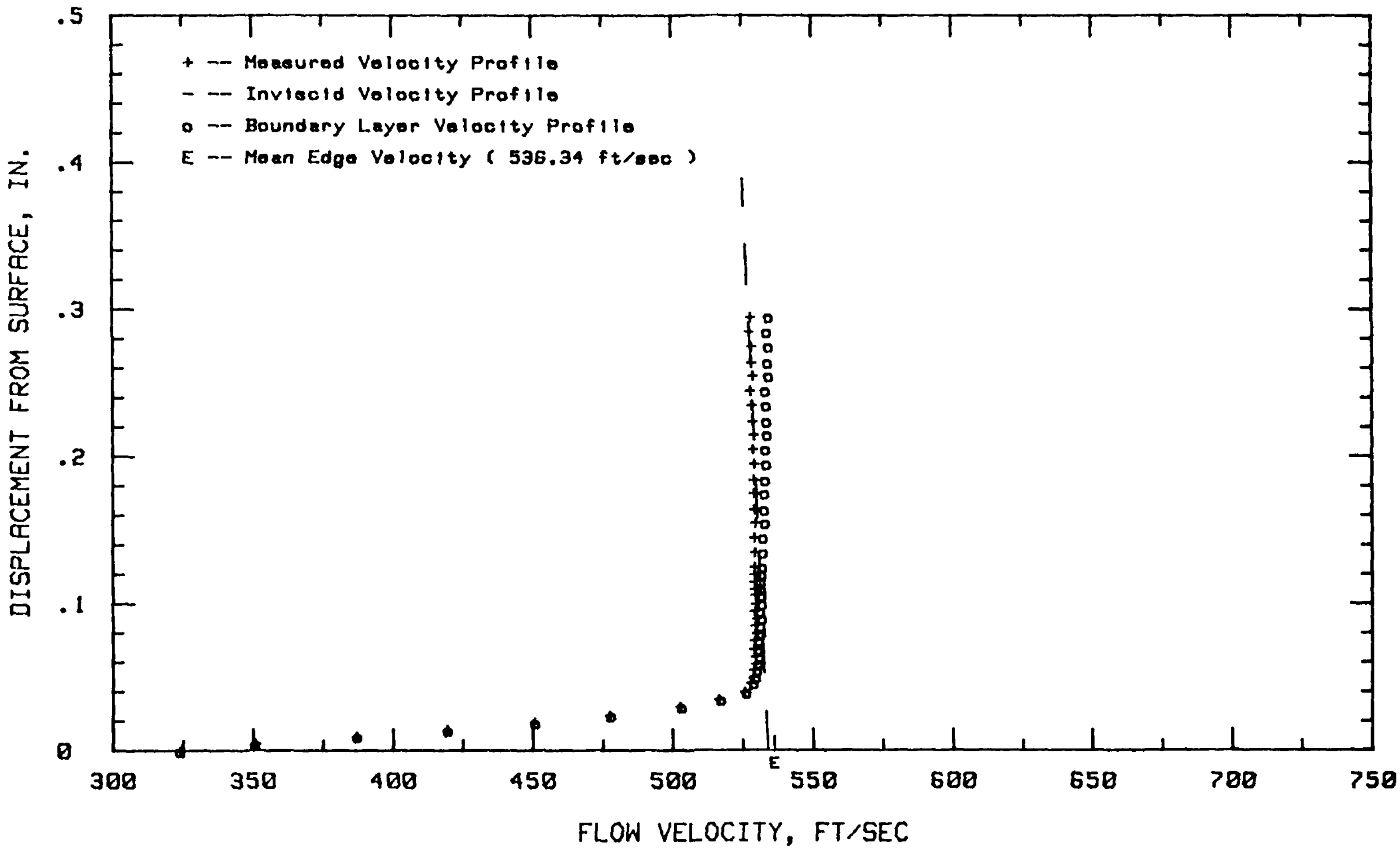

Fig. 77. Boundary Layer Velocity Profiles, i = -3 Deg, 84.37 % Chord

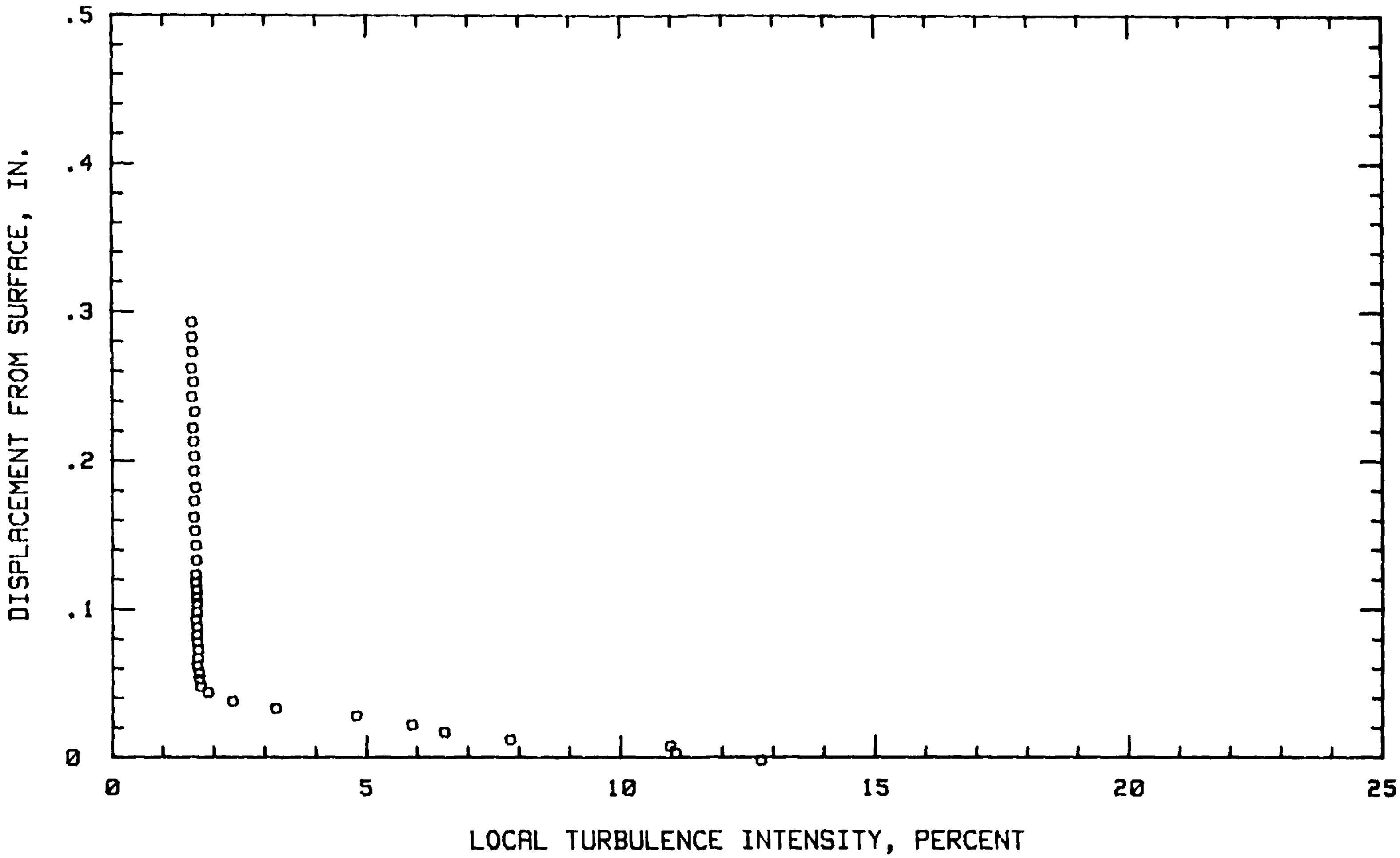

Fig. 78. Boundary Layer Turbulence Intensity Profile, i = -3 Deg, 84.37 % Chord

Appendix J

Boundary Layer Velocity and Turbulence Intensity Profiles

Blade Configuration Number 2

Incidence Angle = -3.0 Degrees

High Free Stream Turbulence

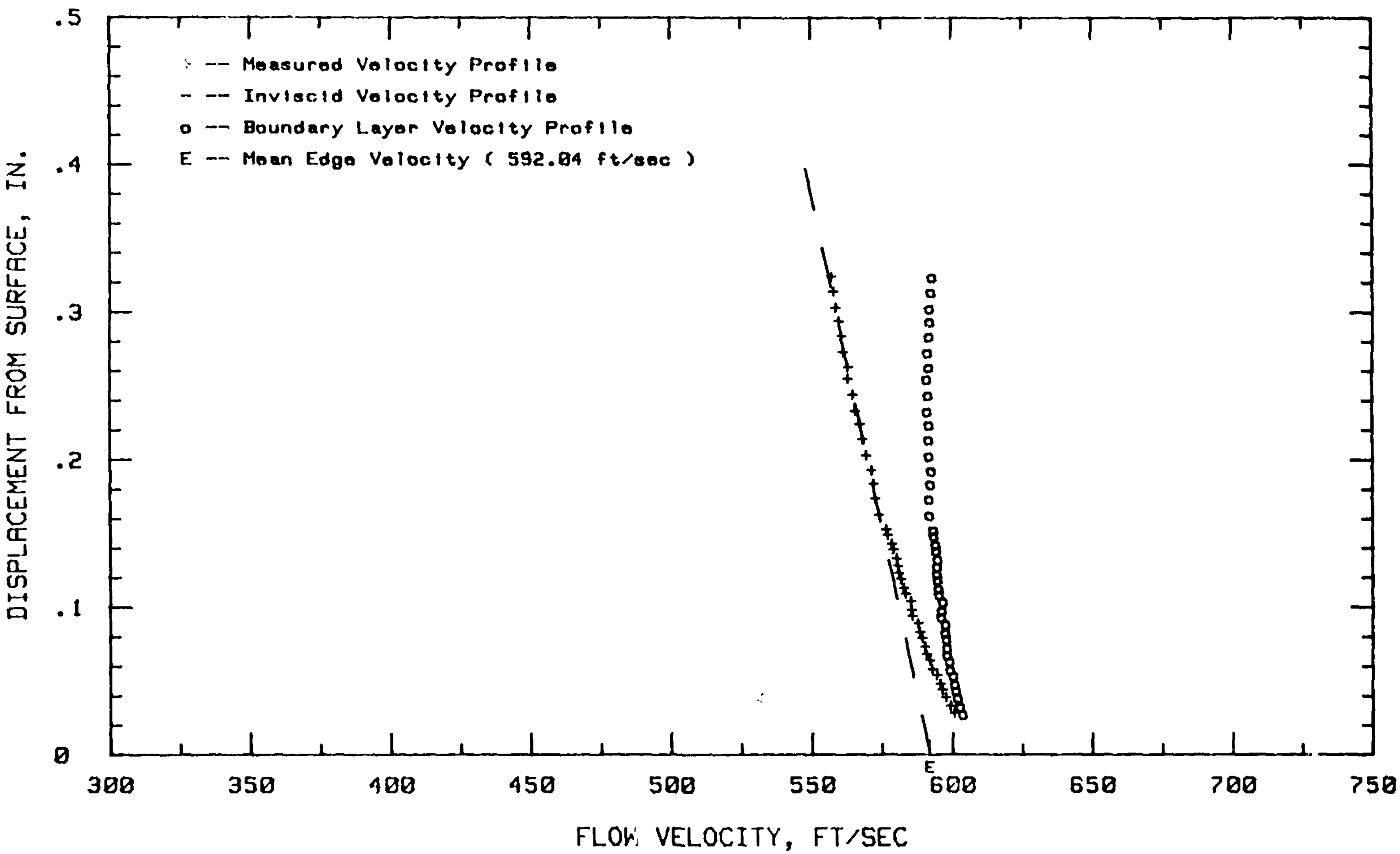

Fig. 79. Boundary Layer Velocity Profiles, i = -3 Deg, 4.68 % Chord

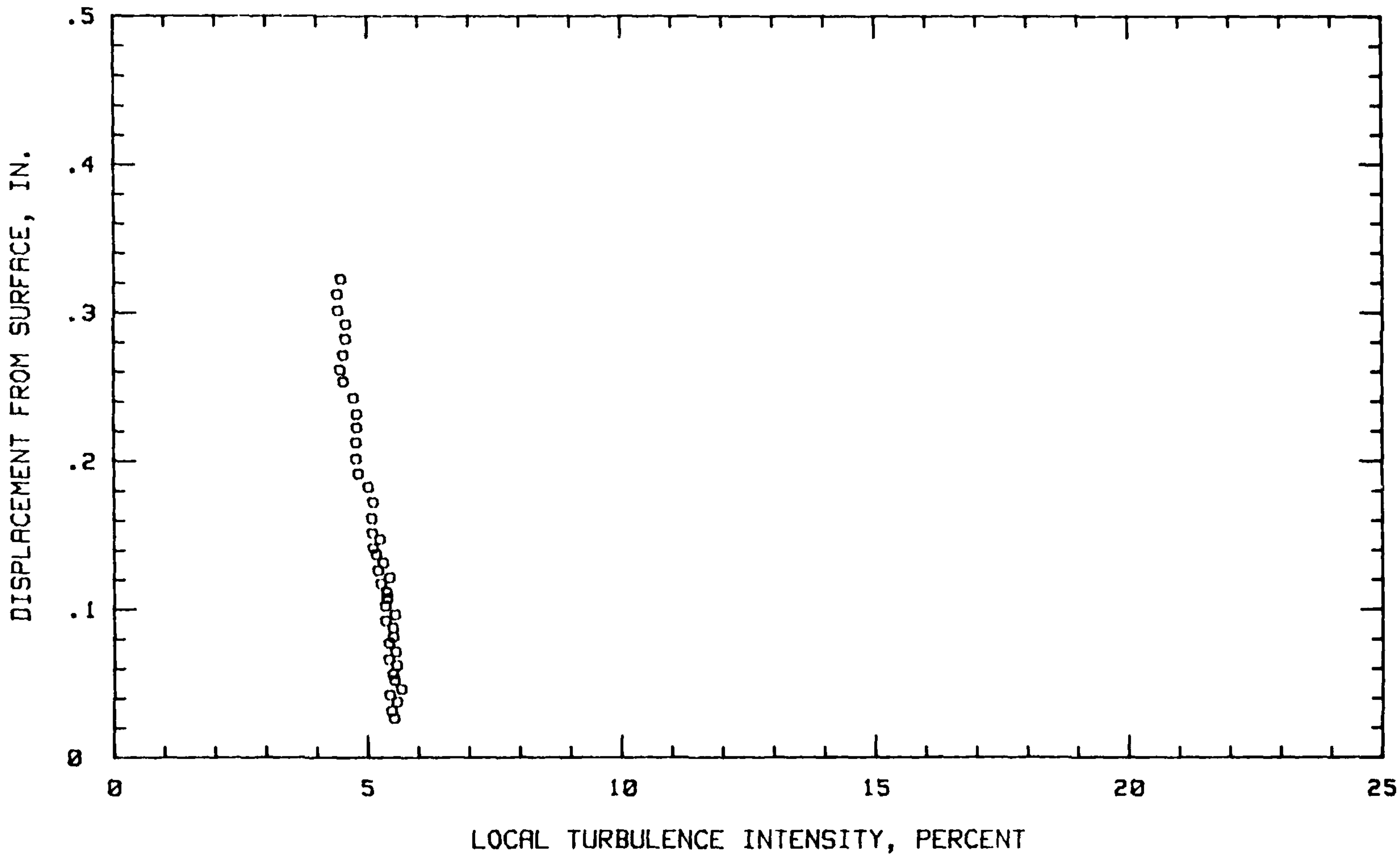

Fig. 80. Boundary Layer Turbulence Intensity Profile, i = -3 Deg, 4.68 % Chord

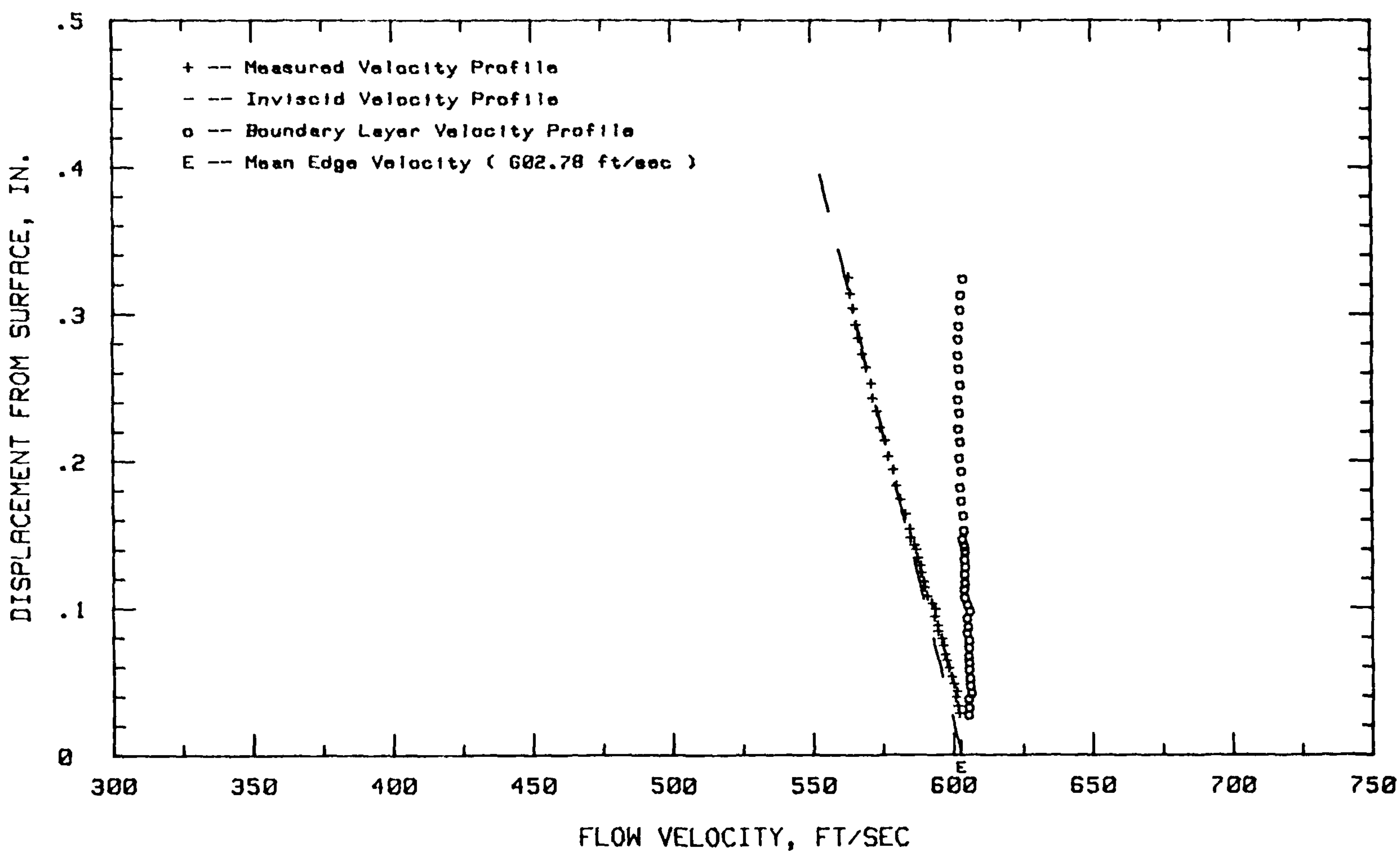

Fig. 81. Boundary Layer Velocity Profiles, i = -3 Deg, 9.37 % Chord

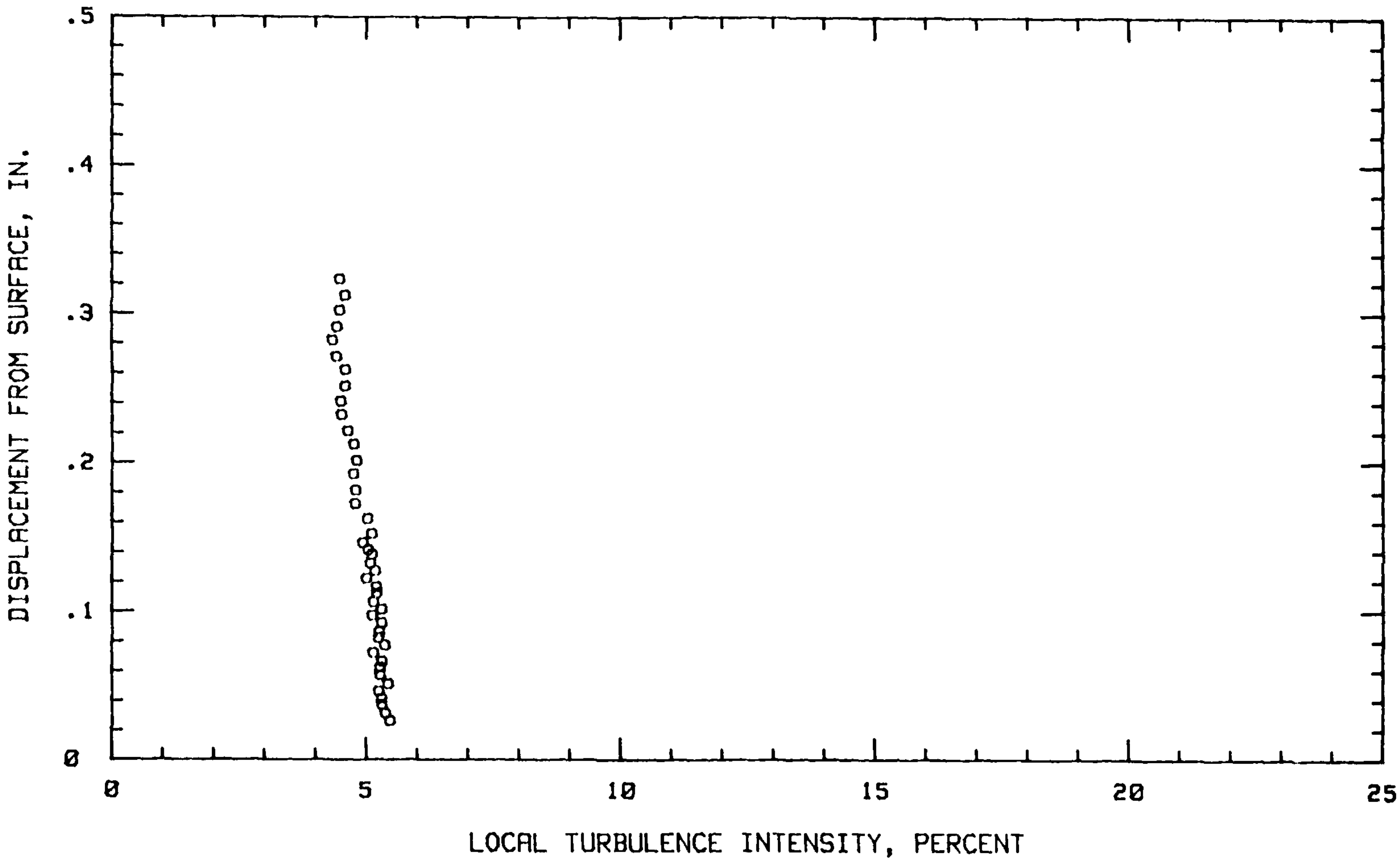

Fig. 82. Boundary Layer Turbulence Intensity Profile, i = -3 Deg, 9.37 % Chord

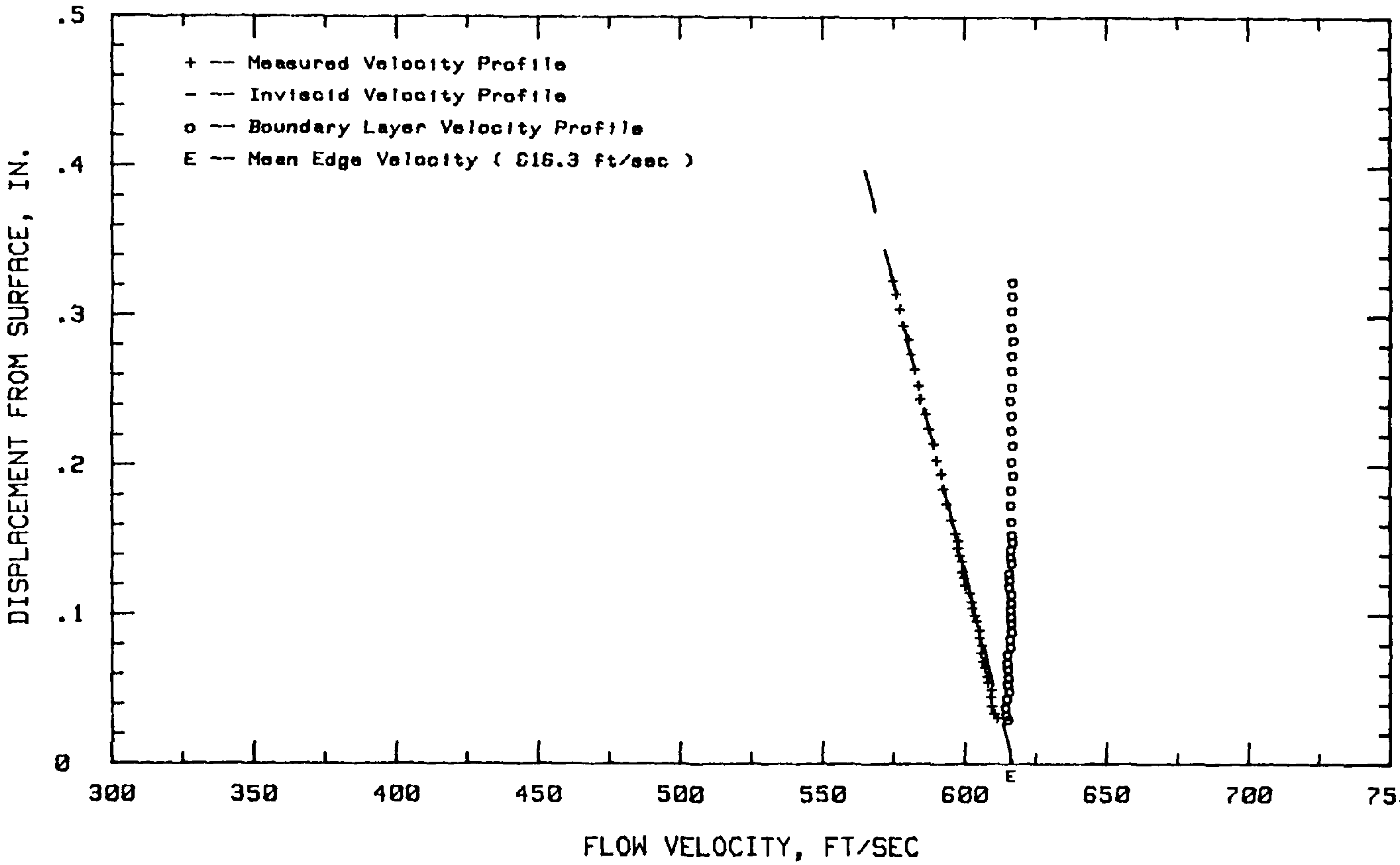

Fig. 83. Boundary Layer Velocity Profiles, i = -3 Deg, 25 % Chord

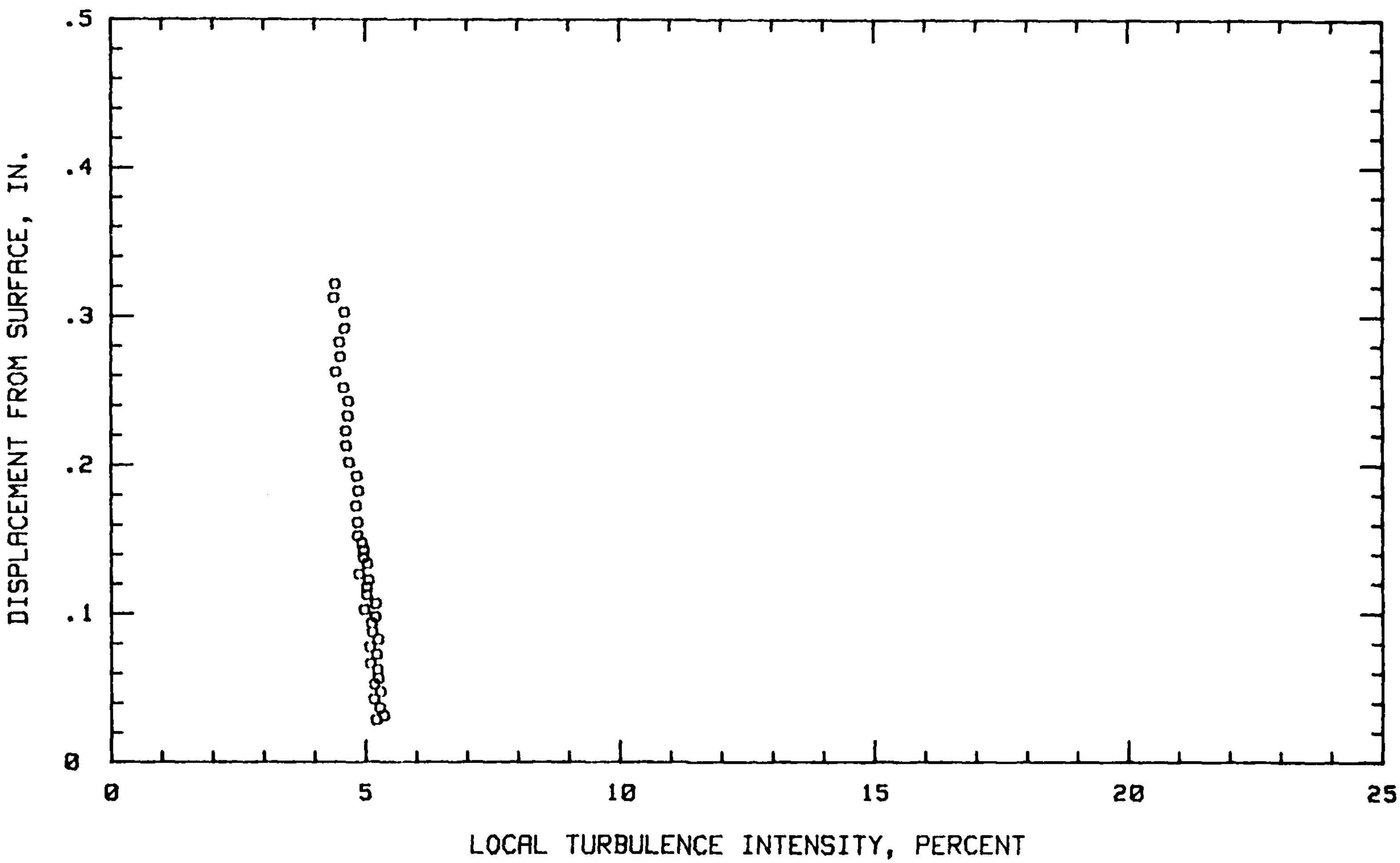

Fig. 84. Boundary Layer Turbulence Intensity Profile, i = -3 Deg, 25 % Chord

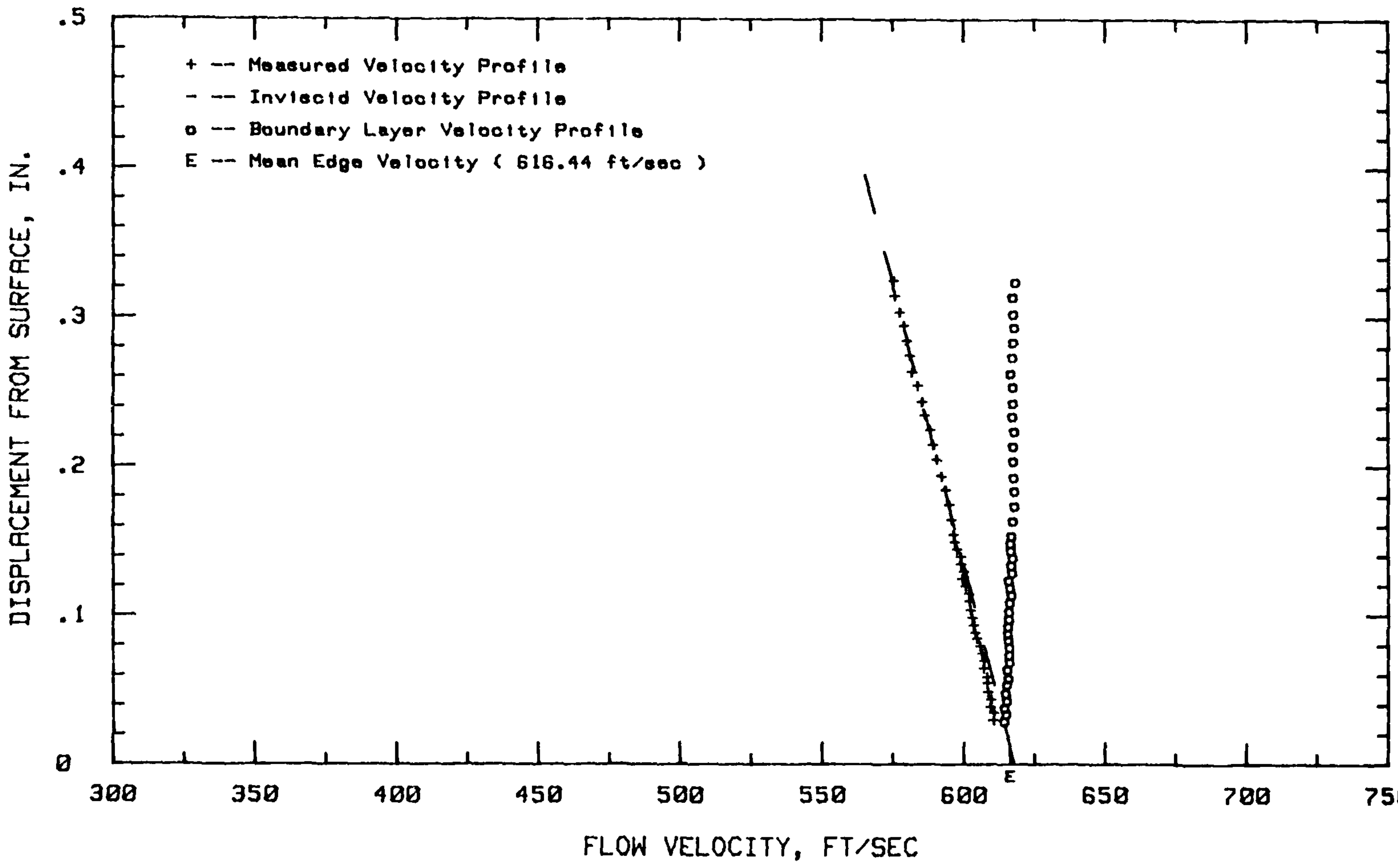

Fig. 85. Boundary Layer Velocity Profiles, i = -3 Deg, 29.68 % Chord

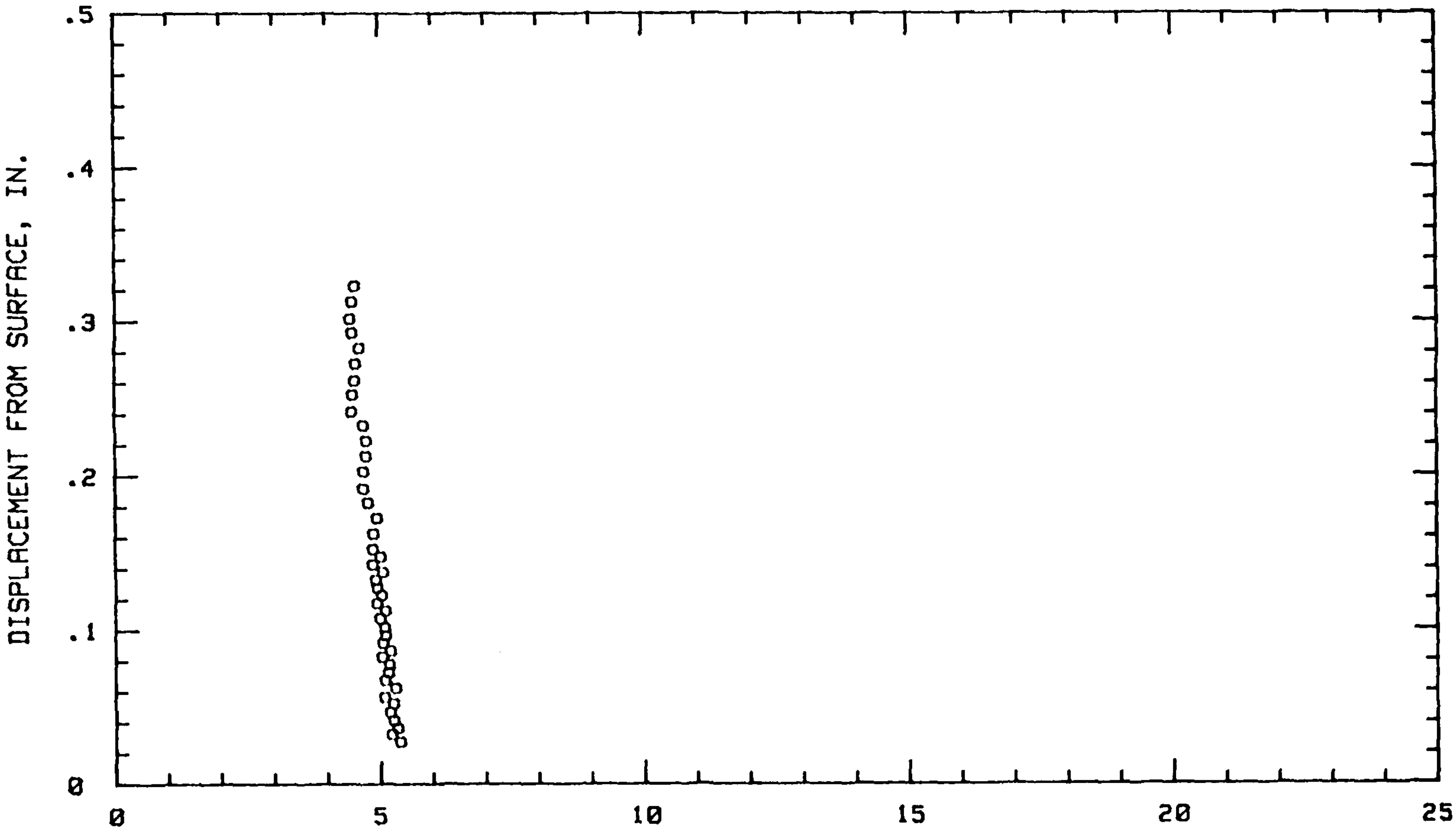

Fig. 86. Boundary Layer Turbulence Intensity Profile, i = -3 Deg, 29.68 % Chord

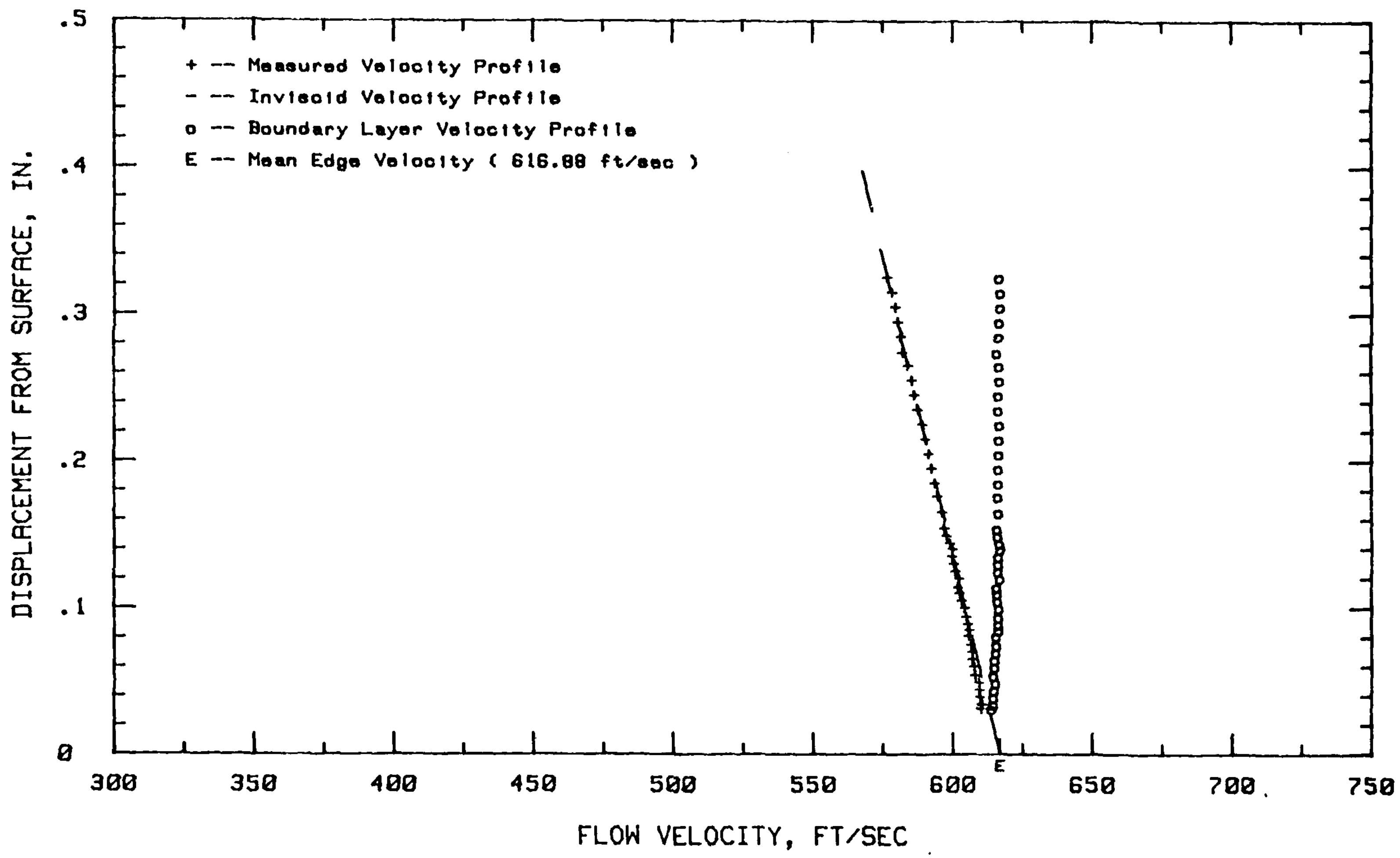

Fig. 87. Boundary Layer Velocity Profiles, i = -3 Deg, 34.37 % Chord

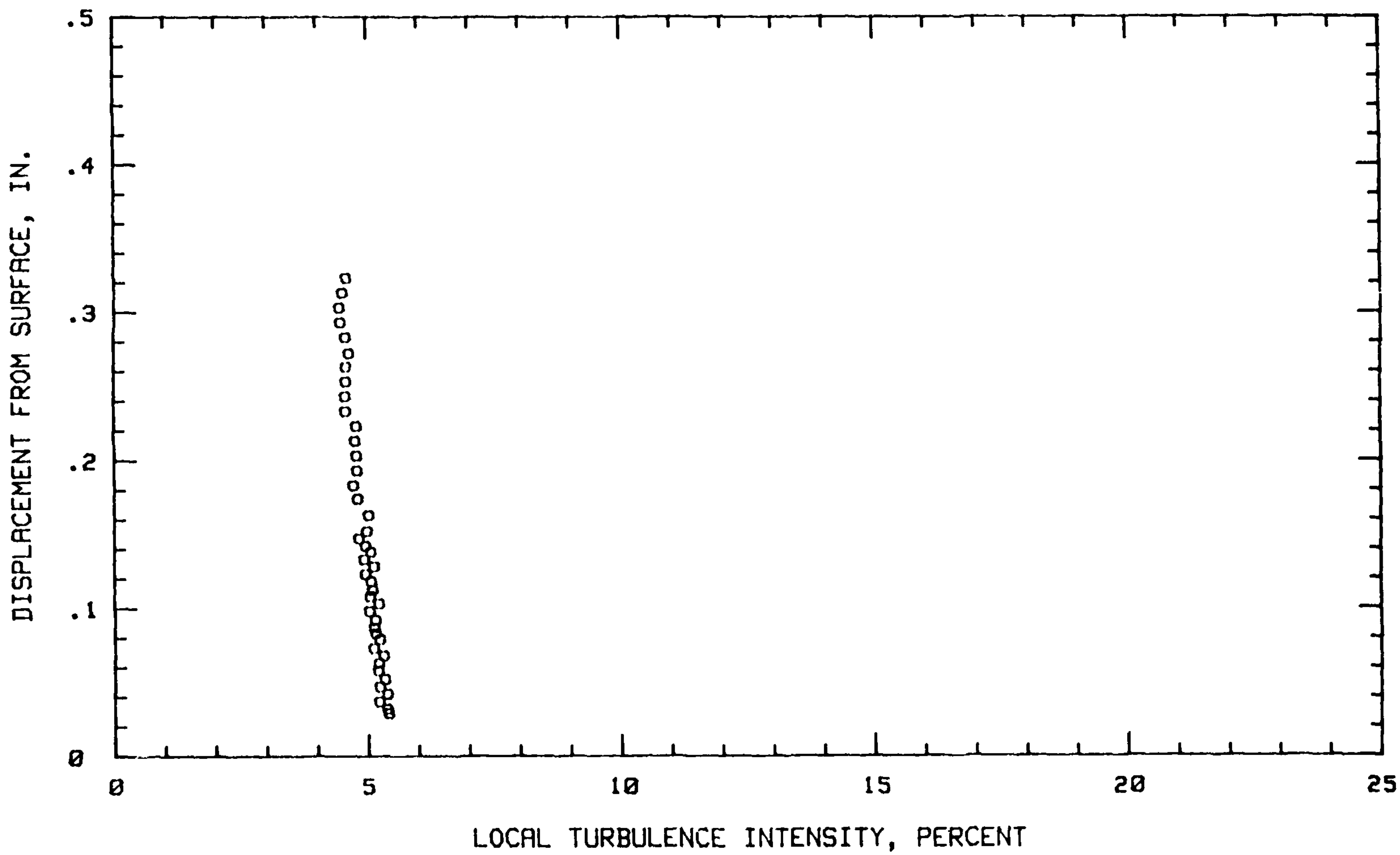

Fig. 88. Boundary Layer Turbulence Intensity Profile, i = -3 Deg, 34.37 % Chord

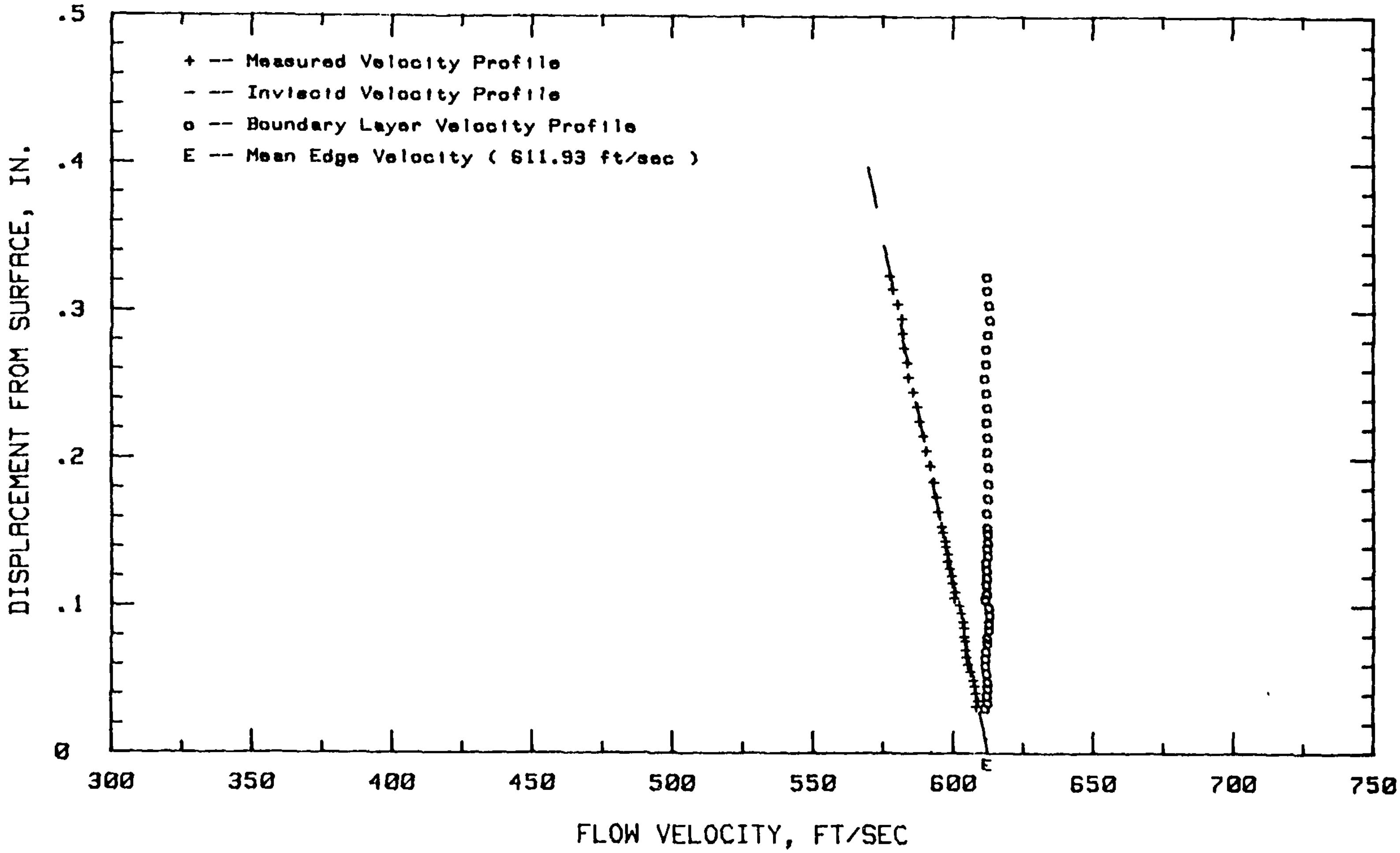

Fig. 89. Boundary Layer Velocity Profiles, i = -3 Deg, 40.62 % Chord

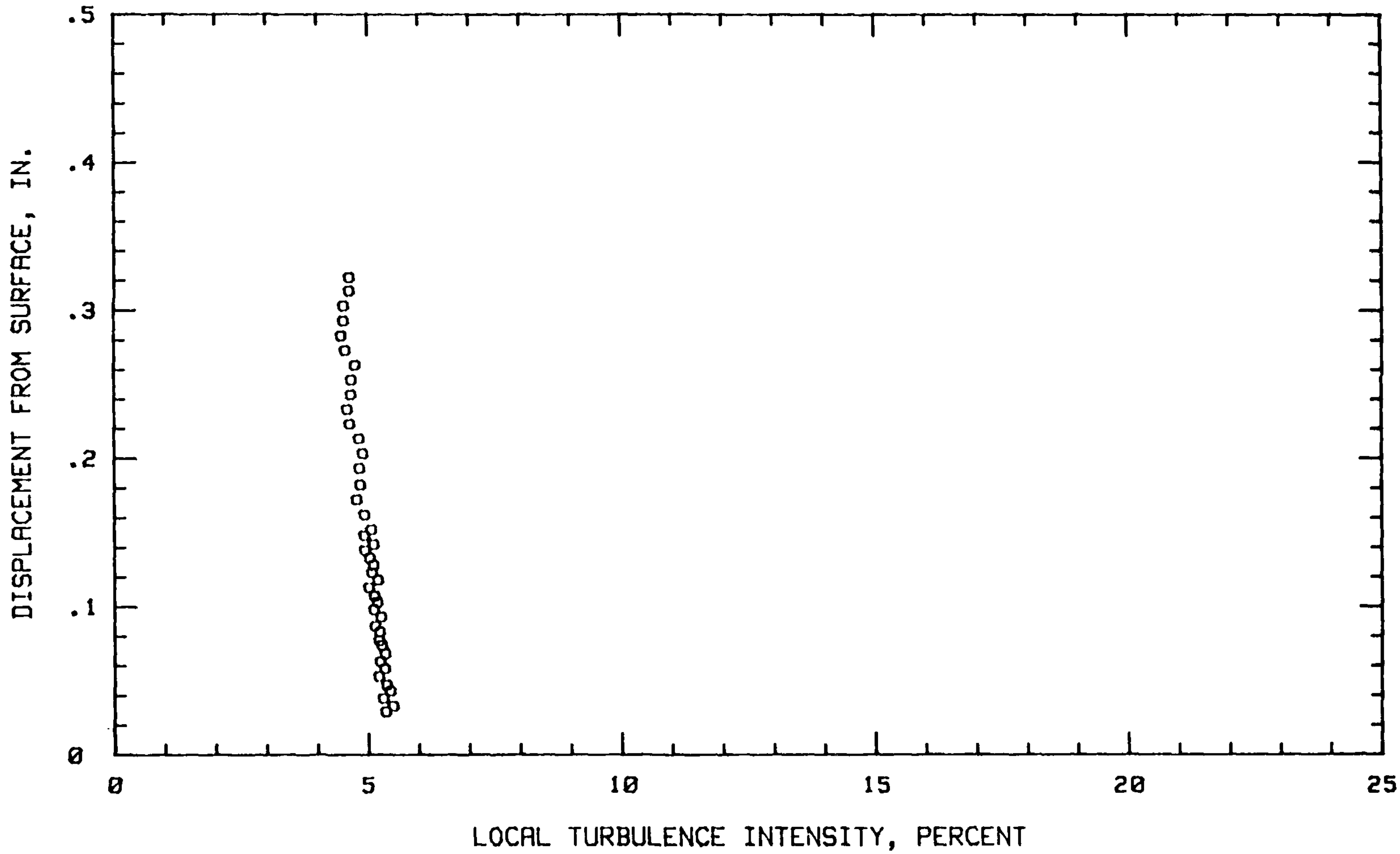

Fig. 90. Boundary Layer Turbulence Intensity Profile, i = -3 Deg, 40.62 % Chord

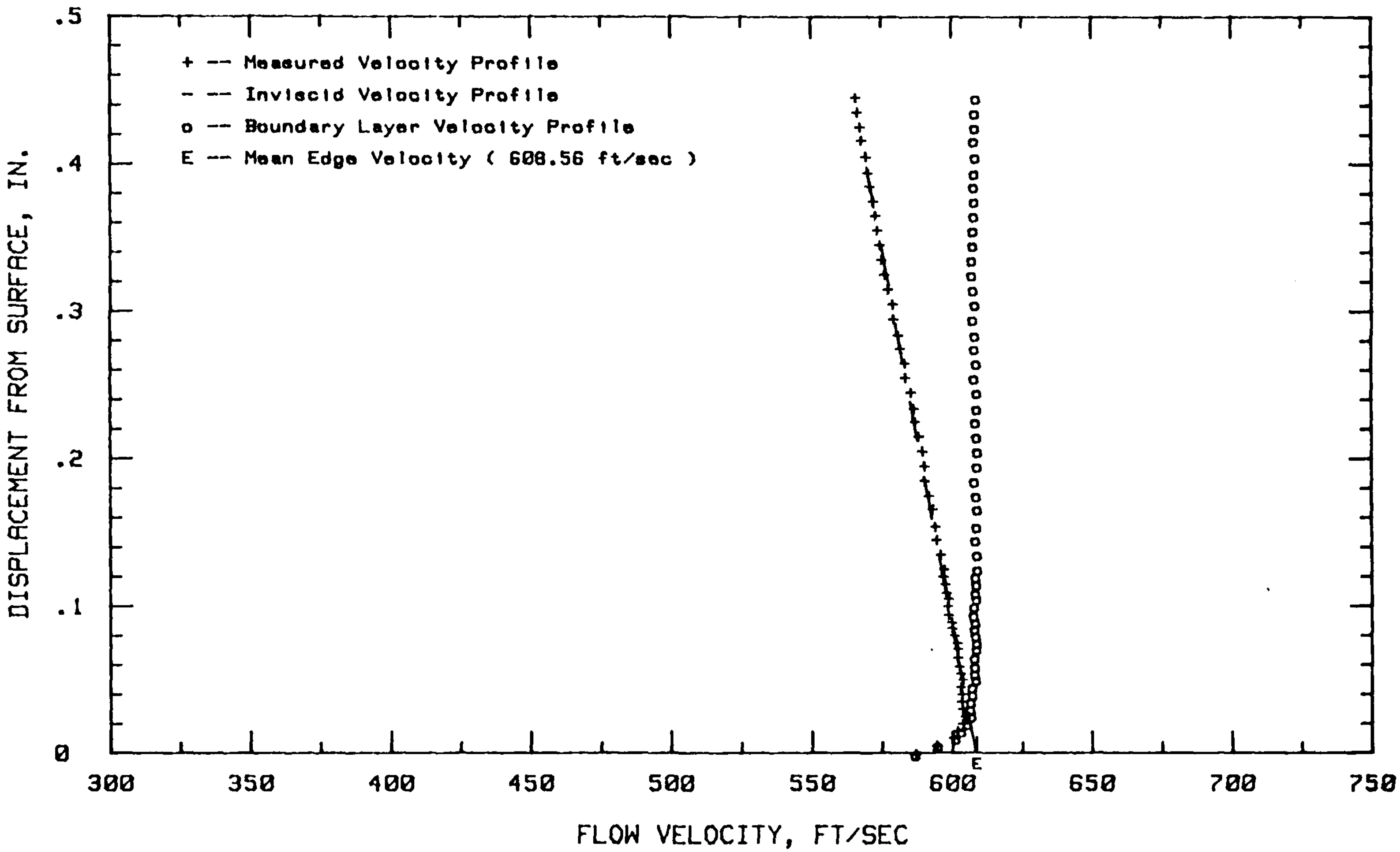

Fig. 91. Boundary Layer Velocity Profiles, i = -3 Deg, 45.31 % Chord

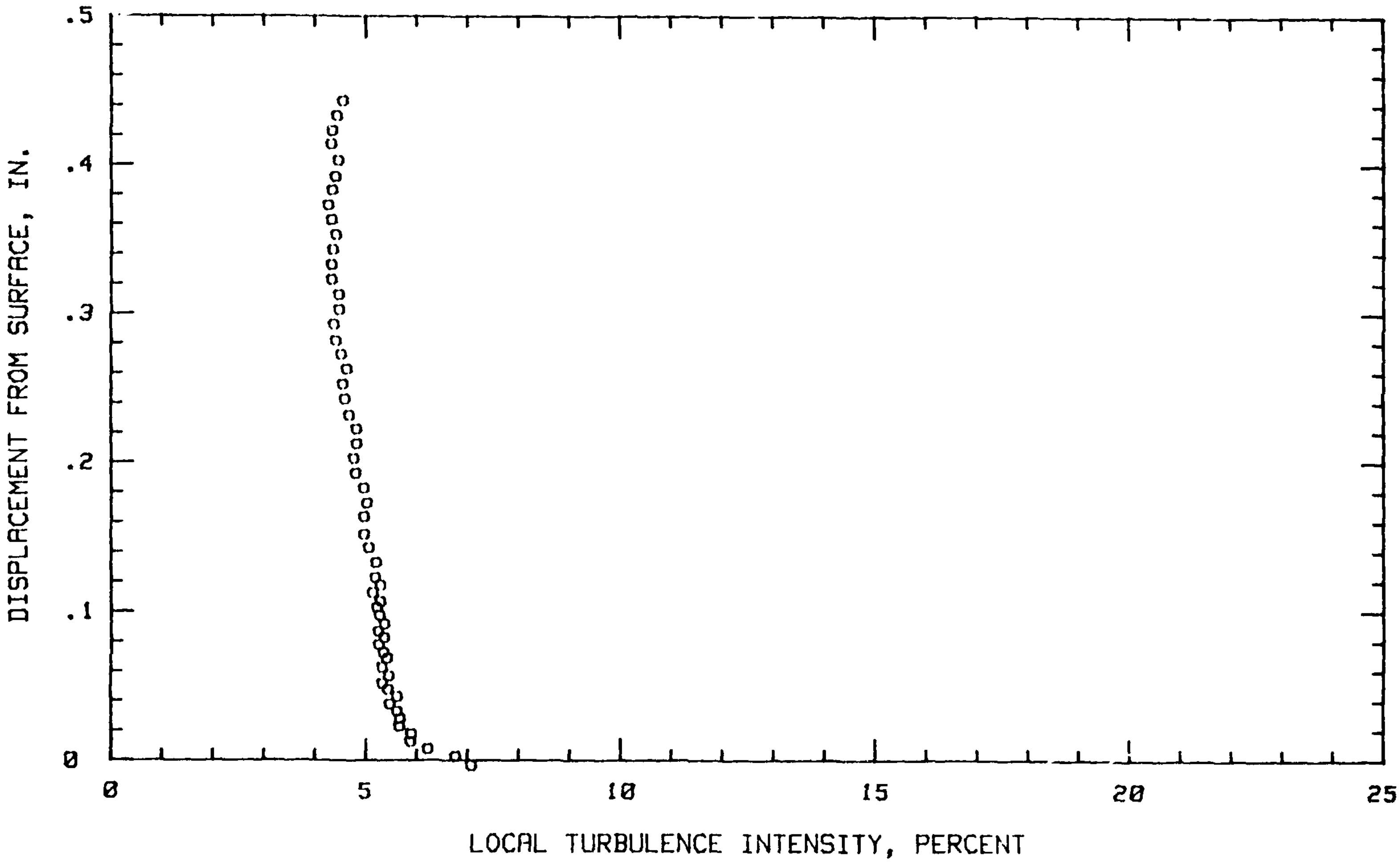

Fig. 92. Boundary Layer Turbulence Intensity Profile, i = -3 Deg, 45.31 % Chord

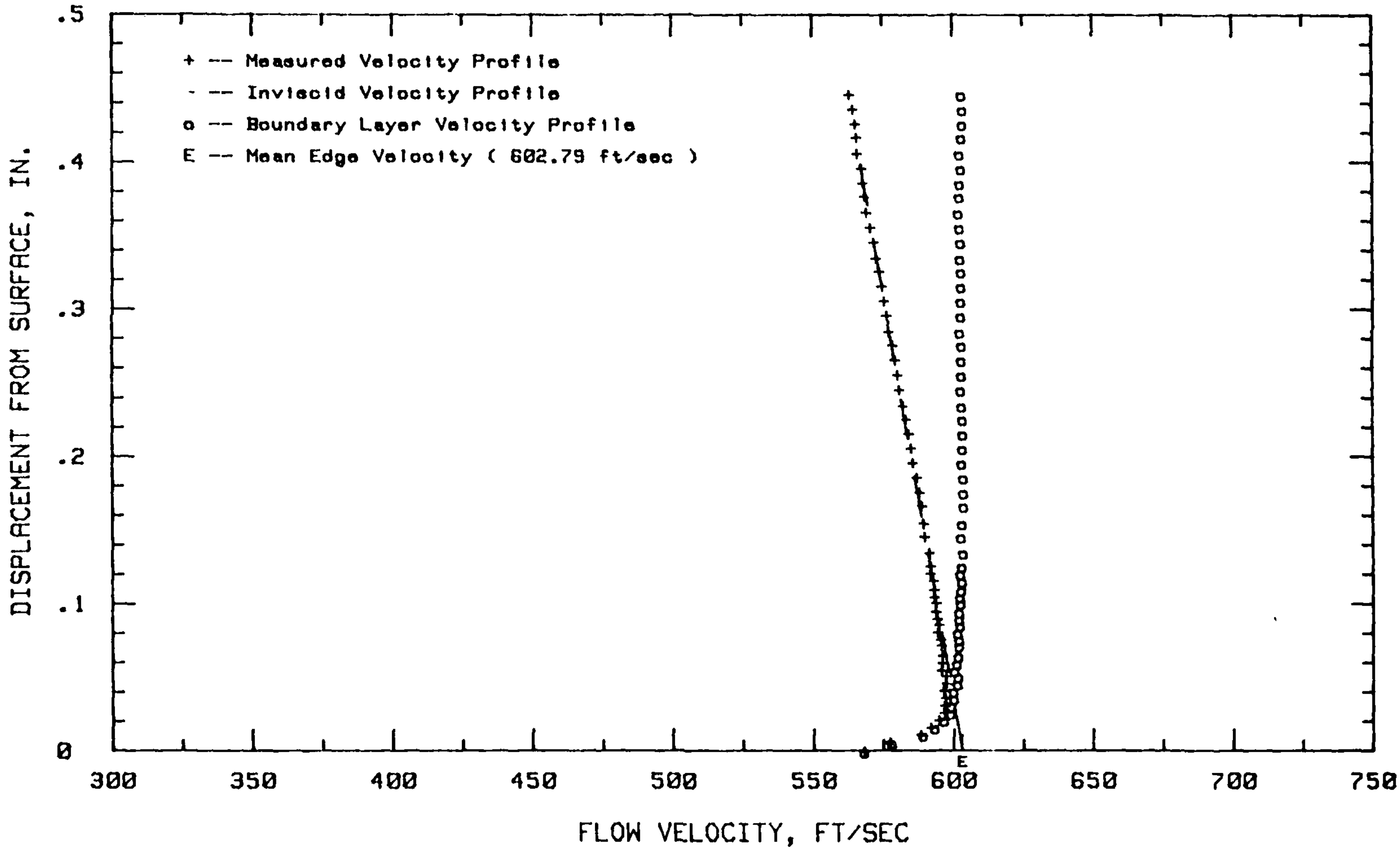

Fig. 93. Boundary Layer Velocity Profiles, i = -3 Deg, 50 % Chord

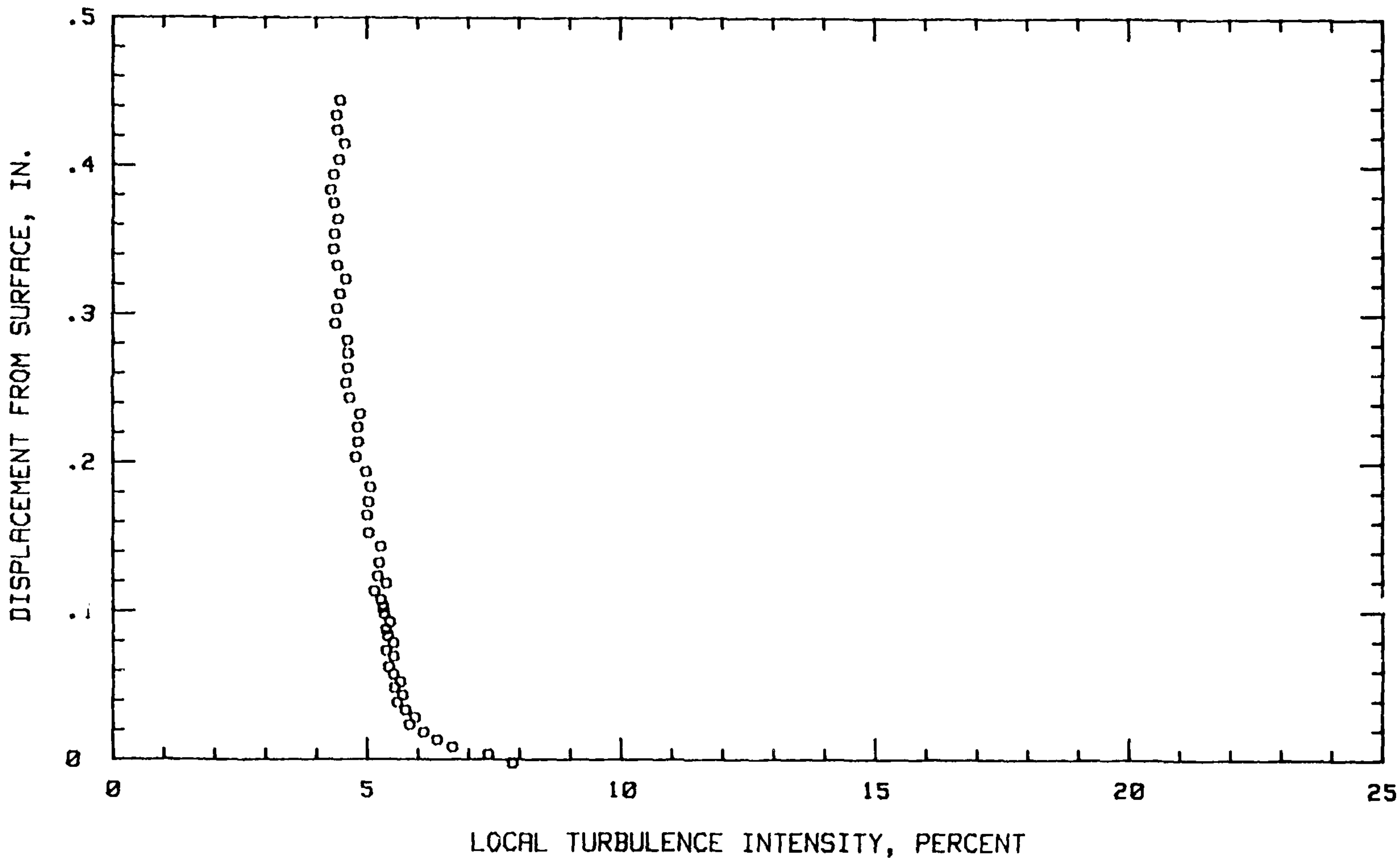

Fig. 94. Boundary Layer Turbulence Intensity Profile, i = -3 Deg, 50 % Chord

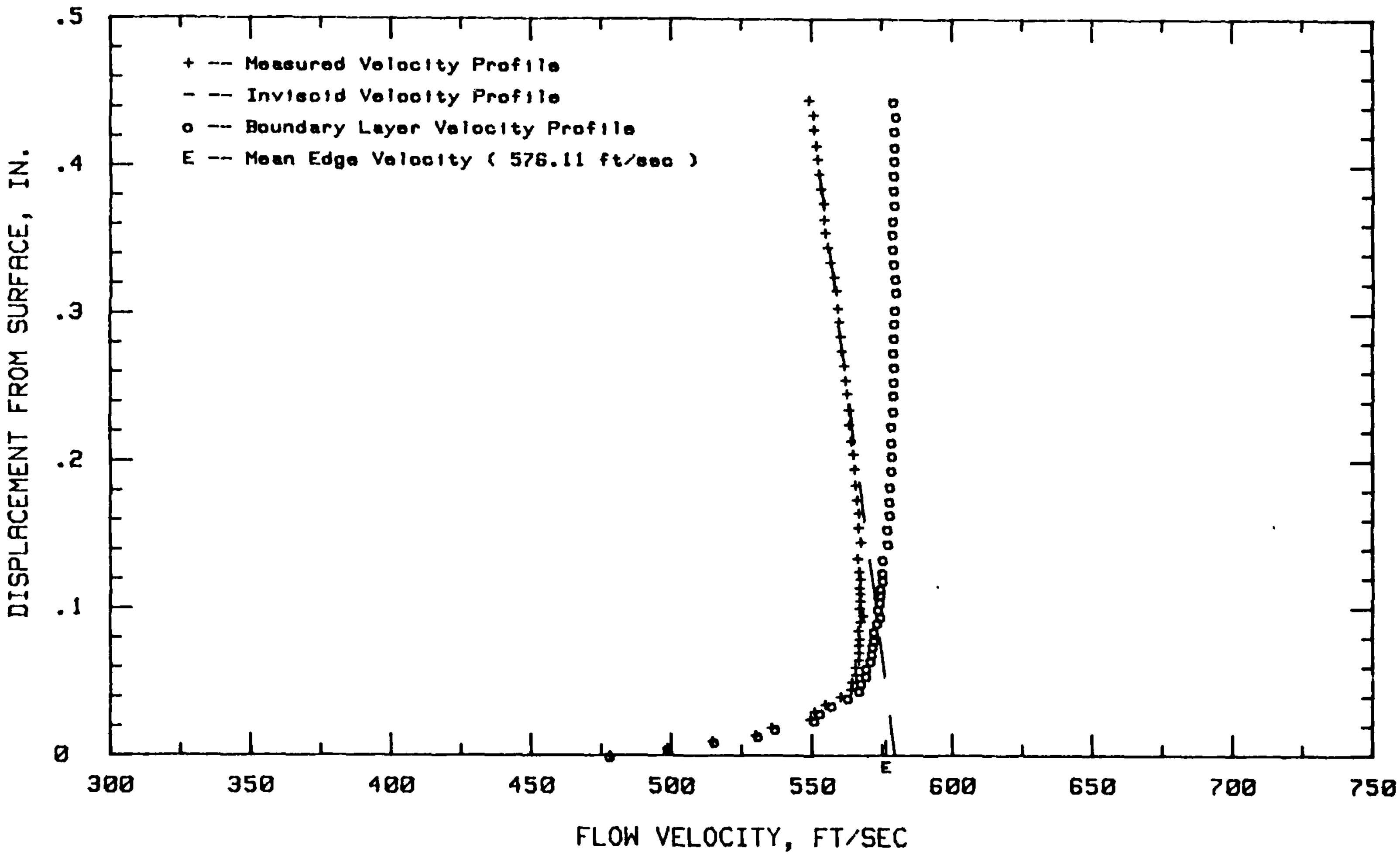

Fig. 95. Boundary Layer Velocity Profiles, i = -3 Deg, 65.62 % Chord

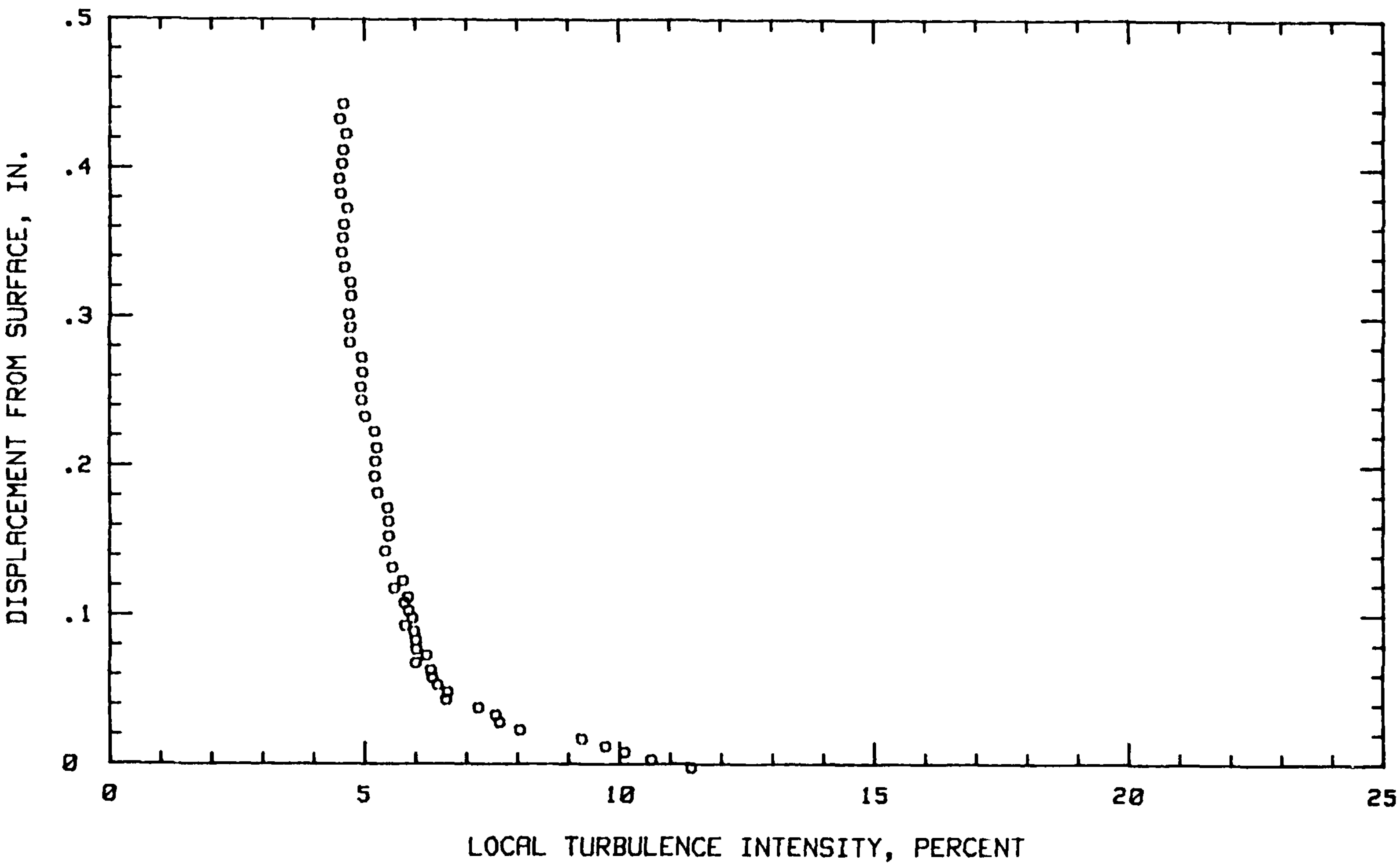

Fig. 96. Boundary Layer Turbulence Intensity Profile, i = -3 Deg, 65.62 % Chord

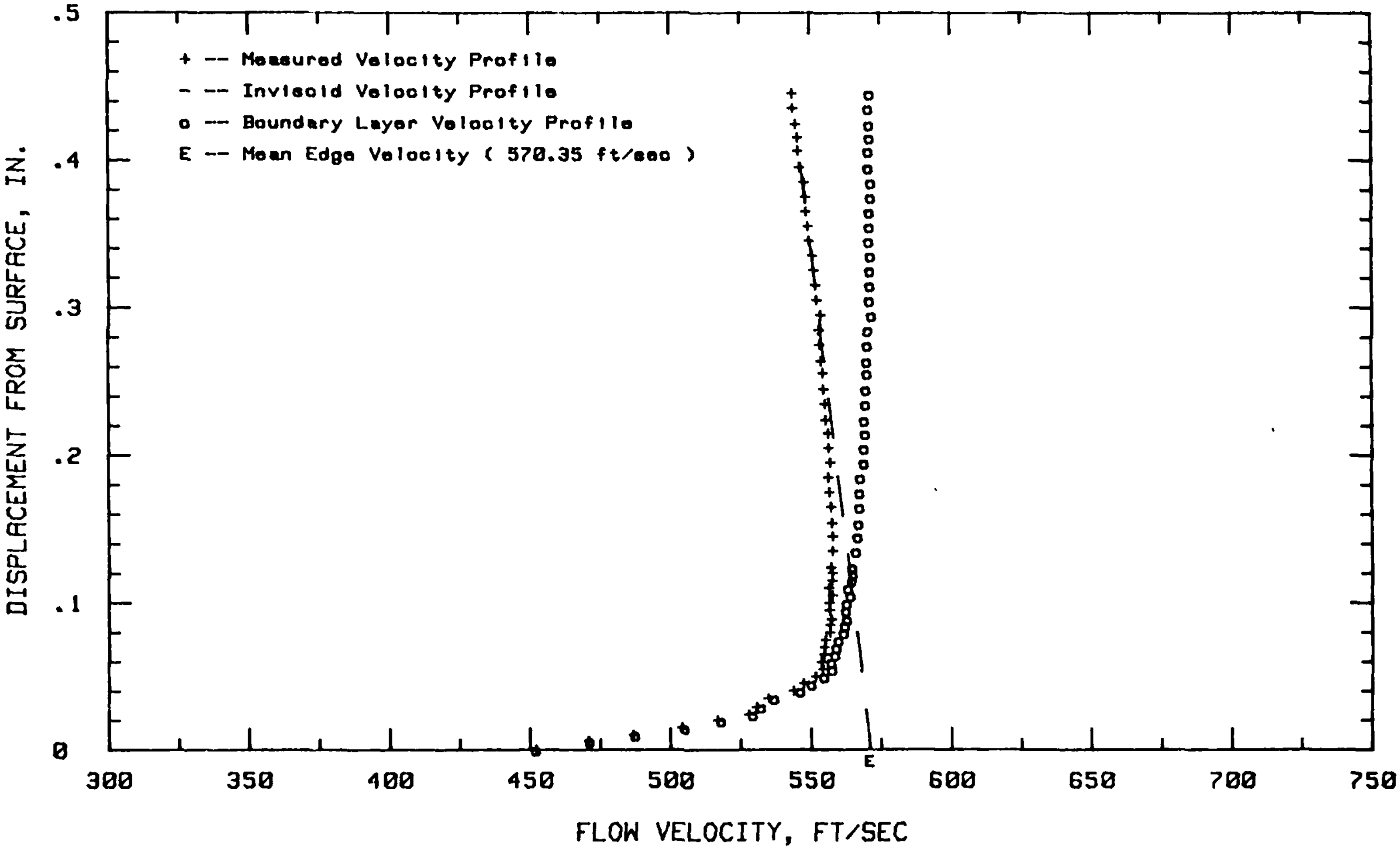

Fig. 97. Boundary Layer Velocity Profiles, i = -3 Deg, 70.31 % Chord

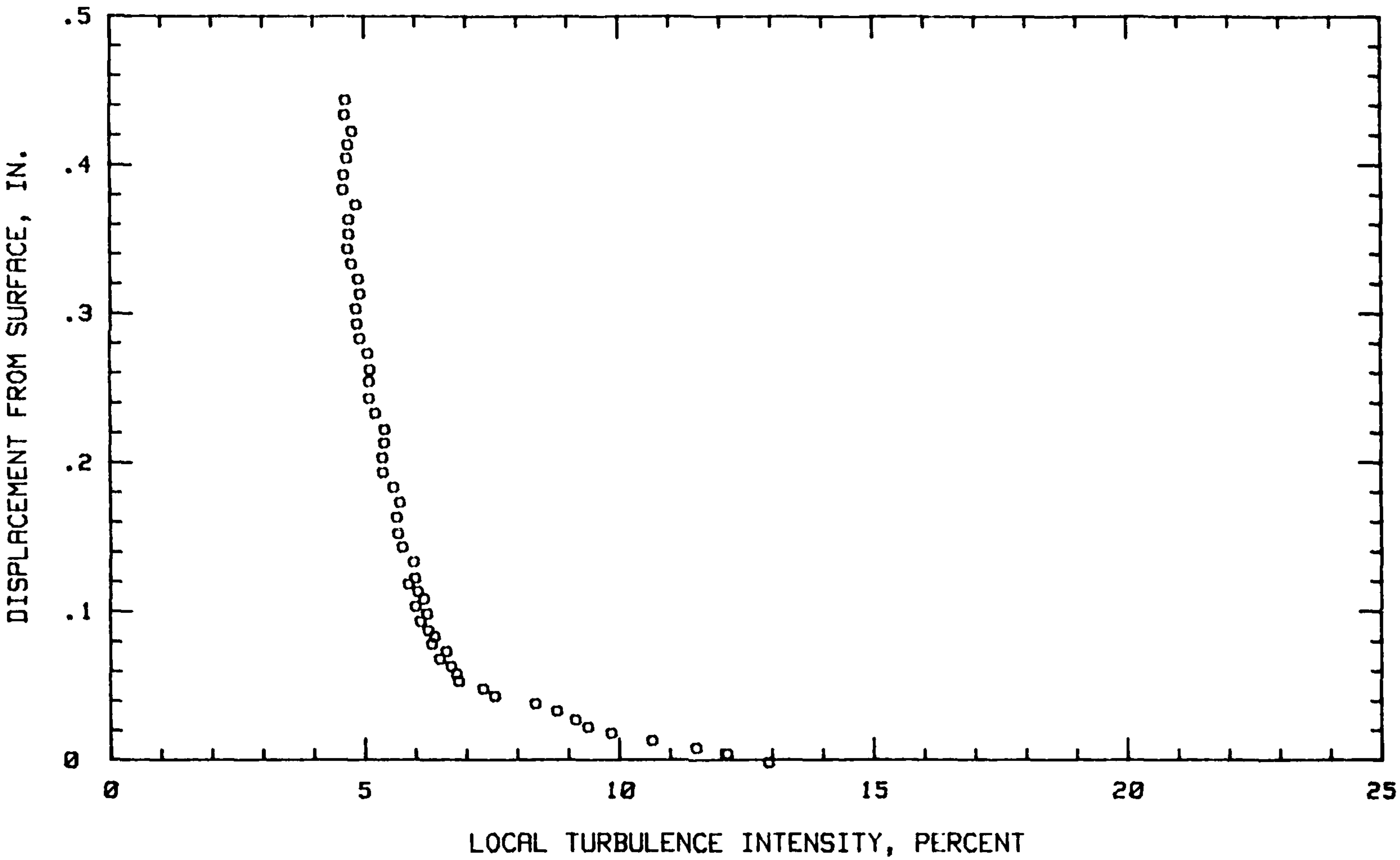

Fig. 98. Boundary Layer Turbulence Intensity Profile, i = -3 Deg, 70.31 % Chord

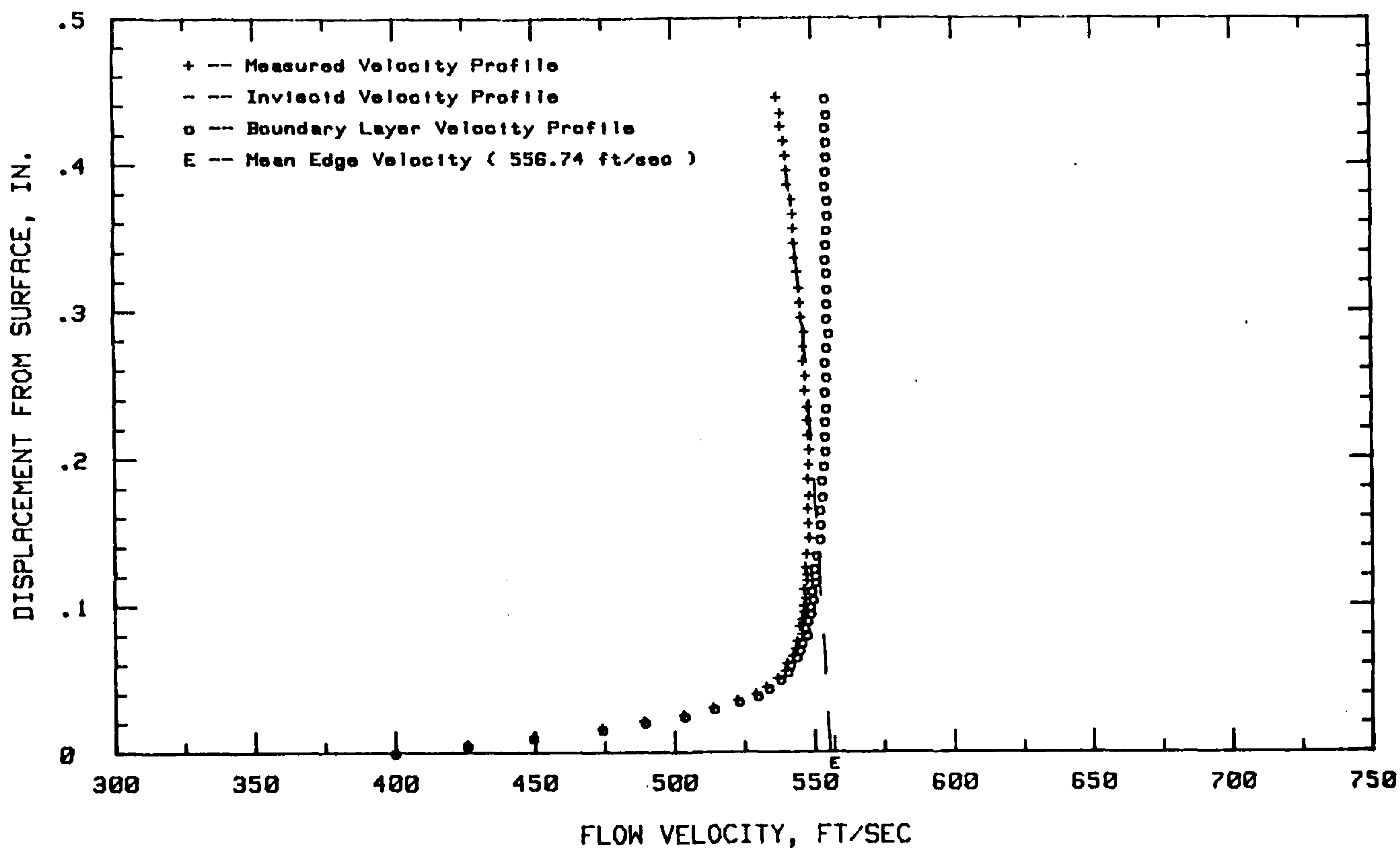

Fig. 99. Boundary Layer Velocity Profiles, i = -3 Deg, 75 % Chord

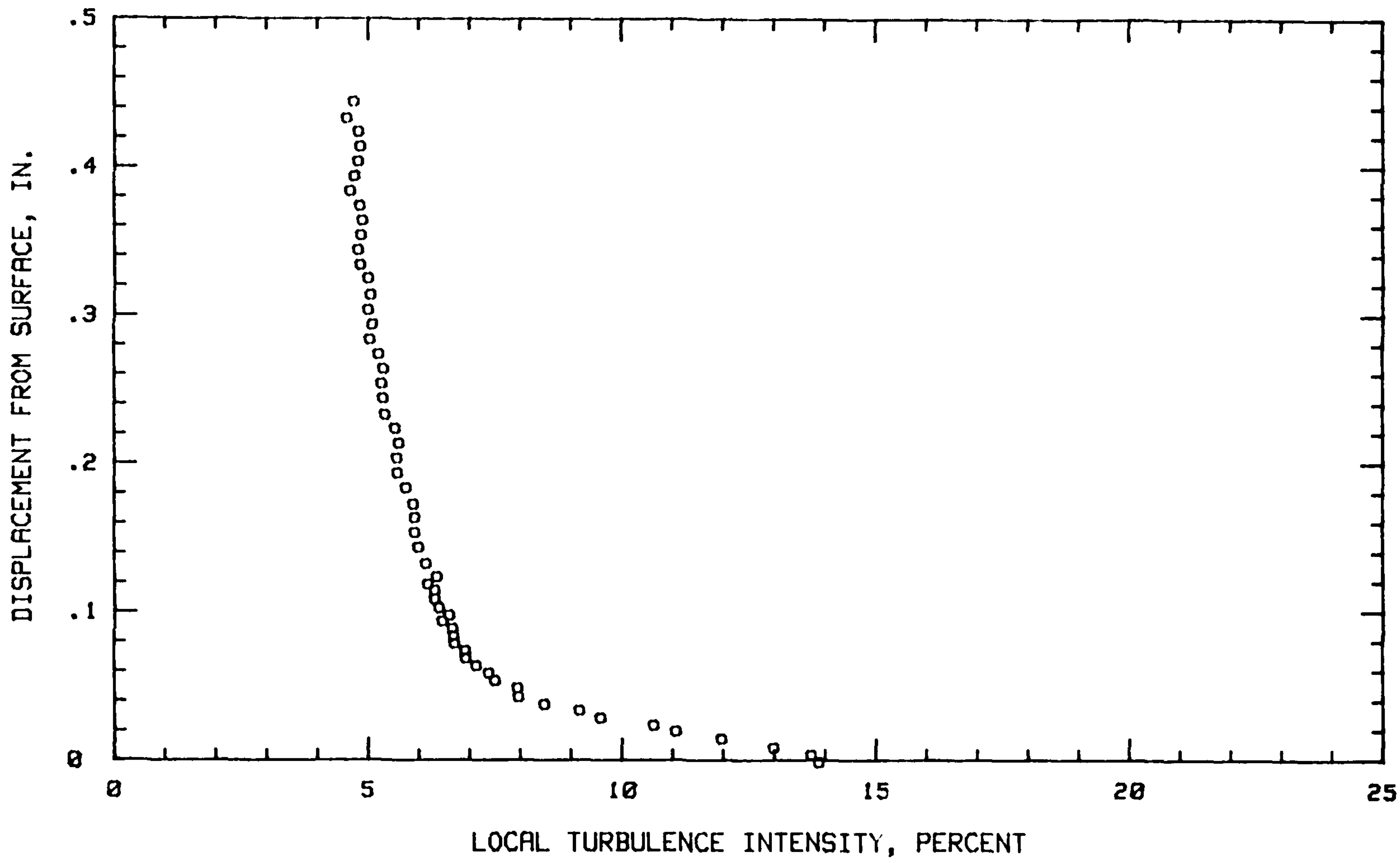

Fig. 100. Boundary Layer Turbulence Intensity Profile, i = -3 Deg, 75 % Chord

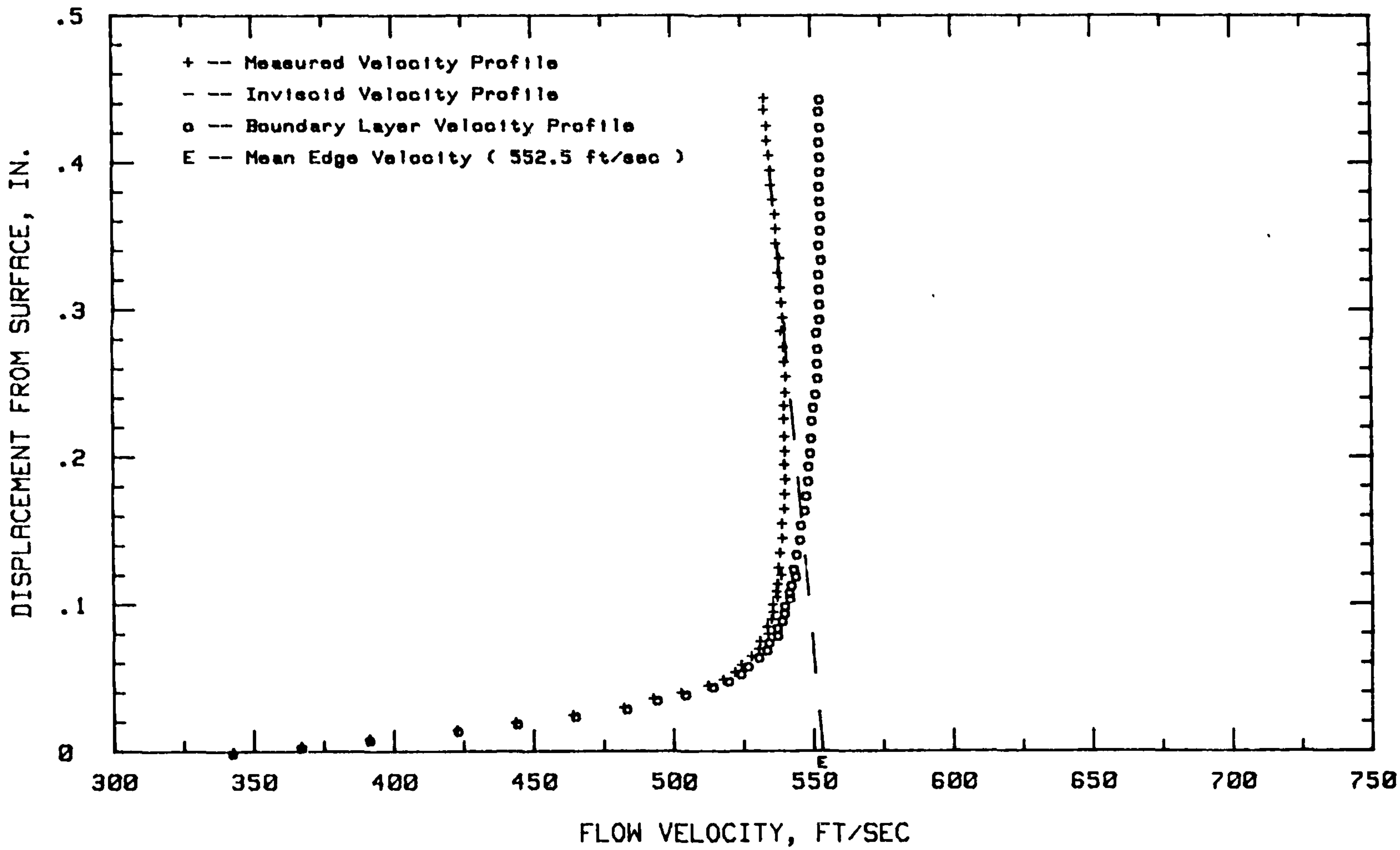

Fig. 101. Boundary Layer Velocity Profiles, i = -3 Deg, 79.68 % Chord

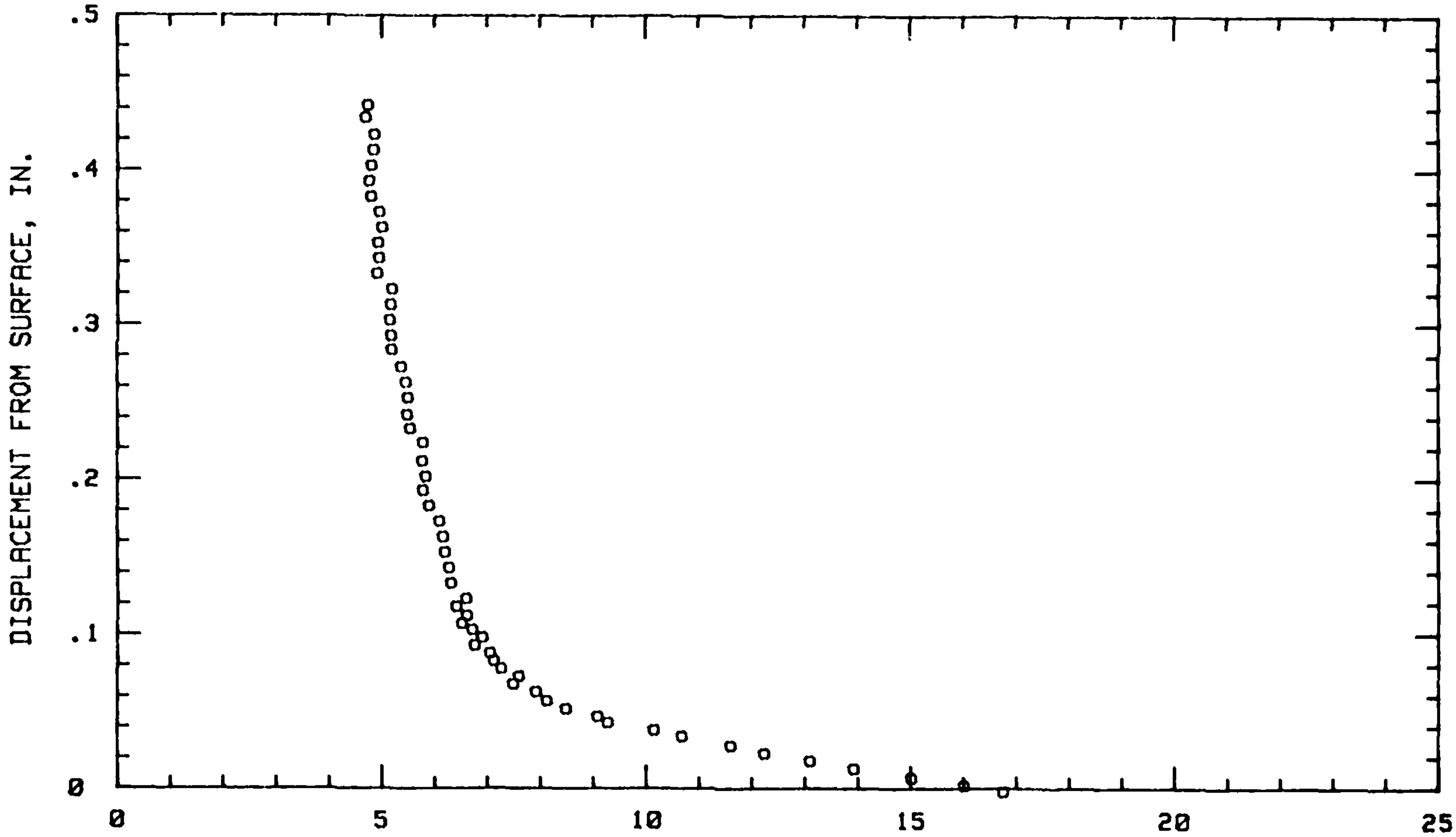

Fig. 102. Boundary Layer Turbulence Intensity Profile, i = -3 Deg, 79.68 % Chord

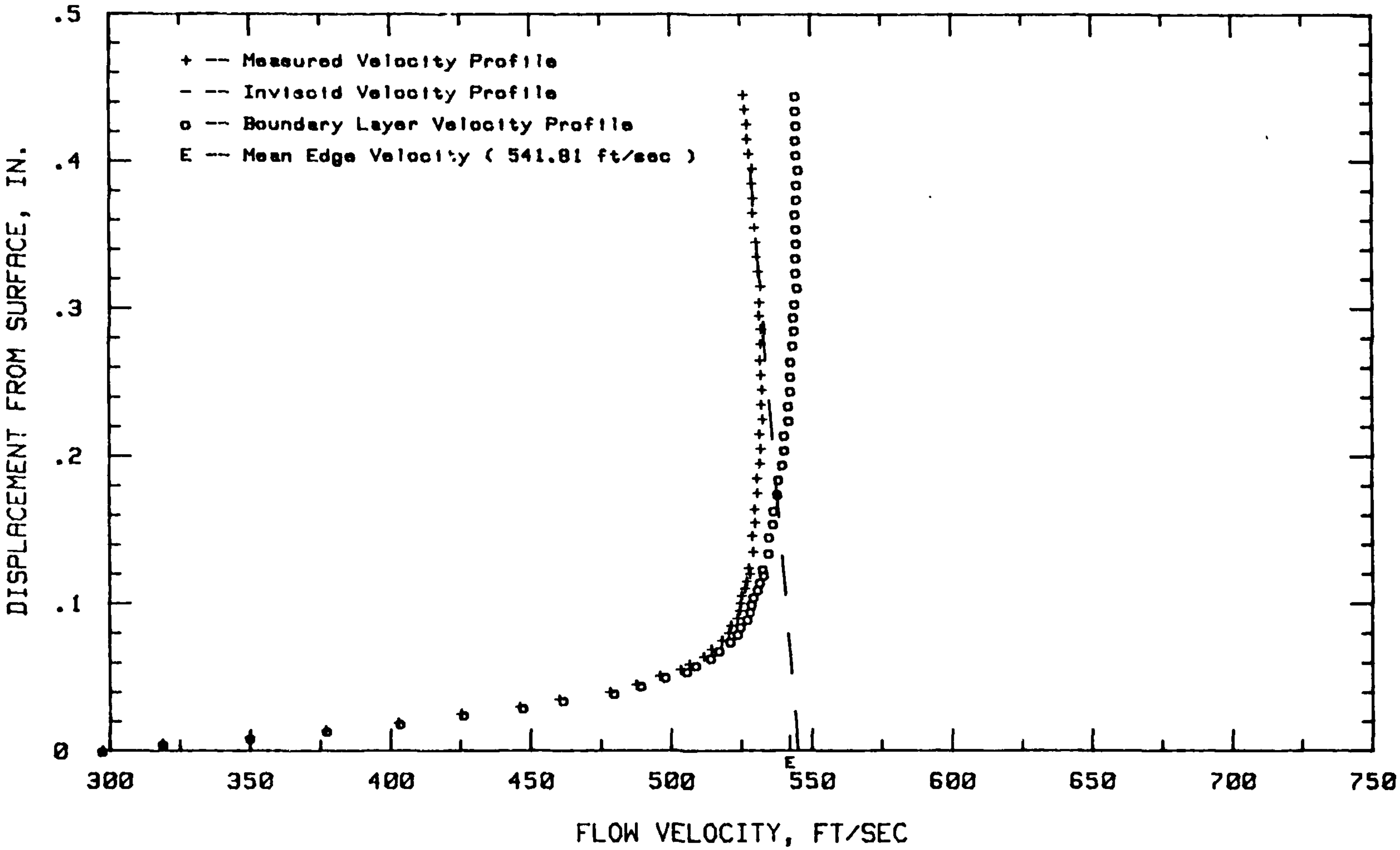

Fig. 103. Boundary Layer Velocity Profiles, i = -3 Deg, 84.37 % Chord

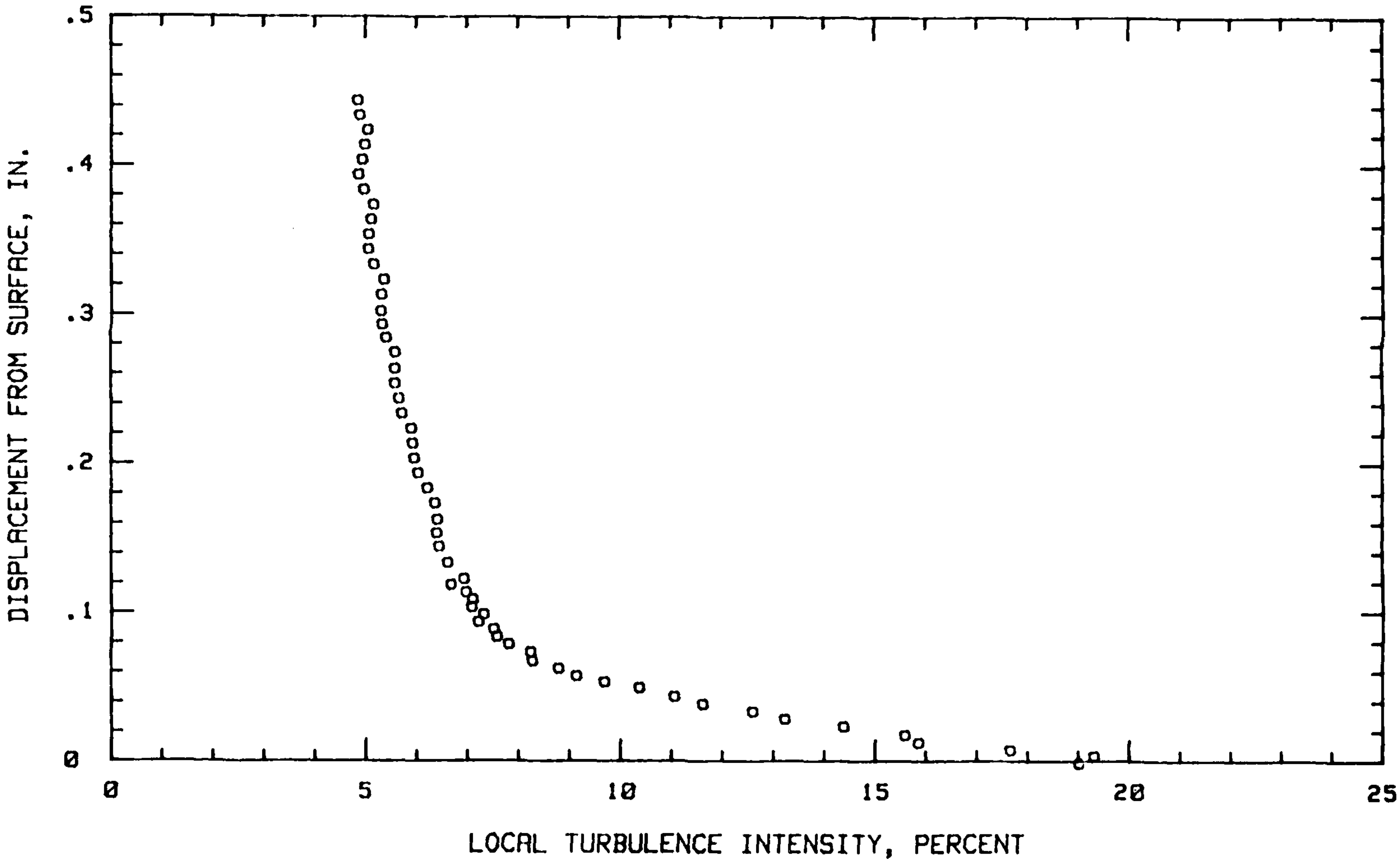

Fig. 104. Boundary Layer Turbulence Intensity Profile, i = -3 Deg, 84.37 % Chord

Appendix K

Boundary Layer Velocity and Turbulence Intensity Profiles

Blade Configuration Number 2

Incidence Angle = Ø.Ø Degrees

Low Free Stream Turbulence

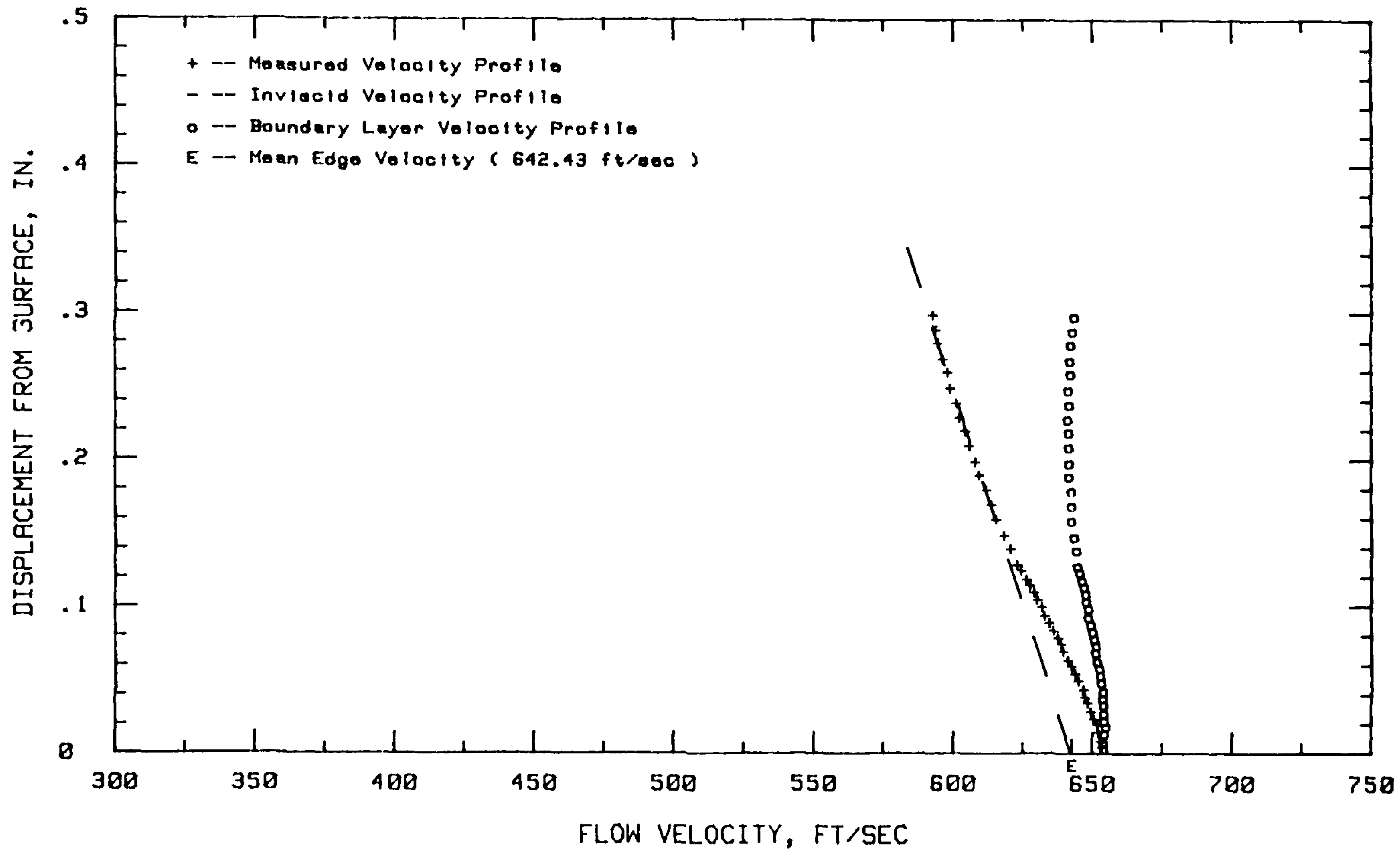

Fig. 105. Boundary Layer Velocity Profiles, i = 0 Deg, 4.68 % Chord

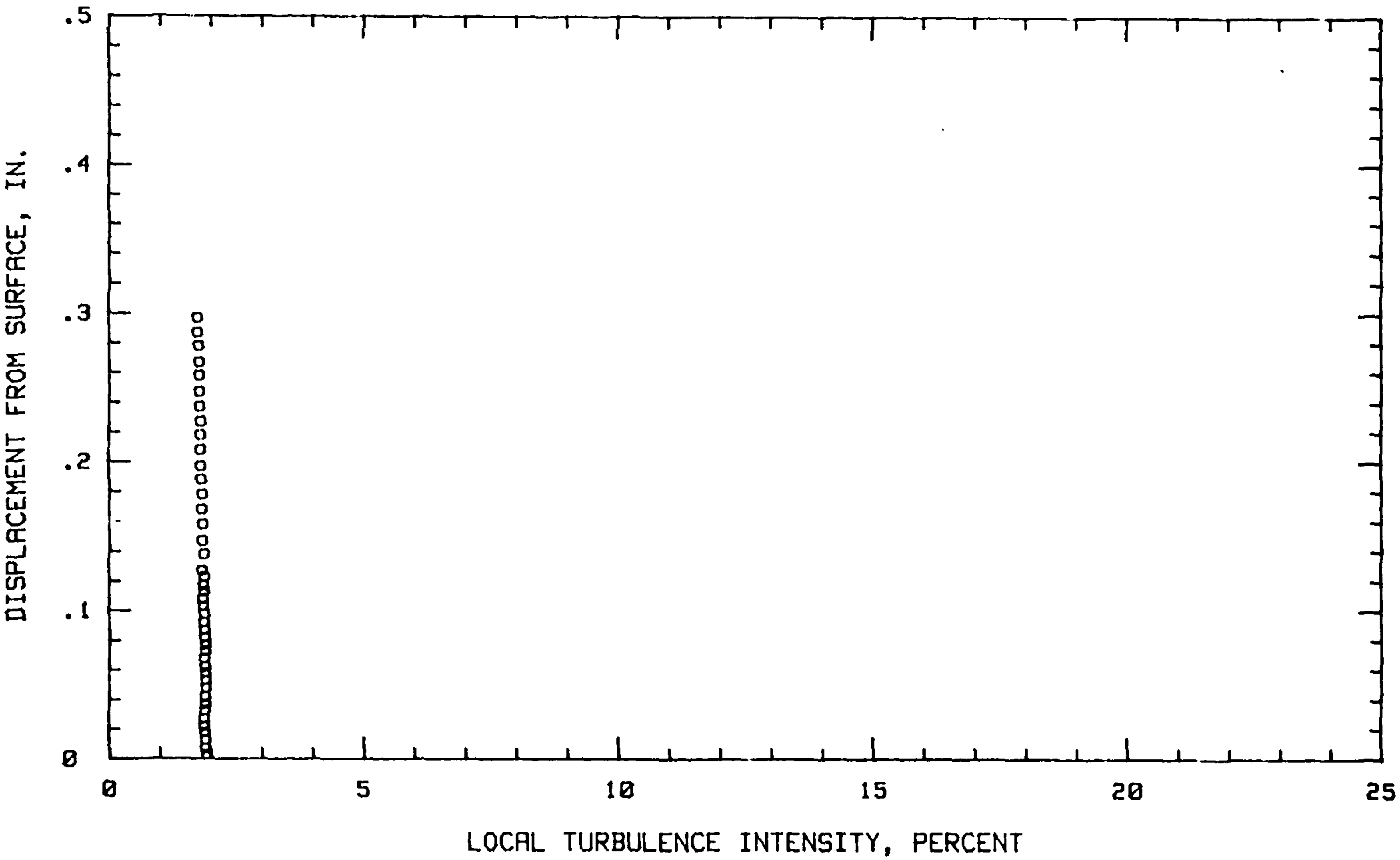

Fig. 106. Boundary Layer Turbulence Intensity Profile, i = 0 Deg, 4.68 % Chord

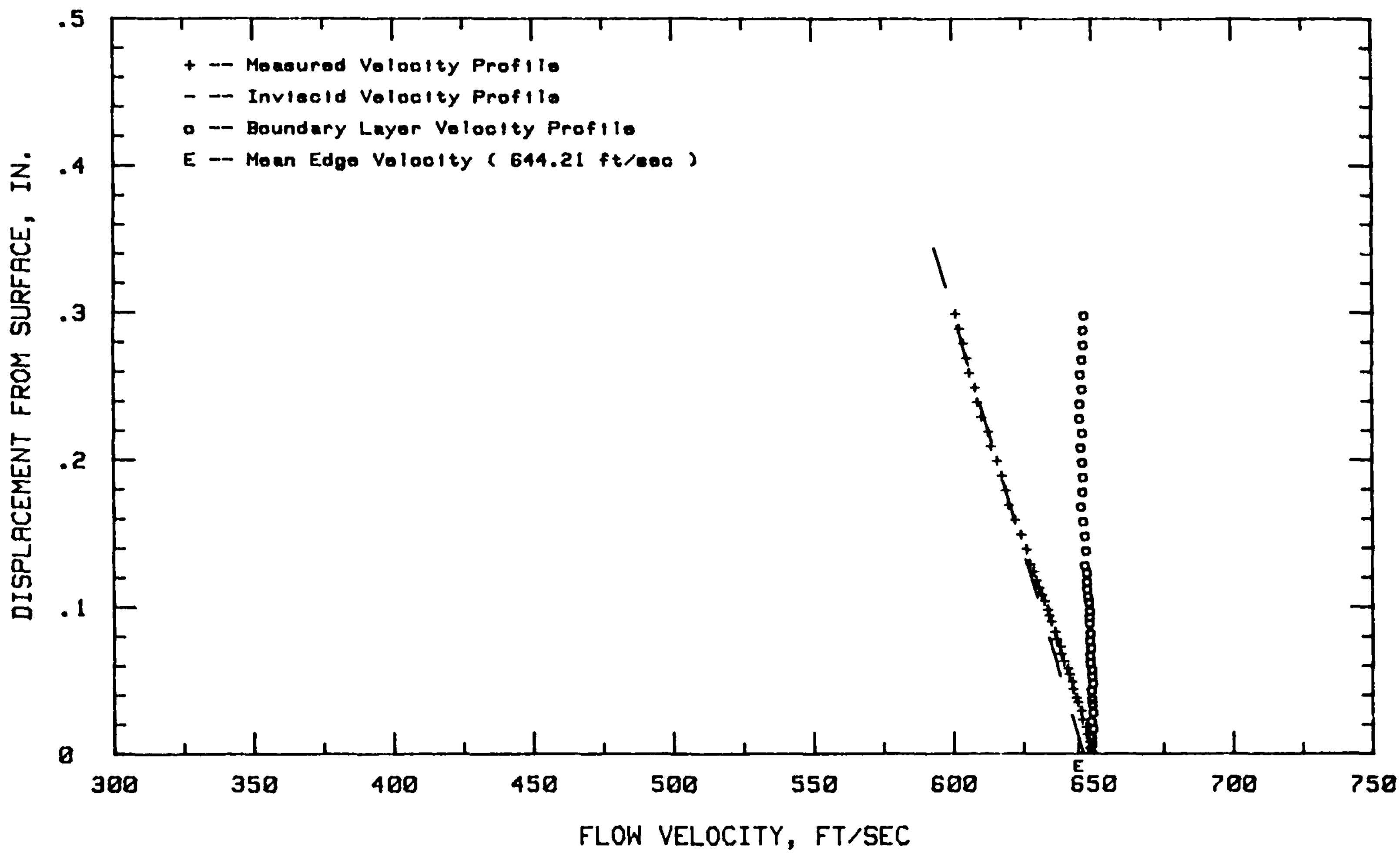

Fig. 107. Boundary Layer Velocity Profiles, i = 0 Deg, 9.37 % Chord

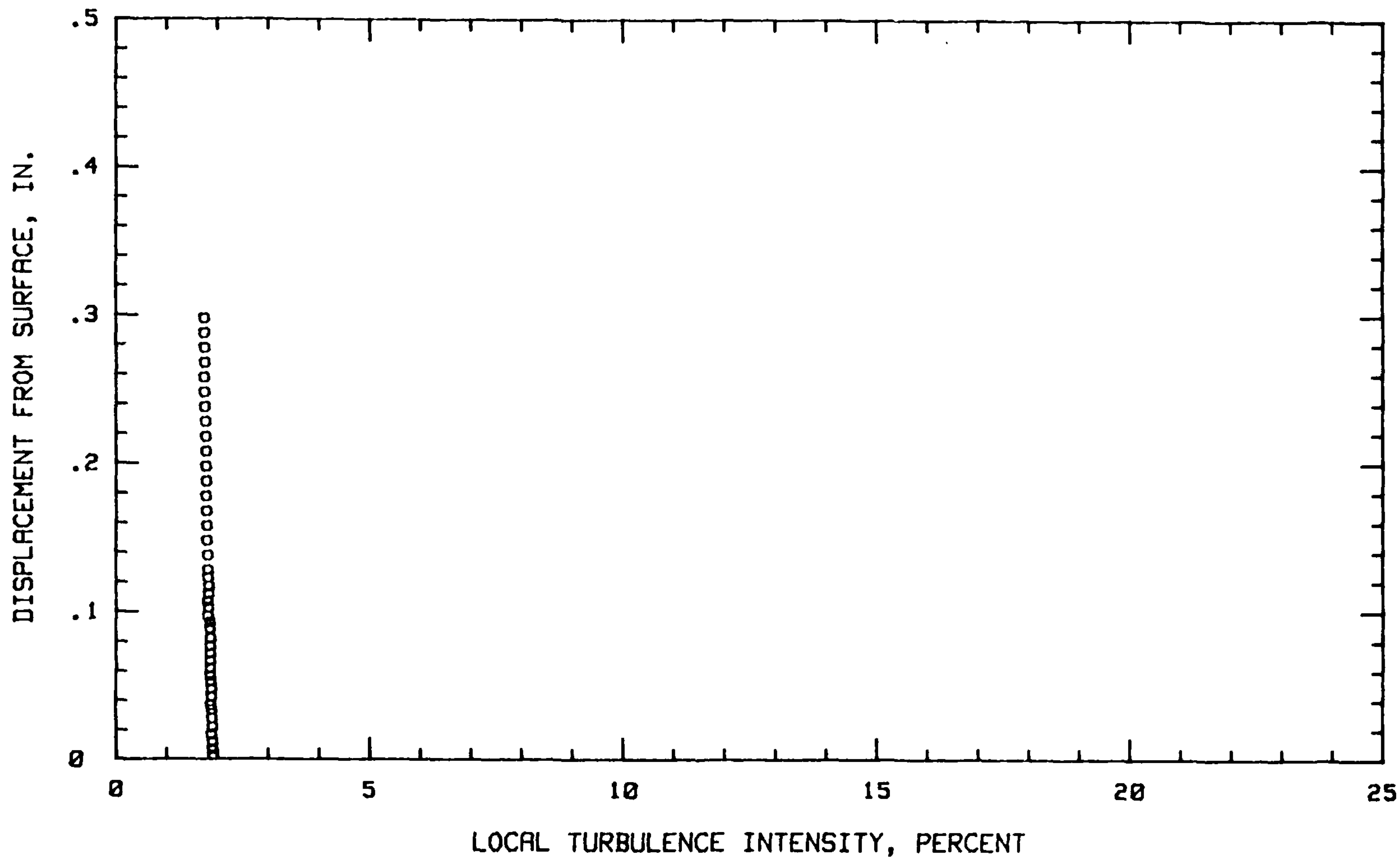

Fig. 108. Boundary Layer Turbulence Intensity Profile, i = 0 Deg, 9.37 % Chord

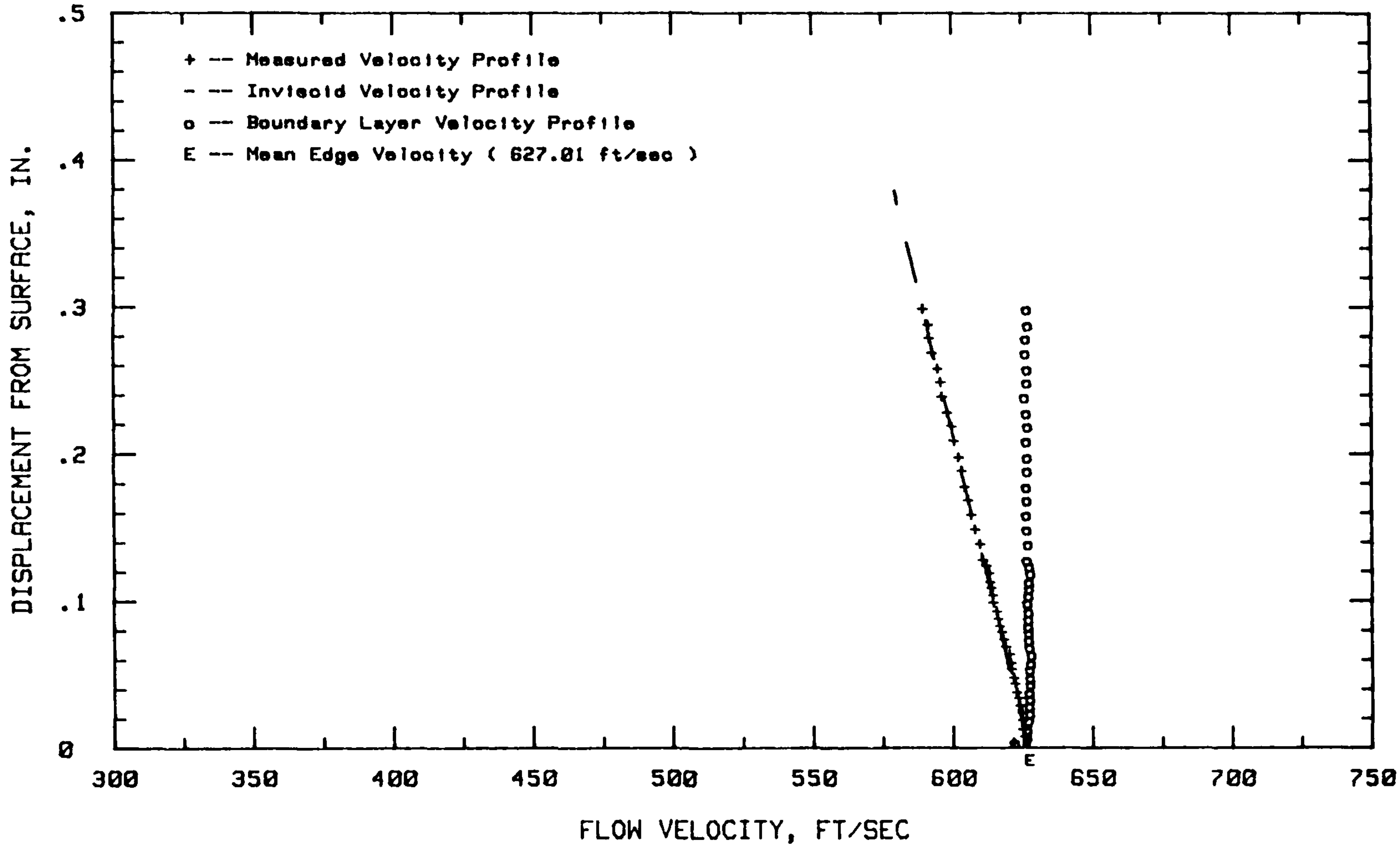

Fig. 109. Boundary Layer Velocity Profiles, ɩ = 0 Deg, 16.51 % Chord

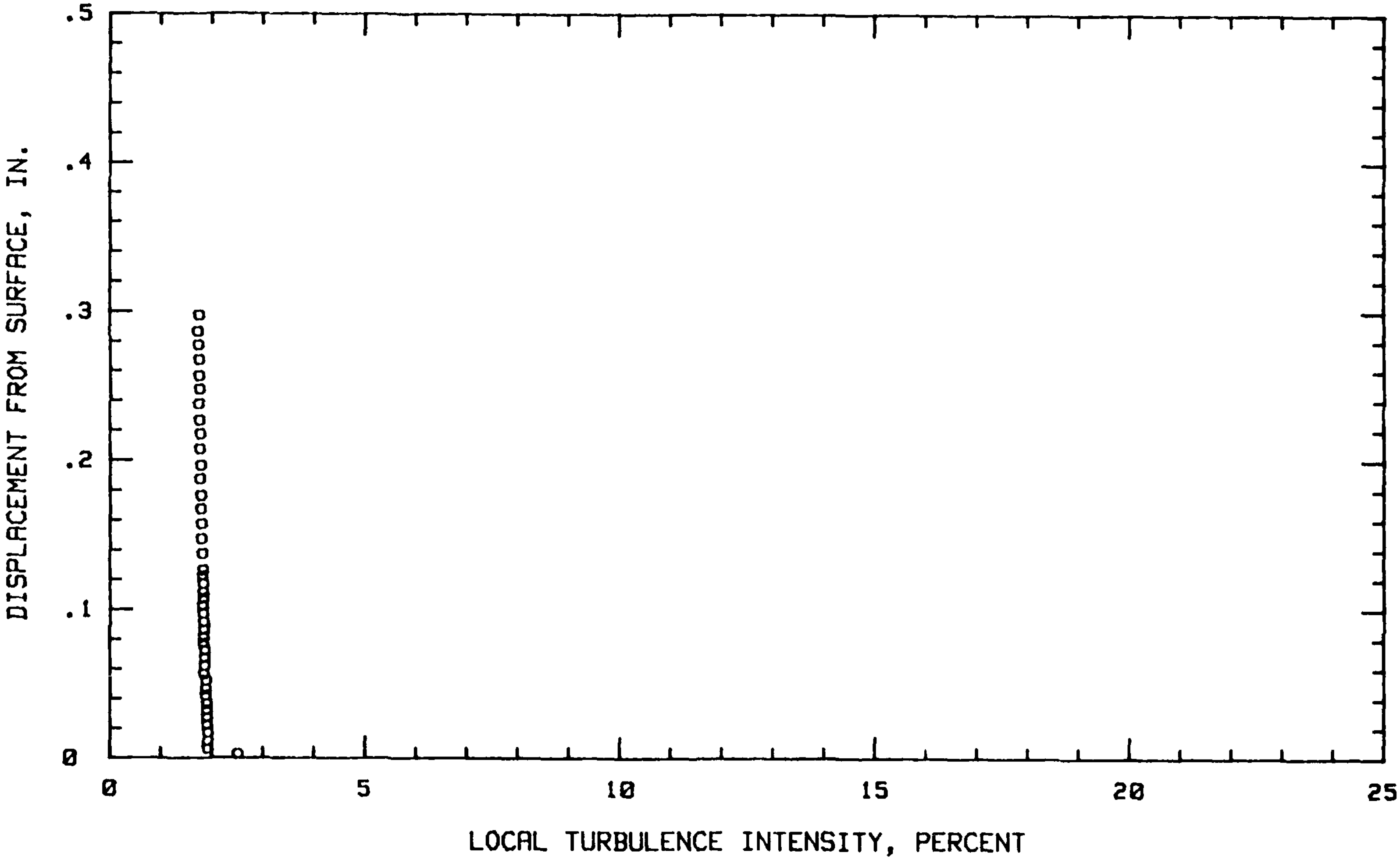

Fig. 110. Boundary Layer Turbulence Intensity Profile, i = 0 Deg, 16.51 % Chord

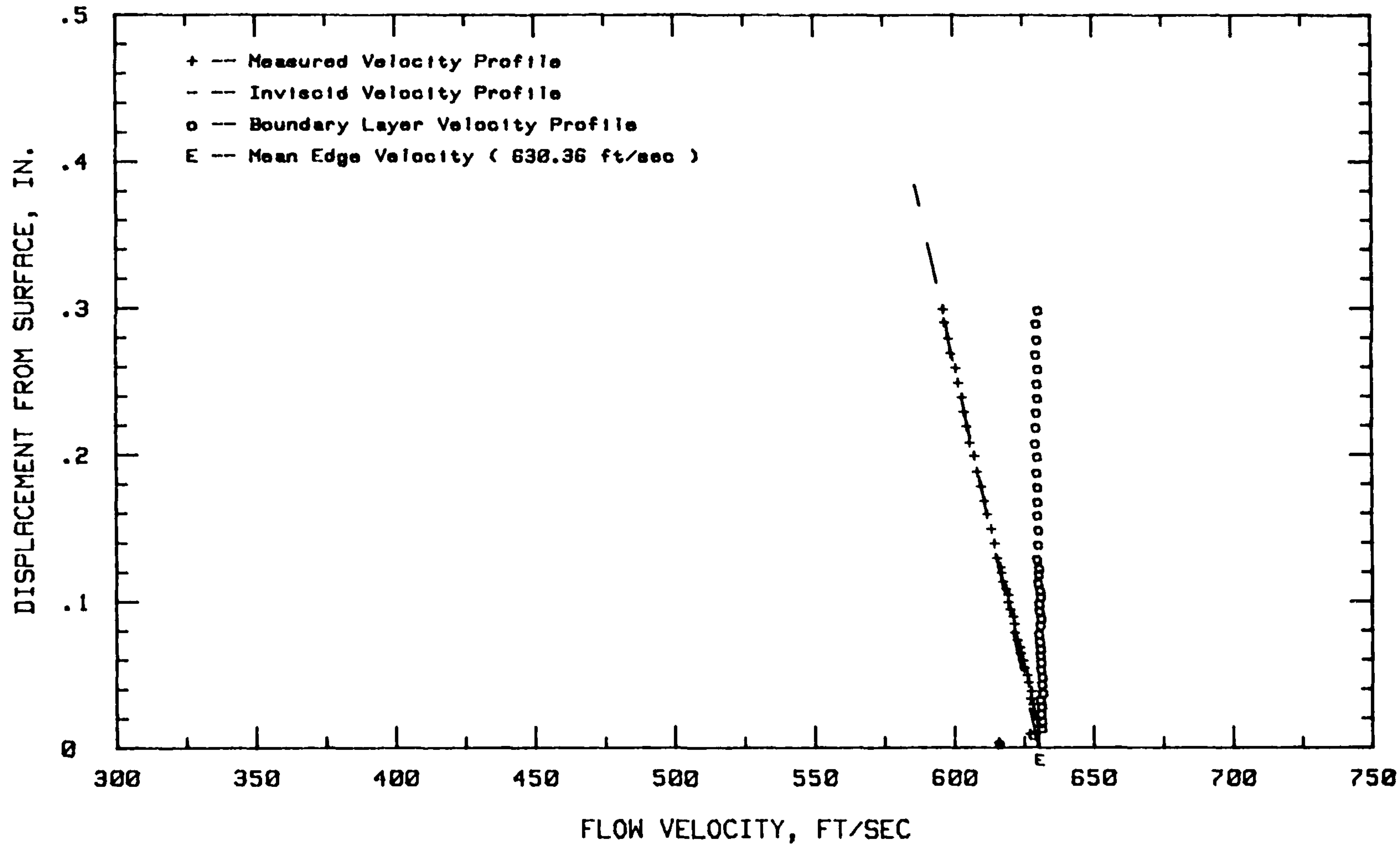

Fig. 111. Boundary Layer Velocity Profiles, i = 0 Deg, 25 % Chord

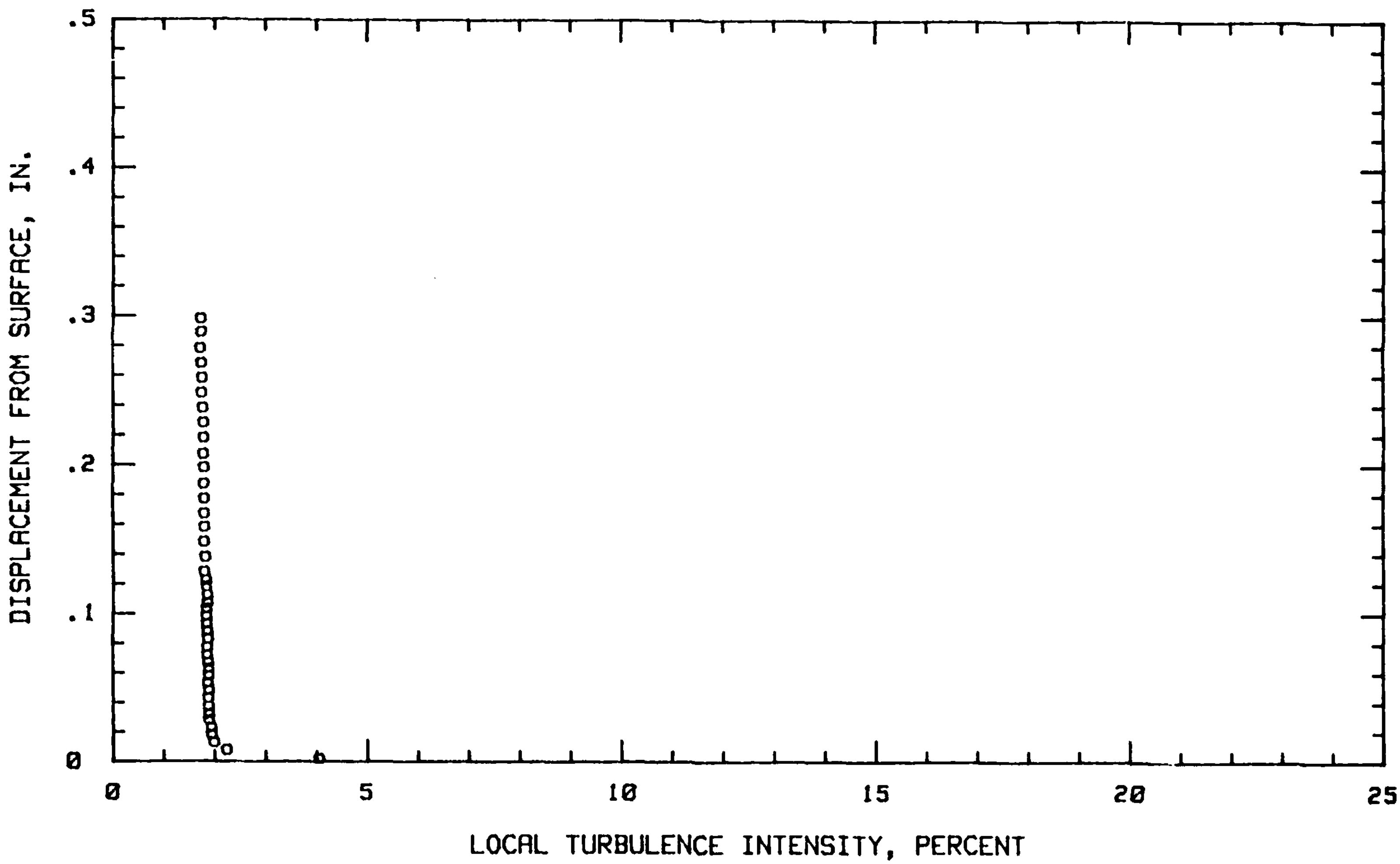

Fig. 112. Boundary Layer Turbulence Intensity Profile, i = 0 Deg, 25 % Chord

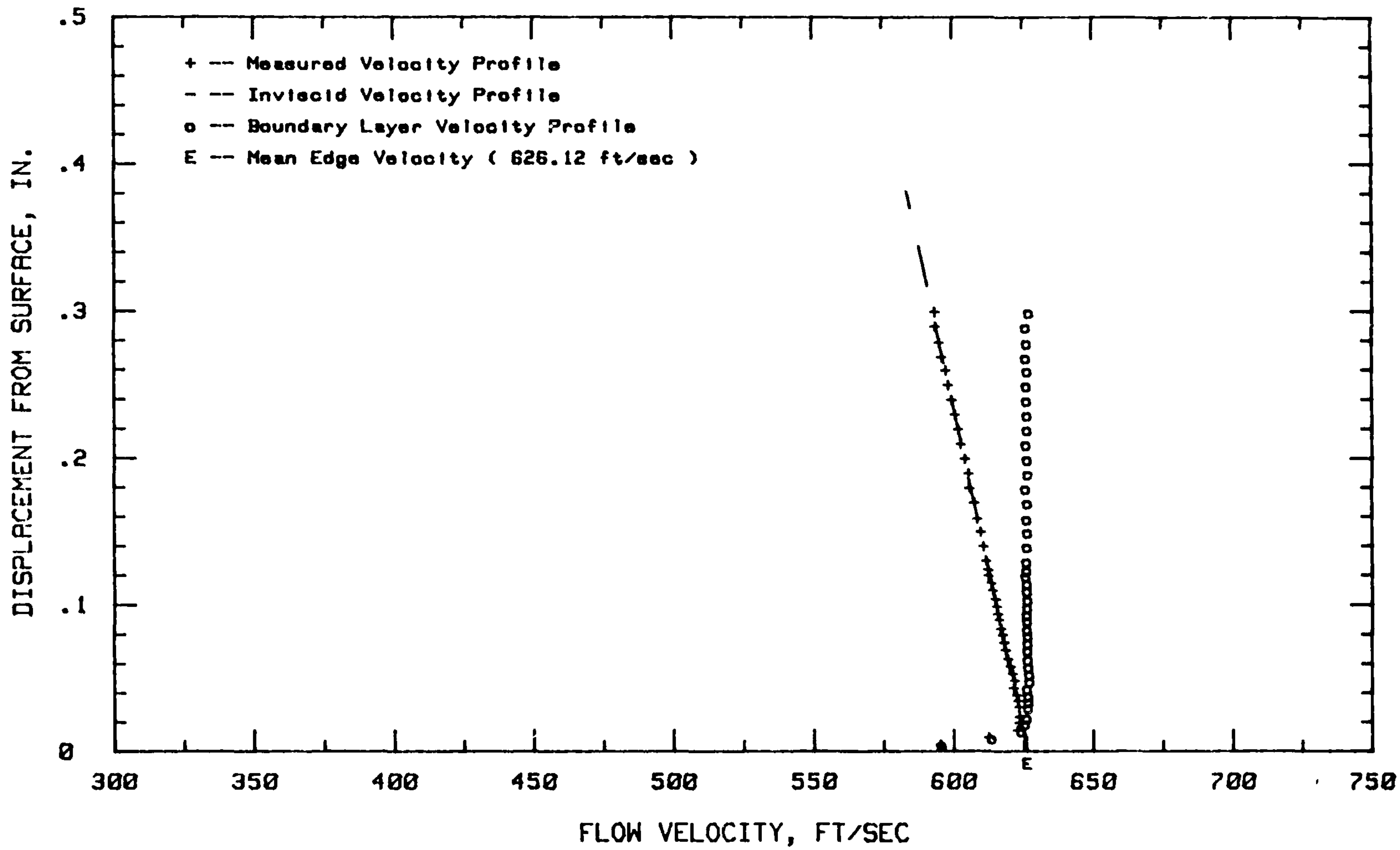

Fig. 113. Boundary Layer Velocity Profiles, i = 0 Deg, 29.68 % Chord

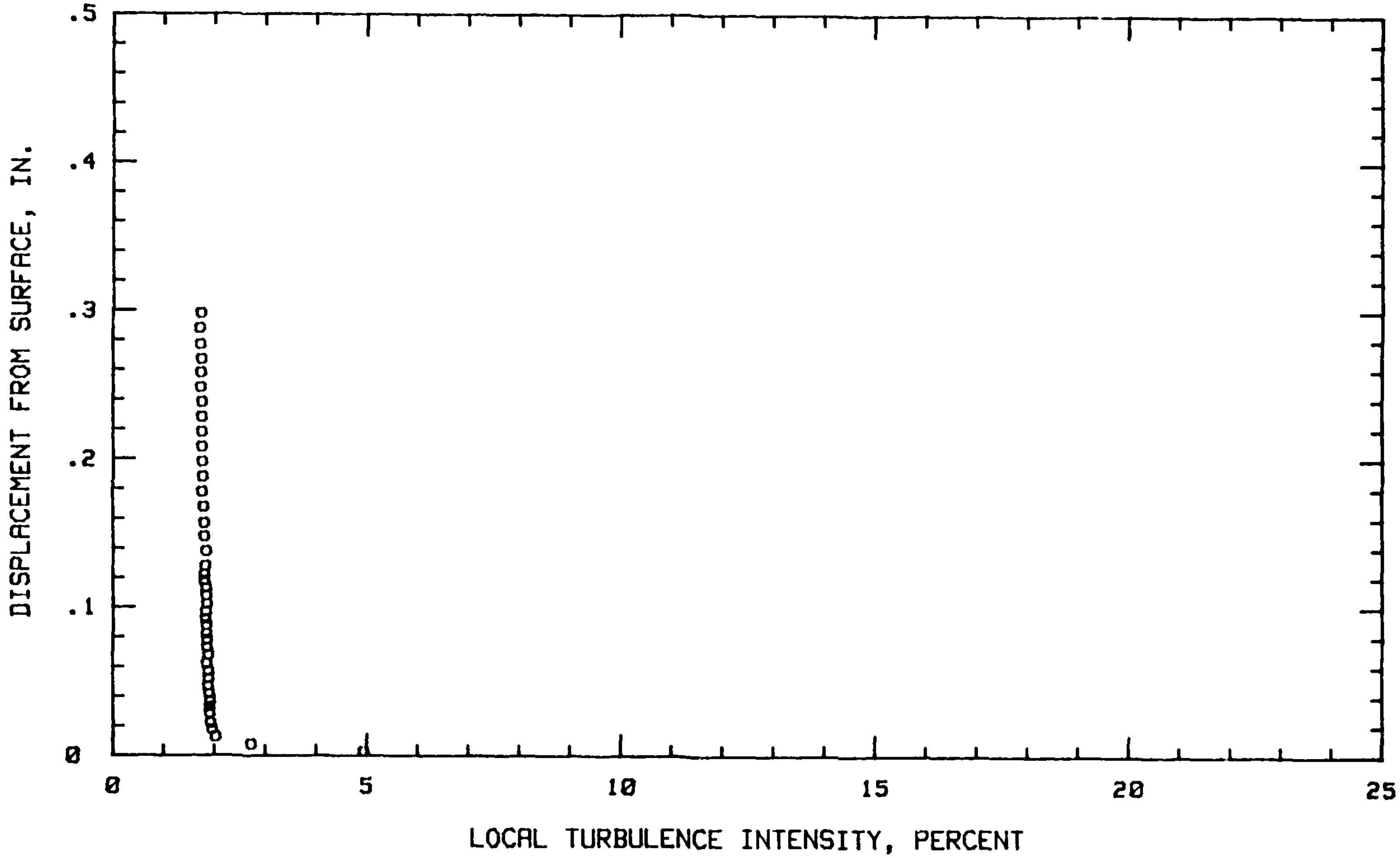

Fig. 114. Boundary Layer Turbulence Intensity Profile, i = 0 Deg, 29.68 % Chord

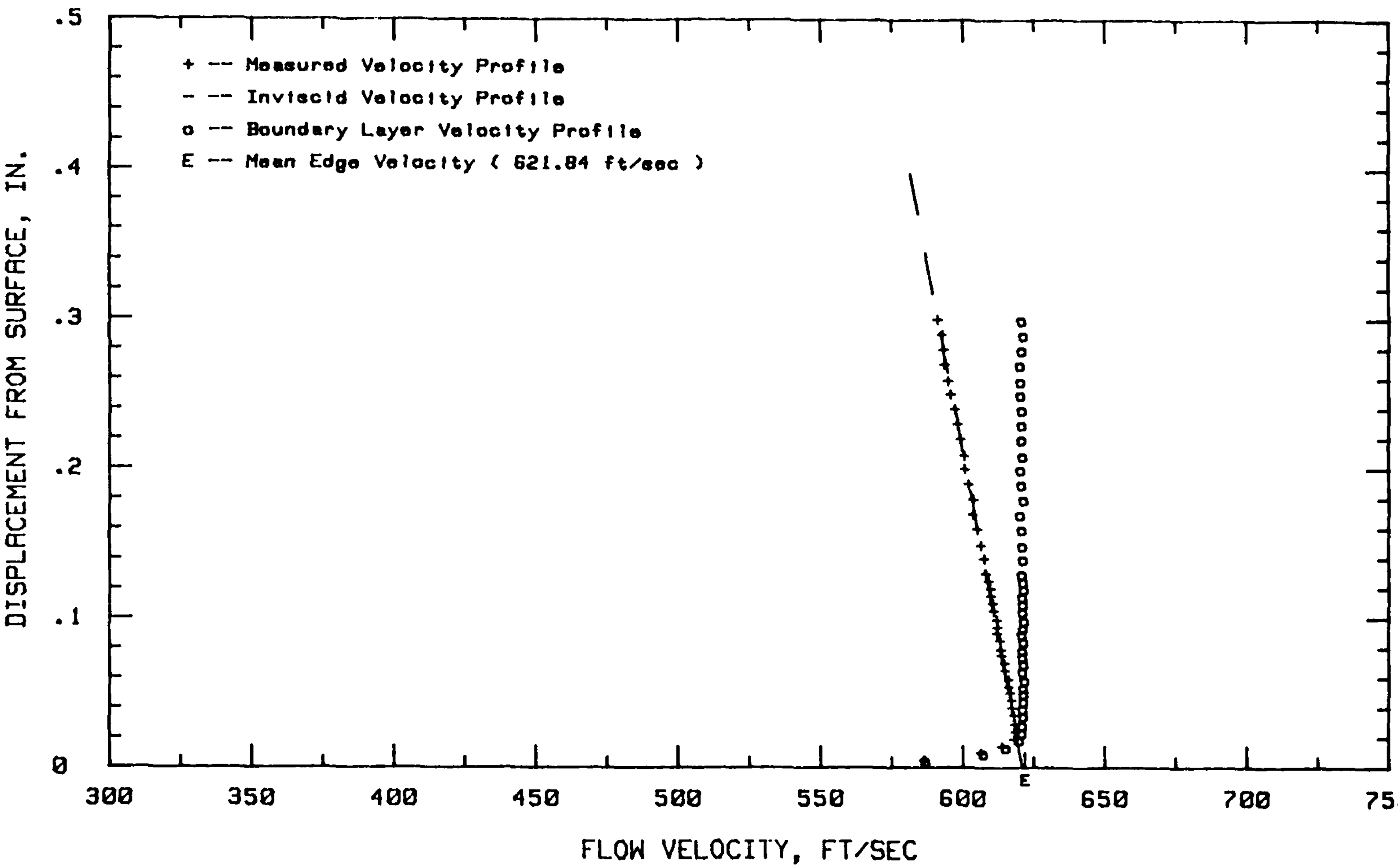

Fig. 115. Boundary Layer Velocity Profiles, i = 0 Deg, 34.37 % Chord

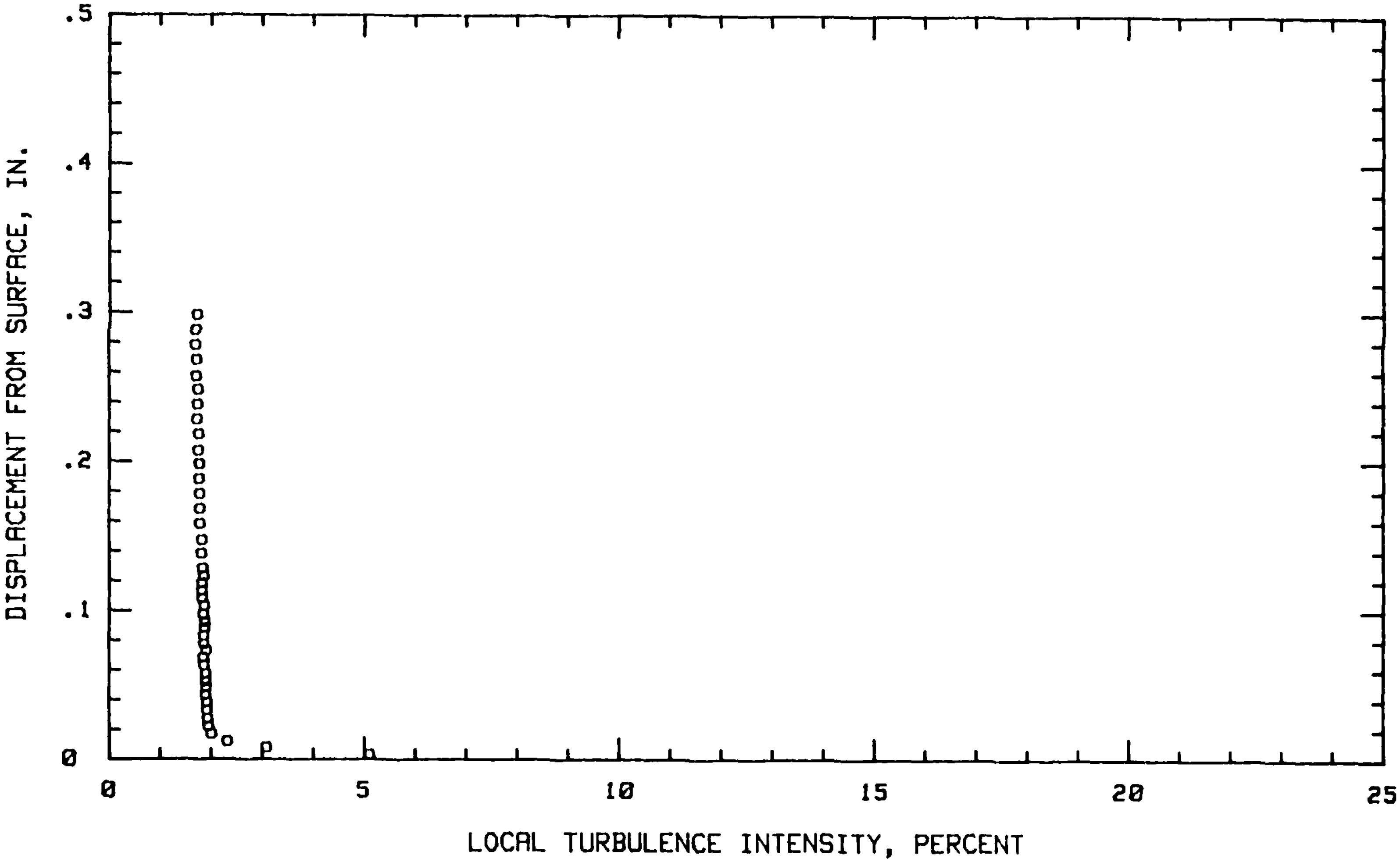

Fig. 116. Boundary Layer Turbulence Intensity Profile, i = 0 Deg, 34.37 % Chord

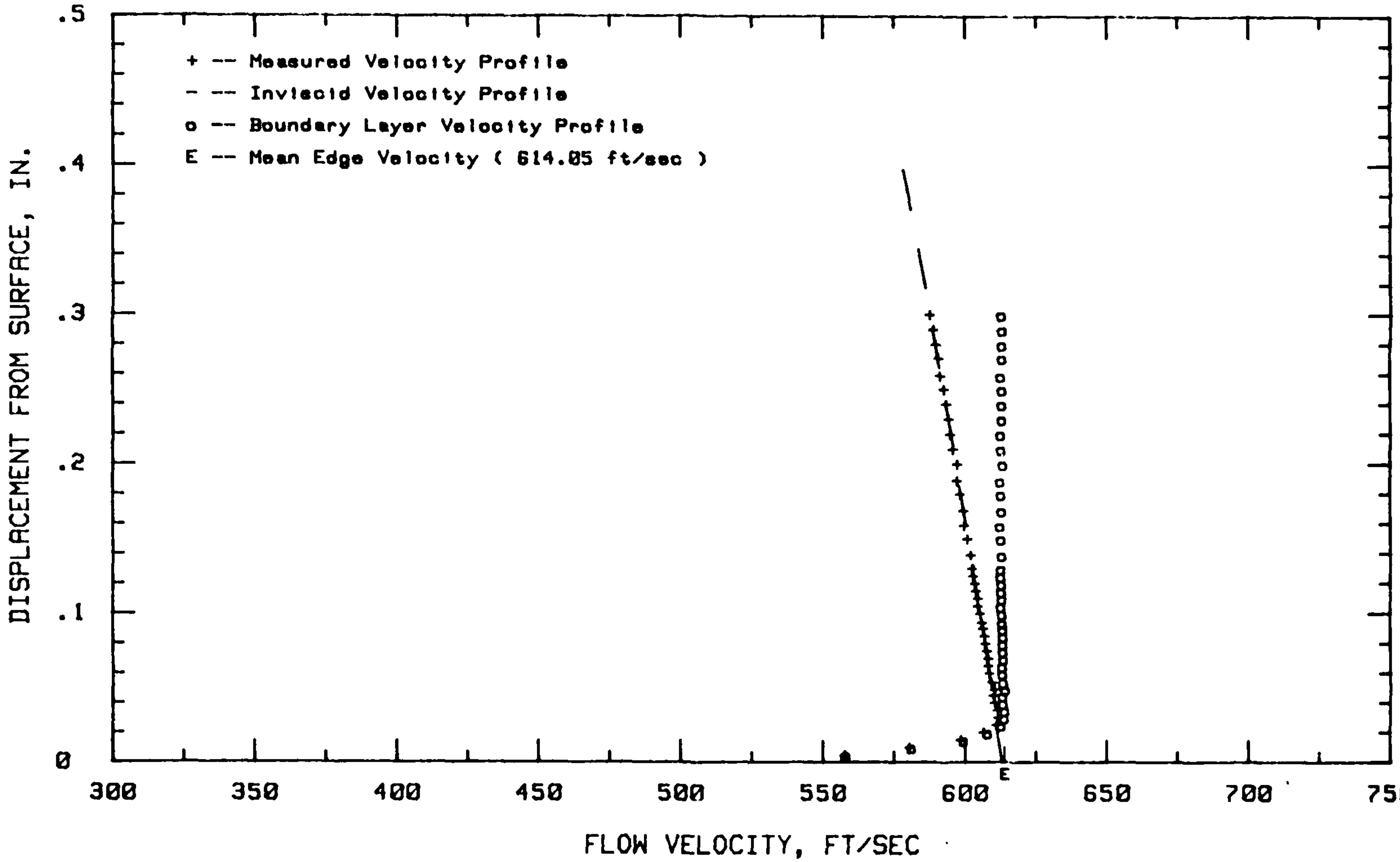

Fig. 117. Boundary Layer Velocity Profiles, i = 0 Deg, 40.62 % Chord

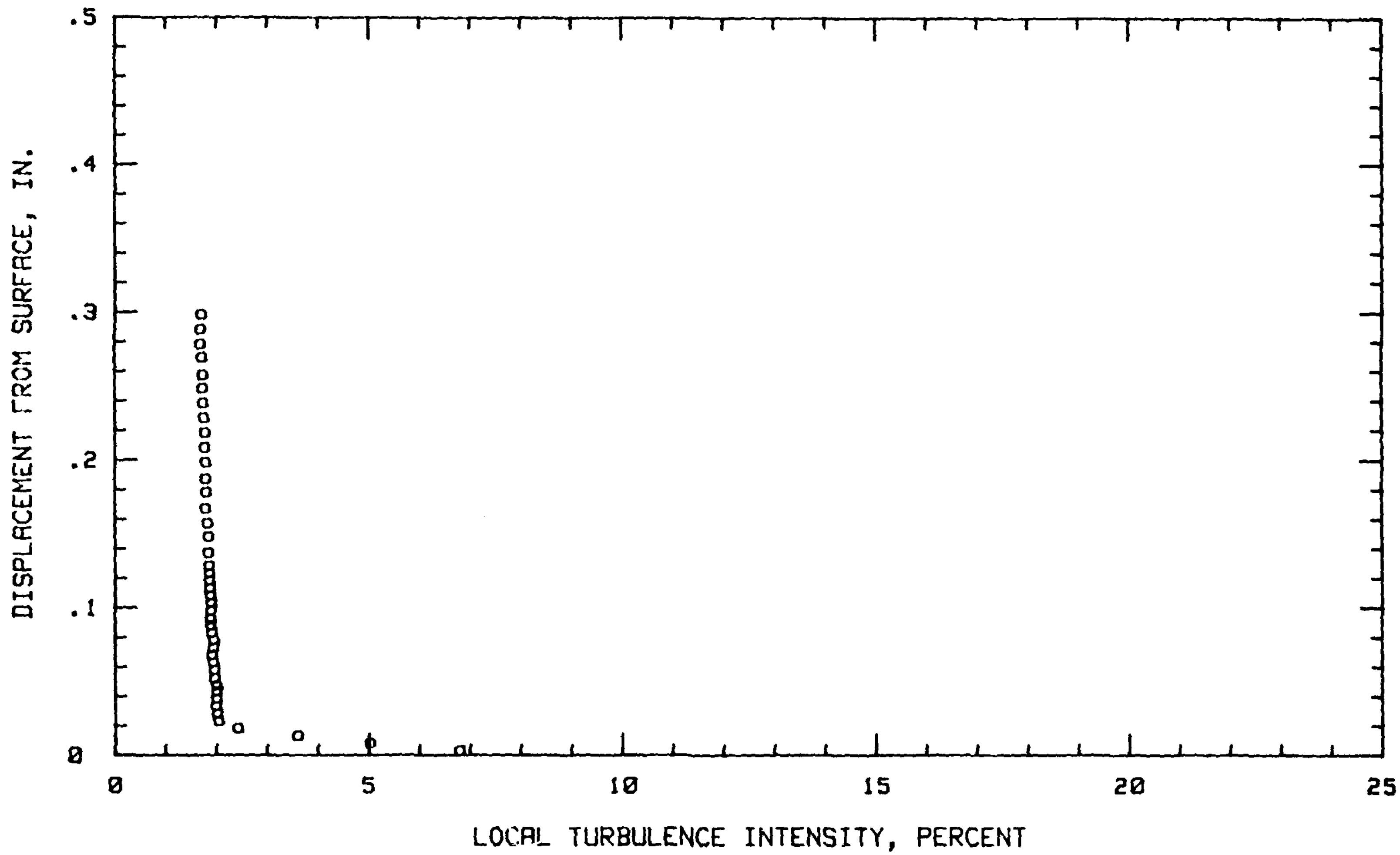

Fig. 118. Boundary Layer Turbulence Intensity Profile, i = 0 Deg, 40.62 % Chord

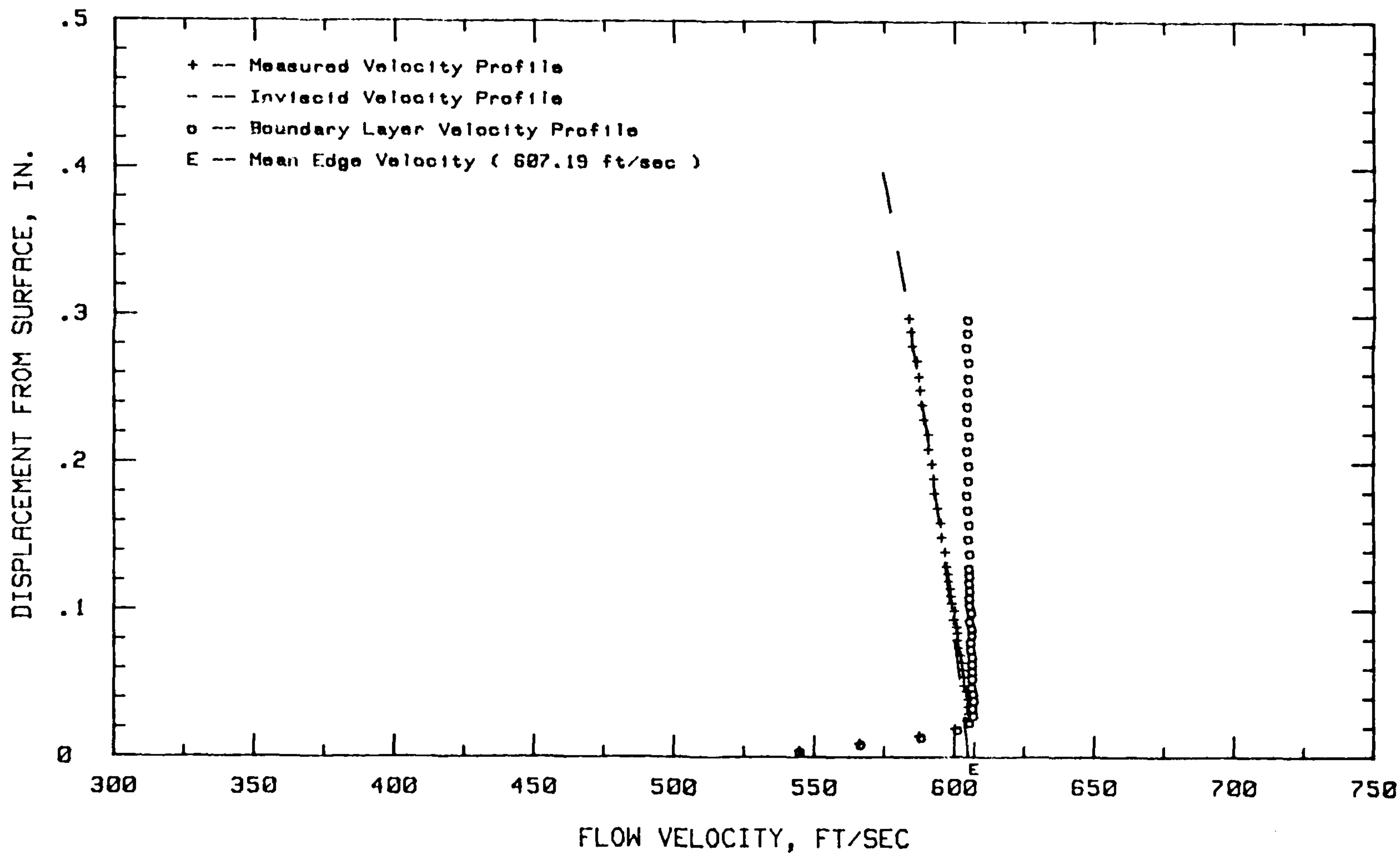

Fig. 119. Boundary Layer Velocity Profiles, i = 0 Deg, 45.31 % Chord

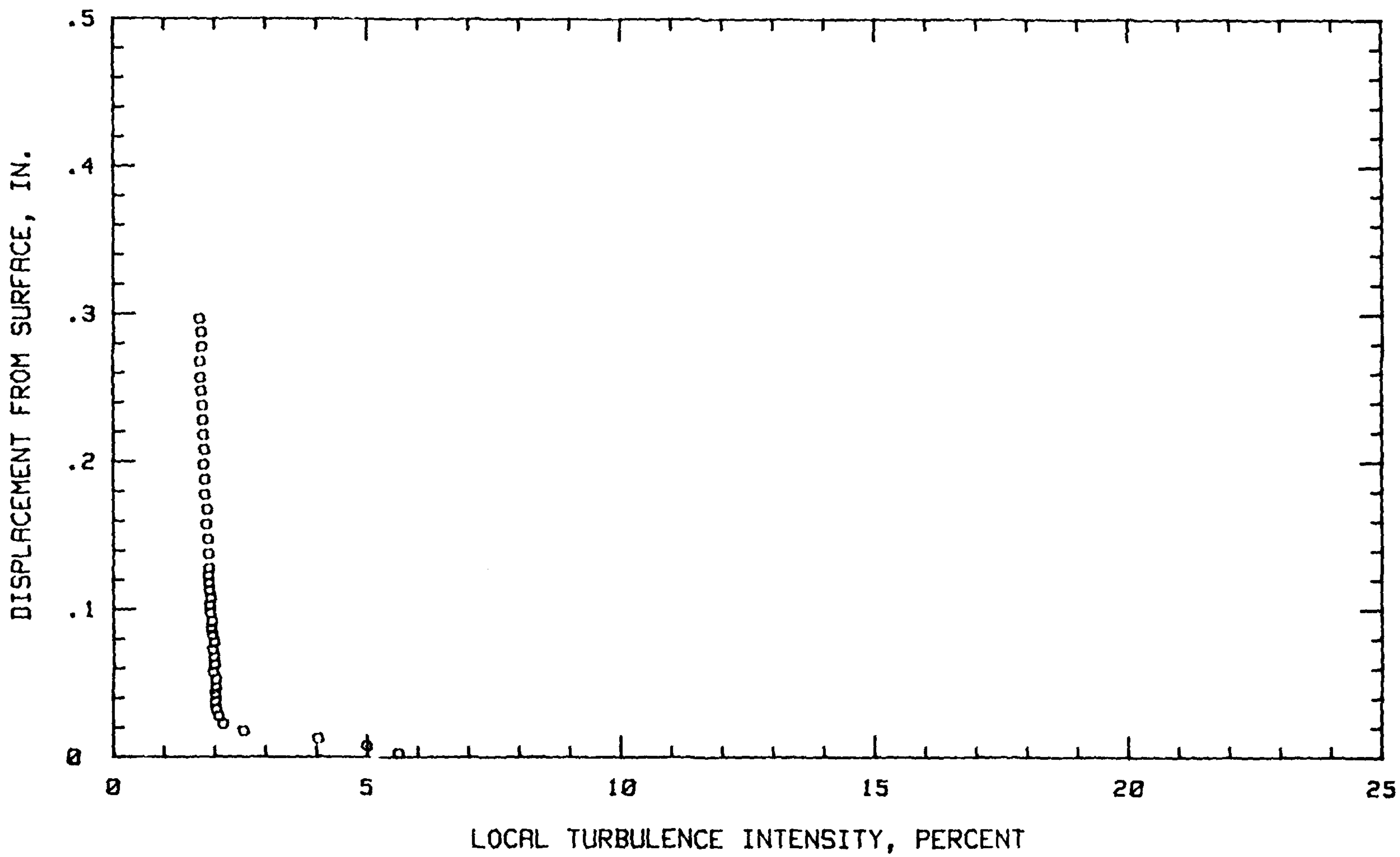

Fig. 120. Boundary Layer Turbulence Intensity Profile, i = 0 Deg, 45.31 % Chord

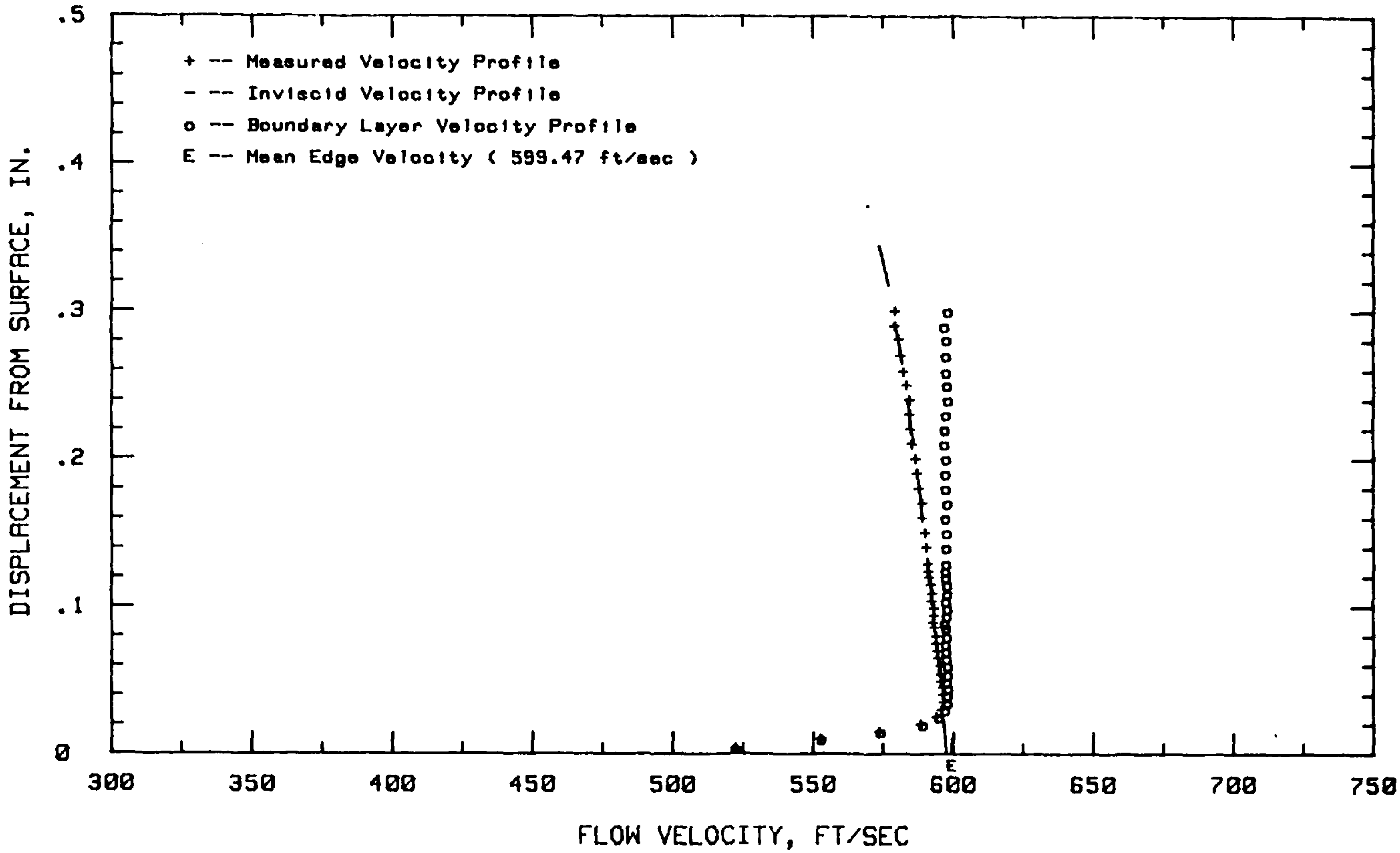

Fig. 121. Boundary Layer Velocity Profiles, i = 0 Deg, 50 % Chord

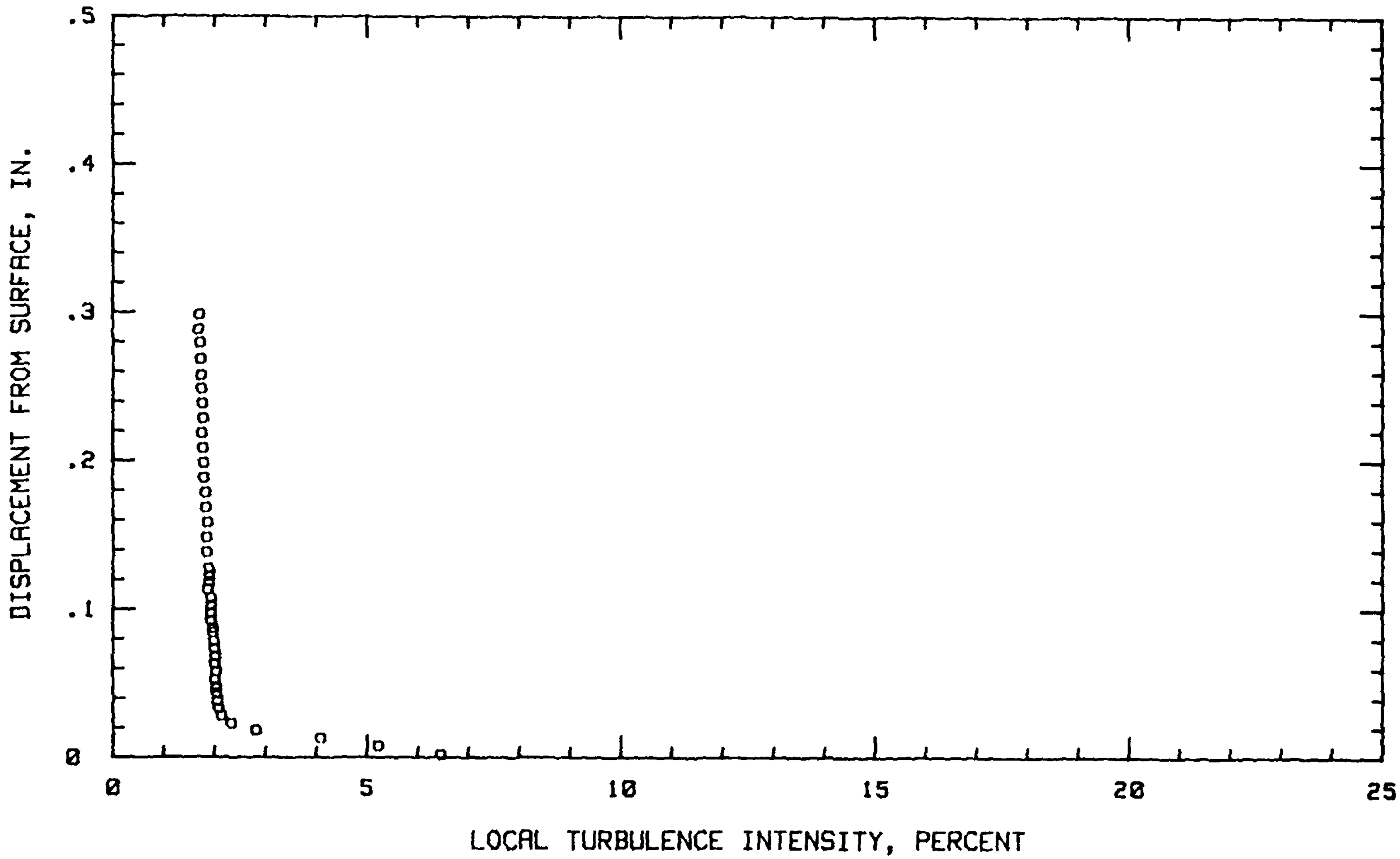

Fig. 122. Boundary Layer Turbulence Intensity Profile, i = 0 Deg, 50 % Chord

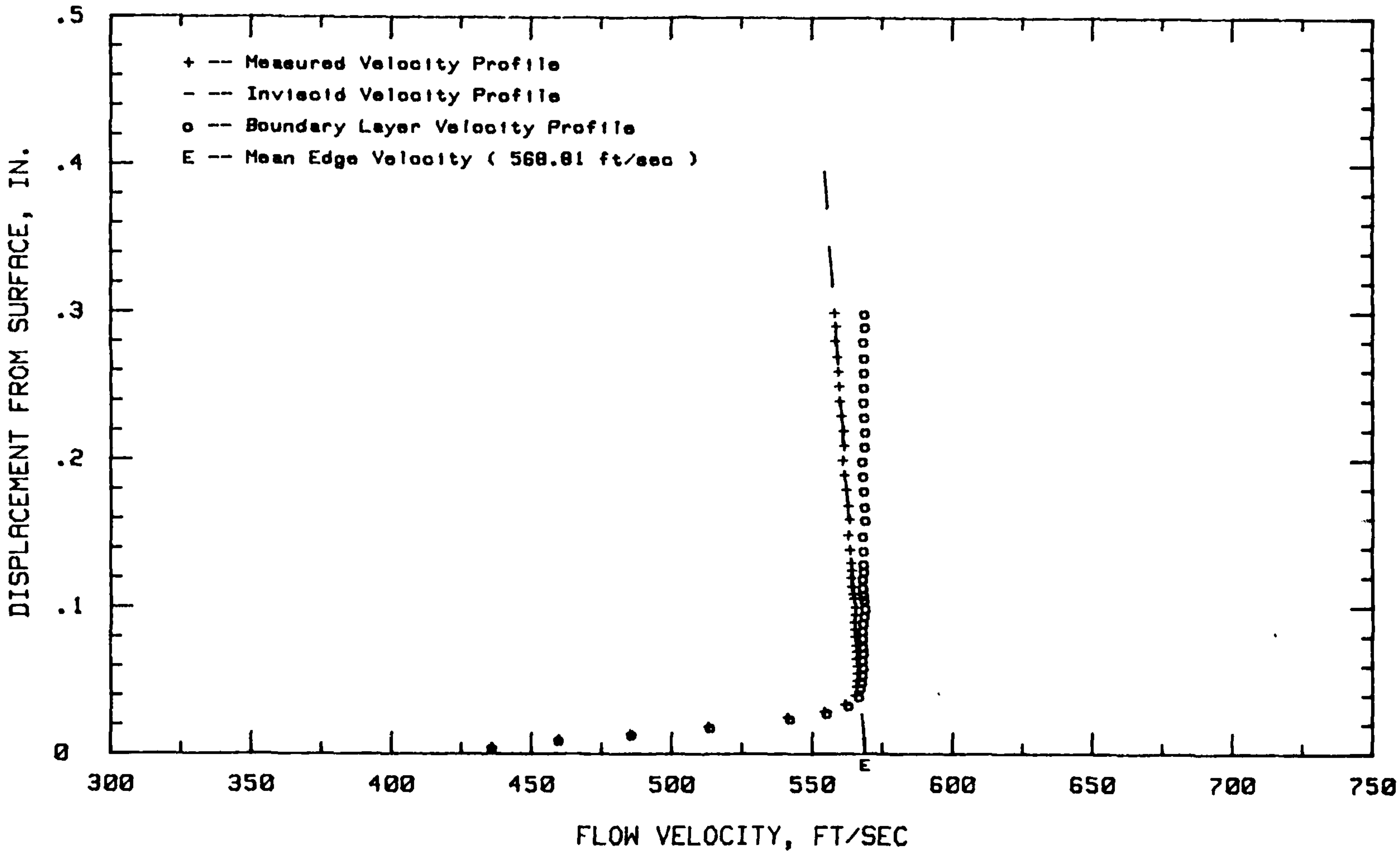

Fig. 123. Boundary Layer Velocity Profiles, i = 0 Deg, 65.62 % Chord

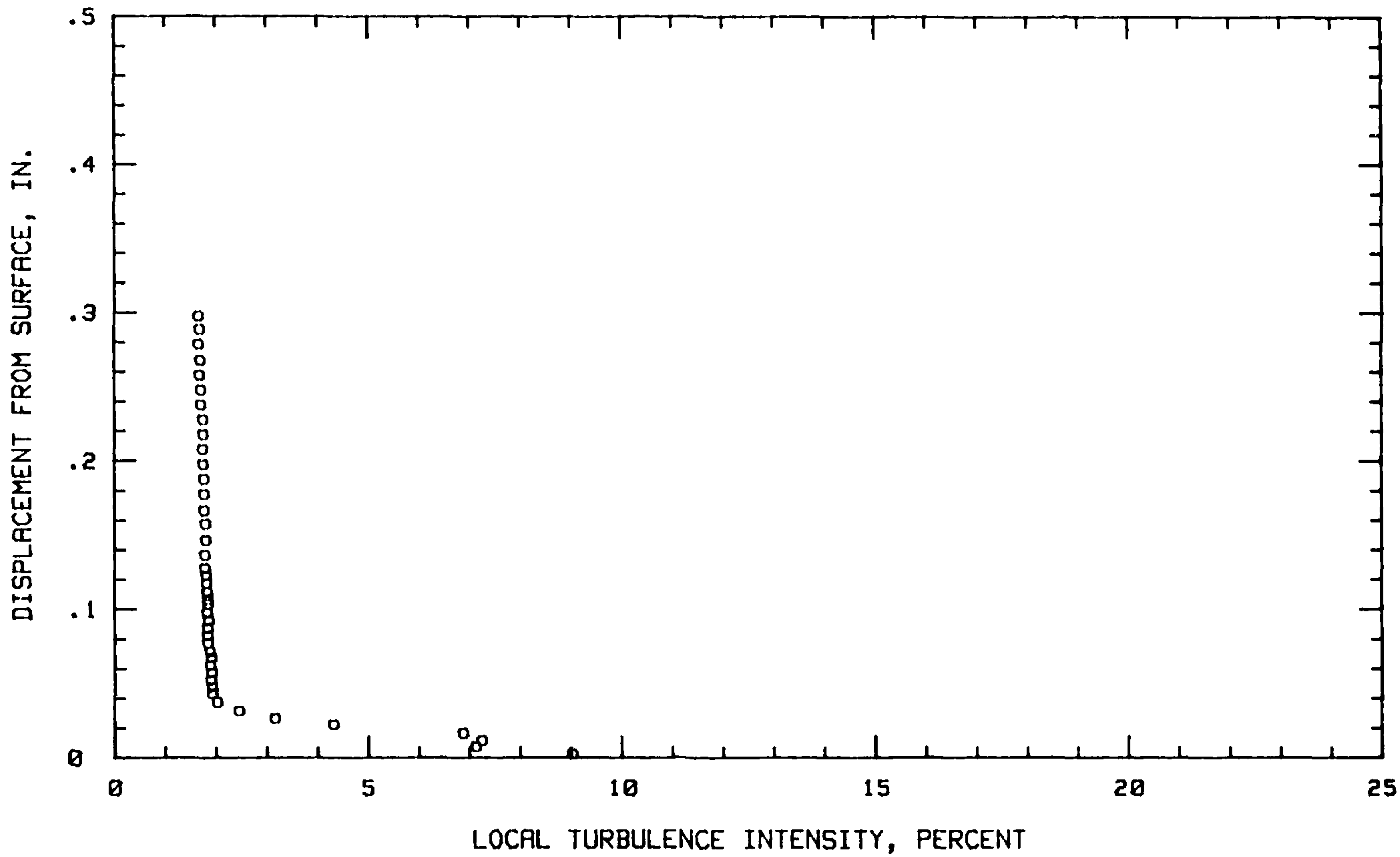

Fig. 124. Boundary Layer Turbulence Intensity Profile, i = 0 Deg, 65.62 % Chord

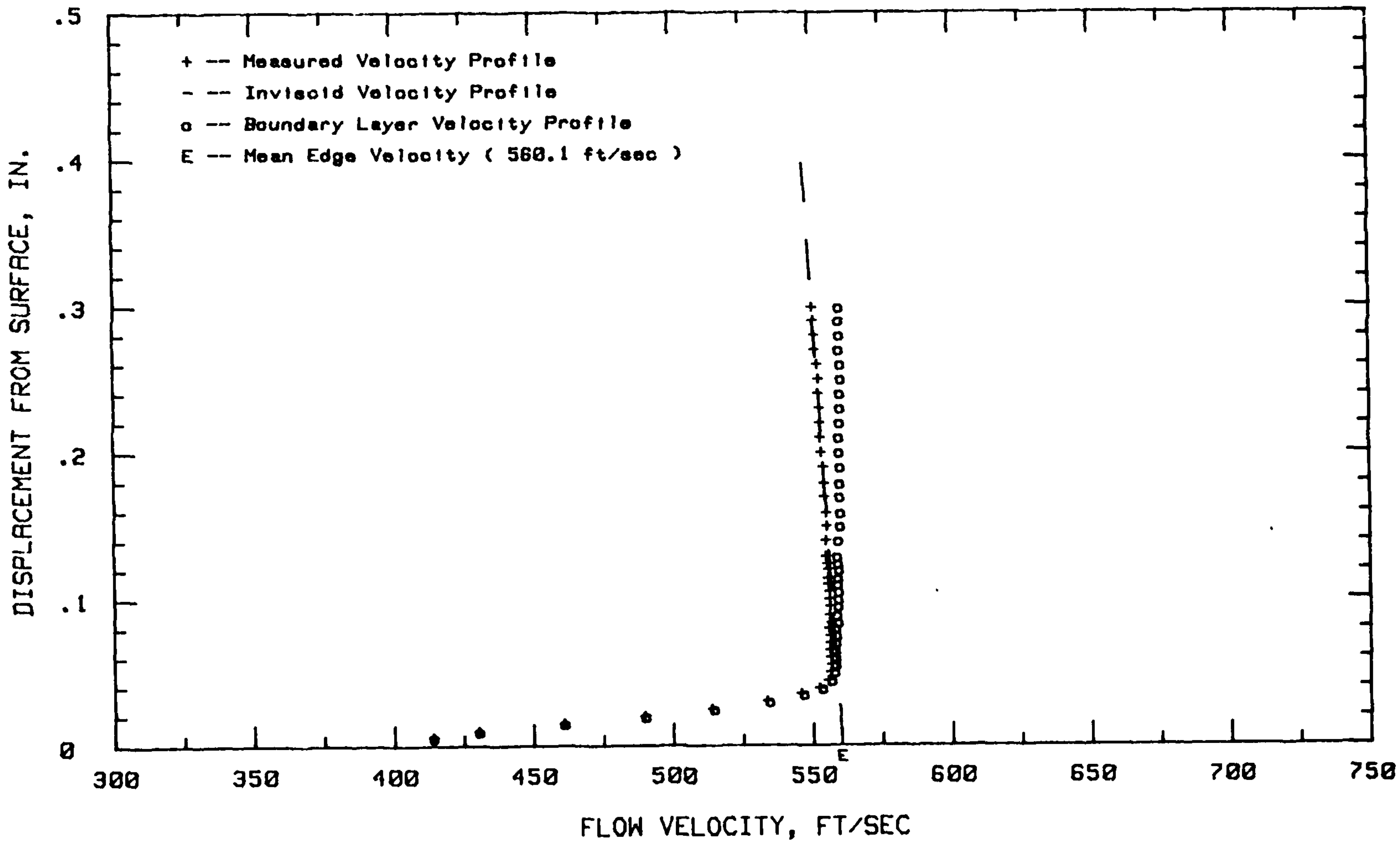

Fig. 125. Boundary Layer Velocity Profiles, i = 0 Deg, 70.31 % Chord

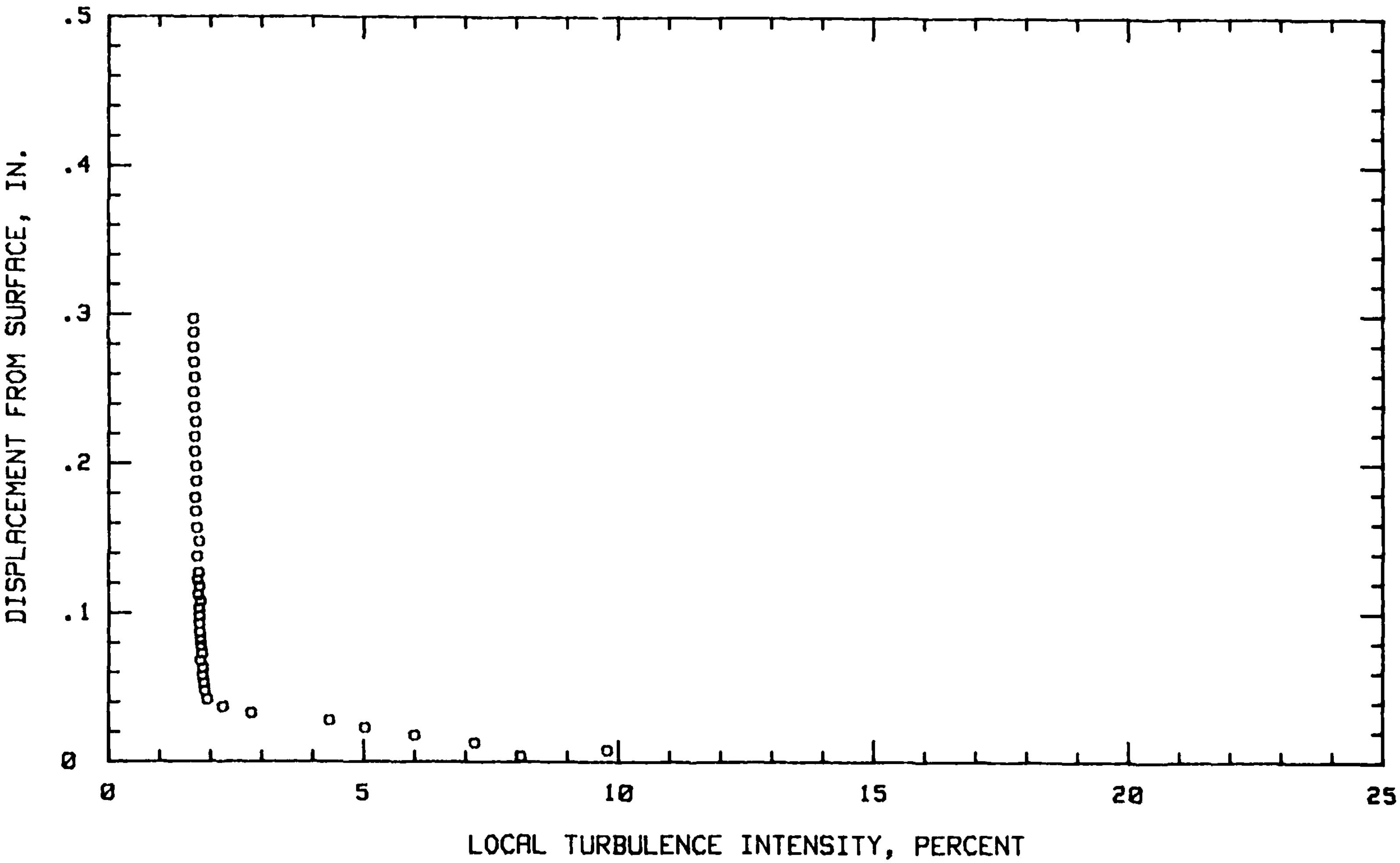

Fig. 126. Boundary Layer Turbulence Intensity Profile, i = 0 Deg, 70.31 % Chord

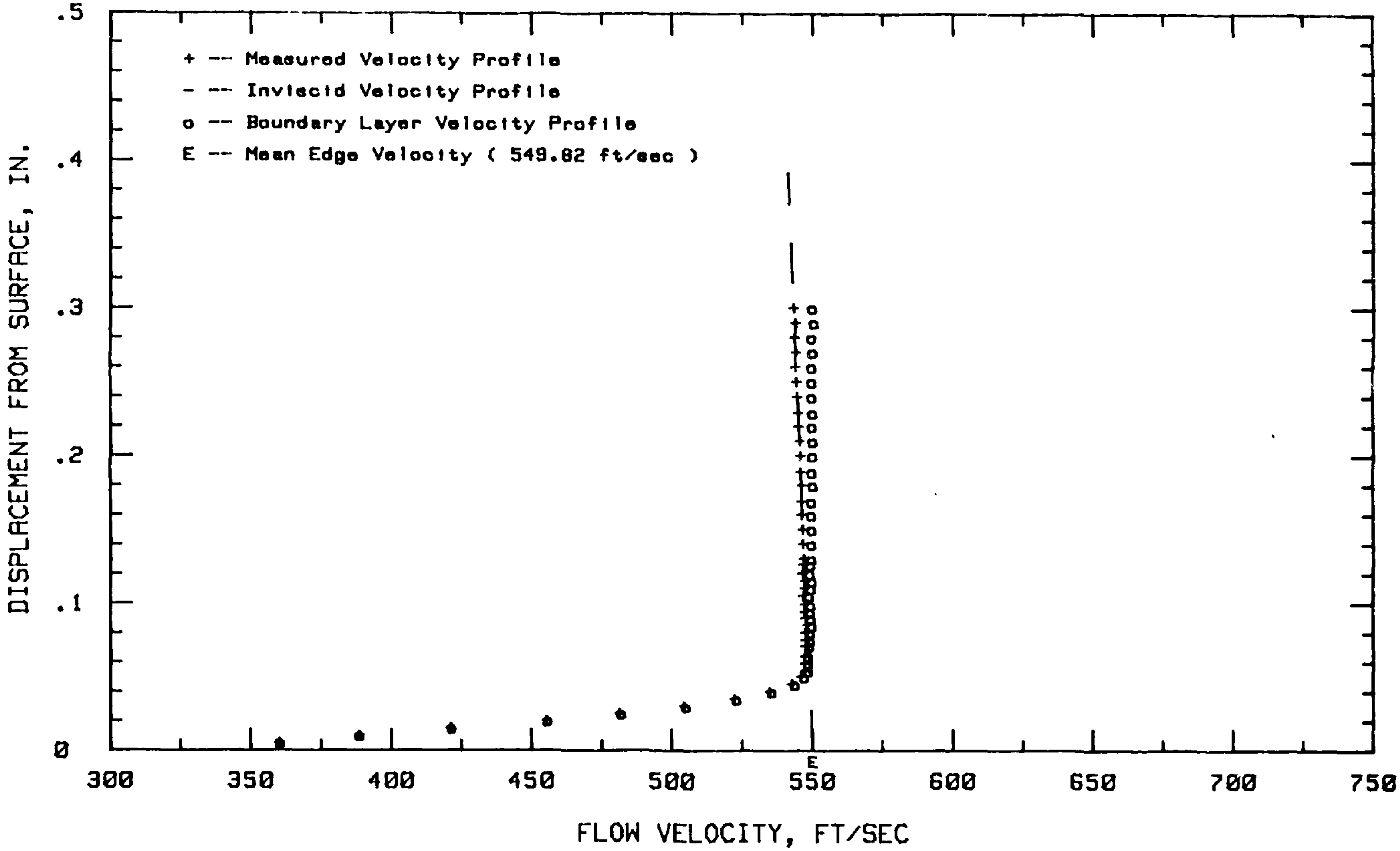

Fig. 127. Boundary Layer Velocity Profiles, i = 0 Deg, 75 % Chord

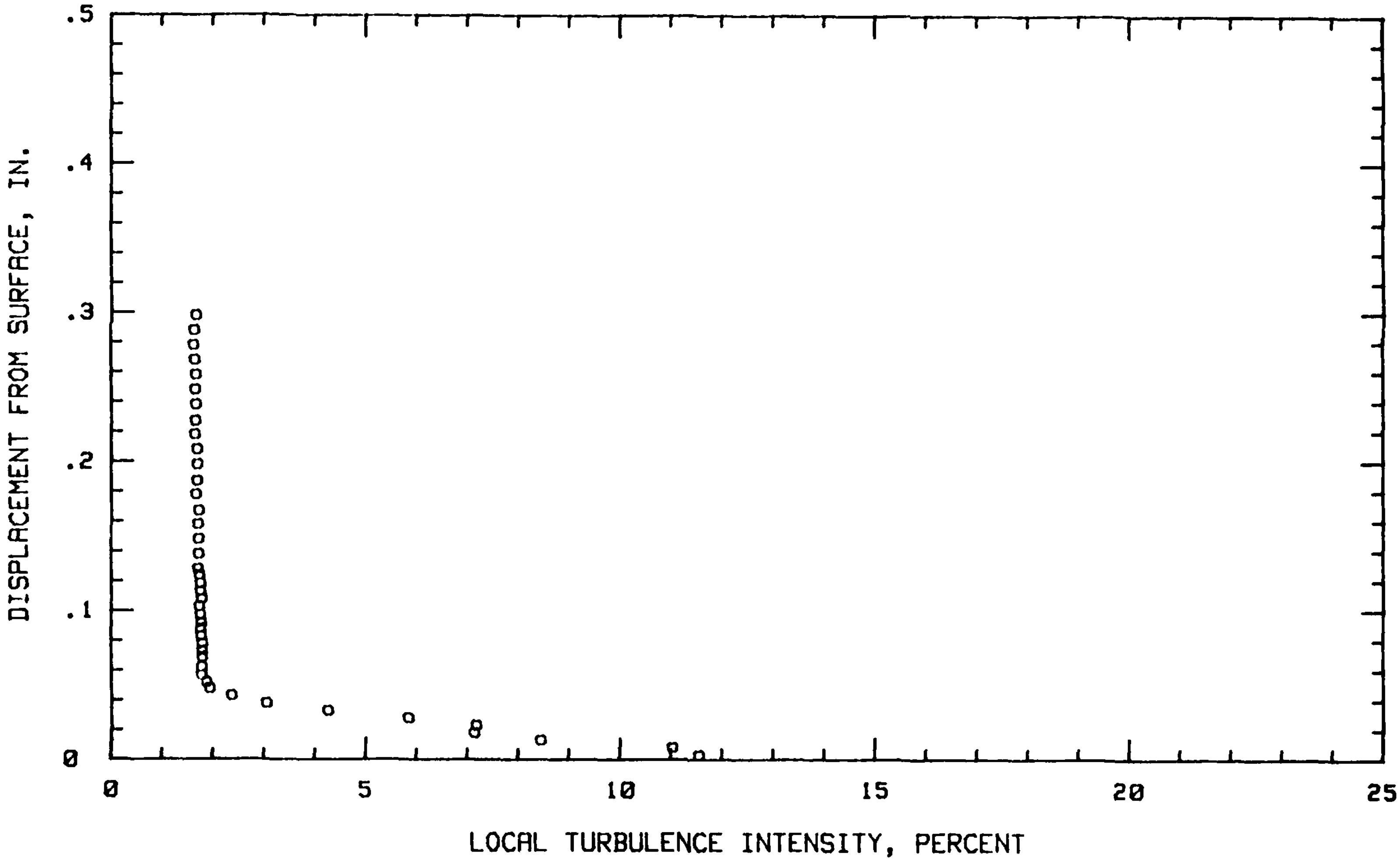

Fig. 128. Boundary Layer Turbulence Intensity Profile, i = 0 Deg, 75 % Chord

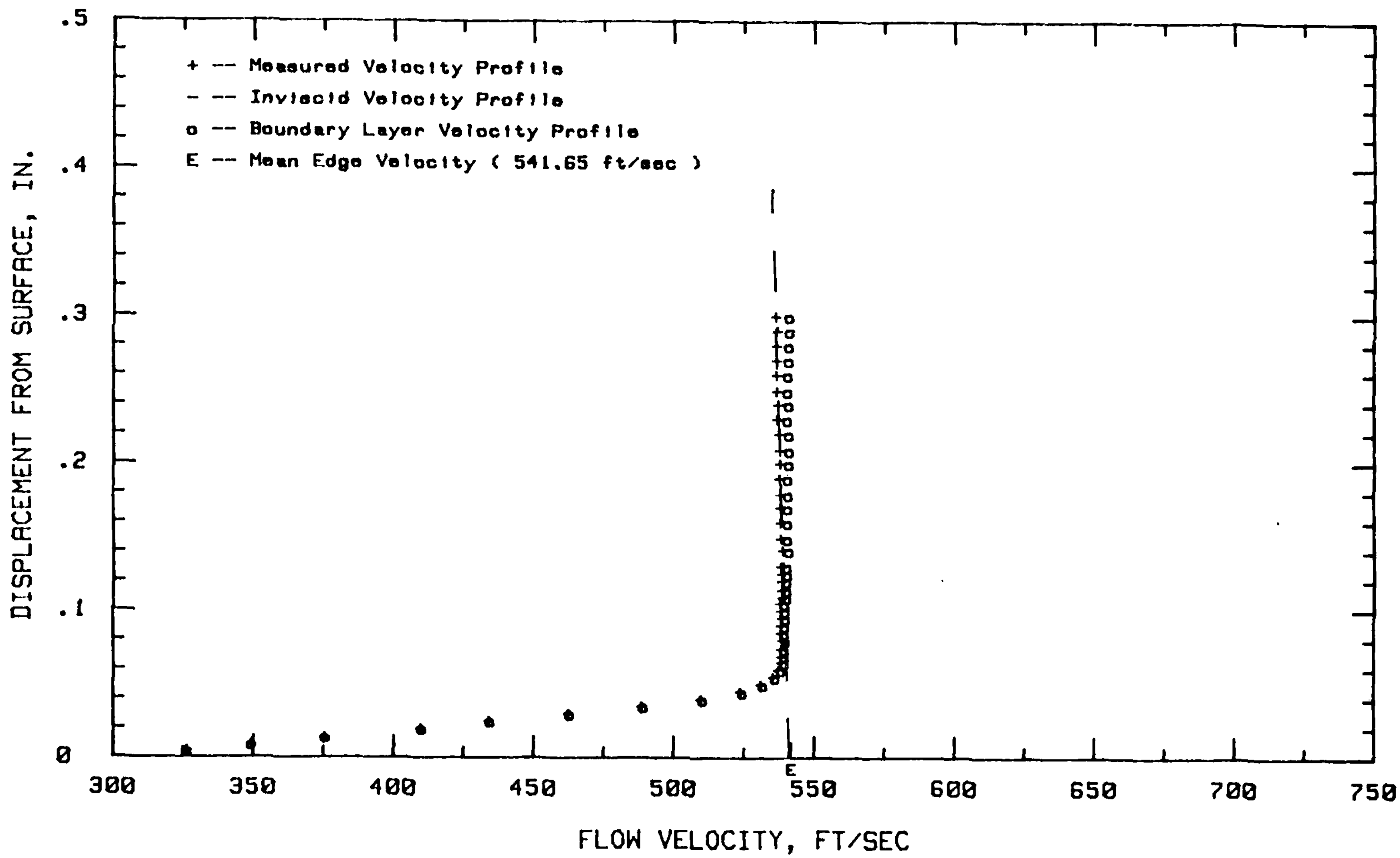

Fig. 129. Boundary Layer Velocity Profiles, i = 0 Deg, 79.68 % Chord

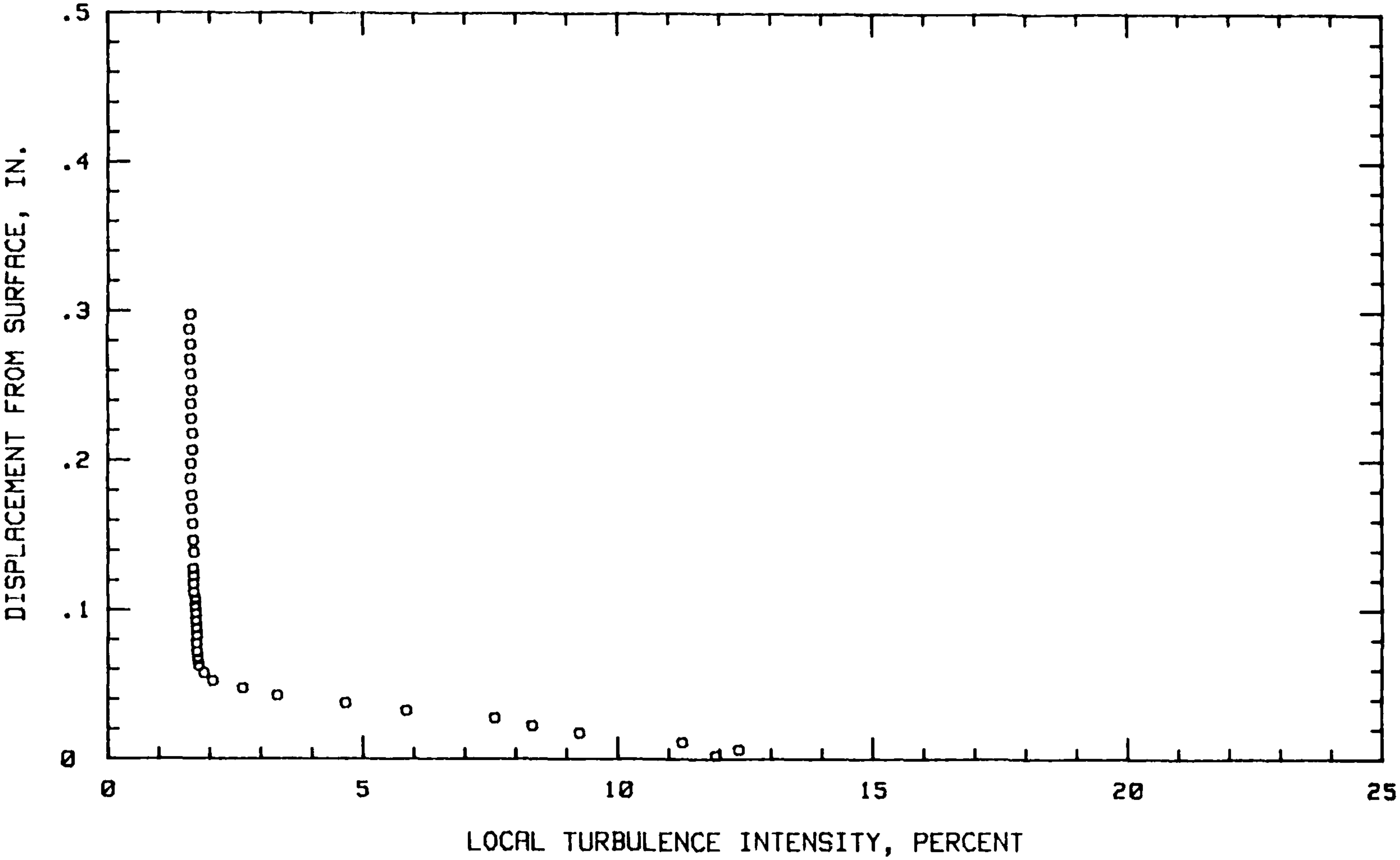

Fig. 130. Boundary Layer Turbulence Intensity Profile, i = 0 Deg, 79.68 % Chord

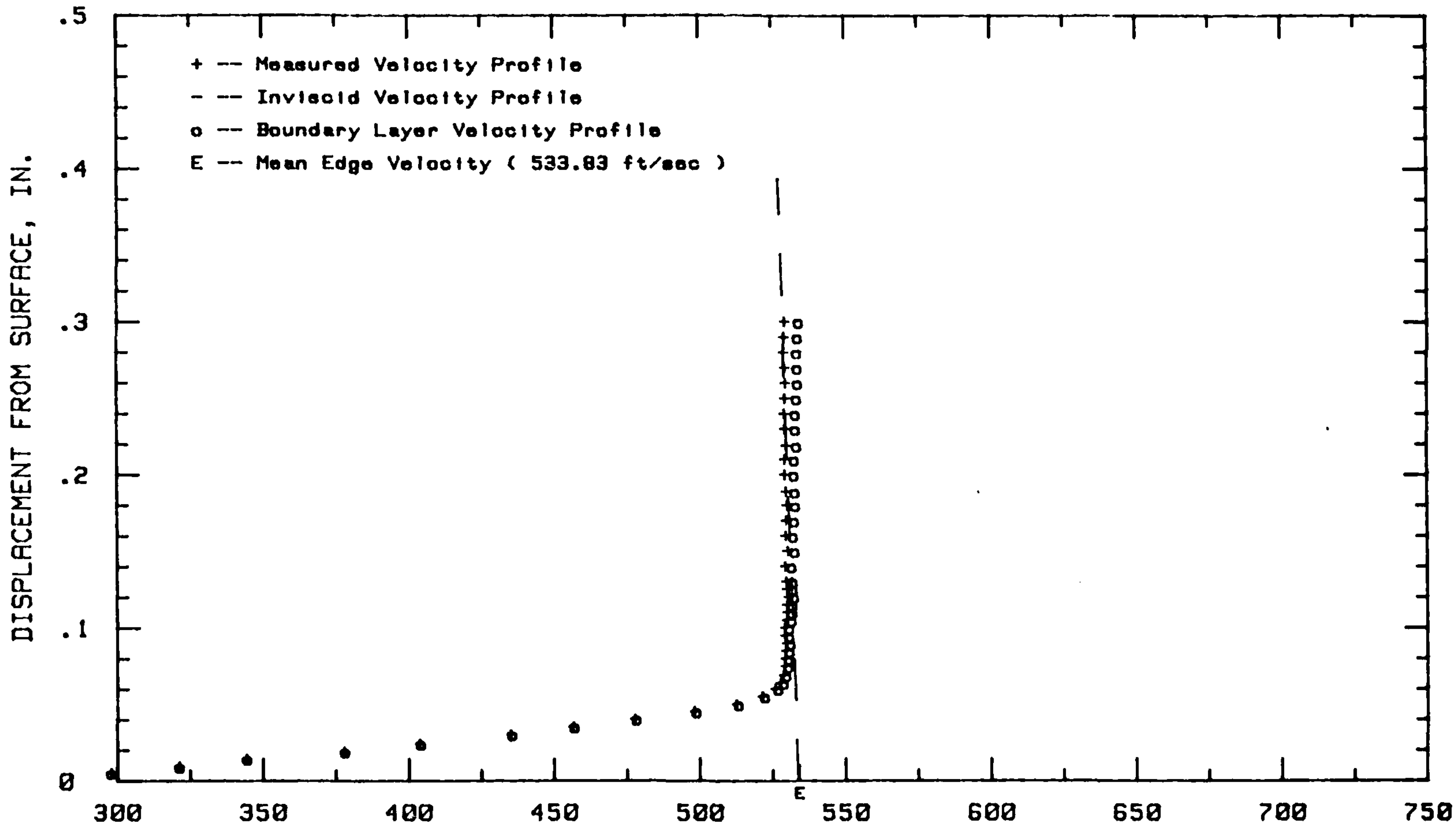

Fig. 131. Boundary Layer Velocity Profiles, i = 0 Deg, 84.37 % Chord

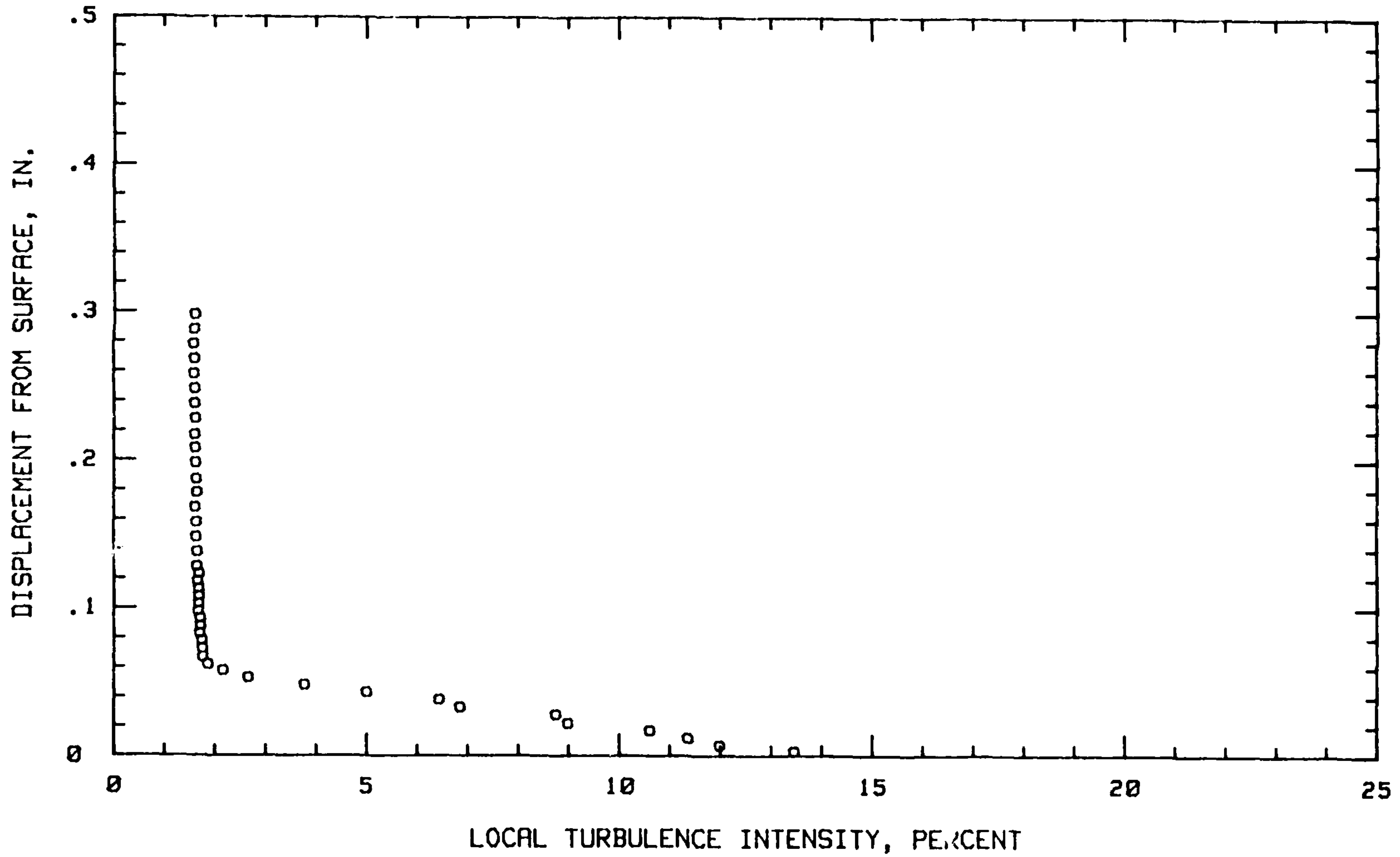

Fig. 132. Boundary Layer Turbulence Intensity Profile, i = 0 Deg, 84.37 % Chord

Appendix L

Boundary Layer Velocity and Turbulence Intensity Profiles

Blade Configuration Number 2

Incidence Angle = Ø.Ø Degrees

High Free Stream Turbulence

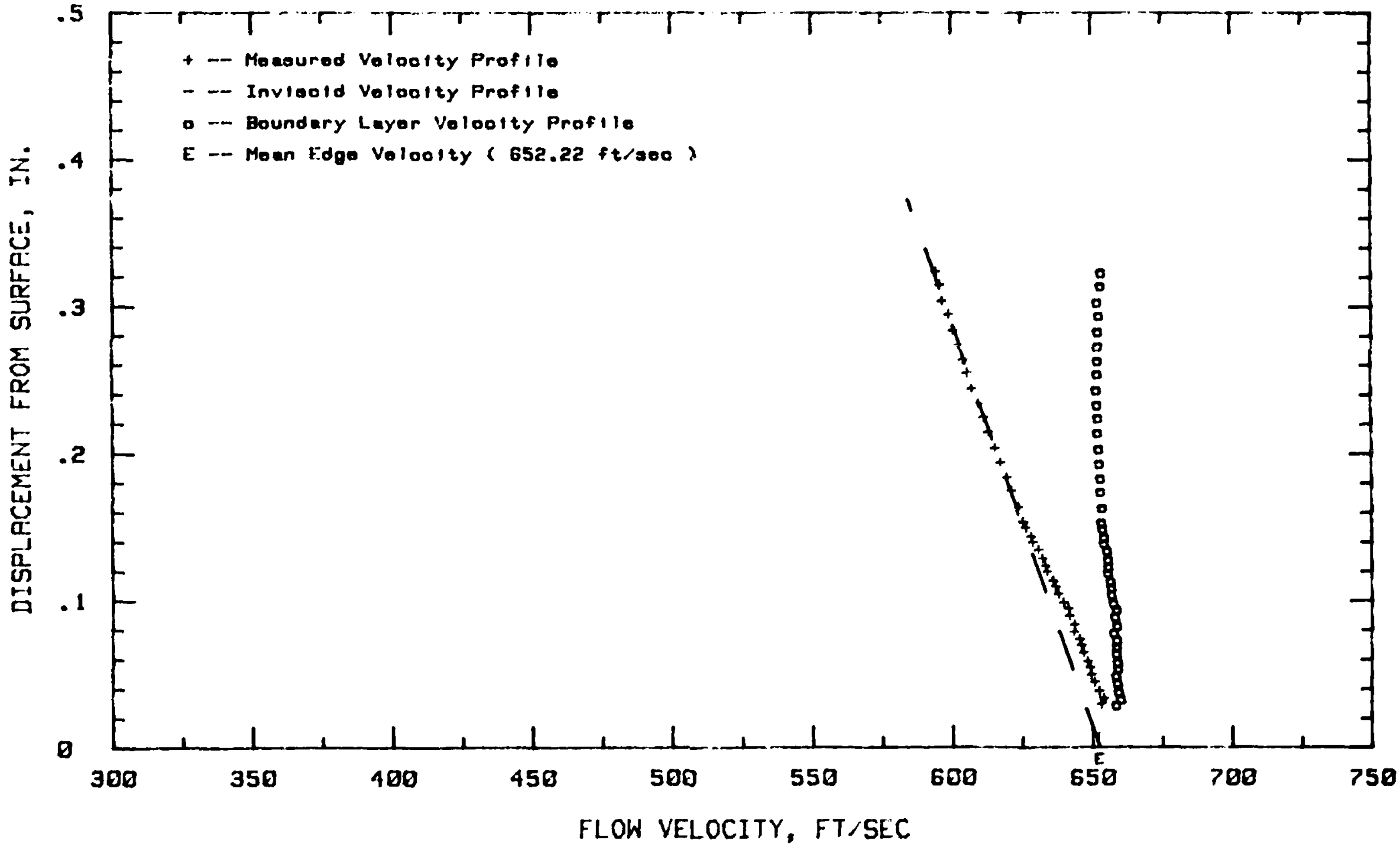

Fig. 133. Boundary Layer Velocity Profiles, i = 0 Deg, 4.68 % Chord

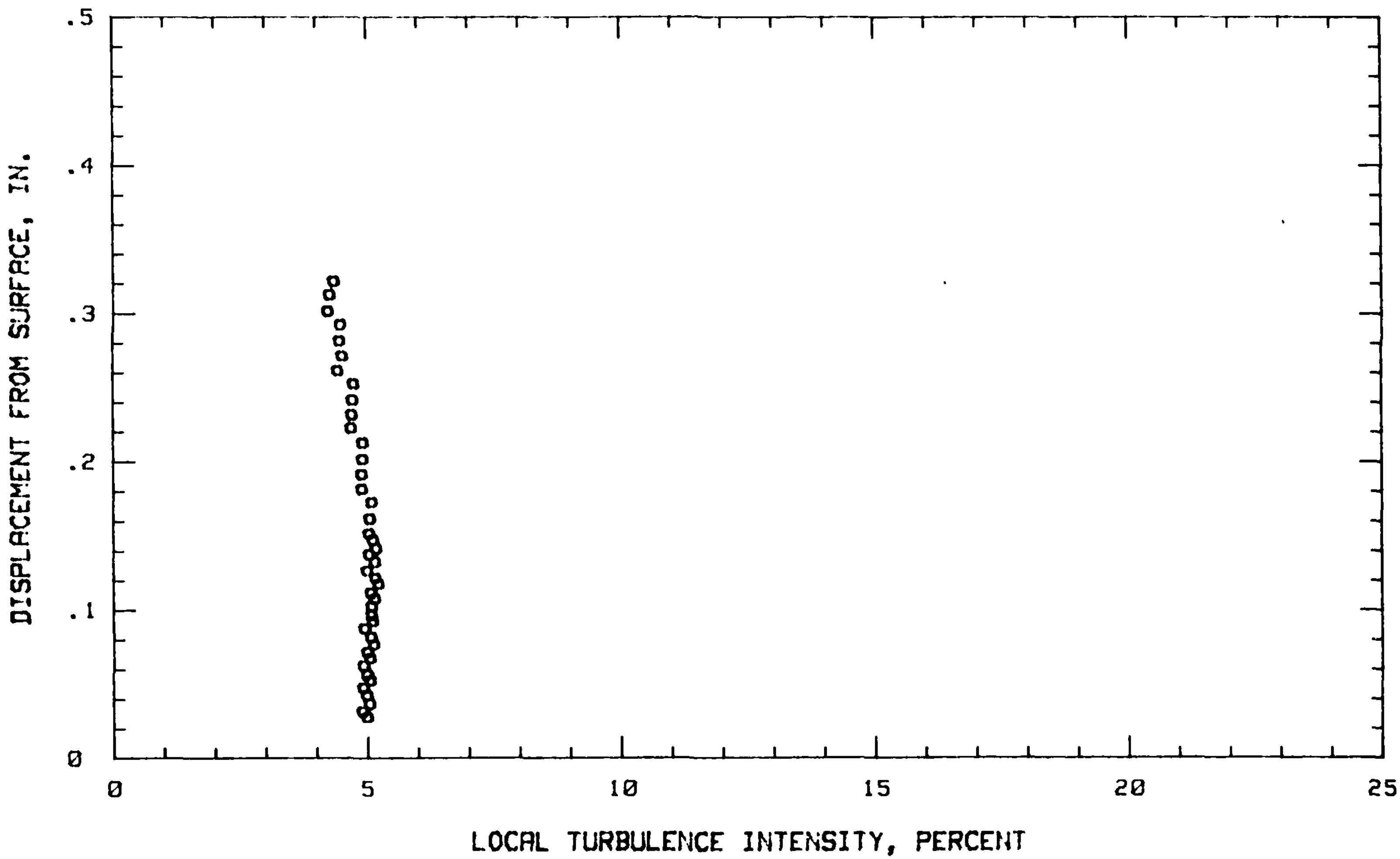

Fig. 134. Boundary Layer Turbulence Intensity Profile, i = 0 Deg, 4.68 % Chord

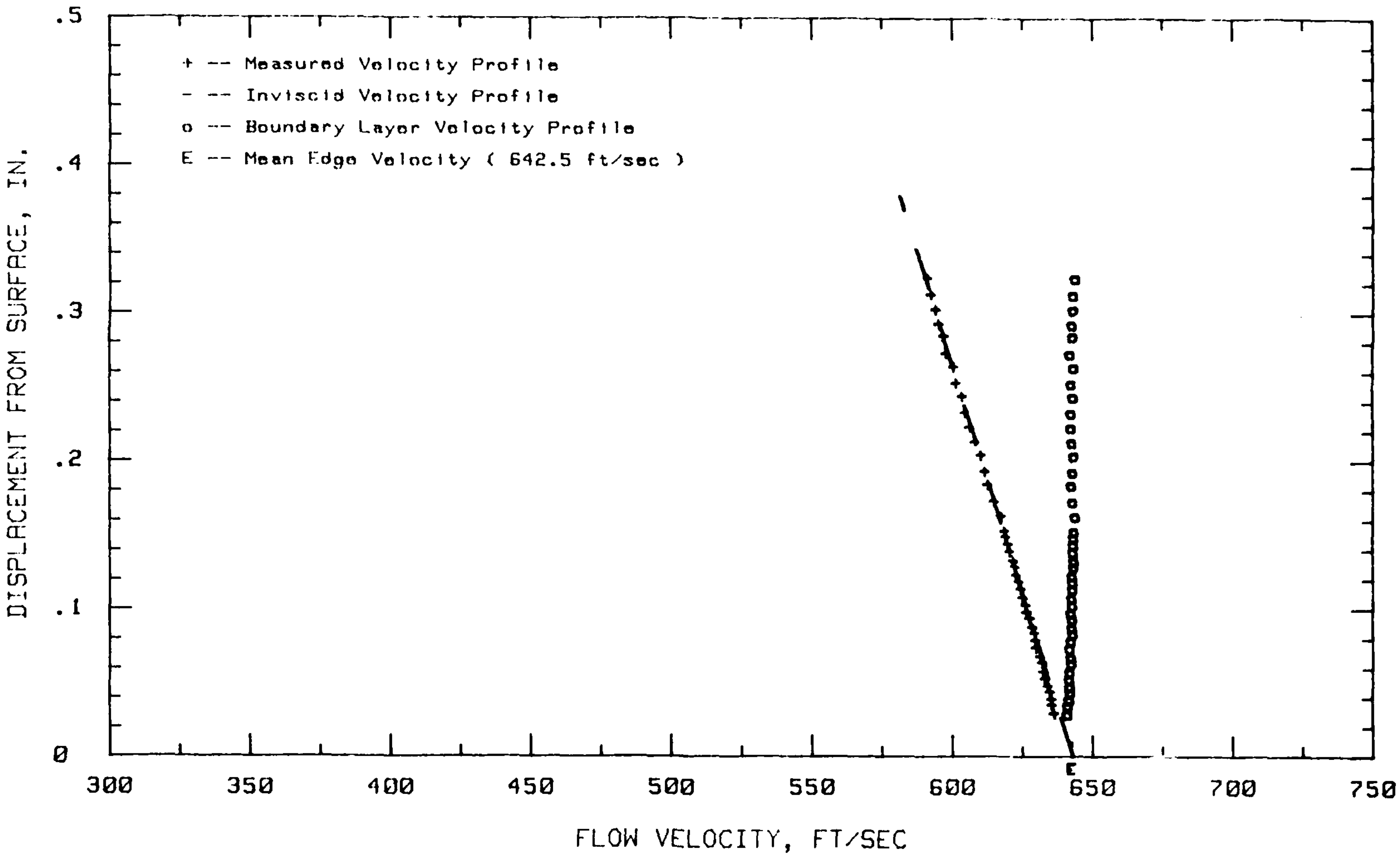

Fig. 135. Boundary Layer Velocity Profiles, i = 0 Deg, 9.37 % Chord

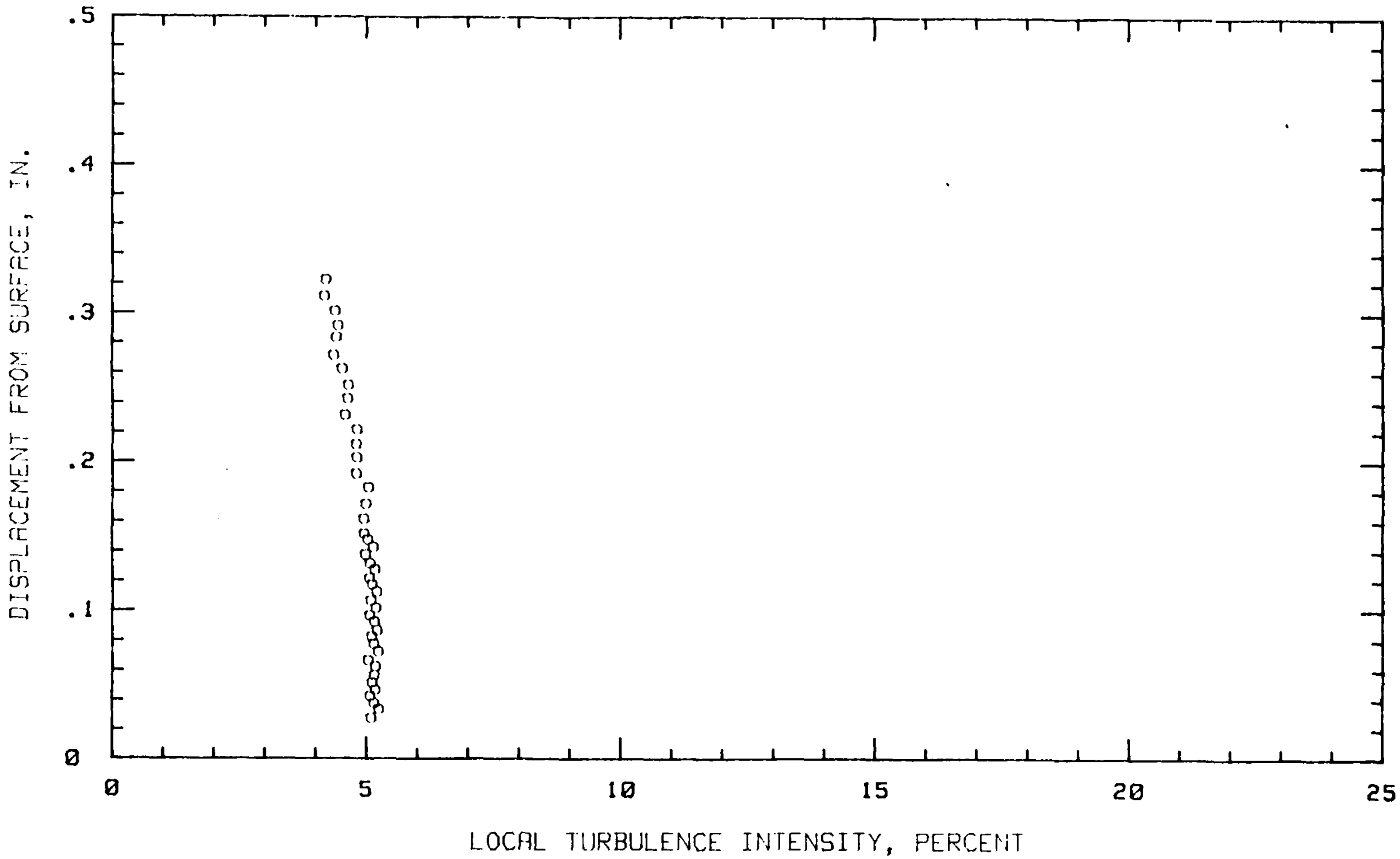

Fig. 136. Boundary Layer Turbulence Intensity Profile, i = 0 Deg, 9.37 % Chord

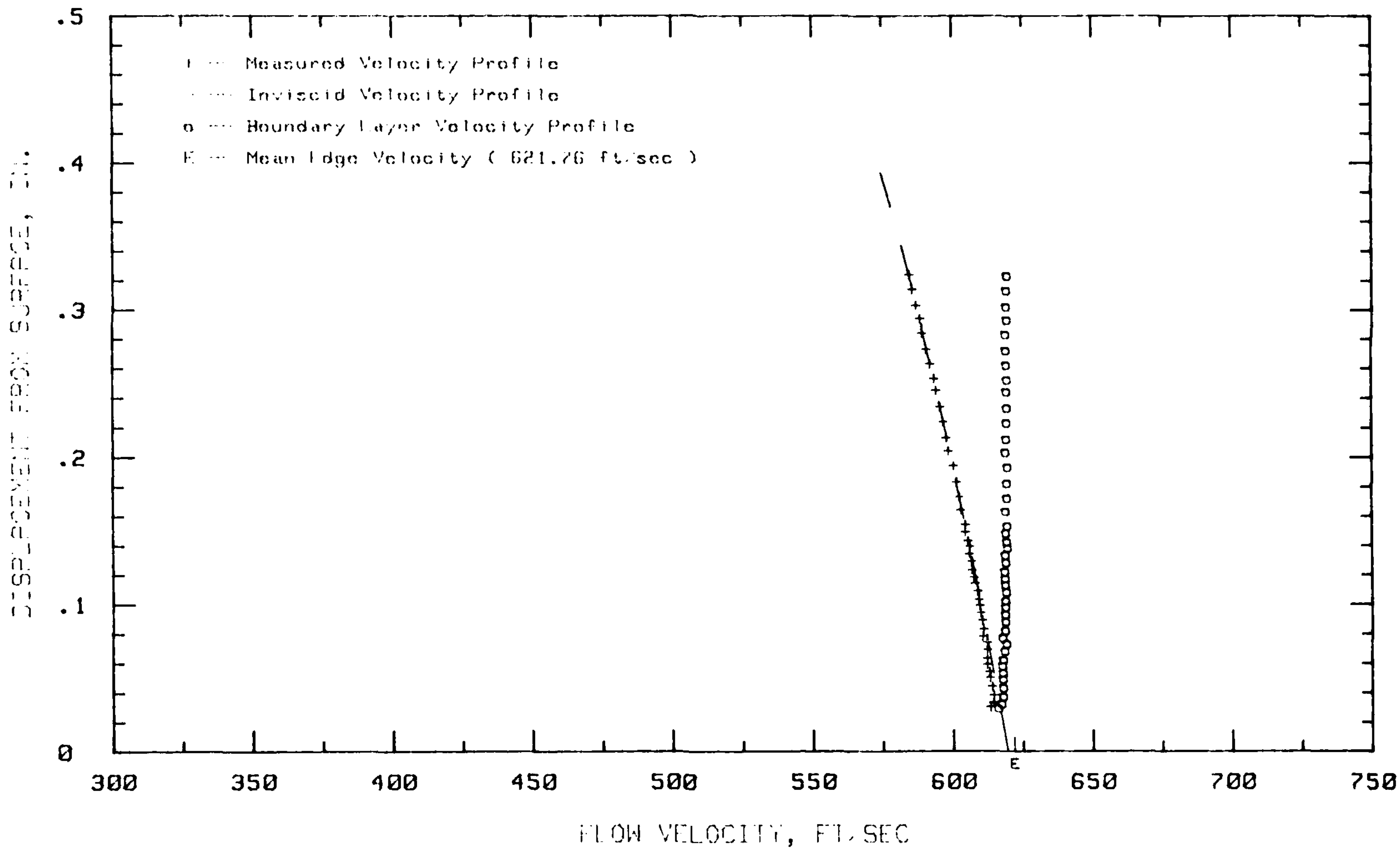

Fig. 137. Boundary Layer Velocity Profiles, α = 0 Deg, 25 % Chord

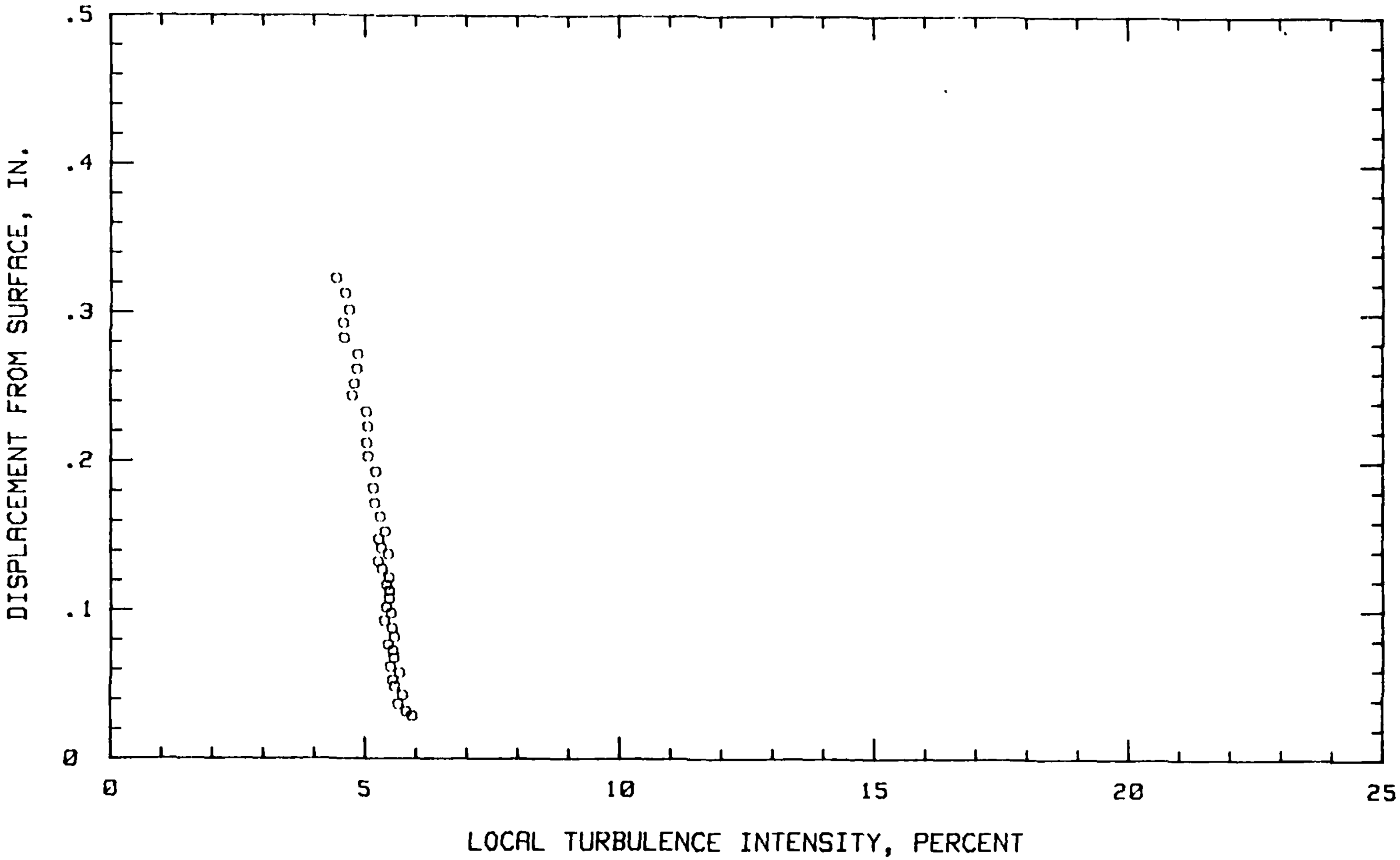

Fig. 138. Boundary Layer Turbulence Intensity Profile, i = 0 Deg, 25 % Chord

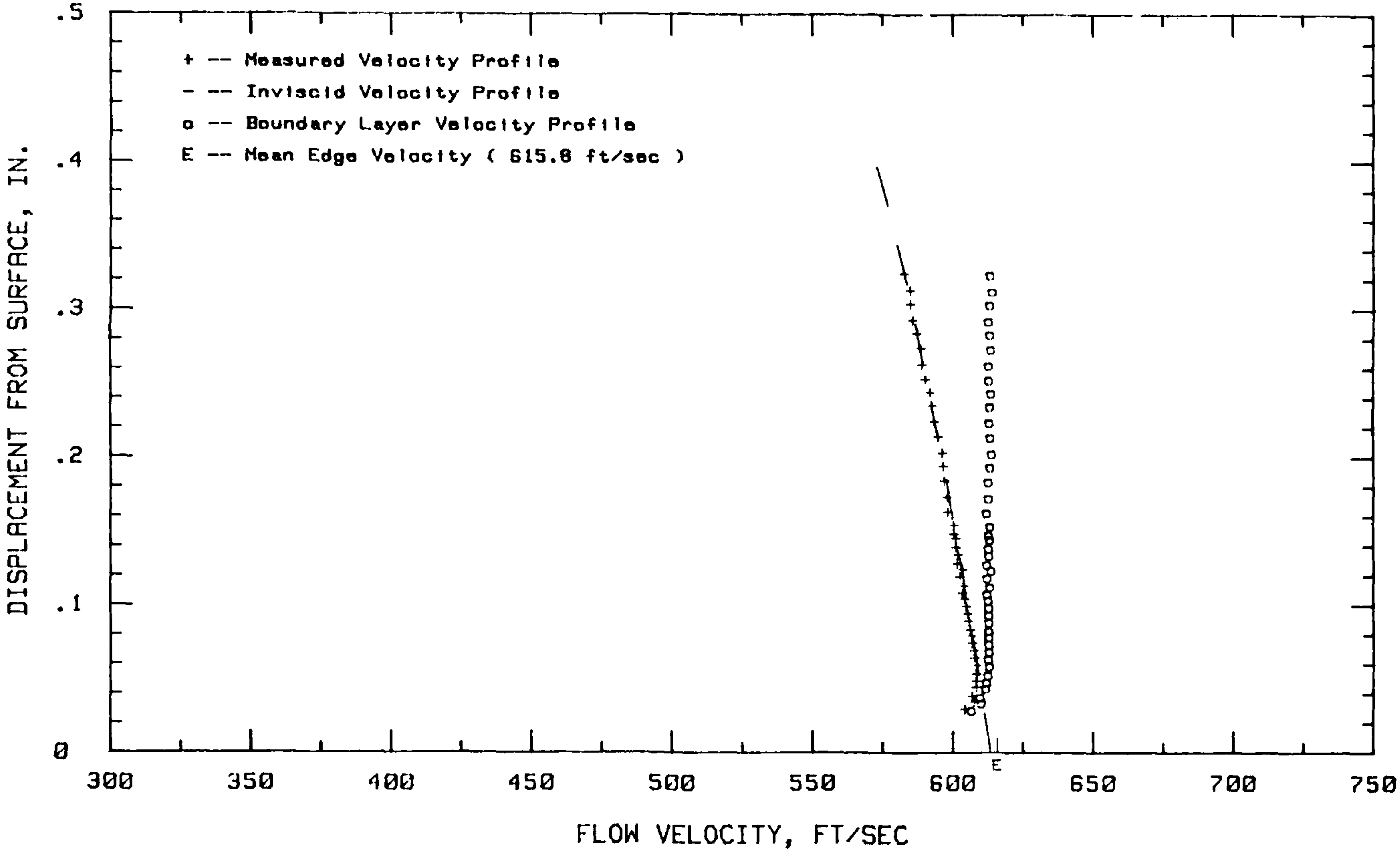

Fig. 139. Boundary Layer Velocity Profiles, i = 0 Deg, 29.68 % Chord

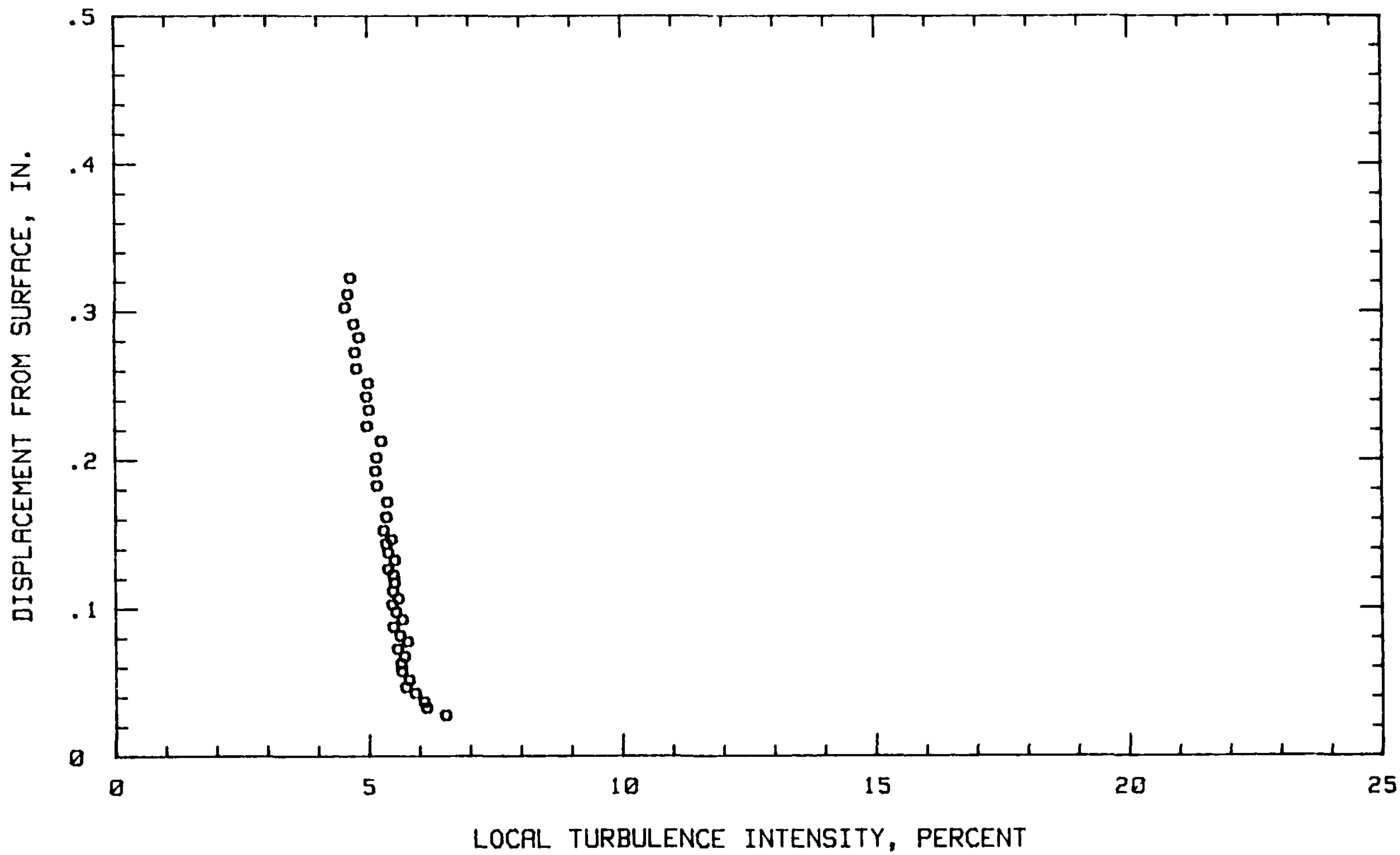

Fig. 140. Boundary Layer Turbulence Intensity Profile, i = 0 Deg, 29.68 % Chord

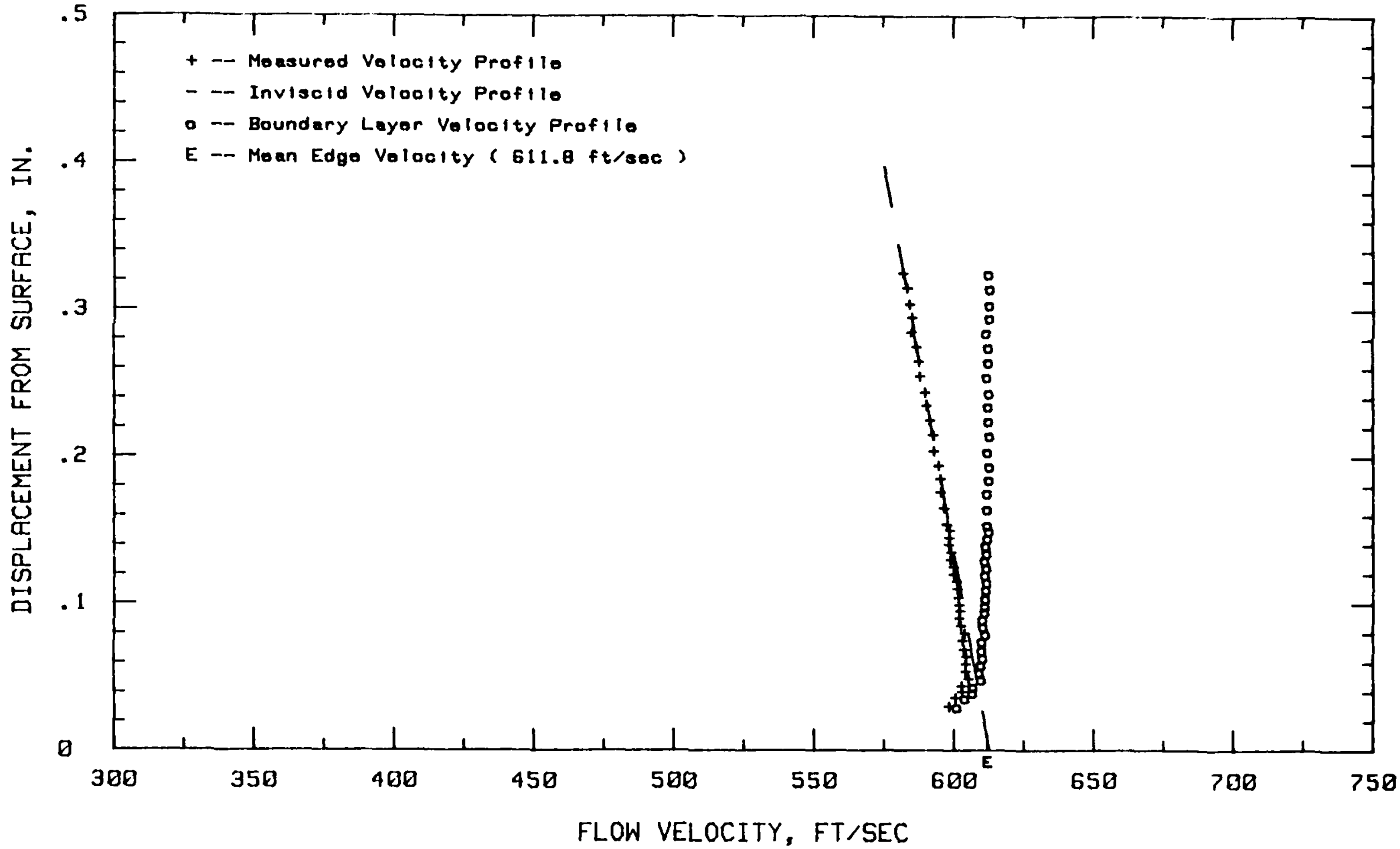

Fig. 141. Boundary Layer Velocity Profiles, i = 0 Deg, 34.37 % Chord

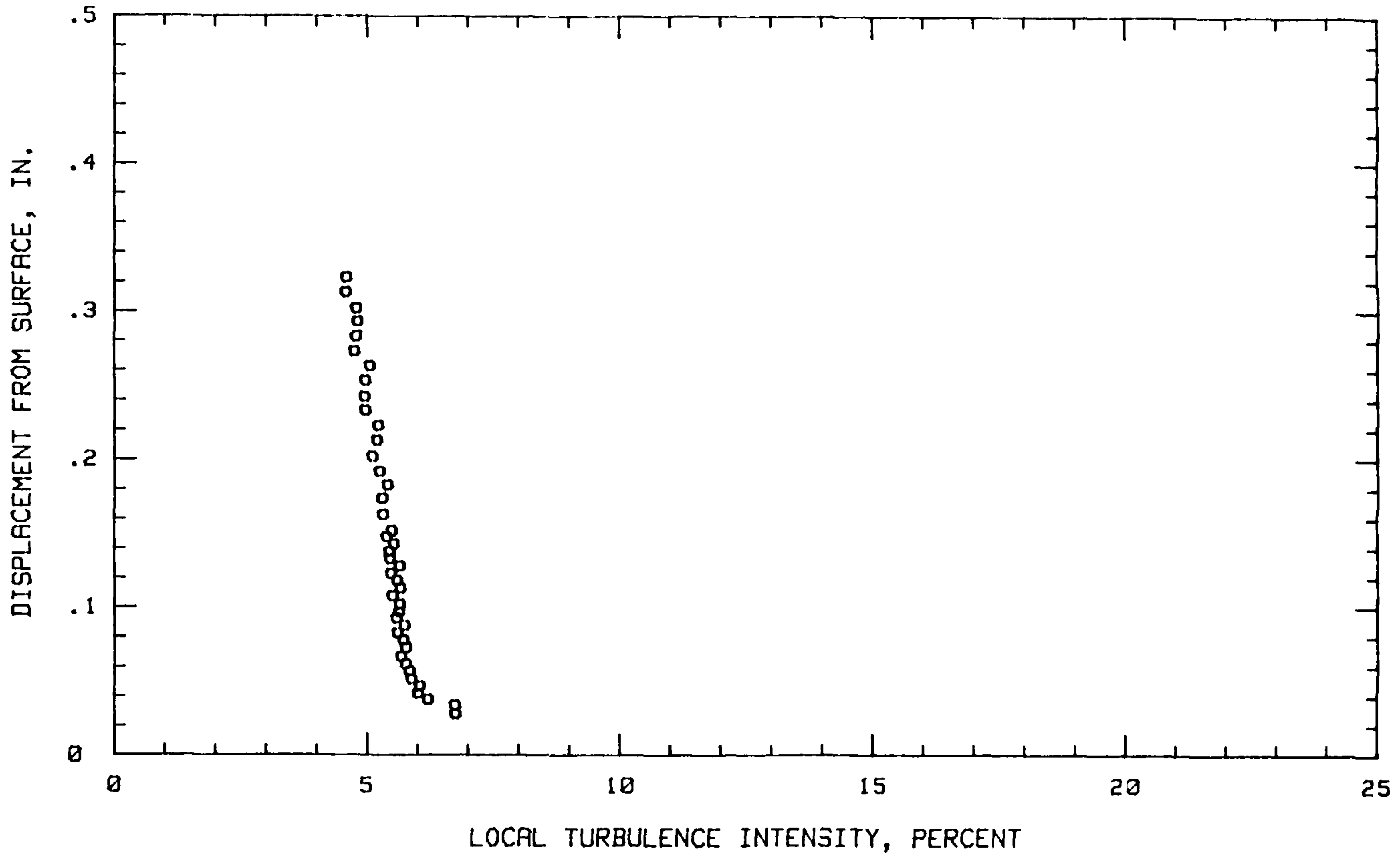

Fig. 142. Boundary Layer Turbulence Intensity Profile, i = 0 Deg, 34.37 % Chord

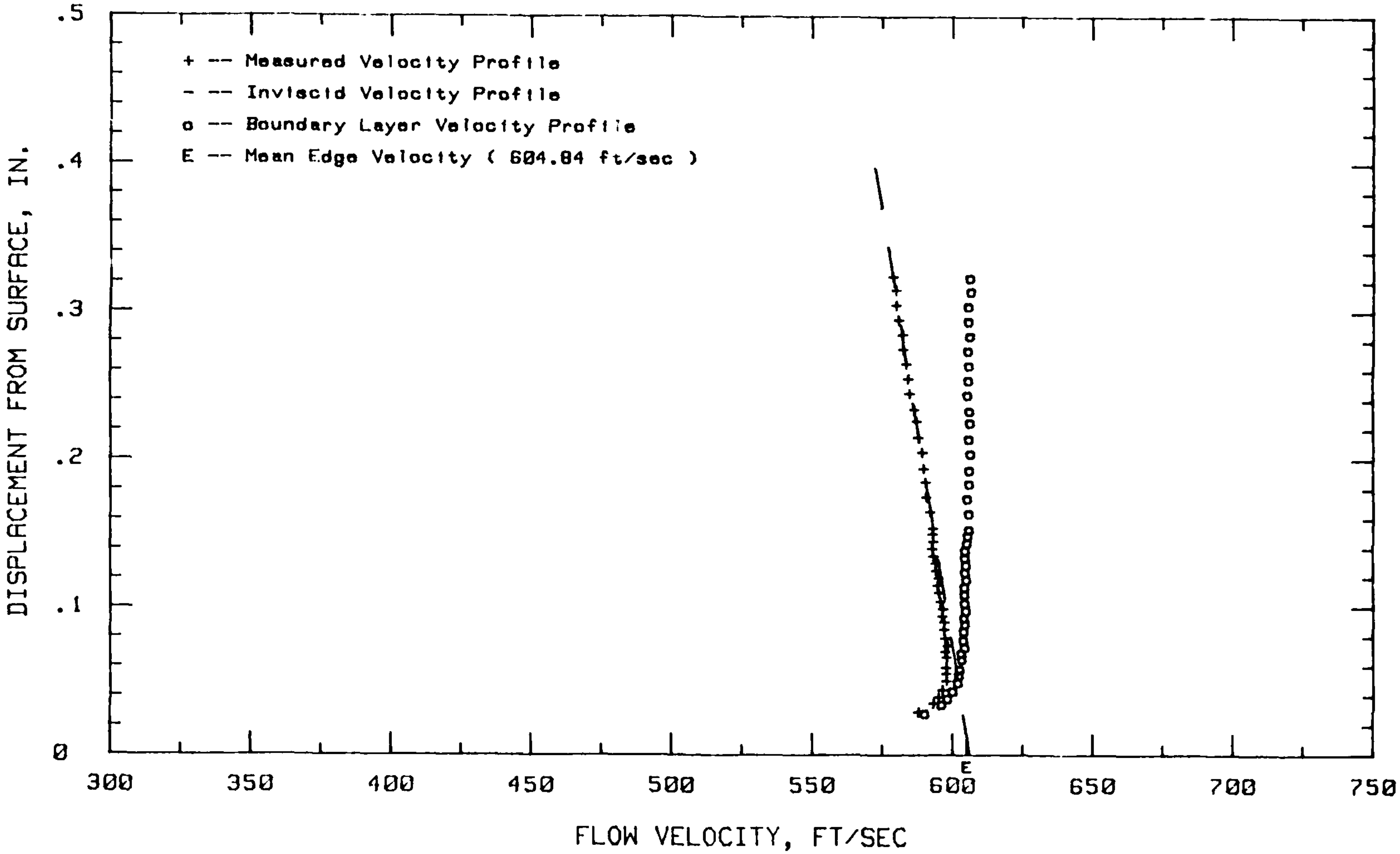

Fig. 143. Boundary Layer Velocity Profiles, i = 0 Deg, 40.62 % Chord

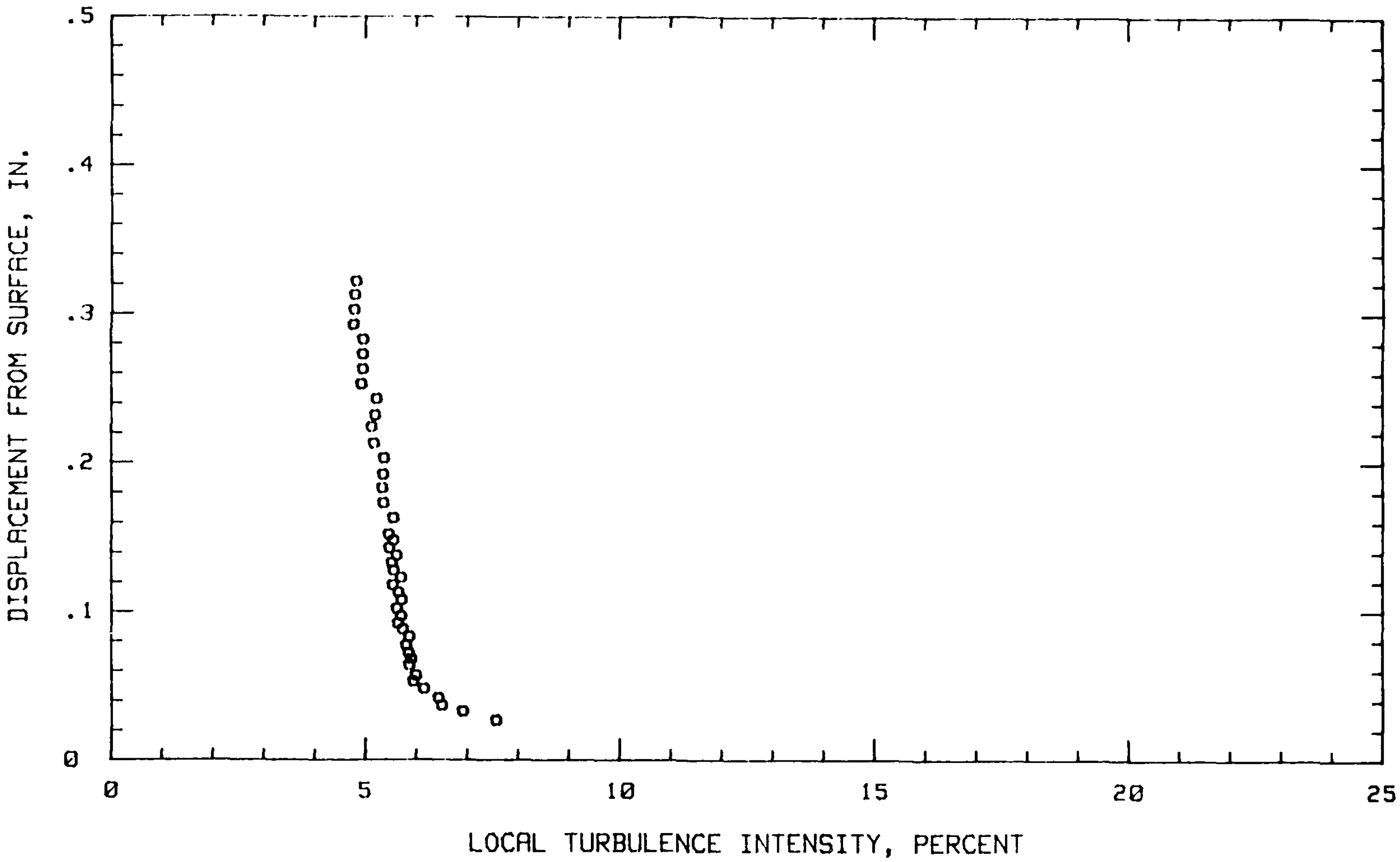

Fig. 144. Boundary Layer Turbulence Intensity Profile, i = 0 Deg, 40.62 % Chord

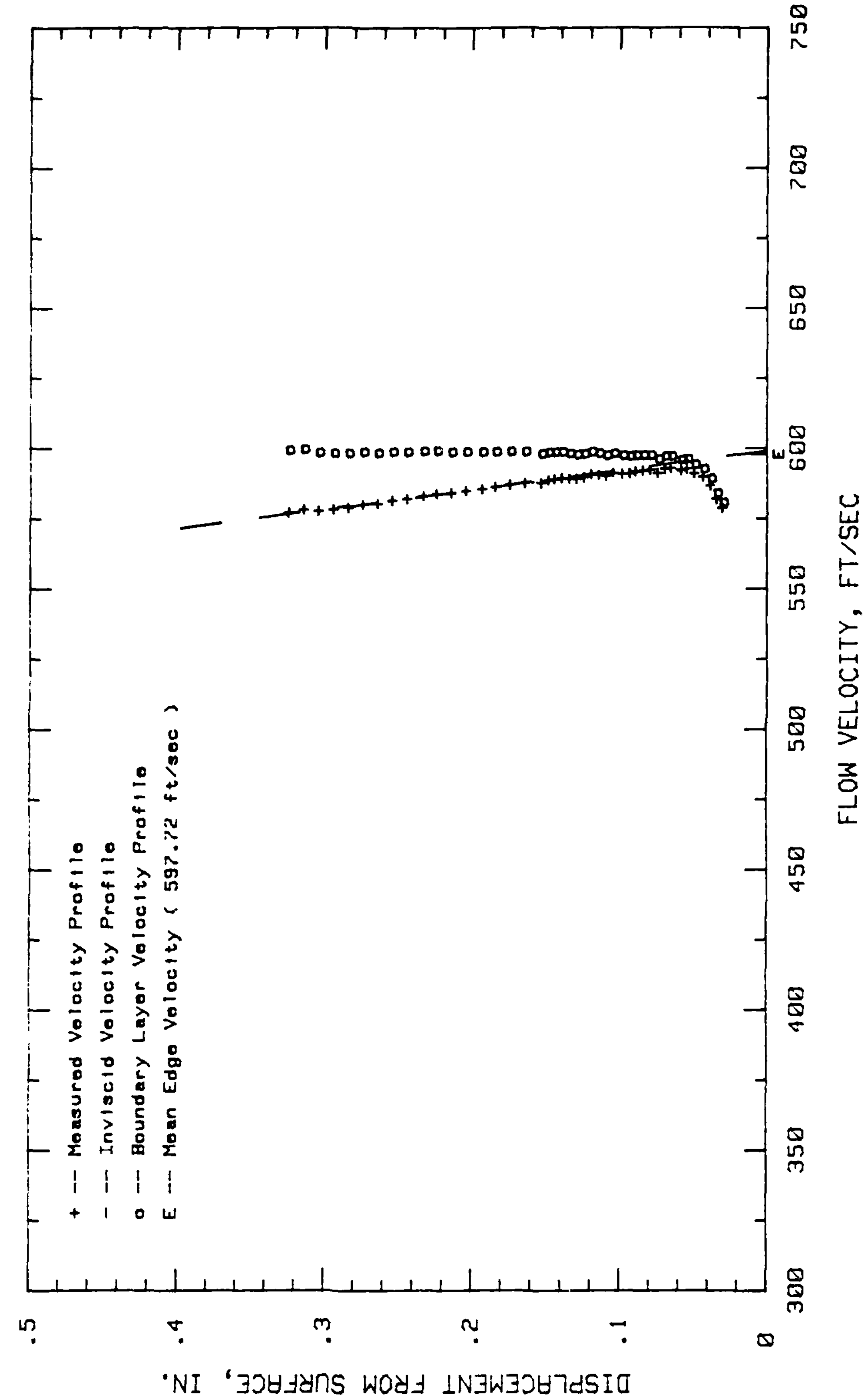

Fig. 145. Boundary Layer Velocity Profiles, i = 0 Deg, 45.31 % Chord

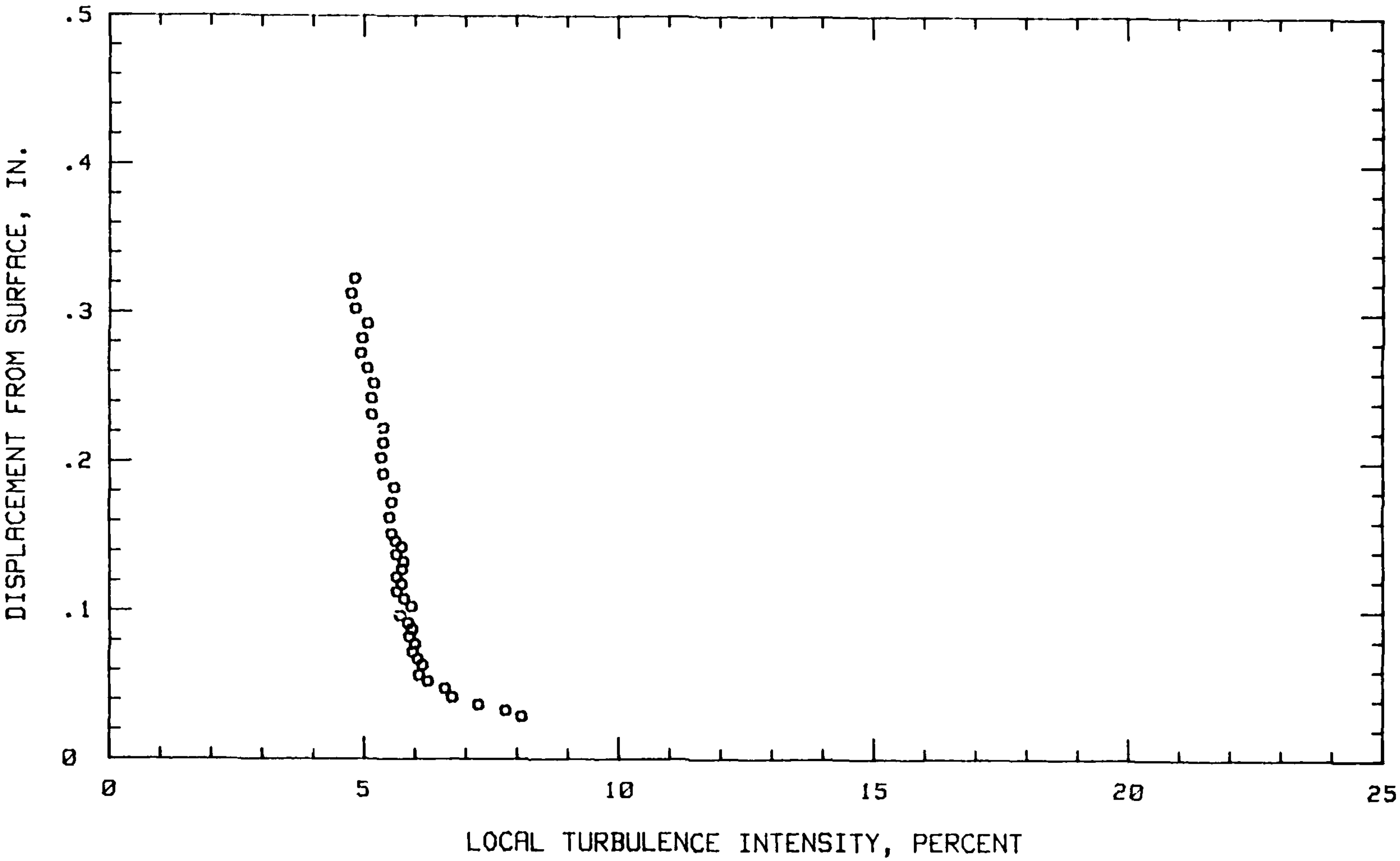

Fig. 146. Boundary Layer Turbulence Intensity Profile, i = 0 Deg, 45.31 % Chord

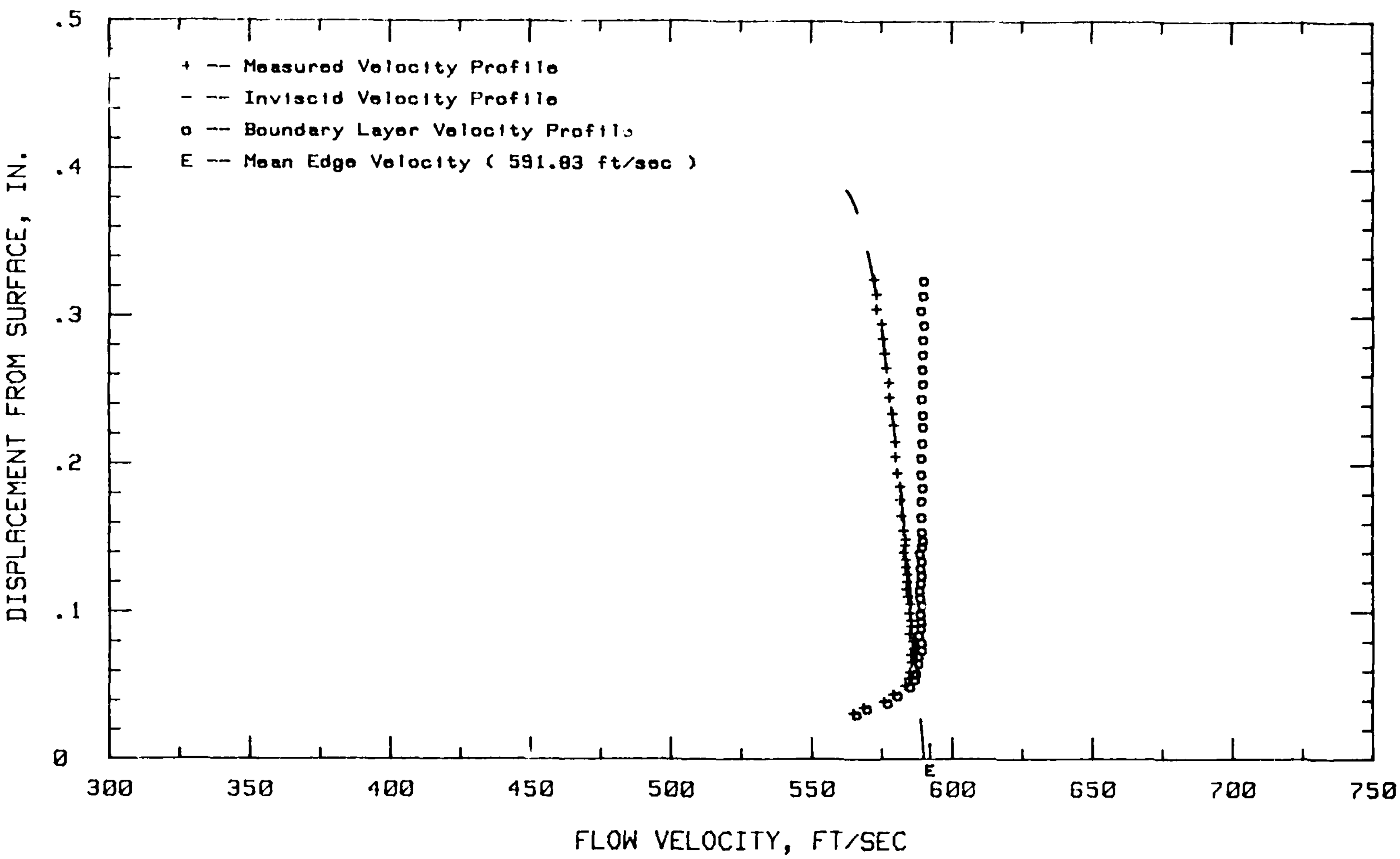

Fig. 147. Boundary Layer Velocity Profiles, i = 0 Deg, 50 % Chord

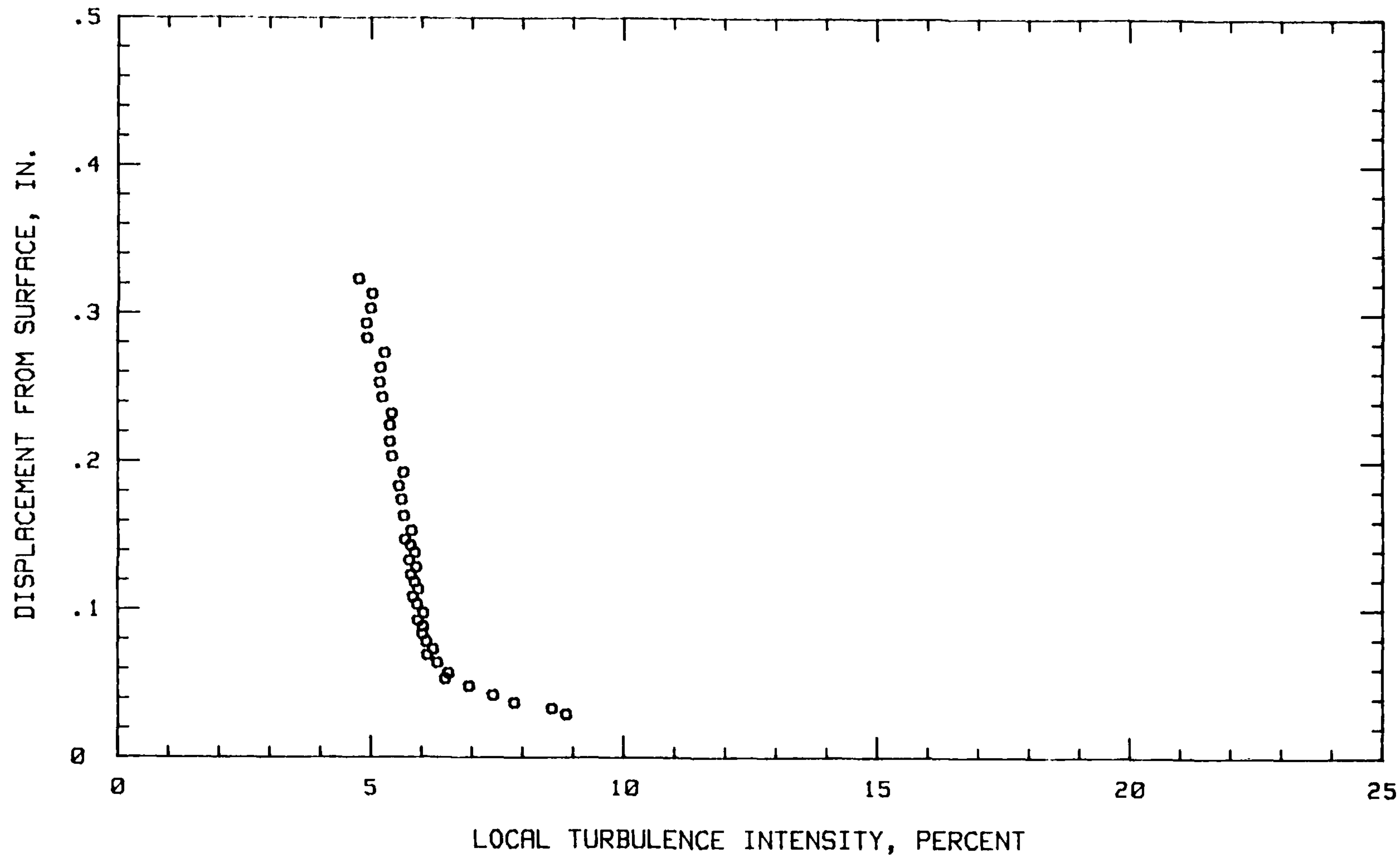

Fig. 148. Boundary Layer Turbulence Intensity Profile, i = 0 Deg, 50 % Chord

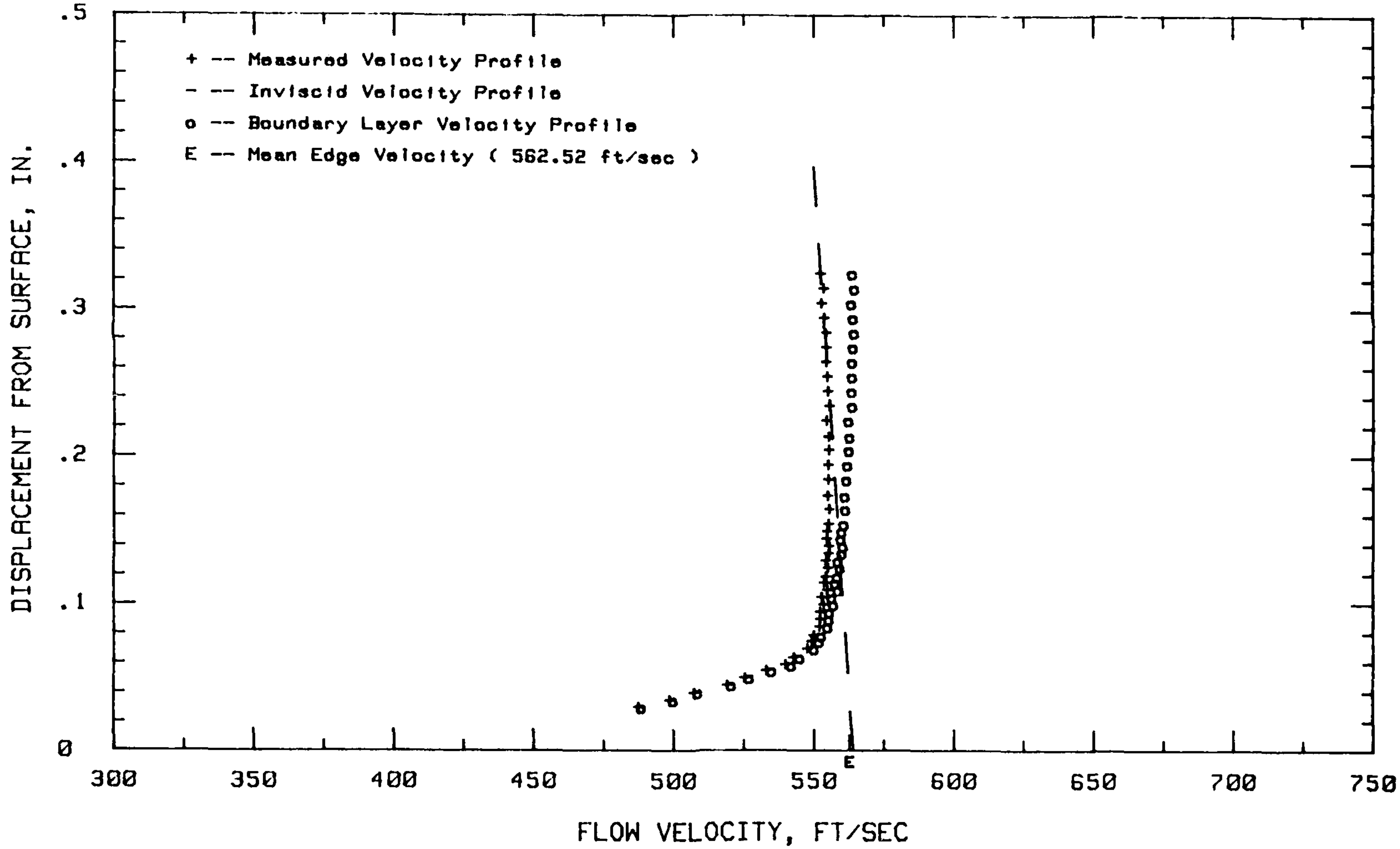

Fig. 149. Boundary Layer Velocity Profiles, i = 0 Deg, 65.62 % Chord

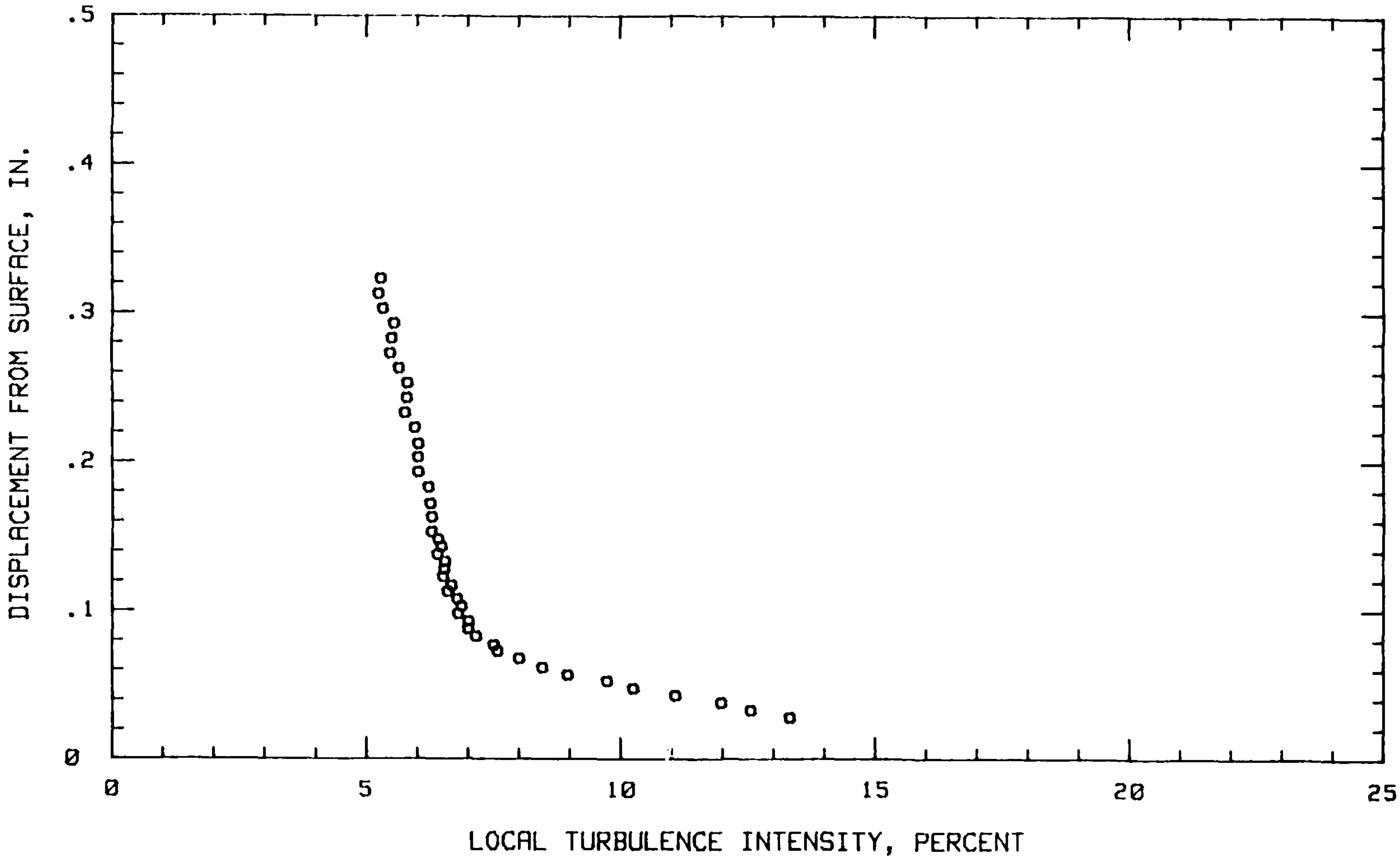

Fig. 150. Boundary Layer Turbulence Intensity Profile, i = 0 Deg, 65.62 % Chord

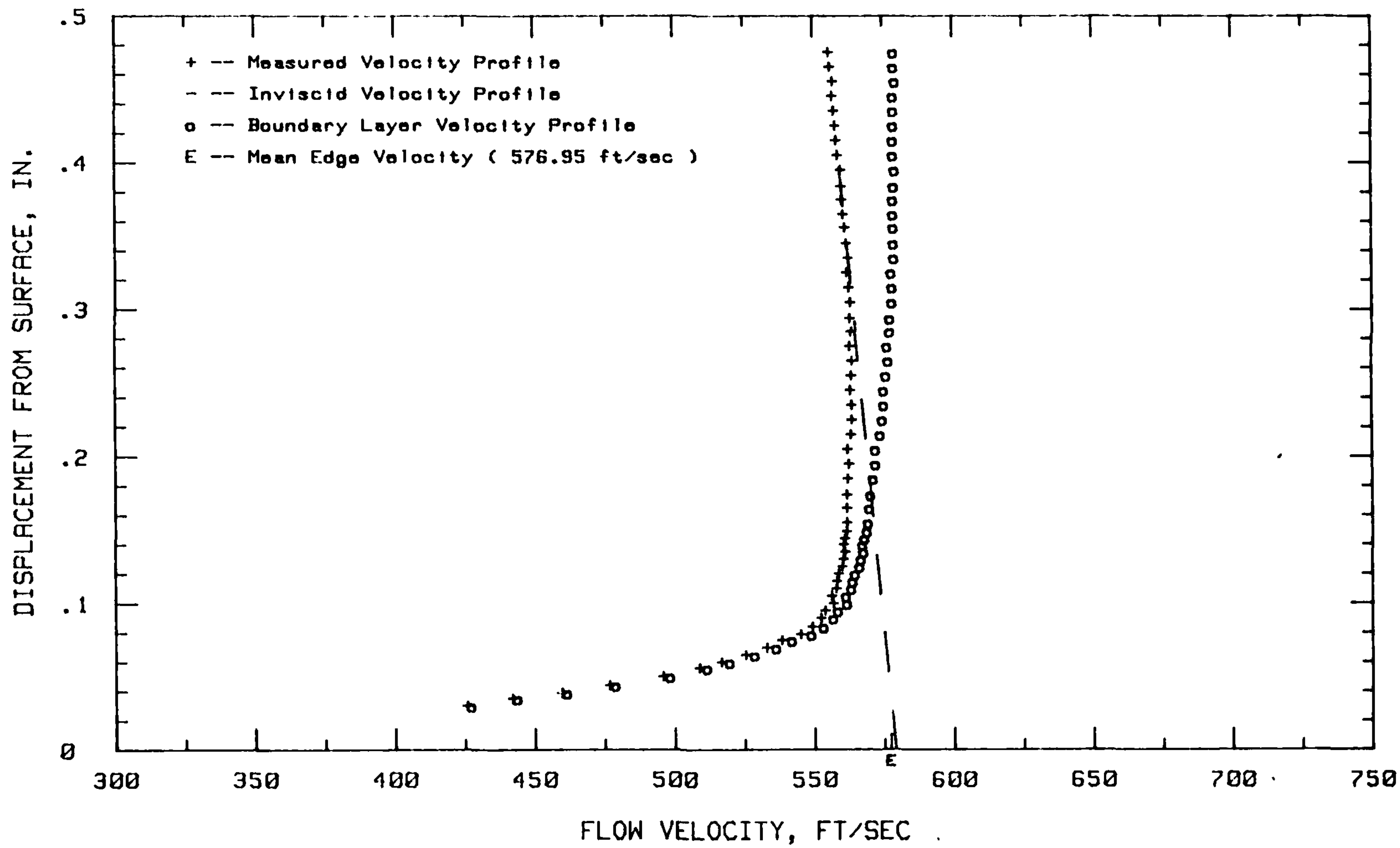

Fig. 151. Boundary Layer Velocity Profiles, i = 0 Deg, 70.31 % Chord

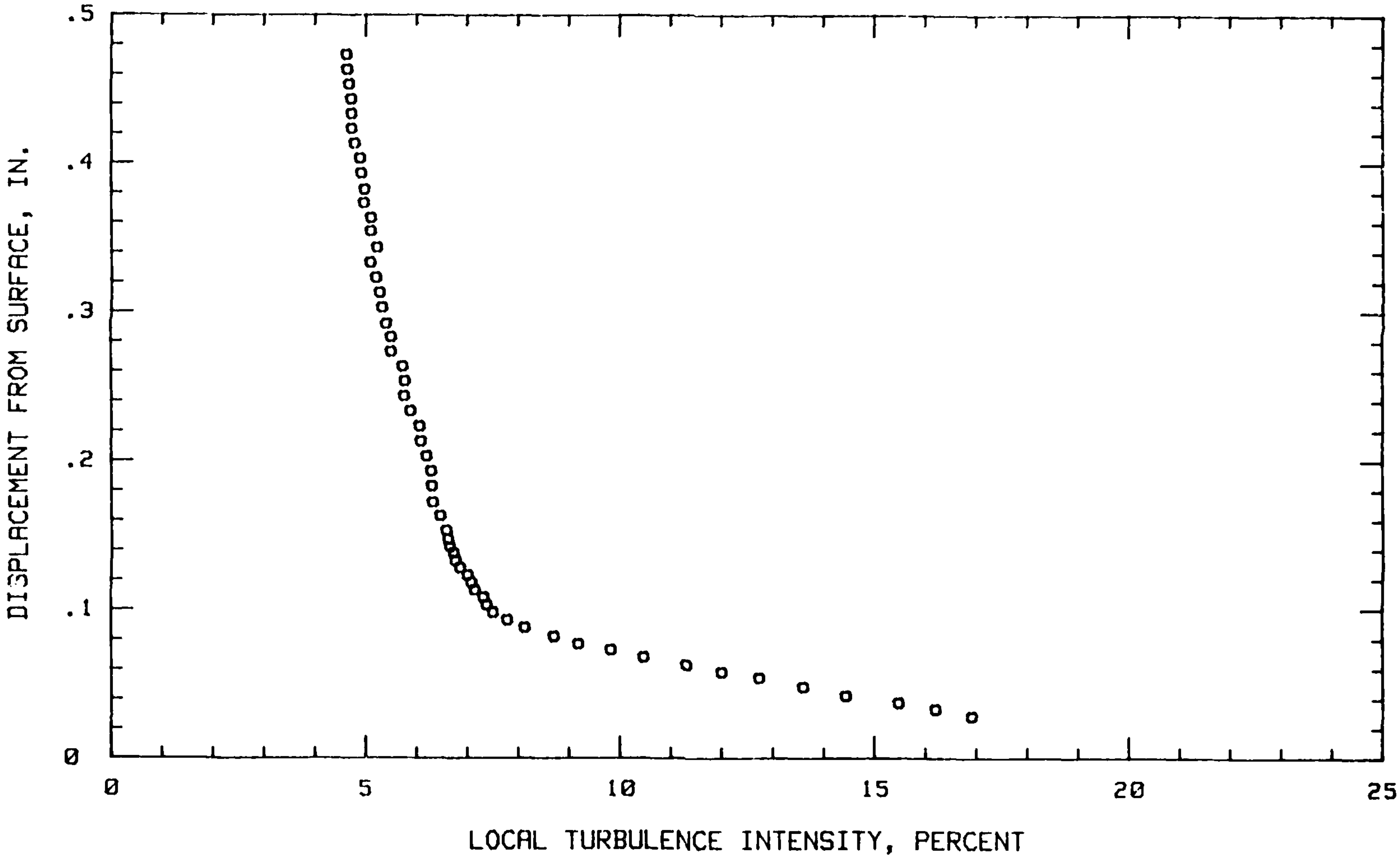

Fig. 152. Boundary Layer Turbulence Intensity Profile, i = 0 Deg, 70.31 % Chord

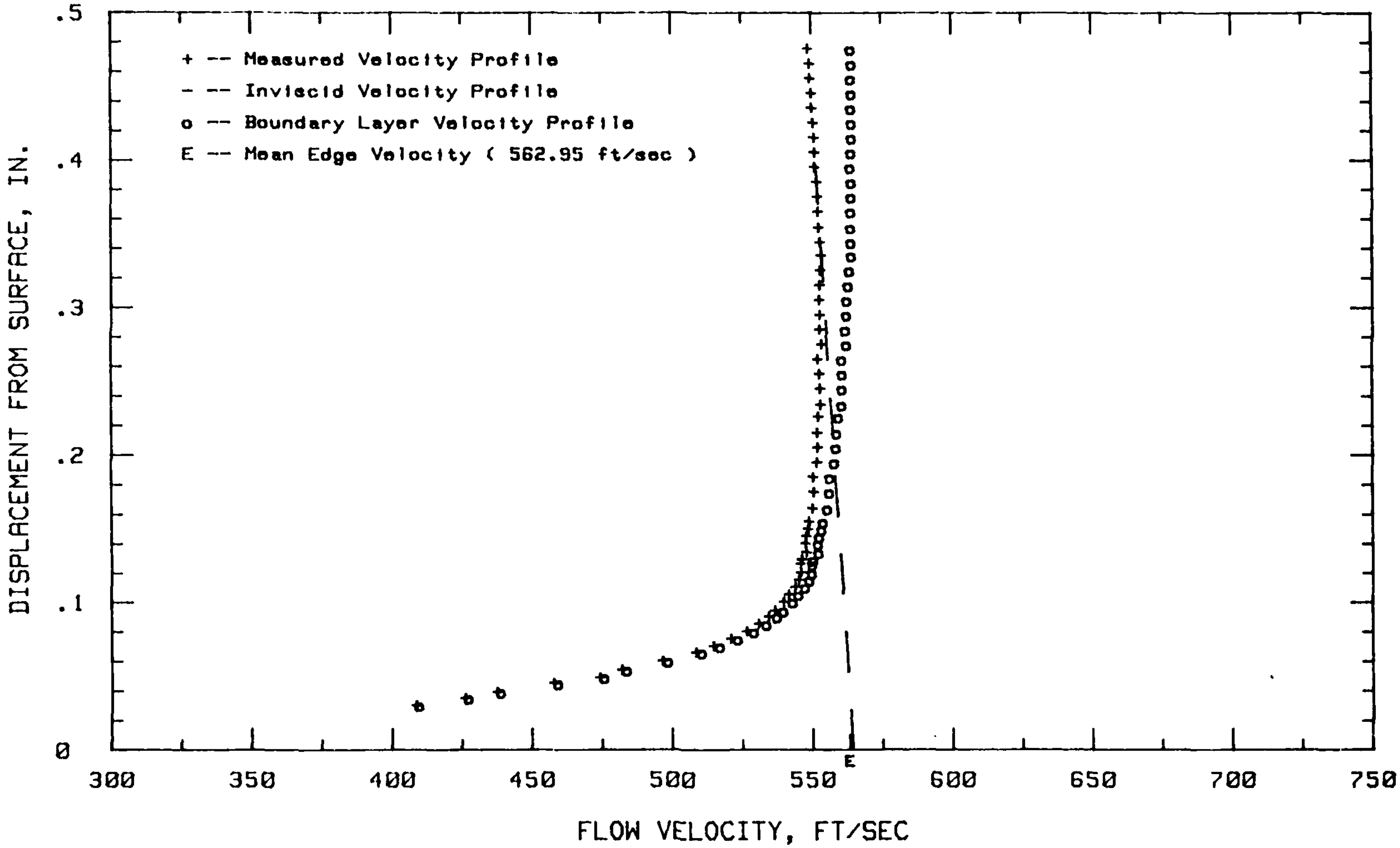

Fig. 153. Boundary Layer Velocity Profiles, i = 0 Deg, 75 % Chord

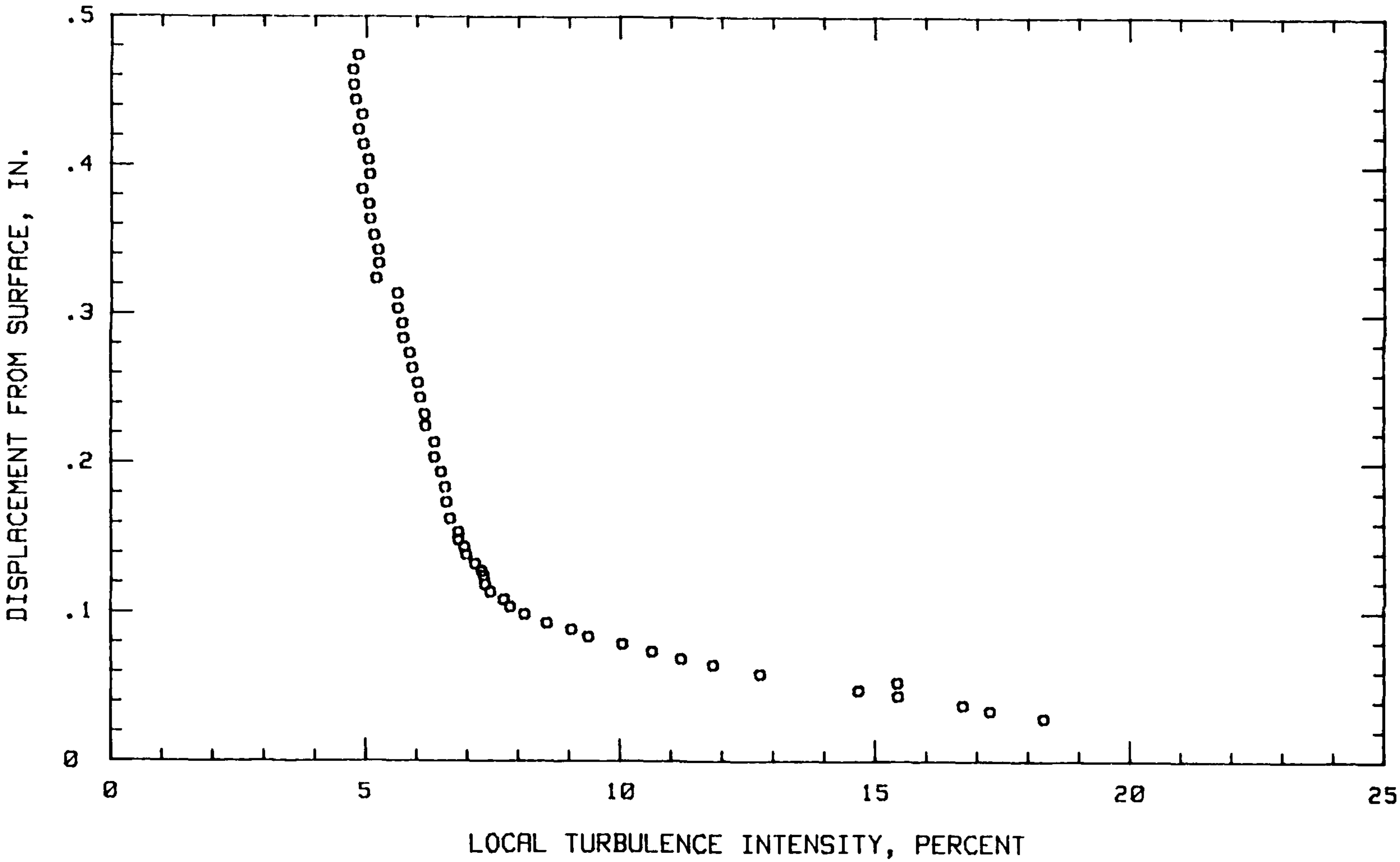

Fig. 154. Boundary Layer Turbulence Intensity Profile, i = 0 Deg, 75 % Chord

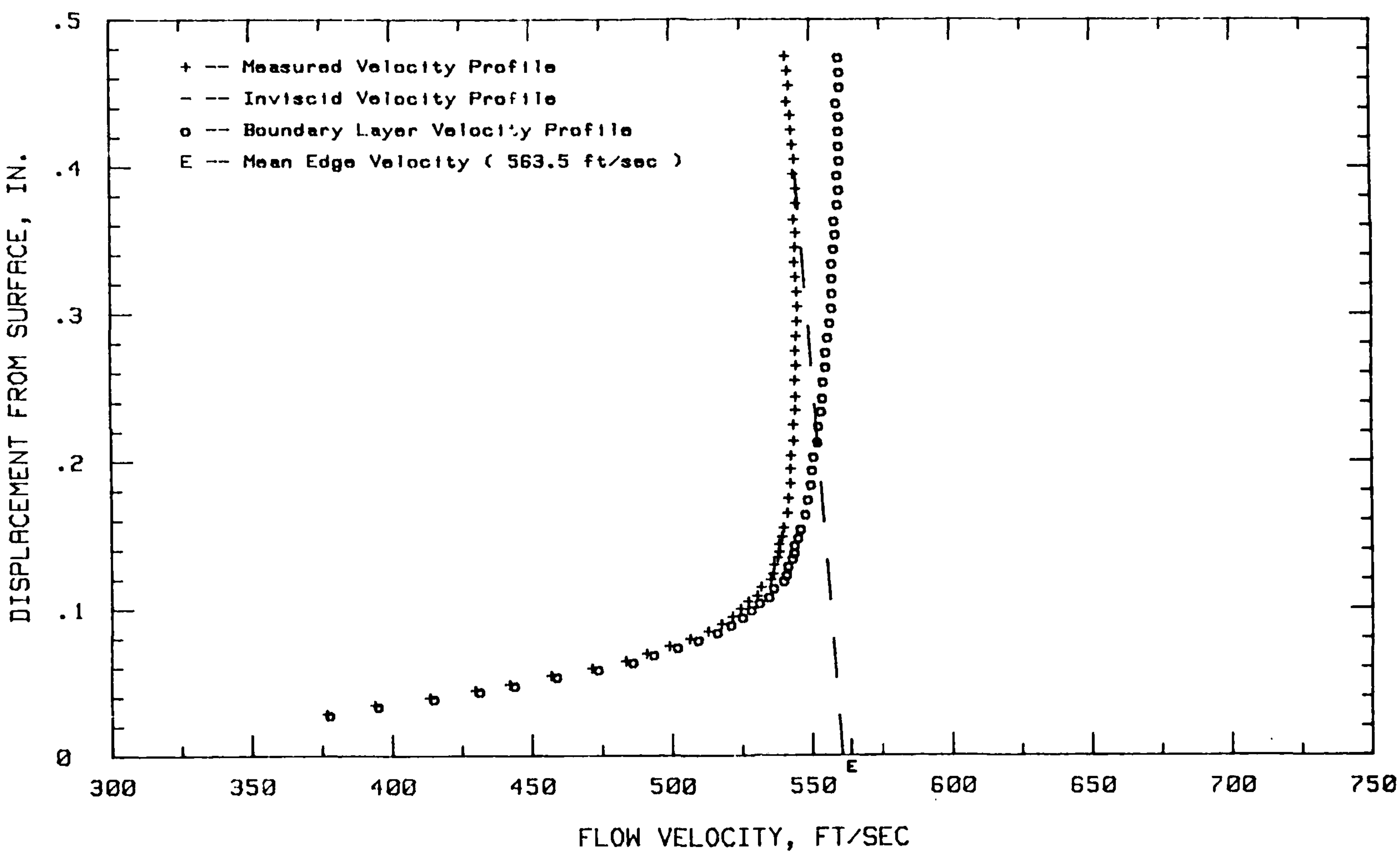

Fig. 155. Boundary Layer Velocity Profiles, i = 0 Deg, 79.68 % Chord

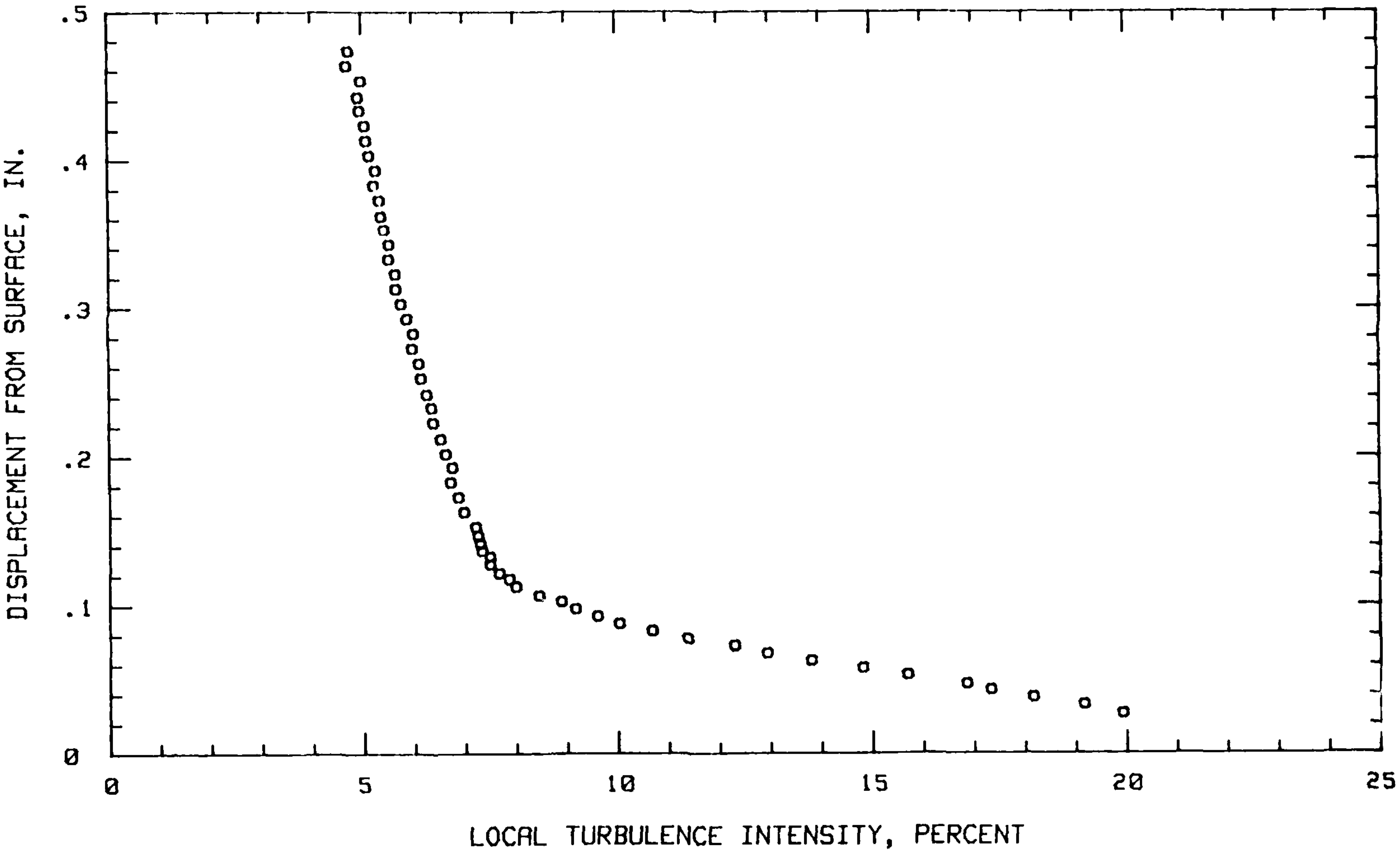

Fig. 156. Boundary Layer Turbulence Intensity Profile, i = 0 Deg, 79.68 % Chord

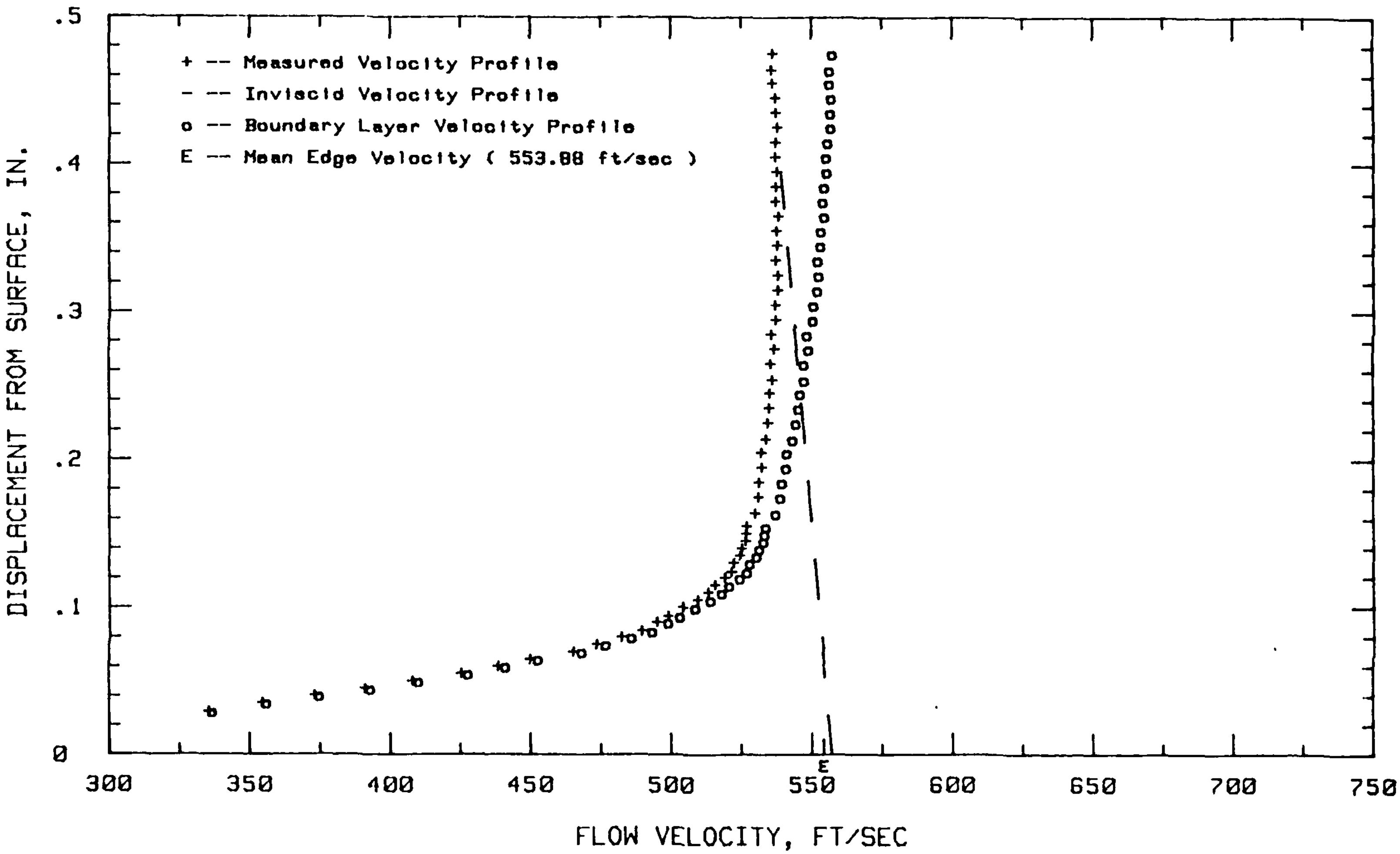

Fig. 157. Boundary Layer Velocity Profiles, i = 0 Deg, 84.37 % Chord

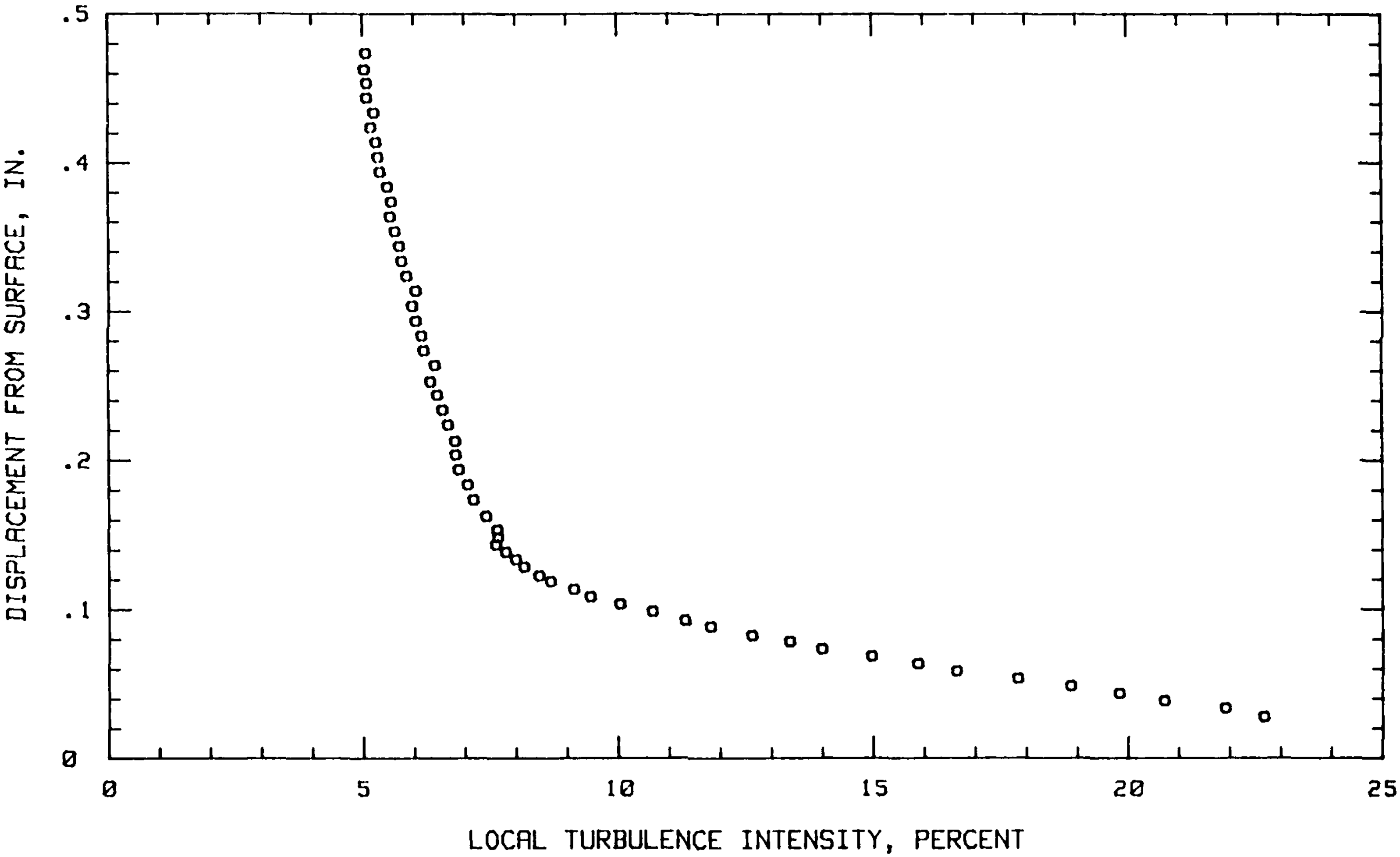

Fig. 158. Boundary Layer Turbulence Intensity Profile, i = 0 Deg, 84.37 % Chord

Appendix M

Boundary Layer Velocity and Turbulence Intensity Profiles

Blade Configuration Number 2

Incidence Angle = +3.0 Degrees

Low Free Stream Turbulence

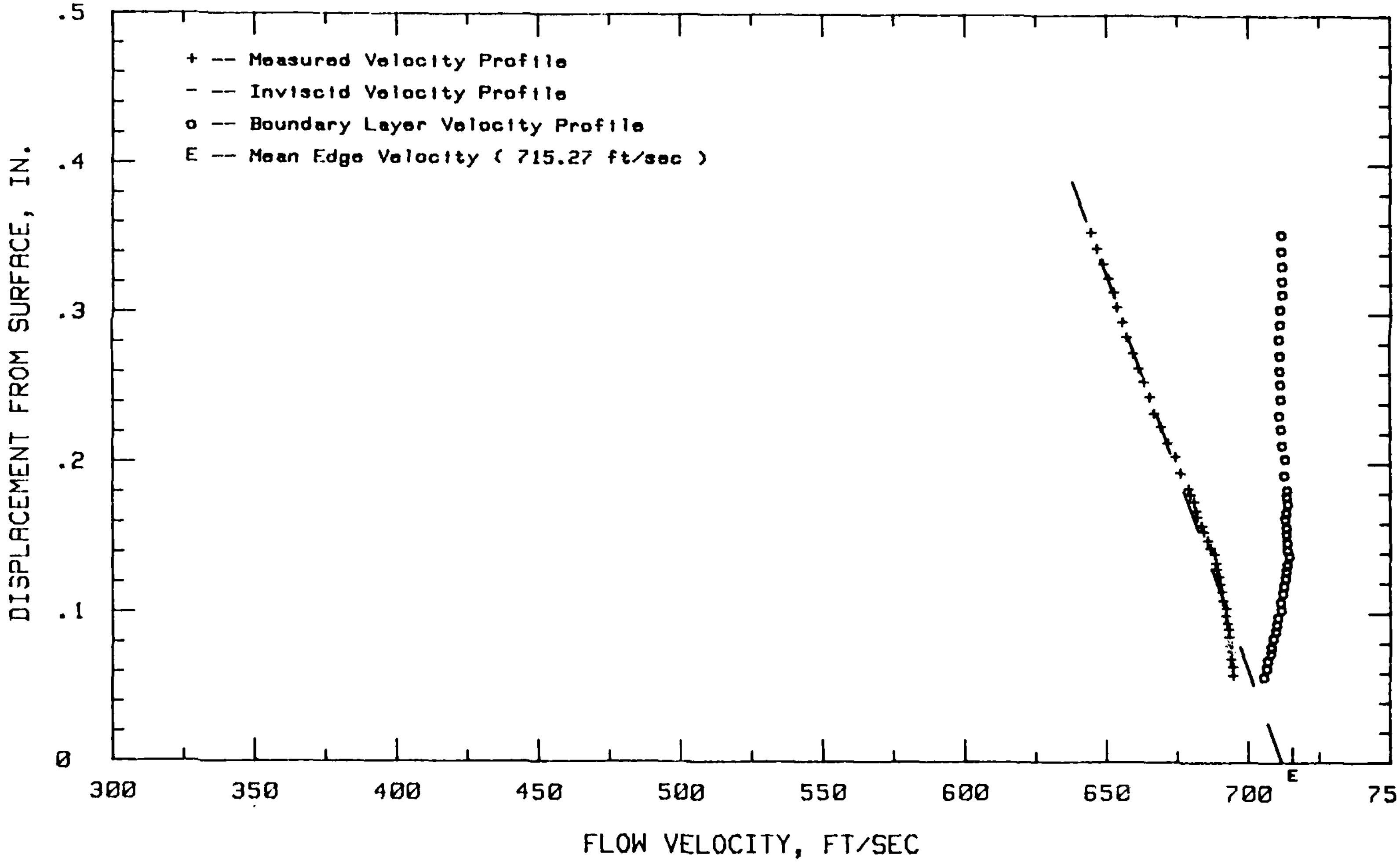

Fig. 159. Boundary Layer Velocity Profiles, i = +3 Deg, 4.68 % Chord

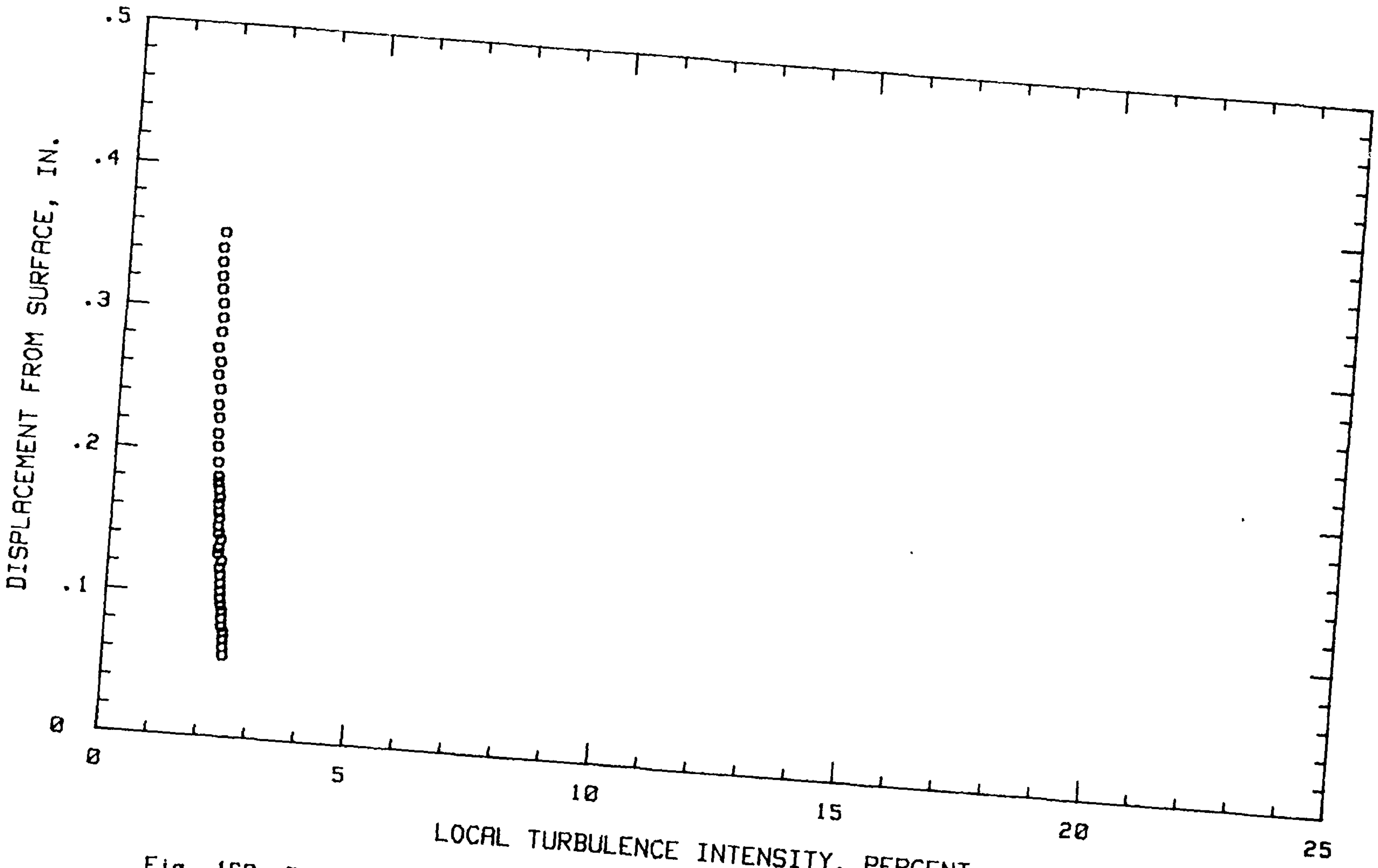

Fig. 160. Boundary Layer Turbulence Intensity Profile, i = +3 Deg, 4.68 % Chord

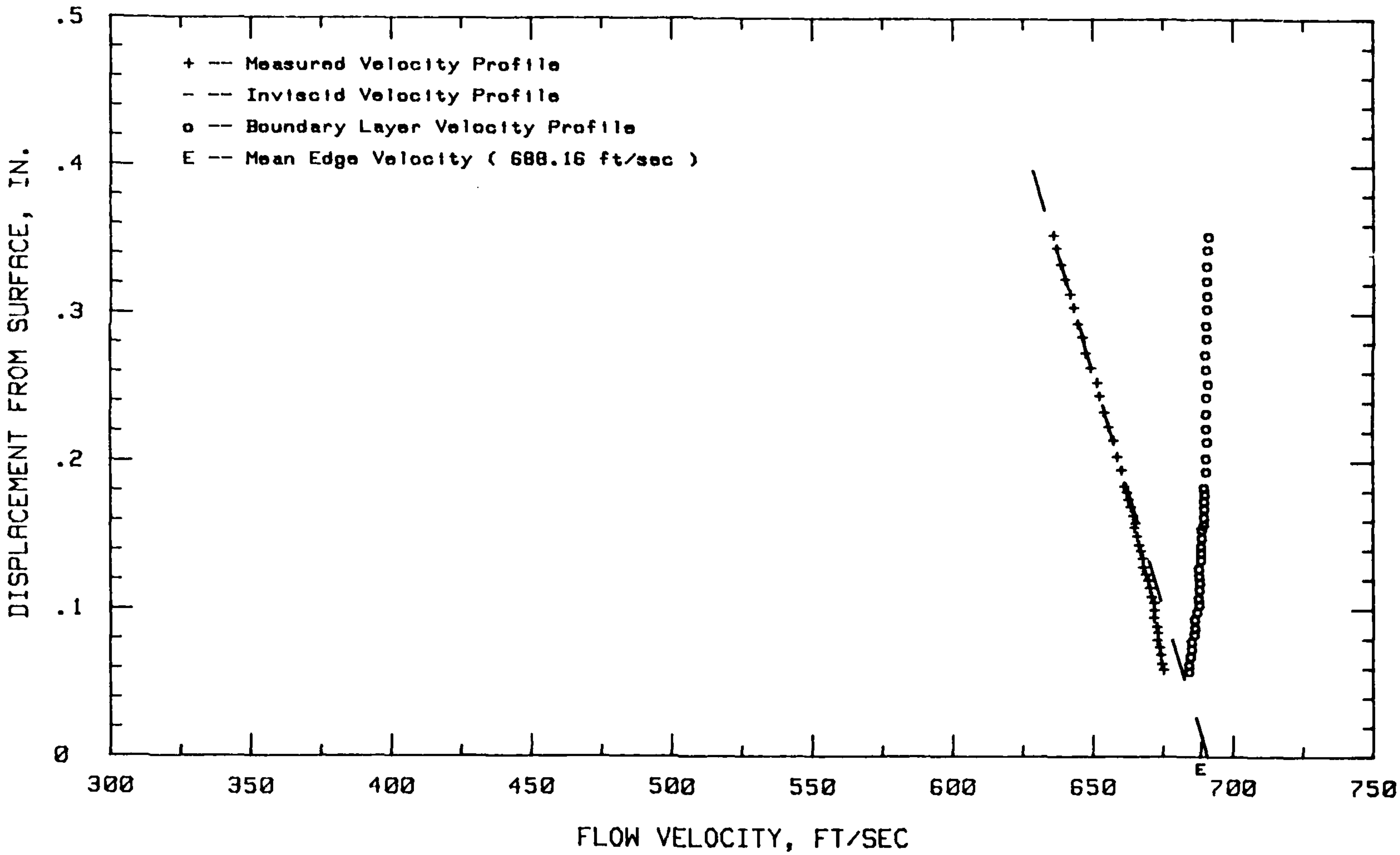

Fig. 161. Boundary Layer Velocity Profiles, i = +3 Deg, 9.37 % Chord

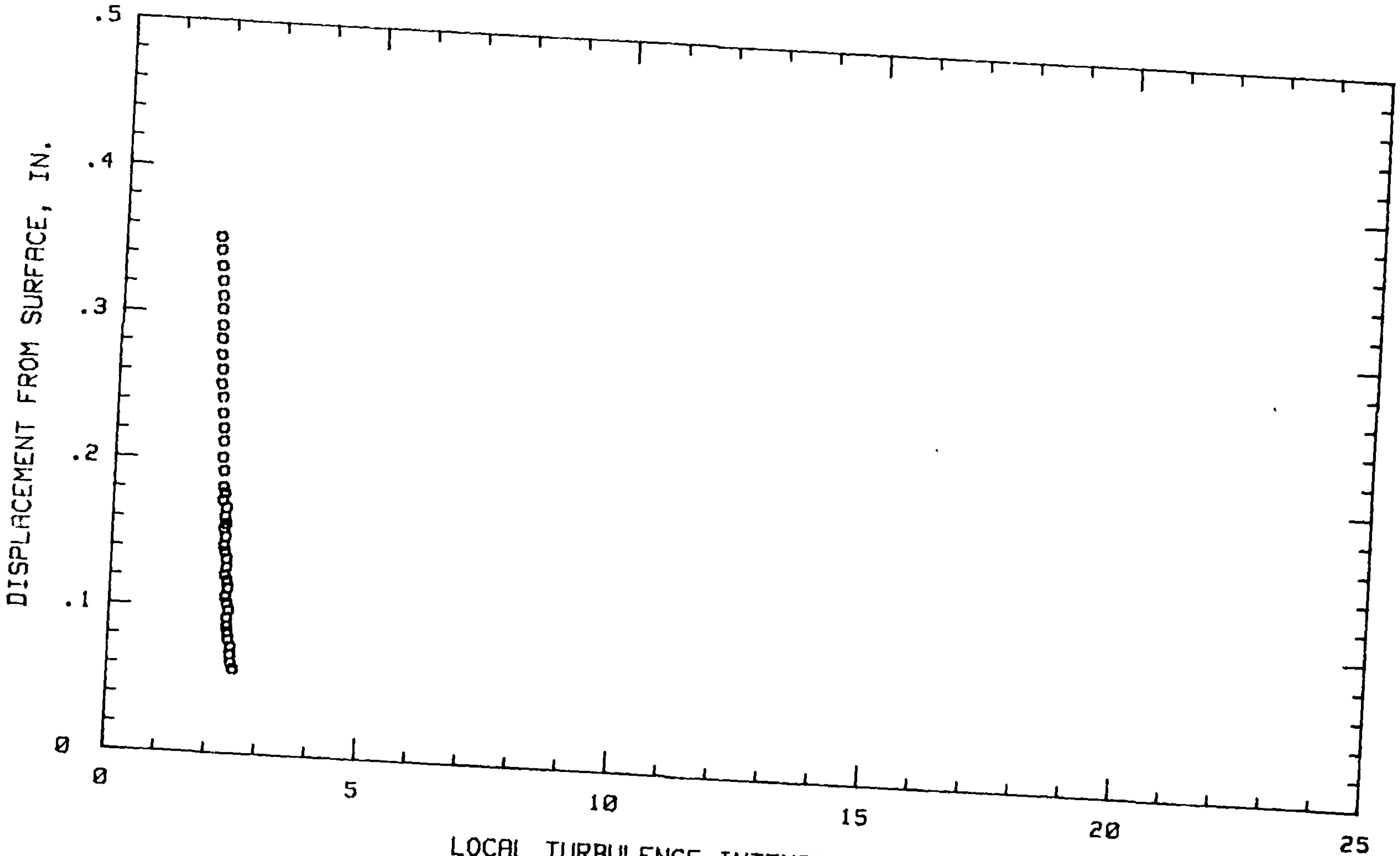

Fig. 162. Boundary Layer Turbulence Intensity Profile, i = +3 Deg, 9.37 % Chord

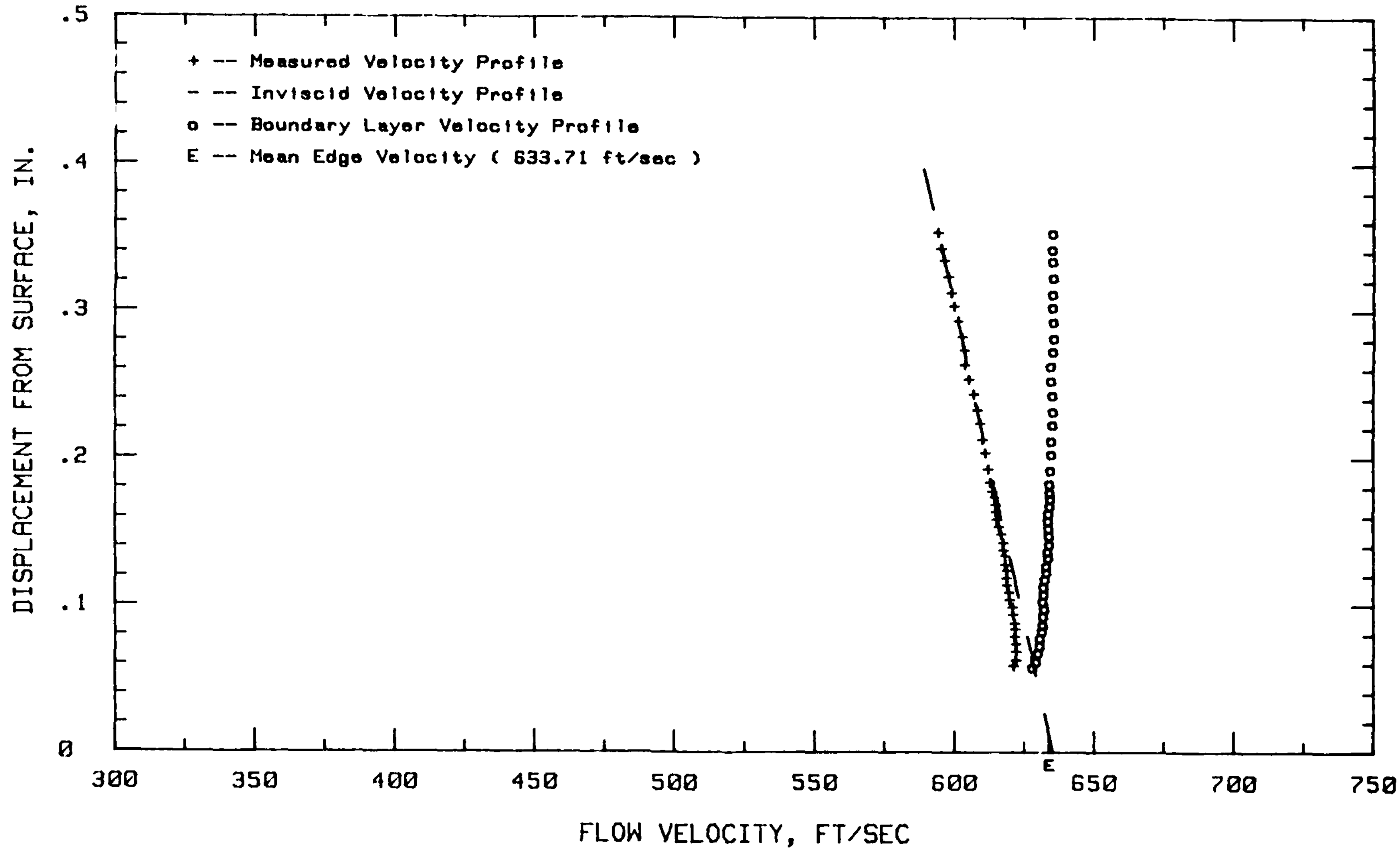

Fig. 163. Boundary Layer Velocity Profiles, i = +3 Deg, 16.51 % Chord

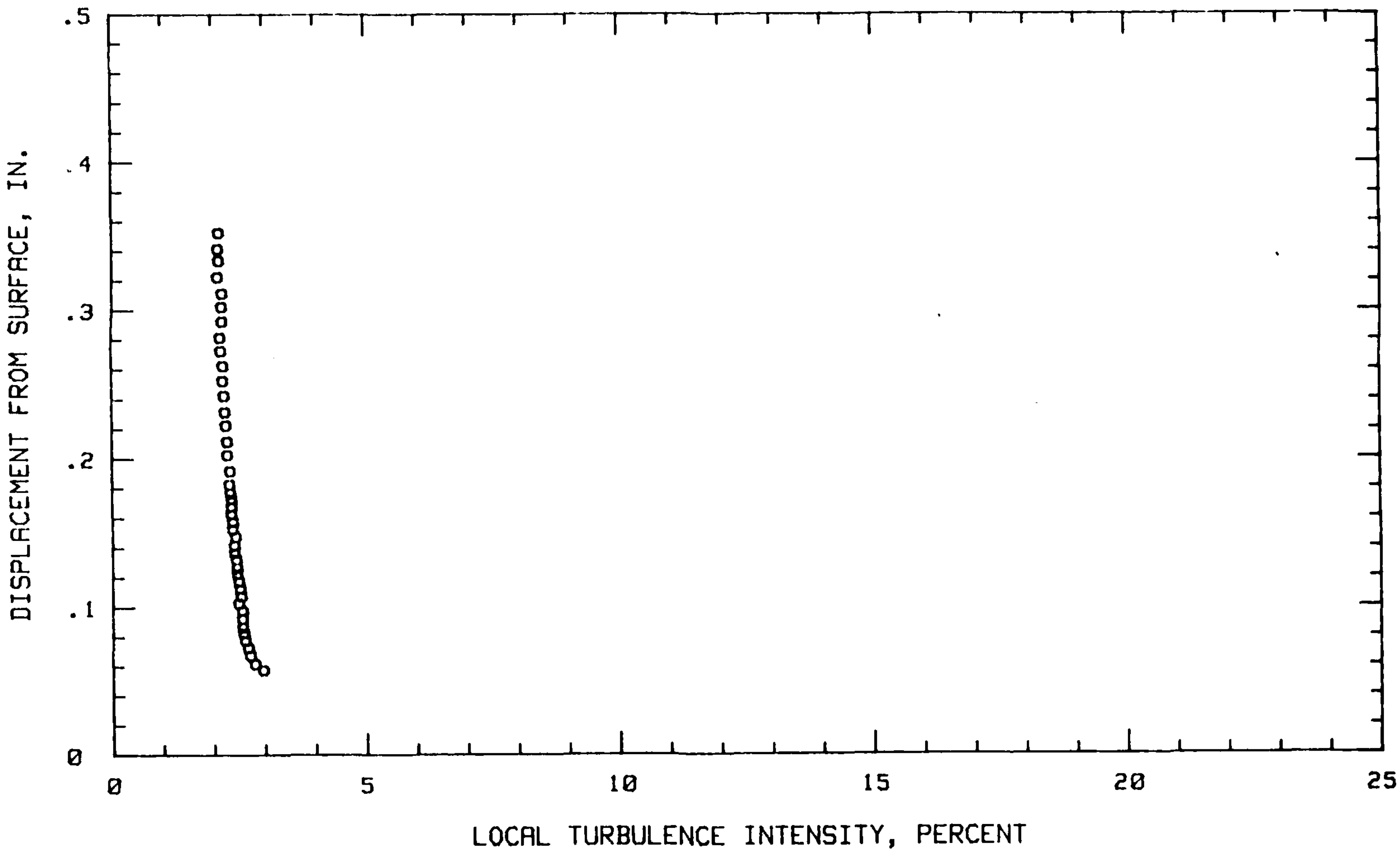

Fig. 164. Boundary Layer Turbulence Intensity Profile, i = +3 Deg, 16.51 % Chord

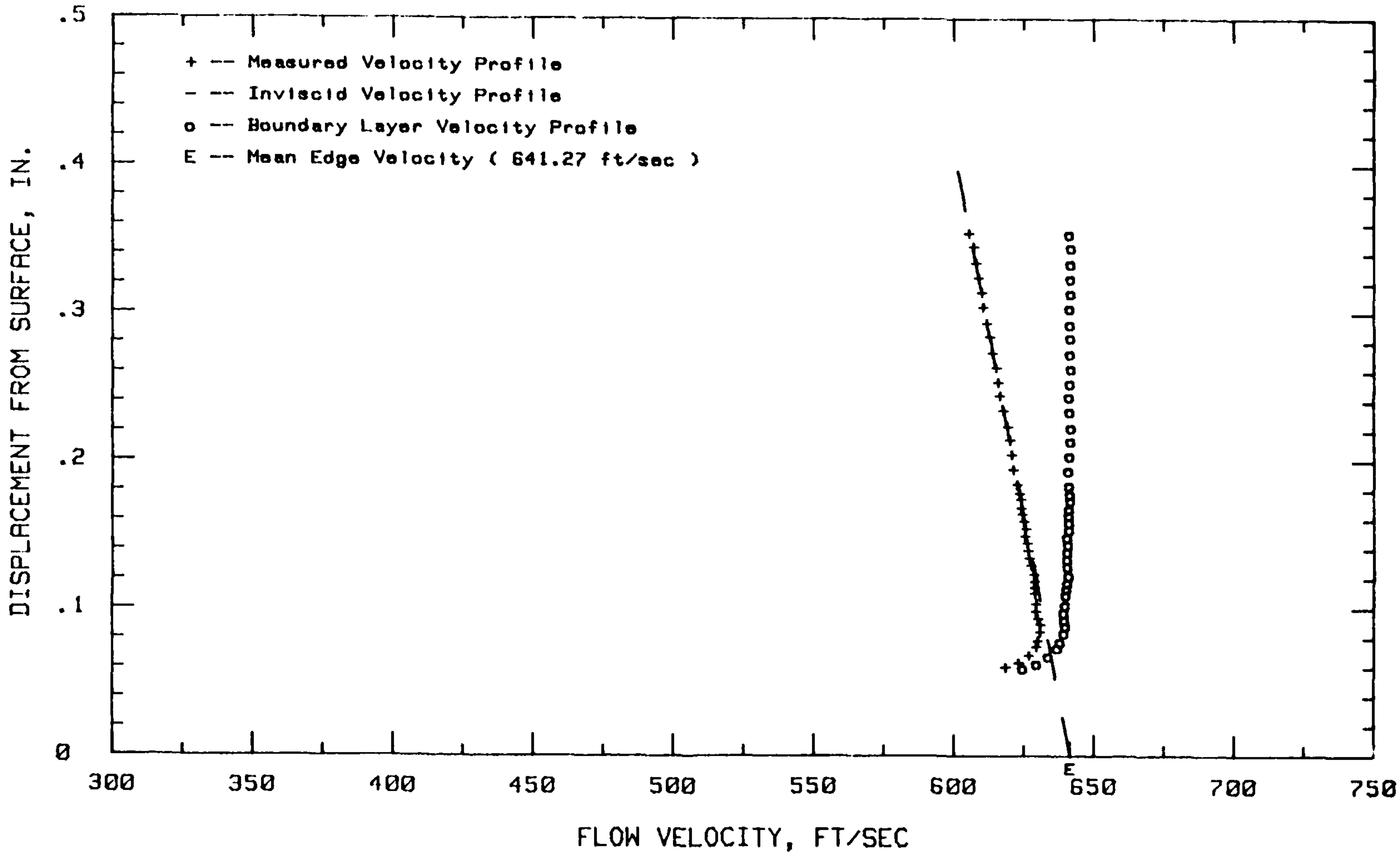

Fig. 165. Boundary Layer Velocity Profiles, i = +3 Deg, 25 % Chord

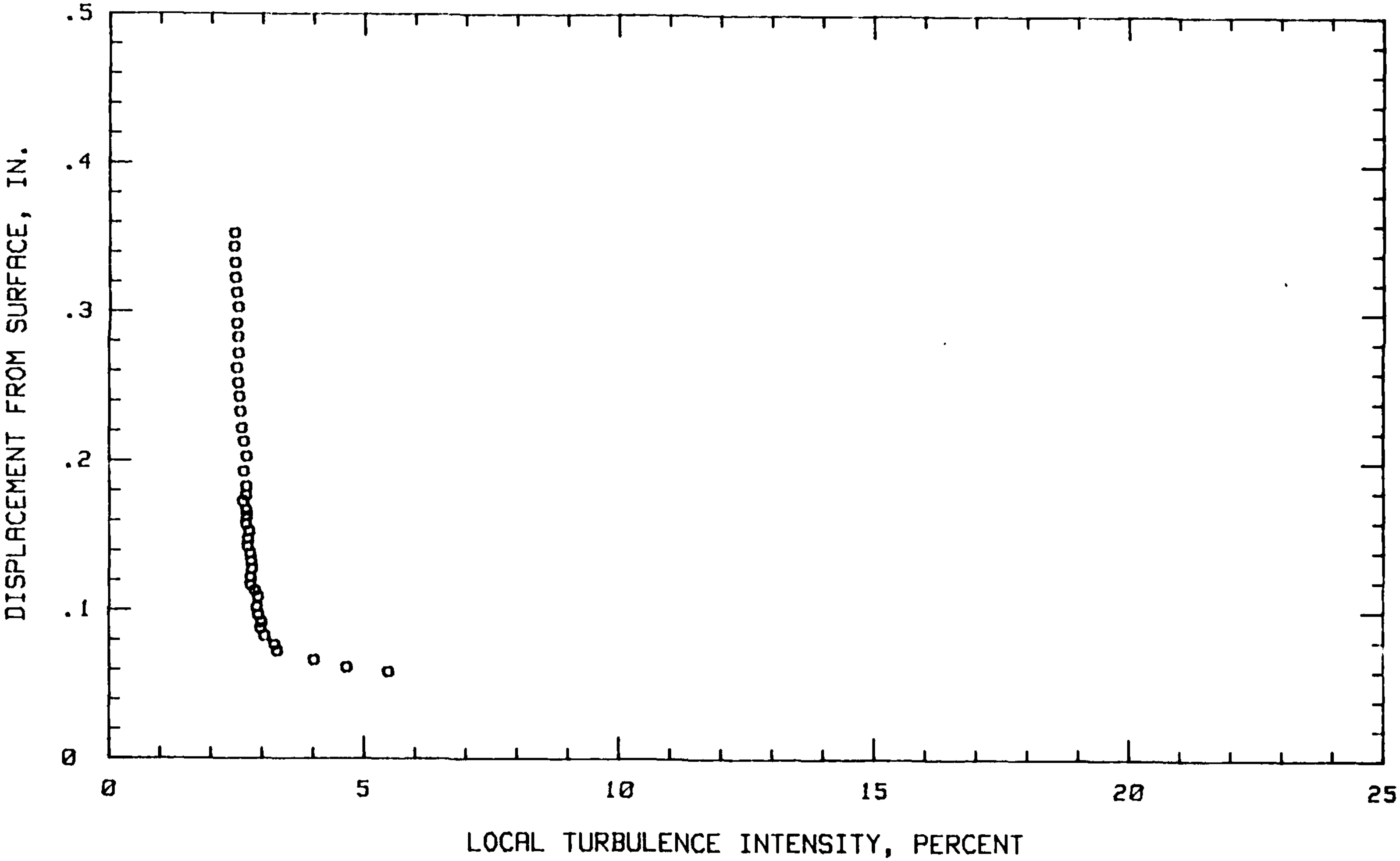

Fig. 166. Boundary Layer Turbulence Intensity Profile, i = +3 Deg, 25 % Chord

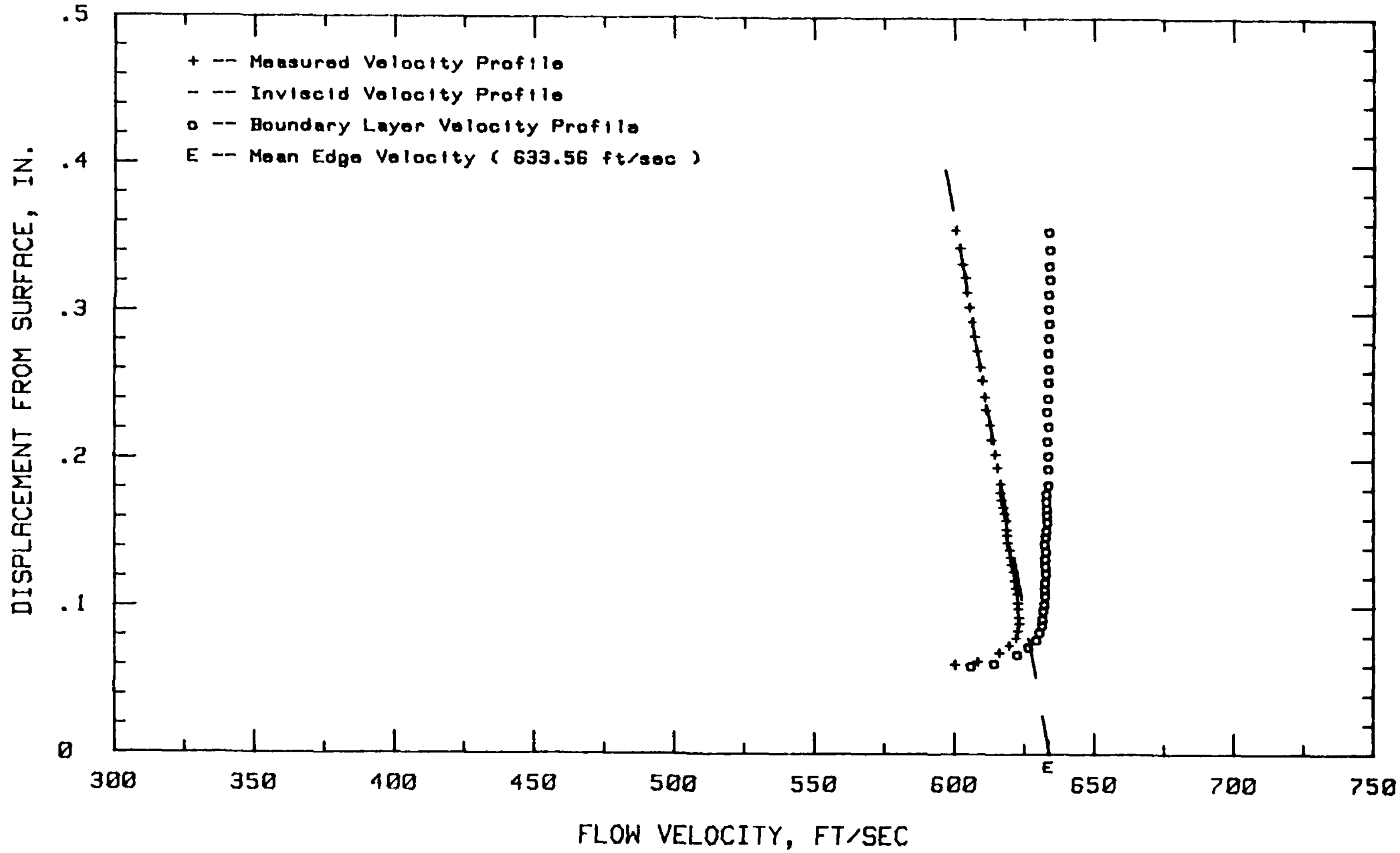

Fig. 167. Boundary Layer Velocity Profiles, i = +3 Deg, 29.68 % Chord

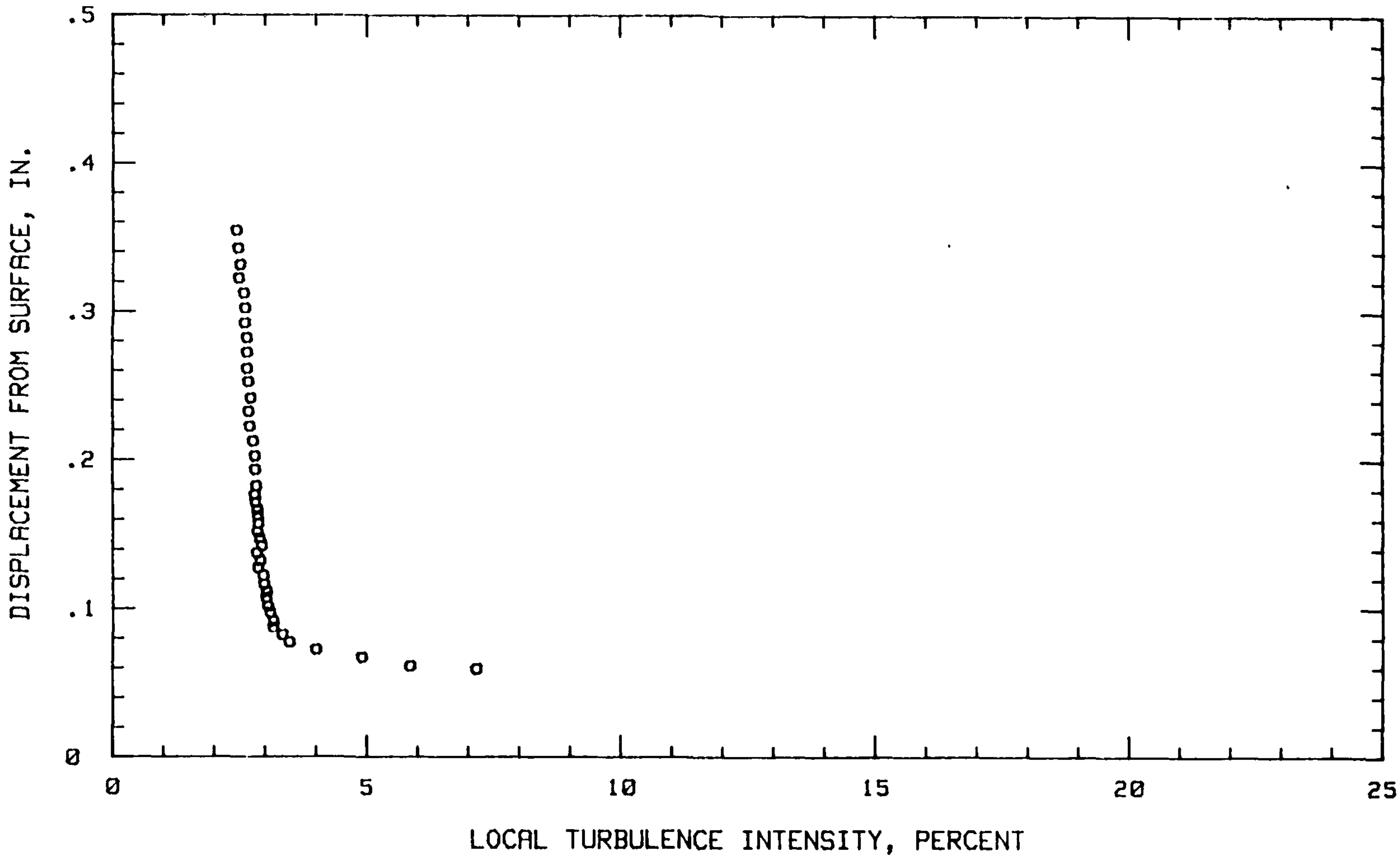

Fig. 168. Boundary Layer Turbulence Intensity Profile, i = +3 Deg, 29.68 % Chord

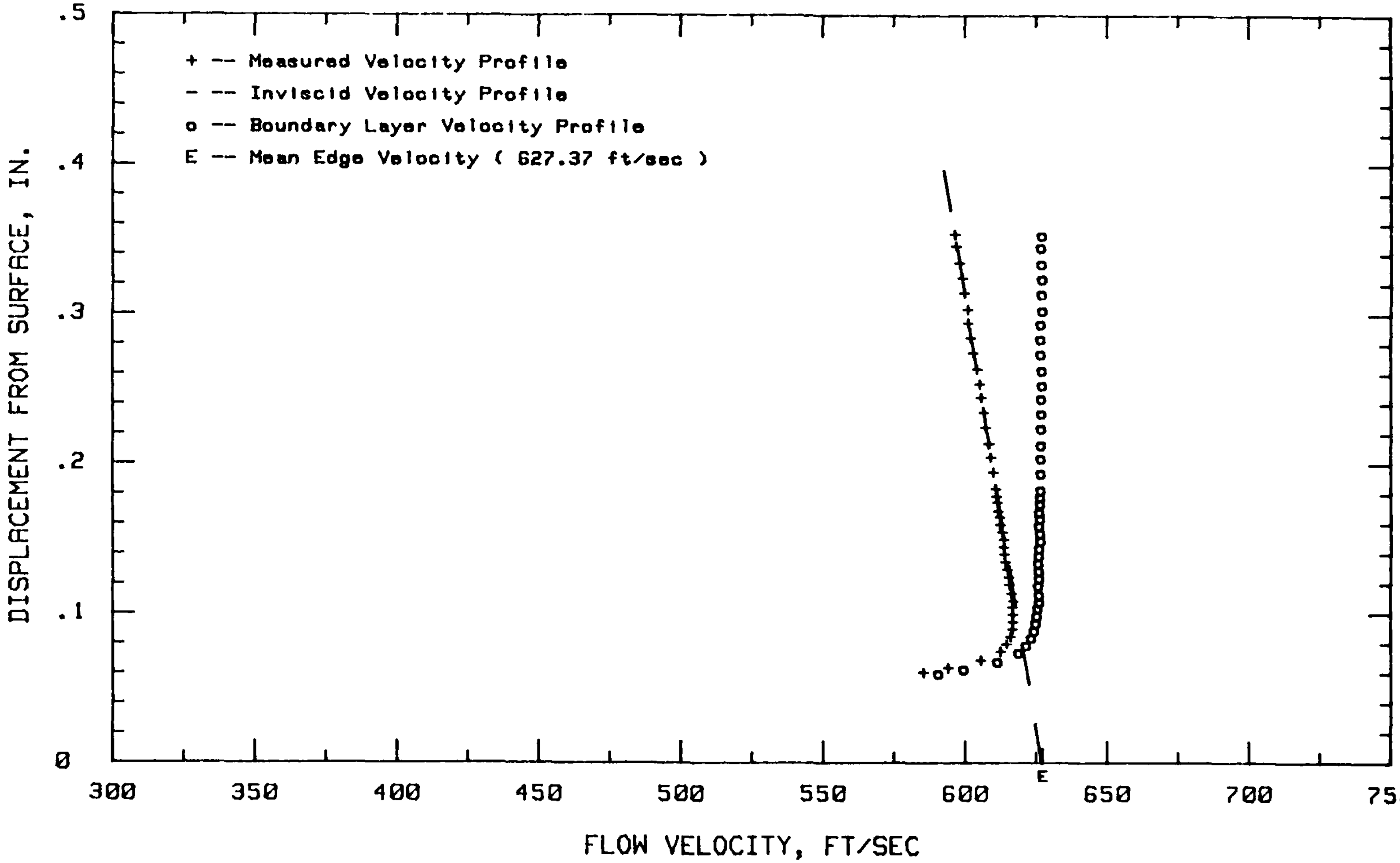

Fig. 169. Boundary Layer Velocity Profiles, i = +3 Deg, 34.37 % Chord

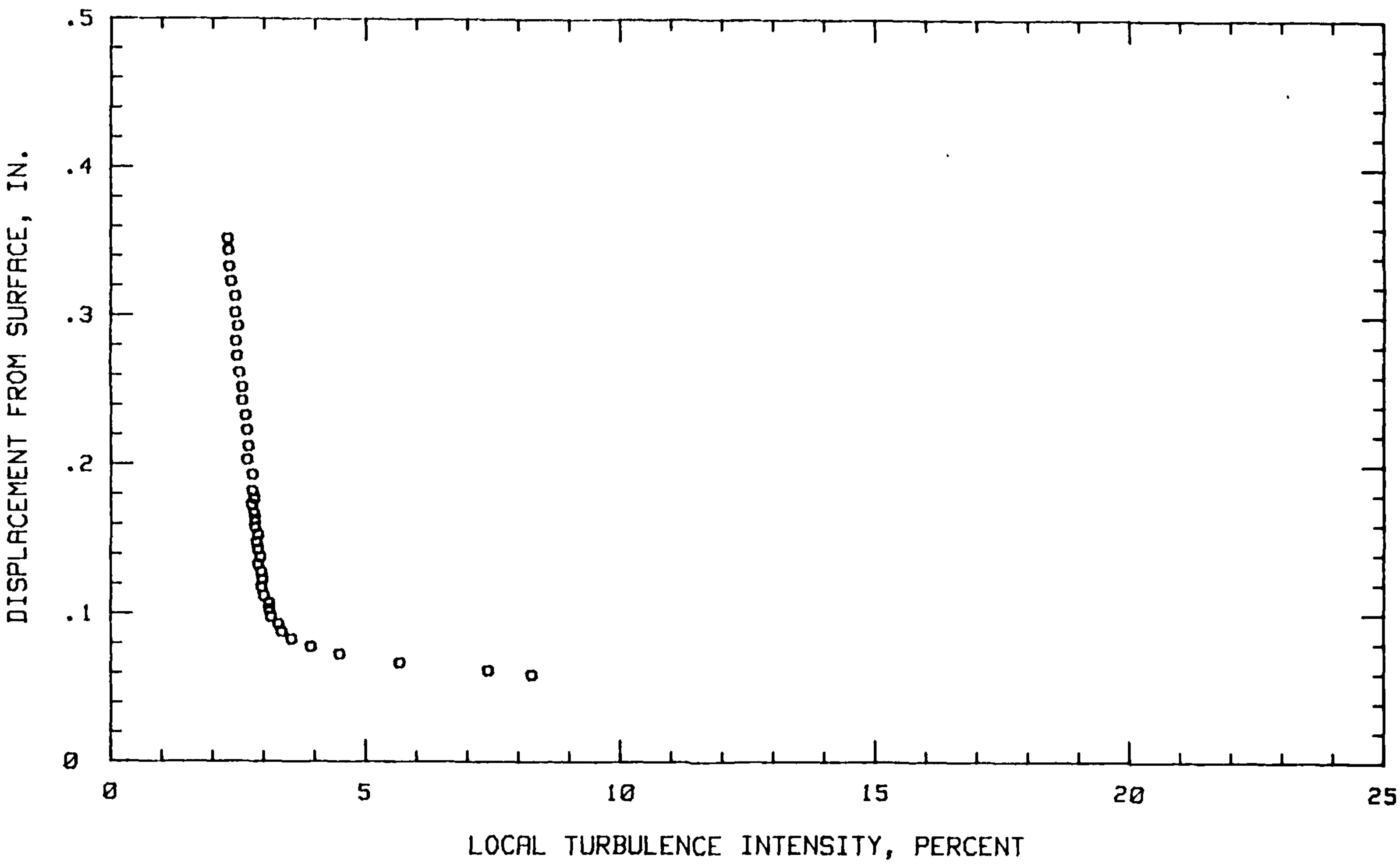

Fig. 170. Boundary Layer Turbulence Intensity Profile, i = +3 Deg, 34.37 % Chord

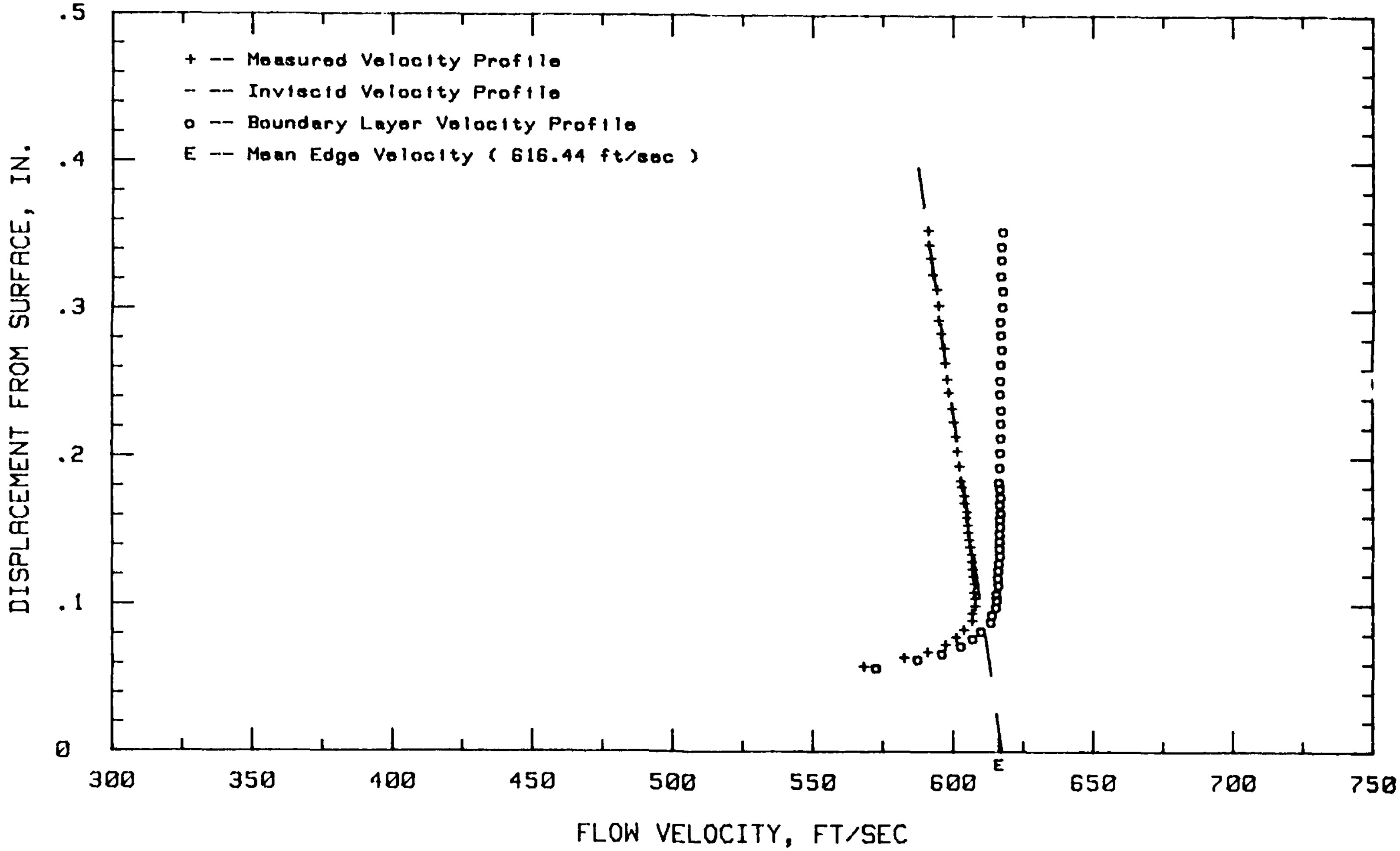

Fig. 171. Boundary Layer Velocity Profiles, i = +3 Deg, 40.62 % Chord

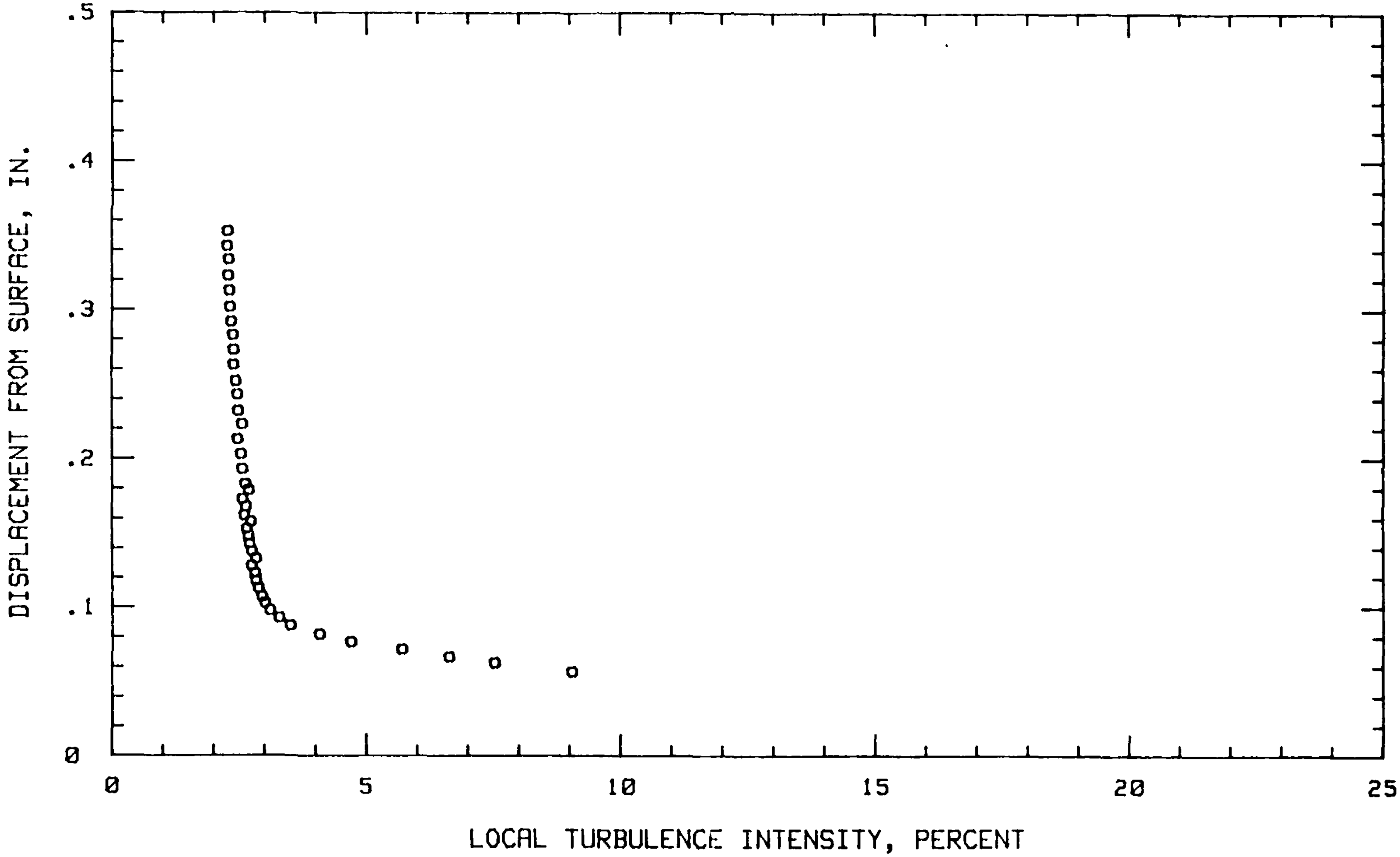

Fig. 172. Boundary Layer Turbulence Intensity Profile, i = +3 Deg, 40.62 % Chord

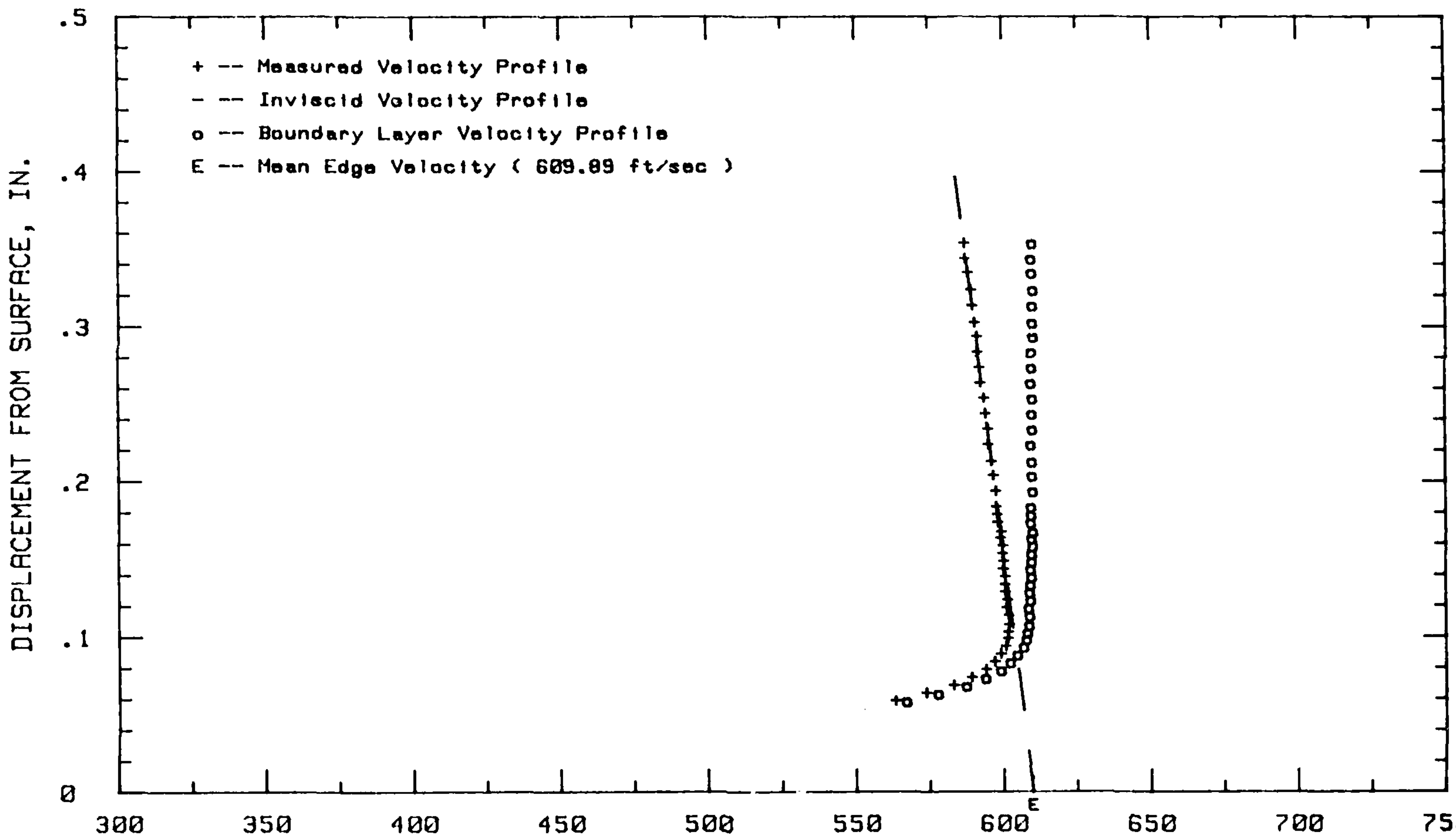

Fig. 173. Boundary Layer Velocity Profiles, i = +3 Deg, 45.31 % Chord

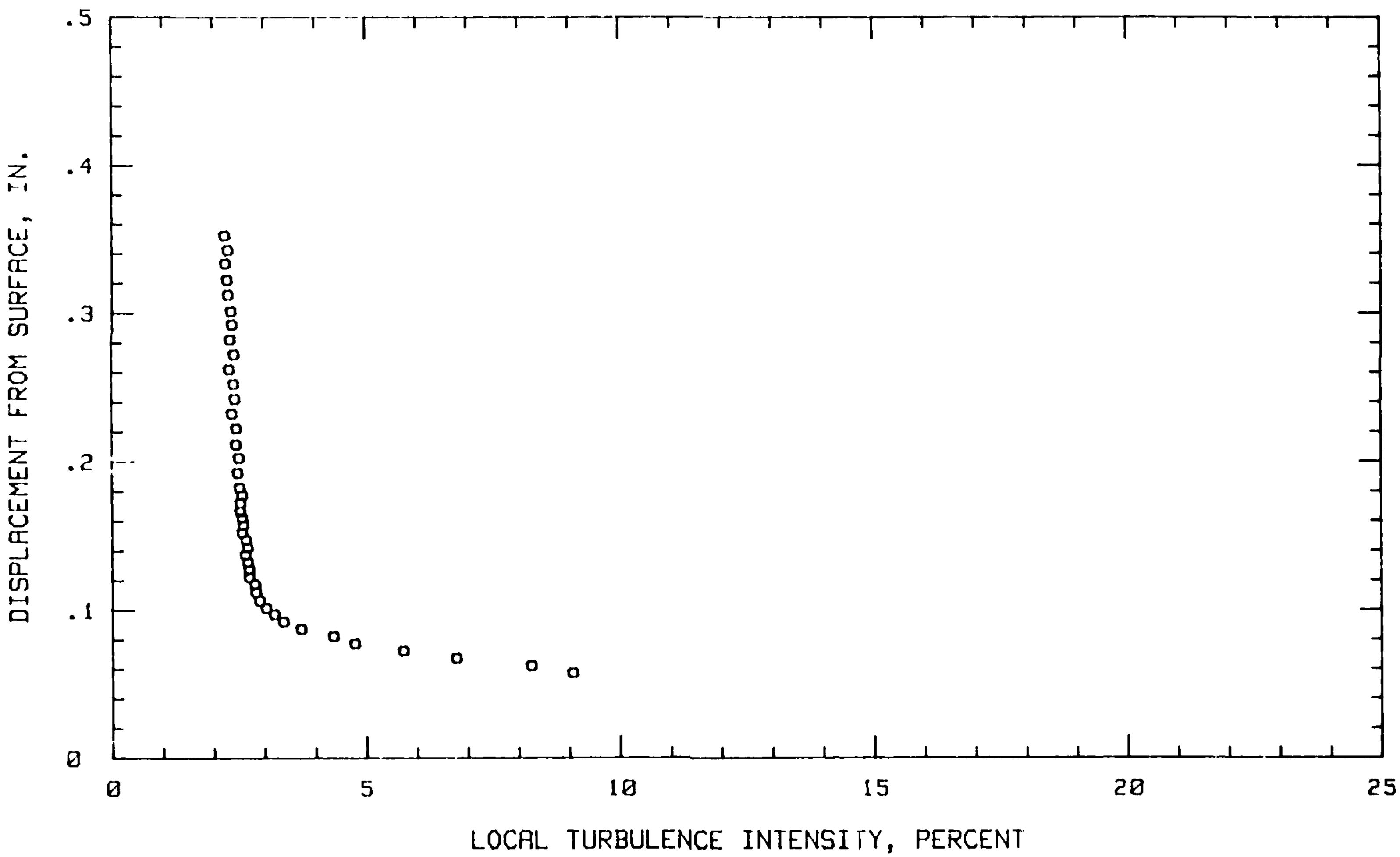

Fig. 174. Boundary Layer Turbulence Intensity Profile, i = +3 Deg, 45.31 % Chord

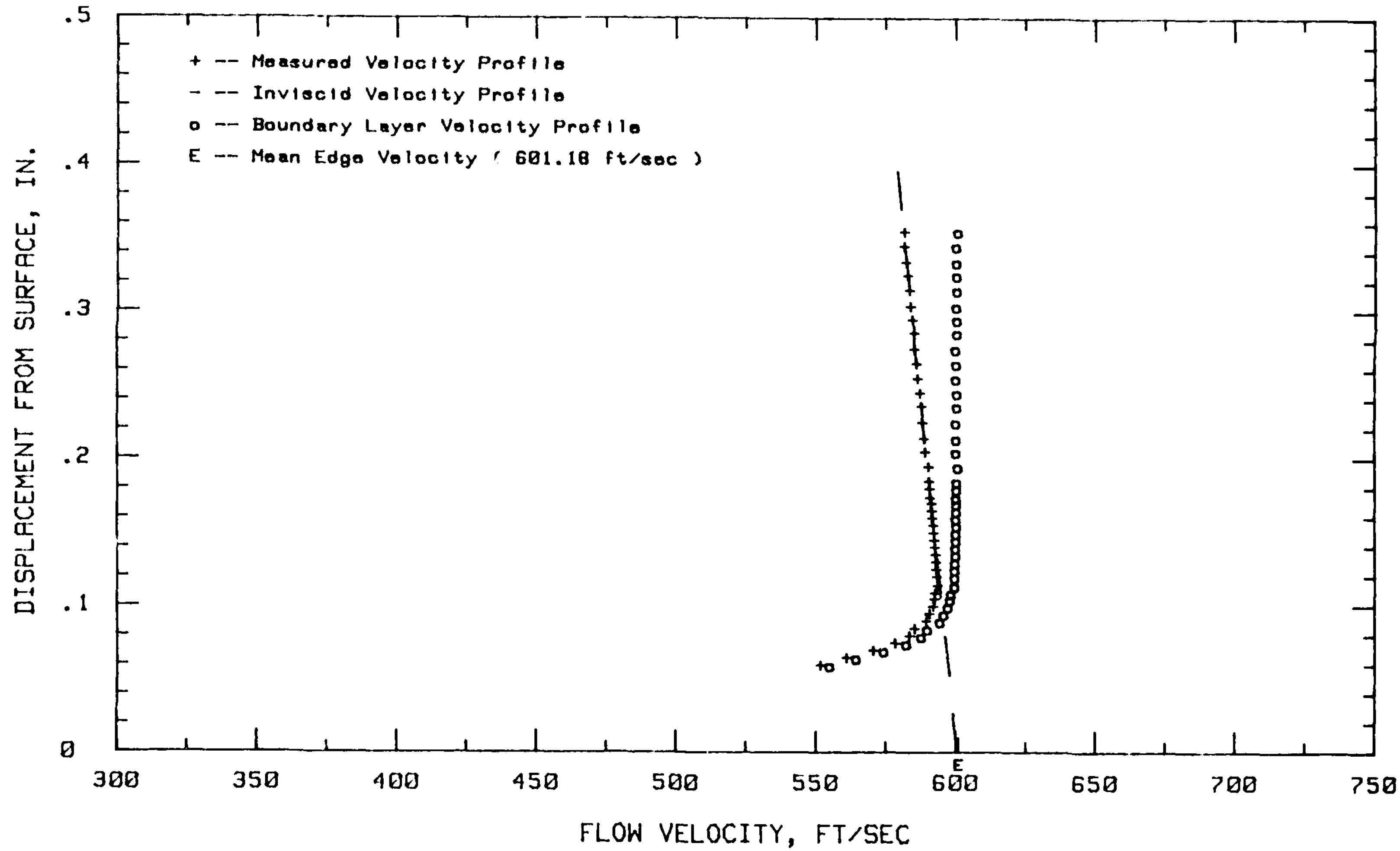

Fig. 175. Boundary Layer Velocity Profiles, i = +3 Deg, 50 % Chord

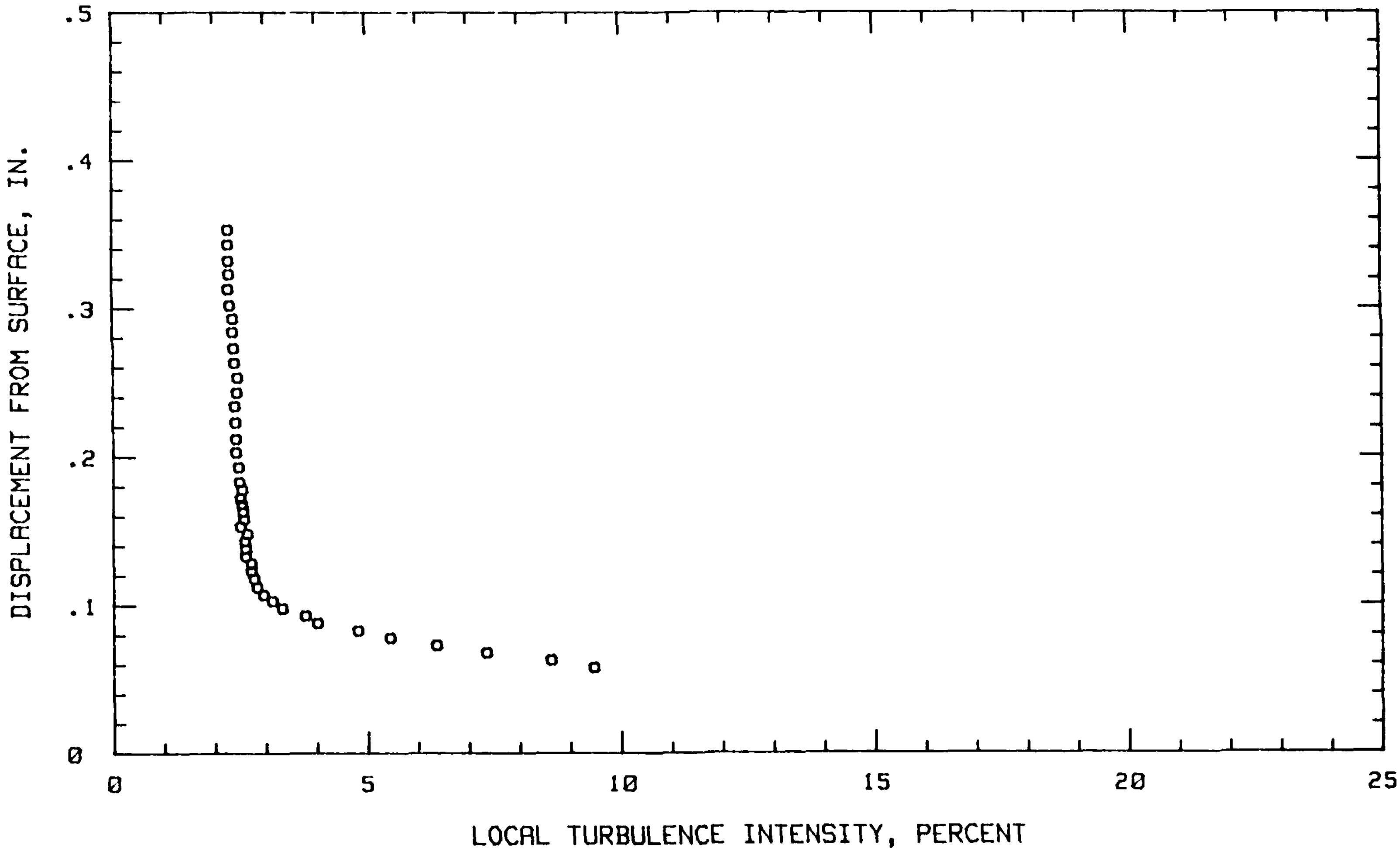

Fig. 176. Boundary Layer Turbulence Intensity Profile, i = +3 Deg, 50 % Chord

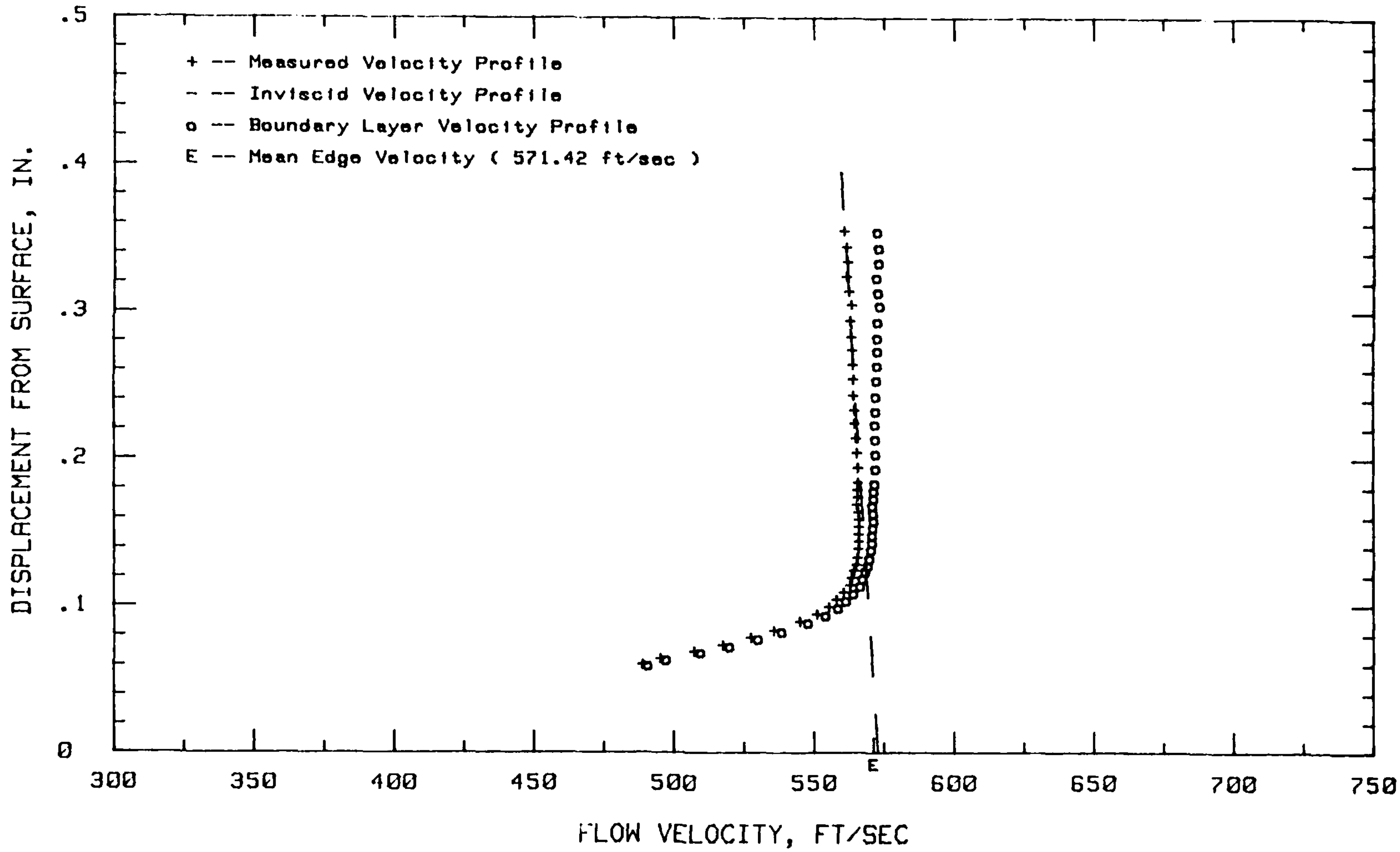

Fig. 177. Boundary Layer Velocity Profiles, i = +3 Deg, 65.62 % Chord

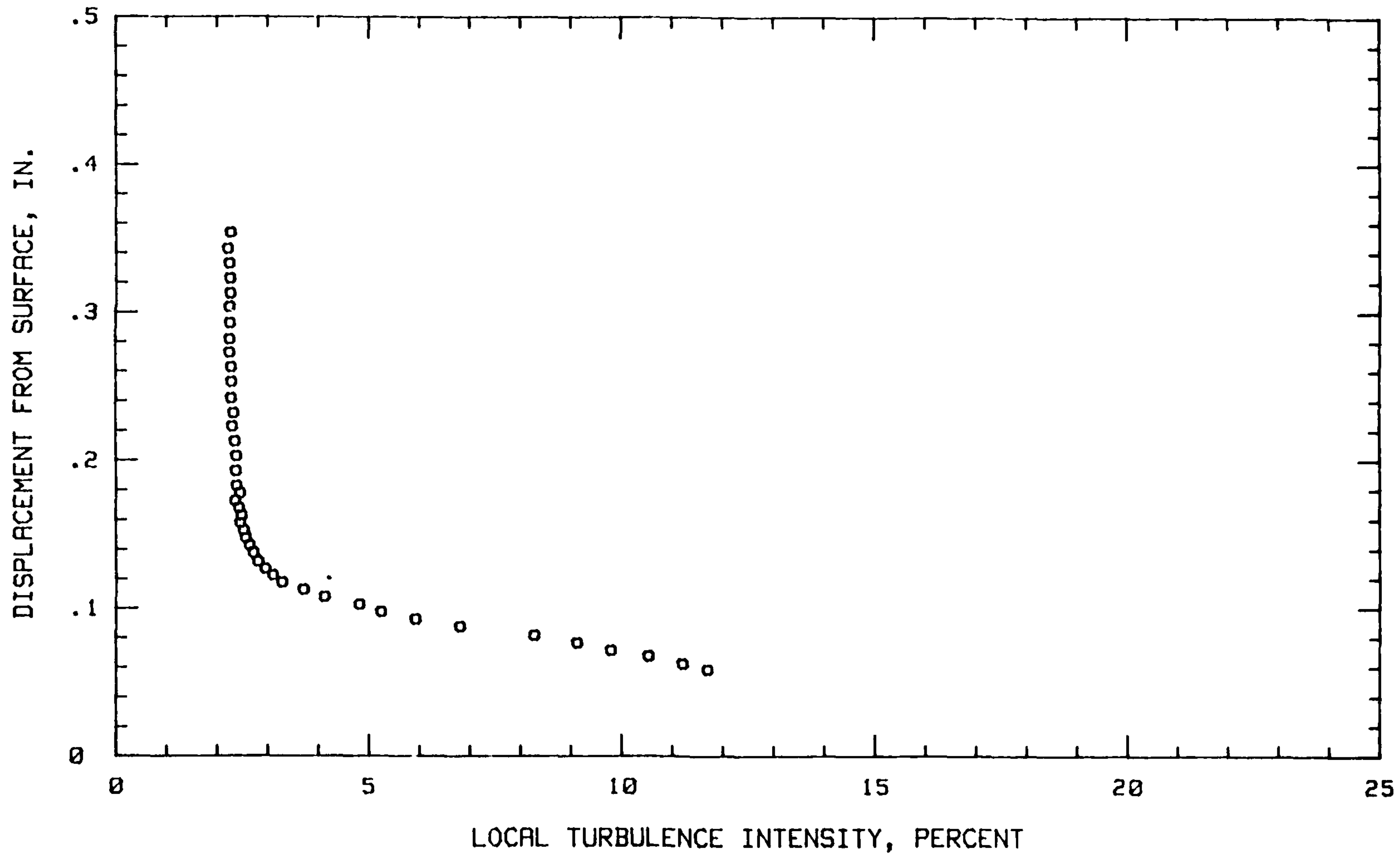

Fig. 178. Boundary Layer Turbulence Intensity Profile, i = +3 Deg, 65.62 % Chord

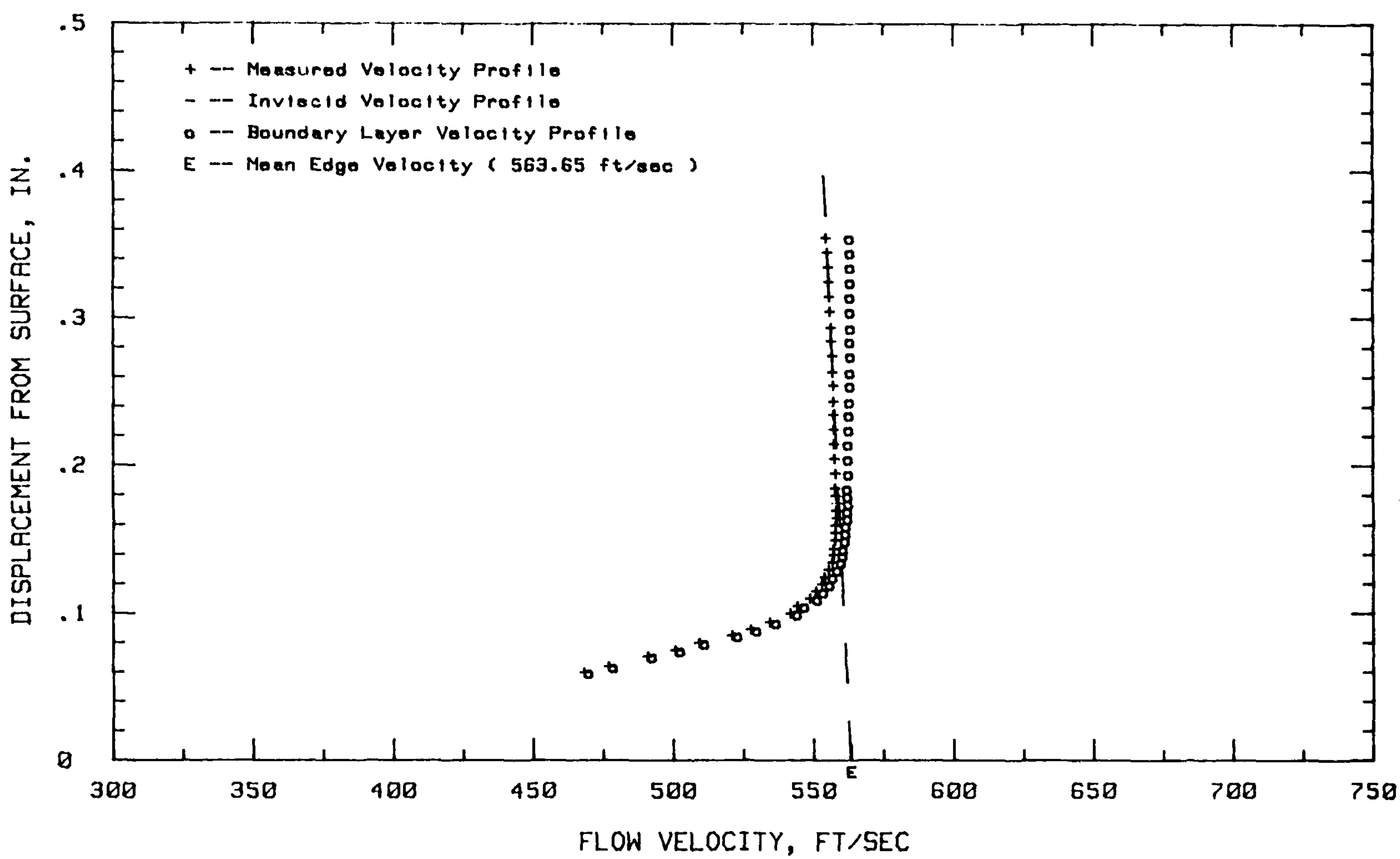

Fig. 179. Boundary Layer Velocity Profiles, i = +3 Deg, 70.31 % Chord

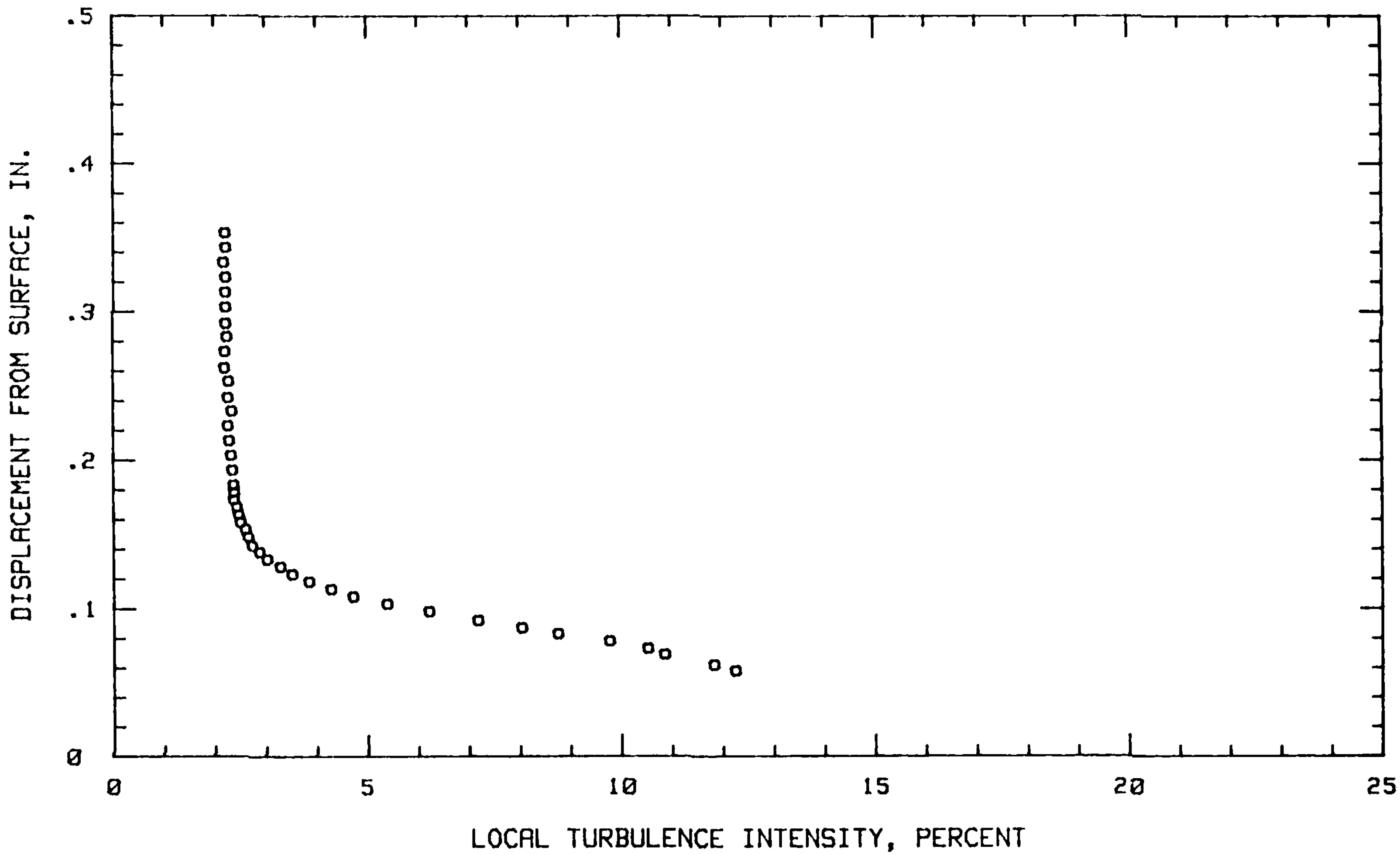

Fig. 180. Boundary Layer Turbulence Intensity Profile, i = +3 Deg, 70.31 % Chord

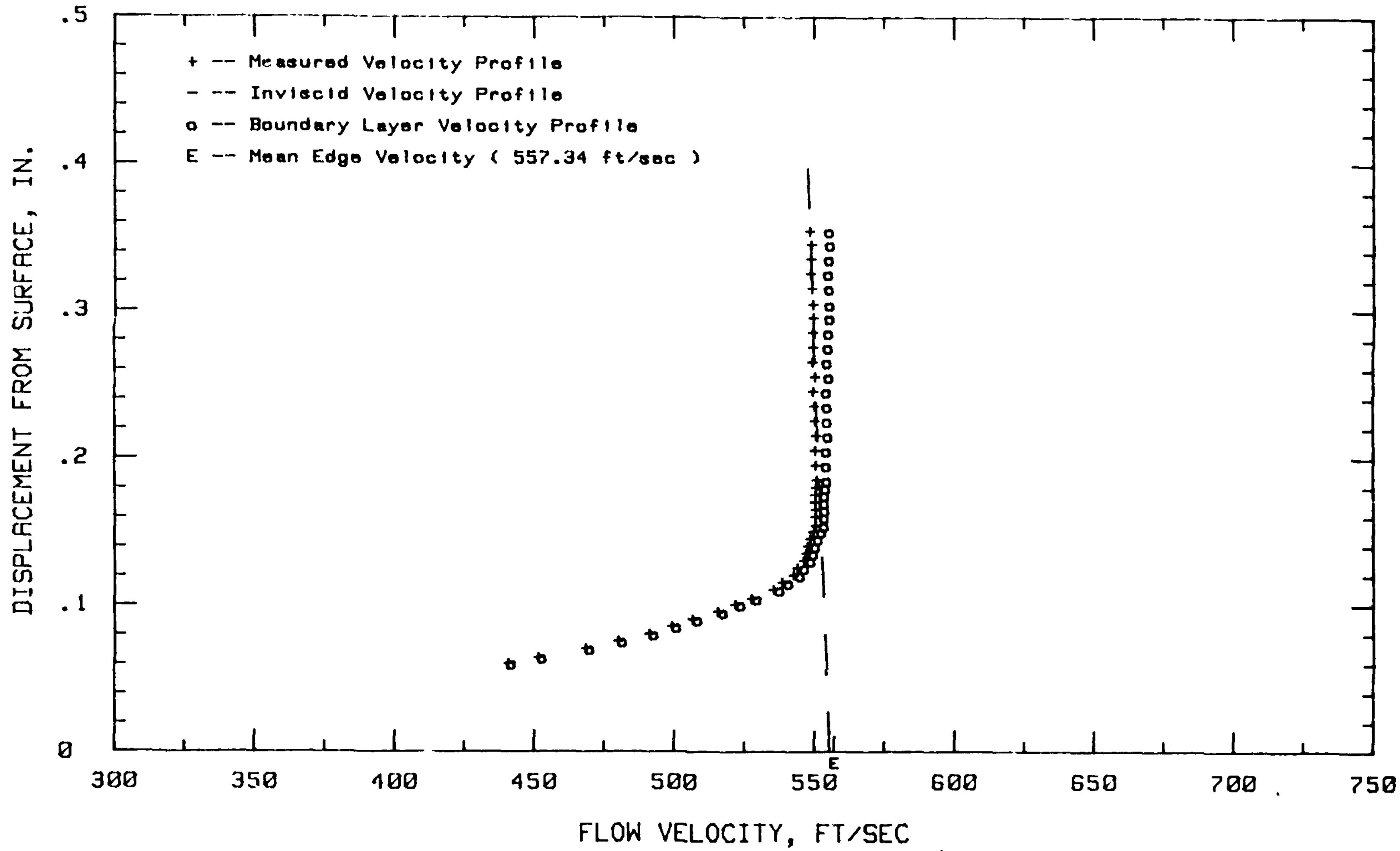

Fig. 181. Boundary Layer Velocity Profiles, i = +3 Deg, 75 % Chord

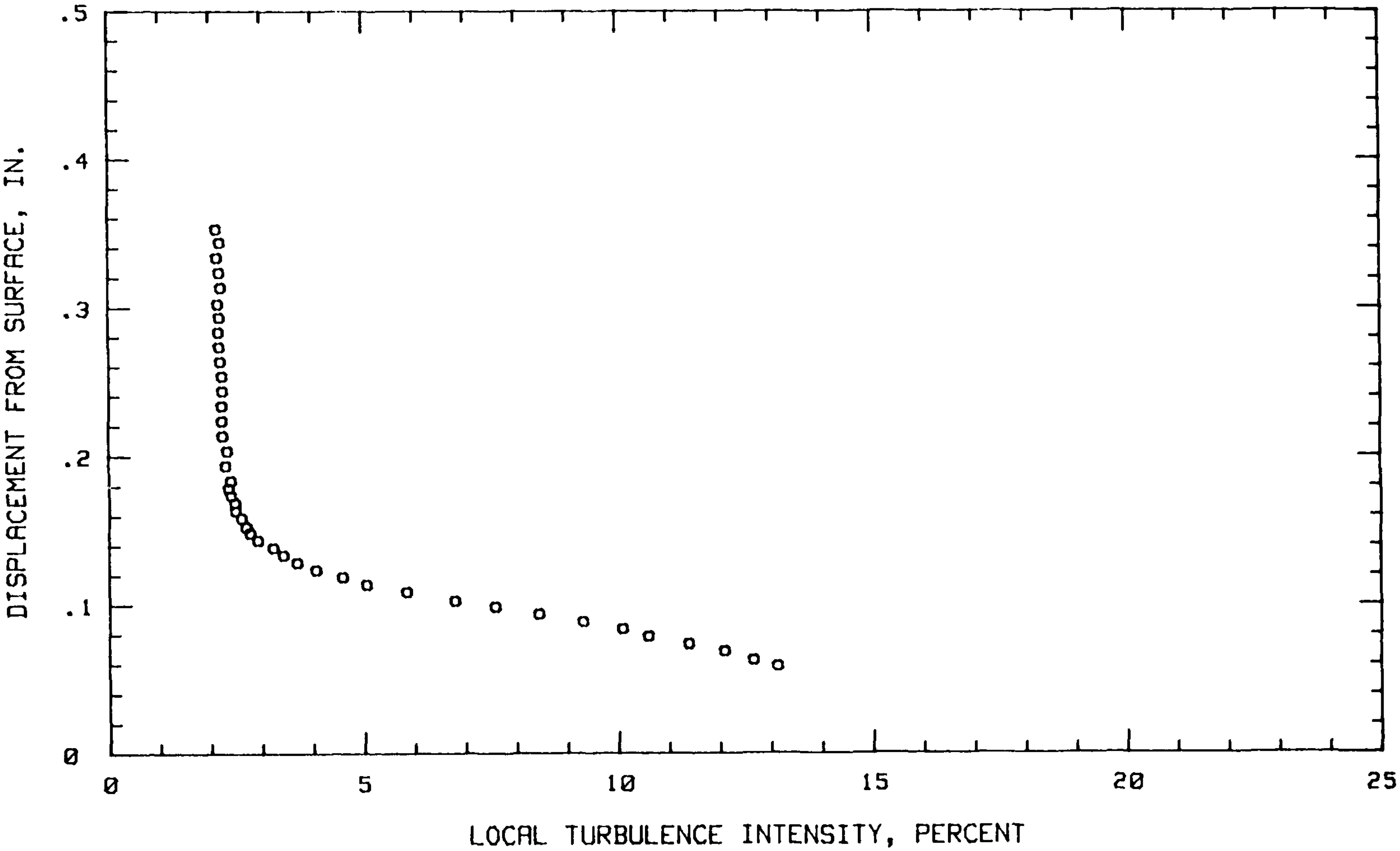

Fig. 182. Boundary Layer Turbulence Intensity Profile, i = +3 Deg, 75 % Chord

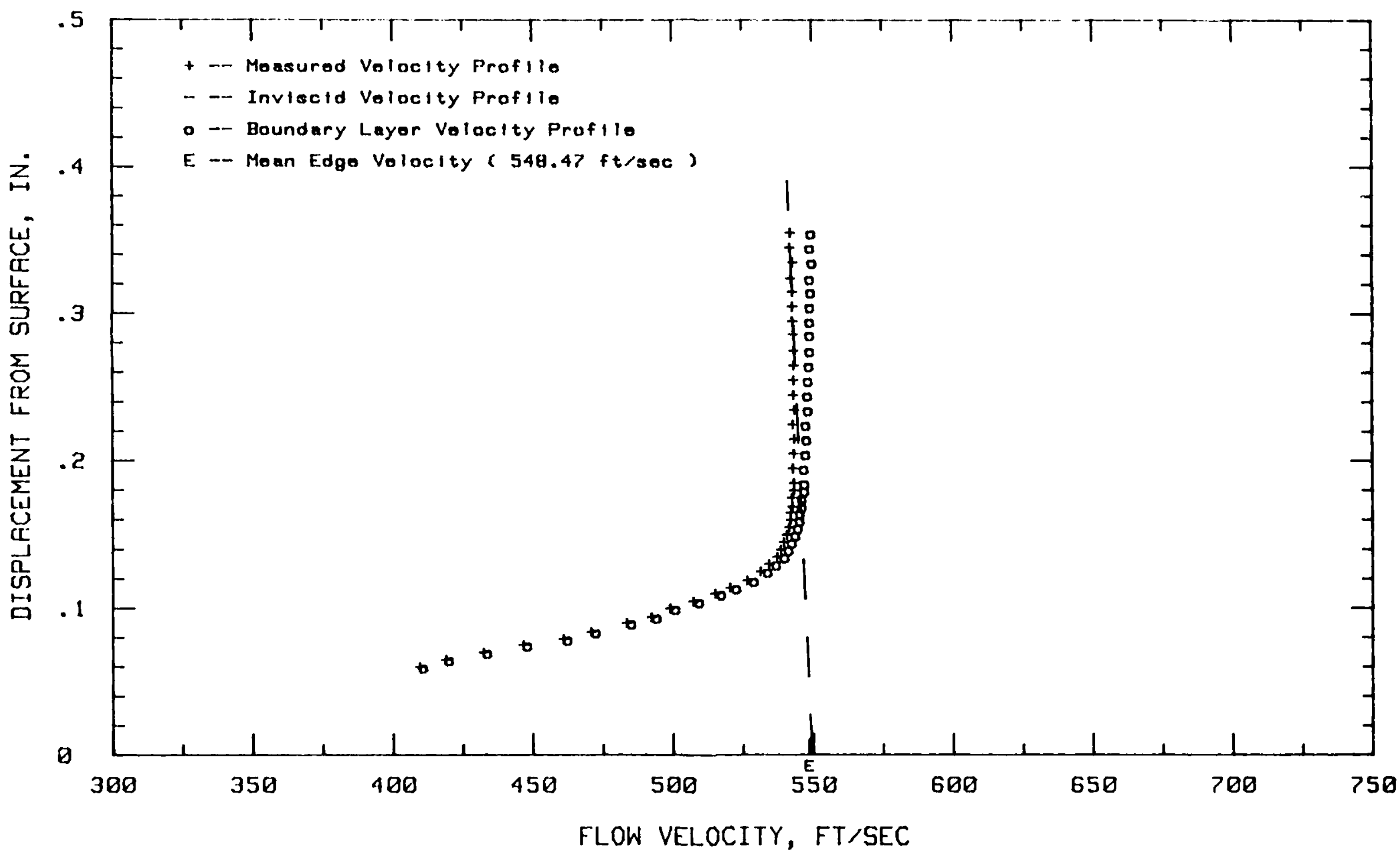

Fig. 183. Boundary Layer Velocity Profiles, i = +3 Deg, 79.68 % Chord

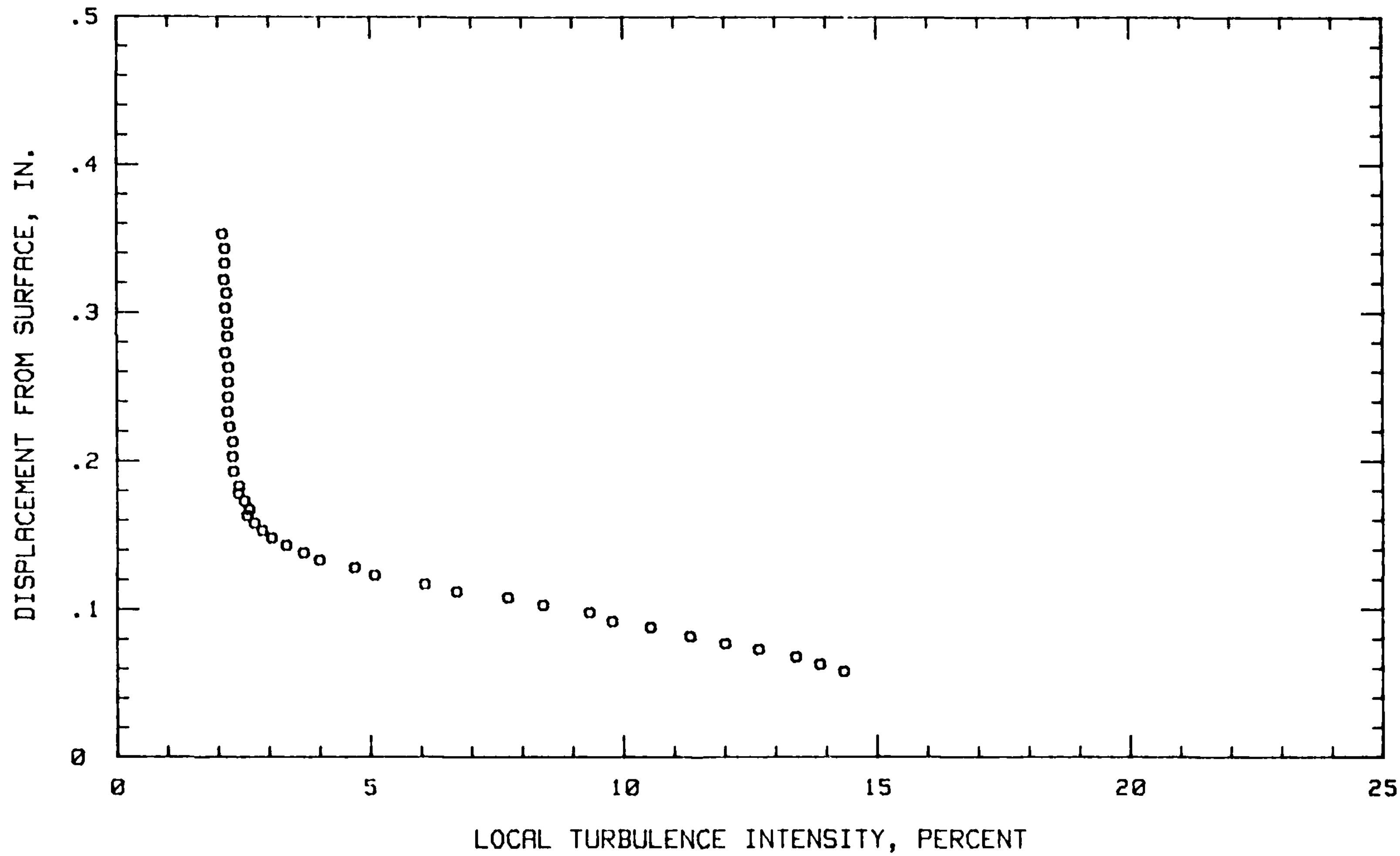

Fig. 184. Boundary Layer Turbulence Intensity Profile, i = +3 Deg, 79.68 % Chord

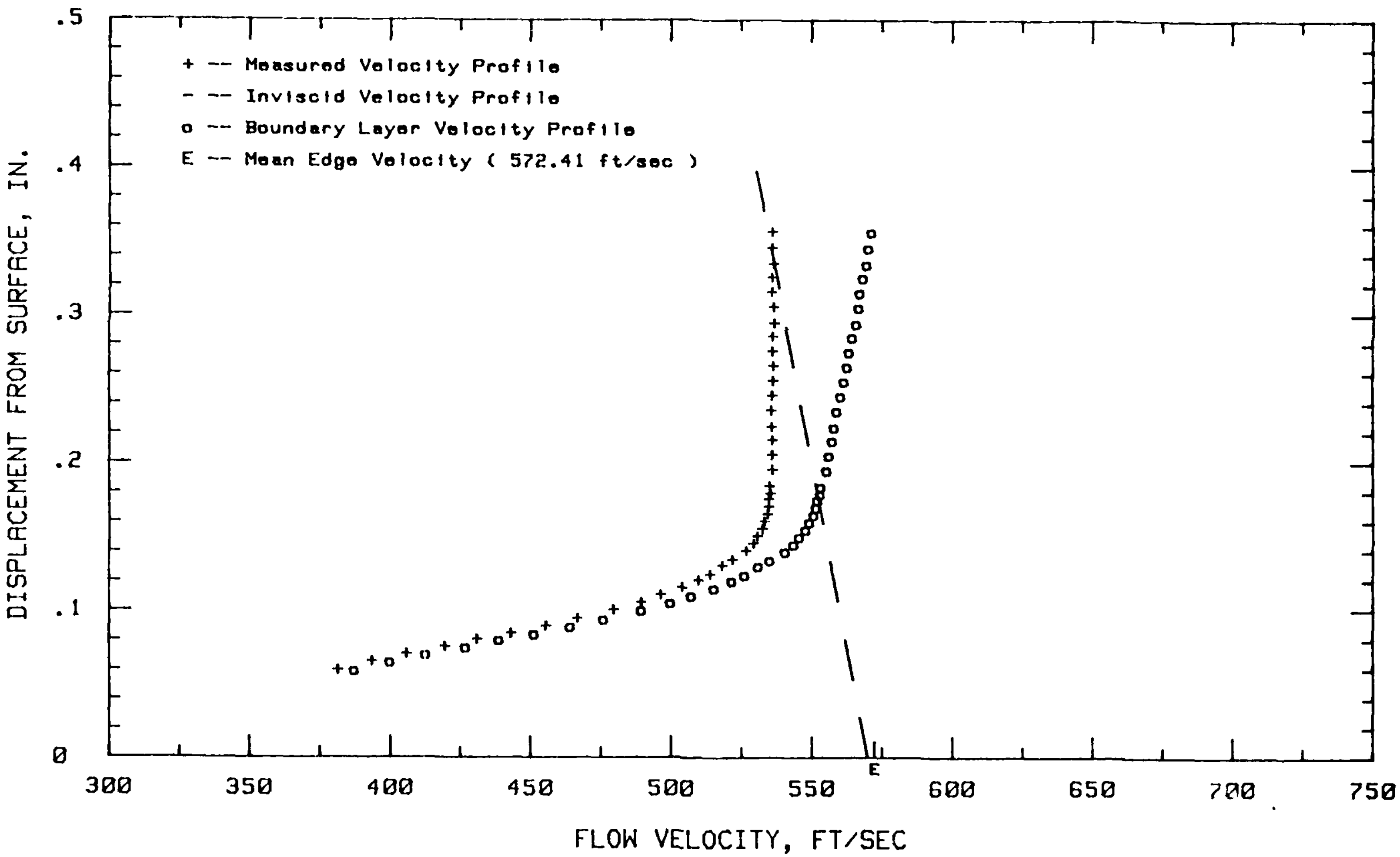

Fig. 185. Boundary Layer Velocity Profiles, i = +3 Deg, 84.37 % Chord

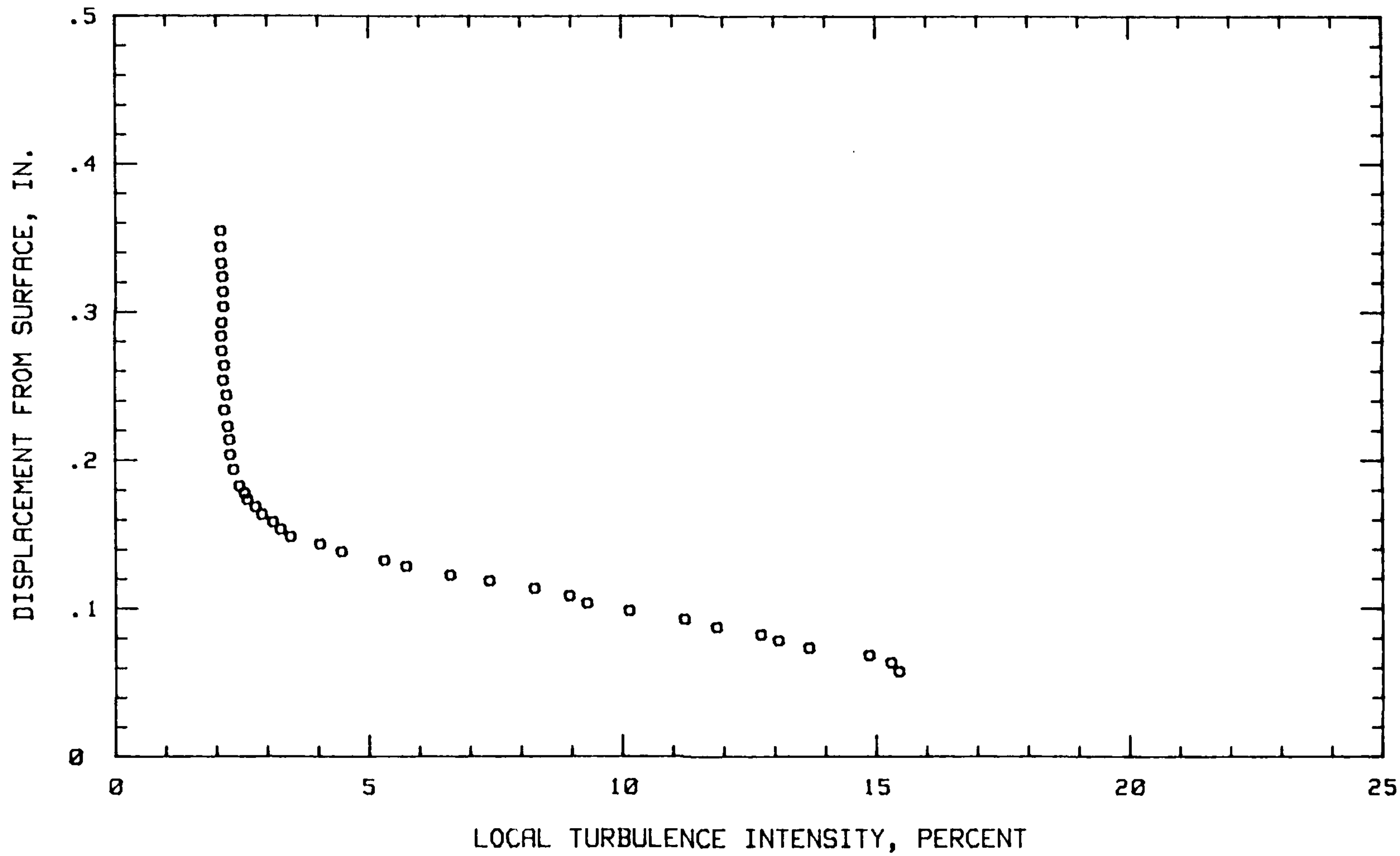

Fig. 186. Boundary Layer Turbulence Intensity Profile, i = +3 Deg, 84.37 % Chord

Appendix N

Boundary Layer Velocity and Turbulence Intensity Profiles

Blade Configuration Number 2

Incidence Angle = +3.0 Degrees

High Free Stream Turbulence

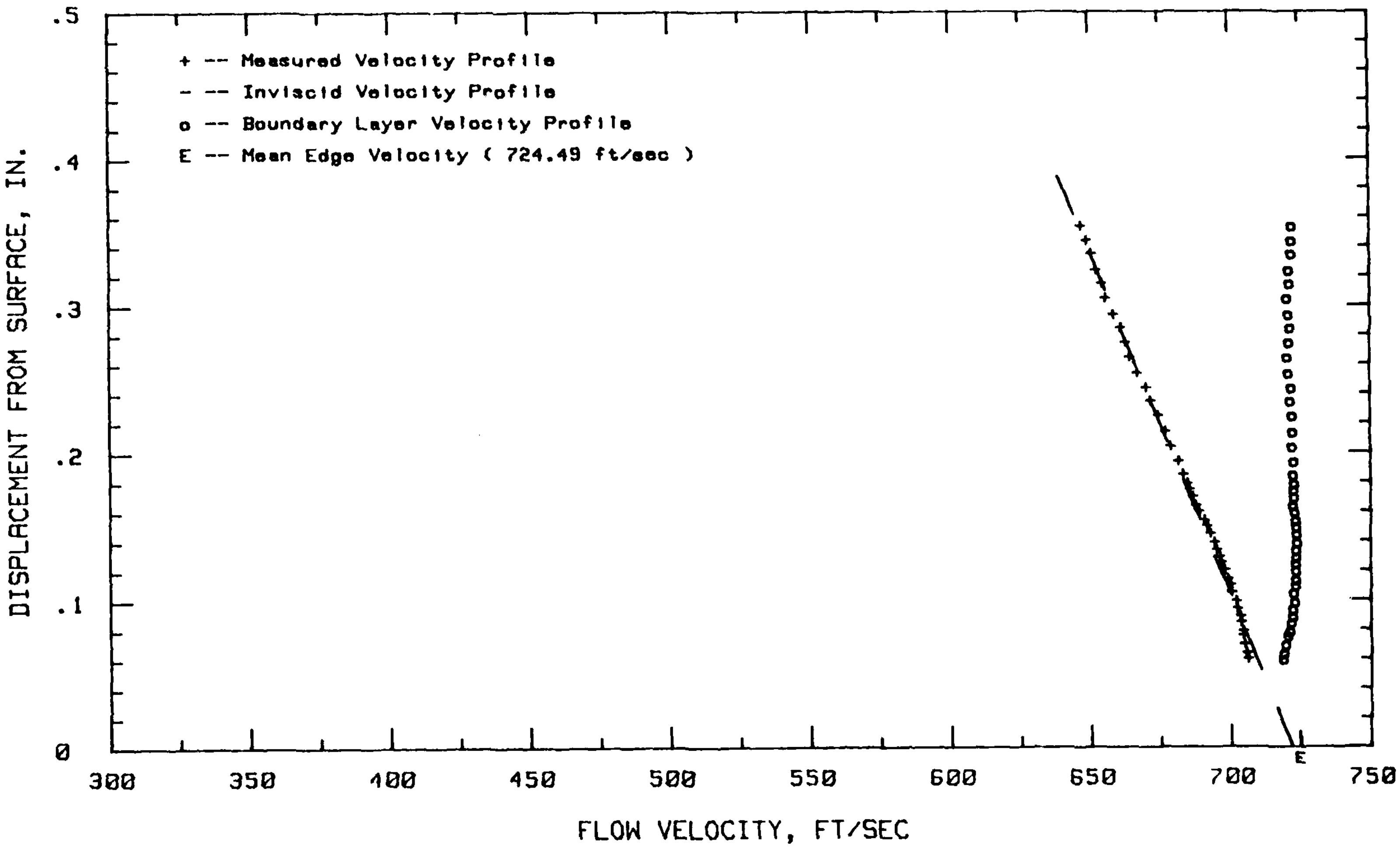

Fig. 187. Boundary Layer Velocity Profiles, i = +3 Deg, 4.68 % Chord

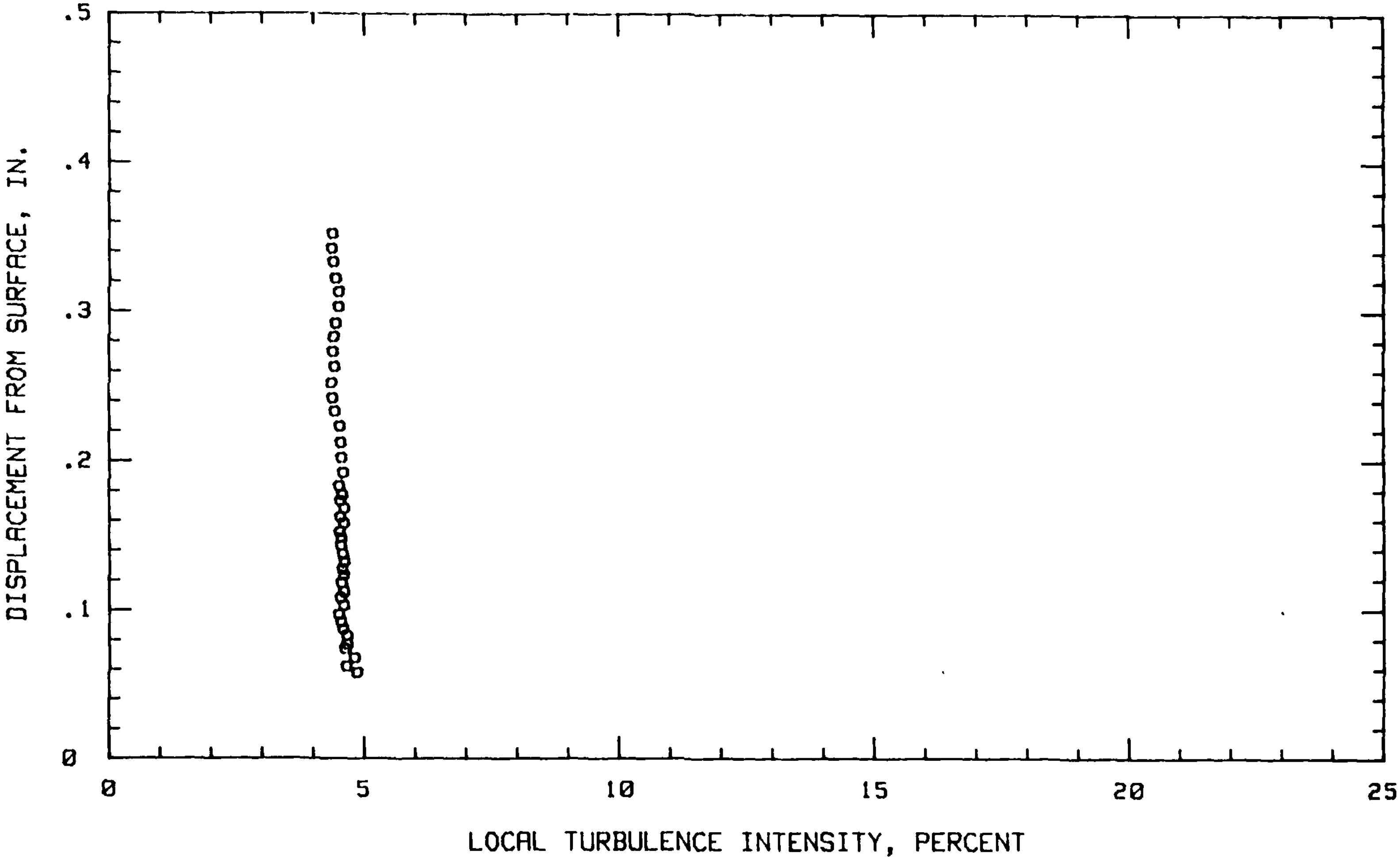

Fig. 188. Boundary Layer Turbulence Intensity Profile, i = +3 Deg, 4.68 % Chord

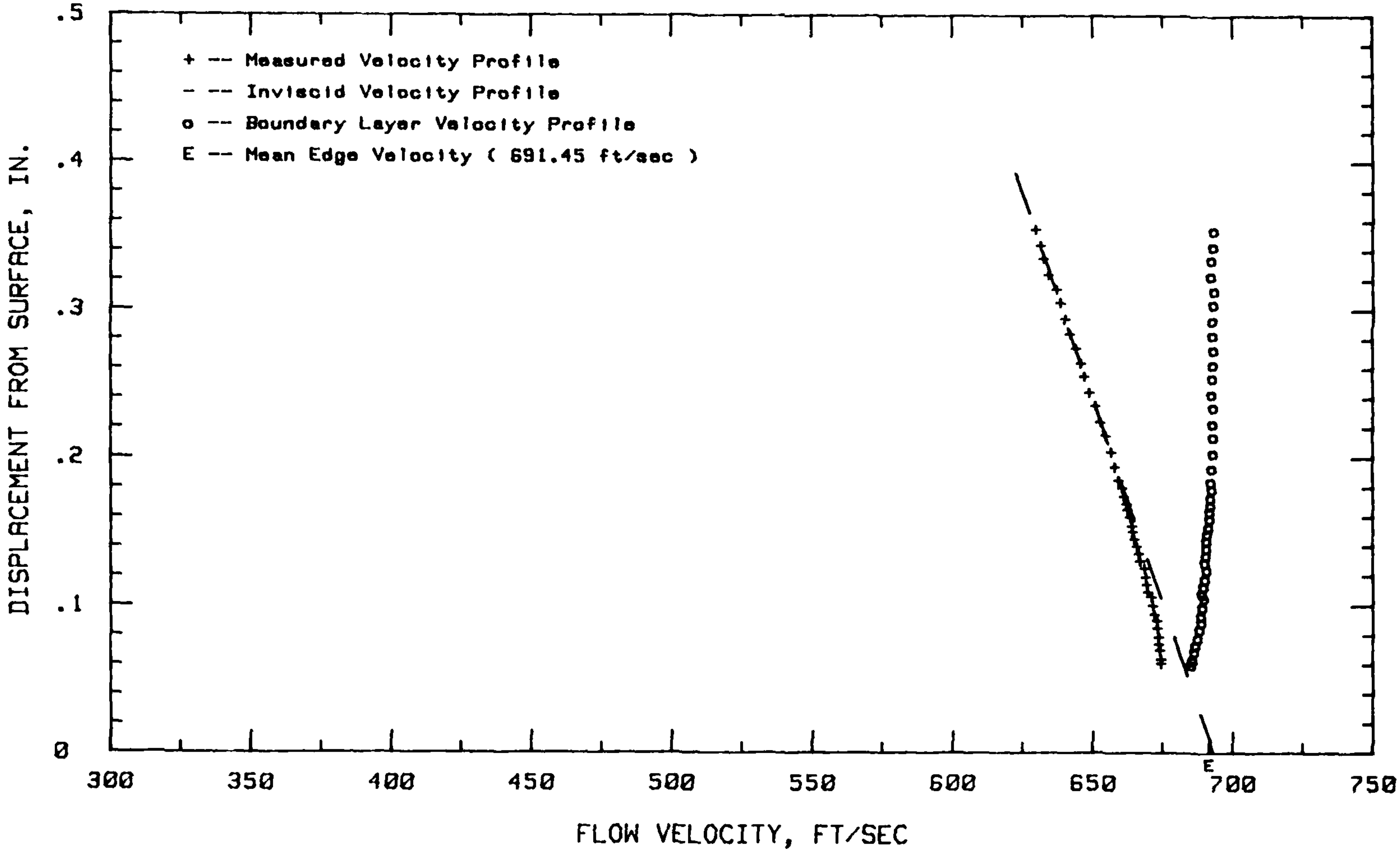

Fig. 189. Boundary Layer Velocity Profiles, i = +3 Deg, 9.37 % Chord

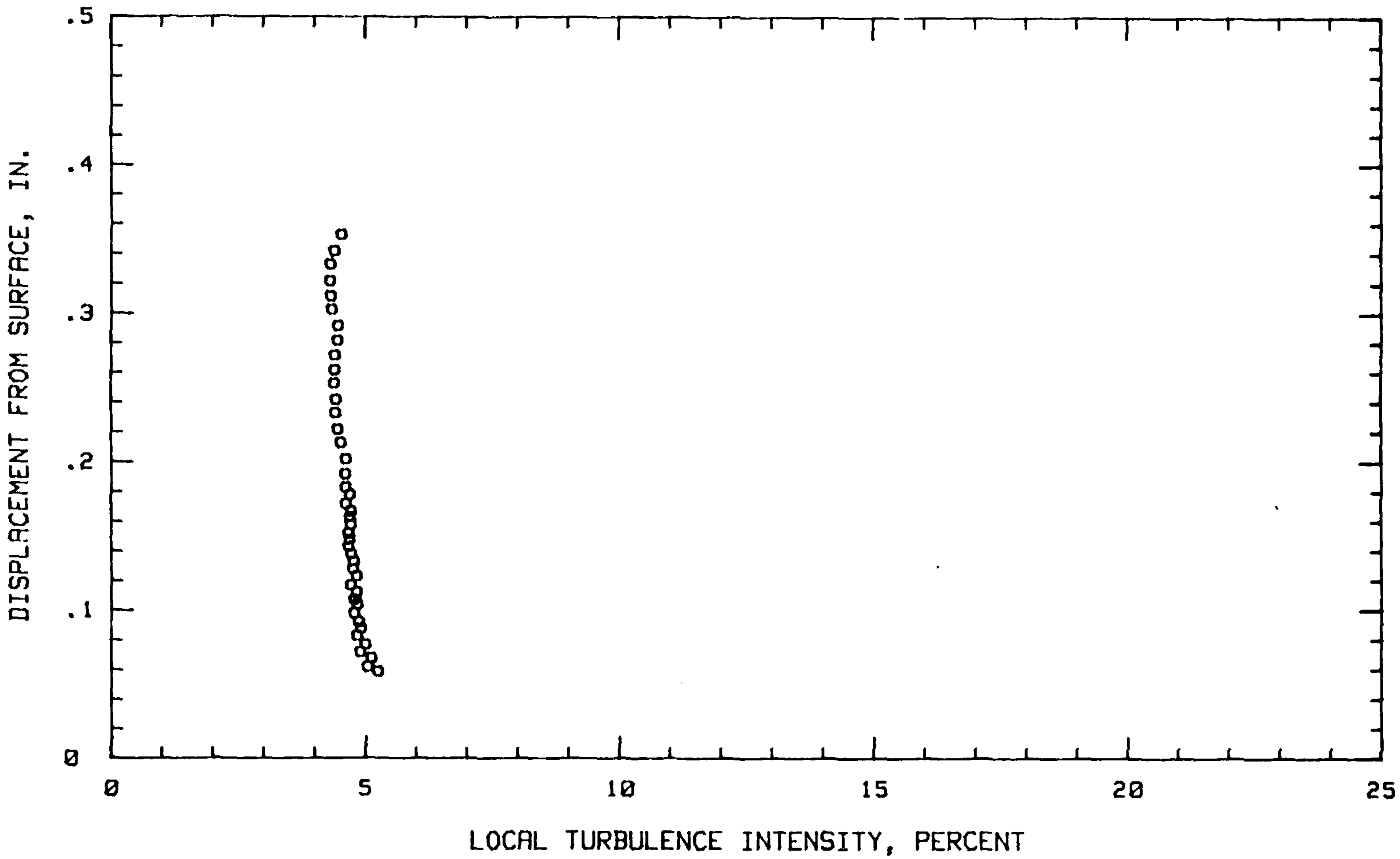

Fig. 190. Boundary Layer Turbulence Intensity Profile, i = +3 Deg, 9.37 % Chord

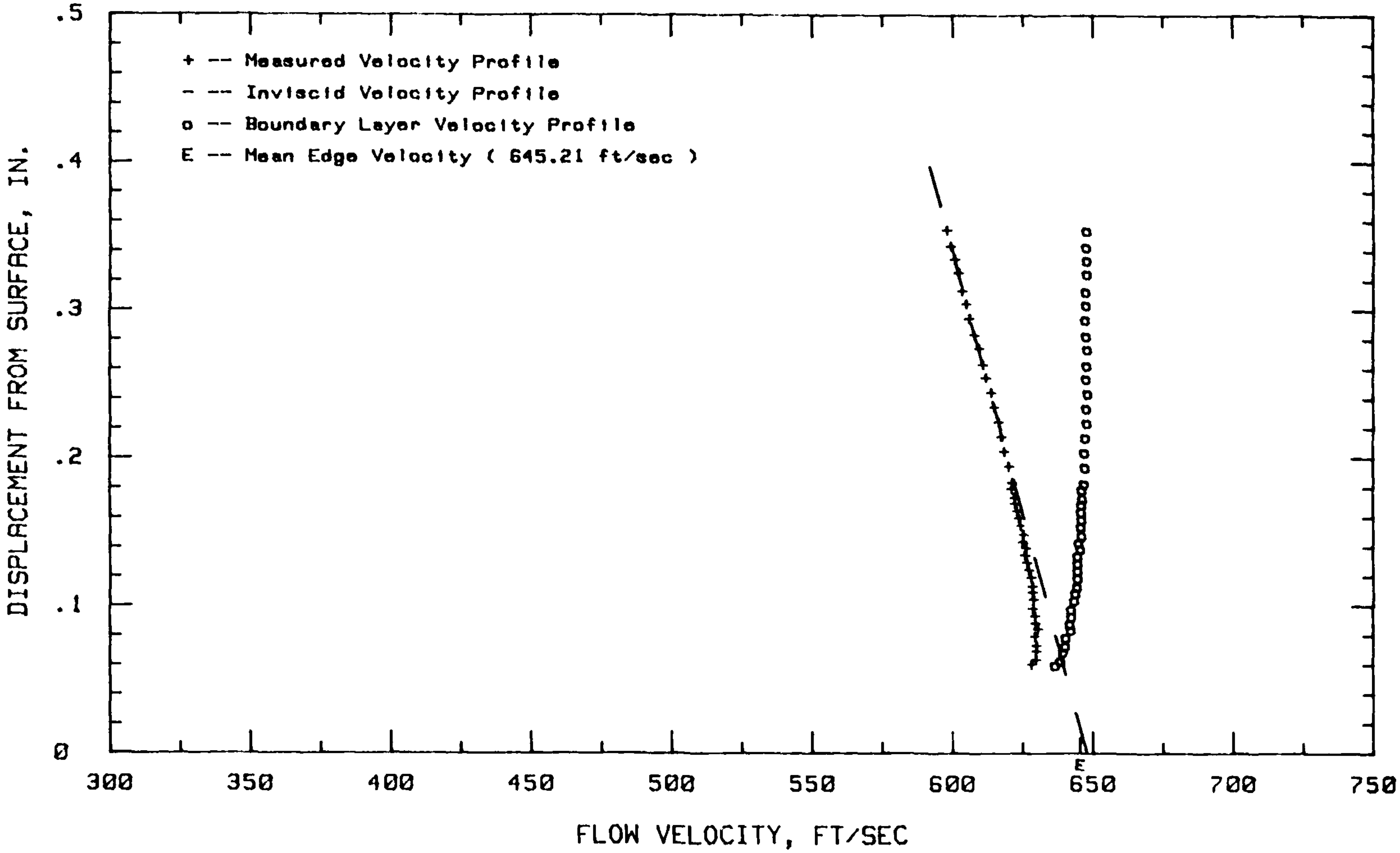

Fig. 191. Boundary Layer Velocity Profiles, i = +3 Deg, 16.51 % Chord

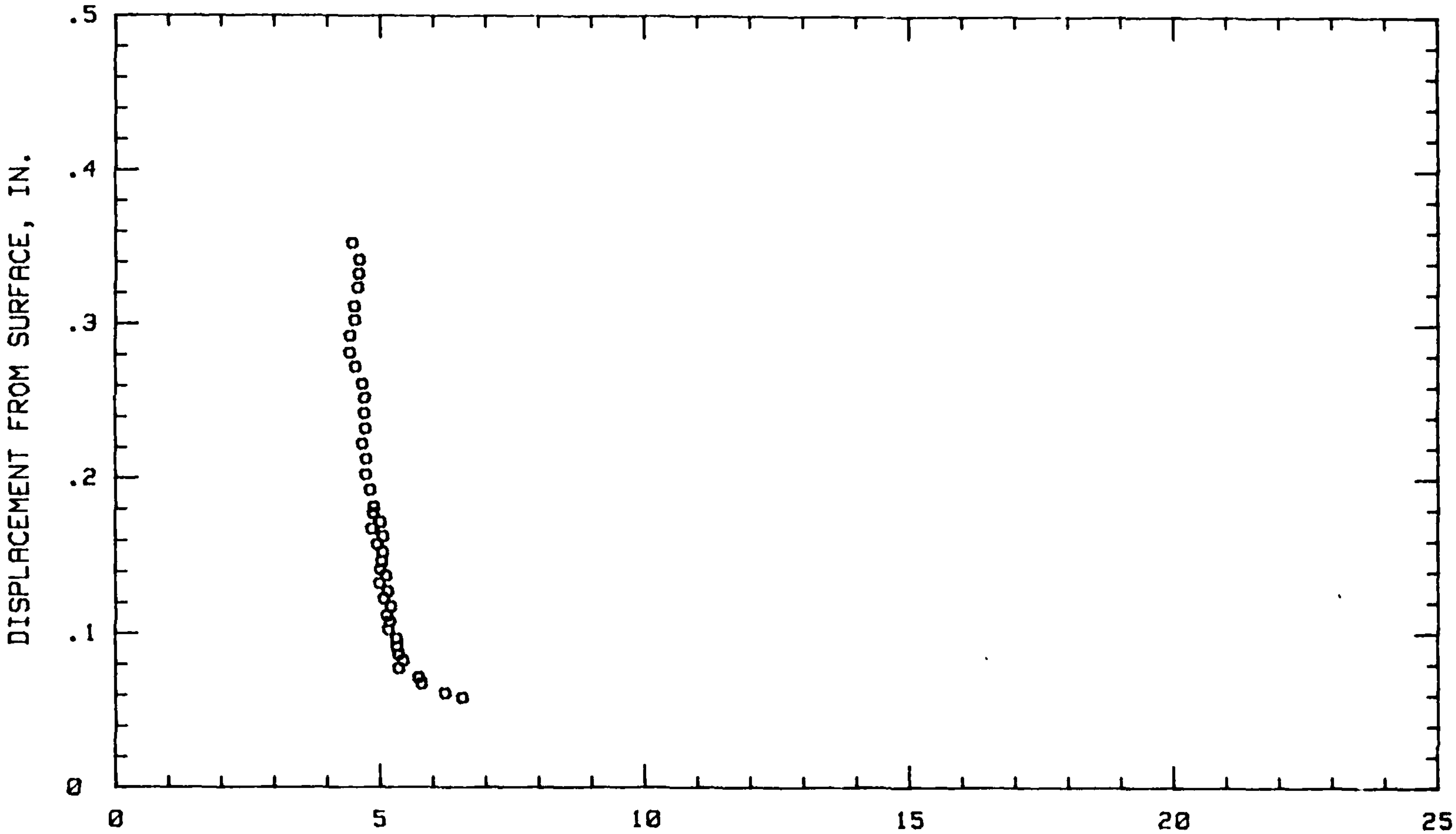

Fig. 192. Boundary Layer Turbulence Intensity Profile, i = +3 Deg, 16.51 % Chord

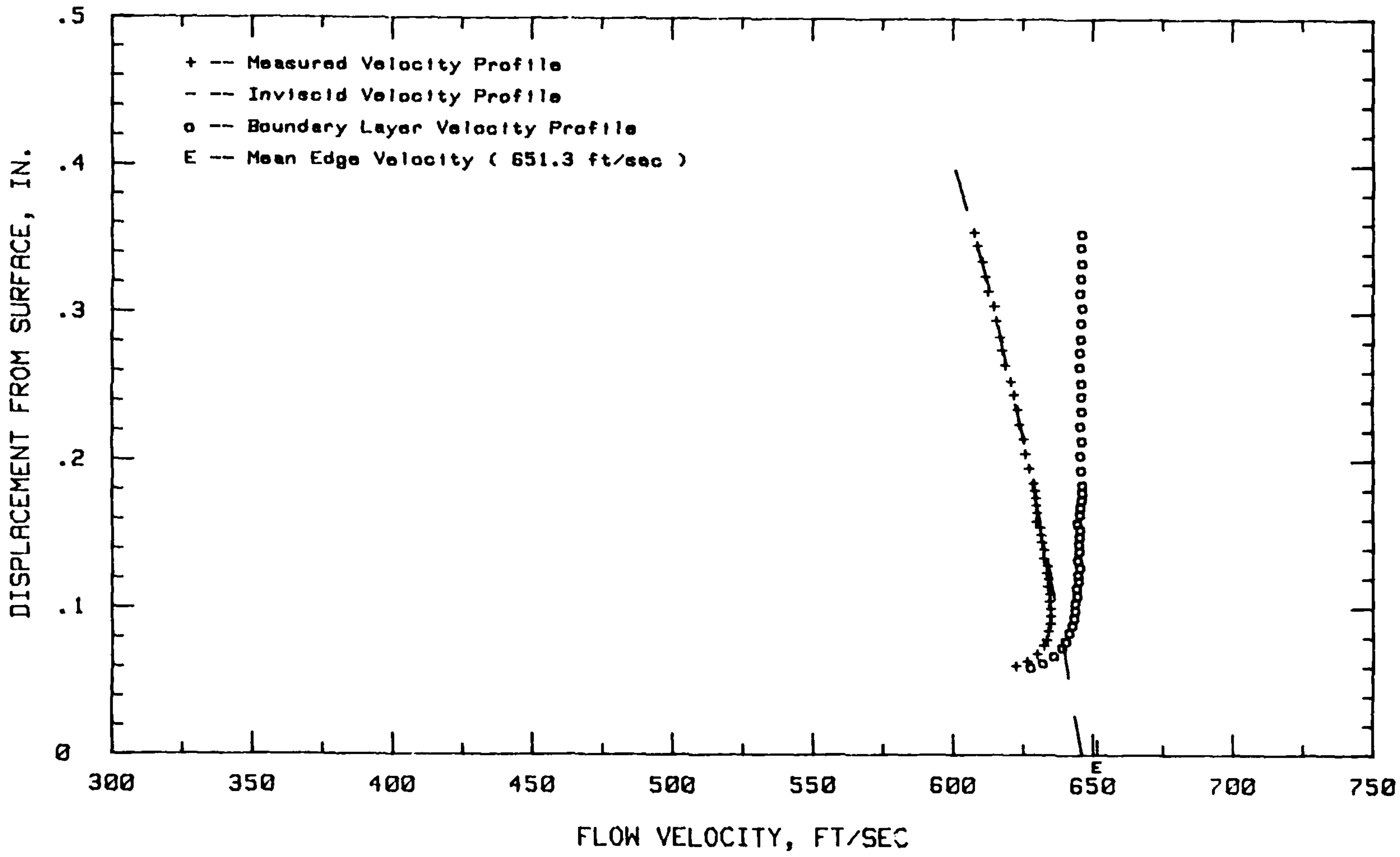

Fig. 193. Boundary Layer Velocity Profiles, i = +3 Deg, 25 % Chord

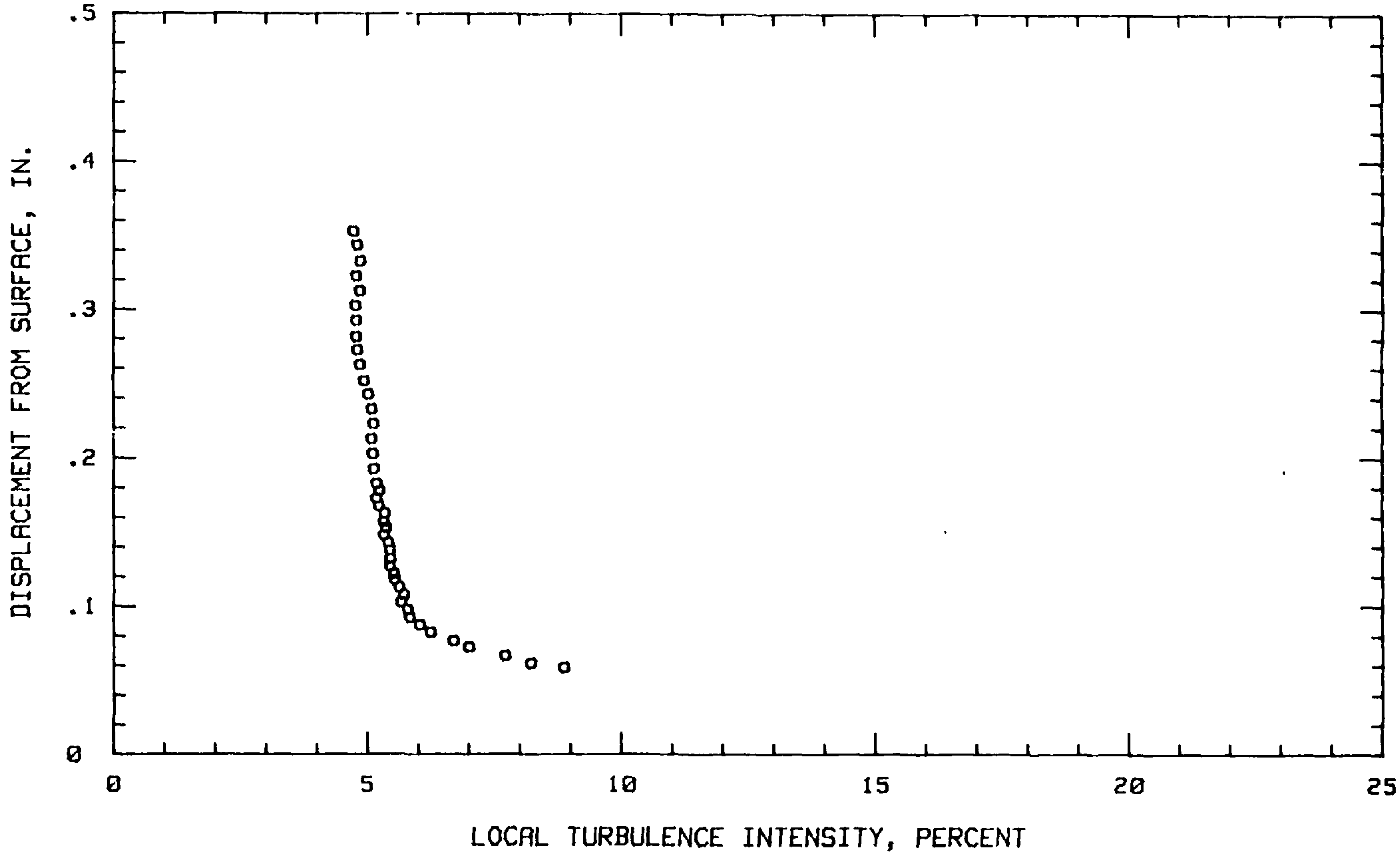

Fig. 194. Boundary Layer Turbulence Intensity Profile, i = +3 Deg, 25 % Chord

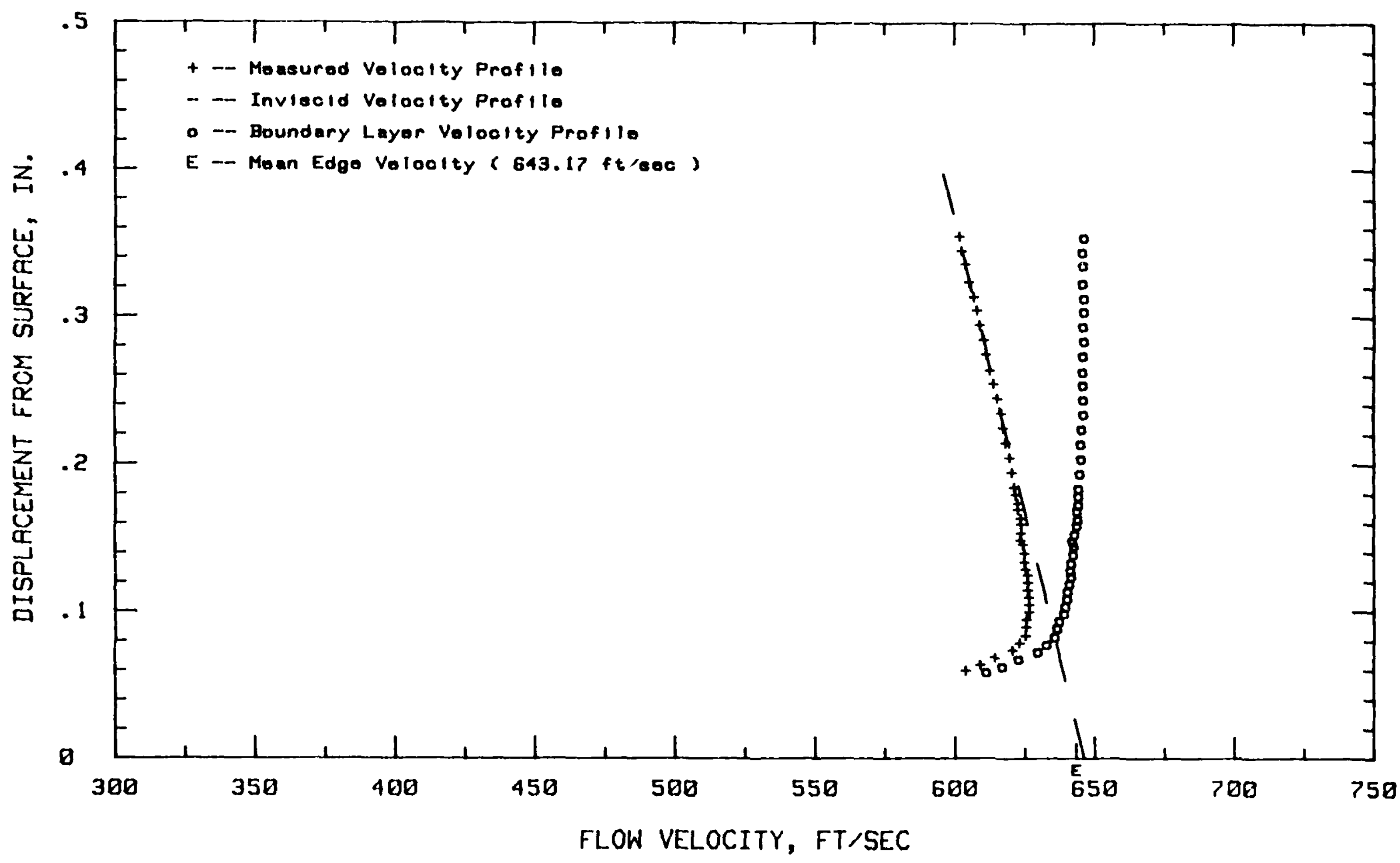

Fig. 195. Boundary Layer Velocity Profiles, i = +3 Deg, 29.68 % Chord

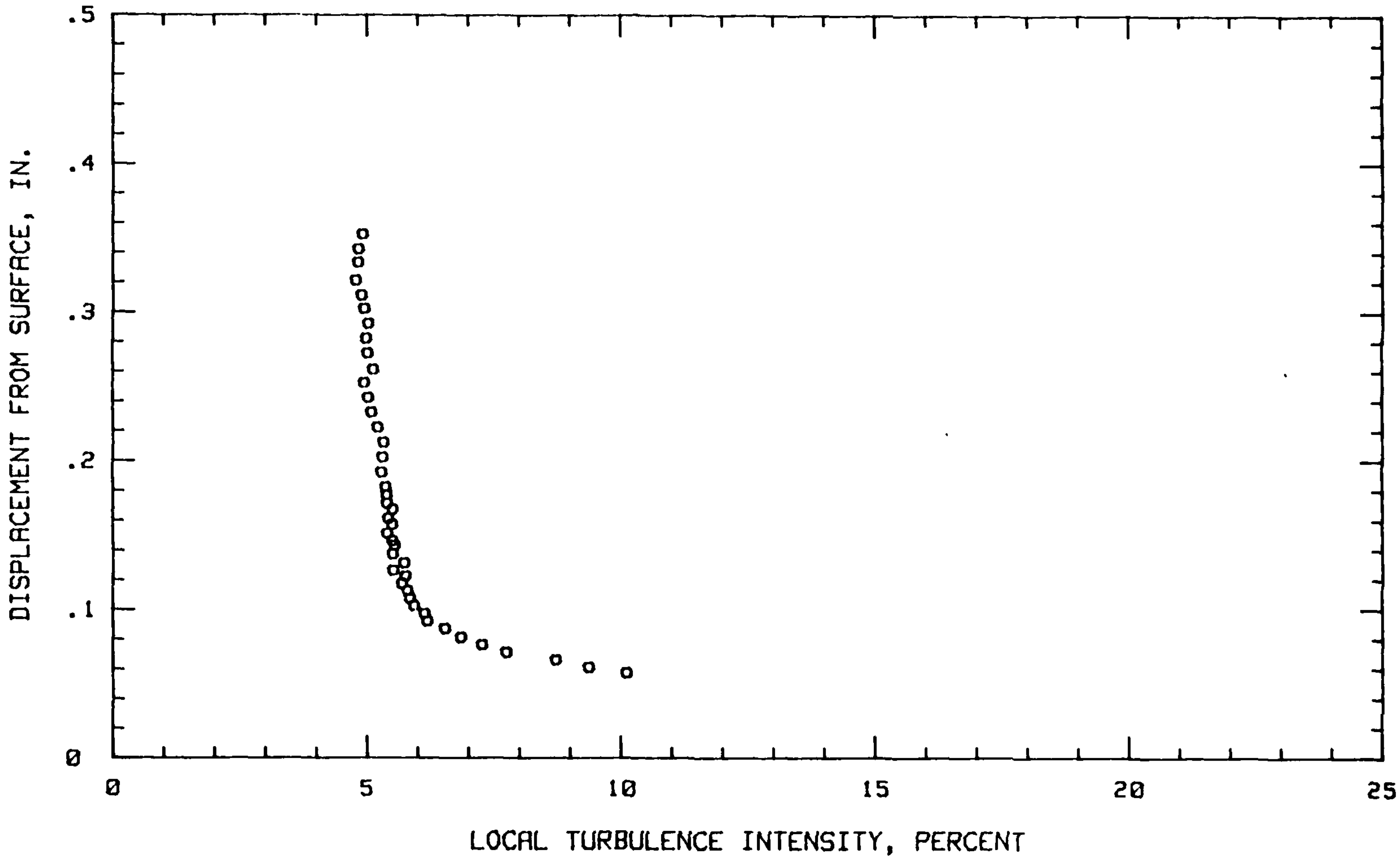

Fig. 196. Boundary Layer Turbulence Intensity Profile, i = +3 Deg, 29.68 % Chord

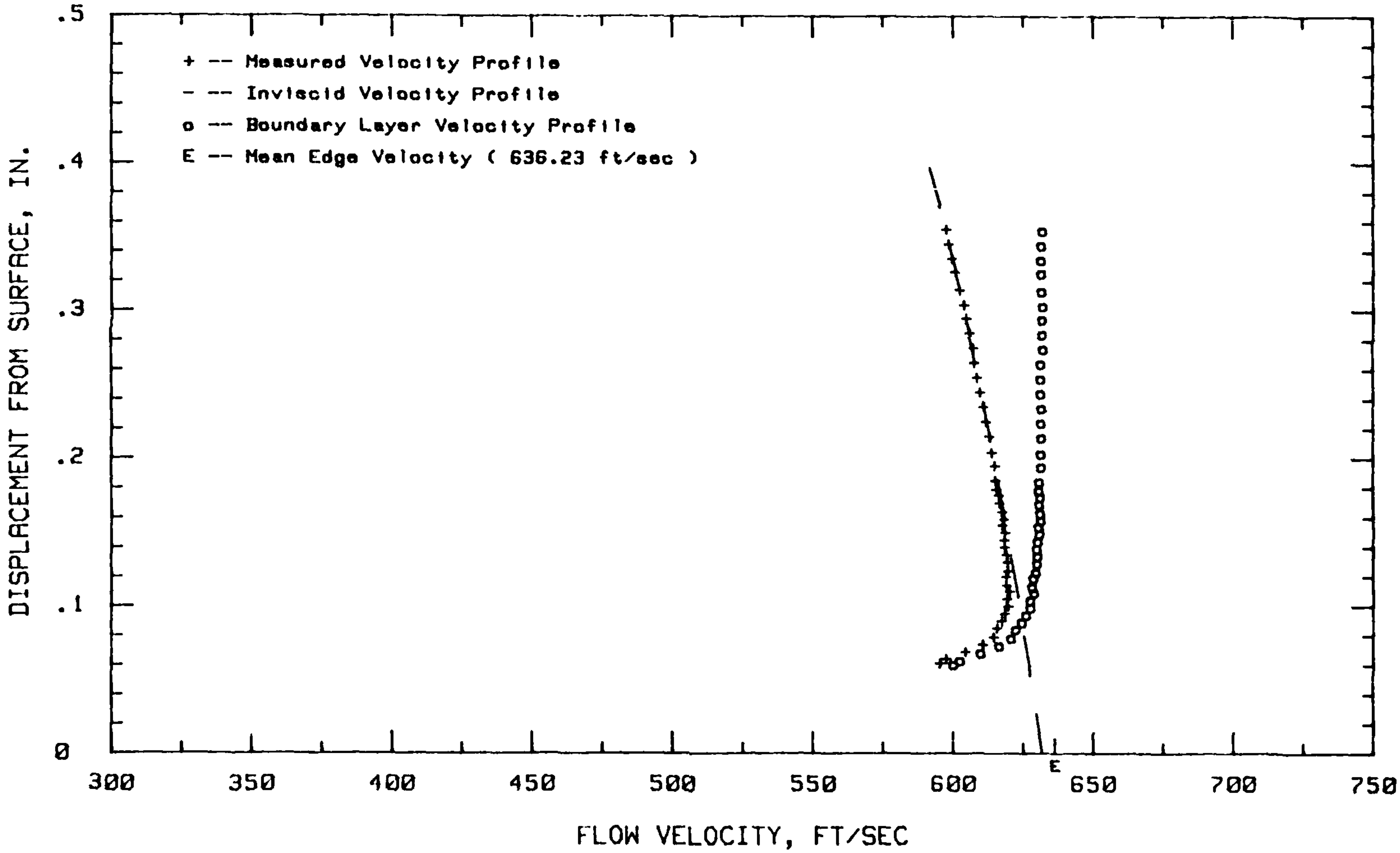

Fig. 197. Boundary Layer Velocity Profiles, i = +3 Deg, 34.37 % Chord

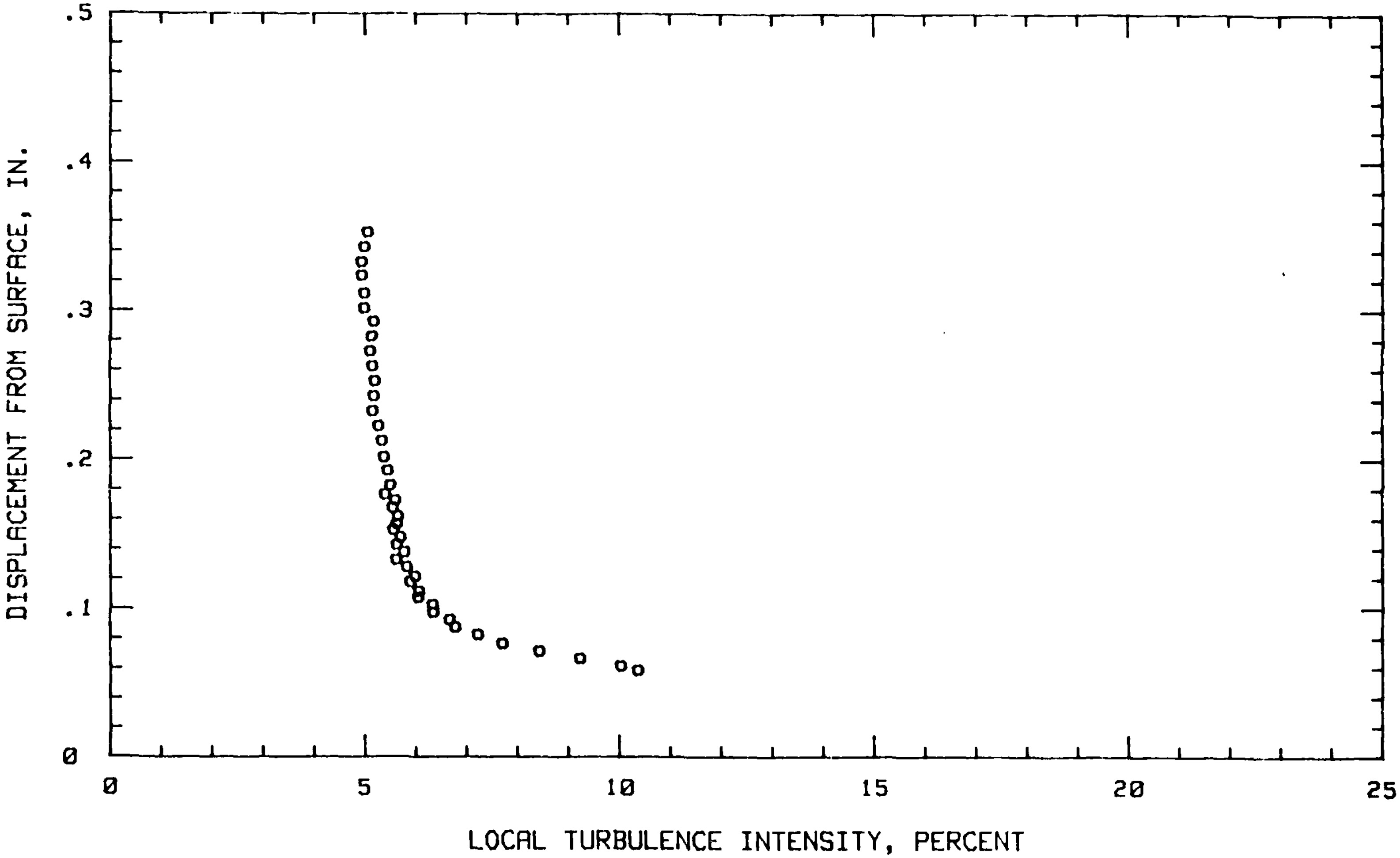

Fig. 198. Boundary Layer Turbulence Intensity Profile, i = +3 Deg, 34.37 % Chord

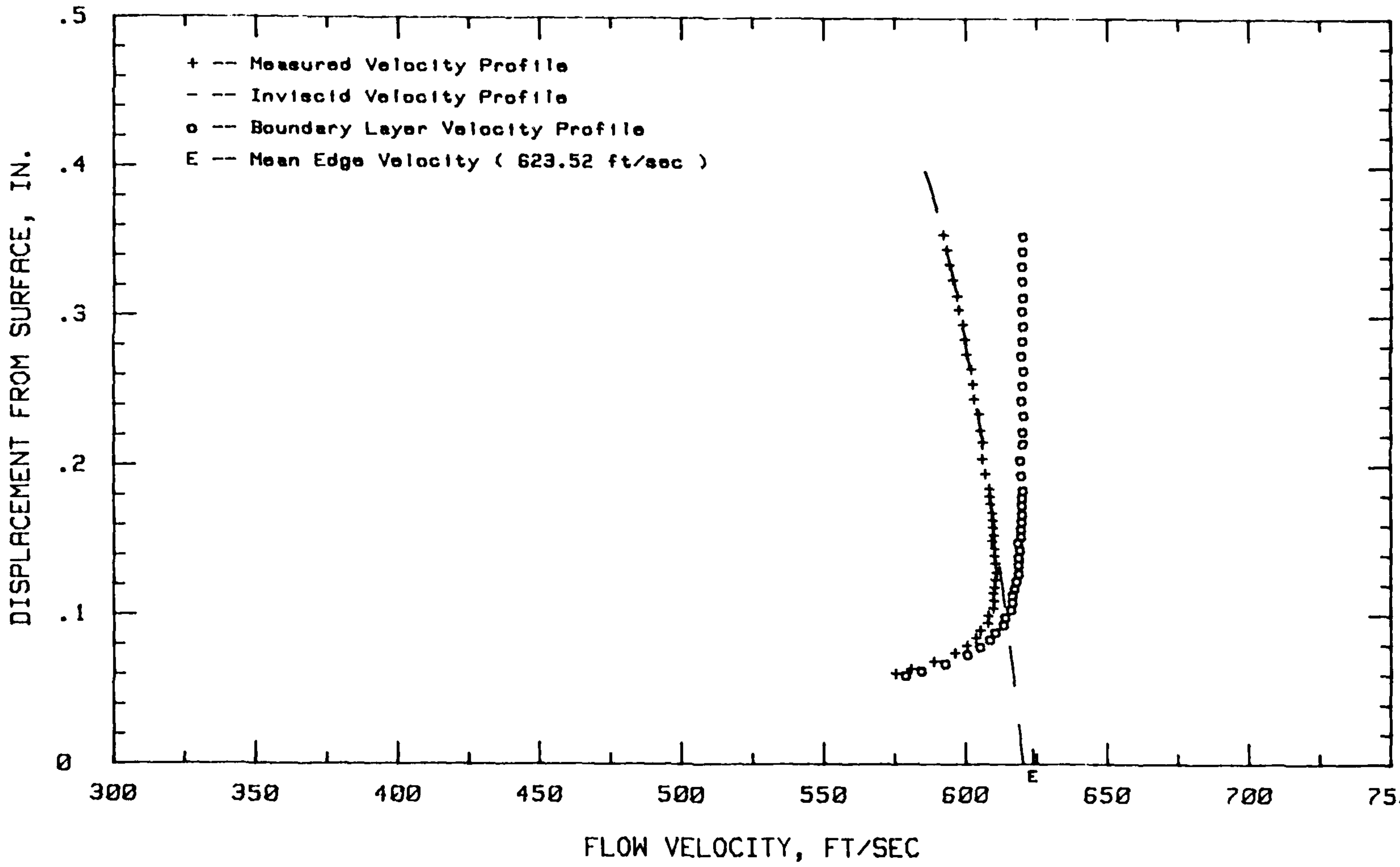

Fig. 199. Boundary Layer Velocity Profiles, i = +3 Deg, 40.62 % Chord

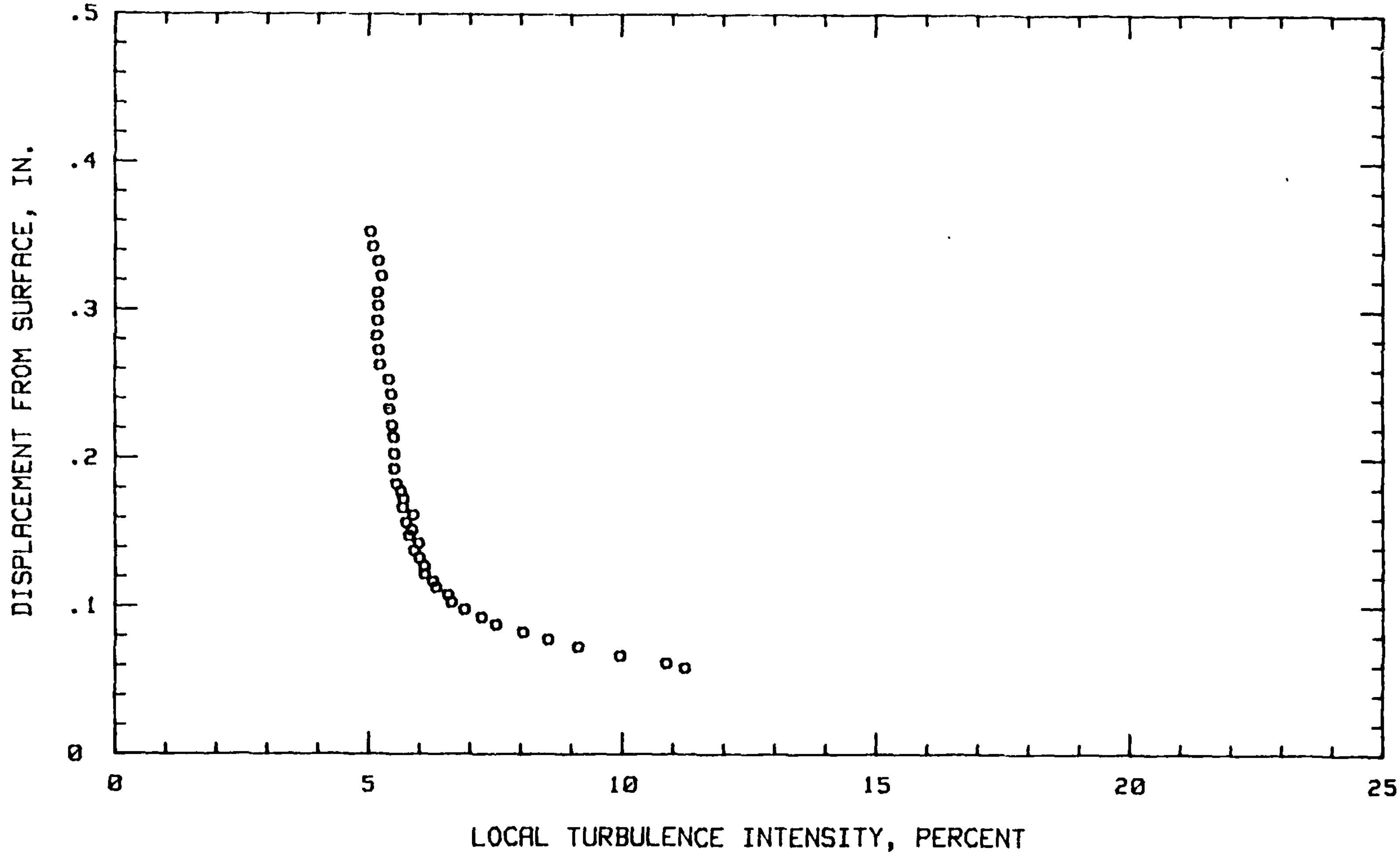

Fig. 200. Boundary Layer Turbulence Intensity Profile, i = +3 Deg, 40.62 % Chord

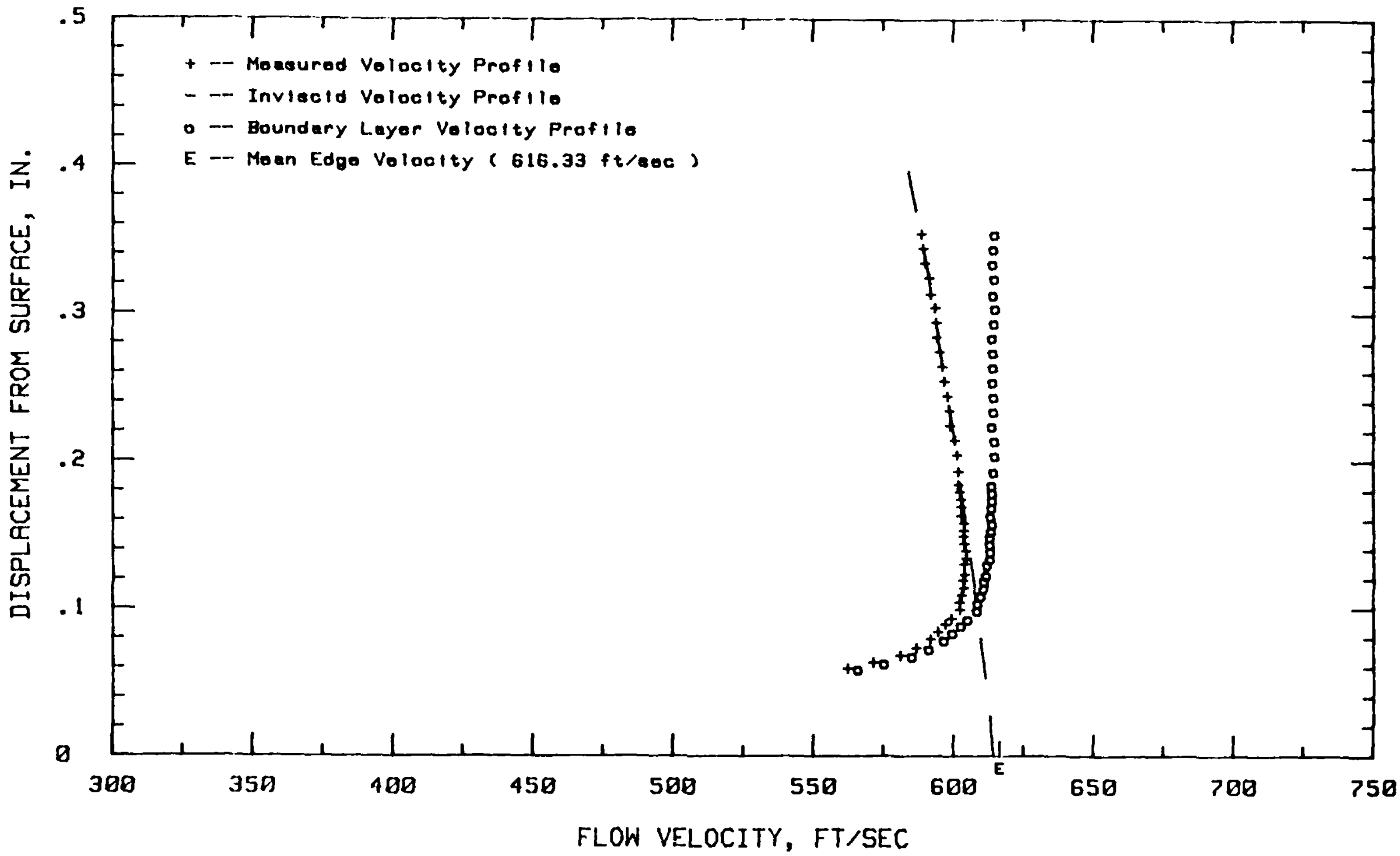

Fig. 201. Boundary Layer Velocity Profiles, i = +3 Deg, 45.31 % Chord

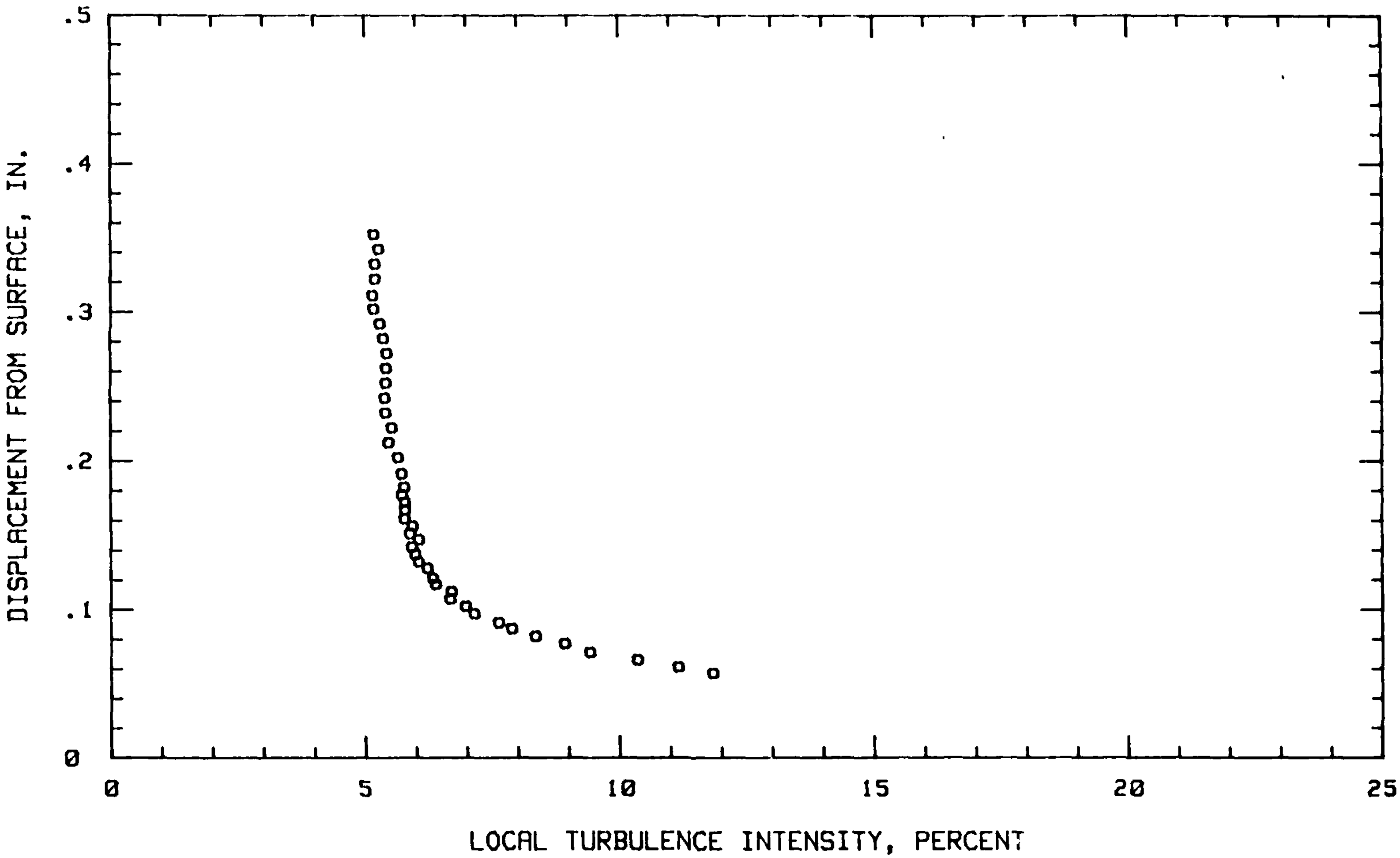

Fig. 202. Boundary Layer Turbulence Intensity Profile, i = +3 Deg, 45.31 % Chord

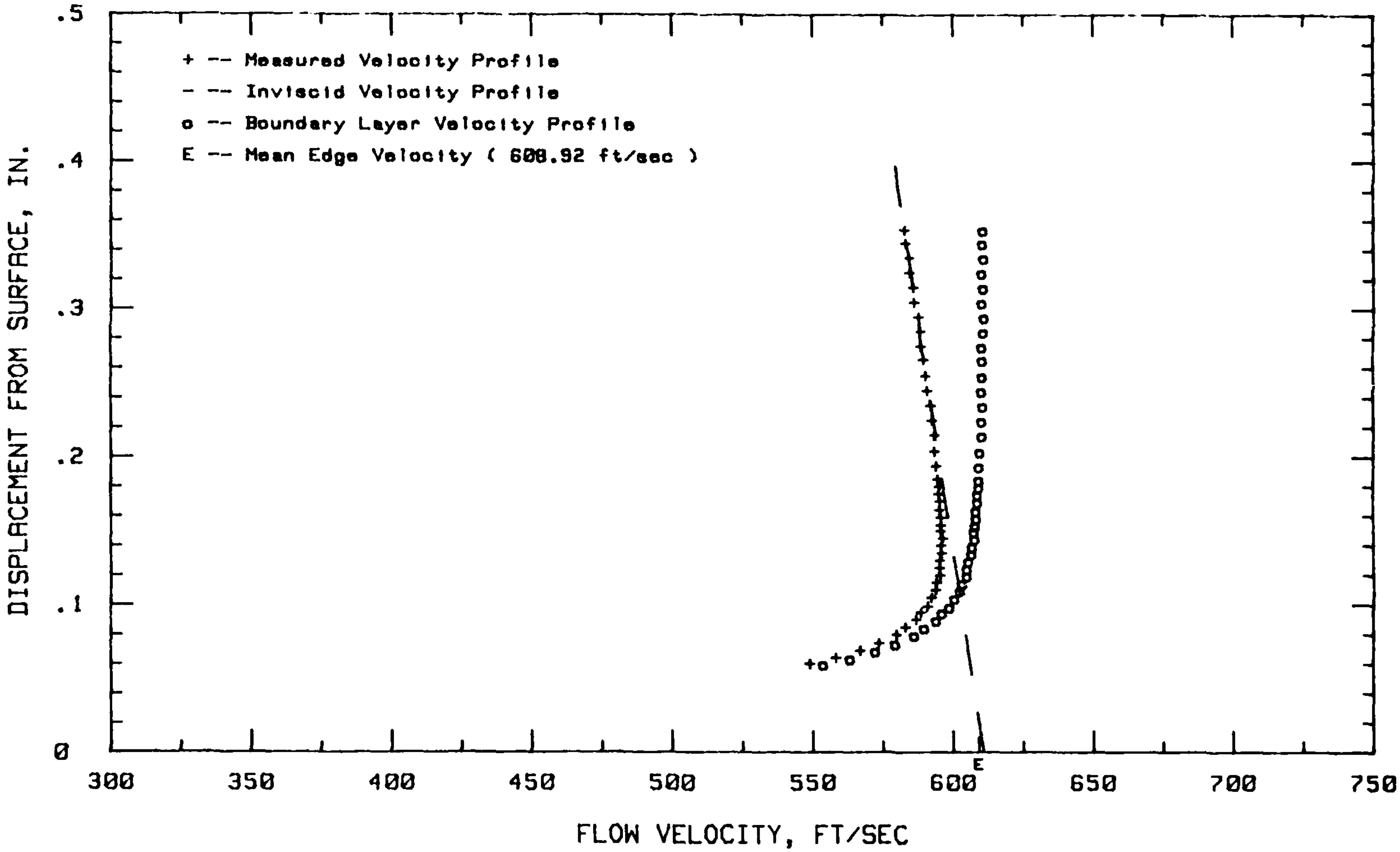

Fig. 203. Boundary Layer Velocity Profiles, ɩ = +3 Deg, 50 % Chord

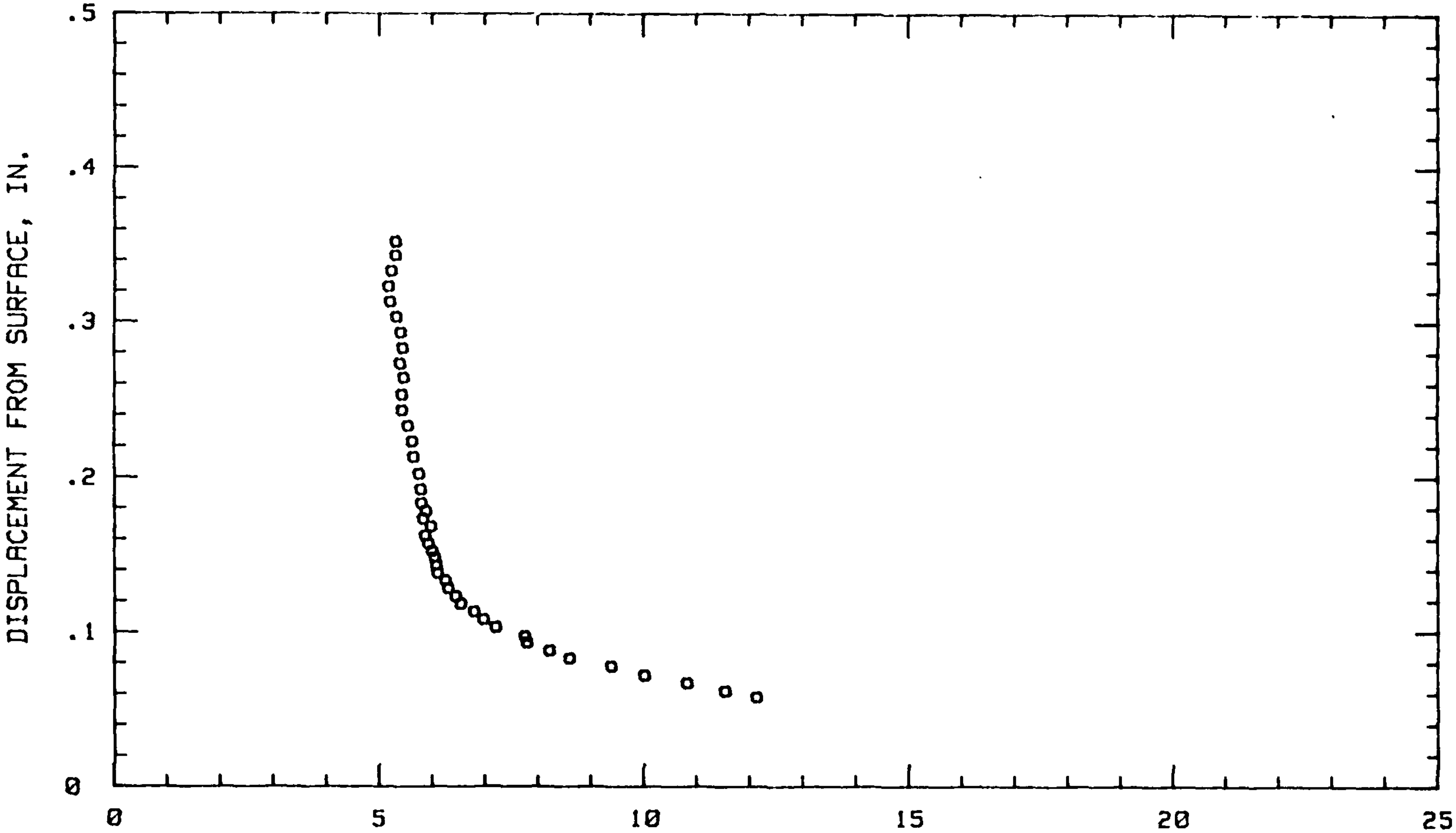

Fig. 204. Boundary Layer Turbulence Intensity Profile, i = +3 Deg, 50 % Chord

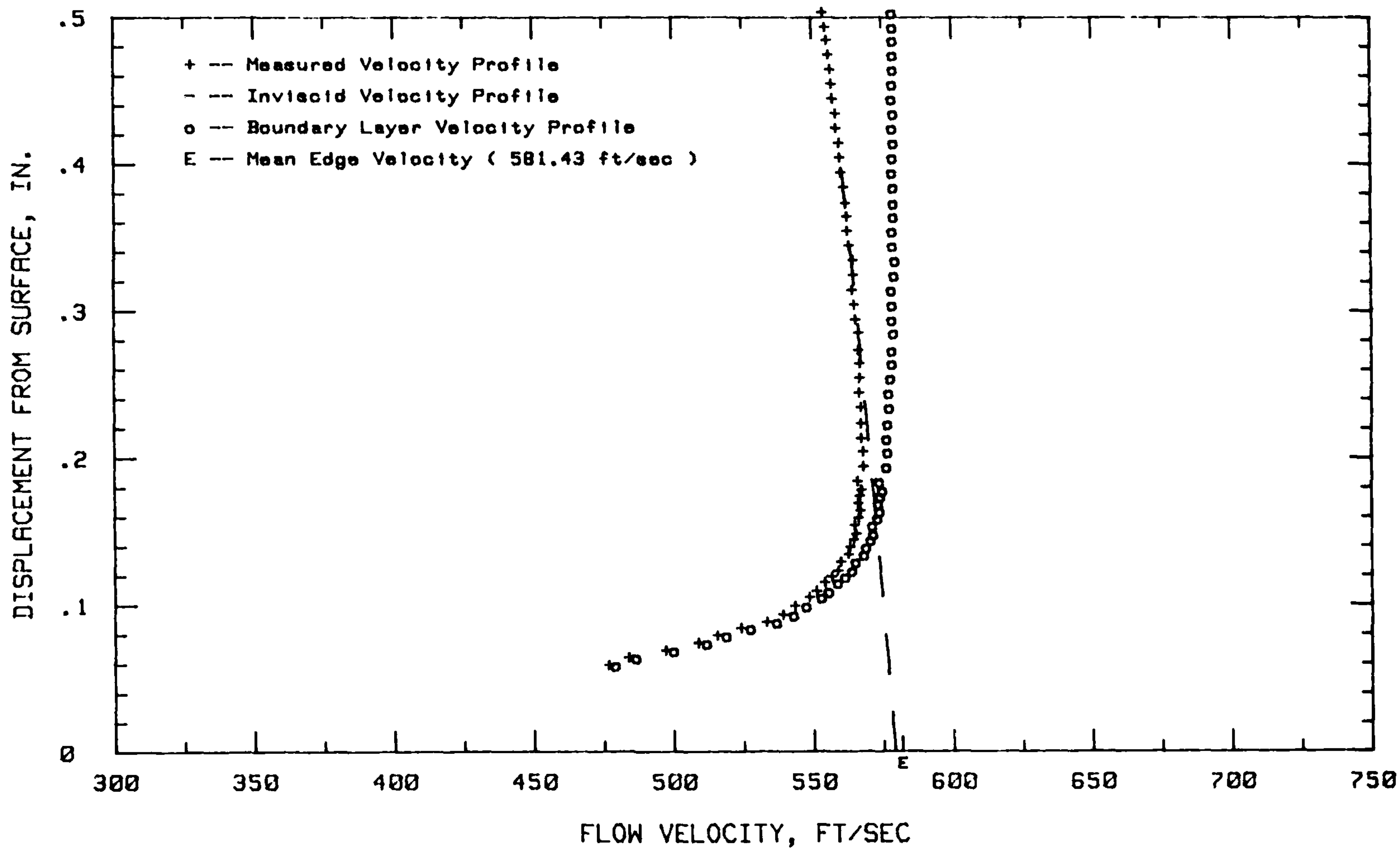

Fig. 205. Boundary Layer Velocity Profiles, i = +3 Deg, 65.62 % Chord

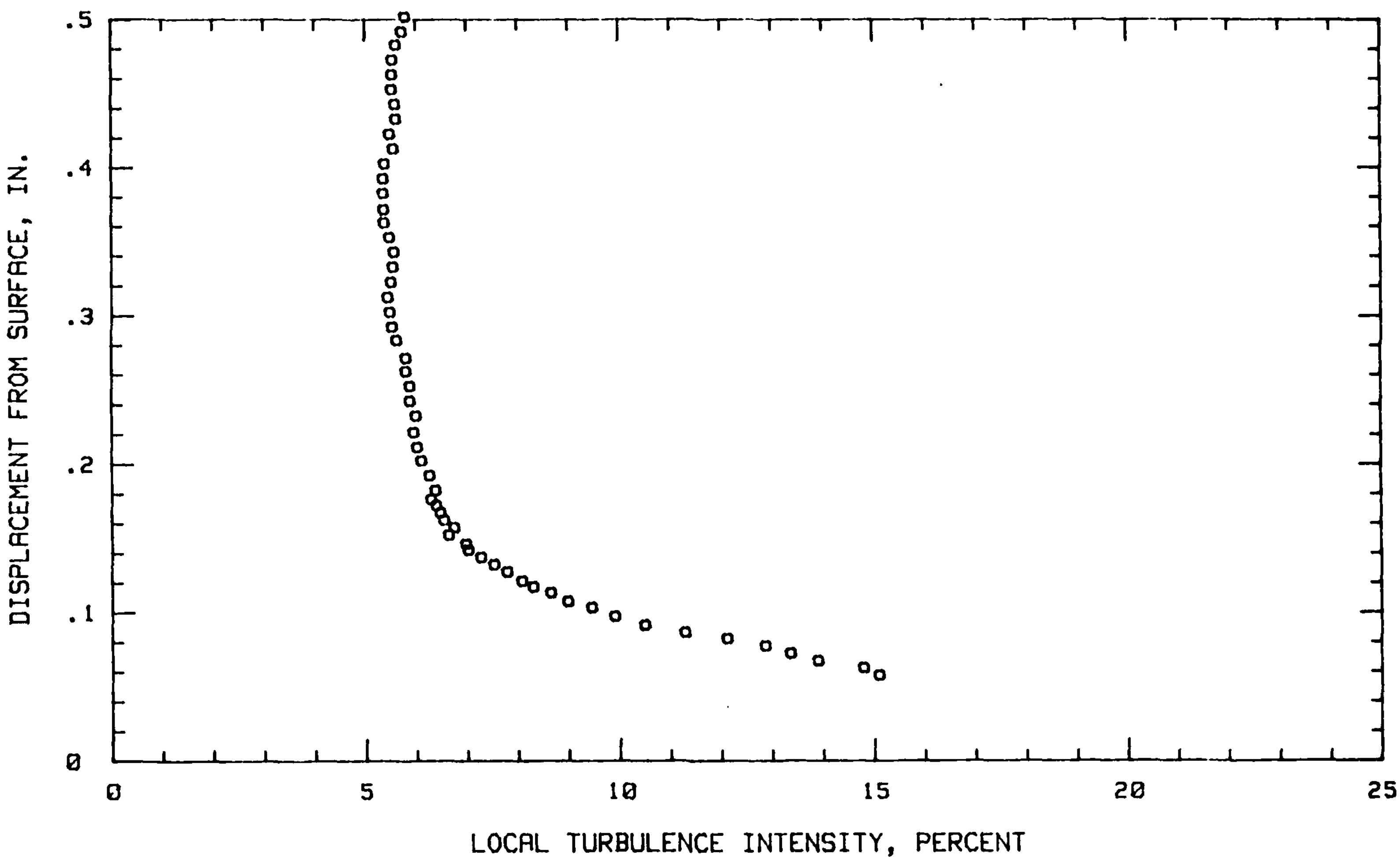

Fig. 206. Boundary Layer Turbulence Intensity Profile, i = +3 Deg, 65.62 % Chord

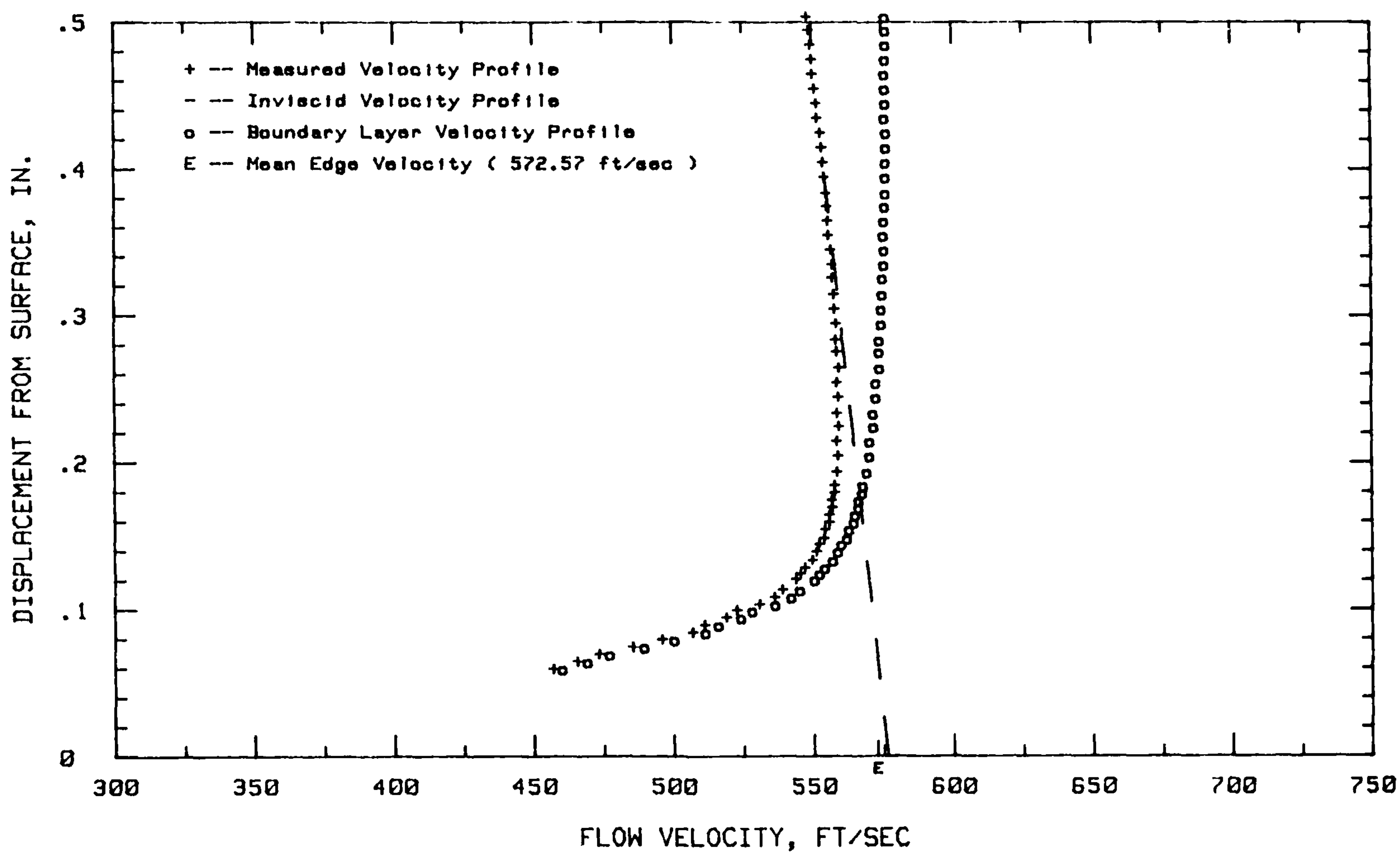

Fig. 207. Boundary Layer Velocity Profiles, i = +3 Deg, 70.31 % Chord

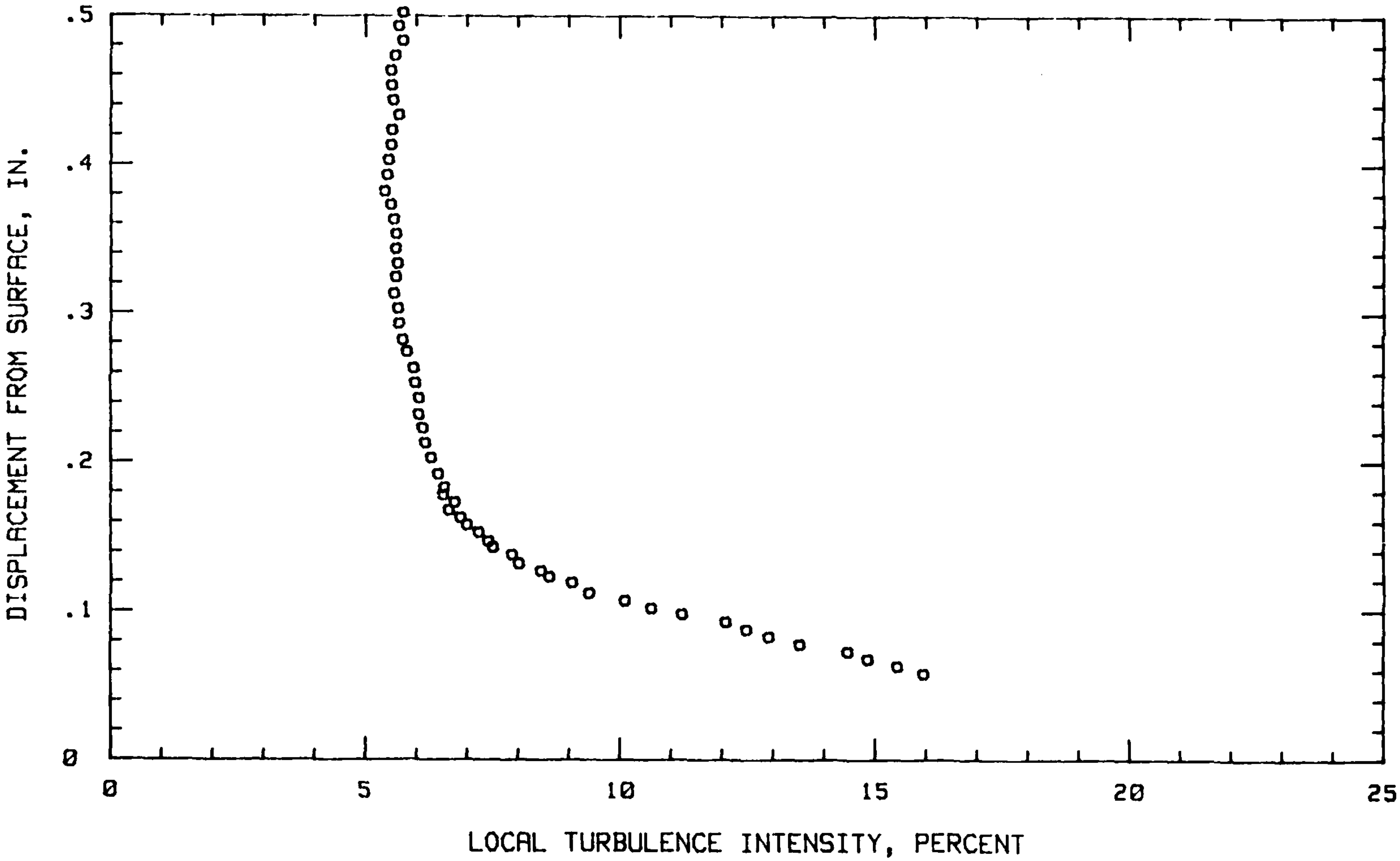

Fig. 208. Boundary Layer Turbulence Intensity Profile, i = +3 Deg, 70.31 % Chord

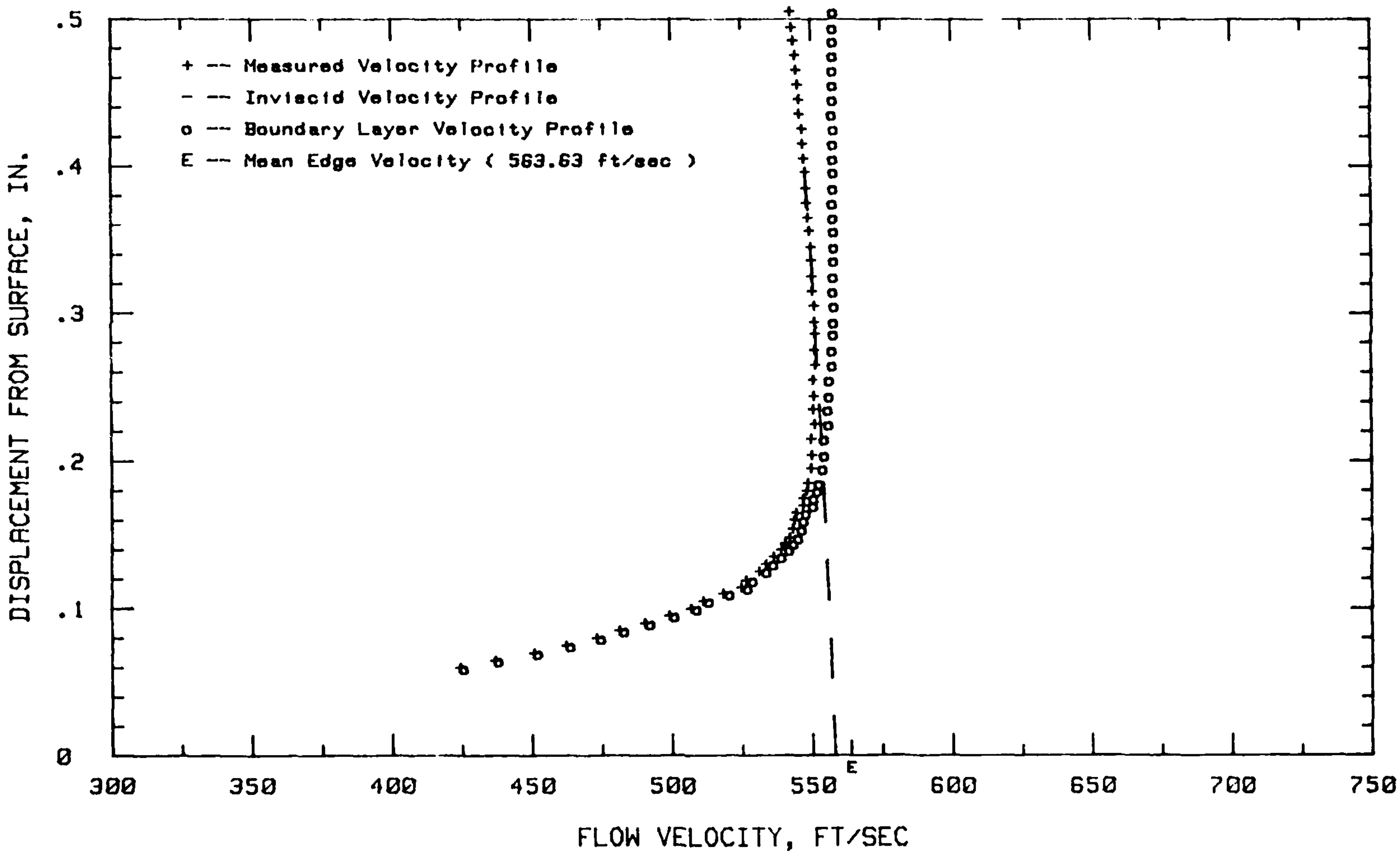

Fig. 209. Boundary Layer Velocity Profiles, i = +3 Deg, 75 % Chord

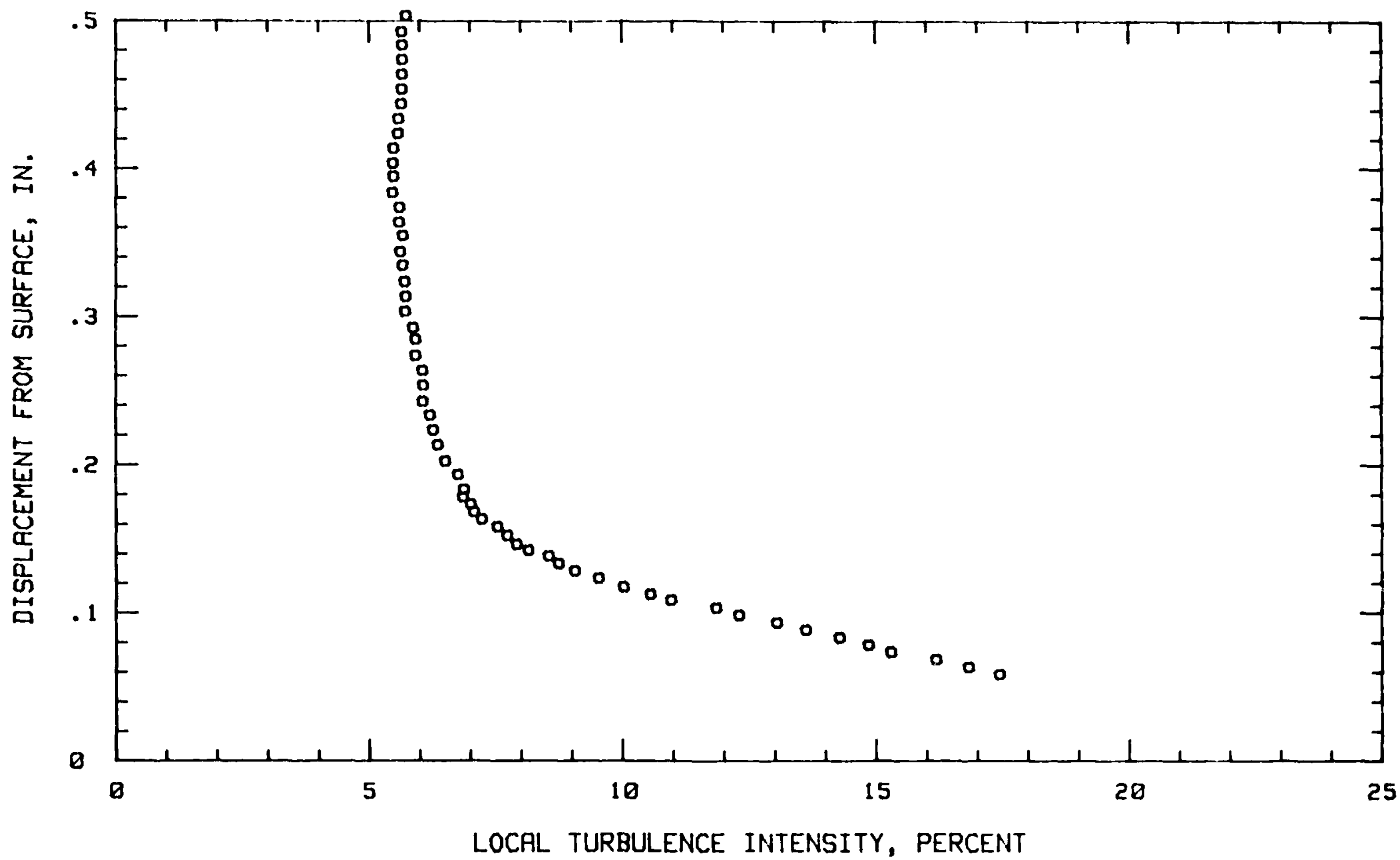

Fig. 210. Boundary Layer Turbulence Intensity Profile, i = +3 Deg, 75 % Chord

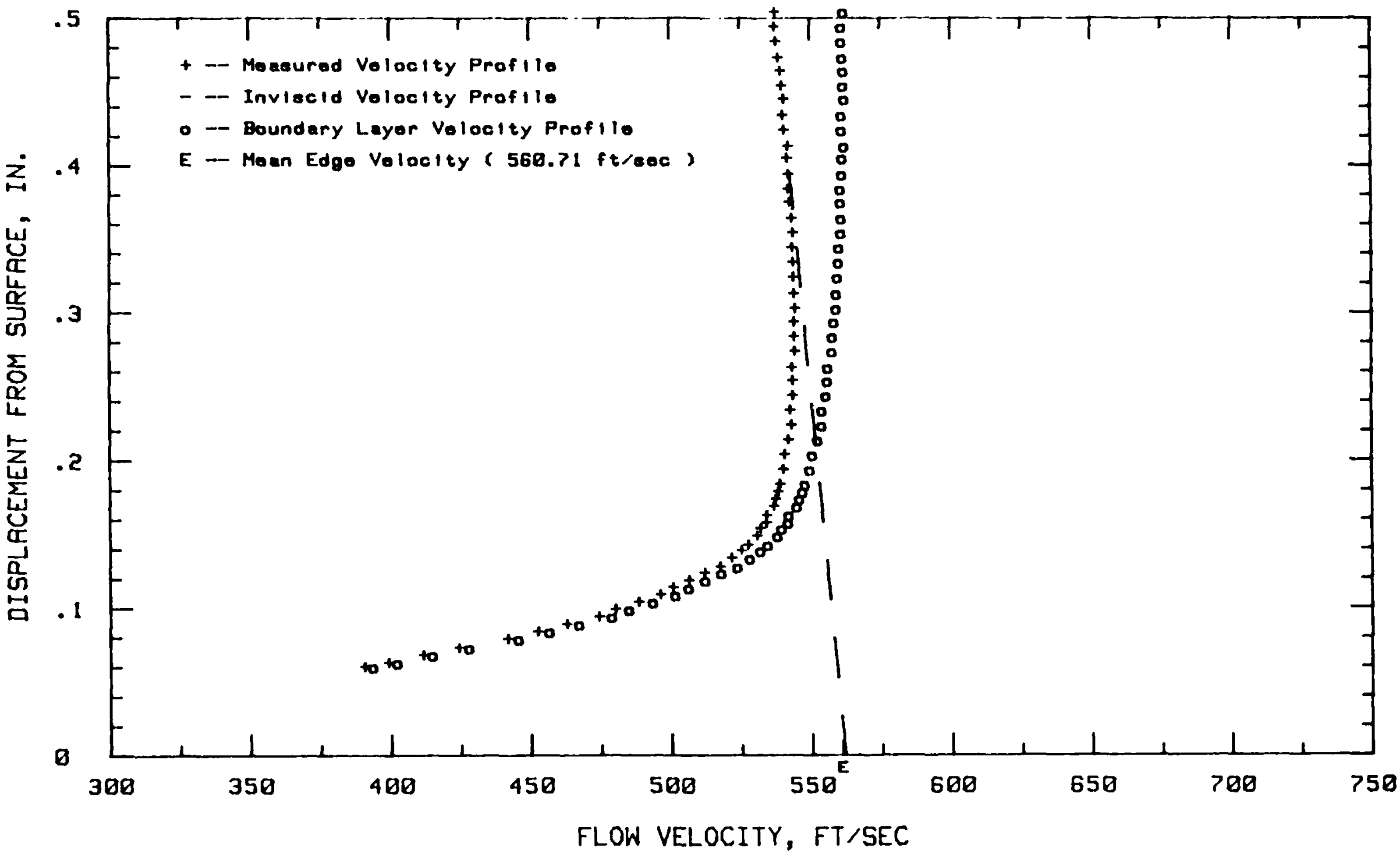

Fig. 211. Boundary Layer Velocity Profiles, i = +3 Deg, 79.68 % Chord

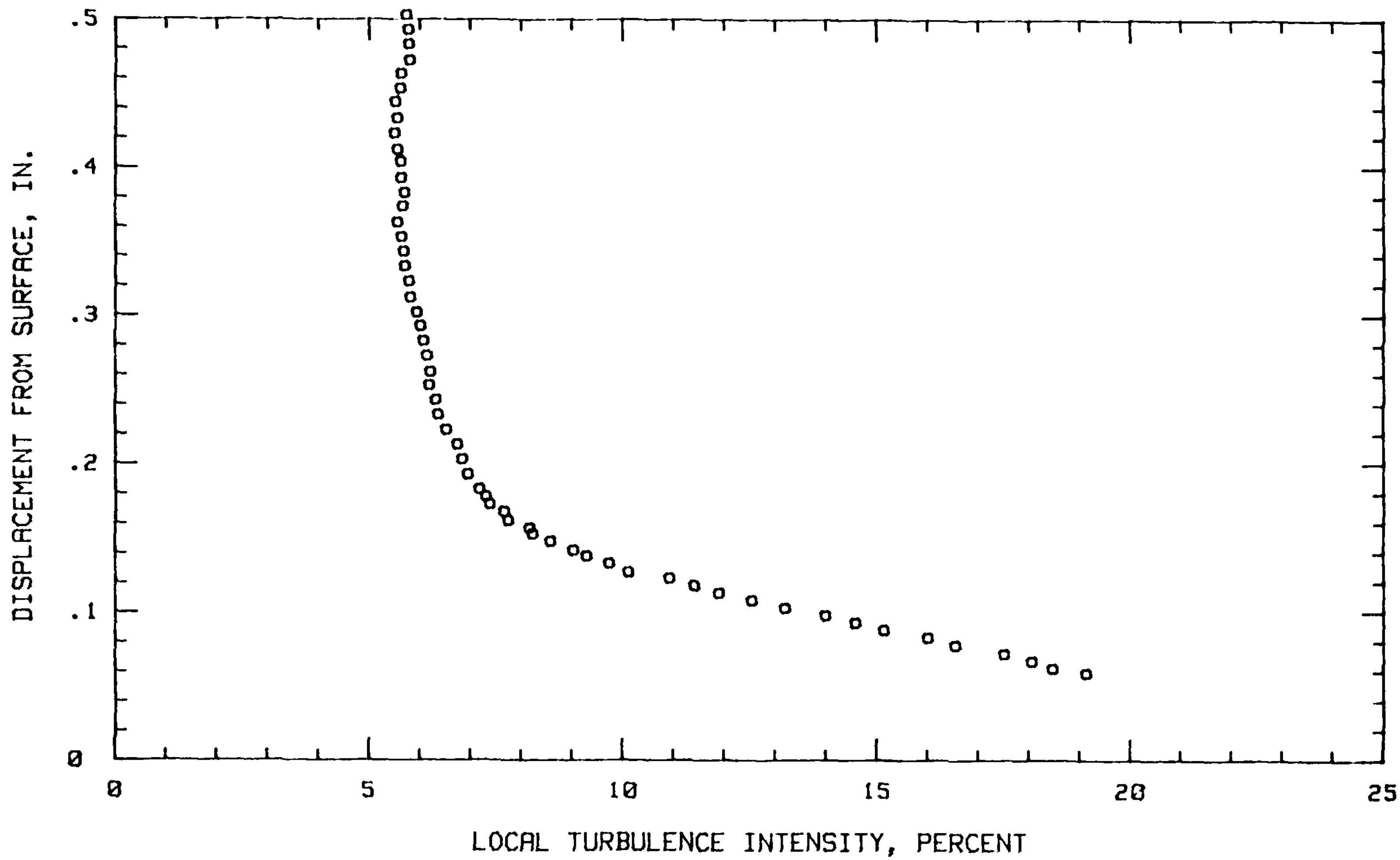

Fig. 212. Boundary Layer Turbulence Intensity Profile, i = +3 Deg, 79.68 % Chord

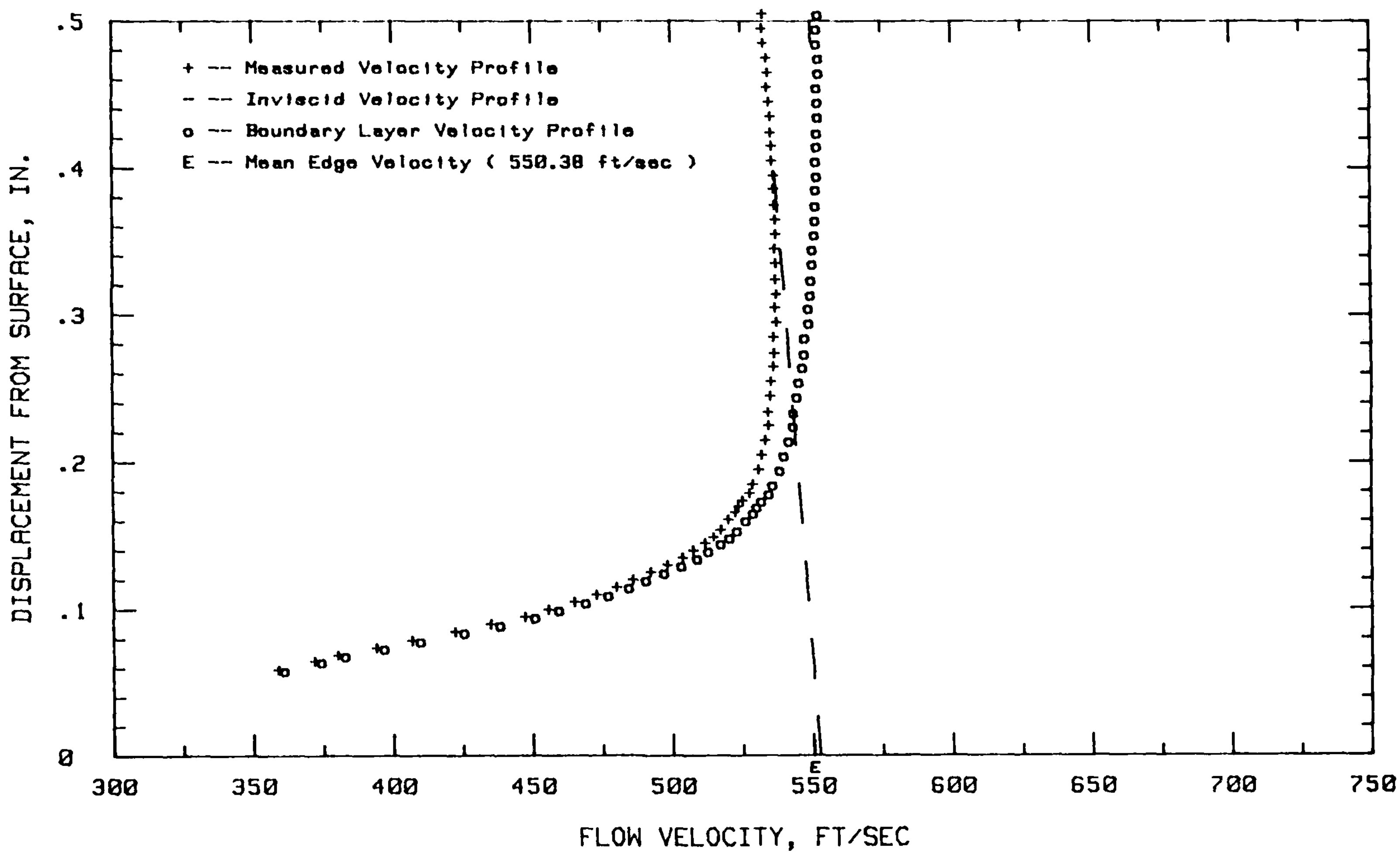

Fig. 213. Boundary Layer Velocity Profiles, i = +3 Deg, 84.37 % Chord

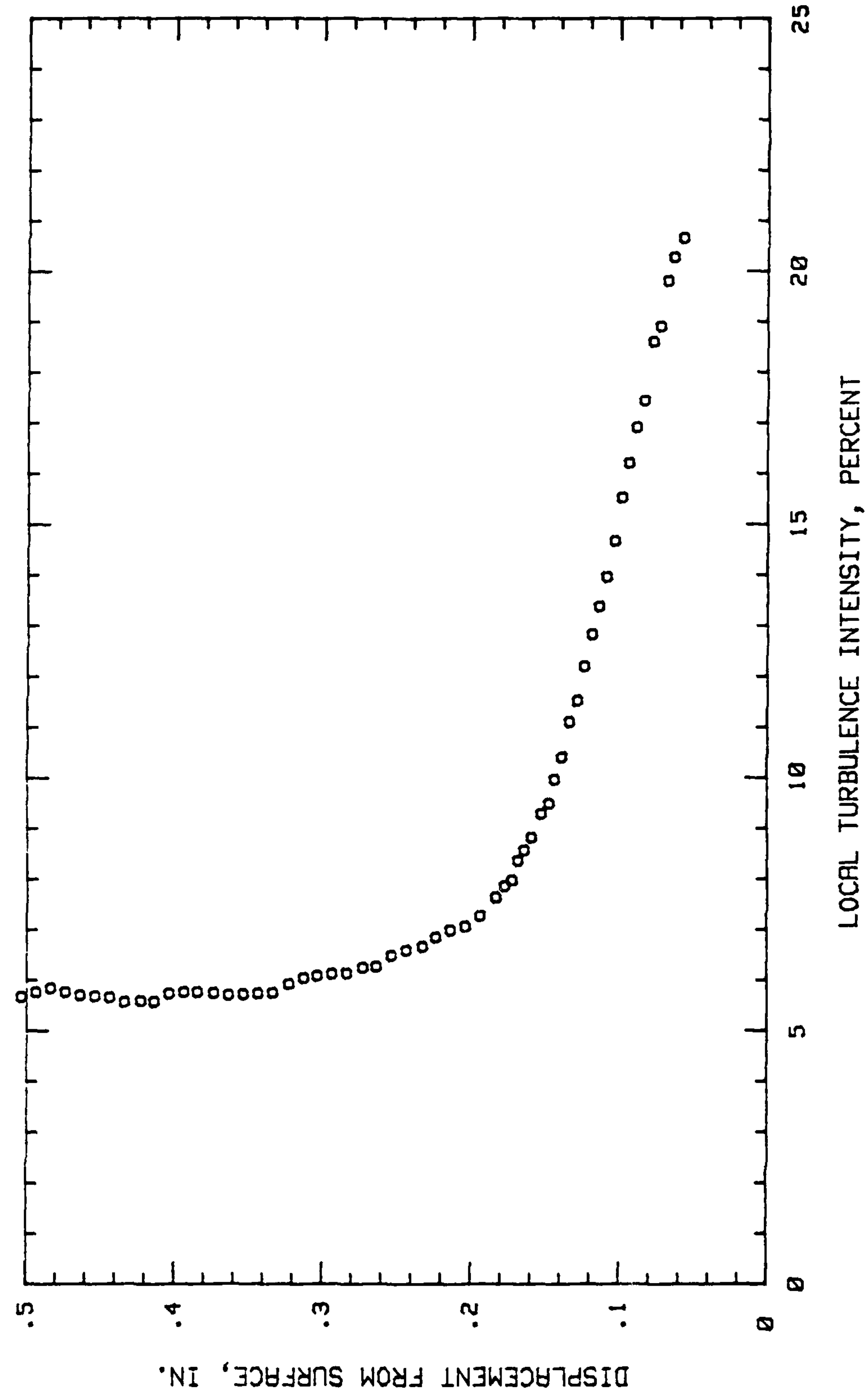

Fig. 214. Boundary Layer Turbulence Intensity Profile, i = +3 Deg, 84.37 % Chord

Bibliography

1. Absar, Salmon. Effect of Free stream Turbulence on a Two-Dimensional Compressor Cascade, with Different Surface Roughness, at High Reynolds Number. MS Thesis GAE/AA/88M-1. School of Engineering, Air Force Institute of Technology (AU), Wright Patterson AFB OH, March 1988.

2. Allison, Dennis M. Design and Evaluation of a Cascade Test Facility. MS Thesis GAE/AA/81D-2. School of Engineering, Air Force Institute of Technology (AU), Wright Patterson AFB OH, June 1982.

3. Bergsten, Daniel E. and Sanford Fleeter. The Effect of Incidence Angle on the Overall Three-Dimensional Aerodynamic Performance of a Classic Annular Airfoil Cascade, NASA CR-168127: Report ME-TSPC-TR-83-02, July 1983.

4. Bradshaw, P. An Introduction to Turbulence and its Measurement. Oxford: Pergamon Press, 1971.

5. Briggs, William B. Effect of Mach Number on the Flow and Application of Compressibility Corrections in a Two-Dimensional Subsonic-Transonic Compressor Cascade Having Varied Porous-Wall Suction at the Blade Tips. NACA TN-2649. Washington: National Advisory Committee for Aeronautics, 1952.

6. Cebeci, Tuncer. G.J. Mosinskis, and A. M. O. Smith. "Calculation of Separation Points in Incompressible Turbulent Flows," Journal of Aircraft, 9: 618-624 (September 1972).

7. Cohen, H. G.F.C. Rogers, and H.I.H. Saravanamuttoo. Gas Turbine Theory (Third Edition). New York: John Wiley & Sons, 1987.

8. Deutsch, Steven. and William C. Zierke. The Boundary Layer on Compressor Cascade Blades. NASA-CR-173514: Semi-Annual Status Report, 1 December 1983 - 1 June 1984.

9. Deutsch, Steven. and William C. Zierke. The Boundary Layer on Compressor Cascade Blades. NASA-CR-174369: Semi-Annual Status Report, 1 June 1984 - 1 December 1984.

10. Erwin, John R. and James C. Emery. Effect of Tunnel Configuration and Testing Technique on Cascade Performance. NACA Report 1016, Washington: National Advisory Committee for Aeronautics, 1951.

11. Genovese, David T. Roughness Effects on Compressor Outlet Guide Vanes at High Reynolds Number and High Turning Angle. MS Thesis GAE/AA/82D-11. School of Engineering, Air Force Institute of Technology (AU), Wright Patterson AFB OH, November 1982.

12. Gostelow, J.P. Cascade Aerodynamics. New York: Pergamon Press, 1984.

13. Herrig, L. Joseph, James C. Emery, and John R. Erwin. Systematic Two-Dimensional Cascade Tests of NACA 65-Series Compressor Blades at Low Speeds. NACA TN-3916. Washington: National Advisory Committee for Aeronautics, 1957.

14. Hewlett-Packard. 3052A Automatic Data Acquisition System Operating Instructions. Volume 1A, undated.

15. Horlock, J.H. Axial Flow Compressors Fluid Mechanics and Thermodynamics. Malabar: Robert E. Krieger, 1985.

16. Kreith, Frank. Principles of Heat Transfer (Second Edition). Scranton: International Textbook Company, 1965.

17. Lieblein, Seymour. "Experimental Flow in Two-Dimensional Cascades," Aerodynamic Design of Axial Flow Compressors (Revised), edited by Irving A. Johnsen and Robert O. Bullock. NASA SP-36. Washington: National Aeronautics and Space Administration, 1965.

18. Lieblein, Seymour. "Incidence and Deviation-Angle Correlations for Compressor Cascades," ASME Journal of Basic Engineering, 82: 575-587 (September 1960).

19. Lieblein, Seymour and William H. Roudebush. Low-Speed Wake Characteristics of Two-Dimensional Cascade and Isolated Airfoil Sections. NACA TN-3771. Washington: National Advisory Committee for Aeronautics, 1956.

20. Lieblein, Seymour and William H. Roudebush. Theoretical Loss Relations for Low-Speed Two-Dimensional-Cascade Flow. NACA TN-3662. Washington: National Advisory Committee for Aeronautics, 1956.

21. Moe, Gary P. Influence of Surface Roughness on Compressor Blades at High Reynolds Number in a Two-Dimensional Cascade. MS Thesis GAE/AA/84D-19. School of Engineering, Air Force Institute of Technology (AU), Wright Patterson AFB OH, December 1984.

22. Oates, Gordon C. Aerothermodynamics of Gas Turbine and Rocket Propulsion. New York: American Institute of Aeronautics and Astronautics, 1984.

23. Poulin, J. Réme. Surface Roughness: Its Effects on the Performance of a Two-Dimensional Compressor Cascade. MS Thesis GAE/AA/86D-13. School of Engineering, Air Force Institute of Technology (AU), Wright Patterson AFB OH, December 1986.

24. Raj, R. and B. Lakshminarayana. "Characteristics of the Wake Behind a Cascade of Airfoils," Journal of Fluid Mechanics, 61: 707-730 (1973).

25. Roudebush, William H. and Seymour Lieblein. "Viscous Flow in Two-Dimensional Cascades," Aerodynamic Design of Axial Flow Compressors (Revised), edited by Irving A. Johnsen and Robert O. Bullock. NASA SP-36. Washington: National Aeronautics and Space Administration, 1965.

26. Sanger, Nelson L. and Raymond P. Shreeve. Comparison of Calculated and Experimental Cascade Performance for Controlled-Diffusion Compressor Stator Blading. NASA TM-87167, 1986.

27. Schlicting, Hermann. Boundary Layer Theory (Seventh Edition). New York: McGraw Hill, 1979.

28. Schlicting, H. and A. Das. "Recent Research on Cascade-Flow Problems," ASME Journal of Basic Engineering, 88: 221-228 (March 1966)

29. Scholz, Norbert. Aerodynamics of Cascades, AGARD-AG-220. Neuilly sur Seine: Advisory Group for Aerospace Research and Development, 1977.

30. Serovy, G.K. "Axial Flow Compressor Aerodynamics," Aerothermodynamics of Aircraft Engine Components, edited by Gordon C. Oates. New York: American Institute of Aeronautics and Astronautics, 1985.

31. Smith, Ralph J. Circuits, Devices, and Systems (Third Edition). New York: John Wiley & Sons, 1976.

32. Tanis, Frederick J. Roughness Effects on Compressor Blade Performance in Cascade at High Reynolds Number. MS Thesis GAE/AA/83D-23. School of Engineering, Air Force Institute of Technology (AU), Wright Patterson AFB OH, November 1983.

33. TSI. General System Information for 1050 Series Anemometry. St. Paul, Minnesota, undated.

34. TSI. Hot Film and Hot Wire Anemometry. Theory and Application Bulletin TB 5. St. Paul, Minnesota, undated.

35. Vonada, John A. School of Engineering, Air Force Institute of Technology. Personal Notes. Wright Patterson AFB OH, 12 March 1982.

36. Whittle, Sir Frank. "The Birth of the Jet Age in Britain," The Jet Age: Forty Years of Jet Aviation, edited by Walter J. Boyne and Donald S. Lopez. Washington City: Smithsonian Institution Press, 1979.

37. Williams, Larry D. Effects of Surface Roughness on Pressure Distribution and Boundary Layer Over Compressor Blades at High Reynolds Number in a Two-Dimensional Cascade. MS Thesis GAE/AA/85D-17. School of Engineering, Air Force Institute of Technology (AU), Wright Patterson AFB OH, December 1985.

38. Zucrow, Maurice J. and Joe D. Hoffman. Gas Dynamics Volume I. New York: John Wiley & Sons, 1976.

Vita

Captain Edward M. Poniatowski was born on [redacted] He graduated from high school in Daytona Beach, Florida in 1975. He enlisted in the United States Army and served as an Observation/Scout Helicopter Crew Chief, until his selection to attend the United States Military Academy Preparatory School. After graduation he was appointed as a cadet at the United States Military Academy, West Point, New York, from which he received the degree of Bachelor of Science in May 1981. Upon graduation he received a commission in the United States Army Field Artillery. He completed the Field Artillery Officer Basic Course, and was assigned to the 2nd Battalion, 33rd Field Artillery (later redesignated as the 4th Battalion, 5th Field Artillery). He served in this unit both in Neu Ulm, Federal Republic of Germany, and Fort Riley, Kansas, in several positions including Battery Fire Direction Officer, Firing Battery Executive Officer, and Service Battery Commander. He then completed the Field Artillery Officer Advanced Course at Fort Sill, Oklahoma, prior to entering the School of Engineering, Air Force Institute of Technology, in June 1987.

[redacted]

UNCLASSIFIED

SECURITY CLASSIFICATION OF THIS PAGE

REPORT DOCUMENTATION PAGE

Form Approved OMB No. 0704-0188

1a. REPORT SECURITY CLASSIFICATION UNCLASSIFIED	1b. RESTRICTIVE MARKINGS
2a. SECURITY CLASSIFICATION AUTHORITY	3. DISTRIBUTION/AVAILABILITY OF REPORT Approved for public release; distribution unlimited
2b. DECLASSIFICATION/DOWNGRADING SCHEDULE	
4. PERFORMING ORGANIZATION REPORT NUMBER(S) AFIT/GAE/AA/88D-31	5. MONITORING ORGANIZATION REPORT NUMBER(S)
6a. NAME OF PERFORMING ORGANIZATION School of Engineering	6b. OFFICE SYMBOL *(If applicable)* AFIT/ENY
7a. NAME OF MONITORING ORGANIZATION	
6c. ADDRESS *(City, State, and ZIP Code)* Air Force Institute of Technology Wright-Patterson AFB, Ohio 45433-6583	7b. ADDRESS *(City, State, and ZIP Code)*
8a. NAME OF FUNDING/SPONSORING ORGANIZATION	8b. OFFICE SYMBOL *(If applicable)*
9. PROCUREMENT INSTRUMENT IDENTIFICATION NUMBER	
8c. ADDRESS *(City, State, and ZIP Code)*	10. SOURCE OF FUNDING NUMBERS

PROGRAM ELEMENT NO.	PROJECT NO.	TASK NO.	WORK UNIT ACCESSION NO.

11. TITLE *(Include Security Classification)*
See Block 19

12. PERSONAL AUTHOR(S)
Edward M. Poniatowski, B.S., Captain, United States Army

13a. TYPE OF REPORT	13b. TIME COVERED	14. DATE OF REPORT *(Year, Month, Day)*	15. PAGE COUNT
MS Thesis	FROM ______ TO ______	1988 December	322

16. SUPPLEMENTARY NOTATION

17. COSATI CODES		
FIELD	GROUP	SUB-GROUP
21	05	

18. SUBJECT TERMS *(Continue on reverse if necessary and identify by block number)*
Cascade Testing, Incidence Angle, Compressor Blade Geometry, Pressure Distribution, Turbulence, Boundary Layer

19. ABSTRACT *(Continue on reverse if necessary and identify by block number)*

Title: The Effects of Incidence Angle and Free Stream Turbulence on the Performance of a Variable Geometry Two-Dimensional Compressor Cascade at High Reynolds Numbers (U)

Thesis Advisor: Dr. William C. Elrod
Professor of Aerospace Engineering

Abstract: See other side

10 Jun 89

20. DISTRIBUTION/AVAILABILITY OF ABSTRACT ☒ UNCLASSIFIED/UNLIMITED ☐ SAME AS RPT. ☐ DTIC USERS	21. ABSTRACT SECURITY CLASSIFICATION UNCLASSIFIED

22a. NAME OF RESPONSIBLE INDIVIDUAL	22b. TELEPHONE *(Include Area Code)*	22c. OFFICE SYMBOL
Dr. William C. Elrod	(513) 255-3517	AFIT/ENY

DD Form 1473, JUN 86 *Previous editions are obsolete.* SECURITY CLASSIFICATION OF THIS PAGE

UNCLASSIFIED

UNCLASSIFIED

The present study investigates the effects of incidence angle and free stream turbulence on the performance of a variable geometry, two-dimensional compressor cascade. A seven-blade cascade of NACA 65-A5Ø6 airfoils with two inch chord, aspect ratio of one, and solidity of 1.5 was used. This cascade used porous side wall suction to establish two-dimensional flow conditions. Flow Unit Reynolds numbers exceeding 2.5 million per foot, and average free stream turbulence levels of one and seven percent were used. Cascade geometry was varied in a manner similar to that used in current variable stator designs: maintaining axial direction and blade spacing constant, while varying incidence angle, stagger angle, and angle of attack. Incidence angles of -3, Ø, and +3 degrees were investigated.

Total pressure loss coefficient decreases through the cascade and may increase in the wake as incidence angle or free stream turbulence increase. The change in loss coefficient with increasing incidence was determined to be insignificant when compared with the change as a result of increased free stream turbulence. Blade suction surface pressure coefficients decrease sharply along the first thirty percent chord as incidence increases. Additionally, the suction surface pressure coefficients show a uniform increase across the blade center span with additional free stream turbulence. Increases in incidence and free stream turbulence result in thicker boundary layers and suggest both earlier transition and intermittent separation on the forward half of the blade. Evidence also suggests that the location of the minimum loss incidence angle may change with additional free stream turbulence.

UNCLASSIFIED